IntechOpen

Nanostructured Solar Cells

Edited by Narottam Das

WEB OF SCIENCE™

NANOSTRUCTURED SOLAR CELLS

Edited by **Narottam Das**

Nanostructured Solar Cells
http://dx.doi.org/10.5772/62516
Edited by Narottam Das

Contributors

Yuguo Tao, Ajeet Rohatgi, Takeo Oku, Masahito Zushi, Kohei Suzuki, Atsushi Suzuki, Taisuke Matsumoto, Yuya Ohishi, Yalin Lu, Zhengping Fu, Qiuping Huang, Xiang Hu, Dazheng Chen, Chunfu Zhang, Carlito Jr. Ponseca, Kaibo Zheng, Ruby Srivastava, Mustafa Can, Serafettin Demic, Ahmet Nuri Ozcivan, Cebrail Özbek, Merve Karakaya, Yang Tang, Lung-Chien Chen, Abdul Kariem Arof, Miroslav Mikolasek, António Vicente, Rodrigo Martins, Narottam Das

Notice

First published in Croatia, 2017 by INTECH d.o.o.
eBook (PDF) Published by IN TECH d.o.o.
Place and year of publication of eBook (PDF): Rijeka, 2019.
IntechOpen is the global imprint of IN TECH d.o.o.
Printed in Croatia

Legal deposit, Croatia: National and University Library in Zagreb

Additional hard and PDF copies can be obtained from orders@intechopen.com

Nanostructured Solar Cells
Edited by Narottam Das
p. cm.
Print ISBN 978-953-51-2935-6
Online ISBN 978-953-51-2936-3
eBook (PDF) ISBN 978-953-51-4110-5

Meet the editor

Narottam Das received his BSc and MSc degrees in electrical and electronic engineering from the Chittagong University of Engineering and Technology, Chittagong, and Bangladesh University of Engineering and Technology, Dhaka, Bangladesh, respectively. He received his PhD degree in systems and information engineering from Yamagata University, Japan, in 2000. Currently, he is a lecturer in Electrical Engineering, School of Mechanical and Electrical Engineering, University of Southern Queensland, Toowoomba, Queensland, Australia, and an adjunct Senior Research Fellow in the Department of Electrical and Computer Engineering, Curtin University, Perth, Australia. During 2014, he was an associate professor in the Department of Electrical and Computer Engineering, Curtin University Sarawak, Malaysia. Earlier, he worked at Curtin University, Edith Cowan University, Perth and Monash University, Melbourne, Australia; NEC Yamagata Ltd., Yamagata, Japan; and Bangladesh Export Import Company, Dhaka, Bangladesh. He is the author/co-author of eight book chapters, more than 135 peer-reviewed journal and international conference papers and more than 20 technical reports at NEC Yamagata Ltd., Japan. He is the editor of the books *Optical Communication Systems*, *Optical Communication* and *Advances in Optical Communication*. Currently, he is a guest editor of the Journal of MDPI, Energies Special Issue "Nano-structured Solar Cells". His research interests include pulse propagation, wave mixing, high-speed communication devices (semiconductor optical amplifiers), plasmonics and plasmonics-based communication devices (metal-semiconductor-metal photodetectors) and high efficiency solar cells (i.e. renewable energy). Dr Das is a senior member of the IEEE Power and Energy Society, Photonics Society, USA; member of the Institute of Engineers, Australia; and a Life Fellow of the Institute of Engineers, Bangladesh.

Contents

Preface

Recently, nanostructured solar cells have been identified as promising candidates for achieving high conversion efficiency in solar or photovoltaics cells due to their small amount of light reflection losses. In relation to the reflection losses, when the period or pitch of a single nano-grating structure is less than the wavelength of the incident light, then the structure behaves like a homogeneous medium with an effective refractive index. Hence, these nano-grating structures can provide gradual changes of the refractive index in several steps that confirm an excellent antireflective coating and light-trapping properties into the substrate compared to planar- or flat-type thin film substrates. There are different types of losses in solar cells that always reduce the conversion efficiency, but the light reflection loss is one of the most important factors that decreases the conversion efficiency of solar cells significantly. Therefore, the nano-grating structures (such as triangular or conical shaped) have a gradual change in refractive index that lead to a reduced amount of light reflection losses over a wide range of wavelengths and the angle of incidences.

This book presents a high-level technical overview of the emerging technologies on renewable energy systems and the conversion efficiency improvement of solar cells. It is intended as an introduction to the field for solar cells or renewable energy and professional or industrial engineers as well as the higher degree research students, research academics and design engineers. Although it is intended for professionals who already have some technical background, it is nevertheless relevant to anyone wishing to understand renewable or solar energy systems and the improvement of its conversion efficiency.

The nano-grating structures have a gradual change in refractive index which acts as a multilayer antireflective coating leading to reduced light reflection losses over broadband ranges of wavelength and angle of incidence. The antireflective coating is an optical coating which is applied to the surface of lenses or any optical devices to reduce the light reflection losses. This coating assists in light-trapping capturing capacity or improves the conversion efficiency of optical devices, such as lenses or solar cells. The multilayer antireflective coatings can reduce the light reflection losses and increase the conversion efficiency of nanostructured solar cells.

Organisation of the book

The authors with whom I have had the pleasure to collaborate have written chapters that report recent developments in nanostructured solar cells and renewable energy. They cover a number of themes which include the general concepts of solar cells or renewable energy; devices used for solar cells, such as nano-structures and nano-gratings; renewable energy systems; and related topics as described above. No book of the current length can encom-

pass the full scope of the subject, but I am pleased at the range of topics that we have been able to include in this book.

In this book, the chapters have been grouped in sections according to the following themes: Nanostructured Solar Cells - General Concepts; Nanostructured Solar Cells - Junction-type Solar Cells, such as single junction and heterojunctions; Nanostructured Solar Cells - Organic and Thin Film Solar Cells, such as organic, thin film and plasmonic-type solar cells; and Nanostructured Solar Cells - Perovskite Solar Cells, such as progresses and the fabrication of perovskite solar cells. These categorisations of parts are not fully perfect because some of the chapters are mixed or overlapped, i.e. like an interdisciplinary research topic. However, all the chapters are within an easily identifiable subject boundary that is a positive sign of the indicators of scientific progress in nanostructured solar cells.

I acknowledge all the contributed authors for their support in this book chapters from different organisations (universities and industries).

I acknowledge Associate Professor Tony Ahfock, Head of School, School of Mechanical and Electrical Engineering, University of Southern Queensland, Toowoomba, Queensland, Australia, and John Curtin Distinguished Professor Syed Islam, Department of Electrical and Computer Engineering, Curtin University, Perth, Australia, for their continuous support and encouragement to complete this task. I also acknowledge Dr Mainul Islam, University of Southern Queensland, Toowoomba, Queensland, Australia, for his continuous support and encouragement to complete this book.

I am very much grateful to Ms. Iva Simcic and Ms. Ana Pantar, book publishing process managers at InTech, for their prompt responses to my queries in regard to completing this book. I wish all of my collaborators every success in their future research activities.

Foremost, I would like to thank my wife Mrs. Varoti Das, son Nishikanta Das and daughter Nandita Das for their strong patience, understanding, continuous encouragement and support to complete this book.

Dr. Narottam Das
School of Mechanical and Electrical Engineering
University of Southern Queensland, Toowoomba, Queensland, Australia

Department of Electrical and Computer Engineering
Curtin University, Perth, WA, Australia

Section 1

Nano-Structured Solar Cells - General Concepts

Chapter 1

Introduction of Nano-Structured Solar Cells

Narottam Das

Additional information is available at the end of the chapter

http://dx.doi.org/10.5772/67467

1. Introduction

Over the decades, nano-structured gratings or materials have opened a promising way to future renewable energy sources with high conversion efficiency, especially nano-structured solar cells. The solar cell uses the advantages of nano-structured gratings for the improvement of light trapping or capturing capacity into the substrate. These nano-structures have been employed for different performance or energy conversion enhancement strategies. These devices can harvest the sunlight energy and convert it directly into the electrical energy/power. These new technologies and infrastructures have been developed for the improvement of solar cell conversion efficiency. This is a useful technology and has several features being relative to other renewable energy resources, such as directly generating electricity from sunlight and supplying electrical power in the form of portable panels/modules and having small-scale up to the large-scale power plants, and it is not being restricted to any particular region. These technologies are expected to contribute significantly for a sustainable future for the next generation.

For example, nano-structured grating shapes or profiles could be classified or categorized as follows: (i) rectangular-shaped nano-grating, (ii) trapezoidal-shaped nano-grating with different aspect ratios (i.e., 0.1–0.9), and (iii) triangular-shaped nano-grating (**Figure 1**).

The term aspect ratio (AspR) is defined as the ratio between the top length over the base length of a rectangle, trapezoid, and/or triangle. It depicts clearly from **Figure 1** that the AspR can be represented by the following equation:

$$\text{AspR} = \frac{a}{b} \tag{1}$$

where, "*a*" is the top length and "*b*" is the base length of the geometric shapes (such as, rectangle, trapezoid, and triangle). For a rectangular-shaped nano-grating profile, the AspR is "1" (i.e., the top and base length of the rectangle is equal) and for the triangular-shaped nano-grating profile, the AspR is "0" (i.e., the top length of the triangle is '0' compared to the base length of the triangle). However, for a trapezoidal-shaped nano-grating, the AspR is $0 < (a/b) < 1$, that is, it lies between '0' and '1' (such as, 0.1–0.9). These nano-grating shapes play an important role for the light trapping inside the substrate that affects the conversion efficiency of solar cells. Therefore, an appropriate design of nano-structured grating is essential to reduce the light reflection losses and improve the conversion efficiency of solar cells.

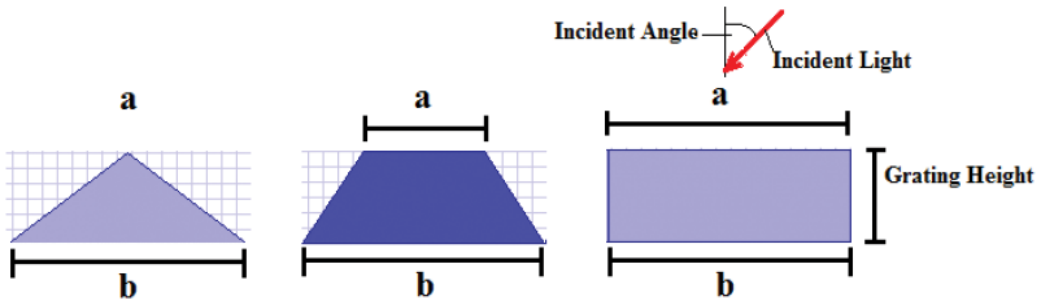

Figure 1. Different types of nano-structured grating shapes or profiles. Where, 'a' is the top length and 'b' is the base length of the geometric shapes (such as, rectangle, trapezoid, and triangle).

The book "Nano-Structured Solar Cells" is divided into four parts.

Part-1 discussed the general concepts of nano-structured solar cells. The requirement to produce solar or renewable energy with low production cost is indispensable dream of avoiding undue reliance on conventional energy systems. The emergence of third generation solar or photovoltaic system is in early stages that can fulfill the requirement of future demand. Solar cells can be considered by dyes, quantum dots, and perovskites for future generations dream.

Part-2 discussed about different junction type nano-structured solar cells. To design a photovoltaic or solar cells, it is essential to understand the background of physics and operation of high-efficiency junction type solar cells. The surface recombination and passivation mechanisms, passivation schemes for cell surfaces are very important. The advanced cell structures and their fabrication schemes are able to achieve high conversion efficiency is demonstrated. These advanced cell design features have become highly active areas of investigation in the photovoltaic or solar energy industry for next generation's renewable or solar energy system.

Part-3 discussed about the organic and thin film nano-structured solar cells. This type of solar cell is one of the new energy sources, and a regenerated energy source is abundant and pollution-free which is environmentally friendly. The organic and thin film solar cell technology represents an alternative way to solve effectively the world's increasing energy shortage problem. The light trapping inside the solar cell is a critical issue for conversion efficiency

improvement. Nano-structured gratings, surface plasmons including localized surface plasmons excited in the metallic nano-particles, and surface plasmon polaritons propagating at metal/semiconductor interfaces have great interests in designing the thin film solar cells. The organic and thin film structured solar cells are able to improve the conversion efficiency of nano-structured solar cells for future generations.

Part-4 discussed the perovskite nano-structured solar cells. Perovskite solar cells are the continuation of dye-sensitized solar cell in terms of the sensitization phenomena as occurred in the functioning molecules. Recently, a breakthrough propose has been performed for the sensitization of perovskite solar cell that is a solid-state structure as offered an equivalent sensitizer used in dye-sensitized solar cell. The energy conversion efficiency of those solid-state cells reached about twofold of its initial amount of generation over past several years. The scientists and researchers from different part of the world followed it very actively. They have introduced an improved efficiency about 20% which was originally started from 4%; this growth is just in 4 years of time. Hence, it seems that the new age for solar conversion devices depending on the recent significant improvement on Perovskite solar cells.

Author details

Narottam Das

Address all correspondence to: narottam.das@usq.edu.au

School of Mechanical and Electrical Engineering, Faculty of Health, Engineering and Sciences, University of Southern Queensland, Toowoomba, Queensland, Australia

Chapter 2

Third-Generation-Sensitized Solar Cells

Muhammad Ammar Mingsukang,
Mohd Hamdi Buraidah and Abdul Kariem Arof

Additional information is available at the end of the chapter

http://dx.doi.org/10.5772/65290

Abstract

The need to produce renewable energy with low production cost is indispensable in making the dream of avoiding undue reliance on non-renewable energy a reality. The emergence of a third-generation photovoltaic technology that is still in the infant stage gives hope for such a dream. Solar cells sensitized by dyes, quantum dots and perovskites are considered to be third-generation technological devices. This research focuses on the development of suitable and reliable sensitizers to widen electromagnetic (EM) wave absorption and to ensure stability of the photovoltaic system. This article discusses the basic principles and the progress in sensitized photovoltaics.

Keywords: third-generation solar cells, sensitized solar cells, dye-sensitized solar cells, quantum dot-sensitized solar cells, perovskite-sensitized solar cells

1. Introduction

Third-generation photovoltaics are able to produce high efficiency photon to electricity conversion devices at a cheaper production cost. Solar cells based on pure Si forms were the first-generation devices with an efficiency of ~27%. Due to the high production cost, researchers searched for new processes and materials that led to the second-generation solar cells comprising copper indium diselenide, amorphous silicon, and polycrystalline solar cells. Production was still expensive, as the fabrication process required a large amount of energy. Production of the third-generation solar cell is cheaper and the cells are reasonably efficient. There are several technologies classified as third-generation solar cell technologies. These include solar cells sensitized by a dye material, solar cells sensitized by quantum dots (QDs) and perovskite-sensitized solar cells. These solar cells have a similar structure consisting of a

photoanode, counter electrode (CE) and a medium for charge transport. The working principle is also similar. Work on sensitized photovoltaics started during the 1970s with the use of organic dyes as the sensitizer. Organic dyes can be natural or synthetic. Natural organic dyes can be obtained from plant sources but the performance is poor and the efficiency is low. Apart from natural organic dyes, synthetic organic dyes can give efficiency as high as 13%. Ruthenium based dye is one of the synthetic organic dyes and is known to give good performance with current density about 20 mA cm^{-2}. As development in dye-sensitized solar cells (DSSCs) continues, an idea to replace organic dyes with inorganic sensitizers resulted in the emergence of quantum dot-sensitized solar cells (QDSSCs) that utilize quantum dots or nano-sized semiconductor crystals with a short band gap and a high extinction coefficient. Later, since 2009, researchers have begun to use perovskite materials as sensitizers. Perovskite works very well with the solid-state hole transfer material and until now its efficiency has reached 21%. However, perovskites are very moisture-sensitive materials and fabrication must be done in very clean and controlled conditions. In sensitized solar cells, the photoanode is a very crucial component because this is where the electrons are generated by the sensitizer. Photoanodes will absorb photons, excite and transport electrons when illuminated. On exiting the photoanode, the electrons will be sent to the cathode and returned to the sensitizer via a hole conductor or a redox mediator in the electrolyte. For DSSCs, the photoanode components are the dye sensitizer, a mesoporous semiconducting oxide layer and a transparent conducting oxide (TCO). Photoanodes for QDSSC and perovskite solar cells have similar components with DSSCs except that quantum dot nano-sized semiconductor crystals and perovskite materials act as the sensitizer. Another difference between them is the redox mediator used in the electrolyte. QDSSC works well with the polysulphide electrolyte instead of the iodide based electrolyte (as in DSSCs) because the iodide-based electrolyte will cause rapid degradation in photocurrent due to the corrosive nature of the iodide ion on many semiconductor materials including quantum dots. Perovskite solar cells use hole conductors instead of a redox mediator electrolyte. **Figure 1** illustrates progress of third-generation devices.

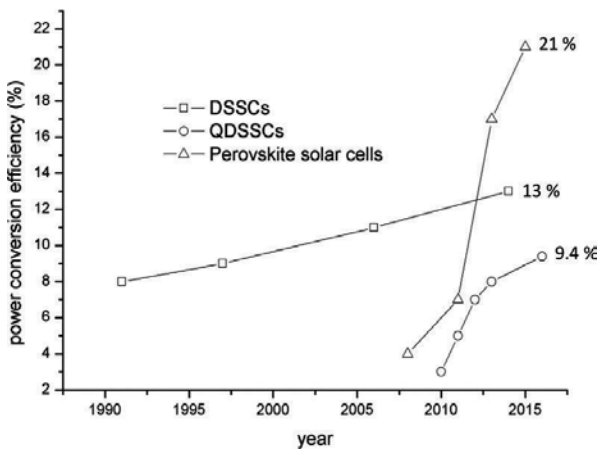

Figure 1. Graphs showing progress of third-generation photovoltaics.

http://dx.doi.org/10.5772/65290

2. Dye-sensitized solar cells (DSSCs)

DSSCs employ oxide semiconductors with wide band gaps and sensitizers that absorb electromagnetic (EM) waves in the visible light. DSSC was first developed in 1972 as a chlorophyll-sensitized zinc oxide (ZnO) electrode solar cell [1]. In 1976, an amorphous silicon photovoltaic was reported for the first time by Carlson and Wronski, and its efficiency was 2.4% [2]. Subsequently, solar energy researchers began to give attention to DSSCs. However, the main dilemma was that a single layer of dye molecules on the surface allowed only 1% incident sunlight absorption that delayed further progress [3]. The breakthrough in DSSC research was in 1991 [4]. The efficiency was 7.1%. About 80% of photons absorbed were converted into electrical current. The cheap cost of production and the simple structure inspired many researchers worldwide to improve the efficiency to a level deemed acceptable for commercialization.

The DSSC operating principle may be compared to the process of photosynthesis with the dye functioning as chlorophyll [4]. In DSSCs, the transport of charges (electrons) to the external circuit begins when electrons exit the semiconducting network layer and ends when the redox mediator in the charge transport medium returns them to the sensitizers. The purity of the semiconducting material is not as crucial as in the earlier generation solar cells.

2.1. DSSC structure

Figure 2 shows the structure of a DSSC. The photoanode consists of a TCO substrate on the top of which is deposited a semiconducting oxide layer (usually TiO_2) and the dye sensitizer. Actually, there are two TiO_2 layers. The first TiO_2 layer is a blocking layer to suppress electron recombining with the ionized dye and/or the mediators. The second layer is mesoporous TiO_2 of 20–30 nm thickness. These particles are larger than the blocking layer particles. The mesoporous TiO_2 layer thickness is about 10 μm. A colloidal TiO_2 paste for the

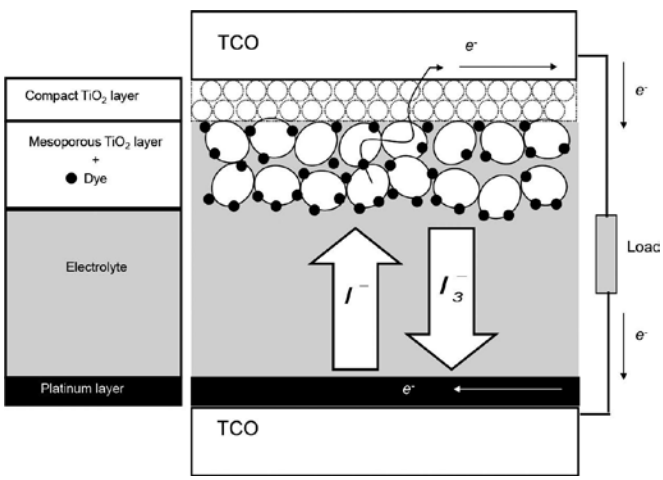

Figure 2. Schematic diagram of the DSSC structure.

second layer can be prepared by grinding TiO_2 of 21 nm size with nitric acid, a polymer of low molecular mass (e.g. polyethylene glycol of molecular mass 200 g/mol) with a little surfactant. This paste will be deposited over the blocking TiO_2 layer and heated at ~450°C for 30 min. To ensure the dye adheres to the mesoporous TiO_2 layer, the TiO_2 films are soaked in the dye solution overnight. The larger surface area of the mesoporous TiO_2 area allows a greater amount of dye to be adsorbed on its surface. An electrolyte usually with an iodide/triiodide couple is needed for DSSC. The electrolyte can be in liquid or gel form. A catalytic active material (usually platinum) is required as the counter electrode to reduce the triiodide ion (I_3^-) to the iodide ion (I^-).

2.2. Working principle of DSSCs

Figure 3 shows the energy levels in the working of a DSSC. The Fermi energy level of TiO_2 will be aligned with the redox energy level when there is no light. Upon illumination, dye molecules (*D*) attached to the mesoporous TiO_2 surface absorbs photons of energy, *hv*. Electrons in the highest occupied molecular orbital (HOMO) of the dye molecules will be excited into the lowest unoccupied molecular orbital (LUMO), see Eq. (1).

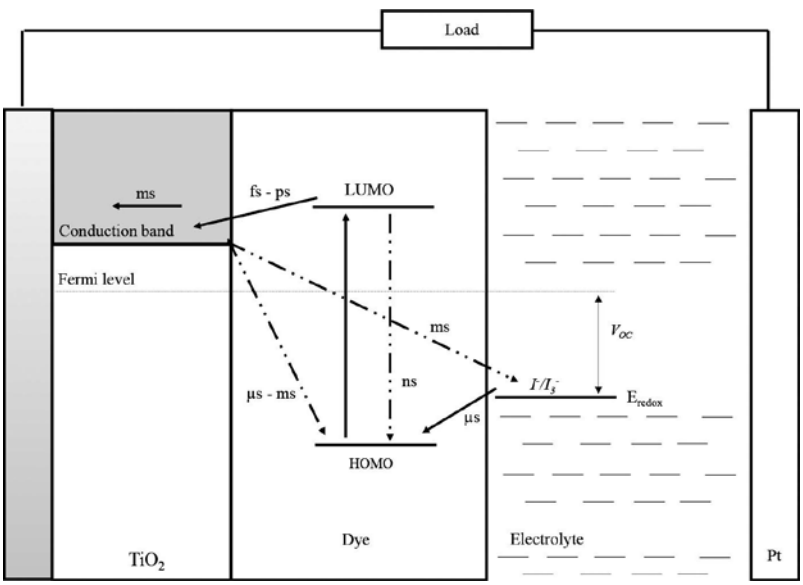

Figure 3. Schematic diagram showing the kinetic processes at the TiO_2/dye/electrolyte interface.

$$D + hv \rightarrow D^* \quad \text{light absorption} \tag{1}$$

Here, D^* is the excited dye molecule. Electrons in the LUMO of the dye will be transferred to the mesoporous TiO_2 within femtoseconds, ~10^{-15} s. This process is called electron injection.

The Fermi level of TiO_2 will be increased towards the conduction band (CB). The dye molecule is now in an oxidized or ionized state (D^+), Eq. (2). The difference in the potential between the Fermi and the redox levels will be manifested as the voltage of the device.

$$D^* \rightarrow e^-_{(TiO_2)} + D^+ \quad \text{electron injection} \tag{2}$$

The transferred electrons percolate through the interconnected nanocrystalline TiO_2 network to the conducting substrate within milliseconds (10^{-3} s). For good performance of the DSSC, this process has to be completed with the recombination reaction displayed in Eqs. (3) and (4).

$$e^-_{(TiO_2)} + D^+ \rightarrow D \tag{3}$$

$$2e^-_{(TiO_2)} + I_3^- \rightarrow 3I^- \tag{4}$$

Eq. (3) describes electron recombination with the ionized dye molecule and Eq. (4) describes electron-triiodide ion recombination. Electrons exit the TCO substrate and travel towards the counter electrode through the external circuit and reduce a triiodide ion in the electrolyte to an iodide ion as shown in Eq. (5).

$$\frac{1}{2}I_3^- + e^-_{(CE)} \rightarrow \frac{3}{2}I^- \tag{5}$$

The iodide ion diffuses to the photoanode and is oxidized back to a triiodide ion regenerating the dye molecule in the process. This process occurs continuously as shown in Eq. (6).

$$D^+ + \frac{3}{2}I^- \rightarrow D + \frac{1}{2}I_3^- \tag{6}$$

2.3. Dye sensitizer

The dye sensitizer is one of the important components of the DSSC. It works as an absorber of light and produces electrons. For good light conversion into electricity, the dye or sensitizer must have the following:

1. A broad absorbance spectrum of solar light for high photocurrent.
2. Anchoring groups such as carboxylate for attachment on the TiO_2 surface so that electron transfer can occur from the LUMO of the dye to the TiO_2 CB.

3. In order for the electrons to be transferred to the oxidized dye molecules efficiently for dye regeneration, the redox level has to be at more negative potential than the HOMO potential of the dye. The LUMO has to be less positive compared to the TiO_2 CB for electron injection.

4. The dye covering the TiO_2 surface should not stack on each other.

2.3.1. Ruthenium sensitizer

Desilvestro et al. [5] was the first to report the use of ruthenium complex tris(2,2′-bipyridyl-4,4′-di-carboxylate)ruthenium(II) dichloride dye in DSSC. The percentage conversion of absorbed incident photons to current (IPCE) for this DSSC was 44%. In 1991, O'Regan and Grätzel, reported IPCE of more than 80% from a DSSC using [Ru(2,2′-bipyridine-4,4′-dicarboxylicacid)$_2$(μ-(CN)Ru(CN) (2,2′-bipyridine)$_2$)$_2$] dye adsorbed on a mesoporous, nanocrystalline TiO_2 surface. The electrolyte contained I^-/I_3^- and the counter electrode was platinum [6]. The efficiency of the DSSC was more than 7%. Nazeeruddin et al. [7] have prepared several ruthenium(II) complexes. These sensitizers are cis-X_2bis(2,2′-bipyridyl-4,4′-dicarboxylate)ruthenium(II) dye sensitizers. X comprises halide anions, CN^- and SCN^-. The cis-di(thiocyanato)bis(2,2′-bipyridyl-4,4′-dicarboxylate) ruthenium(II) dye has been coded as N3. Among all the ruthenium complexes, N3 is a better sensitizer for charge transfer. N3 absorbs a wide wavelength range in the visible light. It has four carboxyl groups that strongly adsorb on the TiO_2 surface and has a long excited state lifetime. The IPCE value exhibits more than 80% between 480 and 600 nm. The electrons are injected into the TiO_2 CB via a metal-to-ligand charge transfer (MLCT) route as shown in **Figure 4**. According to Bryant et al. [8], the carboxylated complexes exhibit two $t_2 \rightarrow \pi^*$ MLCT bands in the near UV and visible region. The absorbance of Ru(2,2′-bipyridine-4,4′-dicarboxylicacid)$_2$(NCS)$_2$, i.e. N3 dye at visible region, $t_2 \rightarrow \pi^*$ is higher than other dihalogeno derivative dyes [7].

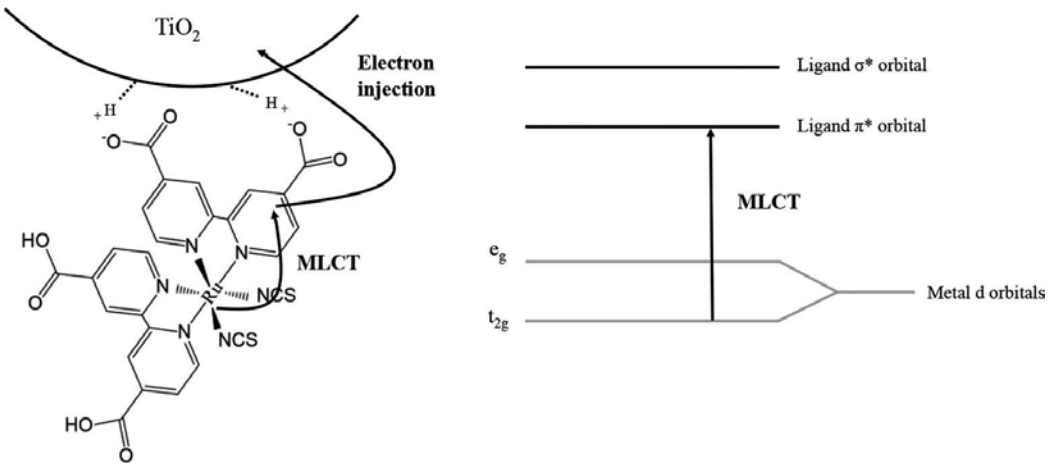

Figure 4. Charge transfer route from dye to TiO_2.

The N3 dye was almost no match in terms of charge transfer ability until Nazeeruddin et al. [9] developed the triisothiocyanato-(2,2′:6′,6″-terpyridyl-4,4′,4″-tricarboxylato) Ru(II) tris(tetrabutylammonium) or 'black dye' and coded as N749. The DSSC with black dye showed a broader IPCE spectrum in the visible region compared to N3. The overall efficiency obtained for this DSSC with black dye was 10.4% under 1 Sun illumination [10].

The substitution of two protons in the carboxyl group of N3 dye with tetrabutylammonium cations resulted in $[Bu_4N]_2[Ru(4\text{-carboxy-4-carboxylate-2,2′bipyridine})_2(NCS)_2]$ or N719 dye. This dye exhibits a higher efficiency than N3 dye [11]. The higher efficiency is related to the higher V_{oc} that resulted from the upshift of the TiO_2 Fermi level. However, the performance of DSSC using N719 dye is still lower than the N749 since N719 does not absorb in the red. To extend the EM absorption region, the dye can be tuned. This can be accomplished by introducing a π^* molecular orbital ligand and by using a strong donor ligand to destabilize the metal t_{2g} orbital [12]. By achieving this, the absorption range can be stretched from visible to the near infrared region. Islam et al. [12] have synthesized ruthenium complexes containing 2,2′-biquinoline-4,4′-dicarboxylic acid where the π^* orbital is lower or at a more positive potential than that containing 2,2′-bipyridine-4,4′-dicarboxylic acid. The DSSC using this sensitizer exhibited lower efficiency due to the dye excited state being at a more positive potential than the CB of TiO_2. This led to reduced electron injection driving force and lowered the photocurrent. The nanocrystalline TiO_2 soaked in $[Bu_4N]_2[cis\text{-}Ru(4\text{-carboxy-2-[2′-(4′-carboxypyridyl)]quinoline})_2(NCS)_2]$ has been investigated by Yanagida et al. [13]. They found that the IPCE spectrum extended up to 900 nm. Unfortunately, the maximum IPCE value obtained for this dye is lower (~40%) compared to the N719 (~80%). This is due to the lower LUMO which is 0.24 V below that of N719.

2.3.2. Porphyrin sensitizer

The porphyrin sensitizer also requires a binding group such as carboxylic acid and 8-hydroxylquinoline (HQ) to adsorb efficiently the TiO_2 semiconductor [14]. The linkers containing carboxylic acid or HQ can be located at *β*-positions or *meso*-positions or both (shown in **Figure 5**).

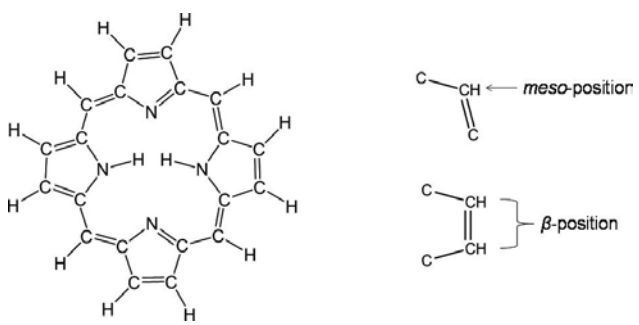

Figure 5. Basic porphyrin structure. The mesoposition is at C—CH═C and β-position is at C—CH═CH—C. The hydrogen at meso- and β-positions will be substituted by functional groups such as diarylamino, fluorene, etc.

Kay and Grätzel were the first to report on DSSC using copper porphyrin [15]. The overall efficiency was 2.6%. The development of porphyrin sensitizers for SSCs gained more attention when Wang et al. [16] reported an efficiency of 5.6% under AM 1.5 illumination using zinc-porphyrin as the sensitizer with the co-adsorbent chenodeoxycholic acid (CDCA). The efficiency was increased to 7.1% reported by the same group for the zinc-porphyrin sensitizer with the aryl group as the electron donor and malonic acid as the acceptor ,which is shown in **Figure 6** [17]. Since then, the research on development of the porphyrin sensitizer increased rapidly. Park et al. [18] have shown that electron injection can be enhanced using two equivalent π-conjugated malonic acid linkers at the β-position. This led to higher J_{sc}.

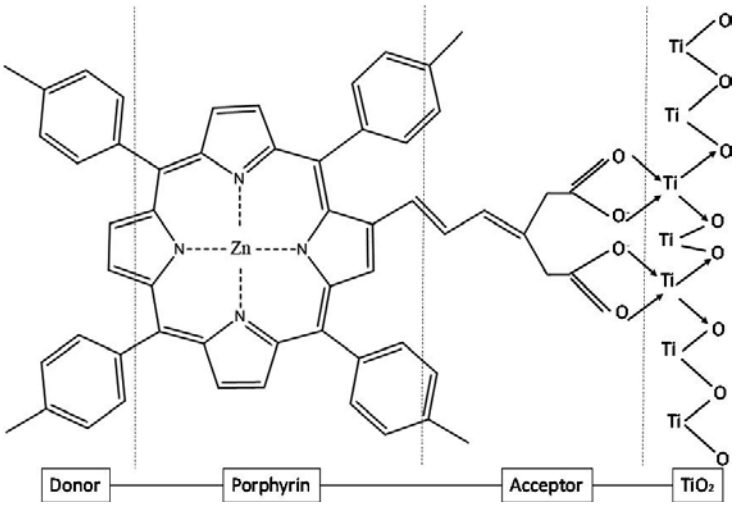

Figure 6. Structure of malonic acid porphyrin substituted at the β-position.

The serious dye aggregation problem for porphyrins on TiO_2 films compared with the ruthenium complexes led to poor DSSC efficiency. The problem was solved by introducing long alkyl chains and 3,5-di-tert-butylphenyl groups to the porphyrin ring at the *meso*-position [19]. By attaching the diarylamino group to the porphyrin ring, the DSSC exhibits an efficiency of 6.0% [20]. The efficiency was further enhanced to 6.8% by attaching two *tert*-butyl groups in the diarylamino group instead of two long alkyl chains (C_6H_{13}) coded as YD2 and co-adsorbed with CDCA. Bessho et al. [21] reported that the efficiency increased up to 11% when a thin reflecting layer of 5 μm thickness was coated on the TiO_2 and sensitized with the YD2 sensitizer.

To further improve the performance of porphyrin based DSSC, light harvesting has to be enhanced which means the HOMO and LUMO energy gap must be decreased. There are two approaches: (1) to fuse or dimerize porphyrins and (2) by coupling a chromophore to the porphyrin ring. Eu et al. [22] have fused two quinoxaline derivatives to the zinc porphyrin to form 5,10,15,20-tetrakis(2,4,6-trimethylphenyl)-6′-carboxyquinoxalino[2, 3-β] porphyrinato-zinc (II) or ZnQMA and 5,10,15, 20-tetrakis(2,4,6-trimethylphenyl)-6′,7′-dicarboxyquinoxali-

no[2, 3-β]porphyrinatozinc (II) or ZnQDA. ZnQMA and ZnQDA based DSSCs exhibit the efficiencies of 5.2% and 4.0% respectively. The IPCE spectrum for both porphyrin sensitizers extended only up to ~700 nm. The fused porphyrin approach has successfully extended the light absorption to wavelengths longer than that in the visible region (~1000 nm) for nickel porphyrins fused with perylene anhydride as reported by Jiao et al. [23]. Unfortunately, the overall efficiency obtained was only 1.36%. The reason for low performance is the dye aggregation that resulted in the LUMO energy to be very close to the TiO_2 CB edge and the short lifespan of the dye excited state.

The introduction of a highly conjugated π-extended chromophore at the *meso*-position can enhance light harvesting of the porphyrin dye. Wu et al. [24] has modified porphyrin by attaching fluorene, acenaphthene and biphenyl to one of the *meso*-positions. A broad IPCE spectrum near 800 nm with stronger response in the 400–500 and 550–750 nm regions were observed for DSSC using these three dyes. They observed that fluorenyl substituents showed the highest efficiency (8.1%). A year before, the same group [25] showed that pyrene-functionalized porphyrin exhibited an efficiency of 10.06% superior to N719 (9.3%). Dye aggregate formation significantly limited the performance of the porphyrin based solar cell. In order to further suppress dye aggregation, a long alkoxy chain zinc porphyrin was employed for protection of the porphyrin core. In 2014, Mathew et al. [26] reported an efficiency as high as 13% for porphyrin-sensitized DSSC. The porphyrin was coded SM315. The mediator used for this DSSC was Co(II/III).

2.3.3. Non-metallic organic dyes

Metal free or non-metallic organic dyes have been studied intensively to replace ruthenium-based sensitizers in DSSC. The metal free organic dyes have a molar extinction coefficient that is usually higher than Ru complexes [27–29]. Metal free dyes have opto-electronic properties that are easily tuned and they are cheaper to produce [30]. The general design principle for dye sensitizer is shown in **Figure 7**.

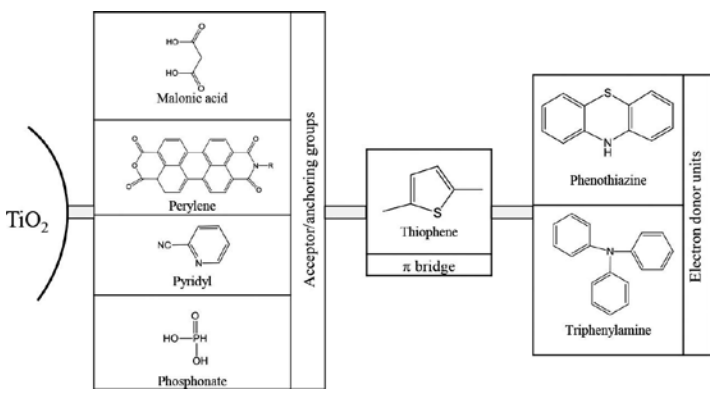

Figure 7. Design structure for non-metallic dye. The electrons from the donor will be transferred to TiO_2 through the π - bridge and the acceptor.

In general, organic dyes can be grouped as neutral and ionic organic dyes. Examples of neutral organic dyes are coumarins, triphenylamine, phenothiazine and indoline. Examples of ionic organic dyes are squarylium, cyanine, hemicyanine and merocyanine.

Tian et al. [31] have synthesized organic dyes with phenothiazine (PTZ) as the electron donor and rhodamine-3-acetic acid or cyanoacrylic acid as the electron acceptor. The DSSC utilizing the dye with cyanoacrylic acid as the anchoring acceptor exhibited 5.5% efficiency. Marszalek et al. [32] reported two novel organic dyes. The dyes comprised of electron donating 10-butyl-(2-methylthio)-10*H*-phenothiazine with and without the vinyl thiophene group (VTP) as the π-bridge. The acceptor used is cyanoacrylic acid. With VTP, the IPCE value observed was up to 80% in the wavelength range between 380 and 750 nm, whereas without VTP, the range was between 380 and 650 nm. This results in higher J_{sc} and efficiency for the DSSC using the VTP attached dye. The photocurrent density enhanced from 11.2 to 15.2 mA/cm^2 and the efficiency reached 7.4%.

Coumarin-based dye is a promising sensitizer for DSSC because it has good photoelectric conversion properties [33]. Wang et al. [33] reported that a DSSC using coumarin dye, 2-cyano-3-(5-{2-[5-(1,1,6,6-tetramethyl-10-oxo-2,3,5,6-tetrahydro-*1H, 4H, 10H*-11-oxa-3a-aza-benzo[*de*] anthracen-9-yl)-thiophen-2-yl]-vinyl}, -thiophen-2-yl)-acrylic acid exhibited an efficiency of 8.2%.

3. Quantum dot-sensitized solar cells (QDSSCs)

As the research on DSSCs progressed, the idea of replacing dyes with QDs emerged. QDs are nano-dimensional structures with a narrow band gap suitable for absorbing light in the visible region. Therefore, when deposited over the mesoporous TiO_2 layer, the excited electrons in the QDs can be transferred to the mesoporous TiO_2. Research on sensitization of a wide band gap semiconductor by using a narrow band gap material such as dye started during the 1960s, but QDs was used for wide band gap semiconductor sensitization for the first time in 1986 by Gerischer et al. [34]. Advancement in research on sensitization led to DSSCs. Based on the highly porous TiO_2 DSSCs introduced by O'Regan and Grätzel [6], QDs were introduced to replace the dye [35–37]. Until now, a lot of research has been geared towards improving QDSSCs performance. The highest efficiency recorded is now around 9% [38, 39].

There are several advantages of inorganic QDs over organic dyes. This is because inorganic QDs are easy to produce and durable [40]. Moreover, the optical band gap of QDs is tuneable [41]. Another special property of QDs is the production of at least two electron-hole pairs per photon with hot electrons. This is due to the impact of ionization in the QD nano-sized semiconducting material [42]. QDs can also reduce dark current and in doing so improve working of the photovoltaic system. This is because the extinction coefficient of QDs is high [43]. The theoretical efficiency for QDSSCs calculated by considering carrier multiplication due to impact of ionization was 44.4% [44].

QDSSCs and DSSCs have a lot of similarities and some differences. The major difference between these two is the sensitizer. QDSSCs utilize nano-sized semiconductor QDs and DSSCs

utilize light absorbing dye. Another difference is material conformity. Some materials that worked effectively in DSSCs are not compatible with QDSSCs and could give a bad impact on the performance of the cells. **Table 1** compares the components for DSSCs and QDSSCs.

Component	QDSSCs	DSSCs
Sensitizer	Sensitizer used is inorganic quantum dots such as CdSe, CdTe, CdS, etc.	Sensitizer include organic dye such as ruthenium based dye, natural dye, etc.
Wide band gap semiconductor	A lot of work on QDSSCs utilized TiO_2 as the one of photoanode components	A lot of work on DSSCs utilized TiO_2 as one of the photoanode components
Electrolyte	Works on QDSSCs, employs the polysulphide redox mediator in the electrolyte due to its stability towards quantum dot	Works on DSSCs employs the iodide based redox mediator in the electrolyte due to its stability towards DSSCs performance
Counter electrode	Metal chalcogenides	Platinum

Table 1. A straightforward comparison between QDSSCs and DSSCs.

3.1. QDSSC structure

Although progress has been made, the efficiency value of QDSSCs has not surpassed that of DSSCs, which is 13% [26]. There is still a lot of improvement to be done in obtaining a better material for QDSSCs. **Figure 8** illustrates schematically the QDSSC device and its components.

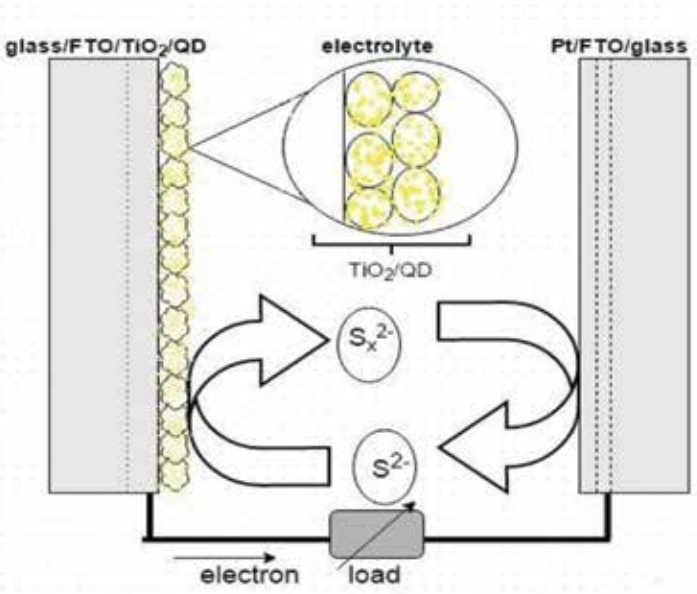

Figure 8. An illustration of QDSSCs with its three main components: photoanode, electrolyte and counter electrode.

3.1.1. Photoanode

In works concerning QDSSCs, very frequently TiO_2 was utilized as the wide band gap semiconductor compared to other oxides. Out of the many QDs chalcogenides, cadmium chalcogenides (CdS, CdSe and CdTe) are most popularly used in QDSSCs [45–47]. Another important component in QDSSC photoanodes is the passivation layer. The passivation layer prevents electron recombination that can improve performance of QDSSCs since the short circuit current density will not be reduced.

Chalcogenides of cadmium can easily be fabricated and have a tuneable band gap that can be achieved by controlling their size [45, 48–50]. CdS, CdSe and CdTe chalcogenide QDs have a band gap 2.3, 1.7 and 1.4 eV, respectively. Hence, incident light in the visible wavelength can be absorbed up to ~540 nm for CdS, ~731 nm for CdSe and ~887 nm for CdTe. **Figure 9** shows the valence band (VB) and conduction bands of cadmium chalcogenide QDs and TiO_2.

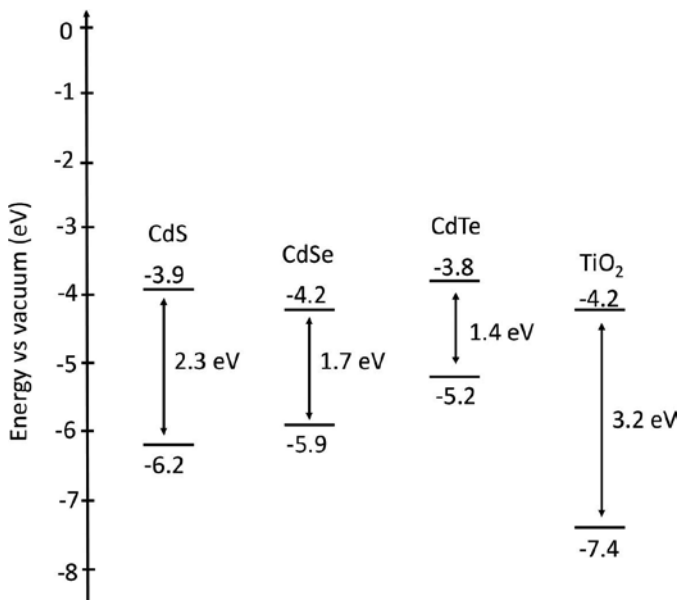

Figure 9. Energy levels of cadmium chalcogenide QDs (CdS, CdSe and CdTe) and TiO_2.

The use of two species of QDs in a single QDSSC has proven to enhance the efficiency, for example, CdS/CdSe, CdTe/CdSe and CdTe/CdS combinations were used as sensitizers [43, 51, 52]. When CdS and CdSe make contact with each other, electron redistribution will occur resulting in the CdS and CdSe band edge to shift to more or less positive potentials, respectively. The shifting of the band edge is referred to Fermi level alignment [43]. This process affects electron injection. The same process also happens in the combinations of CdTe/CdSe and CdTe/CdS. **Figure 10** shows how CdTe/CdSe and CdS/CdSe combinations produce an effective electron injection. Application of co-sensitizing QDs in QDSSCs has shown excellent performance compared to QDSSCs fabricated with a single QD sensitizer [43, 51, 52].

http://dx.doi.org/10.5772/65290

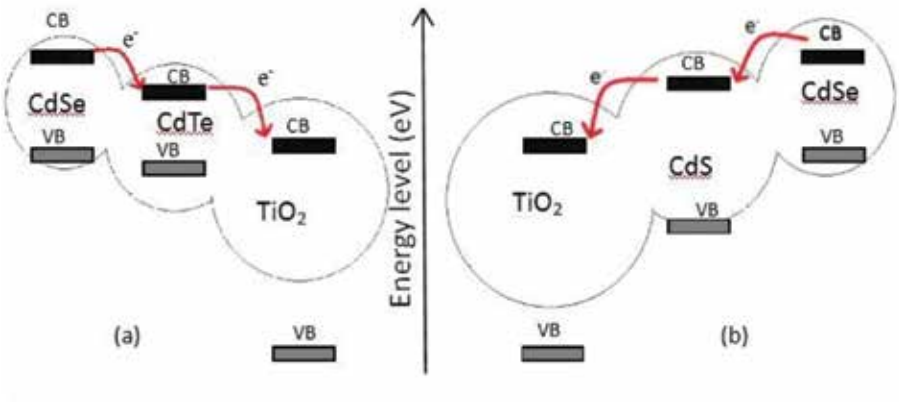

Figure 10. Changing of the band edge level of QDs after electron redistribution of: (a) CdTe/CdSe and (b) CdS/CdSe. This arrangement is necessary for electron injection from CdSe to CB of TiO_2 due to the alignment of the Fermi level.

Although tuning band gap with the size of the QDs is promising in enhancing performance of QDSSCs, this may give rise to stability problem [53]. To avoid this, alloyed cadmium chalcogenide QDs (AB_xC_{1-x}, A = Cd, B and C = S or Se or Te) were used to tailor the band gap of the QDSSCs without having to change the particle size [53, 54]. An example of alloyed cadmium chalcogenide is $CdTe_xS_{1-x}$. The band gap of the $CdTe_xS_{1-x}$ alloyed QD can be adjusted to the range of visible light by changing the tellurium molar ratio and make it exhibit a high potential in photovoltaic application [55]. Another excellent alloyed cadmium chalcogenide used in QDSSCs is $CdSe_xTe_{1-x}$. $CdSe_xTe_{1-x}$has been utilized in QDSSCs by Ren et al. [38] and Yang et al. [39]. Photon-to-electricity efficiency obtained was 9 and 9.4% respectively. Employment of alloyed cadmium chalcogenide in QDSSCs have a very promising future since it will give a better efficiency value and high stability towards performance of QDSSCs.

Even though QDs have many advantages as a sensitizer compared to organic dyes, the efficiency recorded for QDSSCs is still lower compared to DSSCs. Excited electrons in QDs can take one of three possible routes which are: (1) jump into the TiO_2 conduction band which will be beneficial to the performance of the QDSSCs, (2) relax into the valence band by emitting energy and finally (3) combine with redox mediator ions (recombination process) in the electrolyte which are routes detrimental to the QDSSC performance. To overcome recombination, researchers have QDs coated on the surface with ZnS, SiO_2 and amorphous TiO_2 (am-TiO_2) [38, 56, 57]. Ren et al. [38] have introduced a novel strategy to overcome recombination by implementing three passivation layers am-TiO_2/ZnS/SiO_2 resulting in 9% efficiency. Yang et al. [39] utilized the CdS layer as a passivation layer to the CdSeTe QDs and achieved 9.4% efficiency.

3.1.2. Electrolyte

Another important component in QDSSCs is the electrolyte. The electrolyte in QDSSCs functions as a charge carrier transporter between the photoanode and the counter electrode

done via the redox mediators. The redox species in the electrolyte are also responsible for turning the oxidized QD species by donating an electron to the QDs. In QDSSCs, polysulphide electrolytes with S^{2-}/S_x^{2-} are widely utilized by researchers since they can give good performance and stability [58–60]. Performance of QDSSCs can also be improved by utilization of chemical additives in the polysulphide electrolyte. Park et al. [61] reported that by introducing sodium hydroxide (NaOH) into the polysulphide electrolyte of QDSSCs, V_{oc} and *FF* can be increased.

Due to problems that arise from utilization of liquid electrolytes such as leakage and easy vaporization, researchers have begun to use polymer electrolytes. However, the performance of QDSSCs based on the solid polymer electrolyte [62, 63] is low compared to QDSSCs fabricated with liquid electrolytes. This is because solid state electrolytes suffer from low ionic conductivity. Another alternative to the liquid electrolyte is to use gel polymer electrolytes (GPEs). GPE is very competitive since GPE based QDSSC performance is comparable with QDSSCs fabricated with the liquid electrolyte [64–66]. Kim et al. [65] successfully fabricated CdSe/CdS GPE based QDSSCs with 5.45% efficiency, which is comparable with QDSSCs based on the liquid electrolyte. As the GPE based QDSSCs is comparable with QDSSCs fabricated with the liquid electrolyte, utilization of GPE in QDSSCs will be an advantage in terms of providing stability and overcoming problems that arise from liquid electrolytes.

3.1.3. Counter electrode

The counter electrode is another important component in QDSSCs. Electrons from the photoanode are returned to the QD when the electrons react with the redox ions in the electrolyte. In DSSCs, platinum (Pt) is the best material to be used as the CE due to its high stability and high catalytic activity for the triiodide ion to be reduced into the iodide ion. However, Pt CE does not work for QDSSCs. This is because Pt [67]:

1. is not catalytic to the sulphide ion,

2. restrains the charge transfer to polysulphide ions and

3. can react with sulphur.

Hence, researchers look for alternative materials to be used as the CE such as noble metals, carbon based materials and metal chalcogenides [68]. The highest efficiency are presently exhibited by QDSSCs utilizing copper sulphide (Cu_2S) as the CE ($\eta = 9\%$) [39].

3.2. Working principle of QDSSC

Basically, QDSSCs working mechanism is identical with DSSCs. TiO_2 is used in the photoanode. Upon light incident, the QD sensitizers absorb photons to excite electrons into its CB (photoexcitation). Electrons in the CB of QDs will be injected to the CB of TiO_2 and oxidized QDs will be regenerated by receiving electron from S^{2-} ions in the electrolyte [69]. From CB of TiO_2, electrons will leave the photoanode, enter the external circuit and reach the counter

electrode where they will be received by S_x^{2-} ions in the electrolyte (S_x^{2-} transforms into S^{2-}).

As the above process continues, electrons will keep moving through the cell and current is produced. **Figure 11** shows the working mechanism of QDSSCs where only electron movement is shown. Red arrows in **Figure 11** indicate the electron movement.

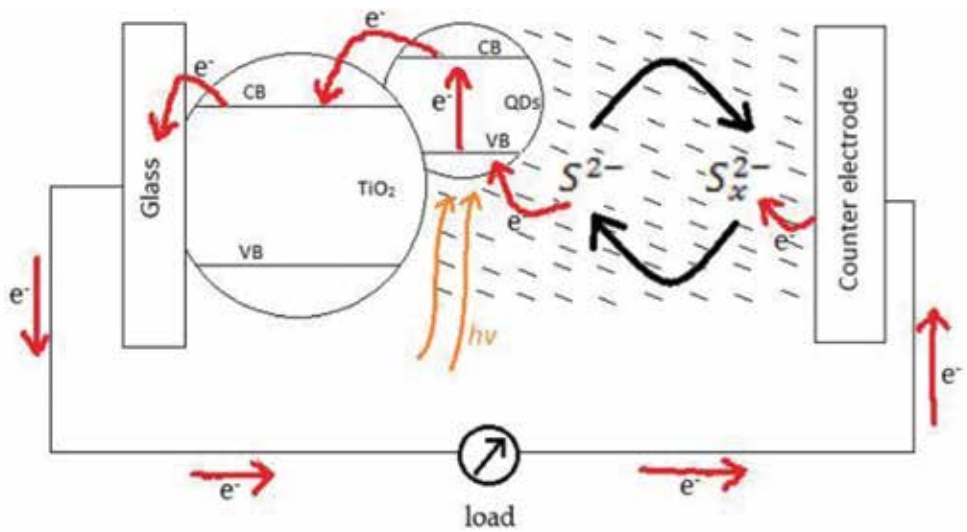

Figure 11. This figure demonstrates the movement of electron starting from QDs excited due to photon absorption.

4. Perovskite-sensitized solar cell

Perovskite is a term for materials that have a similar crystal structure to calcium titanium oxide ($CaTiO_3$), that is, ABX_3 where A and B are cations and X is an anion. A is typically a large cation, such as ethylammonium ($CH_3CH_2NH_3^+$) [70], formamidinium ($NH_2CH{=}NH_2^+$) [71] and methylammonium ($CH_3NH_3^+$) [72]. B is a cation metal of carbon family, such as Ge^{2+}, Sn^{2+} and Pb^{2+} and anion X is a halogen (F, Cl, Br and I).

Perovskite cells are typically fabricated with two structures which are mesoporous and planar structures.

4.1. Mesoporous structure

The mesoporous structure consists of a transparent conducting oxide (TCO) substrate coated with an oxide semiconductor compact layer, mesoporous metal oxide (e.g. TiO_2, Al_2O_3), perovskite sensitizer, hole conductor and gold conductor.

Kojima et al. [73] reported the first perovskite material ($CH_3NH_3PbBr_3$ and $CH_3NH_3PbI_3$) used as a sensitizer in photoelectrochemical cells. The cell consists of mesoporous TiO_2 film having 8–12 μm thickness, iodide/triiodide redox couple liquid electrolyte and platinum counter electrode. The band gap $CH_3NH_3PbBr_3$ is 1.78 eV and that of $CH_3NH_3PbI_3$ is 1.55 eV. They have reported that the solar cells using $CH_3NH_3PbBr_3$ and $CH_3NH_3PbI_3$ sensitizers exhibit the efficiencies of 3.13 and 3.81%, respectively. TiO_2 sensitized with orthorhombic $(CH_3CH_2NH_3)PbI_3$ has been reported by Im et al. [70] to have an optical band gap of 2.2 eV. The cell using the $(CH_3CH_2NH_3)PbI_3$ sensitizer and the electrolyte with the iodide/triiodide redox mediator exhibits an efficiency of 2.4%. Based on the work done by Kojima et al. [73], Im et al. [74] have investigated the effect of TiO_2 film thickness on perovskite photovoltaic performance. The cell with 8.6 μm thick TiO_2 film exhibits an efficiency of 3.37% comparable with that of Kojima et al. [73]. The performance of the cell increases when the TiO_2 film thickness decreases. The cell with 3.6 μm thick TiO_2 film exhibits an efficiency of 6.2%. Unfortunately, the cell exhibited poor stability due to perovskite decomposition and degraded within minutes. In 2012, the stability of $CH_3NH_3PbI_3$-sensitized solar cell over 500 h has been reported by Kim et al. [72]. They have substituted the liquid electrolyte that was previously tried by Kojima et al. [73] with a solid state hole transport layer (*spiro*-MeOTAD). Their results also support the work done by Im et al. [74] where the efficiency of the cell increased with the decrease of TiO_2 thickness and the highest efficiency of 9.7% observed for the cell having TiO_2 thickness of 0.6 μm. Based on the impedance spectroscopy results, they found that the dark current and electron transport resistance increased with the increase in TiO_2 film thickness. Koh et al. [71] have synthesized a novel $(NH_2CH{=}NH_2)PbI_3$ perovskite with an energy band gap of 1.47 eV. Although the band gap of $(NH_2CH{=}NH_2)PbI_3$ is smaller compared to that of $CH_3NH_3PbI_3$, the efficiency of the cell is only 4.3%. The low efficiency is attributed to the energy level mismatch between TiO_2 and the perovskite. The working mechanism of the above perovskite photovoltaics is expected to be similar to DSSC (**Figure 12a**) where the perovskite absorbs light, injects electrons to the CB of TiO_2 and holes to the solid state hole transport material (HTM).

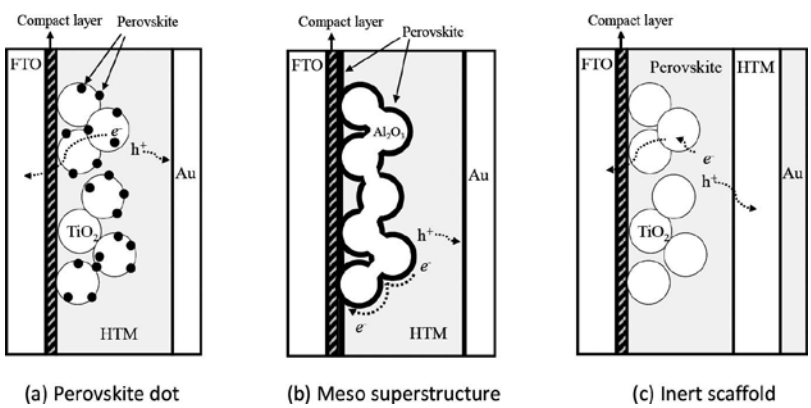

Figure 12. Mesoporous structure of perovskite solar cell. (a) Perovskite dot: the structure is similar to DSSC. (b) Meso superstructure: the CB of the oxide semiconductor used is higher than the perovskite material and its surface is coated completely. (c) Inert scaffold: the perovskite fills the pores and makes a thin layer on the top of TiO_2.

Lee et al. [75] have constructed a meso superstructure (**Figure 12b**) of an organometal halide perovskite solar cell. This structure can be obtained by controlling the perovskite precursor concentration. The cell consists of mesoporous n-type TiO_2, $CH_3NH_3PbI_3Cl$ and p-type *spiro*-OMeTAD hole conductor. The cell exhibited an efficiency of 7.6%. The efficiency was increased up to 10.9% with the substitution of TiO_2 with Al_2O_3. For the TiO_2 based perovskite solar cell, electrons in the $CH_3NH_3PbI_3Cl$ sensitizer is expected to be injected to the CB of TiO_2 and transported to the FTO electrode whereas holes will be transferred to the *spiro*-OMeTAD layer. In the case of Al_2O_3-based perovskite solar cell, electrons will be transferred through the perovskite because Al_2O_3 has a wider band gap (7–9 eV) and the CB of Al_2O_3 is higher than $CH_3NH_3PbI_3Cl$. This shows that the perovskite layer functions as an absorber and n-type component. The authors also reported that the electron diffusion through perovskite is faster than in TiO_2 and thus leads to a higher efficiency. The Mesoporous scaffold structure where the perovskite filled up the pores and formed a dense layer on top of mesoporous TiO_2 (**Figure 12c**) has been reported by Heo et al. [76]. For this structure, they have shown that the $CH_3NH_3PbI_3$ can act both as a light harvester and as a hole conductor which was also previously reported by Etgar et al. [77]. The excitation of $CH_3NH_3PbI_3$ produced excitons, which was then dissociated via electron injection at the $TiO_2/CH_3NH_3PbI_3$ interface. Injected electrons are transported to the FTO electrode through the TiO_2 network and holes are transported through perovskite to HTM and finally arrive at the Au electrode. The highest efficiency reported by Heo et al. [76] was 12% for the cell configuration of FTO/mesoporous TiO_2 layer/$CH_3NH_3PbI_3$/poly-triarylamine/Au. By blending TiO_2 nano-particles with nanorods, the efficiency increased up to 15% [78].

4.2. Planar structure

The planar perovskite solar cell architecture is similar to the mesoporous structure except for the mesoporous metal oxide.

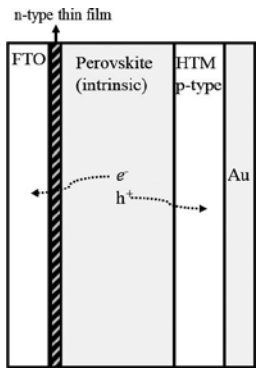

Figure 13. Planar structure of perovskite solar cell. No mesoporous structure involved.

Lee et al. [75] have shown that the perovskite photovoltaic system can still function without the non-blocking TiO_2 layer. Hence, the planar p-i-n and the p-n junction perovskite structures

are possible to construct. **Figure 13** shows an example of the p-i-n junction perovskite solar cell, which consists of an n-type compact metal oxide thin layer, intrinsic perovskite layer and p-type HTM layer. This structure has been demonstrated by Liu et al. [79] using n-type TiO_2 compact layer, perovskite $CH_3NH_3PbI_{3-x}Cl_x$ and p-type *spiro*-MeOTAD. They used vapour deposition technique to deposit the perovskite layer and reported an efficiency of 15%. Murugadoss et al. [80] have reported an efficiency of 8.38% for the $CH_3NH_3PbI_3$ perovskite solar cell using SnO_2 as the compact layer and the CuSCN as hole conductor. The first hole conductor free perovskite solar cell with an efficiency of 5.5% was reported by Etgar et al. [77]. The cell configuration was FTO/compact TiO_2/TiO_2 nanosheet/Perovskite/Au. A year later, the efficiency increased to 8% as reported by the same group after the TiO_2 nanosheet has been replaced with thinner TiO_2 film [81].

4.3. Lead free perovskite solar cell

Perovskite cells have shown a high efficiency of 21%. The perovskite material is very absorptive and moisture sensitive. The main problems are stability and lifetime. Perovskite solar cells are even less stable than organic polymer photovoltaics. Lead is also poisonous and has to be substituted by some other friendlier materials, like Sn. These are among the main challenges faced by researchers. The absorption of tin halide perovskite has been reported up to 1000 nm [82]. By partially substituting lead with tin ($CH_3NH_3Sn_xPb_{1-x}I_3$), the band gap can be reduced by increasing the Sn concentration. Hao et. al [83] has reported an efficiency of 7.37% for $CH_3NH_3Sn_{0.25}Pb_{0.75}I_3$ and 5.44% for $CH_3NH_3SnI_3$ perovskite solar cell. Germanium (Ge^{2+}) perovskites of the form, $CsGeX_3$ (X = Cl^-, Br^-, I^-) with a rhombohedral structure and *R*3*m* symmetry is another candidate for perovskite photovoltaics. However, the maximum efficiency of 3.2% is still far below the performance of $CH_3NH_3PbI_3$ perovskite. Orthorhombic $(C_4H_9NH_3)_2GeI_4$ is another variation of Ge-perovskite. This material shows a photoluminescence signal in the red. Stability is still an issue of concern.

5. Summary

The third-generation-sensitized solar cells have proved that they have the potential to compete with the conventional silicon based photovoltaics. The use of cheap materials with high performance make third-generation-sensitized solar cells a bright candidate as a future photovoltaic technology compared to other third-generation solar cells. The sensitized photovoltaic started with the emergence of DSSC using mesoporous nanocrystalline TiO_2 sensitized with the ruthenium based dye molecule. Since then, the molecular engineering of the dye molecules are extensively studied to improve the DSSC performance. The sensitizer used in the photovoltaic device evolved from organic (dye) to inorganic (quantum dot) and hybrid organic-inorganic (perovskite) sensitizer. The tuneable energy band gap of quantum dots enables them to produce multiple electron-hole pairs per photon. The progress in the performance of perovskite solar cells is very promising. In the beginning, the efficiency of the perovskite solar cell was less than 4%. The efficient reached around 20% within less than 10 years. However, the stability and toxicity issues of lead have to be solved before they can be

commercialized. Tin-based perovskite solar cell is already under investigation to replace the toxic lead.

Acknowledgements

Authors thank University of Malaya, Malaysian Ministry of Higher Education (MOHE) and Malaysian Ministry of Science, Technology and Innovation (MOSTI) for the UMRG grant no. RP003-13AFR, PRGS grant no. PR001-2014A and Science fund project no. 03-01-03-SF0995.

Author details

Muhammad Ammar Mingsukang, Mohd Hamdi Buraidah and Abdul Kariem Arof*

*Address all correspondence to: akarof@um.edu.my

Department of Physics, Faculty of Science, Centre for Ionics University of Malaya, University of Malaya, Kuala Lumpur, Malaysia

References

[1] Tributsch H: Reaction of excited chlorophyl molecules at electrodes and in photosynthesis. *Photochemistry and Photobiology* 1972, 16(4):261–269.

[2] Carlson DE, Wronski CR: Amorphous silicon solar cell. *Applied Physics Letters* 1976, 28(11):671–673.

[3] Fang J, Wu J, Lu X, Shen Y, Lu Z: Sensitization of nanocrystalline TiO_2 electrode with quantum sized CdSe and ZnTCPc molecules. *Chemical Physics Letters* 1997, 270(1–2): 145–151.

[4] Smestad GP, Gratzel M: Demonstrating electron transfer and nanotechnology: A natural dye-sensitized nanocrystalline energy converter. *Journal of Chemical Education* 1998, 75(6):752.

[5] Desilvestro J, Grätzel M, Kavan L, Moser J, Augustynski J: Highly efficient sensitization of titanium dioxide. *Journal of the American Chemical Society* 1985, 107(10):2988–2990.

[6] O'Regan' B, Grätzel M: A low-cost, high-efficiency solar cell based on dye-sensitized colloidal TiO_2 films. *Nature* 1991, 353(6346):737–740.

[7] Nazeeruddin MK, Kay A, Rodicio I, Humphry-Baker R, Mueller E, Liska P, Vlachopoulos N, Graetzel M: Conversion of light to electricity by cis-X2bis(2,2'-bipyridyl-4,4'-dicarboxylate)ruthenium(II) charge-transfer sensitizers (X = Cl^-, Br^-, I^-, CN^-, and SCN^-) on

nanocrystalline titanium dioxide electrodes. *Journal of the American Chemical Society* 1993, 115(14):6382–6390.

[8] Bryant G, Fergusson J, Powell H: Charge-transfer and intraligand electronic spectra of bipyridyl complexes of iron, ruthenium, and osmium. I. Bivalent complexes. *Australian Journal of Chemistry* 1971, 24(2):257–273.

[9] Nazeeruddin MK, Pechy P, Gratzel M: Efficient panchromatic sensitization of nanocrystalline TiO_2 films by a black dye based on a trithiocyanato-ruthenium complex. *Chemical Communications* 1997(18):1705–1706.

[10] Hagfeldt A, Grätzel M: Molecular photovoltaics. *Accounts of Chemical Research* 2000, 33(5):269–277.

[11] Nazeeruddin MK, Zakeeruddin SM, Humphry-Baker R, Jirousek M, Liska P, Vlachopoulos N, Shklover V, Fischer C-H, Grätzel M: Acid–base equilibria of (2,2′-bipyridyl-4,4′-dicarboxylic acid)ruthenium(II) complexes and the effect of protonation on charge-transfer sensitization of nanocrystalline titania. *Inorganic Chemistry* 1999, 38(26): 6298–6305.

[12] Islam A, Sugihara H, Singh LP, Hara K, Katoh R, Nagawa Y, Yanagida M, Takahashi Y, Murata S, Arakawa H: Synthesis and photophysical properties of ruthenium(II) charge transfer sensitizers containing 4,4′-dicarboxy-2,2′-biquinoline and 5,8-dicarboxy-6,7-dihydro-dibenzo[1,10]-phenanthroline. *Inorganica Chimica Acta* 2001, 322(1–2):7–16.

[13] Yanagida M, Yamaguchi T, Kurashige M, Hara K, Katoh R, Sugihara H, Arakawa H: Panchromatic sensitization of nanocrystalline TiO_2 with cis-bis(4-carboxy-2-[2′-(4′-carboxypyridyl)]quinoline)bis(thiocyanato-N)ruthenium(II). *Inorganic Chemistry* 2003, 42(24):7921–7931.

[14] He H, Gurung A, Si L: 8-Hydroxylquinoline as a strong alternative anchoring group for porphyrin-sensitized solar cells. *Chemical Communications* 2012, 48(47):5910–5912.

[15] Kay A, Graetzel M: Artificial photosynthesis. 1. Photosensitization of titania solar cells with chlorophyll derivatives and related natural porphyrins. *The Journal of Physical Chemistry* 1993, 97(23):6272–6277.

[16] Wang Z-S, Sayama K, Sugihara H: Efficient eosin Y dye-sensitized solar cell containing Br-/Br3-electrolyte. *The Journal of Physical Chemistry B* 2005, 109(47):22449–22455.

[17] Campbell WM, Jolley KW, Wagner P, Wagner K, Walsh PJ, Gordon KC, Schmidt-Mende L, Nazeeruddin MK, Wang Q, Grätzel M *et al*: Highly efficient porphyrin sensitizers for dye-sensitized solar cells. *The Journal of Physical Chemistry C* 2007, 111(32):11760–11762.

[18] Park JK, Lee HR, Chen J, Shinokubo H, Osuka A, Kim D: Photoelectrochemical properties of doubly β-functionalized porphyrin sensitizers for dye-sensitized nanocrystalline-TiO_2 solar cells. *The Journal of Physical Chemistry C* 2008, 112(42):16691–16699.

[19] Li L-L, Diau EW-G: Porphyrin-sensitized solar cells. *Chemical Society Reviews* 2013, 42(1): 291–304.

[20] Tan Q, Zhang X, Mao L, Xin G, Zhang S: Novel zinc porphyrin sensitizers for dye-sensitized solar cells: Synthesis and spectral, electrochemical, and photovoltaic properties. *Journal of Molecular Structure* 2013, 1035:400–406.

[21] Bessho T, Zakeeruddin SM, Yeh C-Y, Diau EW-G, Grätzel M: Highly efficient mesoscopic dye-sensitized solar cells based on donor–acceptor-substituted porphyrins. *Angewandte Chemie International Edition* 2010, 49(37):6646–6649.

[22] Eu S, Hayashi S, Umeyama T, Matano Y, Araki Y, Imahori H: Quinoxaline-fused porphyrins for dye-sensitized solar cells. *The Journal of Physical Chemistry C* 2008, 112(11):4396–4405.

[23] Jiao C, Zu N, Huang K-W, Wang P, Wu J: Perylene anhydride fused porphyrins as near-infrared sensitizers for dye-sensitized solar cells. *Organic Letters* 2011, 13(14):3652–3655.

[24] Wu C-H, Pan T-Y, Hong S-H, Wang C-L, Kuo H-H, Chu Y-Y, Diau EW-G, Lin C-Y: A fluorene-modified porphyrin for efficient dye-sensitized solar cells. *Chemical Communications* 2012, 48(36):4329–4331.

[25] Wang C-L, Chang Y-C, Lan C-M, Lo C-F, Wei-Guang Diau E, Lin C-Y: Enhanced light harvesting with [small pi]-conjugated cyclic aromatic hydrocarbons for porphyrin-sensitized solar cells. *Energy & Environmental Science* 2011, 4(5):1788–1795.

[26] Mathew S, Yella A, Gao P, Humphry-Baker R, CurchodBasile FE, Ashari-Astani N, Tavernelli I, Rothlisberger U, Nazeeruddin Md K, Grätzel M: Dye-sensitized solar cells with 13% efficiency achieved through the molecular engineering of porphyrin sensitizers. *Nature Chemistry* 2014, 6(3):242-247.

[27] Wang Z-S, Li F-Y, Huang C-H, Wang L, Wei M, Jin L-P, Li N-Q: Photoelectric conversion properties of nanocrystalline TiO_2 electrodes sensitized with hemicyanine derivatives. *The Journal of Physical Chemistry B* 2000, 104(41):9676–9682.

[28] Wang Z-S, Li F-Y, Huang C-H: Photocurrent enhancement of hemicyanine dyes containing RSO_3-group through treating TiO_2 films with hydrochloric acid. *The Journal of Physical Chemistry B* 2001, 105(38):9210–9217.

[29] Ehret A, Stuhl L, Spitler MT: Spectral sensitization of TiO_2 nanocrystalline electrodes with aggregated cyanine dyes. *The Journal of Physical Chemistry B* 2001, 105(41):9960–9965.

[30] Selopal GS, Wu H-P, Lu J, Chang Y-C, Wang M, Vomiero A, Concina I, Diau EW-G: Metal-free organic dyes for TiO_2 and ZnO dye-sensitized solar cells. *Scientific Reports* 2016, 6:18756.

[31] Tian H, Yang X, Chen R, Pan Y, Li L, Hagfeldt A, Sun L: Phenothiazine derivatives for efficient organic dye-sensitized solar cells. *Chemical Communications* 2007(36):3741–3743.

[32] Marszalek M, Nagane S, Ichake A, Humphry-Baker R, Paul V, Zakeeruddin SM, Gratzel M: Tuning spectral properties of phenothiazine based donor-[small

pi]-acceptor dyes for efficient dye-sensitized solar cells. *Journal of Materials Chemistry* 2012, 22(3):889–894.

[33] Wang ZS, Cui Y, Hara K, Dan-oh Y, Kasada C, Shinpo A: A high-light-harvesting-efficiency coumarin dye for stable dye-sensitized solar cells. *Advanced Materials* 2007, 19(8):1138–1141.

[34] Gerischer H, Lübke M: A particle size effect in the sensitization of TiO_2 electrodes by a CdS deposit. *Journal of Electroanalytical Chemistry and Interfacial Electrochemistry* 1986, 204(1):225–227.

[35] Vogel R, Pohl K, Weller H: Sensitization of highly porous, polycrystalline TiO_2 electrodes by quantum sized CdS. *Chemical Physics Letters* 1990, 174(3):241–246.

[36] Vogel R, Hoyer P, Weller H: Quantum-sized PbS, CdS, Ag_2S, Sb_2S_3, and Bi_2S_3 particles as sensitizers for various nanoporous wide-bandgap semiconductors. *The Journal of Physical Chemistry* 1994, 98(12):3183–3188.

[37] Liu D, Kamat PV: Photoelectrochemical behavior of thin cadmium selenide and coupled titania/cadmium selenide semiconductor films. *The Journal of Physical Chemistry* 1993, 97(41):10769–10773.

[38] Ren Z, Wang J, Pan Z, Zhao K, Zhang H, Li Y, Zhao Y, Mora-Sero I, Bisquert J, Zhong X: Amorphous TiO_2 buffer layer boosts efficiency of quantum dot sensitized solar cells to over 9%. *Chemistry of Materials* 2015, 27(24):8398–8405.

[39] Yang J, Wang J, Zhao K, Izuishi T, Li Y, Shen Q, Zhong X: CdSeTe/CdS type-I core/shell quantum dot sensitized solar cells with efficiency over 9%. *The Journal of Physical Chemistry C* 2015, 119(52):28800-28808.

[40] Lee H, Leventis HC, Moon S-J, Chen P, Ito S, Haque SA, Torres T, Nüesch F, Geiger T, Zakeeruddin SM *et al*: PbS and CdS quantum dot-sensitized solid-state solar cells: "old concepts, new results". *Advanced Functional Materials* 2009, 19(17):2735–2742.

[41] Chang C-H, Lee Y-L: Chemical bath deposition of CdS quantum dots onto mesoscopic TiO_2 films for application in quantum-dot-sensitized solar cells. *Applied Physics Letters* 2007, 91(5):053503.

[42] Nozik AJ: Exciton multiplication and relaxation dynamics in quantum dots: Applications to ultrahigh-efficiency solar photon conversion. *Inorganic Chemistry* 2005, 44(20): 6893–6899.

[43] Lee Y-L, Lo Y-S: Highly efficient quantum-dot-sensitized solar cell based on co-sensitization of CdS/CdSe. *Advanced Functional Materials* 2009, 19(4):604–609.

[44] Hanna MC, Nozik AJ: Solar conversion efficiency of photovoltaic and photoelectrolysis cells with carrier multiplication absorbers. *Journal of Applied Physics* 2006, 100(7):074510.

[45] Jun HK, Careem MA, Arof AK: Quantum dot-sensitized solar cells—perspective and recent developments: A review of Cd chalcogenide quantum dots as sensitizers. *Renewable and Sustainable Energy Reviews* 2013, 22:148–167.

[46] Peter LM: The Grätzel cell: Where next? *The Journal of Physical Chemistry Letters* 2011, 2(15):1861–1867.

[47] Rhee JH, Chung C-C, Diau EW-G: A perspective of mesoscopic solar cells based on metal chalcogenide quantum dots and organometal-halide perovskites. *NPG Asia Mater* 2013, 5:e68.

[48] Yu-Jen S, Yuh-Lang L: Assembly of CdS quantum dots onto mesoscopic TiO_2 films for quantum dot-sensitized solar cell applications. *Nanotechnology* 2008, 19(4):045602.

[49] Barcelo I, Campina JM, Lana-Villarreal T, Gomez R: A solid-state CdSe quantum dot sensitized solar cell based on a quaterthiophene as a hole transporting material. *Physical Chemistry Chemical Physics* 2012, 14(16):5801–5807.

[50] Shen X, Jia J, Lin Y, Zhou X: Enhanced performance of CdTe quantum dot sensitized solar cell via anion exchanges. *Journal of Power Sources* 2015, 277:215–221.

[51] McElroy N, Page RC, Espinbarro-Valazquez D, Lewis E, Haigh S, O'Brien P, Binks DJ: Comparison of solar cells sensitised by CdTe/CdSe and CdSe/CdTe core/shell colloidal quantum dots with and without a CdS outer layer. *Thin Solid Films* 2014, 560:65–70.

[52] Yu X-Y, Lei B-X, Kuang D-B, Su C-Y: Highly efficient CdTe/CdS quantum dot sensitized solar cells fabricated by a one-step linker assisted chemical bath deposition. *Chemical Science* 2011, 2(7):1396–1400.

[53] Wang Y, Hou Y, Tang A, Feng B, Li Y, Liu J, Teng F: Synthesis and optical properties of composition-tunable and water-soluble $Zn_xCd_{1-x}Te$ alloyed nanocrystals. *Journal of Crystal Growth* 2007, 308(1):19–25.

[54] Bailey RE, Nie S: Alloyed semiconductor quantum dots: Tuning the optical properties without changing the particle size. *Journal of the American Chemical Society* 2003, 125(23): 7100–7106.

[55] Badawi A, Easawi K, Al-Hosiny N, Abdallah S: Alloyed $CdTe_{0.6}S_{0.4}$ quantum dots sensitized TiO_2 electrodes for photovoltaic applications. *Materials Sciences and Applications* 2014, 5(1):6.

[56] Yang S-m, Huang C-h, Zhai J, Wang Z-s, Jiang L: High photostability and quantum yield of nanoporous TiO_2 thin film electrodes co-sensitized with capped sulfides. *Journal of Materials Chemistry* 2002, 12(5):1459–1464.

[57] Liu Z, Miyauchi M, Uemura Y, Cui Y, Hara K, Zhao Z, Sunahara K, Furube A: Enhancing the performance of quantum dots sensitized solar cell by SiO_2 surface coating. *Applied Physics Letters* 2010, 96(23):233107.

[58] Jun HK, Careem MA, Arof AK: A suitable polysulfide electrolyte for CdSe quantum dot-sensitized solar cells. *International Journal of Photoenergy* 2013, 2013:10.

[59] Shalom M, Dor S, Rühle S, Grinis L, Zaban A: Core/CdS quantum dot/shell mesoporous solar cells with improved stability and efficiency using an amorphous TiO_2 coating. *The Journal of Physical Chemistry C* 2009, 113(9):3895–3898.

[60] Lee Y-L, Chang C-H: Efficient polysulfide electrolyte for CdS quantum dot-sensitized solar cells. *Journal of Power Sources* 2008, 185(1):584–588.

[61] Park S, Son M-K, Kim S-K, Jeong M-S, Prabakar K, Kim H-J: The effects of electrolyte additives on the cell performances of CdS/CdSe quantum dot sensitized solar cells. *Korean Journal of Chemical Engineering* 2013, 30(11):2088–2092.

[62] Duan J, Tang Q, Sun Y, He B, Chen H: Solid-state electrolytes from polysulfide integrated polyvinylpyrrolidone for quantum dot-sensitized solar cells. *RSC Advances* 2014, 4(105):60478–60483.

[63] Duan J, Tang Q, He B, Chen H: All-solid-state quantum dot-sensitized solar cell from plastic crystal electrolyte. *RSC Advances* 2015, 5(42):33463–33467.

[64] Chen H-Y, Lin L, Yu X-Y, Qiu K-Q, Lü X-Y, Kuang D-B, Su C-Y: Dextran based highly conductive hydrogel polysulfide electrolyte for efficient quasi-solid-state quantum dot-sensitized solar cells. *Electrochimica Acta* 2013, 92:117–123.

[65] Kim H, Hwang I, Yong K: Highly durable and efficient quantum dot-sensitized solar cells based on oligomer gel electrolytes. *ACS Applied Materials & Interfaces* 2014, 6(14): 11245–11253.

[66] Yu Z, Zhang Q, Qin D, Luo Y, Li D, Shen Q, Toyoda T, Meng Q: Highly efficient quasi-solid-state quantum-dot-sensitized solar cell based on hydrogel electrolytes. *Electrochemistry Communications* 2010, 12(12):1776–1779.

[67] Radich JG, Dwyer R, Kamat PV: Cu_2S reduced graphene oxide composite for high-efficiency quantum dot solar cells. Overcoming the redox limitations of S2–/Sn2– at the counter electrode. *The Journal of Physical Chemistry Letters* 2011, 2(19):2453–2460.

[68] Meng K, Chen G, Thampi KR: Metal chalcogenides as counter electrode materials in quantum dot sensitized solar cells: A perspective. *Journal of Materials Chemistry A* 2015, 3(46):23074–23089.

[69] Yin X, Que W, Fei D, Xie H, He Z: Effect of TiO_2 shell layer prepared by wet-chemical method on the photovoltaic performance of ZnO nanowires arrays-based quantum dot sensitized solar cells. *Electrochimica Acta* 2013, 99:204–210.

[70] Im J-H, Chung J, Kim S-J, Park N-G: Synthesis, structure, and photovoltaic property of a nanocrystalline 2H perovskite-type novel sensitizer $(CH_3CH_2NH_3)PbI_3$. *Nanoscale Research Letters* 2012, 7(1):1–7.

[71] Koh TM, Fu K, Fang Y, Chen S, Sum TC, Mathews N, Mhaisalkar SG, Boix PP, Baikie T: Formamidinium-containing metal-halide: An alternative material for near-IR absorption perovskite solar cells. *The Journal of Physical Chemistry C* 2014, 118(30):16458–16462.

[72] Kim H-S, Lee C-R, Im J-H, Lee K-B, Moehl T, Marchioro A, Moon S-J, Humphry-Baker R, Yum J-H, Moser JE *et al*: Lead iodide perovskite sensitized all-solid-state submicron

thin film mesoscopic solar cell with efficiency exceeding 9%. *Scientific Reports*. 2012; 2: 591.

[73] Kojima A, Teshima K, Shirai Y, Miyasaka T: Organometal halide perovskites as visible-light sensitizers for photovoltaic cells. *Journal of the American Chemical Society* 2009, 131(17):6050–6051.

[74] Im JH, Lee CR, Lee JW, Park SW, Park NG: 6.5% efficient perovskite quantum-dot-sensitized solar cell. *Nanoscale* 2011, 3: 4088–4093

[75] Lee MM, Teuscher J, Miyasaka T, Murakami TN, Snaith HJ: Efficient hybrid solar cells based on meso-superstructured organometal halide perovskites. *Science* 2012, 338(6107):643–647.

[76] Heo JH, Im SH, Noh JH, Mandal TN, Lim C-S, Chang JA, Lee YH, Kim H-j, Sarkar A, Nazeeruddin MK *et al*: Efficient inorganic-organic hybrid heterojunction solar cells containing perovskite compound and polymeric hole conductors. *Nat Photon* 2013, 7(6): 486–491.

[77] Etgar L, Gao P, Xue Z, Peng Q, Chandiran AK, Liu B, Nazeeruddin MK, Grätzel M: Mesoscopic $CH_3NH_3PbI_3/TiO_2$ heterojunction solar cells. *Journal of the American Chemical Society* 2012, 134(42):17396–17399.

[78] Islam N, Yang M, Zhu K, Fan Z: Mesoporous scaffolds based on TiO_2 nanorods and nanoparticles for efficient hybrid perovskite solar cells. *Journal of Materials Chemistry A* 2015, 3(48):24315–24321.

[79] Liu M, Johnston MB, Snaith HJ: Efficient planar heterojunction perovskite solar cells by vapour deposition. *Nature* 2013, 501(7467):395–398.

[80] Murugadoss G, Kanda H, Tanaka S, Nishino H, Ito S, Imahori H, Umeyama T: An efficient electron transport material of tin oxide for planar structure perovskite solar cells. *Journal of Power Sources* 2016, 307:891–897.

[81] Laban WA, Etgar L: Depleted hole conductor-free lead halide iodide heterojunction solar cells. *Energy & Environmental Science* 2013, 6(11):3249–3253.

[82] Mitzi DB, Feild CA, Harrison WTA, Guloy AM: Conducting tin halides with a layered organic-based perovskite structure. *Nature* 1994, 369(6480):467–469.

[83] Hao F, Stoumpos CC, Chang RPH, Kanatzidis MG: Anomalous band gap behavior in mixed Sn and Pb perovskites enables broadening of absorption spectrum in solar cells. *Journal of the American Chemical Society* 2014, 136(22):8094–8099.

Chapter 3

Optoelectronics and Bio Devices on Paper Powered by Solar Cells

António T. Vicente, Andreia Araújo, Diana Gaspar,

Lídia Santos, Ana C. Marques, Manuel J. Mendes,

Luís Pereira, Elvira Fortunato and Rodrigo Martins

Additional information is available at the end of the chapter

http://dx.doi.org/10.5772/66695

Abstract

The employment of printing techniques as cost-effective methods to fabricate low cost, flexible, disposable and sustainable solar cells is intimately dependent on the substrate properties and the adequate electronic devices to be powered by them. Among such devices, there is currently a growing interest in the development of user-oriented and multipurpose systems for intelligent packaging or on-site medical diagnostics, which would greatly benefit from printable solar cells as their energy source for autonomous operation.

This chapter first describes and analyzes different types of cellulose-based substrates for flexible and cost effective optoelectronic and bio devices to be powered by printed solar cells. Cellulose is one of the most promising platforms for green recyclable electronics and it is fully compatible with large-scale printing techniques, although some critical requirements must be addressed. Paper substrates exist in many forms. From common office paper, to packaging cardboard used in the food industry, or nanoscale engineered cellulose (e.g. bacterial cellulose). However, it is the structure and content of paper that determines its end use. Secondly, proof-of-concept of optoelectronic and bio devices produced by inkjet printing are described and show the usefulness of solar cells as a power source or as a chemical reaction initiator for sensors.

Keywords: cellulose, optoelectronic and bio devices, paper characterization, inkjet printing, solar cells on paper substrates

1. Introduction

1.1. Printing technology

The e-market for flexible and printed large-area electronics is rapidly growing and it is expected to become a $69 billion market in the next 10 years [1]. The growth is manly supported by the organic light-emitting diodes (OLEDs) and conductive ink industries. Nevertheless, as technology emerges from R&D, new market opportunities with huge growth potential will appear. Two potential markets are the food and health. These industries are facing a paradigm shift as society demands more regulation, quality control, and smart systems to improve life quality while being environmentally friendly and allowing continuous user interface. Printed electronics can be the key to address such demands by imparting products with solutions to acquire, store, and transfer data, communicate and carry out logic functions to take decisions, where recyclability and low cost are key vectors [2].

Printing technologies enable electronics to be readily integrated as a part of other printed media by processing them in the same press. This renders possible low cost products such as radio frequency identification (RFID), intelligent packaging, food quality control devices, or disposable diagnostic kits. Functionality and performance of printed electronics are not intended to compete with silicon-based electronics, nevertheless, mass-printing methods offers economic advantages for large-scale production of appropriate products. Printing technology is highly customizable, it is compatible with the preferable fabrication method in industry—the roll-to-roll (R2R)—does not require large vacuum chambers and has lower capital investment costs when compared with other production methods. It is estimated that a printed electronics facility will cost 100 times less than a conventional silicon electronics plant.

There are various printing techniques, such as inkjet, screen, flexography, gravure, or offset printing, and their features expand the range of applications. The selection of the printing method is dictated either by the requirements concerning printed films or the level of printing system complexity. In the field of electronics, printing techniques are used to apply coatings, to deposit precise patterning, or even to develop microstructures [3]. Inkjet printing patterns material by expelling from the nozzle one picoliter droplet of ink at a time, as the printhead moves over the substrate. It is a method suitable for low-viscosity inks (1–20 cP). Screen printing is a highly versatile technique given its simplicity and reproducibility. To print, a squeegee transfers the ink through a patterned screen onto a substrate. Gravure (or rotogravure), flexography, and offset printing use a rotary printing press. Gravure printing is the most popular process for flexible packaging manufacturing and it consists in applying ink to an engraved cylinder, which is then transferred (directly, or indirectly through a transfer roll) to the substrate. The flexographic technique prints on flexible substrates by ink transfer (with low viscosity, 50–500 cP) from a laser-etched flexible relief plate. Offset printing is the preferable method for newspaper printing. It works on the principle of oil and water repulsion. A plate is damped first in water (nonimage area) and then ink (image area); the ink adheres to the print area, then it is transferred to a rubber blanket and from it to the paper.

http://dx.doi.org/10.5772/66695

1.2. Paper electronics and its thermal management

Electronic devices fabricated on plastics are currently a booming field of research [4–10]. Polyethylene naphthalate (PEN) and polyethylene terephthalate (PET) foils are the most used substrates for printed electronics, because of their high smoothness and good electrical and barrier properties [11, 12]. Physical properties, such as roughness, absorptive capacity, temperature resistance, and flexibility, are also critical. PET foil meets most of these requirements but PEN is also an interesting option given its greater dimensional and thermal stability [13]. PI (polyimide, named Kapton) is another widely used polymeric substrate for flexible thin film solar cells, due to its remarkable chemical and thermal robustness (withstands up to 300–400°C) and bendability [14]. Nonetheless, for low-cost devices, the price of these synthetized materials can be high and its use is ecologically questionable, since they are not biodegradable and are produced from oil-based raw materials.

On the other hand, paper is potentially useful for some specific applications and markets, such as those already mentioned of intelligent packaging and diagnostic kits [15], where low cost (€0.001 dm^{-2} compared with €25 dm^{-2} for silicon or €1–10 dm^{-2} for polymer substrates) and sustainability are highly desirable. Cellulose is the most abundant natural biopolymer on earth, which is recyclable, biodegradable, as well as nontoxic. It is a carbohydrate polymer made up of repeating β-D-glucopyranose units and consists of three hydroxyl groups per anhydroglucose unit (AGU), giving the cellulose molecule a high degree of functionality. The knowledge of the molecular structure of cellulose is of prime importance as it explains the characteristic properties of cellulose, such as hydrophilicity, chirality, biodegradability, and high functionality [16], which are key factors as far as device feasibility is concerned.

Cellulose fibers have remarkable properties, in particular their thermal and mechanical dimensional stability when compared to plastics, for instance. This is of particular interest if alignment is required when printing different functional materials on top of paper substrates. Paper is commonly used as a dielectric for capacitors [17] and supercapacitors [18], as permeable membranes in liquid electrolyte batteries [19, 20], or just as the physical support of energy storage devices [21], as an organic thin film transistor (OTFTs) [22], printed sensors, and RFID tags [23], printed batteries [24], inorganic powder electroluminescence devices [25], foldable printed circuit boards [26], oxide TFTs [27], and flexible low-voltage electric double-layer TFTs [28].

Many end-user devices will then require power sources, either to display information, integration with other devices, or simply to improve their processing capabilities and complexity. Though recent advances in paper batteries aim to suppress those power requirements, full autonomy can only be achieved by coupling a power generator, such as a solar cell. Hence, one can envision the interconnection of several paper functionalities, to accomplish self-sufficient electronic intelligent paper, or enable disposable sensors of complex laboratory functions (lab-on-chip), as seen in **Figure 1**.

Nevertheless, the substrate requirements for printed electronics are much more demanding than for image printing, hence cellulose substrates have numerous challenges. Homogenous,

pinhole-free layers are essential to ensure the desired functionality of the deposited layers, and conventional paper substrates present limitations such as roughness on a length scale of micrometers, porosity, and hydrophilic characteristics. Research has focused on modifying papers for the specific requirements of printed electronics and the paper surface can be modified in a thermal-mechanical manner (i.e., calendered or coated). Normally, the coatings consist of pigments and binders in an aqueous dispersion. However, rendering paper a suitable substrate for active materials can be expensive and may require materials and techniques that are neither cheap nor environmentally friendly [29, 30], diluting the advantage of using a paper substrate over plastic foils for mass production. Moreover, there are reports of chemical interaction/reaction with the selected coating, which degrades the electrical performance of the organic functional layer, as observed when printing PEDOT:PSS on paper [31]. This means that it is difficult to develop a coating, which is chemically compatible with all the inks required to print electronic devices based on organic materials. Another important aspect to consider is the process temperature of the functional materials being deposited on paper which must stay below 200°C in order to avoid cellulose degradation [32].

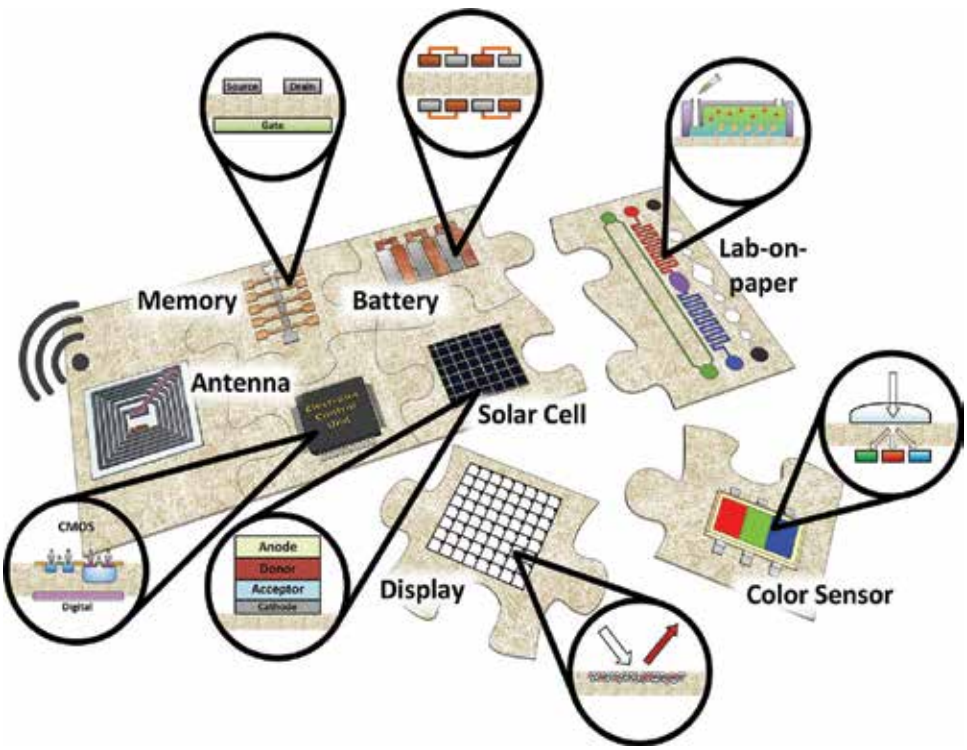

Figure 1. Concept of the multiple integration of devices built with or on paper to perform complex functions. A solar cell coupled with a battery assures full autonomy to a device that requires energy to perform logic operations at the electronic control unit (CMOS), given the signals received from the sensor unit, and then distributes the processed information to be saved in a papermemory or transmitted by an RFID antenna to another device. Other devices/functions can be added according to the final application, such as a display to visually convey messages to the user, or a lab-on-paper diagnostic device.

http://dx.doi.org/10.5772/66695

Though not always using printing deposition techniques, recently, some attempts envisaged to use paper in electronic applications to explore its potential as substrate for low-cost flexible devices [33, 34]. These can complement the functional inks, but their electric performance and stability hardly meet the requirements without specific deposition conditions and encapsulation [29, 35].

Electronics on paper has been investigated since the 1960s, when TFTs were deposited on paper substrates on a roll inside a vacuum chamber [36, 37]. The envisioned applications were flexible circuits for credit cards, electric sensors, toys, and hobby kits; but without any industrial or commercial success since the technology appeared during the boom of the silicon-based CMOS devices that fueled a revolution in the so-called information, communication and telecommunication (ICT) fields. Since then, research on paper-based field effect transistors (FETs) [38–42] has shown that paper could be used as an active component (dielectric). This has established a new approach to the challenge of *paper electronics*, where performance and stability issues are addressed using inorganic semiconductors, not requiring any special paper surface preparation nor device passivation. Likewise, devices with oxide functional materials can also benefit from the fact that cellulose is chemically more compatible with oxides than with many organic semiconductors [43], they bind properly at low temperatures and the natural porosity of paper can be explored in practical applications. Cellulose also provides a high surface area matrix for memories and sensors, for instance, as well as the capacity of electronic charge accumulation at the fiber surface for the integration of electronic components, as demonstrated by our recent research activity [41].

So far, some of the materials and techniques proposed to build electronic devices on paper are assumed to be compatible with low temperature processing and printing deposition. However, there are no reports yet of fully printed devices on paper that are 100% compatible with roll-to-roll processing. Thus, the solution for this challenge is not only the development of materials that can be printed at low temperatures but also to assure that their energy consumption is not high, so that the power sources to be used (solar cells, primary green batteries, and RF energy harvesting) can efficiently meet the energy needs of the device. The integration of multiple fabrication techniques can also maximize the device performance.

When developing electrical circuits, thermal and power dissipation issues, when a large number of electronic circuits/devices are integrated on an area of square millimeters, are another concern, particularly when using organic inks given their sensibility to temperature. Here, the supply voltage used, the overall current passing through the circuit, and the operating frequencies of such circuits are key factors. Resistors along the circuit are the main source of the heat generated and it corresponds to a bottleneck that forces the use of local heat sinks for enhanced dissipation. To overcome this limitation, paper electronics may not target complex and highly demanding applications but rather niche of low power and low frequency applications, where expected power generation remains very low. For instance, a reasonable target for printed paper electronics is to have no more than 10–50 transistors per cm^2, also because the integration density on paper is driven by the resolution of the printing/depositing processes (tens of microns), which are far lower than the traditional photolithography techniques used in the silicon microelectronic field (tens of nanometers).

Finally, contrary to plastic substrates, paper exhibits high dimensional stability over temperature, which is advantageous for electronic components by not introducing complex thermal parasitic effects in the electronic devices' behavior. For example, an optically transparent paper made of cellulose nanofibers has a coefficient of thermal expansion (CTE) of <8.5 ppm [44], which is much lower than plastic (PEN: 18–20 ppm; PET: 22–25 ppm). Besides, paper can also endure annealing cycles at 200°C for short time periods without any noticeable change in physical characteristics.

1.3. Solar-powered photovoltaic paper

The present development of photovoltaic (PV) devices allows the fabrication of solar cells on a wide variety of low-cost recyclable and disposable substrates such as paper, thereby extending PV, coupled with batteries, to a broad range of consumer-oriented portable applications where autonomous energy harvesting is needed (e.g., wearable PV, solar-powered intelligent packaging, internet-of-things systems).

Two main technological challenges can be identified in the field of PV on paper: (1) the requirement of solar cell (SC) fabrication processes employing low temperatures (below 150°C) and (2) the pronounced surface roughness of the fibrous paper structure, which can create defects in the cell layers and consequently deteriorate their electrical conduction. Such challenges are more relevant for inorganic (e.g., silicon, chalcopyrites, kesterites) based solar cells (given the high temperature, between 200°C and 300°C, typically used in the PECVD deposition of thin film silicon devices) and less crucial for organic or dye-sensitized–based cells as these devices can be processed without high temperature and by nonvacuum methods (e.g., screen printing, doctor blading, spin coating, spray deposition, electrochemical deposition) and their performance is more tolerant to the defect density [45], but at the same time more sensible to the substrate chemistry. Regardless of their lower environmental stability and power conversion efficiency, these PV materials are still considered the most suitable option for the development of printable solar cells [46] given their minimum detrimental impact on the cellulose substrate. Barr et al. successfully integrated solar cells directly onto as-purchased papers without pretreatment to fill interfiber spaces. The paper PV arrays produced more than 50 V, enough to power common electronic displays under ambient indoor lighting, and can be flexed and folded without loss of function [47].

Thin film hydrogenated amorphous silicon solar cells have been already successfully implemented on distinct types of cellulose-based substrates, such as liquid-packaging cardboard [48] and printing paper [49] with sunlight-to-electricity conversion efficiencies of 3–4%. This was attained by developing appropriate low-temperature PECVD processes and by coating the paper surface with a hydrophilic mesoporous layer. Such layer can, not only withstand the cells production temperature, but also provide adequate paper sealing and surface finishing for the cell's layers deposition. A key procedure performed in such works is the continuous monitoring of the substances released from the paper substrates during the cell deposition by mass spectrometry, which allows adapting the fabrication processes to mitigate any contamination from the substrate. Transfer printing or lamination is another class of methods that can also be adapted to inorganic and thin film solar cells. With these methods the cell layers are first deposited on a donor substrate, which is compatible with the optimal fabrication condi-

http://dx.doi.org/10.5772/66695

tions (usually high temperature and under vacuum), then they are detached from the original substrate and transferred to another receiver substrate (e.g., a flexible low-temperature tolerant platform such as paper) [50, 51]. For instance, a transfer printing method is applied in the work of Lee et al. where GaAs photovoltaic modules are transferred to a prestrained, structured substrate of PDMS with a power conversion efficiency (PCE) ≥20% [52]. A similar method was employed on cellulose nanocrystal (CNC) substrates to fabricate SCs with a PCE of 4.0% [53], and 5.9% on optimized transparent paper [54].

Another key point to take into account in the fabrication of solar cells on flexible substrates, such as paper, is the front illuminated contact. This transparent contact must be of particular high performance to realize efficient large-area (centimeters scale) devices. Such contact is conventionally composed of a transparent conductive metal oxide (TCO), but research on alternative and inexpensive methods is essential. Examples of such alternatives are metallic networks engineered by soft lithography, such as colloidal lithography or nano-imprint; and the production of conductive transparent paper, for instance by using cellulose nanofibers and printing silver nanowires[55]. The colloidal lithography approach has allowed engineering innovative ultrathin electrodes with a honeycomb lattice structure [56], known as micromesh electrodes (MMEs) [57, 58], which already shows transmittance (T ~91% in visible range) and sheet resistance (Rs ~6.2 Ohm/square) better than the state-of-the-art ITO (Rs ~10 Ohm/square and T ~90%) [59]. Besides, MMEs on flexible polyimide substrates were shown to remain invariant after 1000 cycles of repeat bending to a 2 mm bending radius [64]. As for the conductive paper using cellulose nanofibers and silver nanowires, it presents an optical transparency and electrical conductivity as high as those of ITO glass. The SCs fabricated on such conductive paper exhibited a PCE of 3.2% and generate electrical power even under and after folding.

Lastly, despite all the efforts on solar cell material optimization, efficiencies achieved so far are still considerably below the state-of-the-art (11–13%) on rigid (usually glass) substrates. Advanced light trapping methods employing wavelength-sized photonic structures are regarded as one of the most promising strategy to boost light absorption, allowing thickness reduction while keeping high efficiency [14, 45, 60, 61]. Optically thicker but physically thinner devices imply cheaper and faster fabrication, light-weight and improved flexibility which enables roll-to-roll fabrication on the flexible paper substrates. Besides, thickness reduction can lead to higher open-circuit voltages (and consequently efficiencies) due to lower bulk charge-carrier recombination [62, 63].

2. Cellulose substrates for electronic devices: characterization techniques and properties

Despite the technological applications of paper, there are few contributions regarding cellulose-based substrates characterization, and its applicability in electronic devices. The device and material requirements often limit the choice of the paper substrate, thus a complete understanding of its characteristics, namely, surface morphology, roughness, thermal sta-

bility, flexibility, mechanical strength, and hydrophobicity, is essential to assure the proper device operation.

Paper substrates are generally classified based on their weight or *grammage* and can be divided in three categories, following the suggestion of Tobjörk and Österbacka [43]: Light paper, whose *grammage* is in the range of 12–30 g m^{-2}, or for thickness below 75 μm; standard paper, such as office paper, which is around 80 g m^{-2} and 100 μm thick; and cardboard (or paperboard), when the *grammage* exceeds 200–800 g m^{-2}, or when the thickness is above 300 μm:

- **Light paper**. In this category, one can place two cellulose substrates that are attracting much attention in the recent years: bacterial cellulose (BC) and nanocrystalline cellulose (NCC).

Bacterial cellulose is a bacteria-produced biopolymer composed of ultrafine nanofibers (<100 nm wide); the major perks of this material, comparing to the nanocellulose obtained from wood, is its purity and crystallinity since it is free of lignin, hemicellulose, and other components present in the vegetable cellulose [64–66]. This material can be obtained from several cellulose-producing bacteria, such as *Gluconacetobacter genus, Agrobacterium tumefaciens*, bacteria of the genera *Pseudomonas*, among others; the cellulose is produced extracellularly since the bacteria excretes the cellulose into an aqueous culture medium, of low molecular weight sugars, directly as nanofibers, which form a porous three-dimensional nanocellulose mesh structure [67–69]. The grown layer is then harvested from the medium, cut and dried.

Nanocrystalline cellulose can be obtained primarily from cotton. NCC membranes are prepared through the acid hydrolysis of cellulose process [70]. Cotton is one of the purest cellulose sources, given its higher amount of cellulose (90 wt%), when compared with other vegetal sources that usually contain a mass fraction between 50 wt% (wood) and 80 wt% (flax or hemp) [40, 67, 71]. These membranes are highly transparent, lightweight, and have a smooth surface [40]. The flexibility of some NCC papers and the unique optical properties of nanocrystalline cellulose open a wide range of cost-efficient applications, for instance, smart labels, RFID, smart packaging, or even as support for bio-applications.

- **Standard paper**. There are countless types of paper in this category. The varieties here discussed are the most relevant for this chapter: commercial office paper (COP), raw paper (RP), the *Whatman* filter papers (WFP1 and 4), and the vegetable papers – parchment paper (PP) and tracing paper (TP), with thickness of 60, 135, 180, 205, 52, and 80 μm, respectively. The commercial office paper presented here is an 80 g m^{-2} *grammage* paper made from the Portuguese paper manufacturer the *Navigator* company. Raw paper (63 g m^{-2}) is fabricated by *Felix Schoeller Group*. The W*hatman* filter papers are used worldwide for chromatography and are a registered trademark of *GE Healthcare*. WFP1 and WFP4 *grammage* is 88 and 96 g m^{-2}, respectively. Parchment paper (41 g m^{-2}) is commonly used in baking as a disposable nonstick surface and the tracing paper studied here, with a *grammage* of 90 g m^{-2}, was provided by *Canson*, a manufacturer of fine art paper and is specially adapted to technical drawing.
- **Cardboard**. For this category, the paper studied is called liquid packaging cardboard (LPC) and it is produced by the Finnish company *Stora Enso* [72]. LPC is an aseptic and biodegradable

material widely used in the food packaging and beverage industry throughout the world. This material comprises three layers: the pressed cellulose fibers (cardboard, 240 g m^{-2}), an adhesive layer of low density polyethylene (LDPE, 12 g m^{-2}), and the aluminum sheet (6–7 mm). One major particularity is its robustness to withstand harsh environments, as evidenced by its use as substrate for solar cell deposited by plasma-enhanced chemical vapor deposition (PECVD) [48] and as an efficient surface-enhanced Raman spectroscopy (SERS) platform supporting metal nanoparticles arrays fabricated through thin film annealing [73].

Based on this classification, the following sections present a comprehensive characterization overview and comparison between paper samples of each category.

The assessment of the surface morphology of cellulose substrates can be achieved by scanning electron microscopy (SEM) [39], backed by three-dimensional (3D) profilometry [74] and AFM [38], to evaluate the paper surface, dimension of fibers, thickness, and porosity. Other techniques, such as X-ray diffraction (XRD) [40, 41], differential scanning calorimetry (DSC), thermogravimetric analysis measurements (TGA) [40, 41], and Fourier transform infrared (FTIR) spectroscopy [75, 76], provide information regarding the paper structure and contents. This information in turn can help to understand the optical properties (such as transmittance and haze factor), studied by spectrophotometry [40], or the electrical properties of the cellulose fibers and overall electrical behavior of the paper material. One method to study the electrical properties of cellulose is the fabrication of different transistors (with and on paper) [38–41, 74] and its analysis by impedance spectroscopy [38, 40, 41, 74].

2.1. Light paper

The X-ray diffraction (XRD) diffractogram (**Figure 2a**) provides information regarding the crystallinity index and crystallite size. Bacterial cellulose (BC) and cotton-based nanocrystalline cellulose (NCC) show the presence of characteristic cellulose type I, also defined as native cellulose, given the characteristic peaks at 2θ = 14.7°, 16.9° and 22.9° for BC and 14.7°, 16.8° and 22.7° for NCC. These cellulose type I peaks correspond to the $1\bar{1}0$, 110, and 002 crystallographic planes, respectively. The XRD patterns were collected from 10° to 90° (2θ), with a scanning step size of 0.016°, with a monochromatic CuKα radiation source (wavelength 1.540598 Å). The crystallinity index, I_C, was determined using the method proposed by Segal et al. [77]:

$$I_C = \frac{(I_{(002)} - I_{(\mathrm{am})})}{I_{(002)}} \times 100 \quad (1)$$

where $I_{(002)}$ is the maximum intensity of the diffraction of the (002) lattice peak, taken at a 2θ angle between 21° and 23°, and $I_{(\mathrm{am})}$ is the intensity of the diffraction of the amorphous regions, taken at the minimum on a 2θ angle range between 18° and 20° [40, 41].

The inexistence of lignin and hemicellulose in BC leads to a high crystallinity index (~92%) and a crystallite average size of 5.7 nm, higher than NCC which lies around 80% and has a crystallite average size of 7 nm.

Attenuated total reflectance-Fourier-transformed infrared (FTIR-ATR) spectroscopy provides information regarding the chemical species, chemical bonding state of cellulose, and to infer on the water content. Measurements were recorded using an attenuated total reflectance (ATR) sampling accessory (Smart iTR) with the following conditions: incident angle of 45°; 4000–650 cm^{-1} range; 4 cm^{-1} resolution; 32 scans; 20°C. The FTIR-ATR spectrum (**Figure 2b**) of BC and NCC resembles that typically obtained for plant-based cellulose and depicts the characteristic cellulose absorption peaks, i.e., hydrogen-bonded OH stretching at 3400 cm^{-1}, C–H and C–O stretching vibrations, 2900 and 1060 cm^{-1}, respectively. The O–H bending vibration assigned to the absorbed water is also observed with the presence of a peak at 1640 cm^{-1} [40].

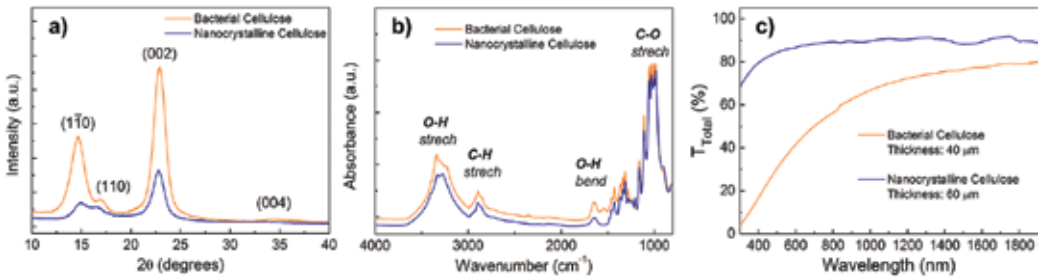

Figure 2. (a) XRD diffractogram of bacterial cellulose (BC) and cotton-based nanocrystalline cellulose (NCC) dried membranes; (b) FTIR spectrum of BC and NCC dried membranes; (c) total transmittance.

The BC membranes have a smooth structure of long entangled filaments of extruded cellulose fibrils with an average width of 20–100 nm (**Figure 3a**) and a surface *RMS* roughness in the order of 60 nm [68, 69, 78]. As for NCC, one can observe a smooth and compact morphology (**Figure 3b**) and also a needle-like structure in the cross-section inset.

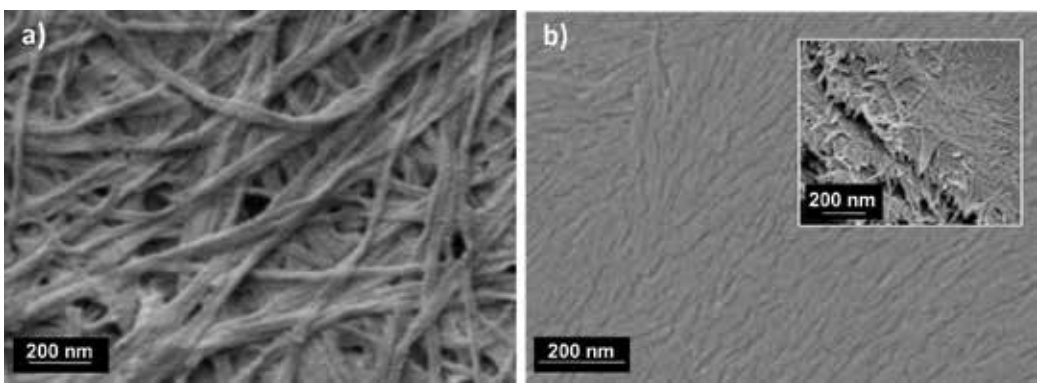

Figure 3. SEM micrograph of the surface morphology of (a) bacterial cellulose and (b) nanocrystalline cellulose membranes (NCC) produced by evaporation and the corresponding cross section (inset). Adapted from Gaspar et al. [40], with permission from IOP Publishing.

The low porosity, roughness in the order of nanometers, and high compactness of the cellulose fibers give these paper substrates a high contact angle (~95°C, accessed through 1 μL of deionized water droplet), which translates in a significant hydrophobicity that is beneficial to microfluidic devices [79], self-cleaning and to prevent the negative effects that the absorption of water can have on electronics devices.

2.2. Standard paper

The SEM micrographs in **Figure 4** show the morphology of the paper samples. COP has a high-density structure of intertwined cellulose fibers, with different shapes and sizes (some wider than 20 μm) and also calcium carbonate agglomerates. RP presents a similar structure and fibril size dispersion, without the presence of calcium carbonate agglomerates. As for the morphology of *Whatman* filter papers (WFP1 and 4), one can observe wide fibers (>20 μm) embedded in a matrix of small ones (<5 μm), whose concentration can be correlated to the intended filter permeability (**Figure 4c** and **d**). Both COP and RP have low porosity and high hydrophobicity (water-contact angle around 100°) when compared to WFP1 and 4 samples, which have a water-contact angle of <10°. The samples with the smoothest, more uniform, and compact surfaces are from parchment (PP) and tracing paper (TP), where the high concentration of small size fibers completely fills the gaps and surface between the larger fibers. The SEM for the PP samples (**Figure 4e**) shows a similar matrix structure of large and small fibers, with dimensions that can exceed 40 μm in width, embedded in a matrix of small ones (<5 μm) but the smoothest and most homogeneous surface is the TP substrate (**Figure 4f**).

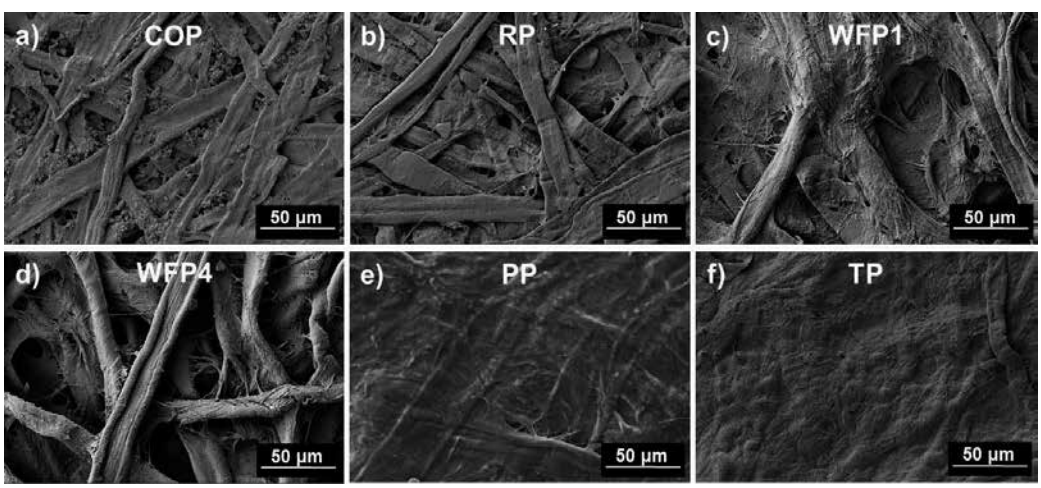

Figure 4. SEM micrographs of the six paper samples: (a) Commercial office paper (CPP), (b) raw paper (RP), (c) *Whatman* filter paper sample 1 (WFP1), (d) *Whatman* filter paper sample 4 (WFP4), (e) parchment paper (PP), and (f) tracing paper (TP).

Figure 5 gathers the 3D profilometry scans of the different paper substrates. As expected, given the fibers' width, the WFP1 and 4 have the surface with the highest root mean square (RMS), exceeding 12 µm. On the opposite side, the TP has the smoothest surface with *RMS* ~4 µm, while COP and RP have similar and slightly higher values of RMS (~5 µm). The COP paper is optimized for printing and therefore has a lower porosity and higher hydrophobicity (water contact angle of 101°) when compared to WFP (water contact angle of <10°), which is hydrophilic in nature, given the dimension of its fibers and high porosity. The high concentration of small size fibers, compactness, and smooth surface of the vegetable papers, PP and TP, also lead to high hydrophobicity (water contact angle of 124° and 95°, respectively).

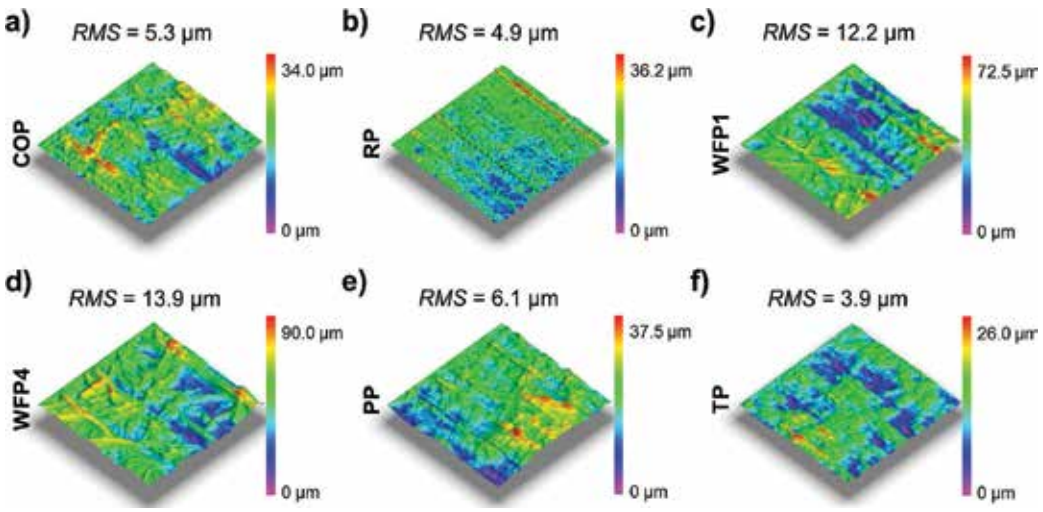

Figure 5. 3D profilometer on a 0.5 × 0.5 mm area of the six paper samples: shown in Figure 4: (a) CPP, (b) RP, (c) WFP1, (d) WFP4, (e) PP, and (f) TP.

The water content and its affinity to the paper substrate also plays an important role as a plasticizer or softening agent, thus influencing paper properties such as flexibility, elasticity, strength, and rigidity, which should be adjusted not only to the fabrication process, but also to the ink impregnation and overall printing quality. A low moisture content give rise to a hard and brittle paper, while a water content too high leads to creasing, delayed ink drying, and poor finish [80].

The analysis of XRD diffraction (**Figure 6a**) highlights the referred differences between COP and the other paper substrates. Besides the common $1\bar{1}0$, 110, and 200 crystallographic planes (respectively at 2θ = 14.7°, 16.8°, and 22.7°) associated to semicrystalline cellulose type I (also referred to as native cellulose), the XRD of COP reveals intense peaks between 28° and 50° related to the presence of calcium carbonate ($CaCO_3$) [41, 81]. Calcium carbonate and clay are typically present in paper manufacturing, either from pigments that are commonly used in papermaking or the water mineral content.

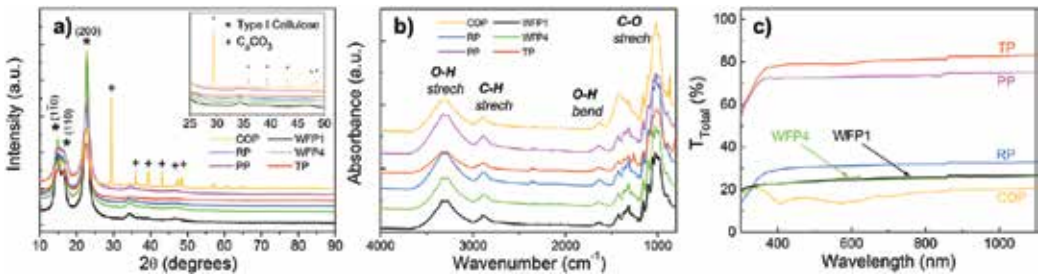

Figure 6. (a) XRD diffractogram of the different papers analyzed in Figures 4 and 5. All paper substrates present the $1\bar{1}0$, (110), and (002) diffraction peaks of cellulose I (native cellulose). COP also shows intense peaks associated with the presence of $CaCO_3$; (b) FTIR spectrum; (c) total transmittance as a function of wavelength.

In the FTIR-ATR spectra (**Figure 6b**), all samples reveal the bands associated to cellulose, such as OH, C–H, and C–O stretching bands, at 3400, 2900, and 1060 cm^{-1}, respectively. It is also observed a peak at 1640 cm^{-1} for the O–H bending vibration which corresponds to the absorbed water [40]. The 3600–3100 cm^{-1} broad band in the region provides information regarding the hydrogen bonds. The peaks from amorphous cellulose are sharper and have lower intensity, which can be correlated with the scission of the intra- and intermolecular hydrogen bonds [75]. Tracing paper is the sample with the most distinctive and low intensity OH stretch band.

Transmittance can also be an important characteristic of paper devices, for example, in OLEDs; the large optical haze is attractive for organic solar cells or in paper touchscreens to eliminate glare under direct light [44]. The total transmittance spectra of the different paper substrates are shown in **Figure 6c**. Tracing and parchment paper are the most translucid, although there is always a fraction of light that is transmitted regardless of the paper substrate. Scattered light is the main component of transmitted light, which translates in a high haze factor.

Information regarding thermal stability can be obtained by thermogravimetry and differential scanning calorimetry (TG-DSC) analysis (~7.5 mg of sample mass, heated at atmospheric pressure, from 25°C to 550°C with a heating rate of 5°C min^{-1}). Results show an initial weight loss (<10%), at temperatures close to 100°C, which corresponds to the desorption of free water from the cellulose fibers. Thermal degradation of cellulose, by depolymerization and the formation and evaporation of levoglucosan, or oxidative decomposition, occurs for temperatures above 300°C and is followed by a weight loss above 70%.

2.3. Cardboard

The liquid packaging cardboard characterization by SEM and 3D profilometry (**Figure 7**) reveals a continuous and crack-free aluminum foil, shaped to the cardboard roughness (*RMS* ~6 μm). As for TG-DSC analysis, published elsewhere [48], there are two endothermic peaks. The first peak, detected at 99.3°C with a weight loss of 6.6%, is related to the release of free water, and the second peak, at 353°C with weight loss of weight loss of 57.7%, is linked to

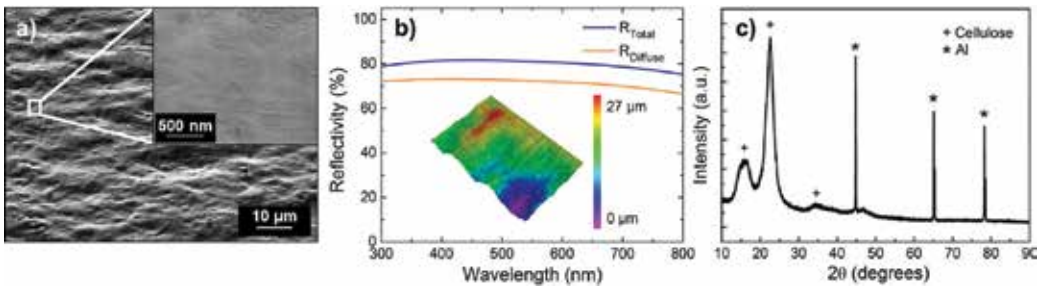

Figure 7. Surface characterization analysis of LPC. (a) SEM. Adapted from Araújo et al. [73], with permission from IOP Publishing. (b) Total and diffuse reflectivity in the visible region. The inset shows the 3D profilometer on a 3 × 2 mm area. Adapted from Vicente et al. [48], with permission from the Royal Society of Chemistry. (c) XRD diffractogram.

the cardboard and LDPE decomposition. It should also be noted that although the weight loss is negligible up to 250°C, the LDPE, responsible for the adhesion of the aluminum foil to the cardboard, starts to degrade at 200°C; thus, the substrate should be considered thermally stable up to 200°C in order to assure that the release of organic species will not influence the device fabrication.

3. Characteristics of electronic devices on paper

Although plasma-based processes, such as physical vapor deposition (PVD) and PECVD, may be relatively complicated and expensive in comparison to what is common in the graphics and printing industries (roll-to-roll), these techniques give rise to higher efficiency devices. Therefore, it is important to develop a better understanding of how these plasma processes can be applied and are influenced by paper substrates, so that a comparison can be established for the same devices produced with organic materials and printing techniques. As an example, in the more recent demonstrations of transistors on paper, there is still typically a trade-off between the transistor performance and its printability. While high-performance conventional silicon-based transistors have been attached to a silicon-coated paper substrate [34], screen printed silicon nanoparticle-based transistors on paper showed rather poor characteristics [82]. Laboratory scale techniques were also used when fabricating conventional organic field-effect transistors (OFETs) operating at high [22] or low voltages [83] on paper substrates, while simple electrochemical organic transistors operating at low voltages have been produced on polyethylene-coated paper [84] and on photo paper [85].

In this section, we provide examples of field effect transistors (FETs) fabricated on the studied substrates described in the previous section and highlight the impact cellulose has on the device properties (**Figure 8**). The transistor is one of the essential active components in electronics and its fabrication complexity makes it an ideal element to test the viability of paper electronics, and since it requires energy to operate, it is also an opportunity for solar power. In the specific case of FETs, paper is not only the support but also an active part of the device—the gate dielectric—according to the electric double layer (EDL) formation due to the mobile

protons within the cellulose matrix [39, 41, 86]. This cellulose role is similar to what happens in electric double-layer capacitors.

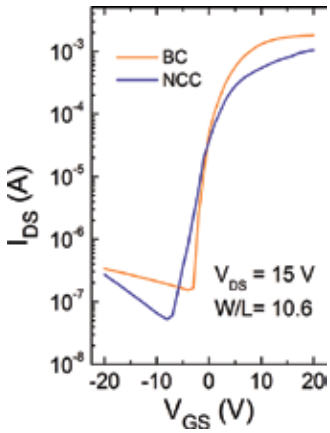

Figure 8. I_{DS}–V_{GS} transfer characteristics obtained at V_{DS} = 15 V for GIZO field effect transistors using bacterial cellulose (BC) and nanocrystalline cellulose (NCC) as gate dielectric.

The transistor fabrication comprises, on one side of the paper, a GIZO (Ga_2O_3-In_2O_3-ZnO) thin film, to create the channel region, followed by the Al e-beam evaporation of the source/drain electrodes (S/D). On the opposite side of the paper substrate, a conductive IZO (In_2O_3-ZnO) thin film is deposited by RF sputtering to work as gate electrode. To ensure the proper functioning, the devices were annealed in air for 30 min at 150°C.

The electronic performance of the BC-based FETs is similar to the FETs reported in the literature using commercial paper as dielectric, reaching a I_{ON}/I_{OFF} modulation ratio above 10^4, whereas NCC-based FETs show a saturation mobility above 7 $cm^2 V^{-1} s^{-1}$, and a I_{ON}/I_{OFF} modulation ratio higher than 10^5 [40].

The creation of the EDL depends on the mobile-free ions present in the paper matrix and fundamentally on the sorbed water within the paper. To infer the role of water content in the paper, due to humidity variations, and relate it with the performance of FETs, Fourier transform infrared (FTIR) spectroscopy was performed under normal atmosphere and in vacuum, for devices fabricated on tracing paper (TP).

In the FTIR-ATR spectra, the bands related to the adsorbed water are mainly located around 700 cm^{-1}, which corresponds to the out-of-plane vibrations of OH groups or to the rotational vibrations of H_2O molecules, whereas OH bending of adsorbed water is ascribed to the band observed at 1635 cm^{-1}. In order to assess the major differences among the samples, the spectra were normalized to the intensity of the 2900 cm^{-1} band, since it is not susceptible to variations in crystallinity or water content [69] (**Figure 9a**). The measurements taken for different vacuum times reveal that there is an abrupt decrease in intensity for the band at 1635 cm^{-1}. This observation is related to the structure compactness, whereas the more porous the structure, the more it facilitates adsorption and desorption of water.

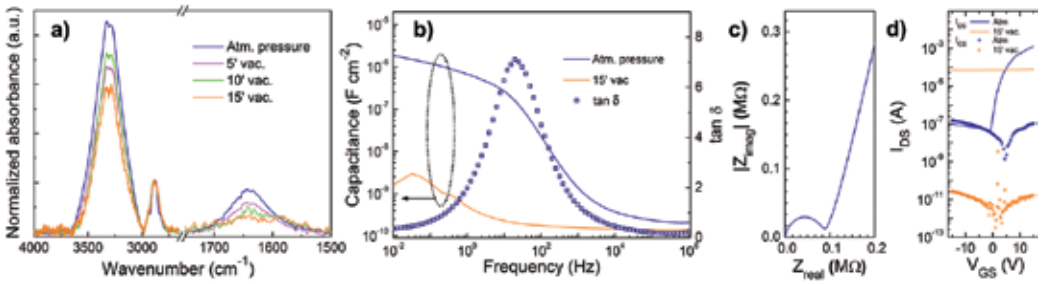

Figure 9. Correlation between electrical properties and water content variation for tracing paper (TP). (a) ATR-FTIR spectra of the water content variation (bands 3600–3000 cm^{-1} and 1635 cm^{-1}); (b) capacitance (C-f), and tan δ (tan δ-f) variation with frequency at atmospheric pressure and after 15 min of vacuum pumping; (c) high frequency region of the Cole-Cole plot; (d) transfer characteristics (V_{DS} = 15 V) of the paper gated GIZO FETs under atmospheric pressure and vacuum. Adapted from Gaspar et al. [74] Copyright Wiley-VCH Verlag GmbH & Co. KGaA. Reproduced with permission.

Water and mobile-free ions are intrinsically linked to EDL formation, when using paper as dielectric. To understand the role of ions and water, spectroscopic impedance can provide information of the paper electrical properties, namely, the capacitance variation with frequency (C-f) and bulk resistance (**Figure 9b**).

The C-f plot was determined between 10 mHz and 1 MHz using an AC excitation voltage of 500 mV [41]. In this frequency range, there is an increase in the capacitance for low frequencies, which is a typical behavior for the electrode polarization as a result of the interaction between the charged electrode surface with the free charges in the paper. For 10 mHz, the capacitance of TP is 1.8 μF cm^{-2}, and when submitted to vacuum, the capacitance decreases more than three orders of magnitude. This difference is explained by the sorbed water which is the main source of protons (H^+) and hydroxyls groups (OH^-) responsible for the behavior at lower frequencies. Drawing a parallel with FTIR-ATR results, it is possible to recognize the high susceptibility of the TP to the water variation content.

The loss tangent (tan δ) allows one to infer the relaxation frequency, by separating the contributions of the bulk material itself from the EDL regime. For high frequencies, the tan δ is low since there is no sufficient time for large dipole creation; whereas for low frequencies, the electric field action drives the ions to form the EDL, which in turn reduces tan δ [40]. The bulk resistance can also be determined from the impedance data through the Cole-Cole plot (**Figure 9c**), where the resistance of bulk material in parallel with the geometric capacitance describe a semicircle at high frequencies; the estimated resistivity for TP is 4.9 × 10^7 Ω cm. A possible explanation for this value relies in the amount of sorbed water, wherein a higher concentration can maximize the ability of free ions to migrate thought the paper matrix [41].

Regarding the other electrical properties of FETs, the saturation mobility on TP (μ_{SAT} = 2.3 cm^2 V^{-1} s^{-1}) is significantly lower compared to those fabricated on light paper (7 cm^2 V^{-1} s^{-1} for NCC).

http://dx.doi.org/10.5772/66695

Thus, the saturation mobility is intimately related to the density of the matrix and fraction of small fibers. The paper morphology also influences similarly the on/off current ratio (TP, $I_{on}/I_{off} = 2.5 \times 10^4$) and minimizes the gate leakage current (I_{GS}).

As for device properties, the FETs characteristics are directly affected by the decrease of water content within the paper bulk (**Figure 9d**). The susceptibility of TP to water loss, due to humidity changes, leads to no current modulation after 15 min of vacuum since the desorbed water does not allow the EDL formation. The compactness and smoothness of small fibers can give paper a higher ability to bind and retain water and ions, allowing the formation of EDLs at the interface of paper, thus enabling the semiconductor to operate under low humidity for a prolonged period [74].

4. Electrochromic devices on paper

The interest in electrochromic materials has grown from the mid-1980s, especially due to the application of these materials in smart windows for energy efficiency and indoor control [87, 88]. Nevertheless, new applications in the field of smart labels and displays have triggered the development of easier and cost-effective deposition processes that simultaneously allow patterning of the active area [89]. Inkjet printing is a good alternative for this purpose since it is processed at low temperatures, is a cost-effective technique, easily scalable for mass production, produces low waste, and can be adapted to different substrates and patterns. Nevertheless, this fabrication method can have some drawbacks as the quality of the deposited film is highly dependent on the ink characteristics, like viscosity and surface tension, combined with the printer specifications and surface properties of the paper substrate [90, 91]. So far, inkjet printed electrochromic films have been applied mostly to organic materials [92], but inorganic materials can also be easily adapted [93, 94].

An electrochemical device comprises two electrodes separated by an electrolyte, and paper can be a viable substrate to produce electrochromic displays as the next proof-of-concept shows. The electrodes are functionalized, by inkjet printing, with the electrochromic material, $WO_3 \cdot H_2O$, and at least one of the supports for the electrodes has to be fully transparent (window layer). In the case of the device shown here, liquid packaging cardboard (LPC) was used as the paper substrate and the transparent support is an ITO-coated PET substrate (for the sake of device operation and proper encapsulation), but nanocrystalline cellulose can be a viable alternative, given its high transparency and low sheet resistance of the TCOs deposited on its surface, as demonstrated by the good quality FETs fabricated on this substrate. The devices are assembled in a sandwich structure, where the ITO-coated PET/WO_3 and LPC/WO_3 are the working and counter electrodes, respectively, with the composite solid polymer electrolyte (fabricated according to Santos et al. [95]) in the middle and double-sided tape for encapsulation and spacing between electrodes. Potentiostat measurements characterize the electrochemical properties and colorimetric data studies the variations in color between different working stages.

Tungsten trioxide (WO_3) is a well-known inorganic electrochromic compound with a very high transmittance modulation, multiple oxidation states, and good cycle stability. The general reaction that describes its electrochromic behavior can be written as follows:

$$WO_3(\text{transparent/white}) + y\,M^+ + y\,e^- \Leftrightarrow M_y WO_3(\text{blue}) \quad (2)$$

The coloration occurs when the tungsten metallic center is reduced, by the application of an external potential, and a small cation ($M^+ = H^+$, Li^+, K^+,…) from the electrolyte intercalates into the material to compensate the charge insertion. The tungsten bronze (M_yWO_3) is then formed, showing the blue color in the electrode. Since this is a reversible process, when a potential with inversed polarity is applied, the reaction occurs in the opposite direction and the material returns to its initial state with a transparent/white color [89]. The full mechanism is still under discussion but the most accepted theory is explained by small polaron transitions for the amorphous material and *Drude*-like free electron scattering for crystalline. The major difference between these two mechanisms is the electron localization or delocalization:

$$W^{VI}O_3 + y\,M^+ + y\,e^- \Leftrightarrow M_y W_x^V W_{1-x}^{IV} O_3 \quad (3)$$

The x represents the number of W sites. However, at higher values of y the reaction gets irreversible and the tungsten bronze turns red or golden [96].

4.1. Liquid packaging cardboard (LPC) electrochromic device assessment

The crystallographic structure of the synthesized WO_3, analyzed by XRD (**Figure 10**), depicts a series of diffraction peaks that can be indexed to the reference pattern from the International Centre for Diffraction Data (ICDD) of the orthorhombic hydrated (or tungstic acid) WO_3 (*ortho*-$WO_3 \cdot H_2O$) with ICDD No. 01–084–0886. Tungstic acid is already known to have a good electrochromic behavior, which is dependent on both the hydration level and crystalline structure [97, 98]. In this work, the terminal W=O and W–H_2O bonds can increase the conduc-

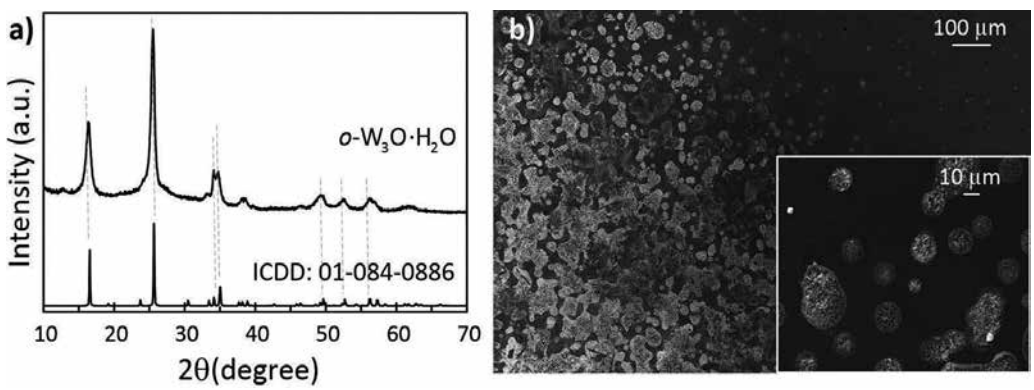

Figure 10. (a) XRD diffractogram of the $WO_3 \cdot H_2O$ deposited film and the corresponding reference ICDD pattern. (b) SEM images of the WO_3 inkjet printed pattern detail on ITO-coated PET substrate.

tivity and diffusion of Li^+ ions, whereas the crystalline structure should improve the stability of the film [99].

The ink produced has to meet the demands of the inkjet printer used. For that, the viscosity and surface tension were between 1.5–2 cP and 30–40 dyne cm^{-1}, respectively, while the filtration assured that the nozzles would not clog during printing. As expected, the printed pattern does not show a continuous film, but the eye resolution cannot detect these irregularities [94]. The patterns were defined as a square with 1 × 1 cm for the LPC and 0.5 cm diameter circle for the ITO-coated PET substrate. This design facilitates the alignment of both electrochromic layers upon encapsulation.

Usually, the coloration of electrochromic materials is studied by UV-Vis spectroscopy; however, due to the opacity of the LPC substrate, the different colors of the device were represented by the CIE 1931 *Yxy* diagram as recommended by the *Commission Internationale de L'Eclairage*. In the CIE diagram, the quantities x and y of Eq. (3) are represented by the two Cartesian coordinates represented and are obtained by analyzing the pictures in *ImageJ* software. The x–y coordinates for each colored and bleached state are represented inside the diagram depicted in **Figure 11a**. It can be observed that there is a notable color difference between the bleached and colored states, especially at −0.6 V, where the reaction becomes irreversible. As the potential increases, the y factor in Eq. (3) also increases and the Li^+ ions become trapped in the crystalline structure of the WO_3.

The electrochemistry of the reaction studied by cyclic voltammetry (**Figure 11b**), under the same potential range (0.3 to −0.3 V and 0.6 to −0.6 V), shows that coloration occurs when the voltage and current decrease until a minimum negative value while bleaching takes place when voltage and current reach a maximum and then stabilize. In this work the capacity of the films is almost ineligible but it can be explained by the small area of the film and consequently the low amount of WO_3 material. The low current and voltage required to govern the on/off stages of the electrochromic device can be easily met by the current state-of-the-art organic [55] and inorganic [48, 49] solar cells fabricated on paper.

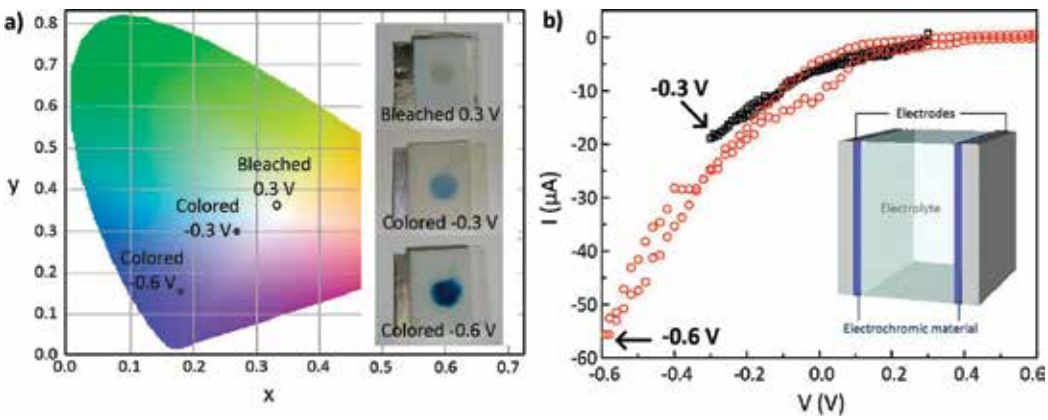

Figure 11. (a) *Yxy* chromaticity diagram for the bleached (0.3 V) and colored samples at both −0.3 and −0.6 V. (b) Cyclic voltammograms of the final devices with LPC/WO_3 and PET ITO/WO_3 electrodes in the potential ranges of 0.3 to −0.3 V and 0.6 to −0.6 V, at a scan rate of 10 and 50 mV s^{-1}, respectively. The inset illustrates the schematic representation of an electrochromic device.

5. Lab-on-paper devices

Lab-on-paper is a novel technology for fabricating simple, low-cost, portable, and disposable analytical devices holding great promise to aid global health, food quality control, and environmental monitoring [81, 100–105]. Lab-on-paper technology requires minimum fluid samples, compared to common devices, and the porous structure of the paper is solely responsible for fluid transportation. This is a crucial aspect of the diagnostic apparatus, since the substrate must facilitate the diffusion and flow of the solutions within the hydrophilic fiber matrix. The movement of fluids is governed by capillary forces, thus without the need for pumps or power [102, 103]. This technology was introduced in 2007 by Martinez et al. [106] as a method for patterning paper to create well-defined, millimeter-sized channels comprising hydrophilic paper bounded by hydrophobic polymer; but the first evidence of the lab-on-paper technology dates back to 1902 with a patent for paper strips impregnated with hydrophobic materials [107]. Earlier diagnostic applications of lab-on-paper comprise the detection of nickel and copper salt concentrations [108], determination of pH for water testing and biological analysis of urine and blood composition [109].

To date, researchers have been focused on adapting new developments in nanotechnology, biotechnology, and materials science to paper-based sensors. The production of practical analytical devices, based on those developments and by simple fabrication techniques, can have a positive impact for creating worldwide applications where they are most needed [100, 104, 106, 110, 111].

The fabrication of lab-on-paper devices starts by defining channels and reaction zones onto paper, in order to control the movement of liquids and to assure the confinement of different reagents. A wide range of diverse patterning techniques was already reported and can be divided in three major patterning principles: (i) physical blocking of pores in paper (e.g., photolithography [106], plotting [112], and laser treatment [113]); (ii) physical deposition of reagent on fiber surface (e.g., inkjet etching [114] and wax printing [104, 115]); and (iii) chemical modification of fiber surface (e.g., plasma treatment [116], inkjet printing [117], and silanization [118]). Each technique has its advantages and limitations which have to be taken under consideration according to the type of device, equipment available, material costs, and the intended application, among other factors.

5.1. Wax printing technology

Among the different patterning techniques, wax printing represents one of the most promising technology for paper patterning, given its simple and fast (5–10 min) fabrication process. The printing process uses a solid wax printer, in which the ink is supplied as solid wax and then melted, before being ejected from the print head, and once it rests on the paper surface it immediately solidifies. Since the wax remains only on the paper surface, the printed paper is then processed on a hot plate (120–140°C, 1–5 min; depending on the type of wax and paper) to allow the wax to diffuse vertically through the entire paper thickness, hence creating the hydrophobic barriers to confine the fluids (**Figure 12**). The wax is formulated from a nontoxic resin-based polymer, composed of a mixture of hydrophobic carbamates, hydrocarbons (e.g., paraffin), and dyes.

http://dx.doi.org/10.5772/66695

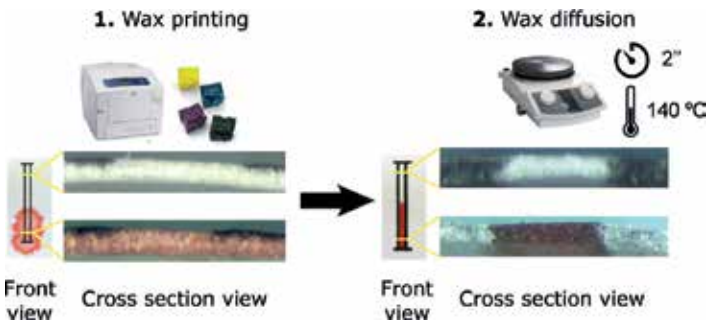

Figure 12. Schematic of the lab-on-paper technology process with wax printing: in the first step, a Xerox ColorQube printer, with solid ink (wax) cartridges, is used to print the sensor layout. The paper sheet is then processed in a hot plate (140°C, 2 min) for melting, in the second step. Digitalized images of the paper front view and the optical micrographs of the cross-section, before and after wax diffusion, show the behavior of the channel when a red dye solution is used and highlight the effect of the hydrophobic barriers. Adapted from Marques et al. [81].

5.2. Applications

The wax printing technology has already been successfully applied in the fabrication of colorimetric paper-based sensors for diagnostic and environmental applications, such as for glucose monitoring, based on enzymatic reactions [104], canine *leishmaniosis* detection through an immunoassay [104], tuberculosis detection by nucleic acid identification [100], and electrochemically active bacteria detection, based on electrochromic detection [81].

5.2.1. Glucose monitoring

Diabetes mellitus is a leading cause of illness and mortality worldwide and a major health problem for most developed societies. This metabolic disorder from insulin deficiency and hyperglycemia results in blood glucose concentrations higher or lower than the normal range (4.4–6.6 mM) [119, 120]. In developed countries where healthcare infrastructure is well established, self-monitoring of blood glucose levels is effective and economically accessible to the public. However, in many resource-limited countries the first priority is generally not given to diabetes care. Even widely used glucose meters and test strips are extremely expensive in those low-income regions; hence, there is an urgent need to develop a simple, low cost, disposable sensor that allows individuals in those countries to self-monitor their blood glucose level [121].

The work of Costa et al. [104] demonstrates how such blood glucose monitor can be fabricated on paper, as a 2D lateral flow device or as a 3D device, using the wax printing technology, for colorimetric analysis. The paper substrate used was *Whatman* filter paper n° 1 (WFP1), which is the most common paper for microfluidic devices. Briefly, the enzyme glucose oxidase (*GOx*) oxidizes glucose to D-glucono-δ-lactone and hydrogen peroxide. The enzyme peroxidase then reacts with the hydrogen peroxide and oxidizes the colorimetric indicators generating a visible color change, which is proportional to the initial amount of glucose in the sample.

Figure 13 illustrates the layers that comprise the paper-based biosensors and compares their sensibility for two different colorimetric indicators: AB (4-aminoantipyrine + 3,5-dichloro-2-hydroxy-benzenesulfonic acid) and KI (potassium iodide).

The 3D device shows important advantages compared to the 2D lateral flow sensor, given its higher coloration homogeneity. The 2D lateral flow sensor, on the other hand, is more subject to some carryover of the colored products that hinder the coloration intensity. This test runs in less than 5 min and a calibration color gradient scale can be printed directly on the paper device in order to compare with test results, allowing the patient to infer an approximate concentration of glucose in the sample. Eventually, a more complex device able to perform a wide range of analysis could take advantage of a solar cell to power sensors, a CMOS to perform logic calculations and a display to show information.

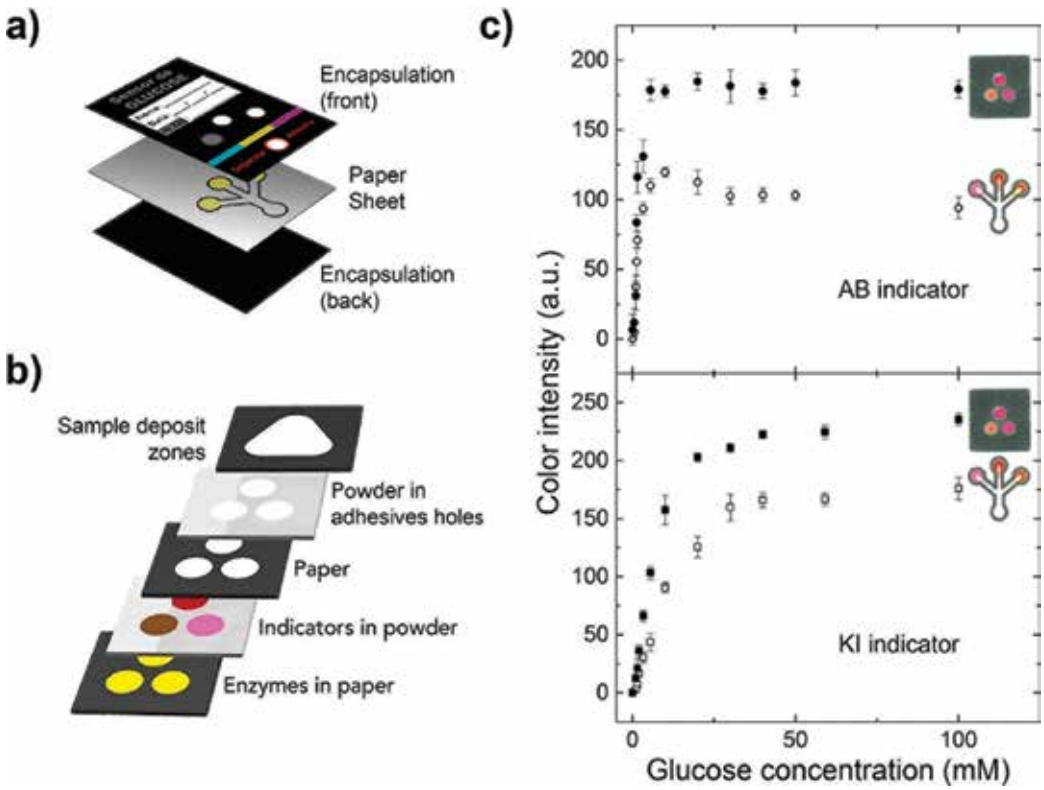

Figure 13. (a) Schematic representation of the 2D lateral flow device—enzyme and colorimetric indicators are deposited together. (b) Schematic representation of the 3D device. (c) Comparison between the 2D and 3D glucose sensors, when tested with increasing glucose concentrations (0.01–100 mM), with the graphical representations of the color intensity of detection zones containing the AB indicator (top) and the KI indicator (bottom). Adapted from Costa et al. [104], with permission from IOP Publishing.

5.2.2. Electrochemically active bacteria detection

Electrochemically active bacteria (EAB) have the ability to extracellularly transfer their electrons produced during microbial respiration [81, 122, 123]. This ability sparked interest given

http://dx.doi.org/10.5772/66695

the multiplicity of applications than can range from bioremediation to electricity production in microbial fuel cells. Although an increasing number of EAB have already been identified, isolated, and characterized, this number is still quite small regarding their ubiquity in the environment. This fact significantly constrains the fundamental knowledge about these bacteria and their role in the environment [81, 124]. To visually detect these bacteria, Marques et al. [81] developed a paper-based sensor, using common office paper (COP) as substrate and tungsten trioxide nanoparticles (WO_3 NPs) as the sensor layer (**Figure 14**), to successfully test the presence of electrochemically active *Geobacter sulfurreducens* DL-1 [125] cells (**Figure 14b**). The change in the WO_3 optical properties (between white and blue) occurs in the presence of EAB which triggers the electron-transfer (redox) process (bioelectrochromic response).

The hexagonal WO_3 NPs, hydrothermally synthesized by microwave, were integrated in a wax-printed office paper platform as an active layer for EAB detection. Common office paper allows a superficial adhesion of the WO_3 NPs, which facilitates the interaction of EAB with the electrochromic nanoparticles, promoting an intense and uniform coloration on the reaction zone, contrarily to chromatography paper (e.g., WFP).

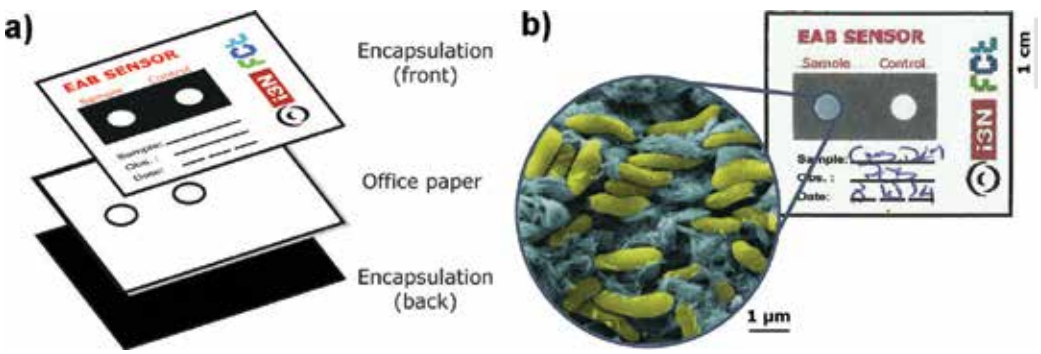

Figure 14. (a) Schematic representation of the common office paper device. (b) Digital photograph of a positive result showing a deep blue color, from the tungsten bronze, on the sample well, and nonresponse on the control well. The amplified SEM image shows the interaction between the *Geobacter sulfurreducens* bacteria (in yellow) and the hexagonal WO_3 nanoparticles (in blue). The SEM image is false-colored for better understanding of the different components. Adapted from Marques et al. [81].

6. Conclusions

Cellulose as a substrate for electronics is a highly promising booming field, not only for its low cost and recyclability, but also because of its compatibility with fast and inexpensive manufacturing printing processes. However, despite the fact that paper properties can be tuned to the intended purpose, there are still numerous challenges to address (e.g., water absorption, need for encapsulation, porosity) usually related with the internal structure, morphology, and chemistry of the fiber surface.

Unlike inorganic platforms (e.g., crystalline silicon, glass), the physical properties of paper-based materials have a considerable degree of polidispersion which can greatly affect the reproducibility of devices employing such materials. Therefore, extensive characterization protocols have to accompany the manufacturing processes, mainly targeted to provide a full

definition of the morphology and composition of the paper as they widely vary and affect immensely the properties of the electrical devices. The analysis of the different devices here described (solar cells, FETs, electrochromic displays, and lab-on-paper) highlight how certain paper substrates are appropriate in some cases, but detrimental to other devices. Nonetheless, in all cases cellulose substrates allow for working devices with similar performance to those produced on plastic or glass. These are exceptional reasons to make electronic device applications on paper a reality and encourage the progress on printed solar cells to power more complex systems such as intelligent packages or diagnostic platforms.

Acknowledgements

This work has been financed by the European Commission under projects of Horizon 2020 program BET-EU (proposal 692373), ERC Start Grant NewFun (proposal 640598), and SYMBIOTIC (proposal 665046 and 60643); the FEDER funds through the COMPETE 2020 Programme and Portuguese Science Foundation (FCT-MEC) through the Projects EXCL/CTM-NAN/0201/2012, EXPL/CTM-NAN/1184/2013, UID/CTM/50025/2013 and PTDC/CTM-ENE/5125/2014. A. T. Vicente acknowledges the support from the Portuguese Foundation for Science and Technology (FCT) and MIT-Portugal through the scholarship SFRH/BD/33978/2009. D. Gaspar acknowledges the support from AdvaMTech PhD program scholarship PD/BD/52627/2014. M. J. Mendes acknowledges support from EU FP7 Marie Curie Action (FP7- PEOPLE-2013-IEF) through the DIELECTRIC PV project (Grant No. 629370). A. Araújo acknowledges the FCT through the scholarship SFRH/BD/85587/2012. The authors want to thank their colleagues Ana Pimentel for DSC-STA measurements, Daniela Gomes for SEM images acquisition, and Rita Branquinho for helping with 3D profilometer data acquisition.

Author details

António T. Vicente*, Andreia Araújo, Diana. Gaspar, Lídia. Santos, Ana C. Marques, Manuel J. Mendes, Luís Pereira, Elvira Fortunato and Rodrigo Martins*

*Address all correspondence to: amv17109@campus.fct.unl.pt or rfpm@fct.unl.pt

CENIMAT/I3N, Department of Materials Science, Faculty of Sciences and Technology, Universidade NOVA de Lisboa and CEMOP/UNINOVA, Campus de Caparica, Caparica, Portugal

References

[1] Das R., Harrop P. Printed, Organic & Flexible Electronics Forecasts, Players & Opportunities 2016-2026. Report IDTechEx. 2016;287.

[2] Martins R., Pereira L., Fortunato E. Frontline Technology: The Future Is Paper Based. Information Display. New York, US: SID Magazine. New York, US, 2014;**30**(2):20-24.

[3] Wojcik P.J. Printable organic and inorganic materials for flexible electrochemical devices [thesis]. Universidade Nova de Lisboa - Faculdade de Ciências e Tecnologia:2013. 285 p. Available from: https://run.unl.pt/handle/10362/13600

[4] De Dobbelaere C., Calzada M.L., Jiménez R., Ricote J., Bretos I., Mullens J., et al. Aqueous solutions for low-temperature photoannealing of functional oxide films: Reaching the 400°C Si-technology integration barrier. Journal of the American Chemical Society. 2011;**133**(33):12922-12925. DOI: 10.1021/ja203553n

[5] Keszler D. Oxide electronics: Transistors pick up steam. Nature Materials. 2011;**10**(1):9-10. DOI: 10.1038/nmat2932

[6] Hardy A., Van Bael M.K. Oxide electronics: Like wildfire. Nature Materials. 2011;**10**(5):340-341. DOI: 10.1038/nmat3016

[7] George A., Stawski T.M., Unnikrishnan S., Veldhuis S. a., ten Elshof J.E. Micro and nanopatterning of functional materials on flexible plastic substrates via site-selective surface modification using oxygen plasma. Journal of Material Chemistry. 2012;**22**(2):328-332. DOI: 10.1039/C1JM14931H

[8] Banger K.K., Yamashita Y., Mori K., Peterson R.L., Leedham T., Rickard J., et al. Low-temperature, high-performance solution-processed metal oxide thin-film transistors formed by a 'sol–gel on chip' process. Nature Materials. 2011;**10**(1):45-50. DOI: 10.1038/nmat2914

[9] Kim M.-G., Kanatzidis M.G., Facchetti A., Marks T.J. Low-temperature fabrication of high-performance metal oxide thin-film electronics via combustion processing. Nature Materials. 2011;**10**(5):382-388. DOI: 10.1038/nmat3011

[10] Nomura K., Ohta H., Takagi A., Kamiya T., Hirano M., Hosono H. Room-temperature fabrication of transparent flexible thin-film transistors using amorphous oxide semiconductors. Nature. 2004;**432**(7016):488-492. DOI: 10.1038/nature03090

[11] Denneulin A., Blayo A., Bras J., Neuman C. PEDOT:PSS coating on specialty papers: Process optimization and effects of surface properties on electrical performances. Progress in Organic Coatings. 2008;**63**(1):87-91. DOI: 10.1016/j.porgcoat.2008.04.009

[12] Huebler A.C., Doetz F., Kempa H., Katz H.E., Bartzsch M., Brandt N., et al. Ring oscillator fabricated completely by means of mass-printing technologies. Organic Electronics. 2007;**8**(5):480-486. DOI: 10.1016/j.orgel.2007.02.009

[13] Khan S., Lorenzelli L., Dahiya R.S. Technologies for printing sensors and electronics over large flexible substrates: A review. IEEE Sensors Journal. 2015;**15**(6):3164-3185. DOI: 10.1109/JSEN.2014.2375203

[14] Lin Q., Huang H., Jing Y., Fu H., Chang P., Li D., et al. Flexible photovoltaic technologies. Journal of Materials Chemistry C. 2014;**2**(7):1233. DOI: 10.1039/c3tc32197e

[15] Martins R., Ferreira I., Fortunato E. Electronics with and on paper. Physica Status Solidi-Rapid Research Letters. 2011;**5**(9):332-335. DOI: 10.1002/pssr.201105247

[16] Peng B.L., Dhar N., Liu H.L., Tam K.C. Chemistry and applications of nanocrystalline cellulose and its derivatives: A nanotechnology perspective. The Canadian Journal of Chemical Engineering. 2011;**89**(5):1191-1206. DOI: 10.1002/cjce.20554

[17] Tanaka Y., Ishii N., Okuma J., Hara R. Electric double-layer capacitor having a separator made from a cellulose fiber. 1999; [Patent] US 5963419 A.

[18] Pushparaj V.L., Shaijumon M.M., Kumar A., Murugesan S., Ci L., Vajtai R., et al. Flexible energy storage devices based on nanocomposite paper. Proceedings of the National Academy of Sciences. 2007;**104**(34):13574-13577. DOI: 10.1073/pnas.0706508104

[19] Lee K.B. Two-step activation of paper batteries for high power generation: Design and fabrication of biofluid- and water-activated paper batteries. Journal of Micromechanics and Microengineering. 2006;**16**(11):2312-2317. DOI: 10.1088/0960-1317/16/11/009

[20] Nyström G., Razaq A., Strømme M., Nyholm L., Mihranyan A. Ultrafast all-polymer paper-based batteries. Nano Letters. 2009;**9**(10):3635-3639. DOI: 10.1021/nl901852h

[21] Kucherovsky J.S., Simmons G.R., Miller J.A., Mlnarik C.F. Method of making a thin film battery. 2002;**1**(12):[Patent] US 6379835 B1.

[22] Kim Y.-H., Moon D.-G., Han J.-I. Organic TFT array on a paper substrate. IEEE Electron Device Letters. 2004;**25**(10):702-704. DOI: 10.1109/LED.2004.836502

[23] Yang L., Rida A., Vyas R., Tentzeris M.M. RFID Tag and RF structures on a paper substrate using inkjet-printing technology. IEEE Transactions on Microwave Theory and Techniques. 2007;**55**(12):2894-2901. DOI: 10.1109/TMTT.2007.909886

[24] Hilder M., Winther-Jensen B., Clark N.B. Paper-based, printed zinc–air battery. Journal of Power Sources. 2009;**194**(2):1135-1141. DOI: 10.1016/j.jpowsour.2009.06.054

[25] Kim J.-Y., Park S.H., Jeong T., Bae M.J., Song S., Lee J., et al. Paper as a substrate for inorganic powder electroluminescence devices. IEEE Transactions on Electron Devices. 2010;**57**(6):1470-1474. DOI: 10.1109/TED.2010.2045675

[26] Siegel A.C., Phillips S.T., Dickey M.D., Lu N., Suo Z., Whitesides G.M. Foldable printed circuit boards on paper substrates. Advanced Functional Materials. 2010;**20**(1):28-35. DOI: 10.1002/adfm.200901363

[27] Lim W., Douglas E.A., Norton D.P., Pearton S.J., Ren F., Heo Y.-W., et al. Low-voltage indium gallium zinc oxide thin film transistors on paper substrates. Applied Physics Letters. 2010;**96**(5):053510. DOI: 10.1063/1.3309753

[28] Lu A., Dai M., Sun J., Jiang J., Wan Q. Flexible low-voltage electric-double-layer TFTs self-assembled on paper substrates. IEEE Electron Device Letters. 2011;**32**(4):518-520. DOI: 10.1109/LED.2011.2107550

[29] Irimia-Vladu M., Sariciftci N.S., Bauer S. Exotic materials for bio-organic electronics. Journal of Materials Chemistry. 2011;**21**(5):1350-1361. DOI: 10.1039/C0JM02444A

[30] Khan M.A., Bhansali U.S., Alshareef H.N. High-performance non-volatile organic ferroelectric memory on banknotes. Advanced Materials. 2012;**24**(16):2165-2170. DOI: 10.1002/adma.201200626

[31] Trnovec B., Stanel M., Hahn U., Hubler A.C., Kempa H., Sangl R., et al. Coated paper for printed electronics. Professional Papermaking. 2009;**6**:48-51.

[32] Shafizadeth F. Alternative pathways for pyrolysis of cellulose. ACS Division of Fuel Chemistry. 1983;**28**(5):285-290.

[33] Manekkathodi A., Lu M.-Y., Wang C.W., Chen L.-J. Direct growth of aligned zinc oxide nanorods on paper substrates for low-cost flexible electronics. Advanced Materials. 2010;**22**(36):4059-4063. DOI: 10.1002/adma.201001289

[34] Kim D.-H., Kim Y.-S., Wu J., Liu Z., Song J., Kim H.-S., et al. Ultrathin silicon circuits with strain-isolation layers and mesh layouts for high-performance electronics on fabric, vinyl, leather, and paper. Advanced Materials. 2009;**21**(36):3703-3707. DOI: 10.1002/adma.200900405

[35] Zocco A.T., You H., Hagen J. a, Steckl A.J. Pentacene organic thin-film transistors on flexible paper and glass substrates. Nanotechnology. 2014;**25**(9):094005. DOI: 10.1088/0957-4484/25/9/094005

[36] Bacon W.S. Now They're printing transistors on paper. Popular Science Magazine. 1968;124-125.

[37] Brody T.P. The thin film transistor - A late flowering bloom. IEEE Transactions on Electron Devices. 1984;**31**(11):1614-1628. DOI: 10.1109/T-ED.1984.21762

[38] Martins R., Ahnood A., Correia N., Pereira L., Barros R., Barquinha P., et al. Recyclable, flexible, low-power oxide electronics. Advanced Functional Materials. 2013;**23**(17):2153-2161. DOI: 10.1002/adfm.201202907

[39] Fortunato E., Correia N., Barquinha P., Pereira L., Gonçalves G., Martins R. High-performance flexible hybrid field-effect transistors based on cellulose fiber paper. IEEE Electron Device Letters. 2008;**29**(9):988-990. DOI: 10.1109/LED.2008.2001549

[40] Gaspar D., Fernandes S.N., de Oliveira A.G., Fernandes J.G., Grey P., Pontes R.V., et al. Nanocrystalline cellulose applied simultaneously as the gate dielectric and the substrate in flexible field effect transistors. Nanotechnology. 2014;**25**(9):094008. DOI: 10.1088/0957-4484/25/9/094008

[41] Pereira L., Gaspar D., Guerin D., Delattre A., Fortunato E., Martins R. The influence of fibril composition and dimension on the performance of paper gated oxide transistors. Nanotechnology. 2014;**25**(9):094007. DOI: 10.1088/0957-4484/25/9/094007

[42] Martins R., Nathan A., Barros R., Pereira L., Barquinha P., Correia N., et al. Complementary metal oxide semiconductor technology with and on paper. Advanced Materials. 2011;**23**(39):4491-4496. DOI: 10.1002/adma.201102232

[43] Tobjörk D., Österbacka R. Paper electronics. Advanced Materials. 2011;23(17):1935-1961. DOI: 10.1002/adma.201004692

[44] Zhu H., Fang Z., Preston C., Li Y., Hu L. Transparent paper: Fabrications, properties, and device applications. Energy Environmental Science. 2014;**7**(1):269-287. DOI: 10.1039/C3EE43024C

[45] Polman A., Knight M., Garnett E.C., Ehrler B., Sinke W.C. Photovoltaic materials: Present efficiencies and future challenges. Science. 2016;**352**(6283):aad4424. DOI: 10.1126/science.aad4424

[46] Ito S. Printable solar cells. Wiley Interdisciplinary Reviews: Energy and Environment. 2015;**4**(1):51-73. DOI: 10.1002/wene.112

[47] Barr M.C., Rowehl J.A., Lunt R.R., Xu J., Wang A., Boyce C.M., et al. Direct Monolithic integration of organic photovoltaic circuits on unmodified paper. Advanced Materials. 2011;**23**(31):3500-3505. DOI: 10.1002/adma.201101263

[48] Vicente A., Águas H., Mateus T., Araújo A., Lyubchyk A., Siitonen S., et al. Solar cells for self-sustainable intelligent packaging. Journal of Material Chemistry A. 2015;3(25):13226-13236. DOI: 10.1039/C5TA01752A

[49] Águas H., Mateus T., Vicente A., Gaspar D., Mendes M.J., Schmidt W.A., Pereira L., Fortunato E., Martins R. Thin film silicon photovoltaic cells on paper for flexible indoor applications. Advanced Functional Materials. 2015;**25**(23):3592-3598. DOI: 10.1002/adfm.201500636

[50] Lee C.H., Kim D.R., Cho I.S., William N., Wang Q., Zheng X. Peel-and-Stick: Fabricating thin film solar cell on universal substrates. Scientific Reports. 2012;**2**:1000. DOI: 10.1038/srep01000

[51] Lee C.H., Kim D.R., Zheng X. Transfer printing methods for flexible thin film solar cells: Basic concepts and working principles. ACS Nano. 2014;**8**(9):8746-8756. DOI: 10.1021/nn5037587

[52] Lee J., Wu J., Shi M., Yoon J., Park S.-I., Li M., et al. Stretchable GaAs Photovoltaics with designs that enable high areal coverage. Advanced Materials. 2011;**23**(8):986-991. DOI: 10.1002/adma.201003961

[53] Zhou Y., Khan T.M., Liu J.-C., Fuentes-Hernandez C., Shim J.W., Najafabadi E., et al. Efficient recyclable organic solar cells on cellulose nanocrystal substrates with a conducting polymer top electrode deposited by film-transfer lamination. Organic Electronics. 2014;**15**(3):661-666. DOI: 10.1016/j.orgel.2013.12.018

[54] Fang Z., Zhu H., Yuan Y., Ha D., Zhu S., Preston C., et al. Novel nanostructured paper with ultrahigh transparency and ultrahigh haze for solar cells. Nano Letters. 2014;**14**(2):765-773. DOI: 10.1021/nl404101p

[55] Nogi M., Karakawa M., Komoda N., Yagyu H., Nge T.T. Transparent conductive nanofiber paper for foldable solar cells. Scientific Reports. 2015;**5**:17254. DOI: 10.1038/srep17254

[56] Gao T., Wang B., Ding B., Lee J., Leu P.W. Uniform and ordered copper nanomeshes by microsphere lithography for transparent electrodes. Nano Letters. 2014;**14**(4):2105-2110. DOI: 10.1021/nl5003075

[57] van de Groep J., Spinelli P., Polman A. Transparent conducting silver nanowire networks. Nano Letters. 2012;**12**(6):3138-3144. DOI: 10.1021/nl301045a

[58] Kim W.-K., Lee S., Hee Lee D., Hee Park I., Seong Bae J., Woo Lee T., et al. Cu mesh for flexible transparent conductive electrodes. Scientific Reports. 2015;**5**:10715. DOI: 10.1038/srep10715

[59] Lyubchyk A., Vicente A., Soule B., Alves P.U., Mateus T., Mendes M.J., et al. Mapping the electrical properties of ZnO-based transparent conductive oxides grown at room temperature and improved by controlled postdeposition annealing. Advanced Electronic Materials. 2016;**2**(1):1500287. DOI: 10.1002/aelm.201500287

[60] Mendes M.J., Morawiec S., Simone F., Priolo F., Crupi I. Colloidal plasmonic back reflectors for light trapping in solar cells. Nanoscale. 2014;**6**(9):4796. DOI: 10.1039/c3nr06768h

[61] Mendes M.J., Araújo A., Vicente A., Águas H., Ferreira I., Fortunato E., et al. Design of optimized wave-optical spheroidal nanostructures for photonic-enhanced solar cells. Nano Energy. 2016;**26**:286-296. DOI: 10.1016/j.nanoen.2016.05.038

[62] Polman A., Atwater H.A. Photonic design principles for ultrahigh-efficiency photovoltaics. Nature Materials. 2012;**11**(3):174-177. DOI: 10.1038/nmat3263

[63] Ferry V.E., Verschuuren M.A., Lare M.C. Van, Schropp R.E.I., Atwater H.A., Polman A. Optimized spatial correlations for broadband light trapping nanopatterns in high efficiency ultrathin film a-Si:H Solar Cells. Nano Letters. 2011;**11**(10):4239-4245. DOI: 10.1021/nl202226r

[64] Abitbol T., Rivkin A., Cao Y., Nevo Y., Abraham E., Ben-Shalom T., et al. Nanocellulose, a tiny fiber with huge applications. Current Opinion in Biotechnology. 2016;**39**(I):76-88. DOI: 10.1016/j.copbio.2016.01.002

[65] Zhou T. Electrically conductive bacterial cellulose composite membranes produced by the incorporation of graphite nanoplatelets in pristine bacterial cellulose membranes. Express Polymer Letters. 2013;**7**(9):756-766. DOI: 10.3144/expresspolymlett.2013.73

[66] Gama M., Dourado F., Bielecki S. Bacterial nanocellulose: From biotechnology to bioeconomy. 1st ed. Oxford, UK: Elsevier, Oxford, UK; 2016. 260 p.

[67] Rojas O.J, editor. Cellulose Chemistry and Properties: Fibers, Nanocelluloses and Advanced Materials. 1st ed. Switzerland: Springer International Publishing; 2016. VII, 333 p. DOI: 10.1007/978-3-319-26015-0

[68] Gama M., Gatenholm P., Klemm D. Bacterial Nanocellulose: A Sophisticated Multifunctional Material. 1st ed. Boca Raton, Florida, US: CRC Press, Boca Raton, Florida, US; 2013. 272 p.

[69] Iguchi M., Yamanaka S., Budhiono A. Bacterial cellulose - A masterpiece of nature's arts. Journal of Materials Science. 2000;**35**(2):261-270. DOI: 10.1023/A:1004775229149

[70] Stephens C.H., Whitmore P.M., Morris H.R., Bier M.E. Hydrolysis of the amorphous cellulose in cotton-based paper. Biomacromolecules. 2008;**9**(4):1093-1099. DOI: 10.1021/bm800049w

[71] Dufresne A. Nanocellulose. From Nature to High Performance Tailored Materials. 1st ed. Berlin, Boston: De Gruyter; 2012. 460 p. DOI: 10.1515/9783110254600

[72] Stora Enso. Available from: www.storaenso.com [Accessed: June, 2016]

[73] Araújo A., Caro C., Mendes M.J., Nunes D., Fortunato E., Franco R., et al. Highly efficient nanoplasmonic SERS on cardboard packaging substrates. Nanotechnology. 2014;**25**(41):415202. DOI: 10.1088/0957-4484/25/41/415202

[74] Gaspar D., Pereira L., Delattre A., Guerin D., Fortunato E., Martins R. Engineered cellulose fibers as dielectric for oxide field effect transistors. Physica Status Solidi (c). 2015;**12**(12):1421-1426. DOI: 10.1002/pssc.201510163

[75] Ciolacu D., Ciolacu F., Popa V.I. Amorphous cellulose – Structure and characterization. Cellulose Chemistry and Technology. 2011;**45**:13-21.

[76] Łojewska J., Miśkowiec P., Łojewski T., Proniewicz L.M. Cellulose oxidative and hydrolytic degradation: In situ FTIR approach. Polymer Degradation and Stability. 2005;**88**(3):512-520. DOI: 10.1016/j.polymdegradstab.2004.12.012

[77] Segal L., Creely J.J., Martin A.E., Conrad C.M. An empirical method for estimating the degree of crystallinity of native cellulose using the X-ray diffractometer. Textile Research Journal. 1959;**29**(10):786-794. DOI: 10.1177/004051755902901003

[78] Luo Y., Zhang J., Li X., Liao C., Li X. The cellulose nanofibers for optoelectronic conversion and energy storage. Journal of Nanomaterials. 2014;**2014**:1-13. DOI: 10.1155/2014/654512

[79] Lisowski P., Zarzycki P.K. Microfluidic paper-based analytical devices (μPADs) and micro total analysis systems (μTAS): Development, applications and future trends. Chromatographia. 2013;**76**(19-20):1201-1214. DOI: 10.1007/s10337-013-2413-y

[80] Willets W, editor. Paper and Paperboard Characteristics, Nomenclature, and Significance of Tests. 3rd ed. West Conshohocken: ASTM International; 1963. 129 p. DOI: 10.1520/STP60B-EB

[81] Marques A.C., Santos L., Costa M.N., Dantas J.M., Duarte P., Gonçalves A., et al. Office paper platform for bioelectrochromic detection of electrochemically active bacteria using tungsten trioxide nanoprobes. Office Paper Platform for Bioelectrochromic Detection of Electrochemically Active Bacteria using Tungsten Trioxide Nanoprobes. 2015;**5**:9910. DOI: 10.1038/srep09910

[82] Härting M., Zhang J., Gamota D.R., Britton D.T. Fully printed silicon field effect transistors. Applied Physics Letters. 2009;**94**(19):193509. DOI: 10.1063/1.3126958

[83] Zschieschang U., Yamamoto T., Takimiya K., Kuwabara H., Ikeda M., Sekitani T., et al. Organic electronics on banknotes. Advanced Materials. 2011;**23**(5):654-658. DOI: 10.1002/adma.201003374

[84] Andersson P., Nilsson D., Svensson P.-O., Chen M., Malmström A., Remonen T., et al. Active matrix displays based on all-organic electrochemical smart pixels printed on paper. Advanced Materials. 2002;**14**(20):1460-1464. DOI: 10.1002/1521-4095(20021016)14:20<1460::AID-ADMA1460>3.0.CO;2-S

[85] Mannerbro R., Ranlöf M., Robinson N., Forchheimer R. Inkjet printed electrochemical organic electronics. Synthetic Metals. 2008;**158**(13):556-560. DOI: 10.1016/j.synthmet.2008.03.030

[86] Martins R., Barquinha P., Pereira L., Correia N., Gonçalves G., Ferreira I., et al. Write-erase and read paper memory transistor. Applied Physics Letters. 2008;**93**(20):203501. DOI: 10.1063/1.3030873

[87] Svensson J.S.E.M., Granqvist C.G. Electrochromic coatings for "smart windows". Solar Energy Materials. 1985;**12**(6):391-402. DOI: 10.1016/0165-1633(85)90033-4

[88] Svensson J.S.E.M., Granqvist C.G. Electrochromic tungsten oxide films for energy efficient windows. Solar Energy Materials. 1984;**11**(1-2):29-34. DOI: 10.1016/0165-1633(84)90025-X

[89] Mortimer R.J. Electrochromic materials. Annual Review of Materials Research. 2011;**41**(1):241-268. DOI: 10.1146/annurev-matsci-062910-100344

[90] Calvert P. Inkjet printing for materials and devices. Chemistry of Materials. 2001;**13**(10):3299-3305. DOI: 10.1021/cm0101632

[91] Hudd A. Inkjet Printing Technologies. In: Shlomo Magdassi, editor. The Chemistry of Inkjet Inks. 1st ed. Israel: World Scientific; 2009. p. 3-18. DOI: 10.1142/9789812818225_0001

[92] Shim G.H., Han M.G., Sharp-Norton J.C., Creager S.E., Foulger S.H. Inkjet-printed electrochromic devices utilizing polyaniline–silica and poly(3,4-ethylenedioxythiophene)–silica colloidal composite particles. Journal of Materials Chemistry. 2008;**18**(5):594-601. DOI: 10.1039/b712766a

[93] Wojcik P.J., Cruz A.S., Santos L., Pereira L., Martins R., Fortunato E. Microstructure control of dual-phase inkjet-printed a-WO3/TiO2/WOX films for high-performance electrochromic applications. Journal of Materials Chemistry. 2012;**22**(26):13268. DOI: 10.1039/c2jm31217d

[94] Santos L., Wojcik P., Pinto J.V., Elangovan E., Viegas J., Pereira L., et al. Structure and morphologic influence of WO3 nanoparticles on the electrochromic performance of dual-phase a-WO3/WO3 inkjet printed films. Advanced Electronic Materials. 2015;**1**(1-2):1400002. DOI: 10.1002/aelm.201400002

[95] Santos L., Nunes D., Calmeiro T., Branquinho R., Salgueiro D., Barquinha P., et al. Solvothermal synthesis of gallium–indium-zinc-oxide nanoparticles for electrolyte-gated transistors. ACS Applied Materials & Interfaces. 2015;**7**(1):638-646. DOI: 10.1021/am506814t

[96] Granqvist C.G. Oxide electrochromics: An introduction to devices and materials. Solar Energy Materials and Solar Cells. 2012;**99**:1-13. DOI: 10.1016/j.solmat.2011.08.021

[97] Choy J.-H., Kim Y.-I., Yoon J.-B., Choy S.-H. Temperature-dependent structural evolution and electrochromic properties of peroxopolytungstic acid. Journal of Materials Chemistry. 2001;**11**(5):1506-1513. DOI: 10.1039/b009119g

[98] Leftheriotis G., Papaefthimiou S., Yianoulis P. The effect of water on the electrochromic properties of WO3 films prepared by vacuum and chemical methods. Solar Energy Materials and Solar Cells. 2004;**83**(1):115-124. DOI: 10.1016/j.solmat.2004.02.019

[99] Yang J., Jiao L., Zhao Q., Wang Q., Gao H., Huan Q., et al. Facile preparation and electrochemical properties of hierarchical chrysanthemum-like WO3·0.33H2O. Journal of Materials Chemistry. 2012;**22**(9):3699-3701. DOI: 10.1039/c2jm15837j

[100] Veigas B., Jacob J.M., Costa M.N., Santos D.S., Viveiros M., Inácio J., et al. Gold on paper–paper platform for Au-nanoprobe TB detection. Lab on a Chip. 2012;**12**(22):4802-4808. DOI: 10.1039/c2lc40739f

[101] Li X., Ballerini D.R., Shen W. A perspective on paper-based microfluidics: Current status and future trends. Biomicrofluidics. 2012;**6**(1):011301. DOI: 10.1063/1.3687398

[102] Zhao W., van der Berg A. Lab on paper. Lab on a Chip. 2008;**8**(12):1988-1991. DOI: 10.1039/b814043j

[103] Liana D.D., Raguse B., Gooding J.J., Chow E. Recent advances in paper-based sensors. Sensors. 2012;**12**(12):11505-11526. DOI: 10.3390/s120911505

[104] Costa M.N., Veigas B., Jacob J.M., Santos D.S., Gomes J., Baptista P.V., et al. A low cost, safe, disposable, rapid and self-sustainable paper-based platform for diagnostic testing: Lab-on-paper. Nanotechnology. 2014;**25**(9):094006. DOI: 10.1088/0957-4484/25/9/094006

[105] Zhou M., Yang M., Zhou F. Paper based colorimetric biosensing platform utilizing cross-linked siloxane as probe. Biosensors and Bioelectronics. 2014;**55**:39-43. DOI: 10.1016/j.bios.2013.11.065

[106] Martinez A.W., Phillips S.T., Butte M.J., Whitesides G.M. Patterned paper as a platform for inexpensive, low-volume, portable bioassays. Angewandte Chemie International Edition. 2007;**46**(8):1318-1320. DOI: 10.1002/anie.200603817

[107] Dieterich K. Testing-paper and method of making same. 1902; [Patent] US 691249 A.

[108] Yagoda H. Applications of confined spot tests in analytical chemistry: Preliminary paper. Industrial & Engineering Chemistry Analytical Edition. 1937;**9**(2):79-82. DOI: 10.1021/ac50106a012

[109] Johnson J.L. Microchemical techniques in solving industrial problems. Mikrochimica Acta. 1967;**55**(4):756-762. DOI: 10.1007/BF01224400

[110] Pelton R. Bioactive paper provides a low-cost platform for diagnostics. Trends in Analytical Chemistry. 2009;**28**(8):925-942. DOI: 10.1016/j.trac.2009.05.005

[111] Jokerst J.C., Adkins J.A., Bisha B., Mentele M.M., Goodridge L.D., Henry C.S. Development of a paper-based analytical device for colorimetric detection of select foodborne pathogens. Analytical Chemistry. 2012;**84**(6):2900-2907. DOI: http://pubs.acs.org/doi/abs/10.1021/ac203466y

[112] Bruzewicz D.A., Reches M., Whitesides G.M. Low-cost printing of poly(dimethylsiloxane) barriers to define microchannels in paper. Analytical Chemistry. 2008;**80**(9):3387-3392. DOI: 10.1021/ac702605a

[113] Martinez A.W., Phillips S.T., Whitesides G.M., Carrilho E. Diagnostics for the developing world: Microfluidic paper-based analytical devices. Analytical Chemistry. 2010;**82**(1):3-10. DOI: 10.1021/ac9013989

[114] Martinez A.W., Phillips S.T., Carrilho E., Thomas S.W., Sindi H., Whitesides G.M. Simple telemedicine for developing regions: Camera phones and paper-based microfluidic devices for real-time, off-site diagnosis. Analytical Chemistry. 2008;**80**(10):3699-3707. DOI: 10.1021/ac800112r

[115] Carrilho E., Martinez A.W., Whitesides G.M. Understanding wax printing: A simple micropatterning process for paper-based microfluidics. Analytical Chemistry. 2009;**81**(16):7091-7095. DOI: 10.1021/ac901071p

[116] Li X., Tian J., Nguyen T., Shen W. Paper-Based Microfluidic Devices by Plasma Treatment. Analytical Chemistry. 2008;**80**(23):9131-9134. DOI: 10.1021/ac801729t

[117] Khan M.S., Fon D., Li X., Tian J., Forsythe J., Garnier G., et al. Biosurface engineering through ink jet printing. Colloids and Surfaces B: Biointerfaces. 2010;**75**(2):441-447. DOI: 10.1016/j.colsurfb.2009.09.032

[118] Glavan A.C., Martinez R.V., Subramaniam A.B., Yoon H.J., Nunes R.M.D., Lange H., et al. Omniphobic "RF Paper" produced by silanization of paper with fluoroalkyltrichlorosilanes. Advanced Functional Materials. 2014;**24**(1):60-70. DOI: 10.1002/adfm.201300780

[119] Wang J. Electrochemical glucose biosensors. Chemical Reviews. 2008;**108**(2):814-825. DOI: 10.1021/cr068123a

[120] Yoo E.-H., Lee S.-Y. Glucose biosensors: An overview of use in clinical practice. Sensors. 2010;**10**(5):4558-4576. DOI: 10.3390/s100504558

[121] Fischer C., Fraiwan A., Choi S. A 3D paper-based enzymatic fuel cell for self-powered, low-cost glucose monitoring. Biosensors and Bioelectronics. 2016;**79**:193-197. DOI: 10.1016/j.bios.2015.12.020

[122] Lovley D.R. Bug juice: Harvesting electricity with microorganisms. Nature Reviews Microbiology. 2006;**4**(7):497-508. DOI: 10.1038/nrmicro1442

[123] Lovley D.R. The microbe electric: Conversion of organic matter to electricity. Current Opinion in Biotechnology. 2008;**19**(6):564-571. DOI: 10.1016/j.copbio.2008.10.005

[124] Yuan S.-J., He H., Sheng G.-P., Chen J.-J., Tong Z.-H., Cheng Y.-Y., et al. A Photometric high-throughput method for identification of electrochemically active bacteria using a WO3 nanocluster probe. Scientific Reports. 2013;**3**:1315. DOI: 10.1038/srep01315

[125] Lovley D.R., Ueki T., Zhang T., Malvankar N.S., Shrestha P.M., Flanagan K.A., et al. Geobacter: The Microbe Electric's Physiology, Ecology, and Practical Applications. In: Poole R.K., editor. Advances in Microbial Physiology. 1st ed. United Kingdom: Elsevier; 2011. p. 1-100. DOI: 10.1016/B978-0-12-387661-4.00004-5

Section 2

Nano-Structured Solar Cells - Junction Type Solar Cells

Chapter 4

Silicon Heterojunction Solar Cells: The Key Role of Heterointerfaces and their Impact on the Performance

Miroslav Mikolášek

Additional information is available at the end of the chapter

http://dx.doi.org/10.5772/65020

Abstract

This chapter is dedicated to the processes linked with the collection of photo-generated carriers in silicon heterojunction (SHJ) solar cells with a focus on the key role of the amorphous silicon/crystalline silicon heterojunction. The intention is to explain the role of carrier inversion at the heterointerface and connect it with the properties of the SHJ to obtain deeper understanding of carrier transport properties and collection, which goes beyond amorphous silicon-based structures and will contribute to understanding the new emerging SHJ based on amorphous silicon oxide and metal oxide emitter layers. The study is extended by a simulation of the TCO/emitter interface with the aim to reveal the effect of parasitic Schottky barrier height on the performance of the SHJ solar cell. In addition, the simulation study of SHJ under concentrated light and varied temperatures is outlined to show the main limitations and prospects of SHJ structures for utilization under concentrated light.

Keywords: amorphous silicon, heterojunction, carrier inversion, open-circuit voltage, ASA simulation

1. Introduction

Among the semiconductor materials with suitable optoelectronic properties for photovoltaic applications, silicon has been the most widely accepted and used in the current production of photovoltaic modules. The basic advantage of silicon is its abundance in nature and mastered silicon wafer fabrication, as well as the compatibility of the technological processes of solar cells with the microelectronics industry. The increasing cost of processed crystalline silicon ingots in the past years became a driving force decreasing the wafer thickness for solar cell

fabrication [1]. However, this trend was stopped due to the bending of thin wafers during high temperature processing of standard silicon solar cells, which results into the increasing efforts focused on the technologies with lower silicon usage. Among them, the silicon heterojunction solar cells (SHJ) provide both high performance together with a perspective of low-cost fabrication and decrease of silicon wafers thickness bellow 100 μm [2]. The advantages of heterojunction between amorphous and crystalline silicon were first introduced into the so-called HIT concept (Hetero-junction with Intrinsic Thin-layer) by former company SANYO (currently SANYO is part of the company Panasonic) in 1992 [3]. The SHJ HIT solar cell is composed of a single thin crystalline silicon wafer, c-Si surrounded by ultra-thin intrinsic silicon layers, a-Si:H(i) and n-type and p-type doped amorphous silicon layers, a-Si:H (**Figure 1**), which can be deposited at temperature below 200°C and so can be used in processing of thin wafers. On the two doped layers, transparent conducting oxide (TCO) layers and metal electrodes are formed with sputtering and screen-printing methods, respectively. The TCO layer on the top also works as an anti-reflection layer.

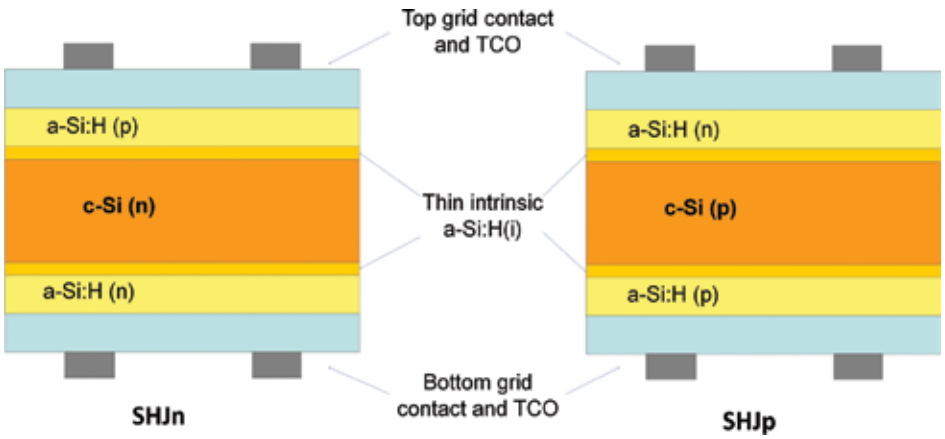

Figure 1. Silicon heterojunction solar cells with on n-type silicon (SHJn) and n-type silicon (SHJp) hetero-junction with intrinsic thin-layer (HIT) solar cell.

Since the first introduction, the HIT solar cells have been the subject of extensive research. Recently, the record efficiency η = 25.6% with open-circuit voltage V_{OC} = 0.74 V, short-circuit current J_{SC} = 41.8 mA/cm^2 and fill factor FF = 82.7% were achieved on the rear junction HIT solar cell by Panasonic, which makes this technology currently the most efficient among silicon-based solar cells [4]. Current strong interest in SHJ concept is motivated by the high conversion efficiency as well as further possibilities for decreasing the fabrication cost. SHJ can be prepared by simple and low temperature fabrication processes, which decreases the thermal budget and thus the cost of the cell. Since the base material of the structure is crystalline silicon, the typical degradation due to the Staebler-Wronski effect observed in amorphous silicon solar cells does not take place in SHJ solar cells, where the base material of the structure is crystalline silicon [5]. Moreover, the HIT cell shows a better temperature coefficient (<–0.25%/K) compared to standard c-Si solar cells (–0.45%/K), which means more power generated in outdoor conditions

http://dx.doi.org/10.5772/65020

for the same nominal conversion efficiency [6]. Since the SHJ HIT has symmetrical front and back structures, the possibility to use it for the bifacial solar module is feasible. The experiments show that bifacial use of the HIT structure brings a performance higher by more than 10% compared to the conventional structures with light incident only from one side [7].

1.1. Current trends in SHJ solar cell development

To make the SHJ solar cells more economically attractive, current efforts are focused on the development of technologies and approaches focused on two main objectives (i) to increase the efficiency and (ii) to decrease the fabrication costs. The utilization of emitters with a large band gap such as amorphous silicon carbide a-SiC:H [8], nanocrystalline silicon oxide nc-SiOx:H [9] or micro-crystalline silicon oxide μc-SiOx:H [10], thus lowering light absorption is a common approach on how to increase J_{SC} and hence the performance of such solar cells. The advantage of this approach is that only low adjustment of production lines is required for replacements of a-Si:H emitter by a-SiC:H or SiOx:H emitter layers. An increase in J_{SC} by about 1 mA/cm^2 was demonstrated by replacing a-Si:H by a-SiC:H [8] or by μc-SiOx:H [10]. However, also in this case the heterojunction with a c-Si substrate plays a crucial role and its fabrication has to be well mastered to benefit from the lower parasitic absorption of light. Another way on how to decrease absorption losses is based on the preparation of the two collection contacts at the bottom side of the silicon substrate forming an inter-digitated back contact silicon heterojunction (IBC-SHJ) solar cells. The beneficial effects of collection electrodes at the bottom of the cell are demonstrated by the best efficiency of 25.6% currently achieved at SHJ solar cells [4]. High J_{SC} = 41.8 mA/cm^2 in such solar cells is attained due to the eliminated absorption losses of a-Si:H layers as well as losses in TCO.

The decrease of fabrication cost can be realized through the replacement of expensive materials by cheaper alternatives. Several groups have investigated alternative materials such as zinc oxide, ZnO [11], and indium zinc oxide, IZO [12], as a replacement of expensive indium tin oxide, ITO. Replacement of silver used in the collection electrodes by copper [1, 13] is another way, and is currently highly investigated to decrease SHJ cost.

Another approach to make SHJ cells more economically attractive is based on the reduction of silicon wafer thickness. The ability of HIT structure to use silicon wafers of low thicknesses and to achieve high performance at the same time was demonstrated already in 2009, when the SHJ HIT solar cell with a conversion efficiency of 22.8% prepared on a 98 μm thick n-type silicon wafer was introduced by former company Sanyo (currently Panasonic) [2].

Nowadays, new advance concepts are emerging based on the replacement of the amorphous emitter by metal oxides [14–16]. Such a concept has the ability to provide both an increase of efficiency as well as a decrease of fabrication cost. Metal oxides provide advantages of large band gaps, thus lower parasitic absorption in the emitter, simpler deposition by thermal evaporation [13] and no requirements of toxic dopant gases during fabrication. Moreover, the deposition of such oxides can be carried out at low temperatures leading to a further decrease of the thermal budget and hence fabrication cost. Metal oxides are widely used as a hole transport layers in organic solar cells [16, 17]. Current attempts to transfer them into the SHJn technology show very promising results with achieved efficiency of η = 22.5% for

molybdenum oxide hole collector MoOx-based SHJ solar cell [18]. The progress in the development of electron selective contacts based on lithium fluoride (LiFx) allows fabrication of dopant-free asymmetric heterocontacts cell (DASH) with conversion efficiency approaching 20% [19].

1.2. Aim of this chapter

Two targets have to be attained for the good performance of solar cells: (i) light has to be absorbed in the absorption layer of the solar cell and (ii) the photo-generated carriers have to be effectively collected by the top and bottom collection electrodes. The first target is focused on the improvement of light management, which with the decreasing of the c-Si substrate thickness starts to be important also for SHJ solar cell. The optimization of TCO [12, 20], tuning of emitter layer band gap [8] and texturization of c-Si [21] are crucial to achieve high J_{SC}. The second target, which is described in detail in this chapter, is focused on the recombination and carrier transport processes in the structure. Such processes determine the collection of the photo-generated carriers and thus the performance of the solar cell. Since the SHJ is formed as a stack of various layers surrounding the absorber c-Si layer, the current transport of photo-generated electron/hole pairs to the collection electrodes is highly influenced by the interfaces between the neighbouring layers. Due to the connection of various materials with different lattice parameters, defect states can be formed at the interface. The difference in the band gap, affinity, doping level and type of adjacent layers results into the formation of heterojunctions/carrier transport barrier. Application of a-Si:H or alternative emitter (such as a-SiC:H, nc-SiOx or metal oxides) in the SHJ solar cell is linked with several challenging requests concerning the quality of this layer and its interfaces with c-Si and TCO. On the one hand, the defect states and band alignment at the a-Si:H/c-Si interface determine the band bending at the c-Si surface and hence recombination and collection of photo-generated carriers [6, 22, 23]. Good quality of the a-Si:H(i) layer as well as a-Si:H/c-Si interface is one of the main challenges in order to achieve high SHJ solar cell efficiency. On the other hand, due to the low specific conductivity of a-Si:H it is required to use conductive TCO as a collection electrode. When the TCO is not chosen carefully regarding the proper work function, or is not properly prepared, the parasitic Schottky barrier can arise at the TCO/a-Si:H interface [24–26]. This parasitic Schottky barrier has an opposite diffusion potential compared to the a-SiH/c-Si junction and thus hinders the collection of photo-generated carriers. As a result, the performance of the SHJ deteriorates.

The aim of this chapter is to explore the processes connected with the collection of photo-generated carriers and to explain the key role of the front a-Si:H/c-Si and TCO/a-Si:H interfaces for carrier recombination processes. ASA simulation is carried out to provide an insight into the charge properties of both a-Si:H/c-Si and TCO/a-Si:H junctions forming the front emitter stack of the SHJ solar cell and to explore their interconnection. Strong emphasis is focused on the presence of carrier inversion at the a-Si:H/c-Si, which is the most determining factor for V_{OC} of SHJ cell. The alternative approaches to obtain high carrier inversion based on field effect passivation and metal oxides are described in the chapter as well. The study is extended by simulation of the SHJ under concentrated light and varied temperatures to explore the

http://dx.doi.org/10.5772/65020

perspective and limitations of n- and p-type silicon-based SHJ structures for utilization in light concentrated applications.

1.3. Simulation set-up

The ASA simulation program was used for characterization of recombination processes in the SHJ structure. This program is designed for the simulation of solar cells based on a-Si:H and c-Si semiconductors. ASA program solves the Poisson equation and continuity equations for electrons and holes in one dimension and includes several physical models which describe the trapping and generation/recombination processes in the structures with consideration of spatial disorder of amorphous silicon [26]. The simulated solar cell structures have the following layer sequence: TCO/a-Si:H(n)/a-Si:H(i)/c-Si(p)/a-Si:H(i)/a-Si:H(p)/TCO/Metal and TCO/a-Si:H(p)/a-Si:H(i)/c-Si(n)/a-Si:H(i)/a-Si:H(n)/TCO/Metal denoted as SHJp and SHJn, respectively. In the simulated models, the thicknesses of 5 and 10 nm were used for a-Si:H(i) and doped a-Si:H(n) and a-Si:H(p) layers, respectively. The band gap of a-Si:H(p) was set to 1.95 eV and the band gaps of a-Si:H(i) and c-Si(n) were set to 1.76 eV in accordance to [27]. The doping activation energies of 0.2 and 0.4 eV were used for a-Si:H(n) and a-Si:H(p) layers, respectively. The gap state densities of amorphous layers have a Gaussian distribution of dangling bonds and an exponential distribution of band tails was set together with additional parameters according to the literature [27]. While the main aim of the simulation is to describe recombination processes in the structure, flat silicon substrate conditions were used in the models. The silicon substrates with thickness of 200 μm, lifetime, τ = 1 ms and concentration of dopants, $N_{dop} = 5 \times 10^{21}$ m^{-3} were used for both SHJp and SHJn structures. TCO was adopted as an optical layer with a thickness of 80 nm. The defect states at the front a-Si:H/c-Si interface was modelled by inserted 1 nm thick highly defective c-Si layer. Flat band conditions at the TCO/a-Si:H interface were used in the initial simulations focused on the study of a-Si:H/c-Si properties. The negligible defect state density of 10^9 cm^{-2} were set at the back c-Si/a-Si:H contact for all simulations. The conduction band offset, $\Delta E_C = 0.15$ eV, and valence band offset, $\Delta E_V = 0.55$ eV, were used as an initial values determining band alignments in SHJp and SHJn structures, respectively. As an illumination source the light with power density of 100 mW/cm^2 and spectrum AM1.5 was used for the output performance simulations.

2. Open circuit voltage and carrier inversion

The output performance of the solar cells can be described by V_{OC}, J_{SC} and FF. All such parameters are linked with the η and define the overall output performance of solar cells. While the main aim of this chapter is to describe the role of heterointerface and inversion at the a-Si:H/c-Si, we will focus on V_{OC} which is strongly affected by recombination properties and carrier transport in the solar cell. The V_{OC} for SHJp solar cells can be expressed by the analytical model as [28, 29]

$$V_{\mathrm{OC}} = \frac{E_{g-Si} - \delta_{Si(p)}}{q} - \frac{kT}{q}\ln\left(\frac{N_C}{\Delta n}.\frac{\frac{D_\mathrm{p}}{L_\mathrm{p}} + S_\mathrm{p}}{\frac{D_\mathrm{p}}{L_\mathrm{p}}}\right) \tag{1}$$

Similarly for SHJn, the V_{OC} is expressed as

$$V_{\mathrm{OC}} = \frac{E_{g-Si} - \delta_{Si(n)}}{q} - \frac{kT}{q}\ln\left(\frac{N_V}{\Delta p}.\frac{\frac{D_\mathrm{n}}{L_\mathrm{n}} + S_\mathrm{n}}{\frac{D_\mathrm{n}}{L_\mathrm{n}}}\right) \tag{2}$$

Symbols in the above equations denote: T is the temperature, q is the elementary charge, k is the Boltzmann constant, $E_{\mathrm{g\text{-}Si}}$ is the band gap of c-Si, N_C and N_V are the effective densities of states in the conduction band of c-Si, $\delta_{Si(p)}$ and $\delta_{Si(n)}$ are the dopant activation energies of c-Si substrate with p-type and n-type doping, respectively, L_p and L_n are diffusion lengths for holes and electrons, respectively, and D_p and D_n are diffusion constants for holes and electrons. Further symbols denote the interface recombination velocities for holes $S_\mathrm{p} = C_\mathrm{p} D_\mathrm{it}$ and electrons $S_\mathrm{n} = C_\mathrm{n} D_\mathrm{it}$, where C_p and C_n are the capture rate coefficients for holes and electrons, respectively, and D_it is the interface defect density. The $\Delta p = \Delta n = g\,.\,\tau_{\mathrm{eff}}$ in the equations denotes the excess carrier concentration, where g is the average photo-generation of the electron-hole pairs in c-Si and τ_{eff} is the effective lifetime of the excess carries.

From the above equations it is apparent that V_{OC} depends on Δn, which is determined by τ_{eff} and g. g is related with the illumination intensity. τ_{eff} is determined by the recombination velocities S_p and S_n and thus by the defect state density at the a-Si:H/c-Si heterointerface, D_it recombination at the rear surface and recombination in the c-Si substrate. The recombination in the c-Si substrate is not the subject of this chapter, instead of this, we focus our attention to the a-Si:H/c-Si interface and inversion layer formed at c-Si surface of this interface. In the case of low recombination in the bulk and at the back surface of c-Si, the main recombination path is at the heterointerface. For such a case, the saturation current of the SHJ, J_{sat}, is determined by the saturation current of interface recombination $J_{\mathrm{sat\text{-}it}}$, which is for SHJp determined by the interface recombination velocity S_n and holes concentration at the heterointerface p_it as

$$j_{\mathrm{sat-it}} = qS_\mathrm{p}p_\mathrm{it} \tag{3}$$

Similarly, by considering interface concentration of electrons n_it for SHJn it can be written

$$j_{\mathrm{sat-it}} = qS_\mathrm{n}n_\mathrm{it} \tag{4}$$

http://dx.doi.org/10.5772/65020

By taking into account the equation for V_{OC}

$$V_{OC} = \frac{AkT}{q} \ln\left(\frac{j_{SC}}{j_{sat}}\right) \tag{5}$$

and substituting $J_{sat\text{-}it}$ as a saturation current, it is possible to write equation which determines the V_{OC} as a function of the interface recombination velocity and effective barrier for recombination at the heterointerface Φ_B [30]

$$V_{OC} = \frac{\Phi_B}{q} - \frac{AkT}{q} \ln\left(\frac{qN_V S_p}{j_{SC}}\right) \tag{6}$$

for SHJp and

$$V_{OC} = \frac{\Phi_B}{q} - \frac{AkT}{q} \ln\left(\frac{qN_C S_n}{j_{SC}}\right) \tag{7}$$

for SHJn, where A represents the diode ideality factor. From the above equation it is obvious that V_{OC} is determined by the Φ_B which should have a high value to obtain high V_{OC}. **Figure 2** show the band diagram of SHJn and SHJp with Φ_B at the heterointerfaces, respectively. In SHJ solar cells the c-Si surface at the heterointerface is inverted or strongly inverted, forming an inversion layer with a high concentration of minority carriers [31, 32] at the heterointerface. From the band diagram, the rate of the inversion is determined by the bending of bands at the surface of c-Si and can be expressed as a distance of the Fermi level from the conduction band level at the heterointerface, $E_i = E_C - E_f$. It is obvious that the car-

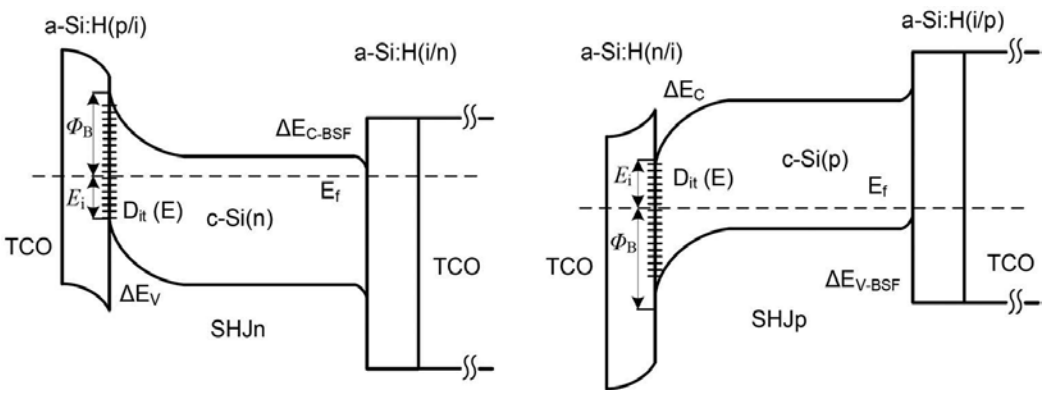

Figure 2. Band diagram of (left) SHJn and (right) SHJp structures with sketched barrier for interface recombination Φ_B at interface defects D_{it}.

rier inversion is linked with Φ_B thus directly related to V_{OC}. For both SHJ, high carrier inversion is required to obtain high value of Φ_B and thus high V_{OC}. Eqs. (1) and (2) do not take into account the influence of a-Si:H layer and indicate that V_{OC} depends on the illumination intensity, recombination properties at the heterointerface, recombination at the rear surface and in the c-Si substrate, and on the dopant activation energy of the c-Si substrate. The properties of the emitter seem to play no role in the V_{OC}. In fact, the parameters like doping, defect density and affinity (or band offset with c-Si) have no direct influence on the V_{OC}. However, all of these parameters affect the charge properties of the space charge region (SCR) of SHJ junction and thus carrier inversion at the heterointerface and consequently V_{OC}. In the following sections, we will describe by means of simulation various SHJ solar cell properties which affect carrier inversion and V_{OC}.

3. Front a-Si:H/c-Si heterointerface

3.1. Front a-Si:H/c-Si: influence of interface defect states

The front a-Si:H/c-Si heterointerface is a key part of the SHJ solar cell which has the main influence on the recombination processes in the structure and thus the output performance. The connection of two materials with different band gaps, lattice and electrical properties results into the formation of band discontinuity and defect states at the interface. Such properties are strongly affecting the carrier transport through that interface. In order to investigate the influence of D_{it} on the carrier inversion and hence recombination activity at the interface, numerical calculations using the program ASA was carried out. **Figure 3(a)** shows V_{OC} and η calculated as a function of D_{it} for SHJp and SHJn solar cell structures. As can be seen, V_{OC} and hence η exhibit a decrease upon the increase of D_{it} for both SHJp and SHJn structures. To explain the recombination processes at the a-Si:H/c-Si interfaces connected with the presence of defect states, it is necessary to consider the band diagram. Analysis will be provided for SHJp structure, however, conclusions are applicable also to SHJn structure. **Figure 3(b)** shows the band diagram of SHJp structure calculated for two values of D_{it}. In the case of SHJp structure with negligibly low $D_{it} = 10^9$ cm^{-2}, the rectification behaviour of the junction is formed due to the presence of the negative and positive space charges in the space charge region (SCR) of the c-Si and a-Si:H part of the junction, respectively. The SHJ solar structure exhibits a high asymmetry of doping, which shifts the SCR into the c-Si part of the junction, leaving a negligible part of the diffusion voltage V_d in the a-Si:H. Due to the presence of band discontinuity in the SHJp solar cell structure, the bands in the c-Si bend downwards and a high concentration of minority electrons is formed at the c-Si surface at the a-Si:H/c-Si interface. Such a layer with a high concentration of minority carriers is called an inversion layer. In the case of high inversion, the concentration of minority electrons is high and the concentration of majority holes is low at the c-Si surface of the heterointerface. For SHJp structure, the photo-generated electrons are collected by the front electrode and transferred through the front heterointerface. High carrier inversion and thus a low concentration of holes results into a low probability of photo-generated electrons to recombine with them. Such a behaviour is characterized by the barrier for interface recombination Φ_B, which is for SHJp

http://dx.doi.org/10.5772/65020

expressed by Eq. (6). The high carrier inversion, in other words high value of Φ_B, leads to low interface recombination. From this it is obvious that carrier inversion plays a crucial role in the V_{OC} of SHJ solar cell. The carrier inversion is changed by introducing a high value of defect states at the interface, $D_{it} = 6 \times 10^{12}$ cm^{-2}. Such defect states affect the charge conditions in the SCR of junction. The defects states at the heterointerface represent traps which are for SHJp structure occupied by electrons forming negative charge Q_i in the SCR at the c-Si part of the junction. Such negative Q_i screens the positive charge in the a-Si:H part of the junction and thus hinders the extension of the SCR in the c-Si. As results, the band bending and electric field in the c-Si part of the junction are lowered, which decreases the carrier inversion at the interface and causes decrease of Φ_B followed by an increase of interfacial recombination. Moreover, due to the lower electric field, the majority of holes have a high probability to diffuse to the interface and contribute to the recombination at the interface [28]. The same mechanism of carrier inversion decrease caused by the presence of Q_i is presented in case of SHJn solar cells (not shown here). However, due to the n-type silicon used in SHJn solar cells and holes collected through the front contact, the Q_i has a positive charge. Comparing both structures (**Figure 3a**), the SHJn structure exhibits a lower sensitivity to D_{it} and a higher efficiency. There are two main sources of such a higher efficiency for the SHJn structure. The first source is the higher FF (not shown here) of SHJn structure compared to SHJp structure. The second reason is the collection of holes through the front heterointerface of SHJn structure, which due to the band alignment exhibits lower interface recombination. The impact of the band alignment on the carrier inversion of SHJ structures is further discussed in Section 3.2.

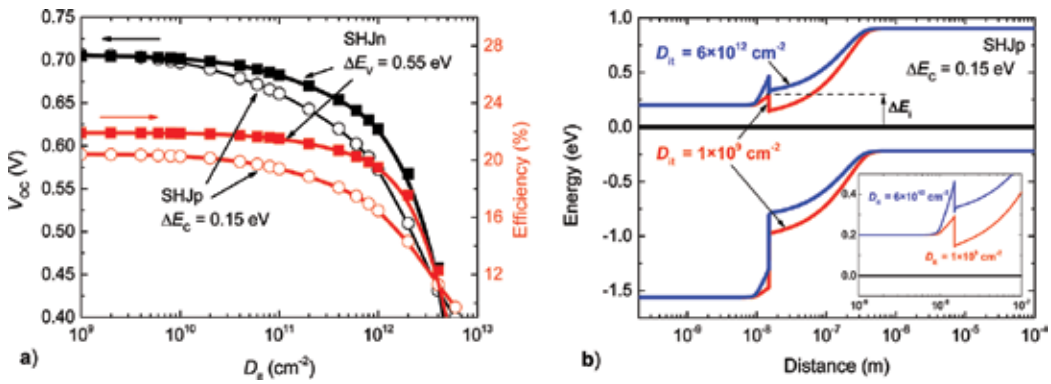

Figure 3. (a) The V_{OC} and η calculated in dependence on D_{it} for SHJn and SHJp structures. (b) Band diagrams calculated for two values of D_{it} for SHJp structure. The inset shows the change of carrier inversion (change in the distance of the conduction band level from the Fermi level at the heterointerface) with the change of D_{it}.

From the above discussion it is clear that the change of the charge properties in the SCR plays the key role for the carrier inversion at the heterointerface and strongly affects V_{OC}. The D_{it} are formed by acceptor and donor types of defects which form negative and positive charges in the c-Si part of SCR, respectively. Our recent study shows that the band bending at the c-Si part of the structure is lowered mainly due to the presence of Q_i with negative charge and Q_i with positive charge for SHJp and SHJn solar cells, respectively [22]. Because of this, the defect

asymmetry at the interface plays also an important role for the recombination processes at the interface [22]. The presence of acceptor defects at the heterointerface is more detrimental for the function of SHJn, while in the case of SHJp structure the donor defects are more affecting the performance of solar cell.

3.2. Front a-Si:H/c-Si: influence of band alignment

Comparing with the standard c-Si-based solar cells, the SHJs are characterized by the formation of a carrier inversion layer of minority carriers at the c-Si surface. The origin of this inversion layer steams from the presence of the band discontinuity at the interface and is the main factor for higher V_{OC} compared to the standard c-Si-based solar cells. In order to describe the impact of band alignment on the V_{OC}, simulation of SHJp solar cells with a varied conduction band offset ΔE_C is presented in **Figure 4(a)**. The impact of non-ideal a-Si:H/c-Si interface is shown as well by using four different values of D_{it}. Clearly, the decrease of ΔE_C results in the decreases of V_{OC}. This effect is stronger, when higher D_{it} is present at the interface. On the other hand, for high ΔE_C, the D_{it} has a weaker impact on the V_{OC}. Such a behaviour can be explained by considering the band bending and carrier inversion in the structure. **Figure 4(b)** shows band diagrams of SHJp solar cells for $D_{it} = 5 \times 10^{11}$ cm^{-2} and two values of ΔE_C. As can be seen, higher ΔE_C results into higher band banding in the c-Si part of the junction and stronger carrier inversion at the heterointerface. Because of this, V_{OC} exhibits higher values for structures with high ΔE_C. Moreover, the strong inversion causes a pronounced suppression of interface recombination since only few majority carries are available for recombination. As a result, the negative impact of D_{it} is less serious for structures with high values of ΔE_C. From this it is obvious that the ability to prepare a-Si:H/c-Si with high ΔE_C should be the way how to suppress the influence of D_{it} and how to attain high V_{OC} and thus the efficiency of SHJ solar cells. However, there are only limited possibilities to modify the band alignment of a-Si:H/c-Si heterointerface based on tuning the hydrogen content in the a-Si:H layer [33]. The literature presents a consensus that ΔE_C at a-Si:H(n)/c-Si(p) heterointerface is below 0.30 eV [23, 34–36].

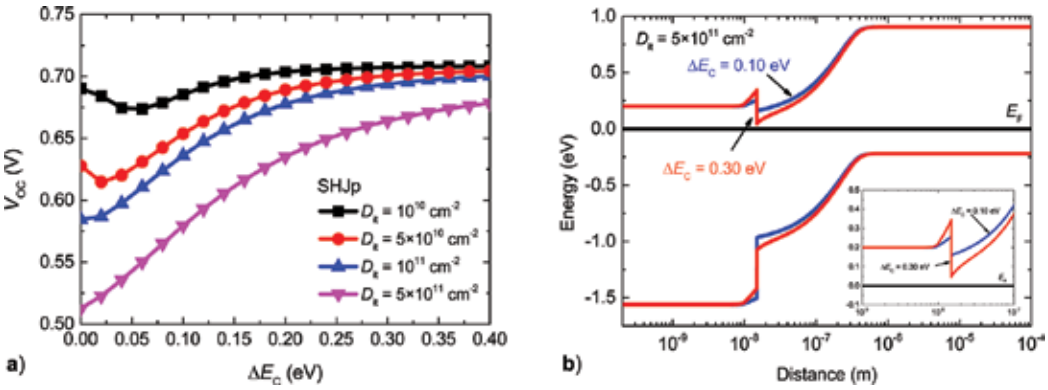

Figure 4. (a) V_{OC} calculated as a function of ΔE_C at the front a-Si:H/c-Si of SHJp solar cell structure. D_{it} is varied as a parameter in the simulations. (b) Band diagrams calculated for two values of ΔE_C and $D_{it} = 5 \times 10^{11}$ cm^{-2} of SHJp solar cell structure. The inset shows the change in the carrier inversion (change in the distance of the conduction band level from the Fermi level at the heterointerface).

Therefore, the critical aspect to obtain high V_{OC} of SHJ structures remains the suppression of defect states at the interface.

In the case of the SHJn structure, the transport of photo-generated minority holes is affected by the valence band offset ΔE_V which, due to the band alignment, has a higher value compared to the ΔE_C of SHJp. Because of this, the SHJn solar cell structures have higher carrier inversion at the interface as well as higher Φ_B and exhibit higher V_{OC} compared to the SHJp structures. Moreover, due to the higher carrier inversion the SHJn structure exhibits a lower sensitivity to D_{it} compared to the SHJp structure (**Figure 3a**).

3.3. Front a-Si:H/c-Si: influence of a-Si:H(i) passivation layer

The most straightforward way to increase the carrier inversion at the c-Si surface is to decrease D_{it}. The a-Si:H emitter with p- or n-type doping is characterized by a high concentration of defects resulting in a high D_{it} at the a-Si:H/c-Si interface. Because of this a thin intrinsic passivation layer of a-Si:H(i) with a significantly lower defect concentration ~5×10^{21} m^{-3} [36] compared to doped a-Si:H layer [27] is inserted at the interface. The quality of the a-Si:H(i) and thus passivation effect increases with the increase of a-Si:H(i) thickness $d_{a\text{-Si:H(i)}}$. However, high $d_{a\text{-Si:H(i)}}$ results in a decrease of FF and performance of SHJ solar cell [37].

A simulation study with a-Si:H(i) inserted at the heterointerface was carried out to describe the impact of $d_{a\text{-Si:H(i)}}$ on the carrier inversion at the c-Si surface and consequently on V_{OC} and the output performance. **Figure 5(a)** shows V_{OC} simulated as a function of $d_{a\text{-Si:H(i)}}$. Three values of D_{it} were used in the simulation as a parameter reflecting the possible passivation effect of a-Si:H(i) layer. In the case of low $D_{it} = 10^9$ cm^{-2}, the change of V_{OC} with $d_{a\text{-Si:H(i)}}$ is negligible. On the other hand, for higher value of D_{it} the decrease of V_{OC} with increase in $d_{a\text{-Si:H(i)}}$ is more relevant. V_{OC} is less sensitive to the presence of D_{it} for low $d_{a\text{-Si:H(i)}}$. This sensitivity to D_{it} increases with increasing $d_{a\text{-Si:H(i)}}$. The band diagrams for $D_{it} = 5 \times 10^{11}$ cm^{-2} and with $d_{a\text{-Si:H(i)}}$ of 10 and 50 nm were calculated to explain the impact of $d_{a\text{-Si:H(i)}}$ on V_{OC} at high D_{it} (**Figure 5b**). The band lines of a-Si:H(i) were aligned for both thicknesses to have the heterointerface at the same place. **Figure 5(b)** shows the decreases of band bending in the c-Si, thus the decrease of the carrier inversion at the heterointerface upon the increase of $d_{a\text{-Si:H(i)}}$ for $D_{it} = 5 \times 10^{11}$ cm^{-2} resulting in the decreases of V_{OC}. The a-Si:H(i) layer has a low concentration of free carriers and thus is a source of a potential drop across this layer, which affects the charge distribution and electric field in the SCR. This potential drop increases with the increase of $d_{a\text{-Si:H(i)}}$. In the case of low $D_{it} = 10^9$ cm^{-2} the strong carrier inversion occurs, in other words a high minority carrier concentration at the c-Si surface screens the potential drop over the a-Si:H(i) layer. Consequently, the potential drop over the a-Si:H(i) layer has a negligible influence on the carrier inversion and thus causes a negligible change of V_{OC} even at high $d_{a\text{-Si:H(i)}}$. In the case of high $D_{it} = 5 \times 10^{11}$ cm^{-2} the carrier inversion is much weaker due to the presence of trapped charge Q_i. Such trapped charge lowers the electric field in the c-Si, hence lowers band bending and decreases the carrier inversion at the c-Si surface. Due to the high Q_i the higher concentration of localized charge in the a-Si:H part of the junction is required to screen the charge in the c-Si. Because of this the potential drop over the a-Si:H(i) becomes more important for the distribution of the diffusion potential in the junction and with an increase of the $d_{a\text{-Si:H(i)}}$ the SCR is more widened

in the amorphous emitter (formed by the intrinsic and doped parts) resulting in an increase of the diffusion voltage in a-Si:H part of the junction and in a decrease of carrier inversion at c-Si surface of the a-Si:H/c-Si interface with increased $d_{\text{a-Si:H(i)}}$. This conclusion is in accordance with experimental observation [38]. V_{OC} decreases as a consequence of weaker carrier inversion. In accordance with this explanation, **Figure 5(b)** shows a more significant decrease of band banding in the c-Si and an increase of the band banding in the a-Si:H followed by a decrease of the carrier inversion at the interface for $d_{\text{a-Si:H(i)}}$ = 50 nm compared to the sample with $d_{\text{a-Si:H(i)}}$ = 10 nm. While the quality and thus passivation properties of the a-Si:H(i) layer increase with the thickness, careful tuning of the thickness and passivation ability is required to achieve high V_{OC} and high output performance. The same principle can be applied to the SHJn structure.

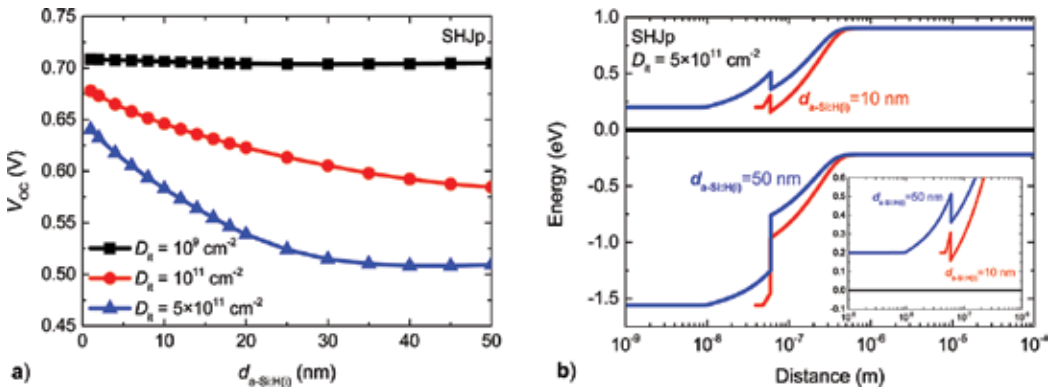

Figure 5. (a) V_{OC} calculated as a function of a-Si:H(i) thickness, $d_{\text{a-Si:H(i)}}$ inserted at the front a-Si:H/c-Si of SHJp solar cell structure. D_{it} is varied as a parameter in the simulations. (b) Band diagrams calculated for two values of $d_{\text{a-Si:H(i)}}$ and D_{it} = 5 × 10^{11} cm^{-2} for SHJp solar cell structure. The inset shows the change in the carrier inversion (change in the distance of the conduction band level from the Fermi level at the heterointerface).

3.4. Alternative concepts to obtain carrier inversion at emitter/c-Si interface

From the above discussion it is clear that high carrier inversion at the emitter/c-Si interface is crucial for high V_{OC} and high output performance of the SHJ solar cell. The high carrier inversion in the SHJ solar cells can be attained through (i) modification of band alignment at the heterointerface or (ii) by a decrease of D_{it} by optimizing the cleaning process or by insertion of a thin passivation a-Si:H(i) layer [6]. In following, we will discuss two alternative concepts of emitters which allow formation of high inversion at the emitter/c-Si interface and offer perspective to achieve high performance. The first one is the hetero-homojunction concept based on the field passivation effect [39, 40] and the second one is the use of alternative emitters based on transition metal oxides TMO with high W_f, which form the hole transport layers in SHJn structures [41].

http://dx.doi.org/10.5772/65020

The first alternative approach is based on the insertion of a highly doped c-Si layer of n^+- and p^+-type doping at the a-Si:H/c-Si interface of SHJp and SHJn solar structure, respectively [39, 40]. Such a highly doped layer with opposite doping of c-Si provides field passivation, and causes a shift of the Fermi level, which leads to an increase in carrier inversion at the c-Si surface. Our recent simulation study shows that by using the field effect passivation it is possible to decrease the sensitivity of V_{OC} to D_{it} and ΔE_C at the a-Si:H/c-Si interface [40]. The main drawback of this approach is, however, the additional technological steps required for preparation of a thin highly doped c-Si layer [42].

TMO with a high work function W_f such as MoOx, V_2O_5 and WO_3 represent alternative materials which can replace the a-Si:H emitter and can provide high carrier inversion at the c-Si surface [41]. The work function of these oxides changes according to the presence of adjacent environment or layer and varies in the range from 6 to 7 eV for as deposited layers and from 5 to 5.3 eV for oxides exposed to air [41]. Due to the intrinsic oxygen vacancies in their structure TMO are acting as n-type semiconductors [41, 43]. However, due to the high W_f TMO provides band alignment with c-Si in the way that acts as a p-contact and allows formation of a depletion silicon surface and strong carrier inversion at the interface in connection with n-type c-Si. Also in the case of SHJ with TMO, the carrier inversion is strongly affected by the defect states at the heterointerface, thus passivation a-Si:H(i) layer is required to insert at the TMO/c-Si interface to provide high performance of such SHJ solar cell structures. The efficiency of 22.5% was obtained for MoOx based on SHJ cell [18]. Despite the high efficiency obtained on TMO-based SHJ, the carrier transport mechanism and collection of photo-generated carriers are still not fully understood. Recent results suggest that regardless of the rectification behaviour caused by the high W_f, classical depletion approximation can be used to describe the rectification behaviour of TMO/c-Si junction [41]. It was shown that measured *I-V* curves can be described by a two-diode model with current transport limited by the recombination in the SCR of c-Si and diffusion of injected minority carriers [41]. However, further research is required to understand the extraction mechanism of photo-generated holes assisted by the gap states in the emitter based on the metal oxide.

4. Front TCO/a-Si:H heterointerface

4.1. Front TCO/a-Si:H: impact of parasitic Schottky barrier

The above simulation study revealed that V_{OC} is strongly determined by the properties at the front a-Si:H/c-Si heterointerface. Defect states and band alignment affect the distribution of the charge in the SCR and thus directly influence the electric field and carrier inversion at the heterointerface. The photo-generated carriers are collected by the front TCO and metal contacts. While TCO can be considered as a degenerated semiconductor, the properties at TCO/a-Si:H have to be also considered for carrier transport [44–46]. The most critical aspect for carrier transport is the possible presence of a parasitic Schottky barrier at the TCO/a-Si:H interface which can arise due to an inappropriate work function of TCO, W_{TCO} [24]. W_{TCO} depends on the material used as a TCO as well as on the deposition conditions used for

preparation. For example, in the case of ITO work functions of 4.2–5.3 eV were reported [45, 47]. The most common way to modify W_{TCO} is by controlling the oxygen pressure or pre- and post-deposition annealing [46]. It was shown that the parasitic Schottky barrier at TCO/a-Si:H interface of value Φ_{TCO} = 0.35 eV can reduce the conversion efficiency by more than 40% due to the deteriorated light current-voltage characteristics, which follows the so-called S-shape [48]. The Φ_{TCO} is partially affected by the carrier doping in the TCO layer, which shifts the Fermi level and thus affects the band alignment at the TCO/a-Si:H. Depending on the magnitude of Φ_{TCO}, different carrier transport mechanisms should provide a good contact TCO/a-Si:H. In the case of low Φ_{TCO}, thermionic emission should take place as a dominant transport mechanism of carriers. In the case of high Φ_{TCO}, tunnelling should take place to assist in the carrier transport. For tunnelling to be active it is necessary to have a high doping at both adjacent parts of the junction [46]. Recently, it was shown that high doping of TCO can result in lowering of the passivation and thus decrease the carrier inversion at the a-Si:H/c-Si, resulting in a decrease of V_{OC} and output performance [46]. Because of this, it is necessary to carefully consider not only the W_{TCO} but also the appropriate carrier doping to achieve a loss-free TCO/a-Si:H interface.

In the following simulation, the TCO is considered as a metal contact and the impact is simulated of low parasitic Φ_{TCO} at the TCO/a-Si:H emitter on the performance of SHJp solar cell. The aim of this simulation is to describe the impact of the Φ_{TCO} on the carrier inversion at the a-Si:H/c-Si of SHJp solar cells with conclusions which can be extended to the SHJn solar cell. **Figure 6(a)** shows V_{OC} simulated as a function of emitter layer thickness d_{emitt} and as a function of Φ_{TCO}. To model the high and low quality of a-Si:H/c-Si interface, two values of negligible low $D_{it} = 10^9$ and high 5×10^{11} cm^{-2} were adopted in the simulations. For the low value of D_{it} a negligible change of V_{OC} with Φ_{TCO} is observed. On the other hand, the change of V_{OC} with Φ_{TCO} is more relevant for high values of D_{it}. With the increase of d_{emitt} the influence of Φ_{TCO} on V_{OC} becomes negligible. Φ_{TCO} has an impact only on SHJp with a high value of D_{it} and low d_{emitt}. To explain such a behaviour, **Figure 6(b)** shows the band diagrams of SHJp structures with Φ_{TCO} = 0.2 eV, $D_{it} = 5 \times 10^{11}$ cm^{-2} simulated for d_{emitt} = 1 and 8 nm. For comparison reasons, the band diagram of SHJp with d_{emitt} = 8 nm and without parasitic Schottky barrier is shown as well. The band lines for both d_{emitt} were aligned to have the heterointerface at the same distance. As can be seen, the structures with Φ_{TCO} = 0 eV and Φ_{TCO} = 0.2 eV simulated with d_{emitt} = 8 nm exhibit the same carrier inversion at the silicon surface of the a-Si:H/c-Si interface. The carrier inversion is, however, significantly lowered when d_{emitt} decreases to 1 nm. The parasitic Φ_{TCO} forms SCR at the TCO/a-Si:H contact and thus is the source of an electric field with opposite direction to the electric field at the a-Si:H/c-Si junction. In the case of low D_{it} the strong carrier inversion at the c-Si surface of a-Si:H/c-Si interface screens the charge and electric field in the SCR of Φ_{TCO}. As a result, Φ_{TCO} has only a negligible impact on the band bending as well as on the carrier inversion and V_{OC} (**Figure 6b**). For D_{it} = 5×10^{11} cm^{-2} the carrier inversion at the a-Si:H/c-Si is significantly lowered due to the presence of Q_i. For such conditions, the distribution of the electric field in the a-Si:H emitter is more sensitive to Φ_{TCO}. In case of high d_{emitt}, the free carriers in the emitter can screen the impact of Φ_{TCO} and the electric field formed in the SCR of Φ_{TCO} barrier, thus no relevant decrease of carrier inversion at a-Si:H/c-Si is observed. With a decrease of d_{emitt} the SCR of

http://dx.doi.org/10.5772/65020

Φ_{TCO} can reach the SCR of SHJp. For such a case, the electric field of Φ_{TCO} lowers the diffusion potential of a-Si:H/c-Si and the parasitic Schottky barrier attracts the holes from the c-Si. As a result, carrier inversion at the interface decreases, leading into a decrease of V_{OC} and thus the overall performance decreases. Simulation results revealed that the negative influence of the parasiticΦ_{TCO} is due to the change of the carrier inversion at the a-Si:H/c-Si interface caused by the electric field of SCR at TCO/a-Si:H contact. Such a change is, however, possible only for low emitter thicknesses which have not sufficient charge for screening of Φ_{TCO}. Obviously, the doping of the emitter layer, in other words, the concentration of free carriers will also affect the screening ability of the emitter. With decrease of the doping, Φ_{TCO} will have more significant impact on the carrier inversion at the a-Si:H/c-Si interface and thus will more rapidly deteriorate the output performance.

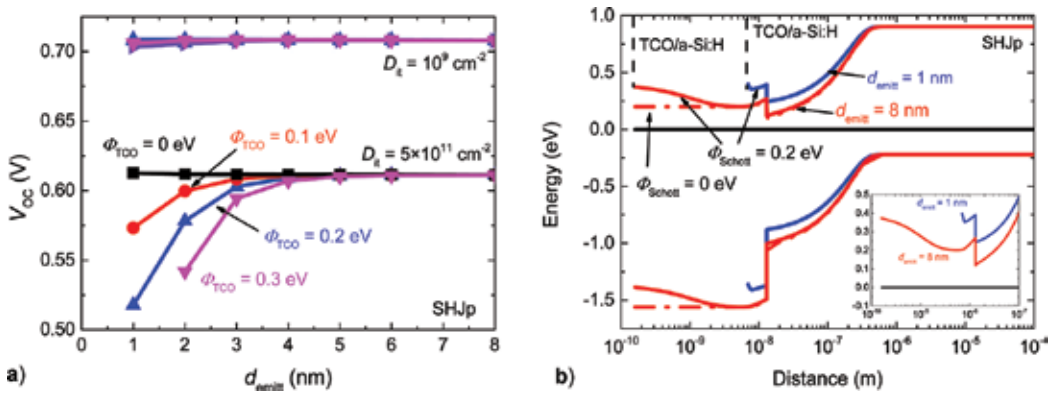

Figure 6. (a) V_{OC} calculated as a function of d_{emitt} of SHJp solar cell structure. Φ_{TCO} is varied as a parameter and two values of D_{it} are used in the simulations. (b) Band diagrams calculated for two values of d_{emitt} and Φ_{TCO} = 0.2 eV for SHJp solar cell structure. The band diagrams are aligned to place the heterointerface at the same distance. The inset shows the change in the carrier inversion.

Similar effect of Φ_{TCO} is presented in SHJn structure. Comparing SHJn and SHJp structures, the main difference is in the dopation type of amorphous emitter and thus required W_f of TCO to obtain good TCO/a-Si:H contact. Due to the presence of n-type a-Si:H emitter in SHJp solar cell, the TCO lower than at least 4.5 eV is required [24]. Typically, TCO materials have W_f higher than 4.5 eV [49, 50], which make the design of SHJp more challenging and require higher thicknesses or higher doping of a-Si:H emitter layer. In case of SHJn solar cells, the minimal W_f = 5.1 eV is required to obtain good TCO/a-Si:H contact [24], resulting in the lower technological obstacles for preparation of good TCO/a-Si:H contact.

5. The role of interfaces in SHJ working under concentrated light

Recently, possible utilization of silicon-based solar cells in light concentration applications became an attractive approach to increase the energy yield from such solar cell structures [51,

52]. Thus, it is of high interest to explore possible aspects connected with the SHJ solar cells for utilizations under concentrated light. Due to the formation of heterojunctions between a-Si:H layers and the c-Si absorption layer, the carrier transport has to overcome barriers at the front and back interfaces of the SHJ structure. Such barriers can significantly affect the collection of photo-generated carriers and thus the solar cell performance at high light intensity. Moreover, the increased light intensity absorbed by the solar cell represents a considerable amount of energy which is partially transformed to thermal energy and causes an increase of cell temperature. Because of this, the impact of the elevated temperature of such a solar cell is considered in the simulations as well. **Figure 7(a)** shows the efficiency as a function of concentrated light expressed in the suns (1 sun = 1000 W/m^2) calculated at 300, 340 and 380 K for both SHJn and SHJp structures. As can be seen, the efficiency at 1 sun decreases with temperature for both SHJ structures. Such decreases are due to the increase of the saturation current caused by an increase of the intrinsic carrier concentration in the c-Si. Saturation current lowers the V_{OC} (see Eq. 5), which consequently results in a decrease of efficiency. In general, the increase of light concentration causes an increase of the light generation g and excess concentration of carriers $\Delta p = \Delta n$, thus results in an increases of V_{OC} according to Eqs. (1) and (2) for SHJp and SHJn, respectively (see Section 2). Simulated results revealed that the efficiency of SHJ structures reach the maximum value at particular light concentration and then starts to decrease. With increased temperature the maximum of the efficiency is shifted to higher values of light concentrations. The temperature dependence of efficiency suggests that the source of efficiency drop at higher light concentrations is the presence of barriers for carrier transport which are partially overcome at higher temperatures by thermionic emission. Such carrier transport limitations are reflected also in FF. **Figure 7(b)** shows FF calculated as a function of light concentration for both SHJn and SHJp structures. The FF exhibits a similar trend to V_{OC}, and decreases significantly at high light concentrations. This drop is more relevant for SHJp structure. Considering the band diagrams of both SHJ structures (see **Figures 2a** and **b**), it can be suggested that different barriers are limiting carrier transport in SHJp and SHJn solar cells. In the case of SHJn, the photo-generated holes are collected through the front heterointerface and photo-generated electrons are collected through the back surface field (BSF) formed in our case by the c-Si/a-Si:H(n) contact. For SHJn structure, the valence band offset at the front a-Si:H/c-Si ΔE_V attains considerable higher values of 0.55 eV compared to the conduction band offset ΔE_C = 0.15 eV at the back BSF contact. It can be assumed that, due to the higher barrier, the front a-Si:H/c-Si heterointerface will be the main limitation factor for the transport of photo-generated carriers. In the case of SHJp structure, photo-generated electrons are collected through the front a-Si:H(n)/c-Si(p) contact, while photo-generated holes are collected through the back c-Si(p)/a-Si:H(p) BSF contact. ΔE_C for minority electrons at the front heterointerface is around 0.15 eV, while the barrier for holes ΔE_{BSF} can reach values around 0.7 eV. Because of this, it can be assumed that the back contact is the limiting factor for the carrier transport for SHJp structure.

ASA simulation was carried out to confirm the negative impact of the front ΔE_V and back ΔE_{BSF} barrier for carrier transport of SHJn and SHJp structures, respectively. **Figure 8(a)** shows the simulated efficiency as a function of light concentration for SHJn at 300 K with considered variation in ΔE_V from 0.65 to 0.45 eV. ΔE_V has a negligible impact on the efficiency at 1 sun light

concentration. With the increase of the light concentration the efficiency exhibits a decrease, which is more relevant for higher ΔE_V values. We can assume that such a decrease of efficiency is connected with limitation of carrier transport through ΔE_V barrier. **Figure 8(b)** shows the efficiency of SHJp calculated as a function of light concentration with a varied barrier for holes ΔE_{BSF}. The results show that the onset of the efficiency decrease is shifted to higher light concentrations with an increase of ΔE_{BSF}. Further simulations revealed (not shown in this chapter) that varying of the front ΔE_C has no impact on the efficiency behaviour with the change of light concentration. Such trends justify the back ΔE_{BSF} barrier to be responsible for the limitation of carrier transport and efficiency losses at high light concentrations of SHJp solar cell structure.

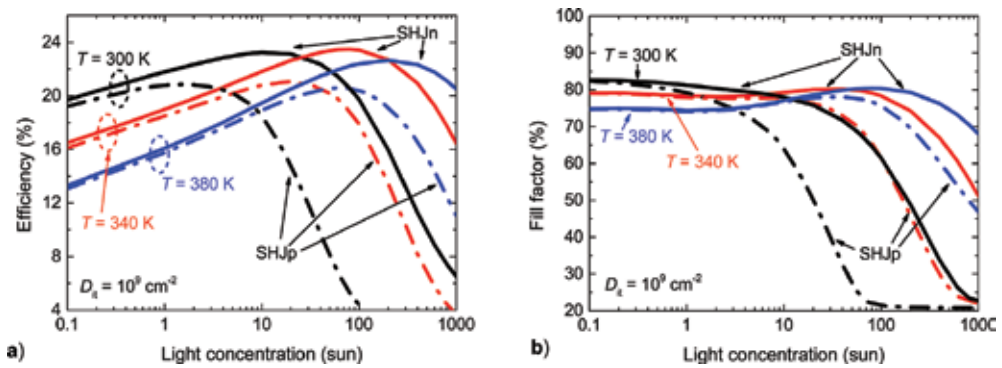

Figure 7. (a) Efficiency η and (b) FF calculated as a function of light concentration at temperatures 300, 340 and 380 K for SHJn (solid lines) and SHJp (dashed lines) structures.

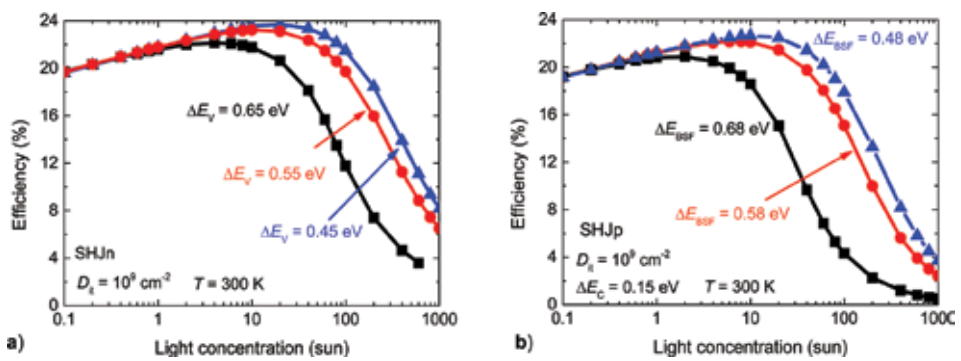

Figure 8. (a) Efficiency η calculated as a function of light concentration for different values of ΔE_V of SHJn solar cell structure. (b) Efficiency η calculated as a function of light concentration for different values of ΔE_{BSF} of SHJp solar cell structure.

From the above discussion it is clear that the presence of barriers for carrier transports has to be taken into account when the SHJ is designed for light concentration applications. While amorphous silicon forms higher ΔE_V than ΔE_C with c-Si, the barriers for collections of holes

are the main source of carrier transport limitations. In the case of SHJn structure such a barrier is formed at the front a-Si:H/c-Si interface while for SHJp structure this barrier is placed at the back c-Si/a-Si:H BSF contact. Due to the presence of thermionic emission causing a temperature-dependent carrier transport mechanism through such barriers, adjustment of the working temperature with light concentration has to be considered in order to attain the highest possible efficiency of SHJ solar cells in concentrated solar applications.

Our recent study shows that the higher operation temperature has a beneficial effect not only in enhancement of the carrier transport through barriers formed by the a-Si:H/c-Si interface but also decreases the negative impact of the parasitic Schottky barrier at the TCO/a-Si:H interface [53]. The negative influence of such barriers is more significant for SHJn structure, where the Schottky barrier depletes the emitter and increases the negative influence of ΔE_V. Thus, the optimization of SHJn solar cell structures for solar applications under concentrated light is more challenging compared to SHJp solar cell structures.

6. Conclusion

This chapter was devoted to a-Si:H/c-Si and TCO/a-Si:H heterointerfaces forming the front emitter stack with the aim to explain the influence of such heterointerfaces on V_{OC} and output performance of SHJp and SHJn solar cells. It was shown that the carrier inversion at the c-Si surface of a-Si:H/c-Si plays a key role for V_{OC} and the output performance. Various properties affecting the carrier inversion in the SHJ solar cells were analysed by means of numerical simulation leading to several conclusions. Low defect states at the interface as well as large band offset for minority carriers at a-Si:H/c-Si heterojunction are crucial to achieve strong carrier inversion and high V_{OC}. The insertion of an a-Si:H(i) passivation layer provides a decrease of the defect states at the interface; however, careful tuning of the passivation layer thickness is required to achieve a strong passivation effect with a negligible negative effect of the potential drop over this passivation layer. The Schottky barrier at the TCO/a-Si:H interface acts as a parasitic junction with opposite direction of the electric field to the electric of a-Si:H/c-Si junction. In the case of weak carrier inversion and small emitter thickness, the effect of the parasitic Schottky barrier is not screened by the charge in the emitter or minority carriers in the inversion layer and the Schottky barrier deteriorates the performance of SHJ solar cell. The simulation of SHJ structures at concentrated light conditions revealed a crucial effect of the barriers for hole collection on the efficiency. Tuning of such barriers together with tuning of the operation temperature is required to achieve a high performance of SHJ solar cells under concentrated light conditions. Due to the higher valence band offset compared to the conduction band offset at the a-Si:H/c-Si interface, higher carrier inversion is observed at the front heterointerface of SHJn solar cells leading to higher V_{OC} and lower sensitivity to defect states at the heterointerface for SHJn solar cells compared to SHJp solar cell. Two alternative concepts with the ability to provide high carrier inversion at the heterointerfaces were presented. The first one is based on the field effect passivation provided by insertion of a highly doped c-Si layer at the interface and the second one is based on the replacement of a-Si:H emitter by metal

oxide with high W_f, which provides favourable band alignment for formation of strong carrier inversion at the heterointerface.

Acknowledgements

This work was supported by the Scientific Grant Agency of the Ministry of Education of the Slovak Republic and of the Slovak Academy of Sciences under project VEGA 1/0651/16 and Slovak Research and Development Agency under the contract APVV-15-0152.

Author details

Miroslav Mikolášek

Address all correspondence to: miroslav.mikolasek@stuba.sk

Faculty of Electrical Engineering and Information Technology, Institute of Electronics and Photonics, Slovak University of Technology in Bratislava, Bratislava, Slovakia

References

[1] Louwen A, Van Sark W, Schropp R, Faaij A: A cost roadmap for silicon heterojunction solar cells. Sol Energy Mater Sol Cells. 2016;147:295–314. DOI: 10.1016/j.solmat.2015.12.026

[2] Sakata H, Tsunomura Y, Inoue H, Taira S, Baba T, Kanno H, et al.: R&d progress of next-generation very thin hit. In: Proceedings of 2010 25th European Photovoltaic Solar Energy Conference and Exhibition/5th World Conference on Photovoltaic Energy Conversion, 6–10 September 2010, Valencia, Spain. 2010. pp. 1102–1105.

[3] Tanaka M, Taguchi M, Marsuyama T, Sawada T, Hanafusa H, Kuwano Y: Development of new a-Si/c-Si heterojunction solar cells: ACJ-HIT (artifically constructed junction-heterojunction with intrinsic thin-layer). Jpn J Appl Phys. 1992;31:3518–3522. DOI: 1347-4065/31/11R/3518

[4] Masuko K, Shigematsu M, Hashiguchi T, Fujishima D, Kai M, Yoshimura N, et al.: Achievement of more than 25% conversion heterojunction solar cell. IEEE J Photovoltaics. 2014;4(6):1433–1435. DOI: 10.1109/JPHOTOV.2014.2352151

[5] Sawada T, Terada N, Tsuge S, Baba T, Takahama T, Wakisaka K, et al.: High-efficiency a-Si/c-Si heterojunction solar cell. Proc 1994 IEEE 1st World Conf Photovolt Energy

Convers – WCPEC (A Jt Conf PVSC, PVSEC PSEC). 1994;2:1219–1226. DOI: 10.1109/WCPEC.1994.519952

[6] Wolf S De, Descoeudres A, Holman ZC, Ballif C: High-efficiency silicon heterojunction solar cells: a review. Green. 2012;0(0):7–24. DOI: 10.1515/green-2011-0018

[7] Mishima T, Taguchi M, Sakata H, Maruyama E: Development status of high-efficiency HIT solar cells. Sol Energy Mater Sol Cells. 2011;95(1):18–21. DOI: 10.1016/j.solmat.2010.04.030

[8] Zhong CL, Luo LE, Tan HS, Geng KW: Band gap optimization of the window layer in silicon heterojunction solar cells. Sol Energy. 2014;108:570–575. DOI: 10.1016/j.solener.2014.08.010

[9] Kirner S, Mazzarella L, Korte L, Stannowski B, Rech B, Schlatmann R: Silicon heterojunction solar cells with nanocrystalline silicon oxide emitter: insights into charge carrier transport. IEEE J Photovolt. 2015;PP(99):1–5. DOI: 10.1109/JPHOTOV.2015.2479461

[10] Mazzarella L, Kirner S, Stannowski B, Korte L, Rech B, Schlatmann R: P-type microcrystalline silicon oxide emitter for silicon heterojunction solar cells allowing current densities above 40 mA/cm^2. Appl Phys Lett. 2015;106(2):023902. DOI: 10.1063/1.4905906

[11] Ruske F, Roczen M, Lee K, Wimmer M, Gall S, Hupkes J, et al.: Improved electrical transport in Al-doped zinc oxide by thermal treatment. J Appl Phys. 2010;107(1):1–8. DOI: 10.1063/1.3269721

[12] Morales-Masis M, Martin De Nicolas S, Holovsky J, De Wolf S, Ballif C: Low-temperature high-mobility amorphous IZO for silicon heterojunction solar cells. IEEE J Photovolt. 2015;5(5):1340–1347. DOI: 10.1109/JPHOTOV.2015.2450993

[13] Geissbühler J, Wolf S De, Faes A, Badel N, Jeangros Q, Tomasi A, et al.: Silicon heterojunction solar cells with copper-plated grid electrodes◎: status and comparison with silver thick-film techniques. IEEE J Photovolt. 2014;4(4):1055–1062. DOI: 10.1109/JPHOTOV.2014.2321663

[14] Bivour M, Temmler J, Steinkemper H, Hermle M: Molybdenum and tungsten oxide: high work function wide band gap contact materials for hole selective contacts of silicon solar cells. Sol Energy Mater Sol Cells. 2015;142:34–41. DOI: 10.1016/j.solmat.2015.05.031

[15] Bullock J, Cuevas A, Allen T, Battaglia C: Molybdenum oxide MoOx: a versatile hole contact for silicon solar cells. Appl Phys Lett. 2014;105(23). DOI: 10.1063/1.4903467

[16] Reddy SS, Gunasekar K, Heo JH, Im SH, Kim CS, Kim DH, et al.: Highly efficient organic hole transporting materials for perovskite and organic solar cells with long-term stability. Adv Mater. 2016;28(4):686–693. DOI: 10.1002/adma.20150372

[17] Li X, Xie F, Zhang S, Hou J, Choy WC: MoOx and V_2Ox as hole and electron transport layers through functionalized intercalation in normal and inverted organic optoelectronic devices. Light Sci Appl. 2015;4(4):e273. DOI: 10.1038/lsa.2015.46

[18] Geissbühler J, Werner J, Martin De Nicolas S, Barraud L, Hessler-Wyser A, Despeisse M, et al.: 22.5% efficient silicon heterojunction solar cell with molybdenum oxide hole collector. Appl Phys Lett. 2015;107(8): 081601. DOI: 10.1063/1.4928747

[19] Bullock J, Hettick M, Geissbühler J, Ong AJ, Allen T, Sutter-Fella CM, et al.: Efficient silicon solar cells with dopant-free asymmetric heterocontacts. Nat Energy. 2016;1:15031. DOI: 10.1038/nenergy.2015.31

[20] Balestrieri M, Pysch D, Becker JP, Hermle M, Warta W, Glunz SW: Characterization and optimization of indium tin oxide films for heterojunction solar cells. Sol Energy Mater Sol Cells. 2011;95(8):2390–2399. DOI: 10.1016/j.solmat.2011.04.012

[21] Kegel J, Angermann H, Sturzebecher U, Conrad E, Mews M, Korte L, et al.: Over 20% conversion efficiency on silicon heterojunction solar cells by IPA-free substrate texturization. Appl Surf Sci. 2014;301:56–62. DOI: 10.1016/j.apsusc.2014.01.183

[22] Mikolášek M, Racko J, Harmatha L, Gašpierik P, Šutta P: Influence of the broken symmetry of defect state distribution at the a-Si:H/c-Si interface on the performance of hetero-junction solar cells. Appl Surf Sci. 2010;256(18):5662–5666. DOI: 10.1016/j.apsusc.2010.03.023

[23] Schmidt M, Korte L, Laades A, Stangl R, Schubert C, Angermann H, et al.: Physical aspects of a-Si:H/c-Si hetero-junction solar cells. Thin Solid Films. 2007;515(19 SPEC. ISS.):7475–7480. DOI: 10.1016/j.tsf.2006.11.087

[24] Zhao L, Zhou CL, Li HL, Diao HW, Wang WJ: Role of the work function of transparent conductive oxide on the performance of amorphous/crystalline silicon heterojunction solar cells studied by computer simulation. Phys Stat Sol A. 2008;205(5):1215–1221. DOI: 10.1002/pssa.200723276

[25] Ritzau KU, Bivour M, Schroer S, Steinkemper H, Reinecke P, Wagner F, et al.: TCO work function related transport losses at the a-Si:H/TCO-contact in SHJ solar cells. Sol Energy Mater Sol Cells. 2014;131:9–13. DOI: 10.1016/j.solmat.2014.06.026

[26] Zeman M, Heuvel J van den, Kroon M, Willemen J, Pieters BE, Krč J, et al.: Advanced Semiconductor Analysis: User's Manual. 2010.

[27] Riesen Y, Stuckelberger M, Haug F-J, Ballif C, Wyrsch N: Temperature dependence of hydrogenated amorphous silicon solar cell performances. J Appl Phys. 2016;119(4): 044505. DOI: 10.1063/1.4940392

[28] Zhong C, Geng K, Luo L, Yang D: An analytical model to explore open-circuit voltage of a-Si:H/c-Si heterojunction solar cells. J Cent South Univ. 2016;23(3):598–603. DOI: 10.1007/s11771-016-3106-0

[29] Zhong CL, Yao RH, Geng KW: Characterization of interface states in a-Si:H/c-Si heterojunctions by an expression of the theoretical diffusion capacitance. J Phys D Appl Phys. 2010;43(49):495102. DOI: 10.1088/0022-3727/43/49/4951

[30] Jensen N, Rau U, Hausner R, Uppal S, Oberbeck L, Bergmann R, et al.: Recombination mechanisms in amorphous silicon/crystalline silicon heterojunction solar cells. J Appl Phys. 2000;87(5):2639–2645. DOI: 10.1063/1.372230

[31] Gudovskikh AS, Ibrahim S, Kleider JP, Damon-Lacoste J, Roca i Cabarrocas P, Veschetti Y, et al.: Determination of band offsets in a-Si:H/c-Si heterojunctions from capacitance-voltage measurements: capabilities and limits. Thin Sol Films. 2007;515(19):7481–7485. DOI: 10.1016/j.tsf.2006.11.198

[32] Maslova OA, Alvarez J, Gushina E V, Favre W, Gueunier-Farret ME, Gudovskikh AS, et al.: Observation by conductive-probe atomic force microscopy of strongly inverted surface layers at the hydrogenated amorphous silicon/crystalline silicon heterojunctions. Appl Phys Lett. 2010;97(25):10–13. DOI: 10.1063/1.3525166

[33] Schulze TF, Korte L, Ruske F, Rech B: Band lineup in amorphous/crystalline silicon heterojunctions and the impact of hydrogen microstructure and topological disorder. Phys Rev B Condens Matter Mater Phys. 2011;83(16):1–11. DOI: 10.1103/PhysRevB.83.165314

[34] Kleider JP, Gudovskikh AS, Roca I Cabarrocas P: Determination of the conduction band offset between hydrogenated amorphous silicon and crystalline silicon from surface inversion layer conductance measurements. Appl Phys Lett. 2008;92(16): 162101. DOI: 10.1063/1.2907695

[35] Essick JM, Cohen JD: Band offsets and deep defect distribution in hydrogenated amorphous silicon-crystalline silicon heterostructures. Appl Phys Lett. 1989;55(12): 1232–1234. DOI: 10.1063/1.101664

[36] Mikolášek M, Jakabovič J, Řeháček V, Harmatha L, Andok R: Capacitance analysis of the structures with the a-Si:H(i)/c-Si(p) heterojunction for solar-cell applications. J Electr Eng. 2014;65(4):254–258. DOI: 10.2478/jee-2014-0039

[37] Page MR, Iwaniczko E, Xu YQ, Roybal L, Hasoon F, Wang Q, et al.: Amorphous/crystalline silicon heterojunction solar cells with varying i-layer thickness. Thin Solid Films. 2011;519(14):4527–4530. DOI: 10.1016/j.tsf.2011.01.293

[38] Mikolášek M, Stuchlíková Ľ, Harmatha L, Vincze A, Nemec M, Racko J, et al.: Capacitance study of carrier inversion at the amorphous/crystalline silicon heterojunction passivated by different thicknesses of i-layer. Appl Surf Sci. 2014;312:152–156. DOI: 10.1016/j.apsusc.2014.03.187

[39] Carrere T, Varache R, Munoz D, Kleider JP: Insertion of a thin highly doped crystalline layer in silicon heterojunction solar cells: simulation and perspectives towards a highly efficient cell concept. J Renew Sustain Energy. 2015;7(1): 011202. DOI: 10.1063/1.4908189

[40] Mikolášek M, Príbytný P, Donoval D, Marek J, Chvála A, Molnár M, et al.: Suppression of interface recombination by buffer layer for back contacted silicon heterojunction solar cells. Appl Surf Sci. 2014;312:145–51. DOI: 10.1016/j.apsusc.2014.05.110

[41] Gerling LG, Mahato S, Morales-Vilches A, Masmitja G, Ortega P, Voz C, et al.: Transition metal oxides as hole-selective contacts in silicon heterojunctions solar cells. Sol Energy Mater Sol Cells. 2016;145:109–115. DOI: 10.1016/j.solmat.2015.08.028

[42] Carrere T, Varache R, Le Perchec J, Denis C, Munoz D, Kleider JP: Silicon Bulk issues during processing of homo-heterojunction solar cells. Energy Procedia. 2015;77:451–457. DOI: 10.1016/j.egypro.2015.07.064

[43] Meyer J, Hamwi S, Kroger M, Kowalsky W, Riedl T, Kahn A: Transition metal oxides for organic electronics: energetics, device physics and applications. Adv Mater. 2012;24(40):5408–427. DOI: 10.1002/adma.201201630

[44] Zhao L, Zhou CL, Li HL, Diao HW, Wang WJ: Design optimization of bifacial HIT solar cells on p-type silicon substrates by simulation. Sol Energy Mater Sol Cells. 2008;92(6): 673–681. DOI: 10.1016/j.solmat.2008.01.018

[45] Bivour M, Schröer S, Hermle M: Numerical analysis of electrical TCO/a-Si:H(p) contact properties for silicon heterojunction solar cells. Energy Procedia. 2013;38:658–669. DOI: 10.1016/j.egypro.2013.07.330

[46] Kirner S, Hartig M, Mazzarella L, Korte L, Frijnts T, Scherg-Kurmes H, et al.: The Influence of ITO dopant density on J-V characteristics of silicon heterojunction solar cells: experiments and simulations. Energy Procedia. 2015;77(1):725–732. DOI: 10.1016/j.egypro.2015.07.103

[47] Klein A, Körber C, Wachau A, Säuberlich F, Gassenbauer Y, Harvey SP, et al.: Transparent conducting oxides for photovoltaics: manipulation of fermi level, work function and energy band alignment. Materials (Basel). 2010;3(11):4892–4914. DOI: 10.3390/ma3114892

[48] Centurioni E, Iencinella D.: Role of front contact work function on amorphous silicon/crystalline silicon heterojunction solar cell performance. IEEE Electron Device Lett. 2003;24(3):177–179. DOI: 10.1109/LED.2003.811405

[49] Minami T, Miyata T, Yamamoto T.: Work function of transparent conducting multicomponent oxide thin films prepared by magnetron sputtering. Surf Coat Technol. 1998;108-109:583–587. DOI: 10.1016/S0257-8972(98)00592-1

[50] Kim JS, Lägel B, Moons E, Johansson N, Baikie ID, Salaneck WR, et al.: Kelvin probe and ultraviolet photoemission measurements of indium tin oxide work function: a comparison. Synth Met. 2000;111:311–314. DOI: 10.1016/S0379-6779(99)00354-9

[51] Descoeudres A, Allebé C, Badel N, Barraud L, Jonathan Champliaud, Debrot F, et al.: Silicon heterojunction solar cells: towards low-cost high-efficiency industrial devices and application to low-concentration PV. Energy Procedia. 2015;77:508–514. DOI: 10.1016/j.egypro.2015.07.072

[52] Paternoster G, Zanuccoli M, Bellutti P, Ferrario L, Ficorella F, Fiegna C, et al.: Fabrication, characterization and modeling of a silicon solar cell optimized for concentrated

photovoltaic applications. Sol Energy Mater Sol Cells. 2015;134:407–416. DOI: 10.1016/j.solmat.2014.12.026

[53] Mikolášek M, Racko J, Harmatha L.: Analysis of low temperature output parameters for investigation ofsilicon heterojunction solar cells. Appl Surf Sci. 2016; DOI: 10.1016/j.apsusc.2016.04.023

Chapter 5

High-Efficiency Front Junction *n*-Type Crystalline Silicon Solar Cells

Yuguo Tao and Ajeet Rohatgi

Additional information is available at the end of the chapter

http://dx.doi.org/10.5772/65023

Abstract

This chapter aims to provide students/workers in the field of photovoltaics with the valuable information and knowledge needed to understand the physics and operation of high-efficiency front junction *n*-type crystalline silicon solar cells. The surface recombination and passivation mechanisms, and several promising passivation schemes for front and back cell surfaces, are addressed and reviewed. The advanced cell structures and their fabrication schemes to achieve higher efficiency are described and discussed, including selective emitter on the front and locally doped back surface filed or carrier selective rear contact composed of tunnel oxide and phosphorus-doped polycrystalline silicon thin film. These advanced cell design features have become highly active areas of investigations in the photovoltaic industry for next-generation production cells.

Keywords: front junction, recombination, surface passivation, selective emitter, tunnel oxide passivated contact, high efficiency

1. Introduction

Solar cells depend upon the photovoltaic effect for their operation that converts the incident energy of sunlight directly into electricity using the electronic properties of semiconducting materials. In the past few decades, silicon wafers have been used to fabricate the overwhelming majority of solar cells in the very dynamic photovoltaic industry because of the abundance and non-toxicity of silicon, the simplicity of cell fabrication process, and the vast amount of processing knowledge developed and accumulated in the microelectronics industry. Simply speaking, silicon wafer-based solar cells generate electricity via absorbing photons and

generating electron-hole pairs that are separated by a *pn*-junction and then flow to electrical contacts on the front and back sides to perform work in external circuit, as shown in the **Figure 1**. In addition, due to several advantages of *n*-type (typically phosphorus-doped) silicon wafers over *p*-type (typically boron-doped), including better tolerance to common impurities (e.g. iron) [1], higher bulk lifetime and no light-induced degradation (LID) [2], *n*-type silicon solar cells with high efficiency can be potentially more cost-effective than *p*-type silicon solar cells. Hence, the focus in this chapter will be on high-efficiency front junction *n*-type crystalline silicon solar cell with both sides passivated and contacted, including their operating principle, advanced cell structures, surface passivation and fabrication schemes.

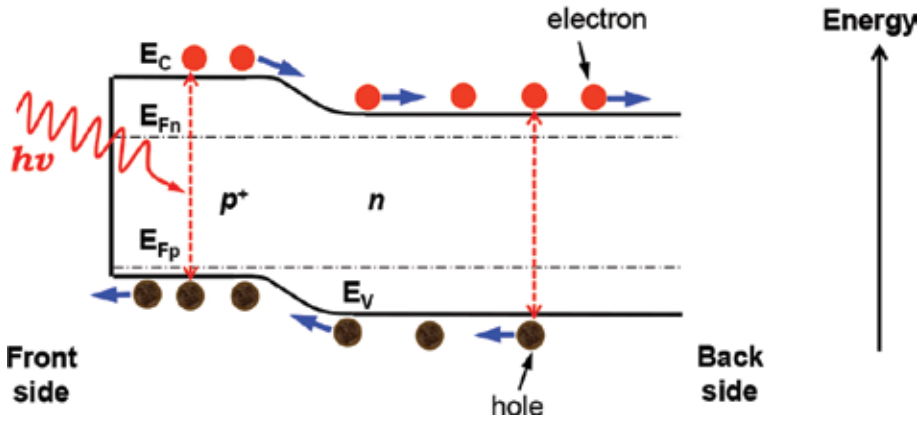

Figure 1. Schematic energy band diagram of a front junction *n*-type silicon solar cell in a non-equilibrium (with illumination), including photon absorption, carrier generation and separation.

2. Operating principle of a front junction *n*-type silicon solar cell

The operating principle of a front junction *n*-type silicon solar cell is described in **Figure 1** via the band diagram. The p^+ emitter region is formed by 'doping' the front side of a *n*-type silicon wafer with boron dopants in high concentration, and the conjunction of the p^+ region and the *n* substrate forms the *pn*-junction. Due to the doping concentration gradient across the *pn*-junction, electrons flow by diffusion from the *n* region into the p^+ region, and holes flow from the p^+ region to the *n* region [3]. This leaves behind exposed charges on ionized boron and phosphorus doping atoms at lattice sites, which form the space charge region. These exposed charges build up an electric field that opposes the natural flow of electrons and holes until and equilibrium scenario is reached with a fixed space charge width and electric field [4]. This built-in electric field also causes a bending of the conduction band (E_C) and the valence band (E_V) (**Figure 1**). When the solar cell is illuminated, photons with energy greater than the silicon band gap energy (E_g) are absorbed to excite electrons from the valence band to the conduction band, which generates an electron-hole pair. The generated electrons and holes can diffuse within the bulk of the solar cell until they reach the space charge region, if they avoid recombination or trapping by defects. Then, the electric field at the *pn*-junction separate

http://dx.doi.org/10.5772/65023

these carriers by sweeping electrons to the *n* region and holes to the p^+ region. In the case of illumination, quasi-Fermi levels (E_{Fn} for electrons and E_{Fp} for holes) are used to analyse the solar cell in non-equilibrium (**Figure 1**). The electrical contact to the front p^+ emitter region is described as an ohmic contact while the metal contact to *n* region, without any heavy doping, is generally a Schottky-type because the metal contact to *n* silicon induces a barrier to majority carrier (electrons) [3]. In order to obtain high cell efficiency, proper doping profiles in both the p^+ and the *n* regions are necessary to reduce the contact resistance and the metal-induced recombination.

2.1. Solar cell parameters

According to the *ideal diode law* (one diode model), an actual silicon solar cell with parasitic series resistance (R_s) and shunt resistance (R_{sh}) can be described by an equivalent circuit containing one diode as shown in **Figure 2** and is often expressed as [3, 4]

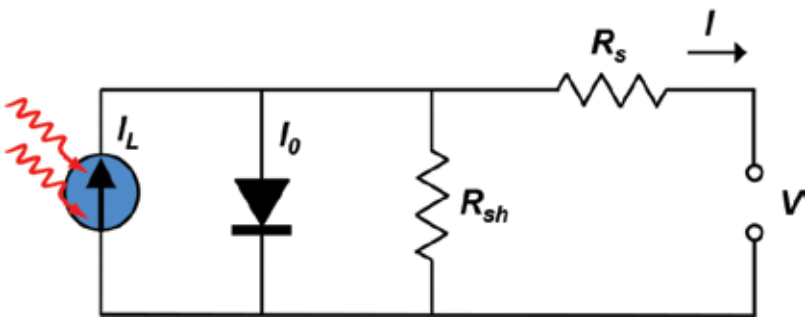

Figure 2. Equivalent circuit of a front junction *n*-type silicon solar cell with parasitic series resistance (R_s) and shunt resistance (R_{sh}) [3, 4].

$$I = I_L - I_0 \left\{ \exp\left[\frac{V + IR_s}{\left(\frac{nkT}{q} \right)} \right] - 1 \right\} - \frac{V + IR_s}{R_{sh}} \tag{1}$$

where I is the terminal current, I_L is the light-generated current with illumination, I_0 is the saturation current (the solar cell leakage current in the dark), V is the terminal voltage, q is the electronic charge, k is the Boltzmann's constant, T is the absolute temperature and n is the ideality factor that is typically in the range of 1 and 2.

The resulting *I-V* curve with illumination is often plotted as output power, as shown in **Figure 3**. The maximum power point (MPP) is also indicated at (V_{mp}, I_{mp}). The fill factor (*FF*) is another important parameter determining cell performance, and it is a metric of the *pn*-

junction quality and the parasitic resistance of a finished silicon solar cell [3]. *FF* is a measure of the squareness of the *I-V* curve and defined as

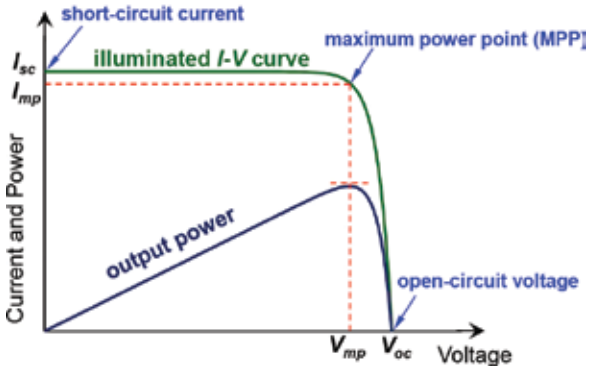

Figure 3. A typical representation of an illuminated *I-V* curve as well as output power curve as a function of voltage, including indication of short circuit current (I_{sc}), open circuit voltage (V_{oc}) and the maximum power point (V_{oc} and I_{sc}) [3, 4].

$$FF = \frac{I_{mp}V_{mp}}{I_{sc}V_{oc}} \tag{2}$$

where I_{mp} and V_{mp} are the corresponding current and voltage at the maximum power point, I_{sc} is the current at short circuit condition ($V = 0$) and V_{oc} is the voltage at open circuit condition ($I = 0$) [3, 4]. Finally, the most important metric of solar cell performance is the energy conversion efficiency and is defined as

$$\eta = \frac{I_{sc}V_{oc}FF}{P_{in}} \tag{3}$$

where P_{in} is the total incident light power striking the solar cell [3]. According to the detailed balance limit of efficiency, the maximum efficiency of an ideal single-junction crystalline silicon solar cell with E_g of 1.12 eV at 25°C is about 30% [5]. Its major fundamental mechanisms of power loss include (1) photons with energy less than 1.12 eV ($<E_g$) cannot be absorbed and directly transmitted through the cell, (2) the excessive energy in photons with high energy ($>E_g$) is wasted via thermallization as the generated electron-hole pair relax back to the edges of carrier band, (3) each absorbed photon creates only one electron-hole pair regardless of its energy, and (4) as shown in **Figure 1**, quasi-Fermi levels (E_{Fn} and E_{Fp}) stay within energy gap ($\left|E_{Fn} - E_{Fp}\right| < E_g$), hence *pn*-junction silicon solar cells are inherently capable of giving voltage output smaller than the potential corresponding to its band gap energy [3, 5].

http://dx.doi.org/10.5772/65023

2.2. *pn*-junction formation

To form the *pn*-junction on *n*-type crystalline silicon wafers, a typical approach is to diffuse boron atoms into the silicon substrates at high temperature. This can be accomplished by several techniques including depositing boron-doped silicon oxide via atmospheric pressure chemical vapour deposition (APCVD) and then thermal annealing at high temperature [6]. The boron emitter can be also formed by spinning-on orthoboric acid (H_3BO_3) solutions [7, 8], which is considered to be a hydrate of boric trioxide (B_2O_3). During the subsequent thermal annealing, the boron oxide reacts with silicon to form SiO_2 and B, which diffuses into silicon at high temperature, as described by

$$2B_2O_3 + 3Si \rightarrow 3SiO_2 + 4B \tag{4}$$

Screen-printed boron emitters have also been explored by printing proper boron-containing paste followed by a thermal drive-in diffusion [9]. Another promising and widely used technology is called 'BBr_3 diffusion' that involves a direct thermal diffusion of boron atom from a liquid boron tribromide (BBr_3) source [10]. In this process, pure nitrogen (N_2) carrier gas flows into a bubbler containing liquid BBr_3, which creates and transports gaseous BBr_3 into the quartz tube and deposits on the surface of silicon wafers loaded in a quartz boat [11]. During this deposition stage, a boron oxide layer is formed on the silicon wafer surface in the oxygen (O_2) ambient according to

$$4BBr_3 + 3O_2 \rightarrow 2B_2O_3 + 6Br_2 \tag{5}$$

This thin boron oxide layer contains very high concentration of inactive boron element on the silicon surface. So, a high temperature anneal (typically ≥950°C) is necessary to activate boron atoms and diffuse them into silicon bulk to form the p^+ region through the reaction (4) [11]. During this process, a SiO_2/B_2O_3 stack or the borosilicate glass (BSG) layer is formed on the surface that has to be removed to achieve better dielectric surface passivation quality. By controlling gas flow rate, diffusion temperature and duration, proper boron dopant profiles can be engineered [12].

Because all of these junction formation technologies suffer from wrap-around or naturally double-sided diffusion process, etching off one side or depositing a mask layer on one side is needed to prevent junction shunting. Therefore, ion implantation has been investigated and implemented as a promising alternative technology that has a unique characteristic to provide single-sided diffusion and facilitates the development of next-generation cells [13]. It can simplify the junction formation process by eliminating the extra processes of masking and etching. In addition, ion implantation offers other technical advantages, including (1) high junction uniformity, (2) flexibly and precisely controlled dopant profiles, (3) elimination of the edge isolation process, (4) capability of patterned doping for selective doping and (5) elimination of the dopant glass (i.e. BSG layer) removal process [14]. It is important to note that ion implantation forms an amorphous layer on the surface [15], therefore, a very high temperature

(≥1000°C) is needed to recover lattice damage and activate dopants [16, 17]. In addition, proper ion dose, implant energy and anneal conditions are essential to obtain desired dopant profiles [18, 19]. Current ion implantation tools have throughput of more than 2000 wafers per h but the capex and maintenance is much higher than the traditional diffusion tubes [13]. **Figure 4** shows two examples of boron emitter profiles measured by electrochemical capacitance-voltage (ECV) profiling technique, revealing that the boron concentration decreases towards the silicon wafer surface due to the higher solubility of boron in the SiO_2 layer than in silicon bulk [20].

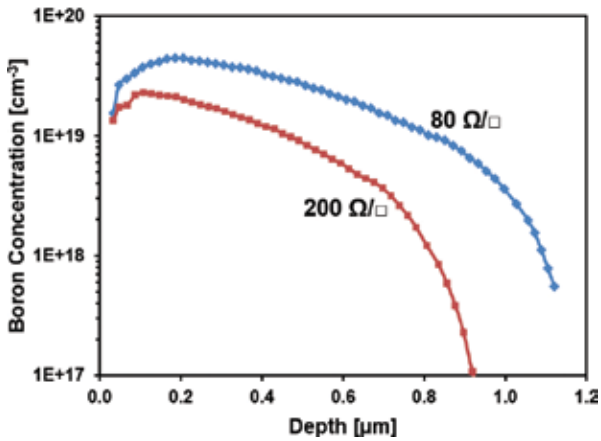

Figure 4. Two measured ECV profiles of ion-implanted boron emitters with sheet resistance of 80 and 200 Ω/□ [16, 20].

2.3. Metallization

In order to extract electrical power from a silicon solar cell, metal contacts have to be applied to the front emitter and the rear base to collect the generated electron-hole pairs. The collected electrons flow through the n^+ regions into the external circuit to power the load and then recombine with the generated holes. In order to minimize the power loss, the electrical contact needs to have low contact resistance with doped silicon regions, low metallic resistance in the formed structure, good adhesion to silicon and reliable solderability for cell interconnection for module production [21]. There are several metallization technologies that are typically used in photovoltaic industry for research and production. First, the screen printing of metal pastes to form electrical contact is the most widely applied technology to manufacture silicon solar cells in photovoltaic industry today because it is very robust, simple, high-throughput, low-cost and reliable method [21]. Its first application dates back to 1970s. In this metallization process, a metal paste is printed through a patterned screen with well-designed openings onto a wafer lying under the screen. This screen acts as a mask, consisting of a mesh of wires partially covered with an emulsion. By properly optimizing some key process parameters, including the snap-off distance between screen and wafer, the printing pressure (pressing the screen against the wafer surface and pushing the metal paste onto wafer surface) and the printing

http://dx.doi.org/10.5772/65023

speed, printed gridline with high aspect ratio can be obtained today with line width of ≤60 μm and height of ~25 μm (**Figure 5(A)**) [16]. Then, the contact formation is realized by a firing process in a conveyor belt furnace that fires the metal pastes through the passivation layer and anti-reflection coating (typically silicon nitride SiNx) on the front. During this firing process, hydrogen (H) is released from the hydrogen-rich SiNx layer into the crystalline silicon to passivate bulk and interface defects to increase the cell performance [23, 24].

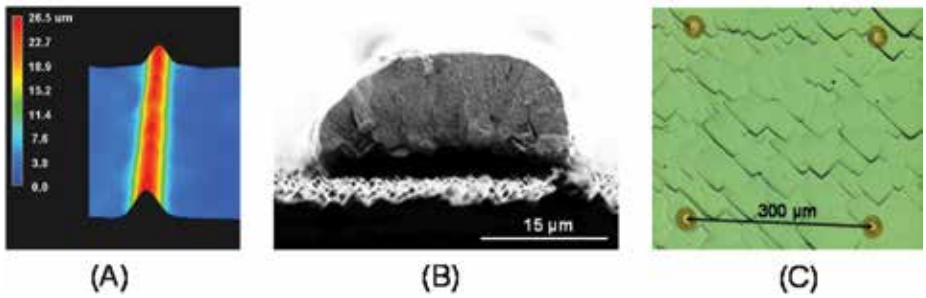

Figure 5. (A) Optical scope image of screen-printed gridline. (B) Scanning electron microscope image of photolithographically defined and plated gridline. (C) Optical scope image of laser-opened point contact pattern for physical vapour deposited metallization [16, 22].

Second contact technology involves metal plating approach that offers low contact resistivity, good gridline conductivity and narrow gridline width (low metal shading). Thus, it is a promising alternative to the screen-printing technology but metal plating typically requires an initial patterning step to create openings in a dielectric masking layer for the subsequent self-aligned metallization [21]. The openings can be defined by photolithography [10] or laser ablation, and then the contacts are applied by electroless plating [25] or a combination of light-induced plating (LIP) and electroplating in an inline plating machine [26]. For industrially feasible plated metallization, nickel (Ni) layer is typically used, first to obtain low contact resistivity and prevent copper (Cu) diffusion followed by copper plating to provide excellent line conductivity and low material cost (compared to silver) [27]. The gridline width after plating is typically around 30 μm, with height of ~15 μm, as shown in **Figure 5(B)**.

Third contact technology involves physical vapour deposition (PVD) that is attractive because of its potential advantages of lower specific contact resistance [28], reduced wafer breakage and processing of thinner wafers due to non-contacting process. In addition, a thin (1~2 μm) PVD aluminium (Al) on the entire rear area is sufficient to meet the required electrical conductance for large area silicon solar cells, which can lead to less wafer bow and less metal material consumption [22]. In order to form the contact between silicon and PVD metal, patterned openings through a dielectric masking layer are needed for the subsequent PVD metallization, which is typically created by laser ablation. **Figure 5(C)** shows an example of rear point contact pattern (300 × 300 μm^2) after laser ablation, with the opening diameter of ≤40 μm and metal coverage of ≤1.4% [22]. To obtain a good solder contact to the PVD Al side, deposition of a double layer of Ni:V/Ag on top of PVD Al layer is often implemented to provide an excellent solderability and long-term stability for module manufacturing [29].

2.4. Optical, resistive and recombination losses in a solar cell

Theoretical maximum J_{sc} of ~44 mA/cm^2 can be achieved for a single-junction crystalline silicon solar cell, if all the striking photons with energy higher than silicon band gap ($E_{photon} \geq E_g$) are absorbed and all the electron-hole pairs generated contribute to the cell current [3]. However, several optical losses can cause lower current density in real cells, including reflection at the front side (metal gridline and front surface), absorption in the metal and dielectric layers on both sides, absorption via free-carrier absorption in highly doped regions and transmission (without being absorbed in the cell). It is important that the front metal shading should be as low as possible without contributing to significant increase in series resistance. Therefore, grid pattern needs to be optimized to minimize the resistive and optical losses. Finally, the size of pyramid on the front side should be as small as possible after the saw damage removal and texturing process to minimize the line width due to spreading of screen-printed metal.

Actual silicon solar cells also suffer from ohmic losses due to parasitic resistance R_s and R_{sh}. R_s is mainly attributed to the sheet resistance of doped regions (p^+ emitter and n^+ back surface field) in the case of two dimensional current flow, bulk resistance of silicon substrate, metallic resistance of gridline and specific contact resistance between silicon and metal. Each of these resistive components can be approximately estimated by using a model and calculation approach [30] to minimize total R_s and achieve high *FF*. R_{sh} is a factor monitoring the non-ideality of the *pn*-junction and some defects near junction, especially edge shunting. Both high R_s and low R_{sh} can result in low *FF* and cause power loss.

Apart from optical and ohmic losses, recombination of generated carriers can reduce J_{sc} and V_{oc} and limit the cell performance. There are two different intrinsic recombinations in semiconductor materials, namely Auger recombination and radiative recombination. Auger recombination is dominant in the heavily doped p^+ and n^+ regions. Auger recombination represents the process in which electron and hole recombine first by band-to-band radiative recombination and use the excess energy to excite another majority carrier (electron) in the conduction band for n^+ silicon or hole in the valence band in the case of p^+ silicon. Then, this excited carrier thermalizes towards the band edge by emitting phonons. Auger recombination strongly depends on majority carrier density; hence it is very effective in the heavily doped regions (p^+ emitter and n^+ back surface field). Radiative recombination refers to a process in which electron makes direct band-to-band transition to recombine with a hole in the valence band while emitting light. Because silicon is an indirect band gap material and a phonon is required for the band-to-band transition, this recombination mechanism is often neglected in silicon solar cell. A third and important bulk recombination mechanism is called SRH recombination (named after Shockley, Read and Hall [31, 32]), which is initiated by the energy levels created within the forbidden gap by impurities or defects. These energy levels form a stepping stair to facilitate the recombination of holes and electrons, which is a function of energy level location, trap density and its capture cross-sections [31, 32]. Generally, mid-gap or deeper traps are more efficient recombination centres. Because all three recombination mechanisms occur in parallel, the silicon substrate bulk lifetime (τ_{bulk}) is expressed as

http://dx.doi.org/10.5772/65023

$$\frac{1}{\tau_{\text{bulk}}} = \frac{1}{\tau_{\text{Auger}}} + \frac{1}{\tau_{\text{radiative}}} + \frac{1}{\tau_{\text{SRH}}} \tag{6}$$

where τ_{Auger} is the Auger lifetime, $\tau_{\text{radiative}}$ is the radiative lifetime and τ_{SRH} is the SRH lifetime.

In addition to these three bulk recombination mechanisms, surface recombination is also very critical for cell performance. This is because dangling bonds present at both surfaces of the wafer induce defect levels within the forbidden band gap. Surface recombination is characterized by a surface recombination velocity that is a function of surface state density and cross-section of surface traps [31]. To account for all the four recombination mechanisms, an effective lifetime (τ_{eff}) is used, and given by

$$\frac{1}{\tau_{\text{eff}}} = \frac{1}{\tau_{\text{bulk}}} + \frac{2s}{d} \tag{7}$$

where s is the surface recombination velocity (SRV) and d is the silicon wafer thickness. All recombination processes not only reduce the maximum short circuit current density (J_{sc}) but also diminish the maximum V_{oc}. According to Eq. (8), the total saturation current density ($J_{0,\text{total}}$) in Eq. (1) strongly influences V_{oc} because

$$V_{\text{oc}} = \frac{nkT}{q} \ln\left(\frac{J_{\text{sc}}}{J_{0,\text{total}}} + 1\right) \tag{8}$$

$$J_{0,\text{total}} = J_{0e} + J_{0b,\text{bulk}} + J_{0b}' \tag{9}$$

where J_{0e}, $J_{0b,\text{bulk}}$ and J_{0b}' are the saturation current density contributions from front emitter, bulk wafer and back side, respectively. These parameter values can be directly measured and extracted from the quasi-steady-state photoconductance (QSSPC) technique [33]. Due to the progress and availability of high lifetime wafers and current photovoltaic industry trend towards thinner wafers for cost reduction, passivation of front and rear surfaces is becoming vitally important for achieving higher efficiency silicon solar cells.

3. Surface passivation of crystalline silicon solar cells

At the silicon wafer surface, the covalent silicon-silicon bonds of crystal lattice are broken during wafer slicing, which creates non-saturated ('dangling') bonds that are often referred as 'surface states' and can easily trap electrons from the conduction band or holes from the valence

band as some of the energy levels are located near mid-gap. In order to keep surface recombination losses at a tolerable level, the wafer surfaces must be electronically well passivated. According to the Shockley-Read-Hall theory [31], the SRV depends on several features, including the properties of the surface states, state density, their capture cross-sections for electrons and holes, the injection level at the surface and the wafer doping level [34]. Therefore, SRV can be decreased by two technical approaches: (1) the chemical passivation by reducing the surface state density via depositing or growing a passivating dielectric film on the silicon surface and (2) the field-effect passivation by reducing the concentration of one charge carrier type (either electrons or holes) at the surface via forming an internal electric field below the silicon surface with doping profile or electrical charges in dielectric insulator. Practically, these two fundamental passivation approaches are often applied together to minimize the SRV. For front junction *n*-type crystalline silicon solar cells, the electronic quality of front boron emitter and back surface are usually expressed and quantified by J_{0e} and J_{0b}'. In a typical solar cell, there are two fundamentally different types of surface regions: metallized and non-metallized. Non-metallized surface regions are usually covered with dielectrics and are referred to as passivated regions. In order to achieve high cell efficiency, both J_{0e} and J_{0b}' should be as low as possible.

3.1. Front boron emitter passivation

In order to take the advantages of high bulk lifetime *n*-type crystalline silicon wafers, excellent passivation of the boron emitter is essential to reduce the SRV or the emitter saturation current density of the passivated region ($J_{0e,\,pass}$). It is well known that aluminium oxide (Al_2O_3) contains a high density of built-in negative charges on the order of $\sim 10^{13}$ cm^{-2} [35], so the majority carrier (hole) is accumulated and minority carrier (electron) concentration is effectively reduced at the Al_2O_3-passivated boron emitter surface, and consequently, the SRH recombination on the surface or the SRV is reduced. Experimentally, very low $J_{0e,\,pass}$ in the range of 10~30 fA/cm^2 has been demonstrated on 150 and 54 Ω/□ is the standard unit to describe a sheet resistivity for emitter or back surface field for silicon solar cells in the photovoltaic field. sheet resistance p^+ emitters with surface doping concentrations around 10^{19} cm^{-3} (prepared by BBr_3) and Al_2O_3 passivation synthesized by plasma-assisted atomic layer deposition (ALD) (**Figure 6**) [36].

It is also shown that with ALD-Al_2O_3 passivation, ion-implanted boron emitters (post-implant anneal at 1040°C for 1 h) demonstrate noticeably higher $J_{0e,\,pass}$ at <150 Ω/□ sheet resistance, but similar passivation performance for ≥150 Ω/□ sheet resistance, compared to the BBr_3-prepared emitters (oxidation anneal at 1050°C). This is due to higher surface doping concentration (~5 × 10^{19} cm^{-3}) resulted from lower oxidation temperature and shorter oxidation time. In addition, thermally grown silicon oxide (SiO_2) also demonstrates decent surface passivation for the boron emitters with $J_{0e,\,pass}$ in the range of 60~110 fA/cm^2. However, silicon nitride (SiNx) deposited by plasma-enhanced chemical vapour deposition (PECVD) does not effectively passivate boron-doped emitters (**Figure 6**) due to the presence of positive built-in charge. Furthermore, hydrogen-rich amorphous silicon yields the passivation performance comparable to SiO_2 [37].

http://dx.doi.org/10.5772/65023

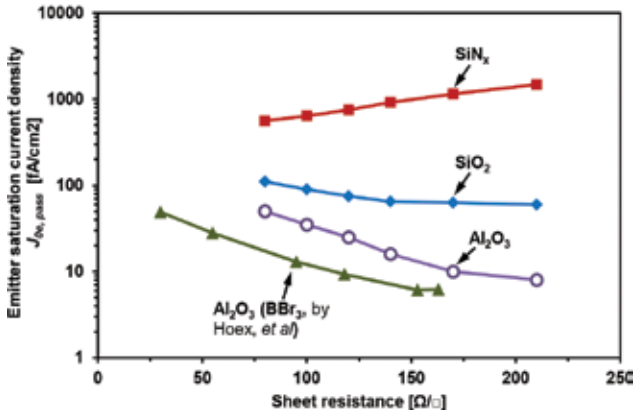

Figure 6. Measured emitter saturation current density on passivated region $J_{0e,pass}$ as a function of the sheet resistance for ion-implanted boron emitters passivated by SiNx, thermal SiO_2 and Al_2O_3. BBr_3-prepared and Al_2O_3-passivated boron emitter reported in Ref. [36] is cited for comparison purpose.

3.2. Rear surface passivation

In practice, there are two different types of surfaces on the rear side of front junction *n*-type silicon solar cells: diffused and non-diffused. Thermal SiO_2 film is very effective in passivating *n*-type silicon surface because it not only reduces the surface state density but also leads to a field-effect passivation due to positive fixed oxide charge [38]. It can reduce non-diffused *n*-type silicon surface SRV values below 10 cm/s [39]. Thermally grown SiO_2 is also very effective in passivating phosphorus-doped silicon surfaces. Since the phosphorus dopants in the diffused back surface of a *n*-type cell have the same polarity as the *n*-type silicon wafer, this doping profile creates a high-low junction (n^+n), the so-called back surface field (BSF). The corresponding electric field formed by the rear high-low junction of a BSF can very effectively shield holes from the rear surface, dramatically reducing rear surface recombination losses.

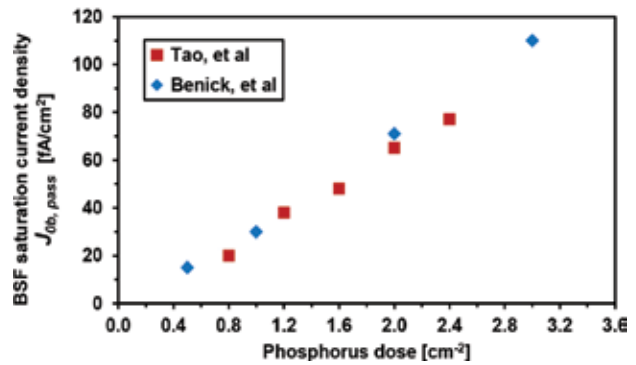

Figure 7. Saturation current density of phosphorus-doped and planarized rear surface $J_{0b,pass}$ as a function of the ion-implanted phosphorus dose [41, 42].

SiNx formed by PECVD provides excellent passivation for *n*-type surfaces because of its field-effect passivation provided by positive interface charges and the properties of the capture cross-sections of the dominant interface defects. Although the surface state density at Si-SiNx interface is much higher than that in the case of thermally grown Si-SiO_2 interfaces, SiNx demonstrates additional advantages for silicon solar cells: (1) excellent anti-reflection coating (ARC) on the rear side, which is suitable for bifacial architecture and (2) releasing large amounts of hydrogen during a high temperature (~800°C) contact firing process to passivate interface and bulk defects ('hydrogen passivation' [40]).

In front junction *n*-type silicon solar cells, phosphorus-doped rear surfaces are typically passivated by the combination of thermal SiO_2 and SiNx stacks. **Figure 7** shows that very low saturation current density has been demonstrated on planarized back surface with ion-implanted BSF $J_{0b,pass}$ of ≤20 fA/cm^2 for low phosphorus dose and $J_{0b,pass}$ of ~80 fA/cm^2 for high phosphorus dose with doping concentration of ~2×10^{20} cm^{-3}, which is compatible with screen printing [41, 42]. The $J_{0b,pass}$ of ≤100 fA/cm^2 has also been reported for SiO_2/SiNx-passivated ion-implanted and $POCl_3$ formed BSF on textured surface [42, 43], which are suitable for fully screen-printed bifacial front junction *n*-type silicon solar cells [17].

3.3. Carrier selective tunnel oxide passivated rear contact

Current high-efficiency front junction *n*-type silicon solar cells are often limited by the recombination in the heavily doped regions and at the metal/silicon contacts. A possible solution for minimizing doping and contact recombination is to insert a passivating material with offset bands between the metal and silicon, also known as passivated contact. One approach to accomplish this is to use an amorphous silicon-based heterojunction (HIT solar cell), which suppresses recombination effectively and which has resulted in outstanding cell V_{oc} of 750 mV [44]. However, this passivation scheme can withstand only low temperature (≤250°C) back-end process, hence is not compatible with the industry standard screen-printing and firing metallization technology [45]. Another approach to achieve a passivated contact involves a chemically grown ultra-thin (~15 Å) tunnel oxide capped with phosphorus-doped n^+ polycrystalline silicon (as shown in **Figure 8(A)**) and metal contact on the entire back side

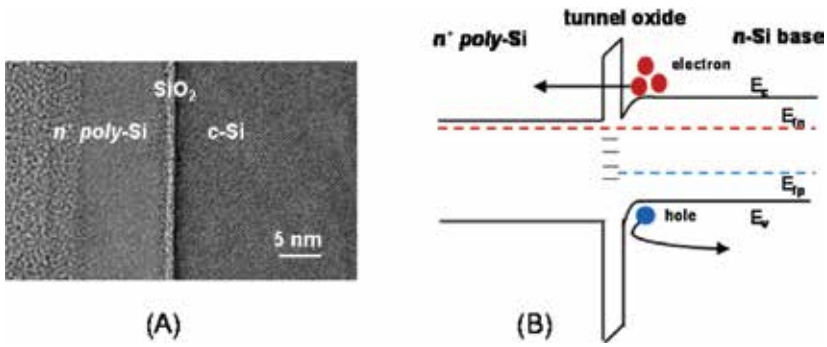

Figure 8. (A) Transmission electron microscopy image and (B) schematic band diagram of tunnel oxide passivated contact structure [45].

http://dx.doi.org/10.5772/65023

of *n*-type silicon cell [45], which is referred to as the tunnel oxide passivated contact (TOPCON) [46, 47].

In this TOPCON structure, four parallel mechanisms contribute to carrier selectivity (as shown in **Figure 8(B)**) [45]. (1) Heavily doped n^+ polycrystalline silicon creates an accumulation layer at the absorber surface due to the work function difference between the n^+ polycrystalline silicon and the n^- silicon absorber. This accumulation layer or band bending provides a barrier for holes to get to the tunnel oxide while electrons can migrate easily to the oxide/Si interface. (2) Tunnel oxide itself provides the second level of carrier selectivity because it presents a 4.5 eV barrier for holes to tunnel relative to 3.1 eV for electrons [48]. (3) There are very few or no states on the other side of the dielectric for holes to tunnel through because the valence band edge of n^- silicon absorber is facing the forbidden gap of n^+ polycrystalline silicon. (4) Even if a hole is able to tunnel through the oxide, it sees much higher resistance due to the n^+ polycrystalline silicon regions to get to the metal contact for recombination while the majority carrier electrons can easily get there. Last but not least, due to the full area metal contact on the back, there is one-dimensional (1D) current flow. This eliminates the lateral transport resistance (2D carrier flow), resulting in much higher *FF*. Therefore, this passivated contact is highly carrier selective and allows the flow of majority carriers via tunnelling while blocking minority carriers.

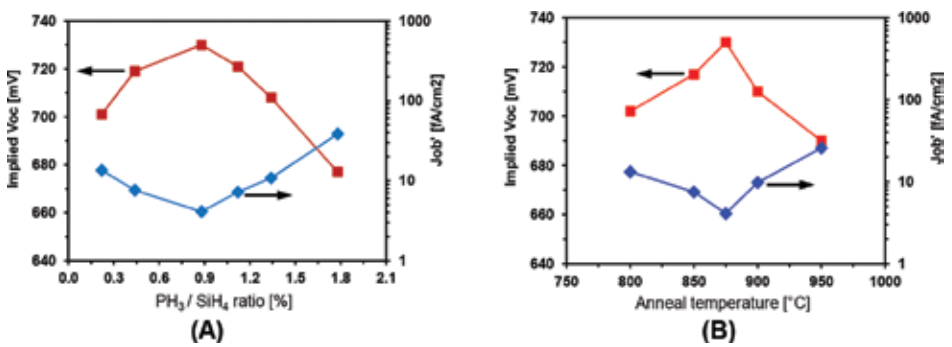

Figure 9. (A) Implied V_{oc} and J_{0b}' as a function of the PH_3/SiH_4 ratio during PECVD. (B) Implied V_{oc} and J_{0b}' as a function of the polysilicon anneal temperature [45].

To obtain an efficiently doped n^+ polycrystalline silicon layer to maintain the quasi-Femi level splitting in silicon absorber (high V_{oc}), a proper PH_3/SiH_4 ratio during PECVD is required for forming the phosphorus-doped amorphous silicon layer [45]. **Figure 9(A)** displays that if the PH_3/SiH_4 ratio is too high (high doping level in as-deposited amorphous silicon layer), the surface passivation quality degrades as indicated by low implied V_{oc} (iV_{oc}) and high saturation current density J_{0b}' obtained on symmetrical TOPCON structure. This is because more phosphorus dopants diffuse from the n^+ polycrystalline silicon layer through the tunnel oxide into the silicon absorber, resulting in high Auger recombination, as well as high recombination at the silicon/SiO_2 interface [49]. However, very low PH_3/SiH_4 ratio also causes inferior surface passivation due to the small band bending or weak accumulation layer created by the reduced

doping in the n^+ silicon layer, resulting in very weak field-effect passivation. In addition, to facilitate the solid-phase crystallization and activate the phosphorus dopants in the as-deposited n^+ amorphous silicon layer, a proper polysilicon anneal temperature is necessary as shown in **Figure 9(B)**. However, a strong degradation in the interface passivation quality is observed if the anneal temperature is too high (≥900°C), again due to more dopant diffusion into the silicon base causing high Auger recombination and possible local disruption of tunnel oxide due to polycrystalline silicon grain growth and more interface defects [45, 46]. It has also been demonstrated that both the tunnel oxide growth temperature in nitric acid and the high temperature firing process can affect the passivation quality. A very low J_{0b}' of ≤5 fA/cm^2 has been achieved by optimizing the TOPCON fabrication processes [50]. Similar passivation performance has also been achieved by depositing intrinsic amorphous silicon layer on top of the tunnel oxide layer followed by ion implantation of phosphorus and thermal annealing [51].

4. High-efficiency front junction *n*-type crystalline silicon solar cells

All front junction *n*-type crystalline silicon solar cell structures fabricated to date feature some degree of surface passivation. In the following section, we discuss several types of advanced high-efficiency front junction solar cells that have been developed on *n*-type silicon substrates.

4.1. Passivated emitter with rear totally diffused (PERT) cells

Even though *p*-type silicon solar cells dominate the PV market today, in recent years, several academic groups and companies have started to investigate front junction *n*-type crystalline silicon solar cells. The schematic of front junction *n*-type PERT 'passivated emitter rear totally diffused' [52, 53] cell is shown in **Figure 10**. PERT cell structure featuring a bifacial architecture is shown in **Figure 10(A)**, which can collect radiation from the rear side of the solar cell, hence has the potential to achieve an increased energy yield (5~20%) in certain module configurations. The PERT cell structure in **Figure 10(B)** shows the rear point contact that can reduce the rear metal-induced recombination due to lower metal coverage, as well as reduce the lateral resistance due to smaller contact pitch [22].

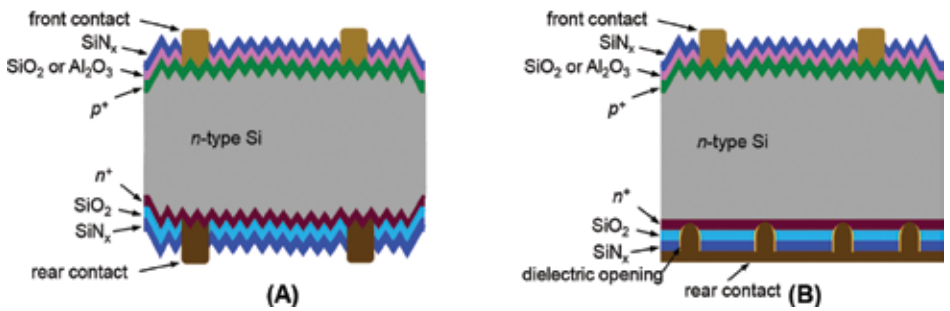

Figure 10. (A) Schematic of front junction *n*-type PERT cell with bifacial feature [52, 53]. (B) Schematic of front junction *n*-type PERT cell with rear point contacts [22].

Table 1 shows that 21.9% cell efficiency has been reported on thermal SiO_2-passivated boron emitter formed by BBr_3 diffusion [53] while 22.7% cell efficiency has been achieved via Al_2O_3-passivated boron emitter formed by ion implantation and photolithography on small area *n*-type float zone (Fz) substrates [54] with rear point contacts. To make manufacturable *n*-type PERT cells, screen-printing metallization has been applied on large area *n*-type Czochralski (Cz) silicon substrate with excellent cell efficiencies approaching 21% featuring bifacial architecture [17, 55], as listed in **Table 1**.

Literature	η (%)	V_{oc} (mV)	J_{sc} (mA/cm^2)	*FF* (%)	Area (cm^2)	Structure	Year
[54]	21.9	695	41.1	76.5	4 (FZ)	Rear point contact	2002
[55]	22.7	691	40.9	80.2	4 (FZ)	Rear point contact	2014
[56]	20.5	655	39.5	79.1	239 (CZ)	Bifacial	2014
[57]	21.0	665	39.8	79.3	239 (CZ)	Bifacial	2015

Table 1. Light *I-V* results of high-efficiency front junction *n*-type PERT silicon solar cells.

The detailed characterization and analysis show that the 22.7% efficient PERT cell is largely limited by the rear side recombination (J_{0b}') due to the totally diffused BSF layer ($J_{0b,\text{pass}}$), with J_{0b}' ($J_{0b,\text{pass}} + J_{0b,\text{metal}} = 29 + 4$) = 33 fA/cm^2, J_{0e} ($J_{0e,\text{pass}} + J_{0e,\text{metal}} = 12 + 16$) = 28 fA/cm^2 and $J_{0b,\text{bulk}}$ = 10 fA/cm^2 [54]. Therefore, to further improve the cell performance, the recombination in this heavily doped full BSF layer needs to be reduced. This can be accomplished by locally diffused BSF (PERL) structure on the rear side.

4.2. Passivated emitter with rear locally diffused (PERL) cells

The concept of 'passivated emitter rear locally diffused (PERL)' structure was introduced and developed in 1990s [56], in order to reduce the recombination from the rear side. The PERL schematic is shown in **Figure 11(A)**, which can diminish the heavy doping effect by using locally phosphorus-diffused area and decrease the metal-induced recombination simultaneously via heavy doping (n^{++}) underneath the contact metal. By upgrading from PERT to PERL structure, the J_{0b}' can be significantly reduced (from 33 to 15 fA/cm^2), which can lead to an increase in V_{oc} from 691 to 704 mV [10]. However, because the rear metal contact of PERL cell is restricted to a small fraction (<1%) of the rear surface, the carrier flow towards contact is constricted, which is beneficial for minority carriers (holes) but detrimental for majority carriers (electrons). On one hand, for minority carriers, such constriction is equivalent to reducing the conductance in the direction of the rear contact, which facilitates the build-up of their concentration inside the solar cell resulting in higher V_{oc}. However, for majority carriers, a lower conductance causes higher lateral resistive losses resulting in lower *FF* [57]. Hence, a trade-off between V_{oc} and *FF* needs to be considered. By optimizing the cell fabrication process to reduce contact resistance, a 23.9% efficient front junction PERL cell on small area *n*-type Fz substrate with photolithography contacts was reported [58] with V_{oc} of 705 mV and *FF* of 82.5%. The detailed characteriza-

tion and analysis shows that this 23.9% efficient PERL cell is limited by metal recombination on the front ($J_{0e,\text{metal}}$) and the rear side recombination J_{0b}', with total J_{0e} of 30 fA/cm^2 ($J_{0e,\text{pass}} = 10, J_{0e,\text{metal}} = 20$), $J_{0b,\text{bulk}}$ = 10 fA/cm^2 and J_{0b}' = 15 fA/cm^2 [54]. To further reduce recombination losses, selective emitter with heavier and deeper boron doping profile underneath front contact metal is typically implemented, as shown in **Figure 11(B)**, which can dramatically decrease the front metal-induced recombination (from 1800 to 200 fA/cm^2) resulting in $J_{0e,\text{metal}}$ reduction from 20 to 2 fA/cm^2 on the contacted region assuming ~1.1% metal coverage [10, 59].

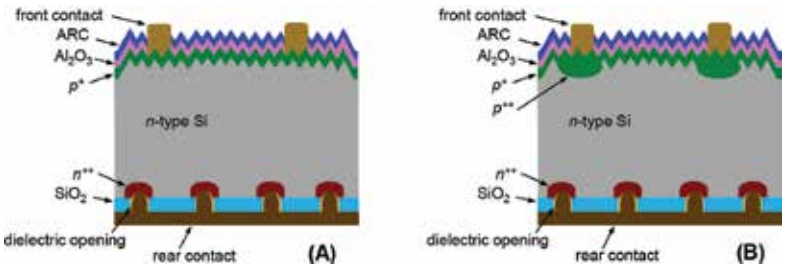

Figure 11. Schematic of front junction *n*-type PERL cell (A). (B) Front junction *n*-type PERL cell with selective emitter [56, 58].

4.3. Tunnel oxide passivated contact cells

The implementation of polysilicon tunnel junction as an alternative to either totally or locally diffused junction to reduce the recombination at the contact of silicon solar cells has been reported in the 1980s [60]. Because of its excellent surface passivation and carrier selectivity, a full area TOPCON shown in **Figure 12(A)** was applied, which also enables one-dimensional (1D) carrier transport on the rear side to eliminate *FF* losses due to 2D/3D carrier transport in the PERT and PERL cells.

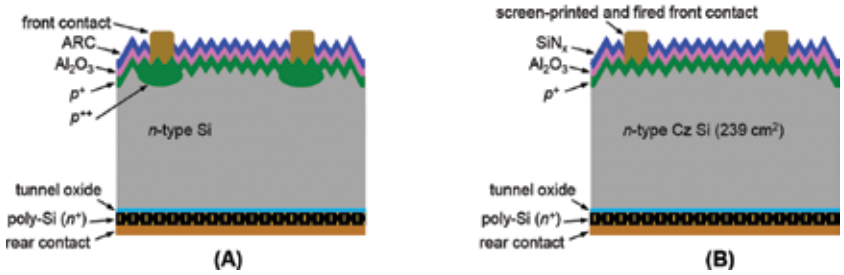

Figure 12. (A) Schematic of front junction *n*-type TOPCON cell with selective emitter [59, 61]. (B) Schematic of large area front junction *n*-type TOPCON cell with screen-printed and fired front contact [45].

In addition, because both the heavy doping effect and the metal-induced recombination are minimized in TOPCON structure, J_{0b}' is dramatically reduced from ≥15 fA/cm^2 in a PERL cell

to ≤8 fA/cm² in TOPCON cell [50, 54, 59]. A small area (4 cm²) 24.9% efficient TOPCON cell has been reported [59] with selective boron emitter and photolithography contacts on the front in conjunction with TOPCON back (**Figure 12(A)**). This cell had a V_{oc} of 719 mV, J_{sc} of 41.5 mA/cm² and *FF* of 83.4% [59]. More recently, an efficiency of 25.1% is reported by moving the busbars outside the cell with J_{sc} of 42.1 mA/cm² [61].

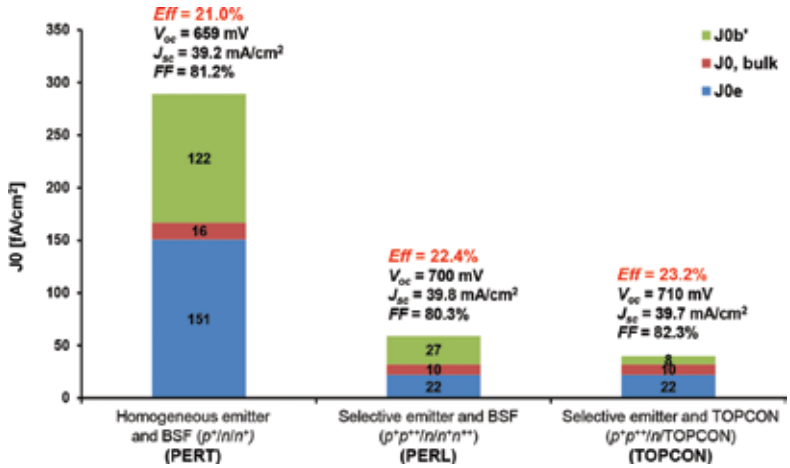

Figure 13. Simulated J_0 decomposition with each technology for large area front junction *n*-type PERT, PERL and TOPCON cells [62, 63].

To implement TOPCON on a more manufacturable cell structure, large area front junction n-type Cz silicon solar cells have been developed with ion-implanted boron emitter, SiNx antireflection coating and screen-printed front contact, as shown in **Figure 12(B)**, and cell efficiency of 21.4% with evaporated rear contact has been reported [45]. **Figure 13** shows the simulated road map to achieve ≥23% efficient large area front junction *n*-type silicon solar cells, including the reduction of all the J_0 components (J_{0e}, $J_{0b,\,bulk}$ and J_{0b}') in the cell [62, 63]. It is clearly shown that selectively doping is one of the most manufacturable and elegant way to reduce J_0 of the metallized and diffused regions simultaneously. This is because heavy diffusion underneath grid reduces metal J_0 and light diffusion in between the gridlines reduces J_0 of the diffused region. The 2D modelling shows that the cell efficiency can be increased from 21.0 to ~22.5% (bifacial architecture) by applying selectively doped emitter and BSF on large area *n*-type Cz wafers. Moreover, implementing TOPCON structure on the rear side can raise the cell efficiency over 23% with screen-printed contact on the front in combination with improved bulk material (10 Ω-cm, 3 ms lifetime).

5. Summary and outlook

In this chapter, the physics and operation of front junction *n*-type silicon solar cells is described, including detailed cell parameters, *pn*-junction formation, metallization approaches and

fundamental power loss mechanisms. To reduce surface recombination velocity for achieving high cell efficiency, Al_2O_3 has been approved to be very efficient on passivating heavily boron-doped front emitter and thermal SiO_2 is very effective to passivate phosphorous-diffused regions. In addition, to minimize the metal-induced recombination, implementation of selective boron emitter on the front side and locally-diffused back surface field on the rear side are preferred. Furthermore, TOPCON passivation scheme shows even better performance by simultaneously reducing the metal-induced recombination and the heavy doping effect, and allowing for 1D carrier transport. However, it is only suitable for being applied on the rear side of solar cell because the heavily doped polysilicon layer can absorb significant amount of incoming photons (hence low J_{sc}), if it is located on the front side.

High-efficiency front junction *n*-type silicon solar cells, including PERT, PERL and TOPCON cells, are reviewed and analysed. In combination with low-cost screen-printed metallization technology, PERT bifacial cell structure with homogeneous doping profiles on both front and back sides is a promising candidate of next-generation solar cells for industrial application in terms of process simplicity and energy yield while the recently developed cell structure with TOPCON on the rear and selective boron emitter on the front demonstrates the promise of this technology option for higher cell efficiency.

Acknowledgements

The authors would like to thank all other group members of UCEP in Georgia Tech and R&D department of Suniva, Inc. for their great support. This work was supported by the DOE FPACE I and the FPACE II contracts, as well as the DOE Solarmat1 and the DOE Solarmat2 contracts.

Author details

Yuguo Tao* and Ajeet Rohatgi

*Address all correspondence to: yuguo.tao@ece.gatech.edu

Georgia Institute of Technology, School of Electrical and Computer Engineering, University Center of Excellence for Photovoltaics, Atlanta, GA, USA

References

[1] Macdonald D, Geerligs LJ. Recombination activity of interstitial iron and other transition metal point defects in p-and n-type crystalline silicon. Applied Physics Letters. 2004; 85(18):4061–4063.

[2] Glunz SW, Rein S, Lee JY, Warta W. Minority carrier lifetime degradation in boron-doped Czochralski silicon. Journal of Applied Physics. 2001; 90(5):2397–2404.

[3] Green MG. Solar Cells: Operating Principles, Technology, and System Applications. Englewood Cliffs, NJ: Prentice-Hall, Inc.; 1982; 288 p.

[4] Green MA, Wenham SR, Watt ME. Applied Photovoltaics. Australia: National Library of Australia, Centre for Photovoltaic Devices and Systems, UNSW; 1997.

[5] Shockley W, Queisser HJ. Detailed balance limit of efficiency of p-n junction solar cells. Journal of Applied Physics. 1961; 32(3):510–519.

[6] King R, Gruenbaum P, Sinton R, Swanson R. Passivated emitters in silicon solar cells. In: 21st IEEE Photovoltaic Specialists Conference; Kissimmee, FL, USA; 1990. p. 227–232.

[7] Kim DS, Das A, Nakayashiki K, Rounsaville B, Meemongkolkat V, Rohatgi A. Silicon solar cells with boron back surface field formed by using boric acid. In: 22nd European Photovoltaic Solar Energy Conference; Milan, Italy; 2007.

[8] Das A, Ryu K, Rohatgi A. 20% Efficient screen-printed n-type solar cells using a spin-on source and thermal oxide/silicon nitride passivation. IEEE Journal of Photovoltaics. 2011; 1(2):146–152.

[9] Ryu K, Upadhyaya A, Ok YW, Xu H, Metin L, Rohatgi A. High efficiency n-type solar cells with screen-printed boron emitters and ion-implanted back surface field. In: 38th IEEE Photovoltaic Specialists Conference (PVSC); Austin, TX; 2011. p. 2247–2249.

[10] Benick J, Hoex B, Van de Sanden MC, Kessels WM, Schultz O, Glunz SW. High efficiency n-type Si solar cells on Al2O3-passivated boron emitters. Applied Physics Letters. 2008; 92(25):253501–253504.

[11] Schiele Y, Fahr S, Joos S, Hahn G, Terheiden B. Study on boron emitter formation by BBr3 diffusion for n-type Si solar cell applications. In: 28th European Photovoltaic Solar Energy Conference and Exhibition; Paris, France; 2013. p. 1242–1247.

[12] Werner S, Lohmuller E, Belledin U, Vlooswijk AHG, Naber RCG, Mack S, Wolf A. Optimization of BBr3 diffusion processes for n-type silicon solar cells. In: 31st European Photovoltaic Solar Energy Conference; Hamburg, Germany; 2015.

[13] Hieslmair H, Latchford I, Mandrell L, Chun M, Adibi B. Ion implantation for silicon solar cells. Cell. 2010; 18:17.

[14] Rohatgi A, Meier DL, McPherson B, Ok YW, Upadhyaya AD, Lai JH, Zimbardi F. High-throughput ion-implantation for low-cost high-efficiency silicon solar cells. Energy Procedia. 2012; 15:10–19.

[15] Hermle M, Benick J, Rüdiger M, Bateman N, Glunz SW. N-type silicon solar cells with implanted emitter. In: 26th European Photovoltaic Solar Energy Conference; Hamburg, Germany; 2011. p. 875–878.

[16] Tao Y, Rohatgi A. High-efficiency large area ion-implanted n-type front junction Si solar cells with screen-printed contacts and SiO_2-passivated boron emitters. In: 40th IEEE Photovoltaic Specialist Conference; Denver, CO, USA; 2014. p. 3654–3658.

[17] Boscke TS, Kania D, Schollhorn C, Stichtenoth D, Helbig A, Sadler P, Braun M, Dupke M, Weis M, Grohe A, Lossen J. Fully ion implanted and coactivated industrial n-type cells with 20.5% efficiency. IEEE Journal of Photovoltaics. 2014; 4(1):48–51.

[18] Florakis A, Janssens T, Rosseel E, Douhard B, Delmotte J, Cornagliotti E, Poortmans J, Vandervorst W. Simulation of the anneal of ion implanted boron emitters and the impact on the saturation current density. Energy Procedia. 2012; 27:240–246.

[19] Müller R, Benick J, Bateman N, Schön J, Reichel C, Richter A, Hermle M, Glunz SW. Evaluation of implantation annealing for highly-doped selective boron emitters suitable for screen-printed contacts. Solar Energy Materials and Solar Cells. 2014; 120:431–435.

[20] Taniguchi K, Kurosawa K, Kashiwagi M. Oxidation enhanced diffusion of boron and phosphorus in (100) silicon. Journal of the Electrochemical Society. 1980; 127(10):2243–2248.

[21] Hahn G, Joos S. State-of-the-art industrial crystalline silicon solar cells. In: Willeke GP, Weber ER, editors. Semiconductors and Semimetals. 1st ed. London, UK: Elsevier Inc.; 2014. p. 1–62.

[22] Tao Y, Payne A, Upadhyaya VD, Rohatgi A. 20.7% efficient ion-implanted large area n-type front junction silicon solar cells with rear point contacts formed by laser opening and physical vapor deposition. Progress in Photovoltaics: Research and Applications. 2014; 22(10):1030–1039.

[23] Jiang F, Stavola M, Rohatgi A, Kim D, Holt J, Atwater H, Kalejs J. Hydrogenation of Si from SiNx (H) films: characterization of H introduced into the Si. Applied Physics Letters. 2003; 83(5):931–933.

[24] Hahn G, Käs M, Herzog B. Hydrogenation in crystalline silicon materials for photovoltaic application. Solid State Phenomena. 2010; 156:343–349.

[25] Mason N, Artigao A, Banda P, Bueno R, Fernandez JM, Morilla C, Russell R. The technology and performance of the latest generation buried contact solar cell manufactured in BP Solar's Tres Cantos facility. In: 19th European Photovoltaic Solar Energy Conference; Paris, France; 2004.

[26] Lennon A, Yao Y, Wenham S. Evolution of metal plating for silicon solar cell metallisation. Progress in Photovoltaics: Research and Applications. 2013; 21(7):1454–1468.

[27] Bartsch J, Kamp M, Hartleb D, Wittich C, Mondon A, Steinhauser B, Feldmann F, Richter A, Benick J, Glatthaar M, Hermle M. 21.8% efficient n-type solar cells with industrially feasible plated metallization. Energy Procedia. 2014; 55:400–409.

[28] Katkhouda K, Martinez-Limia A, Bornschein L, Koseva R, Geppert T, Grohe A, Krokoszinski HJ, Schaaf P. Aluminum-based rear-side PVD metallization for nPERT silicon solar cells. IEEE Journal of Photovoltaics. 2014; 4(1):160–167.

[29] Jung V, Heinemeyer F, Kšntges M. Long-term stable encapsulated solder joints on an Al/Ni: V/Ag metallization for silicon solar cells. Energy Procedia. 2012; 21:84–91.

[30] Meier DL, Good EA, Garcia RA, Bingham BL, Yamanaka S, Chandrasekaran V, Bucher C. Determining components of series resistance from measurements on a finished cell. In: Conference Record of the 2006 IEEE 4th World Conference on Photovoltaic Energy Conversion; Waikoloa, HI; 2006. p. 1315–1318.

[31] Shockley W, Read Jr WT. Statistics of the recombinations of holes and electrons. Physical Review. 1952; 87(5):835.

[32] Hall RN. Electron-hole recombination in germanium. Physical Review. 1952; 87(2):387.

[33] Sinton RA, Cuevas A. Contactless determination of current–voltage characteristics and minority-carrier lifetimes in semiconductors from quasi-steady-state photoconductance data. Applied Physics Letters. 1996; 69(17):2510–2512.

[34] Aberle AG. Surface passivation of crystalline silicon solar cells: a review. Progress in Photovoltaics: Research and Applications. 2000; 8(5):473–487.

[35] Agostinelli G, Delabie A, Vitanov P, Alexieva Z, Dekkers HF, De Wolf S, Beaucarne G. Very low surface recombination velocities on p-type silicon wafers passivated with a dielectric with fixed negative charge. Solar Energy Materials and Solar Cells. 2006; 90(18):3438–3443.

[36] Hoex B, Schmidt J, Bock R, Altermatt PP, Van de Sanden MC, Kessels WM. Excellent passivation of highly doped p-type Si surfaces by the negative-charge-dielectric Al_2O_3. Applied Physics Letters. 2007; 91(11):112107.

[37] Altermatt PP, Plagwitz H, Bock R, Schmidt J, Brendel R, Kerr MJ, Cuevas A. The surface recombination velocity at boron-doped emitters: comparison between various passivation techniques. In: 21st European Photovoltaic Solar Energy Conference; Dresden, Germany; 2006. p. 647–650.

[38] Aberle AG, Glunz S, Warta W. Impact of illumination level and oxide parameters on Shockley-Read-Hall recombination at the Si-SiO_2 interface. Journal of Applied Physics. 1992; 71(9):4422–4431.

[39] Stephens AW, Aberle AG, Green MA. Surface recombination velocity measurements at the silicon-silicon dioxide interface by microwave-detected photoconductance decay. Journal of Applied Physics. 1994; 76(1):363–370.

[40] Kimura K. Recent developments in polycrystalline silicon solar cells. In: 1st International Photovoltaic Science and Engineering Conference; Kobe, Japan; 1984. p. 37–42.

[41] Benick J, Müller R, Bateman N, Hermle M, Glunz S. Fully implanted n-type PERT solar cells. In: 27th European Photovoltaic Solar Energy Conference and Exhibition; Frankfurt, Germany; 2012. p. 676–679.

[42] Tao Y, Ok YW, Zimbardi F, Upadhyaya AD, Lai JH, Ning S, Upadhyaya VD, Rohatgi A. Fully ion-implanted and screen-printed 20.2% efficient front junction silicon cells on 239 cm n-type CZ substrate. IEEE Journal of Photovoltaics. 2014; 4(1):58–63.

[43] Wolf A, Kimmerle A, Werner S, Maier S, Belledin U, Meier S, Biro D. Status and perspective of emitter formation by POCl3 diffusion. In: 31st European PV Solar Energy Conference and Exhibition; Hamburg, Germany; 2015.

[44] Taguchi M, Yano A, Tohoda S, Matsuyama K, Nakamura Y, Nishiwaki T, Fujita K, Maruyama E. 24.7% record efficiency HIT solar cell on thin silicon wafer. IEEE Journal of Photovoltaics. 2014; 4(1):96–99.

[45] Tao Y, Upadhyaya V, Huang YY, Chen CW, Jones K, Rohatgi A. Carrier selective tunnel oxide passivated contact enabling 21.4% efficient large-area n-type silicon solar cells. In: 43rd IEEE Photovoltaic Specialist Conference; Portland, OR, USA; 2016.

[46] Feldmann F, Bivour M, Reichel C, Hermle M, Glunz SW. Passivated rear contacts for high-efficiency n-type Si solar cells providing high interface passivation quality and excellent transport characteristics. Solar Energy Materials and Solar Cells. 2014; 120:270–274.

[47] Moldovan A, Feldmann F, Zimmer M, Rentsch J, Benick J, Hermle M. Tunnel oxide passivated carrier-selective contacts based on ultra-thin SiO_2 layers. Solar Energy Materials and Solar Cells. 2015; 142:123–127.

[48] Lee WC, Hu C. Modeling CMOS tunneling currents through ultrathin gate oxide due to conduction-and valence-band electron and hole tunneling. IEEE Transactions on Electron Devices. 2001; 48(7):1366–1373.

[49] Steinkemper H, Feldmann F, Bivour M, Hermle M. Numerical simulation of carrier-selective electron contacts featuring tunnel oxides. IEEE Journal of Photovoltaics. 2015; 5(5):1348–1356.

[50] Tao Y, Upadhyaya V, Chen CW, Payne A, Chang EL, Upadhyaya A, Rohatgi A. Large area tunnel oxide passivated rear contact n-type Si solar cells with 21.2% efficiency. Progress in Photovoltaics: Research and Applications. 2016; 24:830–835.

[51] Romer U, Peibst R, Ohrdes T, Lim B, Krugener J, Wietler T, Brendel R. Ion implantation for poly-Si passivated back-junction back-contacted solar cells. IEEE Journal of Photovoltaics. 2015; 5(2):507–514.

[52] Zhao J, Wang A, Green MA. 24.5% efficiency silicon PERT cells on MCZ substrates and 24.7% efficiency PERL cells on FZ substrates. Progress in Photovoltaics: Research and Applications. 1999; 7(6):471–474.

[53] Zhao J, Wang A, Altermatt PP, Green MA, Rakotoniaina JP, Breitenstein O. High efficiency PERT cells on n-type silicon substrates. In: 29th IEEE Photovoltaic Specialists Conference; New Orleans, LA, USA; 2002. p. 218–221.

[54] Benick J, Steinhauser B, Muller R, Bartsch J, Kamp M, Mondon A, Richter A, Hermle M, Glunz S. High efficiency n-type PERT and PERL solar cells. In: 40th IEEE Photovoltaic Specialist Conference; Denver, CO; 2014. p. 3637–3640.

[55] Institute for Solar Energy Research in Hamelin (ISFH). Ion implanted, co-annealed and fully screen-printed bifacial n-type PERT solar cells with efficiencies of 21% and bifaciality factors exceeding 97% [Internet]. Sep 4th, 2015. Available from: http://www.isfh.de

[56] Zhao J, Wang A, Green M. 24% efficient PERL structure silicon solar cells. In: 21st IEEE Photovoltaic Specialists Conference; Kissimmee, FL; 1990. p. 333–335.

[57] Cuevas A. Electrons and holes in solar cells with partial rear contacts. Progress in Photovoltaics: Research and Applications. 2014; 22(7):764–774.

[58] Glunz SW, Benick J, Biro D, Bivour M, Hermle M, Pysch D, Rauer M, Reichel C, Richter A, Rüdiger M, Schmiga C. N-type silicon-enabling efficiencies>20% in industrial production. In: 35th IEEE Photovoltaic Specialists Conference; Honolulu, HI; 2010. p. 50–56.

[59] Hermle M, Feldmann F, Eisenlohr J, Benick J, Richter A, Lee B, Stradins P, Rohatgi A, Glunz SW. Approaching efficiencies above 25% with both sides-contacted silicon solar cells. In: 42nd IEEE Photovoltaic Specialist Conference; New Orleans, LA; 2015. p. 1–3.

[60] Yablonovitch E, Gmitter T, Swanson RM, Kwark YH. A 720 mV open circuit voltage SiOx:c-Si:SiOx double heterostructure solar cell. Applied Physics Letters. 1985; 47(11): 1211–1213.

[61] Glunz SW, Feldmann F, Richter A, Bivour M, Reichel C, Steinkemper H, Benick J, Hermle M. The irresistible charm of a simple current flow pattern -25% with a solar cell featuring a full-area back contact. In: 31st European Photovoltaic Solar Energy Conference and Exhibition; Hamburg, Germany; 2015.

[62] Chen CW, Hermle M, Benick J, Tao Y, OK YW, Upadhyaya A, Tam A, Rohatgi A. Modeling the potential of screen-printed front and tunnel oxide passivated back contact Cz silicon solar cell. Progress in Photovoltaics: Research and Applications. Forthcoming.

[63] Tam AM, Huang Y, OK Y, Rohatgi A. Design of selective emitter profiles for high efficiency solar cells under manufacturing technology constraints. In: 43rd IEEE Photovoltaic Specialist Conference; Portland, OR; 2016.

Chapter 6

Ultrafast Time-Resolved Measurements of Hybrid Solar Cells

Kaibo Zheng and Carlito S. Ponseca

Additional information is available at the end of the chapter

http://dx.doi.org/10.5772/65022

Abstract

The early time charge carrier dynamics in quantum dot-sensitized and organo-metal halide perovskite solar cells are presented in this chapter. Using transient spectroscopy techniques, i.e., absorption, photoluminescence, and photoconductivity, we probed the generation mechanism, charge injection, mobility, and recombination of charges in the time scales of subpicosecond (ps) to a nanosecond. In few ps, electron injection from quantum dot to *n*-type metal oxide (MO) is complete while hole injection to *p*-type MO required hundreds of ps. The injection process is dictated by the band alignment, density of states of MO and the charge transfer state at the interface. For organo-metal halide perovskite material, there is a distribution of exciton binding energy brought about by the nonuniformity in the quality of the sample. As a result, varying amount of exciton and highly mobile charges may be generated depending on the morphology of the film. In the sample presented here, we found that 30% of photo-generated charges are excitons, which then dissociates within 2–3 ps. The rest of the photons are instantaneously converted into highly mobile charges (μ_e = 12.5 $cm^2 V^{-1} s^{-1}$ and μ_h = 7.5 $cm^2 V^{-1} s^{-1}$), and at the appropriate excitation fluence, the photoconductivity remains constant up to 1 ns. The time scale and mechanism of charge injection from perovskite into organic electrodes are also presented.

Keywords: transient absorption, photoluminescence, photoconductivity, THz spectroscopy, mobility

1. Introduction

The emergence of different photovoltaic technologies has been driven by the desire to find an alternative solar cell technology that can be manufactured using simple laboratory processes

and at lower cost. This has led to conceptualization and development of hybrid solar cells, a structure where an organic molecule is used as light absorber and then attached to a metal oxide (MO). The earliest of this type is the dye-sensitized solar cell also known as the Graetzel-type solar cell. Upon light excitation, the dye generate excitons wherein electrons are injected into metal oxide (usually TiO_2) while holes traverse in liquid iodine electrolyte. This field has branched out to many material substitutions, two of which will be discussed in this chapter. On one hand, organic dyes were replaced by quantum dots, whose absorption spectra highly depends on its miniscule size, have now reached an overall power conversion efficiency (PCE) of 11.3% according to the solar cell efficiency chart of the National Renewable Energy Laboratory (NREL), USA. On the other hand, organo-metal halide perovskite solar cells adopt a perovskite crystal structure (usually orthorhombic), but has organic molecules, e.g., methyl ammonium, within its unit cell. Since its first discovery about 6 years ago, it has become one of the most serious competitors of silicon solar cells having a PCE 22.1% (NREL).

In this chapter, we present the ultrafast charge dynamics of these materials from the subpicosecond (ps) to a nanosecond (ns) time scale. Using transient spectroscopy techniques, the evolution of the charges from photoexcitation to recombination will be discussed. This chapter is divided into two main sections. First, results on quantum dot (QD) sensitized solar cell will be presented. This will include the electron injection in an *n*-type metal oxide (MO) acceptor as well as the hole injection to a p-type MO. The influence of single layer and multiple layers of QD on excitation transfer will be also examined. The second section will focus on the nature of photogenerated charges in organo-metal halide perovskite (OMHP), mobility and lifetime of charge carriers, and the mechanism and time scale of charge injection from perovskite material to organic electrodes.

2. Dynamics of charge carriers in QD-sensitized solar cells

Semiconductor nanocrystals, so-called quantum dots (QD), are confined quantum objects whose optoelectronic properties are dependent on their sizes [1]. Due to recent progress in chemical solution processing techniques for synthesis of colloidal QDs [2], it has attracted increasing attention on its fundamental properties [3] and applications [4]. The QDs can be utilized as imaging markers [5], as building blocks in light-emitting diode devices, [6] lasers and light harvesters in solar cells devices [7, 8]. Particularly, the potential application in photovoltaic devices has become the focus of the field over the past decade. One of the reasons for this is the possibility of breaking the Shockley-Queisser thermodynamic limit of single junction solar cells via multiple exciton generation (MEG) [9] or hot electron transfer (HET) [10]. Besides, the efficiencies of colloidal QD-based solar cells have been rapidly improving [11]. In this work, we would only discuss colloidal QDs and would refer it simply as QD. The recent progress in the understanding of the photo-induced dynamic processes in QD-based solar cell components is summarized in this section. Electron injection dynamics in QD—metal oxide (MO) composites is investigated followed by the studies of hole transfer dynamics and trapping. We also analyze excitation transfer in the films of QDs. The article is mainly based

on the studies of Cadmium chalcogenide QDs as well as some progress made for systems such as lead chalcogenide QDs in solar cell application.

2.1. Electron injection from QD to MO

Electron injection from QD to MO is a process responsible for charge separation in the vast majority of QD-sensitized solar cells (the so-called *n*-type solar cells). The first study can be found already in the 1990s [12]. The idea of using QD-MO heterojunction in solar cells was directly inspired by the study of dye-sensitized solar cells. As a key factor in photovoltaic process that would greatly determine its efficiency, electron injection in this system has been widely studied [13–19]. Time-resolved spectroscopy techniques are commonly used methodology to analyze electron injection dynamics including transient absorption (TA) or time-resolved photoluminescence (TRPL). However, combining such experiments with other spectroscopic techniques would be more useful to obtain more thorough picture of the overall injection process. The typical systems to study in QD-MO hetero-junction are CdSe QDs attached to a suitable wide band-gap MO (i.e., TiO_2 or ZnO) [20]. Generally speaking, the electron population in the QDs plays a domination role in the TA signal of CdSe QDs in the visible region [20]. Thus, one can easily distinguish the difference between electron and hole dynamics. Other than the CdSe, the PbS and PbSe QDs are also widely studied [21–23]. The band gap of the lead chalcogenide QDs is much narrower allowing it to harvest more photons over the whole sunlight spectrum. The narrower band gap is also favorable in studying the MEG process [24]. It should be noted that in the lead chalcogenide QDs, the transient absorption signal have features from both electron and hole dynamics. Therefore, a more careful identification of the spectral features including both interband and intraband transitions are highly needed [21].

By using the TA and TRPL measurements, it is possible to track down the density of mean electron population in QDs after excitation [20]. Decrease in the population, however, does not imply electron injection. For instance the electron trapping results in such decay as well. Identification of the electron injection itself can therefore become a complicated issue. The conventional techniques (visible TA or TRPL) can only be used to probe the electron population in QDs. However, one can also monitor electron population in MO by combining other spectroscopy techniques to directly show electron transfer. Blackburn et al. [19] provided a good example in QD-MO system. In that work, they tracked the population in MO using the TA in far IR region (around 5 μm wavelength) and it can therefore be used to detect the arrival of electrons. However, QDs have features in this spectral region as well. It is therefore necessary to correctly normalize and subtract QD-MO and QD signals to extract the true injection kinetics. Another suitable probe for the electron injection is a terahertz (THz) light source, which also has been applied previously on the dye-sensitized MOs. Absorbance in THz wave is correlated to the change in photoconductivity, and therefore we can use it to probe the evolution of the mobile charges in the system. In QDs, the charges are highly localized with rather low THz absorption. However, due to the relatively large mobility of the electrons in MO, the THz absorption would be much larger (especially for ZnO) [25, 26]. In this scenario, we utilized THz spectroscopy to probe the electron injection from QD to MO. By observing

simultaneous depopulation of electrons in QDs (probed by visible TA) with population of mobile charges in the system (probed by THz) one can directly show the electron transfer process and estimate the transfer rate [25]. This is illustrated in **Figure 1(b)**.

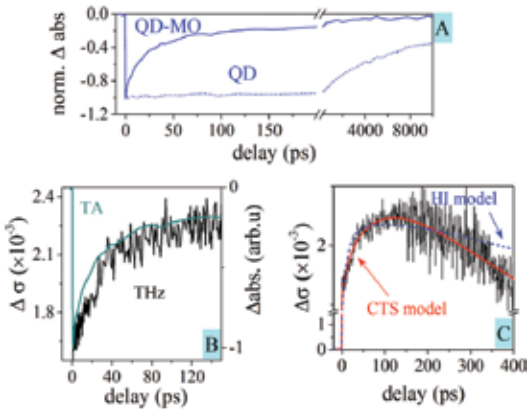

Figure 1. (A) Comparison of slow TA decay kinetics for bare CdSe QDs in solution (dotted line) and significantly faster decay kinetics of CdSe QD-ZnO system (solid line) indicates electron injection. (B) Overlapping decays of TA (cyan line) and THz kinetics (black line) demonstrating the electron transfer from QD to MO. (C) Model of the THz kinetics to exclude the possible hetereogeneous injection and confirm the injection via CTS (red line). Figures are reproduced from Ref. [25]. Copyright American Chemical Society, 2012.

In QDs, one cannot ignore the effect of electron-hole Coulomb interaction— for example, the exciton binding energy in conventional CdSe QDs can reach hundreds of meV, which is much larger than their bulk value [27]. Such Coulomb interaction prevents electron injection process [16]. In dye-sensitized or polymer solar cells with the similar high exciton binding energy, a so-called charge transfer state (CTS) has been observed [28]. This CTS formation indicates the build-up of an electron-cation bound complex after electron injection. The further movement of the injected electrons would follow the dissociation of such complex. The CTS is therefore important to the charge separation and collection. We have reported this CTS formation in the CdSe QD-ZnO system whose details can be found in Ref. [25]. The combination of THz and TA spectroscopy provided here is a direct evidence of that type charge transfer. A two-component dynamics can be observed in both pump-probe and the THz spectroscopy. The explanation that assumes injection of the electrons from two classes of QDs (the so-called heterogeneous injection, HI), cannot simultaneously reproduce both the transient kinetics. In constrast, the injection of electrons via a CTS can fully explain both TA and THz dynamics— see **Figure 1(c)**. The formation of the CTS greatly depends on the binding energy. Therefore, in PbS QDs with low exciton binding energy, the CTS would be negligible which explains the faster injection process [21–23].

2.2. Hole injection in *p*-type solar cells

In *n*-type solar cells, the hole transfer from QDs to liquid electrolyte is usually 2–3 orders of magnitude slower than the corresponding electron injection [29]. Thus, the hole dynamics

http://dx.doi.org/10.5772/65022

becomes the limiting factor for the photo-conversion efficiency [30]. To circumvent this, *p*-type solar cells are becoming popular, wherein QDs are attached to *p*-type MOs, e.g., NiO where holes are injected and extracted at the electrodes [31]. The lifetime and the pathway of the photo-generated holes are therefore essential for the photon-to-current conversion efficiency. It has been recently reported that the photon-to-current conversion efficiency is relatively low, about 17% only [32]. In this section, we give an overview of our studies on the hole dynamics in QDs, specifically the hole trapping process and the injection to *p*-type MOs.

To rigorously confirm the hole injection rates, complementary analysis using both TRPL and TA is necessary. It should be noted that the DOS of conduction band at the band-edge transition of CdSe QDs is significantly smaller than the DOS of valence band. Moreover, the hole states are much more closely spaced in QDs [9, 33]. Therefore, the signal of TA bleaching is dominated by the electron filling while hole contribute much less. Moreover, the PL measurements are sensitive to both charge carriers. It is therefore through TA kinetics that we are able to ascertain or preclude the role of electron depopulation in PL quenching as shown in **Figure 2** [34].

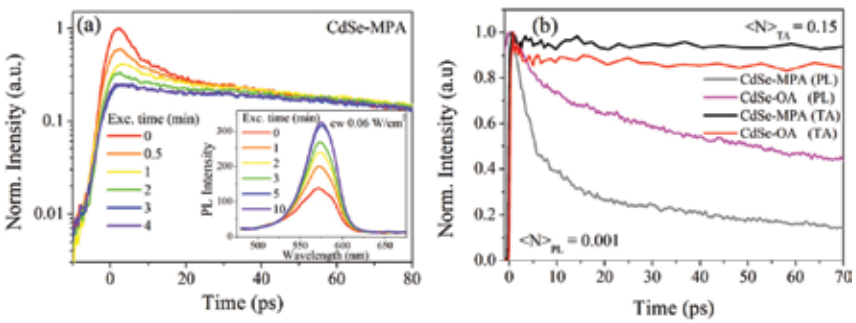

Figure 2. (a) PL decay kinetics trace of CdSe QDs after continuous laser excitation. The inset shows the evolution of the steady-state PL intensity. (b) TA kinetics at the band-edge bleach and PL decay of CdSe QDs with different capping agent attached to QD. Figures are reproduced from Ref. [34]. Copyright American Chemical Society, 2012.

In *p*-type dye-sensitized solar cells, the hole injection to MO can occur if it is energetically favorable [35, 36]. In QD-sensitized solar cells, the hole injection would also be restricted by the fast hole trapping. However, such hole trapping is likely to be greatly self-passivated. One example is the self-passivation by continuous light soaking. The effect is commonly explained by surface passivation induced by the chemical changes of the QD surface during photoirradiation [37].

Compared with electron injection in *n*-type MOs, the hole injection in *p*-type MOs such as NiO turns out to be much slower reaching hundreds of picoseconds that is due to the weaker electronic coupling, heavier effective mass of holes and less driving force for the charge transfer [37]. The driving force of QD is changed depending on its size, which means it also influences the holes' injection rate. The influence does not come from the difference in energy levels as the valence band of QDs tends to be pinned when attached to MOs [38]. The difference in the driving forces, mainly originate from the size-dependent Coulomb energy wherein larger driving force is found in larger QDs since Coulomb coupling is weaker.

2.3. Excitation transfer

Due to large exciton binding energy in CdSe QDs, initial photo-generated charge species behave like excitons [39]. The motion of such excitons between the QDs occurs via Förster resonant energy transfer (FRET), which is essential for the function of optical devices with densely packed QD films including light emitters and solar cells [40–42].

In QD-sensitized MOs, it is conventionally believed that electron injection only occurs from QDs directly attached to the MO surface while multilayer QD attachment would hinder the electron collection process. However, in the system of QD-MO with multiple layer QDs attachement, it is found the excitation transfer (Förster energy transfer) also occurs within the aggregates of QDs [41]. This transfer process can be traced in TA as an additional long-lived (5 ns) excited states depopulation (see **Figure 3**). Such energy transfer has also been reported in tandem-layered cadmium chalcogenide QD solar cells, which can be an effective complement to improve the solar cell efficiency [40].

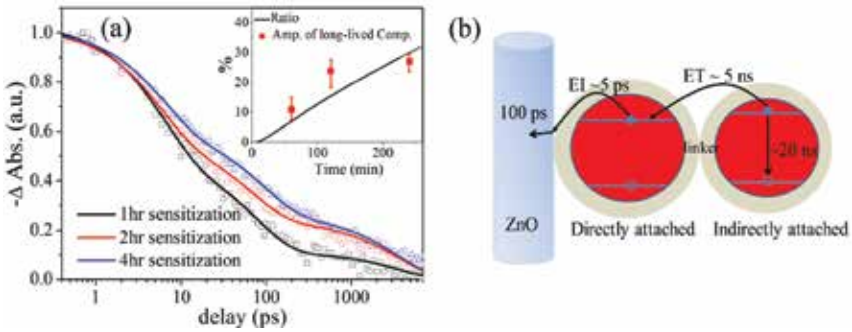

Figure 3. Energy transfer between indirectly attached QDs in QD-MO photoanodes. (a) TA kinetics of QD-ZnO NWs with different sensitization times. The inset illustrates the long-lived TA component (red dots) extracted from the exponential fit of the kinetics. The consistence between the TA amplitude and the number of indirectly attached QDs indicates indirect exciton depopulation with ns time scale. (b) Main photoinduced processes, including direct electron injection and energy. Figures are reproduced from Ref. [41]. Copyright American Chemical Society, 2012.

2.4. Outlook

QDs provide great opportunities for the development of optoelectronic devices. Moreover, the booming of QD solar cell research will surely put forward photo-induced dynamics questions waiting to be revealed in the future. For example, the band alignment assembly in lead chalcogenide QD devices currently holds the highest record of solar cell efficiency. The general principles of the device have been revealed but the atomistic details are still to be understood. The conventional spectroscopic techniques used in investigating the photo-induced dynamics are usually very different from the solar illumination conditions. These include the excitation intensity, the loading of circuit, medium conditions, etc. Systematic studies of charge carries dynamics under real solar cell functioning conditions may provide more useful reference for device application. Another issue of future research is to utilizing the "green" elements in the materials to replace the toxic Cd and Pb, which are overwhelmingly used in recent studies. All

in all, many challenges remain to be faced before the QD solar cells can be considered as a real viable solar technology. However, recent advances in QD research give ground for optimism.

3. Dynamics of charge carriers in organo-metal halide perovskite solar cells

From its first use as a light absorber in a dye-sensitized solar cell, the PCE of organo-metal halide perovskite (OMHP) has now reached to 22.1%. Such remarkable rise has dazzled scientists and engineers that have now considered OMHP to be one of the most serious competitors to the current solar cell industry leader, silicon. In spite of this, there are fundamental photophysical processes, especially in the ultrafast time scale, that is yet to be fully explained. Details of transient spectroscopy techniques used to unravel these processes can be found in Ref. [25].

3.1. Intrinsic properties of OMHP

Shown in **Figure 4(a)** is the rise of transient photoconductivity of methyl ammonium lead triiodide ($MAPbI_3$), $MAPbI_3/Al_2O_3$, and $MAPbI_3/TiO_2$ measured using time-resolved THz spectroscopy (TRTS). Notice that the rise in $MAPbI_3$ and $MAPbI_3/Al_2O_3$ is a two-step process, one that is instrument limited (about 70% of the total amplitude), while the second is about 2–3 ps (about 30% of the total amplitude). We note that molecular excitons that are tightly bound are neutral by definition, and therefore would not contribute to the transient photoconductivity obtained here. However, if photo-generated species are either loosely bound or mobile, or both, TRTS would be able to detect it. The instantaneous rise therefore means that highly mobile charges are created within the response of our instrument. The next question is how to explain the additional 2–3 ps rise. This can be understood in two ways. One, is that from the 70% highly mobile charges, these carriers become faster, that is gaining more mobility during that time scale. This would show in the technique as increase in photoconductivity. Another explanation is that there is a distribution of binding energy in the sample. The implication of this is that, there is a nonuniformity in the quality of film wherein in some parts have defect-free area that promotes generation of mobile charges. Area of the film with high defect density would tend to have exciton that is more tightly bounded. In fact, it has been reported that binding energy of exciton in these materials vary between few meV [43] and 50 meV [44] depending on the preparation conditions. As a result of heterogeneity in its binding energy, photo-generated species dissociates at different rates. This explains the two-component rise in the photoconductivity kinetics shown in **Figure 4(a)**. In this scenario, 70% are directly converted to mobile charges while the 30% are generated via exciton dissociation. For $MAPbI_3/TiO_2$, the transient photoconductivity rises in a single-step instrument-limited time scale. This means that, unlike the first two samples, mobile charges are readily created. This is reminiscent of our previous results on electron injection from QD to ZnO [25] as well as the injection rate of electrons from RuN3 dye attached to TiO_2 [45]. Similarly, we assign the single step rise of the transient photoconductivity as evidence of subpicosecond injection of electrons from the OMHP to TiO_2. There is favorable band energy alignment between the energy of perovskite

and metal oxide that helps in the separation of any bound electron-hole pair allowing injection in the ultrafast time scale.

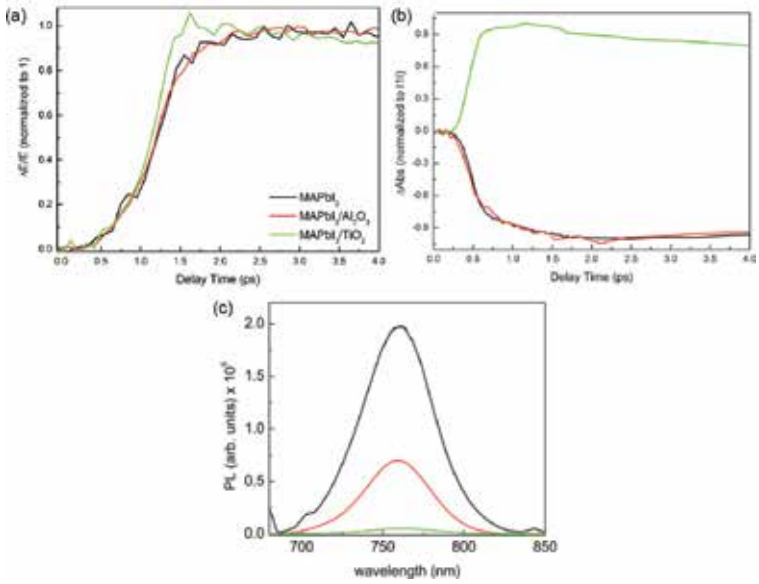

Figure 4. (a) Transient photoconductivity kinetics of neat $MAPbI_3$, $MAPbI_3/Al_2O_3$, and $MAPbI_3/TiO_2$. Normalized to 1 (λ_{pump} = 400 nm, I_{exc} = 1.7 × 10^{13} ph/cm^2 per pulse). (b) Transient absorption kinetics (λ_{pump} = 603 nm, λ_{probe} = 970 nm, I_{exc} = 6.0 × 10^{14} ph/cm^2 per pulse). (c) Photoluminescence spectra (λ_{pump} = 550 nm) of the three samples. Reprint with permission from Ref. [46]. Copyright 2014, American Chemical Society.

To verify the above assertions, we also obtained the transient absorption kinetics of the three samples, shown in **Figure 4(b)**. For $MAPbI_3$ and $MAPbI_3/Al_2O_3$, the kinetics is characterized by two-step decrease whose time scale is identical to that of the rise in the transient photoconductivity. This means that the processes in both kinetics should be at least similar if not identical. Since the absorption kinetics is negative for the two samples, it means that something is being bleached or being emitted. Furthermore, as shown in **Figure 4(c)**, for the same two samples, the emission spectra of the steady state photoluminescence are quite high. The two-step stimulated emission in the transient absorption kinetics show that not all charges are created simultaneously while the bright photoluminescence in steady state PL means these charges eventually meet and recombine radiatively. In the case of $MAPbI_3/TiO_2$, the positive one-step rise in the transient absorption kinetics supports our conclusion that there is instantaneous charge generation while the very low PL count reiterates our assertion that electrons are injected into TiO_2 and does not recombine radiatively with holes left in the perovskite.

We further analyzed and take the transient photoconductivity of the three samples at different excitation fluences and at up to 1 ns. Plotted in **Figure 5(a)** is the transient photoconductivity per photon absorbed per pulse for the first 40 ps. For the first two samples, $MAPbI_3$ and the $MAPbI_3/Al_2O_3$, the obtained mobility is 20 cm^2 V^{-1} s^{-1} while for $MAPbI_3/TiO_2$, it is 7.5 cm^2 V^{-1} s^{-1}. For the $MAPbI_3$, both electrons and holes are generated in the perovskite material. This is

http://dx.doi.org/10.5772/65022

also true for $MAPbI_3/Al_2O_3$ sample, since the alignment of band energies of Al_2O_3 and perovskite is not favorable for charge transfer, both electrons and holes remain in the perovskite material. Therefore, 20 $cm^2\ V^{-1}\ s^{-1}$ is the sum of the mobility of both charges in the perovskite. For $MAPbI_3/TiO_2$, where there is an ultrafast electron injection as discussed above, electrons are transferred to TiO_2 and its mobility becomes 0.1 $cm^2\ V^{-1}\ s^{-1}$ only, since it adopts the property of the accepting material. The implication is that the measured mobility of 7.5 $cm^2\ V^{-1}\ s^{-1}$ in $MAPbI_3/TiO_2$ should be coming from holes left in perovskite since electrons are already in the TiO_2. Now, knowing that the hole mobility is 7.5 $cm^2\ V^{-1}\ s^{-1}$ and the total mobility is 20 $cm^2\ V^{-1}\ s^{-1}$, one can concludes that the electron mobility should be 12.5 $cm^2\ V^{-1}\ s^{-1}$ in both $MAPbI^3$, and $MAPbI^3/Al^2O^3$. This is the first report where both the electron and hole mobilities are measured in OMHP materials [46].

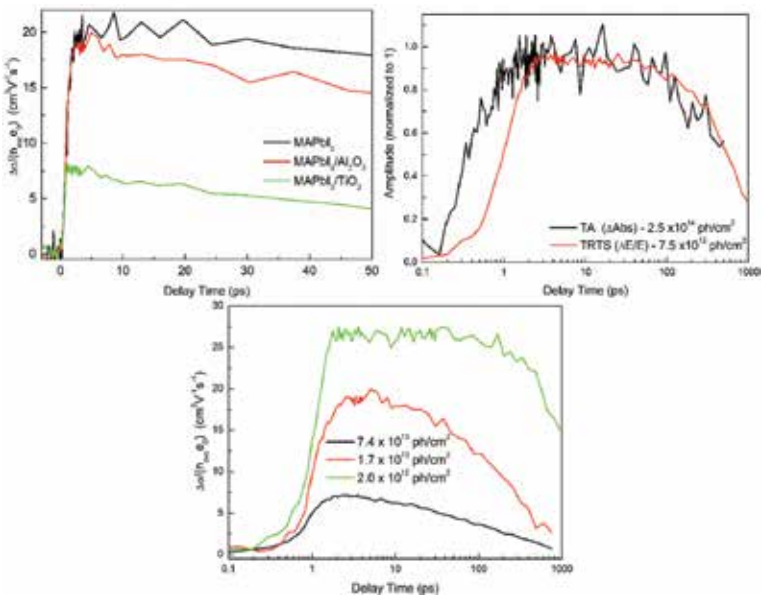

Figure 5. (a) Transient photoconductivity of neat $MAPbI_3$, $MAPbI_3/Al_2O_3$, and $MAPbI_3/TiO_2$ per photon absorbed. (b) Comparison TA and TRTS kinetics for neat $MAPbI_3$ showing that similar decay rates up to 1 ns. (c) Intensity dependence transient photoconductivity of $MAPbI_3/Al_2O_3$. Reprint with permission from Ref. [46]. Copyright 2014, American Chemical Society.

We then compared the kinetic traces of $MAPbI_3$ using transient absorption and photoconductivity up to 1 ns, at very similar excitation conditions, which are plotted in **Figure 5(b)**. From about 3 ps to 100 ps, both of the traces are flat which then started to decay at similar rate until 1 ns showing that the charge dynamics should be identical. Transient absorption monitors the population or depopulation of charge carries while transient photoconductivity measures the product of charge concentration and mobility. From 3 ps to 100 ps, where the two traces are flat means that neither the population of the charges nor the mobility of the carriers is changing. However, for time scale longer than 100 ps, the decay starts to manifest. In this case, the transient absorption kinetics shows that charges are disappearing. Similarly, the decay in

transient photoconductivity should manifest the same phenomenon. Ergo, the mobility of charges in perovskite should have remained constant, at least up to 1 ns, otherwise its decay should be more substantial than just the corresponding transient absorption. This is a very important finding since mobility of charges usually decay in emerging photovoltaic materials due to the defects in the film as well as its high exciton binding energy. In the case of OMHP, it seems to suggest that there is at least less defects in these films that favor the charge to maintain its mobility up to 1 ns. For organic solar cell material, we have previously shown that mobility is 50% slower in half of nanosecond [48].

We then want to determine the influence of reduced excitation fluence to the decay of the transient photoconductivity as we have shown previously that there are nonlinear effects at high fluency in organic solar cells [48]. Shown in **Figure 5(c)** is the transient conductivity of $MAPbI_3/Al_2O_3$ at three different intensities. For 7.4×10^{13} ph/cm^2 per pulse, the mobility is around 5 cm^2 V^{-1} s^{-1} and its decay started early at about 5 ps. For intensity of 1.7×10^{13} ph/cm^2 per pulse, a mobility of 20 cm^2 V^{-1} s^{-1} was obtained and the onset of decay is prolonged to around 10 ps. At the lowest excitation condition of 2.0×10^{12} ph/cm^2 per pulse, the highest mobility is measured 25 cm^2 V^{-1} s^{-1} and decay did not start until after 300 ps. This shows how essential the excitation intensity dependence measurements in transient spectroscopy. At high excitation conditions, nonlinear effects as such charge pair annihilation or second order nongeminate recombination dominates as the main channel of charge depopulation. This is the reason for the behavior of the transient photoconductivity shown above. At high excitation, mobility is low, i.e., at the earliest time scale, charges recombine right away since the resulting charge density at this condition is quite high. Moreover, the onset of decay is early. On the other hand, at the lowest excitation intensity, charges are rather sparse with each other (low charge density) and the probability of it recombining is low. This is the rationale of the high mobility at the early time scale. For the same reason, recombination is also delayed to at least 300 ps. The difference between the mobility of $MAPbI_3$ (20 cm^2 V^{-1} s^{-1}, **Figure 5a**) and $MAPbI_3/Al_2O_3$ (25 cm^2 V^{-1} s^{-1}, **Figure 5c**) can be explained by the better film morphology in $MAPbI_3/Al_2O_3$. The metal oxide Al_2O_3 acts like a scaffolding creating a more continuous film than the bare $MAPbI_3$.

Another, interesting feature of this material is the very small differences in the mobility of electrons and holes. In contrast with organic solar cells, this difference in mobility can be few orders of magnitude. Due to this, a built-in electric field is produced since one of the charge specie, usually the electrons, arrives earlier in the electrode while the holes, being slow, is still traversing the polymer molecule, arriving later in the counterelectrode. As shown in the above results, electrons and holes in OMHP have a difference in the mobility of just about half, i.e., μ_e = 12.5 cm^2 V^{-1} s^{-1} and μ_h = 7.5 cm^2 V^{-1} s^{-1}. This indicates that both charges arrive in their respective electrodes almost at the same time, avoiding the built-up electric field. This again is advantageous for solar cell operation since it will be able to collect more charges.

3.2. Injection into organic electrodes

Similar to other emerging photovoltaic technologies, there are significant efforts on using organic molecules, like PCBM and Spiro-OMeTAD as electrodes. In this section, we will show

http://dx.doi.org/10.5772/65022

the mechanism and time scale of electron and hole injection in these organic electrodes. Plotted in **Figure 6(a)** is the transient photoconductivity of $MAPbI_3$, $MAPbI_3$/PCBM, and $MAPbI_3$/Spiro-OMeTAD per photon absorbed per pulse. It can be seen that for $MAPbI_3$ mobility obtained is 15 cm^2/Vs and remained flat for the first ns. We note that the difference in the mobility measured here with respect to the $MAPbI_3$ sample discussed above (20 cm^2/Vs). It has been reported by Wang et al. [49] that depending on the preparation conditions, the concentration and type of defects could differ significantly. In fact, they found that thermal annealing alone should be able to shift the property of perovskite material from an *n*-type to intrinsic to *p*-type semiconductor. This means that no two-perovskite samples are made identical to each other, more so, when prepared by different groups despite following the same recipe. Having said that, the transient photoconductivity measurements of all perovskite samples we studied in the past gave a rather consistent result, i.e., from 15 to 25 cm^2/Vs. We surmise that these differences do not significantly alter the interpretation of the photophysical properties of the materials we presented here.

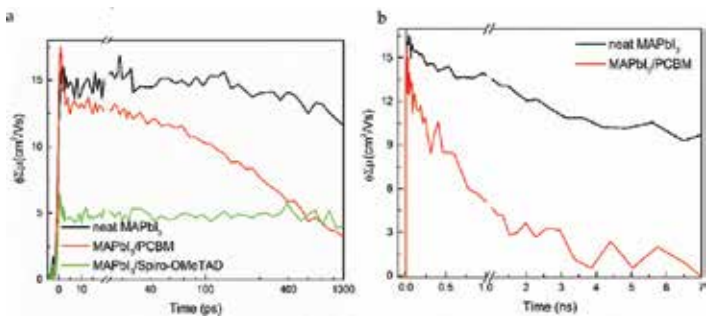

Figure 6. Transient photoconductivity of (a) neat $MAPbI_3$, $MAPbI_3$/PCBM, and $MAPbI_3$/Spiro-OMeTAD per photon absorbed per pulse (λ_{pump} = 590 nm) up to 1 ns and (b) of neat $MAPbI_3$ and $MAPbI_3$/with 7 ns time window. Reprint with permission from Ref. [47]. Copyright 2014, American Chemical Society.

Also plotted in **Figure 6(a)** is the transient photoconductivity of $MAPbI_3$/Spiro-OMeTAD. Spiro-OMeTAD is an organic hole transporting material that is widely used for highly efficient perovskite-based solar cell material despite its reported very low conductivity, 10^{-8} S/cm [50]. The measured mobility from this sample is about 5 cm^2/Vs, which is a third of that obtained from the $MAPbI_3$ only, but it stayed constant for 1 ns. Upon photoexcitation, electrons and holes are generated in the perovskite material. In the presence of an acceptor material that has favorable band energy alignment, charges may be injected. In this case, there is a 0.5 eV difference in the band edge between the valence bands of perovskite and Spiro-OMeTAD, leading us to conclude that there is an efficient hole injection. The injection rate is ultrafast since the mobility is reduced to three times in the earliest time scale. This is also supported by the fact that decent PCE are reported to these devices, which means that holes are really transferred from perovskite to Spiro-OMeTAD. Moreover, since holes are injected to the Spiro-OMeTAD and the conductivity of this material is very small, this means that the mobility of 5 cm^2/Vs should be the mobility of electrons. This value of electron mobility is again different from the sample presented in the previous section. However, we reiterate that different

preparation conditions yield different film quality manifesting as different values in their mobility, among other properties. As to the flat transient photoconductivity trace of this sample, it can be understood such that electrons remain in the perovskite material and did not encounter either defects where they can be trapped or holes which they can recombine with.

The transient photoconductivity trace of $MAPbI_3$/PCBM is characterized by mobility similar to $MAPbI_3$, 15 cm^2/Vs, but is decaying to almost a third in 1 ns. The initial value of the mobility implies that both electrons and holes are generated in the perovskite. The decay could then be assigned as due to second order geminate recombination. However, this type of recombination is excitation dependent. If this is the case, both the transient photoconductivity of $MAPbI_3$ and $MAPbI_3$/Spiro-OMeTAD should also be decaying at the same rate since the excitation fluence used for these three samples are the same. Since this is not the case, one can discount this possibility. In addition and as shown in **Figure 6(b)**, where a higher excitation fluence is used for $MAPbI_3$ and $MAPbI_3$/PCBM but for a longer time window of 7 ns, the decay in $MAPbI_3$/PCBM is faster than $MAPbI_3$ only, showing that there is an additional mechanism that causes the decay other than the second order recombination. It has been reported that the energy difference between the conduction bands of PCBM and perovskite is only 0.2 eV. As such, injection is still possible, but unlike in perovskite/Spiro-OMeTAD interface, this injection can be slower since the driving force is at least two times less. This slower injection rate of electrons from perovskite to PCBM could be one of the mechanisms of the decay. Furthermore, one should also take into account the electron mobility in PCBM, which is 10^{-3} cm^2/Vs [51–55]. This implies that while electrons are slowly injecting into the PCBM, the low mobility of the PCBM causes the electrons to be pinned at the interface. In this scenario, holes that are in perovskite could easily recombine with the electrons pinned at the interface of PCBM which could also have a ns time scale. We surmised that the ns decay of the transient photoconductivity shown in **Figure 6** is a convolution of the electron injection and recombination of the pinned electrons at the interface with the holes left in the perovskite material both occuring in the time scale of few ns.

3.3. Outlook

There are many studies that have reported the very impressive properties of perovskite-based solar cells and these have inspired material scientists and engineers to pursue this field of study. However, this should be taken as only the start of a longer, more detailed investigations in the future. It is only very recently that evidence of the influence of preparation conditions is getting the attention it deserves. In organic solar cells, preparation routes dictate the morphology, therefore, the quality of the film, which now appear to be very similar to perovskite solar cells.

4. Conclusion

Ultrafast time-resolved studies of two of the most important hybrid solar cell technologies, quantum dot-sensitized and perovskite-based solar cells, were discussed in this chapter. The mechanism and time scale of charge generation, nature of charged species, mobility, injection,

http://dx.doi.org/10.5772/65022

and recombination were obtained using transient absorption, photoluminescence, and photoconductivity measurements. For quantum dot-sensitized solar cell materials, electron injection is a two-step process; first, a few ps injection at the interface between QD and ZnO, while the second step is a charge transfer state-mediated 200 ps injection from the interface to the bulk of the ZnO material. For multiple layers of QDs, excitation transfer is confirmed while hole injection is shown to be dictated by the band alignment at the interface but limited by fast hole trapping. For organo-metal halide perovskite, almost ideal solar cell characteristics were found, i.e., ultrafast generation charges, high mobility of electrons and holes that is maintained for at least 1 ns, and balanced transport. Using organic electrodes, electron injection from perovskite to PCBM is found to be in the sub-ns while the sub-ps hole injection is obtained from perovskite to Spiro-OMeTAD. The time scale of charge transfer was found to be dependent on the driving force between the interface of perovskite and organic electrodes. Despite the seemingly convincing time-resolved measurement results, we surmise that more thorough investigations are warranted. This is in the broader context of further understanding the influence of preparation conditions to the ultrafast charge carrier dynamics of the solar cell technologies discussed here.

Acknowledgements

This work was supported by the Swedish Energy Agency, the Knut and Alice Wallenberg Foundation, and the Swedish Research Council. Collaboration within nanoLund and Lund Laser Center is acknowledged. We also acknowledge support from by NPRP grant # NPRP7-227-1-034 from the Qatar National Research Fund (a member of Qatar Foundation) and Laserlab-Europe (EU-H2020 654148).

Author details

Kaibo Zheng[1,2] and Carlito S. Ponseca[1*]

*Address all correspondence to: carlito.ponseca@chemphys.lu.se

1 Division of Chemical Physics, Lund University, Lund, Sweden

2 Gas Processing Center, College of Engineering, Qatar University, Doha, Qatar

References

[1] Leutwyler W, Bürgi S, Burgl H Semiconductor clusters, nanocrystals and quantum dots. *Science* 1996; 271:933–937.

[2] Murray CB, Kagan CR Synthesis and characterization of monodisperse nanocrystals and close-packed nanocrystal assemblies. *Annu Rev Mater Sci* 2000; 30:545–610.

[3] Scholes GD Selection rules for probing biexcitons and electron spin transitions in isotropic quantum dot ensembles. *J Chem Phys* 2004; 121:10104–10110.

[4] Prabhakaran P, Kim W J, Lee KS, Prasad PN Quantum dots (QDs) for photonic applications. *Opt Mater Exp* 2012; 2:578.

[5] Zrazhevskiy P, Gao X Quantum dot imaging platform for single-cell molecular profiling. *Nat Commun* 2013; 4:1619.

[6] Tessler N, Medvedev V, Kazes M, Kan S, Banin U Efficient near-infrared polymer nanocrystal light-emitting diodes. *Science* 2002; 295:1506–1509.

[7] Kamat P Quantum dot solar cells. The next big thing in photovoltaics. *J Phys Chem Lett* 2013; 4:908–918.

[8] Kramer IJ, Sargent EH The architecture of colloidal quantum dot solar cells: materials to devices. *Chem Rev* 2014; 114:863–882.

[9] Klimov V Spectral and dynamical properties of multiexcitons in semiconductor nanocrystals. *Annu Rev Phys Chem* 2007; 58:635–673.

[10] Ross RT Efficiency of hot-carrier solar energy converters. *J Appl Phys* 1982; 53:3813.

[11] Chuang CH M, Brown PR, Bulović V, Bawendi MG Improved performance and stability in quantum dot solar cells through band alignment engineering. *Nat Mater* 2014; 13:796–801.

[12] Kietzmann R, Willig F, Weller H, Vogel R, Nath DN, Eichberger R, Liska P, Lehnert J Picosecond time resolved electron injection from excited cresyl violet monomers and Cd3P2 quantum dots into TiO_2. *Mol Cryst Liq Cryst* 2006; 194:169–180.

[13] Robel I, Kuno M, Kamat P Size-dependent electron injection from excited CdSe quantum dots into TiO_2 nanoparticles. *J Am Chem Soc* 2007; 129:4136–4137.

[14] Guijarro N, Shen Q, Giménez S, Mora-Seró I, Bisquert J, Lana-Villarreal T, Toyoda T, Gómez R Direct correlation between ultrafast injection and photoanode performance in quantum dot sensitized solar cells. *J Phys Chem C* 2010; 114:22352–22360.

[15] Abdellah M, Žídek K, Zheng K, Chábera P, Messing ME, Pullerits T Balancing electron transfer and surface passivation in gradient CdSe/ZnS core–shell quantum dots attached to ZnO. *J Phys Chem Lett* 2013; 4:1760–1765.

[16] Tvrdy K, Frantsuzov PA, Kamat PV Photoinduced electron transfer from semiconductor quantum dots to metal oxide nanoparticles. *Proc Natl Acad Sci* 2011; 108:29–34.

[17] Leschkies KS, Divakar R, Basu J, Enache-Pommer E, Boercker JE, Carter CB, Kortshagen UR, Norris DJ, Aydil ES Photosensitization of ZnO nanowires with CdSe quantum dots for photovoltaic devices. *Nano Lett* 2007; 7:1793–1798.

[18] Tisdale WA, Zhu XY Surface chemistry special feature: artificial atoms on semiconductor surfaces. *Proc Natl Acad Sci* 2011; 108:965–970.

[19] Blackburn JL, Selmarten DC, Nozik AJ Electron transfer dynamics in quantum dot/titanium dioxide composites formed by in situ chemical bath deposition. *J Phys Chem B* 2003; 107:14154–14157.

[20] Klimov VI *Nanocrystal Quantum Dots* Klimov V I, Ed CRC Press, Boca Raton, FL 2010.

[21] Pattantyus-Abraham AG, Kramer IJ, Barkhouse AR, Wang X, Konstantatos G, Debnath R, Levina L, Raabe I, Nazeeruddin MK, Grätzel M, Sargent EH Depleted-heterojunction colloidal quantum dot solar cells. *ACS Nano* 2010; 4:3374–3380.

[22] Yang Y, Rodríguez-Córdoba W, Xiang X, Lian T Strong electronic coupling and ultrafast electron transfer between PbS quantum dots and TiO_2 nanocrystalline films. *Nano Lett* 2012; 12:303–309.

[23] Tisdale WA, Williams KJ, Timp BA, Norris DJ, Aydil ES, Zhu XY Hot-electron transfer from semiconductor nanocrystals. *Science* 2010; 328:1543–1547.

[24] Luther JM, Beard MC, Song Q, Law M,Ellingson RJ, Nozik AJ Multiple exciton generation in films of electronically coupled PbSe quantum dots. *Nano Lett* 2007; *7*:1779–1784.

[25] Žídek K, Zheng K, Ponseca CS, Messing ME, Wallenberg LR, Chábera P, Abdellah M, Sundström V, Pullerits T Electron transfer in quantum-dot-sensitized ZnO nanowires: ultrafast time-resolved absorption and terahertz study. *J Am Chem Soc* 2012; 134:12110–12117.

[26] Cánovas E, Moll P, Jensen SA, Gao Y, Houtepen AJ, Siebbeles LDA, Kinge S, Bonn M Size-dependent electron transfer from PbSe quantum dots to SnO2 monitored by picosecond terahertz spectroscopy. *Nano Lett* 2011; 11:5234–5239.

[27] Meulenberg RW, Lee JRI, Wolcott A, Zhang JZ, Terminello LJ, van Buuren T Determination of the exciton binding energy in CdSe quantum dots. *ACS Nano* 2009; 3:325–330.

[28] Němec H, Rochford J, Taratula O, Galoppini E, Kužel P, Polívka T, Yartsev A, Sundström V Influence of the electron-cation interaction on electron mobility in dye-sensitized ZnO and TiO_2 nanocrystals: a study using ultrafast terahertz spectroscopy. *Phys Rev Lett* 2010; 104:1–4.

[29] Chakrapani V, Baker D, Karmat P Understanding the role of the sulfide redox couple (S2-/Sn2-) in quantum dot sensitized solar cells. *J Am Chem Soc* 2011; 133:9607–9615.

[30] Kamat PV, Christians JA, Radich JG Quantum dot solar cells: hole transfer as a limiting factor in boosting the photoconversion efficiency. *Langmuir* 2014; 30:5716–5725.

[31] Wang Z, Shakya A, Gu J Sensitization of P-GaP with CdSe quantum dots: light-stimulated hole injection. *J Am Chem Soc* 2013; 135:9275–9278.

[32] Barceló I, Guillén E, Lana-Villarreal T, Gómez R Preparation and characterization of nickel oxide photocathodes sensitized with colloidal cadmium selenide quantum dots. *J Phys Chem C* 2013; 117:22509–22517.

[33] Malko AV, Mikhailovsky AA, Petruska MA, Hollingsworth JA, Klimov VI Interplay between optical gain and photoinduced absorption in CdSe nanocrystals. *J Phys Chem B* 2004; 108:5250–5255.

[34] Rowland CE, Schaller RD Exciton fate in semiconductor nanocrystals at elevated temperatures: hole trapping outcompetes exciton deactivation. *J Phys Chem C* 2013; 117:17337–17343.

[35] Morandeira A, Boschloo G, Hagfeldt A, Hammarström L Coumarin 343-NiO films as nanostructured photocathodes in dye-sensitized solar cells: ultrafaste transfer, effect of the I^{3-}/I^{-} redox couple and mechanism of photocurrent generation. *J Phys Chem C* 2008; 112:9530–9537.

[36] Li L, Gibson EA, Qin P, Boschloo G, Gorlov M, Hagfeldt A, Sun LC Double-layered NiO photocathodes for p-type DSSCs with record IPCE. *Adv Mater* 2010; 22:1759–1762.

[37] Zheng K, Zidek K, Abdellah M, Zhang W, Chabera P, Lenngren N, Yartsev A, Pullerits T Ultrafast charge transfer from CdSe quantum dots to p-type NiO: hole injection vs hole trapping. *J Phys Chem C* 2014; 118:18462–18471.

[38] Carlson B, Leschkies K Valence band alignment at cadmium selenide quantum dot and zinc oxide (1010) interfaces. *J Phys Chem C* 2008; 112:8419–8423.

[39] Meulenberg R, Lee J, Wolcott A Determination of the exciton binding energy in CdSe quantum dots. *ACS Nano* 2009; 3:325–330.

[40] Santra PK, Kamat PV Tandem-layered quantum dot solar cells: tuning the photovoltaic response with luminescent ternary cadmium chalcogenides. *J Am Chem Soc* 2013; 135:877–885.

[41] Zheng K, Zídek K, Abdellah M, Torbjörnsson M, Chábera P, Shao S, Zhang F, Pullerits T, Fast monolayer adsorption and slow energy transfer in CdSe quantum dot sensitized ZnO nanowires. *J Phys Chem A* 2012; 117:5919–5925.

[42] Choi S, Jin H, Bang J, Kim S Layer-by-layer quantum dot assemblies for the enhanced energy transfers and their applications toward efficent solar cells. *J Phys Chem Lett* 2012; 3:3442–3447.

[43] Lin Q, Armin A, Nagiri RR, Burn PL, et al. Electro-optics of perovskite solar cells. *Nat Photonics* 2014; 9:106–112.

[44] Sum TCT, Mathews N. Advancements in perovskite solar cells: photophysics behind the photovoltaics *Energy Environ Sci* 2014; 7:2518–2534.

[45] Nemec H, Rochford J, Taratula O, et al. Influence of the electron-cation interaction on electron mobility in dye-sensitized ZnO and TiO_2 nanocrystals: a study using ultrafast terahertz spectroscopy. *Phy Rev Lett* 2010; 104:197401.

[46] Ponseca CS, Savenije TJ, Abdellah M, et al. Organometal halide perovskite solar cell materials rationalized: ultrafast charge generation high and microsecond-long balanced mobilities and slow recombination. *J Am Chem Soc* 2014; 136:5189–5192.

[47] Ponseca CS, Hutter EM, Piatkowski P, Cohen B, Pascher T, Douhal A, Yartsev A, Sundstrom V, Savenije TJ Mechanism of charge transfer and recombination dynamics in organo metal halide perovskites and organic electrodes, PCBM and spiro-OMeTAD: role of dark carriers. *J Am Chem Soc* 2015; 137:16043-16048.

[48] Ponseca CS, Yartsev A, Wang E, Andersson MR, et al. Ultrafast terahertz photoconductivity of bulk heterojunction materials reveals high carrier mobility up to nanosecond time scale. *J Am Chem Soc* 2012; 134:11836–11839.

[49] Wang Q, Shao Y, Xie H, Lyu L, Liu X, Gao Y, Huang J Qualifying composition dependent p and n self-doping in $CH_3NH_3PbI_3$. *Appl Phys Lett* 2014; 105:163508.

[50] Nguyen WH, Bailie CD, Unger EL, McGehee MD Enhancing the hole-conductivity of Spiro-OMeTAD without oxygen or lithium salts by using Spiro (TFSI) 2 in perovskite and dye-sensitized solar cells. *J Am Chem Soc* 2014; 36:10996–11001.

[51] Gao P, Grätzel M, Nazeeruddin MK Organohalide lead perovskites for photovoltaic applications. *Energy Environ Sci* 2014; 7:2448–2463.

[52] Von Hauff E, Dyakonov V, Parisi J Study of field effect mobility in PCBM films and P3HT:PCBM blends. *Sol Energy Mater Sol Cells* 2005; 87:149–156.

[53] Mihailetchi VD, Xie H, De Boer B, et al. Charge transport and photocurrent generation in poly(3-hexylthiophene): methanofullerene bulk-heterojunction solar cells. *Adv Funct Mater* 2006; 16:699–708.

[54] Warman JM, De Haas MP, Anthopoulos TD, De Leeuw DM The negative effect of high-temperature annealing on charge-carrier lifetimes in microcrystalline PCBM. *Adv Mater* 2006; 18;2294–2298.

[55] Savenije TJ, Ferguson AJ, Kopidakis N, Rumbles G Revealing the dynamics of charge carriers in polymer:fullerene blends using photoinduced time-resolved microwave conductivity. *J Phys Chem C* 2013; 117:24085–24103.

Section 3

Nano-Structured Solar Cells - Organic and Thin Film Solar Cells

Chapter 7

Plasmonic Thin Film Solar Cells

Qiuping Huang , Xiang Hu , Zhengping Fu and Yalin Lu

Additional information is available at the end of the chapter

http://dx.doi.org/10.5772/65388

Abstract

Thin film solar cell technology represents an alternative way to effectively solve the world's increasing energy shortage problem. Light trapping is of critical importance. Surface plasmons (SPs), including both localized surface plasmons (LSPs) excited in the metallic nanoparticles and surface plasmon polaritons (SPPs) propagating at the metal/semiconductor interfaces, have been so far extensively investigated with great interests in designing thin film solar cells. In this chapter, plasmonic structures to improve the performance of thin film solar cell are reviewed according to their positions of the nanostructures, which can be divided into at least three ways: directly on top of thin film solar cell, embedded at the bottom or middle of the optical absorber layer, and hybrid of metallic nanostructures with nanowire of optical absorber layer.

Keywords: thin film solar cells, light trapping, localized surface plasmons (LSPs), surface plasmon polaritons (SPPs), light absorption enhancement

1. Introduction

Photovoltaic technology, the conversion of solar energy to electricity, can help to solve the energy crisis and reduce the environmental problems induced by the fossil fuels. Worldwide photovoltaic production capacity at the end of 2015 is estimated to be about 60 GW [1] and is expected to keep rising. Yet, there is great demand for increasing the photovoltaic device efficiency and cutting down the cost of materials, manufacturing, and installation. Materials and processing represent a large fraction of the expense. For example, material costs account for 40% of the total module price in the bulk crystalline silicon solar cells. Thin film solar cells have emerged as a means to reduce the material costs. To date, thin film solar cells are made

from various active inorganic materials, including amorphous and polycrystalline silicon, GaAs, $CuIn_xGa_{1-x}Se_2$ and CdTe, hybrid lead halide perovskites, as well as organic semiconductors. As the thickness of the absorbing semiconductor is decreased, the absorption naturally reduces at energies close to the band gap of the semiconductor. This is particularly a problem for thin film silicon solar cells. Thus, the compromise between enhancing the absorbance of broader solar lights and reducing the usage of narrower band gap semiconductor materials has to be taken in a thin film solar cell. And novel designs of thin film solar cells in which broadband light can be trapped inside to increase the absorption are highly needed to break the compromise balance.

In the past decade, a few light-trapping techniques have been investigated, among which a typical example is using a pyramidal surface texture [2]. However, such surface texture is intended for active light-harvesting layers, which are thicker than the wavelength of sunlight in the visible and near-infrared regions. The improved light trapping is balanced by the surface roughness that is almost the same order as the film thickness and by the increased surface recombination due to the larger surface area. Recently, the use of metallic nanostructures, which support surface plasmons (SPs) [3], has been regarded as an efficient way for enabling light trapping inside the active layer of a thin film solar cell and has consistently drawn an increasing amount of attention. SPs are coherent electron oscillations that propagate along the interface between a metal and a dielectric or semiconductor material. And SPs cause the electromagnetic field strongly confined at the metal/dielectric or semiconductor interface, with their intensity having an exponential dependence on the distance away from the interface. Thus near-field electromagnetic field enhancement and the enhanced scattering cross section (SCS) can be obtained through excitation of SPs. The larger electrical field means a stronger absorption, and a larger scattering cross section redirects more incident sunlight into the absorbing layer, resulting in a much larger light absorption in a much thinner semiconductor layer. Hence, both localized surface plasmons (LSPs) [4] excited in metallic nanoparticles and surface plasmon polaritons (SPPs) [5] propagating at the periodic metal/semiconductor interfaces have been so far widely investigated with great interests in designing high-efficient thin film solar cells [6–9].

In early work using plasmonic structures to improve the light absorption of photovoltaic devices, Au or Ag nanoparticles [5, 10] and nanograting [11] have been introduced into the front side of solar cells [5, 10–12]. Such efforts have common disadvantages that resonances can only occur at certain wavelengths, and the use of metallic nanostructures directly on top of solar cells will block a fairly large amount of total incident light. And then a layer of antireflection coating was combined into the surface metallic grating, to reduce the reflected light and thus to improve sunlight absorption [13]. The fractal-like pattern of Ag nano cuboids with several feature sizes [14] was employed to simultaneously excite low-index and high-index SP modes along the silicon-silver interface to achieve broadband absorption. On the other hand, Wang et al. [15] achieved a broadband and polarization-insensitive absorption enhancement by placing a metallic nanograting at the bottom of the optically active layer. In such design, planar waveguide modes, the Fabry-Pérot (FP) resonance, and the SPP resonance were effectively coupled, and photons blocking by the surface nanostructures can be avoided.

In Ref. [16], Ag nanocone was employed to enhance light trapping, and the simulated results showed that the normalized scattering cross section of the rear located Ag nanocone is higher than that of the front located one. Incorporation of embedded metal nanostructures for light trapping in thin film solar cell has been extensively investigated, such as, with nucleated silver nanoparticles embedded at rear side of amorphous silicon cells [17], using nanosphere [18], silver nanopillars [19], silver triangular [20], gold paired-strips [21] embedded grating structures, placing metal nanoparticles inside the active layer of solar cells [22], and with a metallic hole array inserted into a tandem solar cell [23]. Furthermore, combination of surface texture with embedded metal nanoparticles was also designed to trap light [24]. More plasmonic structures for light trapping in thin film solar cells will be described in the following sections in detail.

In this chapter, the theoretical formalisms about the SPPs and LSPs will be first described, followed by a summarize of plasmonic structures to improve the performance of thin film solar cell according to their positions of the nanostructures, which can be divided into at least three ways: (1) directly on top of thin film solar cell, (2) embedded at the bottom or middle of the optical absorber layer, and (3) combined with nanowire of optical absorber layer. Finally, conclusions are given.

2. Theory of surface plasmon

2.1. Surface plasmon polaritons

It has been more than a century since the electrons in solids were first regarded as hot dense plasma to explain some natural phenomenon like the color of metals and the temperature-dependent conductivity. Decades later since then, the word 'Plasmon' is carried out to describe a quantum of plasma oscillations, which are longitude density fluctuations that propagate through the volume of metal. The so-called volume plasmons have an eigen frequency $\omega_p = \sqrt{ne^2/m\varepsilon_0}$, when n is the electron density, at the order of 10 eV. They can be excited by both free electron beams and ultraviolet photons. In the 1950s, this was a fascinating phenomenon and has been well-studied theoretically and experimentally with electron-loss spectroscopy.

Probably as a result of the well investigations, in 1957, Rufus Ritchie [25] first predicted the existence of surface plasmons, which made up the other half of plasmon physics and is referred to as 'Plasmonics' nowadays. Surface plasmons are indeed the electron charges that perform coherent fluctuations on the metal boundary and are localized in the normal direction of the boundary within the Thomas-Fermi screening length. Polarized light source is frequently used to efficiently and conveniently excite a surface plasmon wave. Therefore, surface plasmon can also be treated as a collective set of surface plasmon polaritons (SPPs). Surface plasmon polariton is thus the elementary 'particle' of this unique surface phenomenon and will be investigated in the following.

Consider the simplest geometry sustaining SPPs, that is, a single and flat interface between a non-absorbing dielectric space with positive real dielectric constant ε_2 and a conductive space with complex dielectric function $\varepsilon_1(\omega)$. Maxwell's equations of macroscopic electromagnetism read:

$$\nabla \times \overline{E}\left(\vec{r},t\right) + \mu \frac{\partial \overline{H}\left(\vec{r},t\right)}{\partial t} = 0 \tag{1a}$$

$$\nabla \cdot \left(\mu \overline{H}\left(\vec{r},t\right)\right) = 0 \tag{1b}$$

$$\nabla \times \overline{H}\left(\vec{r},t\right) - \varepsilon_0 \varepsilon(\vec{r}) \frac{\partial \overline{E}\left(\vec{r},t\right)}{\partial t} = 0 \tag{1c}$$

$$\nabla \cdot \left(\varepsilon_0 \varepsilon(\vec{r}) \overline{E}\left(\vec{r},t\right)\right) = 0 \tag{1d}$$

There are two fundamental sets of solutions, which are termed as transverse magnetic (TM) and transverse electric (TE), respectively. Let us first look into TE solutions:

where $z > 0$:

$$E_y\left(z\right) = A_2 e^{i\beta x} e^{-k_2 z} \tag{2a}$$

$$H_x\left(z\right) = -iA_2 \frac{1}{\omega \mu_0} k_2 e^{i\beta x} e^{-k_2 z} \tag{2b}$$

$$H_z\left(z\right) = A_2 \frac{\beta}{\omega \mu_0} e^{i\beta x} e^{-k_2 z} \tag{2c}$$

And where $z < 0$:

$$E_y\left(z\right) = A_1 e^{i\beta x} e^{k_1 z} \tag{3a}$$

http://dx.doi.org/10.5772/65388

$$H_x(z) = iA_1 \frac{1}{\omega\mu_0} k_1 e^{i\beta x} e^{k_1 z} \tag{3b}$$

$$H_z(z) = A_1 \frac{\beta}{\omega\mu_0} e^{i\beta x} e^{k_1 z} \tag{3c}$$

Here the perpendicular component of wave vector $k_i(z)$ is denoted as k_i, with $i = 1, 2$ for short. Boundary condition requires the continuity of E_y and H_x at the interface $z = 0$, thus we have

$$A_1 = A_2 \tag{4a}$$

$$A_1(k_1 + k_2) = 0 \tag{4b}$$

Since k_i is positive, the only solution of Eq. (4) is $A_1 = A_2 = 0$. Hence, there are no possible surface modes for TE polarization. Now let us examine the result for TM polarization. Similarly, respective expressions for the field components in TM solutions are:

where $z > 0$:

$$H_y(z) = A_2 e^{i\beta x} e^{-k_2 z} \tag{5a}$$

$$E_x(z) = iA_2 \frac{1}{\omega\varepsilon_0\varepsilon_2} k_2 e^{i\beta x} e^{-k_2 z} \tag{5b}$$

$$E_z(z) = -A_2 \frac{\beta}{\omega\varepsilon_0\varepsilon_2} e^{i\beta x} e^{-k_2 z} \tag{5c}$$

and where $z < 0$:

$$H_y(z) = A_1 e^{i\beta x} e^{k_1 z} \tag{6a}$$

$$E_x(z) = -iA_1 \frac{1}{\omega\varepsilon_0\varepsilon_1} k_1 e^{i\beta x} e^{k_1 z} \tag{6b}$$

$$E_z(z) = -A_1 \frac{\beta}{\omega \varepsilon_0 \varepsilon_1} e^{i\beta x} e^{k_1 z} \tag{6c}$$

Boundary condition requires the continuity of H_y and $\varepsilon_i E_z$ at the interface $z = 0$, thus we have

$$A_1 = A_2 \tag{7a}$$

$$\frac{k_1}{k_2} = -\frac{\varepsilon_1}{\varepsilon_2} \tag{7b}$$

Different from the TE case, we can expect some non-null solution from Eq. (7). Note that the wave equation for TM modes reads:

$$\frac{\partial^2 H_y}{\partial z^2} + \left(k_0^2 \varepsilon - \beta^2\right) H_y = 0 \tag{8}$$

To fulfill Eq. (8) with the expression for H_y shown in Eqs. (5a) and (6a), we thus have

$$k_1^2 = \beta^2 - k_0^2 \varepsilon_1 \tag{9a}$$

$$k_2^2 = \beta^2 - k_0^2 \varepsilon_2 \tag{9b}$$

Combing this and Eq. (7), the solution at the boundary $z = 0$ is finally reached with propagating constant being:

$$\beta = k_0 \sqrt{\frac{\varepsilon_1 \varepsilon_2}{\varepsilon_1 + \varepsilon_2}} \tag{11}$$

Note that the metallic character of $\varepsilon_1(\omega)$ requires that ε_1 should be complex and its real part $\mathrm{Re}(\varepsilon_1) < 0$. Therefore, it is obvious that β is also complex, and its imaginary part indicates strong attenuation while propagating. By expanding $\varepsilon_1(\omega)$ into $\varepsilon_1' + i \cdot \varepsilon_1''$ and assuming $\left|\varepsilon_1'\right| \gg \varepsilon_1''$ as most metals do in reality, we further have

http://dx.doi.org/10.5772/65388

$$\beta = \beta' + i \cdot \beta'' = k_0 \sqrt{\frac{\varepsilon_1' \varepsilon_2}{\varepsilon_1' + \varepsilon_2}} + i k_0 \frac{\varepsilon_1''}{2(\varepsilon_1')^2} \left(\frac{\varepsilon_1' \varepsilon_2}{\varepsilon_1' + \varepsilon_2} \right)^{3/2} \tag{12}$$

Here, β'' determines the attenuation of SPPs. On the other hand, one can say the reason for SPPs being surface mode is that SPPs will quickly vanish once it 'leaves' the surface. The energy is tightly bounded to the interface and travels only for a small amount of length, typically in the order of 1–10 wavelengths. This behavior is in nature similar to the well-known evanescence wave, and in fact, SPPs can be efficiently excited by the impact of evanescence wave when the momentum match between SPPs and the evanescent wave is satisfied. Unlike the old method using electron beam, optical way to excite SPPs is of much more convenience and efficiency and has paved the way for plasmonics into application.

2.2. Localized surface plasmons

If the interface supporting SPPs that we discussed above shrinks to the scale of nanometer and forms a closed surface like sphere or ellipsoid, there would be no SPPs existing as the dispersive relationship and boundary condition have changed. However, by simply assuming the electrons in such a tiny metal object to be a neutral plasma, one should expect that an intrinsic resonance similar to the volume plasma resonance still existed for it. In that case, electrons would also collectively oscillate with the impact photons. In fact, this behavior is reasonable and termed 'localized surface plasmon' (LSP). LSP should be in nature different from SPP because SPP can propagate along the interface while LSP is totally bounded and cannot propagate at all. In general, LSP does not consist of 'polaritons' as SPP does, hence we will call LSP directly in the following text.

Considering a metal sphere with radius R, which is much smaller than the incident light's wavelength, we could treat the incident electromagnetic field as a static electric field. Hence, under this static field approximation, the eigen modes for LSP can be solved from Laplace equations. The electrostatic potential from Laplace equations thus reads [26]:

$$\phi_{<}(r,\theta,\phi) = \sum_{l=0}^{\infty} \sum_{m=-l}^{l} a_{lm} r^l Y_{lm}(\theta,\phi) \tag{13a}$$

where $0 \le r \le R$ and

$$\phi_{>}(r,\theta,\phi) = \sum_{l=0}^{\infty} \sum_{m=-l}^{\infty} b_{lm} \frac{1}{r^{l+1}} Y_{lm}(\theta,\phi) \tag{13b}$$

Here $Y_{lm}(\theta,\phi)$ is the spherical harmonics, a_{lm} and b_{lm} are the coefficients. At the sphere surface, boundary condition requires φ and $\varepsilon \partial\varphi/\partial r$ to be continuous, thus we arrive at the dispersive relation for LSP:

$$\frac{\mathrm{Re}\,\varepsilon\left(\omega_{LSP}\right)}{\varepsilon_0}+\frac{l+1}{l}=0 \tag{14}$$

Assuming $\varepsilon(\omega_{LSP})$ has a Drude form, i.e., $\varepsilon\left(\omega_{LSP}\right)=1-\frac{\omega_p^2}{\omega^2}$ thus Eq. (14) turns into:

$$\omega_l=\omega_p\left[\frac{l}{\varepsilon_0\left(l+1\right)+l}\right] \tag{15}$$

where l stands for the angular momentum index. For a small enough sphere where the static field approximation is well satisfied, l thus equals to 1, which means that the dipole excitation is mainly responsible for LSP. With the increase in radius, the interaction between multipoles is becoming more and more important. Eventually at infinite radius, the frequency of LSP reaches that of SPPs at a semi-infinite metal-dielectric interface.

Similar to SPPs, LSPs exhibit an impressive local field enhancement as all energy is bounded. However, LSPs exist much more common than SPPs, as LSP does not require a specific polarization direction of the incident electromagnetic wave. A lot of applied techniques thus are developed on the basis of LSP enhancement, such as surface enhanced Raman spectroscopy (SERS), tip enhanced fluorescence spectroscopy (TEFS), and tip enhanced Raman spectroscopy (TERS).

3. Plasmonic light trapping in thin film solar cells

Metallic nanoparticles placed on the top of a solar cell will scatter the incident sunlight to couple and trap freely propagating plane waves into the active absorbing thin film, by folding the light into the thin film. When metallic nanoparticles are embedded inside of active layer, they can be treated as subwavelength antennas in which the plasmonic near-field is coupled to the absorbing layer, which will increase the effective absorption cross section. A patterned metallic structure on the backside of a thin absorber layer can couple sunlight into SPP modes, as well as the planar waveguide modes. Taking these light trapping effects into considerations, various structures have been designed to increase the light absorption of thin film solar cells.

3.1. Metallic nanostructures on top of thin film solar cell

When small metal nanoparticles are placed close to the surface of solar cell, light will mainly scatter into the dielectric with a larger permittivity [27]. The optical path length, thus, can be increased due to the scattered light obtains an angular spread in the dielectric. With a metallic reflector on the backside of the solar cell, the reflected light from the backside can couple to the surface nanoparticles and will reradiate into the active layer partly. In 2006, Yu et al. [12] deposited Au nanoparticles above the amorphous silicon film with thickness of only 240 nm.

http://dx.doi.org/10.5772/65388

They observed an 8.1% increase in short-circuit current density and an 8.3% increase in energy conversion efficiency with a modest density of Au particles. Moreover, finite-element electromagnetic simulations showed that substantially larger improvements should be attainable for higher nanoparticle densities. Ag nanoparticles were placed on top of a 1.25 μm thick Si-on-insulator solar cell; a broadband absorption enhancement and a 16-fold enhancement at 1050 nm were reported [10]. Atwater et al. [28] demonstrated that on GaAs thin cells with Ag nanoparticles located at the surface yielded a significant enhancement for wavelengths longer than 600 nm and exhibited an improvement of 8% for the short circuit current density. In addition, Au nanopillar [29] or Ag nanoparticle [30] was also used to excite the localized particle plasmon to enhance the light trapping in the organic solar cells, like P3HT: PCBM.

3.1.1. Effect of nanoparticle material, size, shape, and surrounding conditions

The surface nanoparticle material, size, shape, refractive index of the medium and distance from the active layer are key factors determining the scattering and coupling effect [6, 31–33]. In Ref. [33], the relationship between the normalized scattering cross section (SCS) and the spherical particle size in both air and silicon was investigated. The plasmonic resonance exhibits an obvious red-shift effect in Si compared to that in air. Additionally, the resonance peaks red shift and broaden with increasing particle size, which will significantly enhance the light trapping in the red and near-IR region. Typically, a relatively high scattering efficiency can be obtained with a particle size of ~100 nm. The particle shape also has effect on the efficiency. As shown in **Figure 1(a)**, cylindrical and hemispherical particles bring about much stronger light absorption enhancements than spherical particles [31], which may due to the fact that the average spacing to the substrate is smaller for these geometries than for spheres, and this allows efficient coupling of the scattered light into semiconductor substrates. The plasmon resonance peak always corresponds to the best light harvesting effect, and such resonance peak can be changed with the refractive index of the surrounding material. Plasmon resonances of Ag or Au nanoparticles locate at 350 and 480 nm, respectively, which can be red shifted over the entire 500–1500 nm by placing them in SiO_2, Si_3N_4, or Si [34–36]. When the distance between the nanoparticles and the absorbing layer increase, the light scattered into the absorbing layer will decrease [31]. However, such decrease is not significant. The carrier recombination occurs at the metal can be avoided due to separation by the dielectric layer. Moreover, increasing the distance between the nanoparticles and the absorbing layer can increase the SCS because large distance prevents destructive interference effects between the incident and reflected fields. Besides, it is demonstrated that Ag particles are better choice than Au, because Ag not only offers a lower price but also leads to much higher light absorption enhancement. Besides the noble metal, Al nanoparticles on front side of silicon solar cell show a 28.7% photon absorption enhancement in Si wafers, which is much larger than that induced by Ag or Au [37]. By combined with SiN_x anti-reflection coating, Al nanoparticles can even produce a 42.5% enhancement, which provides a low cost and high efficiency solution for practical larger-scale implementation of plasmonic nanoparticles for solar cell performance enhancement. Furthermore, it is experimentally demonstrated [38] that the use of periodic arrays of Al nanoparticles placed in the front of a thin Si film (shown in **Figure 1(b)**) causes a broadband photocurrent enhancement ranging from the ultraviolet to the infrared with respect

to the reference cell. Single particle resonances contribute to the enhancement in the infrared spectral range, and the collective resonances lead to an efficient coupling of light in the ultraviolet-blue range [38], thus a broadband enhancement can be realized.

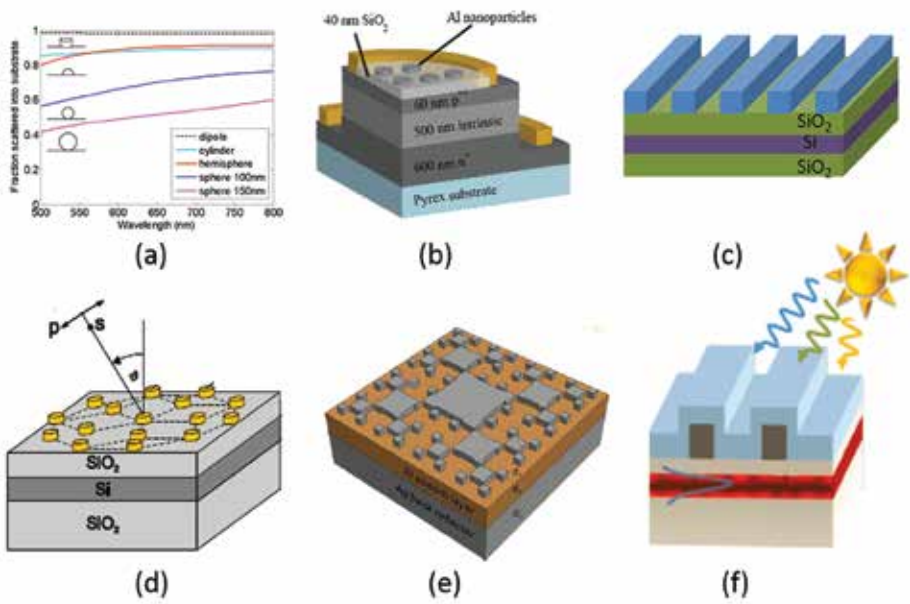

Figure 1. Various metallic nanostructures on top of thin film solar cells. (a) Fraction of light scattered into the substrate for different sizes and shapes of Ag particles on Si [31]; (b) Al nanoparticles placed on front of a thin Si film [38]; (c) Ag strips on the top of Si thin film cell [39]; (d) 2D quasiperiodic gold disks on top of the Si layer [43]; (e) a fractal-like pattern of silver nano cuboids on top of Si thin film cell [14]; (f) combination of AR coatings and gratings on top of ultrathin Si cell [44]. Figures reproduced with permission: (a) © 2008 AIP; (b) © 2015 OSA; (d), (e) © 2013 OSA; (f) © 2011 ACS.

3.1.2. Other surface nanostructures

In addition to metal nanoparticles, other structures such as gratings have also been employed for light trapping. Pala et al. [39] investigated the effect of periodic array of Ag strips (with the structure shown in **Figure 1(c)**) on the absorption enhancement in the Si thin film cell based on the finite-difference frequency-domain (FDFD) method. The simulation results show that the broadband light absorption benefits from the high near-fields surrounding the nanostructure and the effective coupling to waveguide supported by the thin Si film. Light absorption enhancement can be obtained both in the transverse electric (TE) and transverse magnetic (TM) polarized plane wave. For TM illumination, the Ag strips can effectively concentrate light in their vicinity at frequencies near their surface plasmon resonance, which depends on the strip geometry and its dielectric environment. And the sizes of Ag strips in the range from 50 to 100 nm are optimal. The lateral spacing of the strips governs the excitation of waveguide modes, while the number of allowed waveguide modes is determined by the thickness of the

Si layer. For TE illumination, only waveguide modes are excited, and the absorption enhancement directly results from an increased interaction length of the light with the Si film. Other structures like plasmonic cavity with subwavelength hole arrays [40] and nanotoroid arrays [41] were also employed in the P3HT: PCBM and silicon thin film solar cells, respectively.

3.1.3. Random nanostructures

Most plasmonic nanostructures designed on the front surface of thin film cells are always periodically distributed. Nishijima et al. [42] numerically and experimentally investigated the effect of periodic and random particle patterns on the plasmonic resonance. For the periodic arrays, the extinction peak (corresponding to the plasmonic resonance) value decreases with increasing periodicity, and the peak wavelength is red-shifted. The increasing disorder results in increasing extinction and a broader plasmon resonance, which may be due to grating-like diffraction losses. Light absorption is enhanced by more than two orders of magnitude for the random configuration of nanodiscs, demonstrated by the FDTD (finite-difference time-domain) simulations. The random structures applied to solar cell have advantages of simple and low-resolution fabrication. In Ref. [43], absorption enhancement by introducing 2D quasiperiodic and 2D periodic gold disks on top of the Si layer (with structure presented in **Figure 1(d)**) was compared. The simulation results present that, due to much more isotropic than the square lattice, the Penrose tiling structure can excite much more waveguide modes for absorbance spectra dependent on the azimuthal angle as well as the angle of incidence. Therefore, enhancement factor throughout the day as well as over the year may vary little. For the quasiperiodic lattice, the enhancement factor varies from 15.8 to 16.2 during summertime, whereas the variation ranges between 15.4 and 16.6 for the periodic lattice. Consequently, the performance of the solar cell with a quasicrystalline arrangement is expected to be more stable than that with a periodic one. An ultra-thin silicon solar cell coated by a fractal-like pattern of silver nanocuboids (as shown in **Figure 1(e)**) was investigated through FDTD simulation in Ref. [14], in which a broadband absorption is achieved due to the exists of multiple cavity modes and SP modes in the structure. The cavity modes come from Fabry-Pérot resonances at the longitudinal and transverse cavities, respectively. Low-index and high-index SP modes, which propagate along the silicon-silver interface, are simultaneously excited due to several feature sizes distributed in the fractal-like structure.

3.1.4. Combination of AR coating and metal nanostructures

Surface metal nanostructures have also been integrated with the antireflection (AR) coatings to enhance performance of plasmonic solar cells [44–46]. A detailed comparison between traditional AR coatings, plasmonic gratings, and structures that combine AR coatings and gratings on ultrathin Si absorbing layers (as shown in **Figure 1(f)**) was presented by FDTD simulations in Ref. [44]. Plasmonic gratings exhibit strong, narrow-band light absorption enhancement, while the traditional AR coatings result in more modest, broadband light absorption enhancement. The AR coatings even lead to stronger absorption than the gratings alone for the thicker films. However, the combination of AR coatings and gratings surpasses enhancements of either of these structures individually. The reason for this improvement

originates mainly from the enhanced absorption within the propagating periodic modes rather than the localized resonances for the structures. Al nanoparticles [45] located above a 75 nm silicon nitride antireflection coating in a 1 μm silicon film also provide a strong broadband light absorption enhancement.

3.2. Metallic nanostructures embedded inside the active layer

Designing the metallic nanostructures on top of solar cells has the problem of blocking a fairly large amount of total incident solar photons. While the metal nanostructures are placed at the bottom of optically active layer, they can be treated as back reflector and support SPP modes at the metal/semiconductor interface, as well as couple light into the photonic modes. Ferry et al. demonstrated [47] by numerical simulations that a single subwavelength scattering objects on the metallic back surface of a 200 nm Si thin film can enhance absorption by a factor of 2.5 over a large area for the portion of the solar spectrum near the Si band gap. The incident light is coupled into an SPP mode as well as a photonic mode that propagates inside the Si waveguide. And the coupling effect of each mode can be controlled by the height of the scatter. The photonic modes suffer from only very small losses in the metal. While for the ultrathin Si solar cell with thickness smaller than 100 nm, the photonic mode approaches its cutoff frequency and all the scattered light is converted into SPPs. The fraction of light coupled to both SPP and photonic modes increases with increasing wavelength because the incoming light at shorter wavelengths is directly absorbed in the Si layer.

Furthermore, Wang et al. [15] demonstrated that a broadband and polarization insensitive absorption enhancement was achieved in an α-Si cell with hybrid gratings of Ag and indium tin oxide (ITO) at the bottom of the a-Si layer (as presented in **Figure 2(a)**), which were originated from the effective coupling of planar waveguide modes, the Fabry-Pérot (FP) resonance and the SPP resonance. Similar to Ref. [47], the improvement mainly occurs at certain long wavelengths. The FP resonance inside the α-Si layer is excited both for TE or TM polarizations when both layer thickness and the incidence wavelength satisfy the resonance condition. Since the FP resonance is typically dependent on the thickness of α-Si layer, the added Ag nanograting will change the cavity thickness and cause the resonance red shift. Therefore, adjusting the Ag nanograting will be a practical means to tune the FP resonance to better fit the solar spectrum without changing the α-Si layer thickness. The excitation of guiding modes in the planar α-Si layer slab waveguide can lead to strong enhancement in the near-infrared regime for both TE and TE illuminations by adding the Ag nanograting. Such enhancement region red shifts with a thicker Si layer, a larger grating period, and a thicker Ag nanograting. The presence of the Ag nanograting provides more absorption enhancement for TM illumination, as SPPs are excited at both Si/Ag and ITO/Ag interfaces. Plasmonic wavelength is less dependent on α-Si thickness and red shifts as the grating's period increases. The absorption over the solar spectrum by such design shows an up to 30% broadband absorption enhancement when comparing to bare thin film cells, and the total enhancement under an unpolarized illumination varies little between 24 and 31% with an incident angle changing from 0 to 82°.

http://dx.doi.org/10.5772/65388

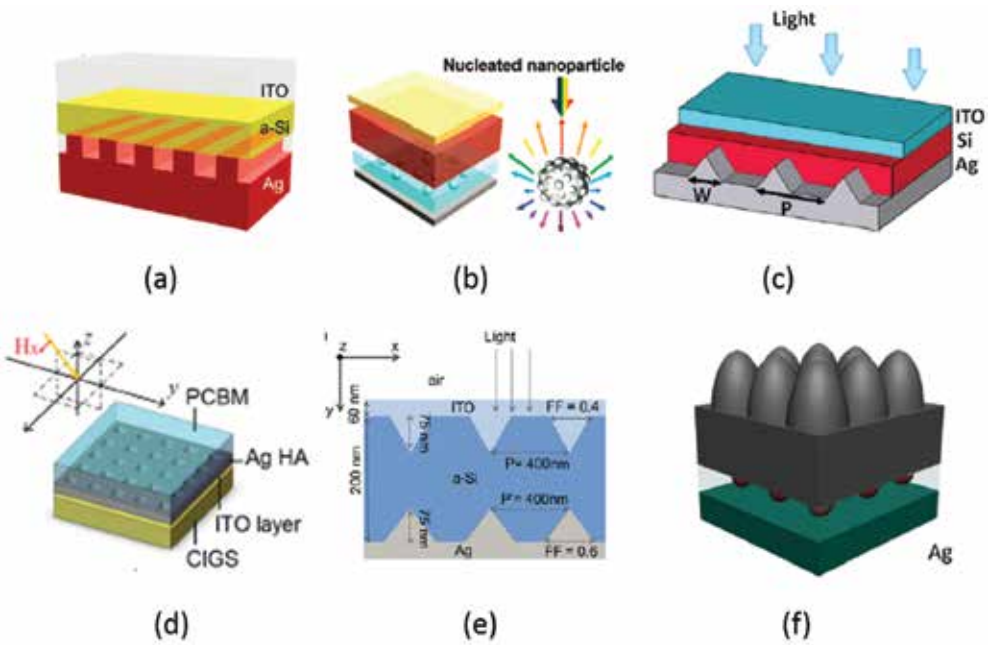

Figure 2. (a) Ag gratings at the bottom of thin film Si [15]; (b) nucleated Ag particles is embedded inside the ZnO layer at the rear side of the a-Si:H cell [17]; (c) Ag triangular corrugations at the bottom of a 100 nm c-Si cell [20]; (d) an Ag hole-array is inserted into a PCBM/CIGS tandem solar cell [53]; (e) Ag triangular gratings at the back side of cell and triangular ITO gratings at the front a-Si cell [65]; (f) the biomimetic silicon moth-eye structure combined with rear located Ag hemispherical particles in 2 μm thick c-Si cell [24]. Figures reproduced with permission: (a) © 2010 ACS; (b) © 2012 ACS; (c) © 2012 OSA; (d) © 2014 OSA; (e) © 2012 APS; (f) © 2016 OSA.

3.2.1. Various nanostructures at the bottom of active layer

Various plasmonic structures embedded at the back of active layer were proposed and investigated to enhance the solar cell absorption. Metal nanoparticles like nanospheres are widely employed [17–19, 48–50]. In Ref. [17], Chen et al. proposed a novel structure of glass/transparent conductive oxide (TCO)/p-i-n a-Si:H/ZnO:Ag, in which the nucleated Ag particles were embedded inside the ZnO layer at the rear side of the cell (as shown in **Figure 2(b)**). The simulations showed clearly that smaller nanoparticles (20–100 nm) have smaller scattering/absorption cross-sectional ratio but more equivalence in their scattering intensity versus angle distribution, while larger nanoparticles possess dominant scattering but focused primarily in limited scattering angles. Therefore, the proposed particle in Ref. [17] has a larger core with the surface simultaneously covered evenly with half-truncated small particles (1/5 size of the large particle). The larger particle brings about a larger scattering coefficient in the longer wavelength because of the excitation of the dipolar and quadrupolar plasmonic modes. And the smaller particle provides larger angle scattering for shorter wavelength light. The experimental results demonstrated that, compared with these of the randomly textured solar cells without nanoparticles, a broadband light absorption enhancement and prominent perform-

ance including a 23% improve of the energy conversion efficiency and a 14.3% increase in the short-circuit photocurrent density were achieved in the solar cells designed with 200 nm nucleated Ag nanoparticles with 10% coverage density. The surface coverage of the nucleated Ag particles at the rear side of cell should be set at the optimal range because too small coverage seems to be insufficient to cause significant light scattering, while too large may lead to obvious particle absorption.

In addition, an 80 nm thick Ag layer with triangular corrugations was designed on the bottom of a 100 nm thick c-Si layer, and the triangular corrugations (as shown in **Figure 2(c)**) were penetrated into the active Si layer [20]. Similar to Ref. [15], SPP mode and optical resonances contributed to the absorption enhancement. The FDTD simulation demonstrates that SPPs are excited at the Ag/Si interface of the triangular gratings, and the coupling of the excited SPP resonance with the FP resonance modes is observed for the TM illumination. For TE light, the excited cavity mode is demonstrated, and the coupling between waveguide and cavity modes is observed. Such triangular corrugations sustain large absorption enhancement factors (33.8–43.3%) up to relatively wide incidence angles, with enhancement higher than that using the Ag strip grating [15]. In Ref. [21], the FEM (finite element method) simulations demonstrated that the absorption enhancement with Au paired-strip grating embedded at back side of solar cell is higher than that with the Au single-strip grating. And the enhancement depends on the absorber layer thickness and the refractive index of the surrounding medium. Other structures like dual plasmonic nanostructures [51] are employed in single organic solar cells, in which Au nanoparticles are embedded in the active layer, and an Ag nanograting is used as the plasmonic back reflector. Through the collective excitation of Floquet modes, SPP, LSP, and their hybridizations, broadband absorption enhancement was observed both by experiment and simulation.

3.2.2. Metal nanostructures embedded in the middle of active layer

Absorption enhancement by plasmonic nanostructures embedded at the back side of active absorbing layer mainly focused on the long wavelength range, due to that the short wavelength part has mostly been absorbed by the solar cell. Therefore, plasmonic nanostructures embedded in the middle of the cell were also investigated [52–56]. Zhang et al. [53] proposed a structure that an Ag hole-array was inserted into a PCBM/CIGS tandem solar cell (as shown in **Figure 2(d)**). Such metallic hole array is expected to reflect the short-wavelength photons back to the top cell and transmit long-wavelength photons to the bottom cell through the extraordinary optical transmission (EOT) effect, as well as act as an intermediate electrode to allow a fabrication of hybrid organic-inorganic tandem solar cell. The simulation by FEM method demonstrates that for the cell including 100 nm PCBM/50 nm Ag hole-array/100 nm ITO/100 nm CIGS, the absorption inside the top subcell is always enhanced with different Ag hole array period, due to the back reflection of the Ag array, and for the bottom subcell, the absorption for the longer wavelength range (>650 nm) is greatly enhanced, originating from the EOT effect. When varying the period in the range from 200 nm to 1.5 μm, five resonant mechanisms are identified to participate in the EOT, including SPP mode, magnetic plasmon polaritons, LSP, and optical waveguide modes. It is shown that the thickness of Ag array or

that of ITO, the duty cycle of the holes also affects the optical performance of the cell. More than 40% integrated power enhancement can be achieved in a variable structural parameter range. Recently, metal nanoparticles are also placed at the middle of Si active layer [56] or the perovskite solar cell layer [55] to provide absorption enhancement.

3.2.3. Other effect in the embedded plasmonic nanostructure

Similar to plasmonic nanoparticles at the front side of solar cell, refractive index of the surrounding medium has effect on the plasmonic resonance and hence the absorption [57, 58]. Park et al. [57] applied the Ag nanoparticles on the rear side of p-Si tin film and investigated the optimum surface condition for plasmonic enhanced light absorption through experiment and simulation. It is found that the existence of SiO_2 layer between Si and Ag particles has a major effect on the SCS and hence the absorption in the cells. Peak of SCS with nanoparticles on the thermal SiO_2 is located at the light wavelengths <700 nm, while nanoparticles on the native SiO_2 layer and directly on Si show peaks of SCS at wavelengths >700 nm. The sample with nanoparticles on the native SiO_2 has the highest short-circuit current density enhancement. The simulation in Ref. [59] reveals that by tuning the thickness of Si and transparent conductive oxide layers in the ITO/a-Si:H/Ag nanoparticles/ZnO:Al/Ag mirror structure, the driving field intensity experienced by the embedded plasmonic particles can be enhanced up to a factor of 14. The effect of light losses induced by the rear located Ag nanoparticle on the light trapping of Si wafer was studied by Zhang et al. [60]. The light losses include the intrinsic absorption loss from Ag particles and the additional absorption loss induced by the void plasmons in the Al reflectors. The study reveals that Ag particles are effective to enhance the photocurrent in cells with planar front surface, while the absorption enhancement is substantially influenced by the plasmonics in the textured cells.

3.2.4. Comparison of plasmonic nanostructures located at different positions

Although the absorption enhancement can be achieved more or less by plasmonic nanostructure located at various positions of solar cell active layer, it is meaningful to compare the enhancement among the different locations of nanostructures [16, 61–64]. In early reports, metallic particle shapes such as spheres, hemispheres, and cylinders are commonly employed. It is usually seen that the SCS for the front located particles is obviously larger than that for the rear located particles when the dielectric spacer between metallic particles and absorbing layer is relatively thick [63, 64]. However, the front located particles involve a detrimental Fano effect resulting from the interference effects between the scattered light and the incident light, which reduces light absorption below the plasmon resonance wavelength. Using the rear located nanoparticles can avoid the Fano effect. Hence, the ideal design is to make the SCS value of the rear located particles higher than that of the front located particles for a wide range of the electric spacer thickness. Yan et al. [16] adopted an Ag nanocone as the plasmonic particles in the c-Si/Al_2O_3/Ag nanocone solar cell structure. The particles are treated as the front located particles when light is incident on the particles from air, while it is described as the rear ones if light is illuminated from the Si side. The FDTD simulation shows that the ratio of SCS between the rear and the front located particles at the resonance wavelength is near two

when the Al_2O_3 spacer thickness is 30 nm. And the ratio increases to three as the Al_2O_3 spacer thickness is 10 nm.

3.2.5. Combination of front and rear nanostructures

Dual-interface nanostructures [65–72] including the rear metal plasmonic grating/nanoparticles and the front dielectric grating or metal particles have also been adopted to enhance absorption efficiency in thin film solar cell. For example, in Ref. [65], an Ag triangular grating at the back side of cell and a triangular ITO grating at the front a-Si are combined (as shown in **Figure 2(e)**). The simulation presents that the ITO triangles focus on the short-wavelength incident light and subsequently spread it inside the active layer, and a combination of dielectric waveguide mode and FP resonance arises at 660 nm. Additionally, an absorption peak at 760 nm resulting from the waveguide mode and a peak at 810 nm corresponding to the plasmonic mode are observed. An integrated absorption for TM illumination of the AM 1.5 G spectrum in the 400–950 nm region is 83.1%. Having different periods at specific interfaces provides more efficient diffraction into both plasmonic and dielectric guide modes. Other similar structures like rear located Ag strip grating combined with silicon front surface trapezoidal [70] or strip [69] texture are reported too to enhance light trapping in Si thin film cell.

In Ref. [66], the Ag nanohemisphere is deposited on the rear of a nanohole-textured Si thin film. The role of Si nanohole is to absorb the light at the short wavelength, due to antireflection effect and light trapping properties. Long-wavelength light absorption benefits from the excitation of the LSP induced by the rear located Ag hemisphere. By adjusting parameters of Si nanohole and Ag hemisphere, the short-circuit current density can reach to 25.4 mA/cm^2. Shi et al. [71] combined silicon front surface grating and the rear-located bilayer Ag nanohemispheres. In that case, the grating and metal nanoparticles are optimized, and a short-circuit current density as high as 29.7 mA/cm^2 is obtained with a 1-μm thick c-Si cell. Similarly, Zhang et al. [24] propose a hybrid structure based on the biomimetic silicon moth-eye structure combined with rear located Ag hemispherical particles in the 2 μm thick c-Si cells (as shown in **Figure 2(f)**). The FDTD simulation results present the integrated light absorption enhancement over the solar spectrum is 69% compared with the cells with the conventional light trapping design, which is larger than these in only silicon moth-eye structure (58%) and only Ag hemisphere (41%). The photocurrent is as large as 33.4 mA/cm^2, which is higher than these in most structures.

3.3. Hybrid of metallic nanostructures with nanowire of optical absorber layer

Reducing the use of both active absorbing and non-earth abundant materials in thin film solar cell is pursued. A nanowire optical antenna absorber was proposed in Ref. [73], which demonstrated that the absorption of sunlight in Si nanowires can be significantly enhanced over the bulk Si. The active layer in the thin film solar cell structures was designed into nanostructures in quite a few researches [73–78], such as Si nanowire array with a wire-embedded Ag back reflector [76] and silicon nanocone hole solar cell with back located square Ag particle [78]. Wang et al. [75] patterned the entire $CuIn_xGa_{(1-x)}Se_2$ (CIGS) thin film cell into

http://dx.doi.org/10.5772/65388

an 1D nanograting array, with Ag strips on top of CIGS gratings and Ag planar acting as the surface and rear electrodes, respectively (as shown in **Figure 3(a)** and **(b)**). For TE illuminations, the observed larger absorption enhancement compared to the conventional cell mainly results from the scattering by the top electrode as well as the coupling with the multiple internal reflection resonance. As thickness of the CIGS layer increases, the light absorption enhancement shows a red shift and becomes broader and stronger simultaneously. In the case of TM light, SPPs are excited and lead to that most incoming light is transmitted through the Ag nanowire array. The transmitted light is confined in the CIGS wires, which results in a broadband absorption enhancement. Similar to the TE case, the SPP-related enhancement presents a red shift as the CIGS thickness increases. As the nanograting period and width increase, both magnitude and bandwidth of the enhancement first increase and then reduce beyond certain points. Such CIGS nanograting solar cell can enhance the overall current density over 250% compared to the bare thin film cells. In Ref. [77], the structure of Si nanowire/Si layer/ZnO:Al/Ag nanohemispheres back reflector (as shown in **Figure 3(c)**) is investigated through simulations. The nanohemispheres Ag back reflector can excite LSP resonance and cause scattering of light, giving rise to light absorption in Si. The short-circuit current density reaches to 28.4 mA/cm^2, demonstrating an enhancement of 22% compared with a Si nanowire solar cell with a planar back reflector.

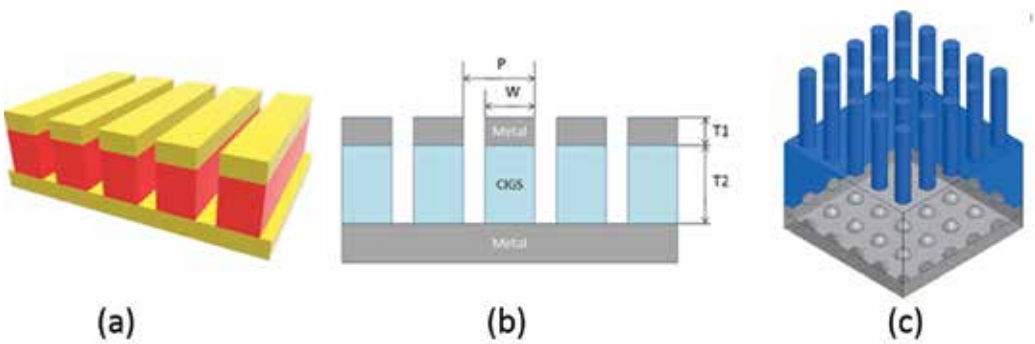

Figure 3. (a) The entire thin film cell $CuIn_xGa_{(1-x)}Se_2$(CIGS) is patterned into a 1D nanograting array, with Ag strips on top of CIGS gratings and Ag planar acting as surface and rear electrodes [75]; (b) cross-sectional view of (a); (c) Ag nanohemispheres at the bottom of Si nanowire cells [77]. Figures reproduced with permission: (a)–(c) © 2012 OSA.

4. Conclusions

In this chapter, we have summarized the advances in the research of light trapping and the plasmonic enhancement of thin film solar cells. Metallic nanoparticles can excite localized surface plasmons, which benefit for light scattering and light concentration to enhance the light absorption in thin film cell. A corrugated metallic film like grating on the absorber layer can couple sunlight into surface plasmon polaritons to enhance light absorption too. The light

enhancement by these plasmonic modes is strongly related to the material, size, shape, refractive index of the medium, position in the absorber layer of metallic nanoparticles, and metallic corrugated nanostructures.

The position of metal nanostructures has significant effect on the plasmonic solar cells. The metallic nanoparticles like hemispheres and cylinders on the front side of thin film solar cell have larger normalized scattering cross section than that for the rear located particles when the dielectric spacer between metallic particles and absorbing layer is relatively thick. However, the front located particles involve a detrimental Fano effect resulting from the interference effects between the scattered light and the incident light, which reduces light absorption below the plasmon resonance wavelength. The rear located nanoparticles can avoid such Fano effect. Therefore, careful designs like using rear located Ag nanocone can achieve larger SCS than that at front side. On the other hand, adopting the embedded metallic nanostructures can obtain broadband and polarization insensitive absorption enhancement benefiting from the effective coupling of planar waveguide modes, FP resonance and SPPs resonance. Furthermore, dual-interface hybrid structure based on the nanostructures of front surface absorber combined with rear located nanoparticles or nanograting may be an excellent way to enhance light absorption in thin film solar cells. Anyway, new plasmonic nanostructures still need to be investigated to further achieve broadband and polarization insensitive absorption enhancement at wide incident angles.

Acknowledgements

This work was supported by the National Basic Research Program of China (2012CB922000).

Author details

Qiuping Huang[1,3], Xiang Hu[1], Zhengping Fu[1] and Yalin Lu[1,2,3,4*]

*Address all correspondence to: yllu@ustc.edu.cn

1 Advanced Applied Research Center, Hefei National Laboratory for Physical Science at the Microscale, University of Science and Technology of China, Hefei, Anhui, PR China

2 National Synchrotron Radiation Laboratory, University of Science and Technology of China, Hefei, Anhui, PR China

3 Synergetic Innovation Center of Quantum Information & Quantum Physics, University of Science and Technology of China, Hefei, Hefei, PR China

4 Laser and Optics Research Center, Department of Physics, United States Air Force Academy, Colorado, USA

References

[1] International Technology Roadmap for Photovoltaic [Internet]. 2016. Available from: http://www.itrpv.net/Reports/Downloads/

[2] Green M. A. Lambertian light trapping in textured solar cells and light-emitting diodes: analytical solutions. Prog. Photovolt. 2002;10:235–41.

[3] Barnes W. L., Dereux A., Ebbesen T. W. Surface plasmon subwavelength optics. Nature. 2003;424:824–30.

[4] Rockstuhl C., Fahr S., Lederer F. Absorption enhancement in solar cells by localized plasmon polaritons. J. Appl. Phys. 2008;104:123102–7.

[5] Schaadt D. M., Feng B. , Yu E. T. Enhanced semiconductor optical absorption via surface plasmon excitation in metal nanoparticles. Appl. Phys. Lett. 2005;86:063106–3.

[6] Atwater H. A., Polman A. Plasmonics for improved photovoltaic devices. Nat. Mater. 2010;9:205–13.

[7] Spinelli P., Ferry V. E., Groep J., Lare M., Verschuuren M. A., Schropp R., Atwater H. A., Polman A. Plasmonic light trapping in thin-film Si solar cells. J. Opt. 2012;14:024002.

[8] Guo C., Sun T., Gao F., Liu Q., Ren Z. Metallic nanostructures for light trapping in energy-harvesting devices. Light Sci. Appl. 2014;3:e161.

[9] Tran H. N., Nguyen V. H., Nguyen B. H., Vu D. L. Light trapping and plasmonic enhancement in silicon, dye-sensitized and titania solar cells. Adv. Nat. Sci.: Nanosci. Nanotechnol. 2016;7:013001.

[10] Pillai S., Catchpole K. R., Trupke T., Green M. A. Surface plasmon enhanced silicon solar cells. J. Appl. Phys. 2007;101:093105–8.

[11] Pala R. A., White J., Barnard E., Liu J., Brongersma M. L. Design of plasmonic thin-film solar cells with broadband absorption enhancements. Adv. Mater. 2009;21:1–6.

[12] Derkacs D., Lim S. H., Matheu P., Mar W., Yu E. T. Improved performance of amorphous silicon solar cells via scattering from surface plasmon polaritons in nearby metallic nanoparticles. Appl. Phys. Lett. 2006;89:093103–3.

[13] Munday J. N., Atwater H. A. Large integrated absorption enhancement in plasmonic solar cells by combining metallic gratings and antireflection coatings. Nano Lett. 2010;11:2195–201.

[14] Zhu L., Shao M., Peng R., Fan R., Huang X., Wang M. Broadband absorption and efficiency enhancement of an ultra-thin silicon solar cell with a plasmonic fractal. Opt. Express. 2013;21:A313.

[15] Wang W., Wu S., Reinhardt K., Lu Y., Chen S. Broadband light absorption enhancement in thin-film silicon solar cells. Nano Lett. 2010;10:2012–18.

[16] Yan W., Stokes N., Jia B., and Gu M. Enhanced light trapping in the silicon substrate with plasmonic Ag nanocones. Opt. Lett. 2013;38:395.

[17] Chen X., Jia B., Saha J. K., Cai B., Stokes N., Qiao Q., Wang Y., Shi Z., Gu M. Broadband enhancement in thin-film amorphous silicon solar cells enabled by nucleated silver nanoparticles. Nano Lett. 2012;12:2187–92.

[18] Xu Q., Johnson C., Disney C., Pillai S. Enhanced broadband light trapping in c-Si solar cells using nanosphere-embedded metallic grating structure. IEEE J. Photovol. 2016;6:61–7.

[19] Mailhes R., Nychyporuk T., Lemiti M., Lysenko V. Plasmon-induced enhancement of optical absorption in silicon thin films due to embedded silver nano-pillars. Europhys. Lett. 2014;108:58005.

[20] Battal E., Yogurt T. A., Aygun L. E., Okyay A. K. Triangular metallic gratings for large absorption enhancement in thin film Si solar cells. Opt. Express. 2012;20:9458–64.

[21] Yang Z. Y. and Chen K. P. Effective absorption enhancement in dielectric thin-films with embedded paired-strips gold nanoantennas. Opt. Express. 2014;22:12737–49.

[22] Mopurisetty S. M., Bajaj M., Ganguly S. Beyond optical enhancement due to embedded metal nanoparticles in thin-film solar cells. Appl. Phys. Express. 2016;9:032301.

[23] Zhang X., Huang Q., Hu J., Knize R. J., Lu Y. Hybrid tandem solar cell enhanced by a metallic hole-array as the intermediate electrode. Opt. Express. 2014;22:A1400.

[24] Zhang Y., Jia B., Gu M. Biomimetic and plasmonic hybrid light trapping for highly efficient ultrathin crystalline silicon solar cells. Opt. Express. 2016;24:A506.

[25] Ritchie R. H. Plasma losses by fast electrons in thin films. Phys. Rev. 1957;106:874.

[26] Zayats A. V., Igor I. S., Alexei A. M. Nano-optics of surface plasmon polaritons. Phys. Rep. 2005;408:131–314.

[27] Mertz J. Radiative absorption, fluorescence, and scattering of a classical dipole near a lossless interface: a unified description. J. Opt. Soc. Am. B. 2000;17:1906.

[28] Nakayama K., Tanabe K., Atwater H. A. Plasmonic nanoparticle enhanced light absorption in GaAs solar cells. Appl. Phys. Lett. 2008;93:121904.

[29] Shu J. T., Mihaela B., Danilo B. R., Warren N. H., Huang C. K., Raymond J. P. Effect of gold nanopillar arrays on the absorption spectrum of a bulk heterojunction organic solar cell. Opt. Express. 2010;18:A528.

[30] Ren W., Zhang G., Wu Y., Ding H., Shen Q., Zhang K., et al. Broadband absorption enhancement achieved by optical layer mediated plasmonic solar cell. Opt. Express. 2011;19:26536.

[31] Catchpole K. R., Polman A. Design principles for particle plasmon enhanced solar cells. Appl. Phys. Lett. 2008;93:191113.

[32] Catchpole K. R., Polman A. Plasmonic solar cells. Opt. Express. 2008;16:21793–800.

[33] Pillai S., Green M. A. Plasmonics for photovoltaic applications. Sol. Energ. Mater. Sol. C Cells. 2010;94:1481–6.

[34] Beck F. J., Polman A., Catchpole K. R. Tunable light trapping for solar cells using localized surface plasmon. J. Appl. Phys. 2009;105:114310.

[35] Xu G., Tazawa M., Jin P., Nakao S., Yoshimura K.,Wavelength tuning of surface plasmon resonance using dielectric layers on silver island films. Appl. Phys. Lett. 2003;82:3811.

[36] Mertens H., Verhoeven J., Polman A., Tichelaar F. D. Infrared surface plasmons in two-dimensional silver nanoparticle arrays in silicon. Appl. Phys. Lett. 2004;85:1317.

[37] Zhang Y., Ouyang Z., Stokes N., Jia B., Shi Z., Gu M. Low cost and high performance Al nanoparticles for broadband light trapping in Si wafer solar cells. Appl. Phys. Lett. 2012;100:151101.

[38] Uhrenfeldt C., Villesen T. F., Tetu A., Johansen B., and Larsen A. N. Broadband photocurrent enhancement and light-trapping in thin film Si solar cells with periodic Al nanoparticle arrays on the front. Opt. Express. 2015;23:A525.

[39] Pala R. A., White J., Barnard E., Liu J., Brongersma M. L. Design of plasmonic thin-film solar cells with broadband absorption enhancements. Adv. Mater. 2009;21:3504–9.

[40] Chou S. Y., Ding W. Ultrathin, high-efficiency, broad-band, omni-acceptance, organic solar cells enhanced by plasmonic cavity with subwavelength hole array. Opt. Express. 2012;21:A60.

[41] Burford N., and Shenawee M. E. Optimization of silver nanotoroid arrays for the absorption enhancement of silicon thin-film solar cells. Plasmonics. 2015;10:225.

[42] Nishijima Y., Rosa L., Juodkazis S. Surface plasmon resonances in periodic and random patterns of gold nano-disks for broadband light harvesting. Opt. Express. 2012;20:11466.

[43] Bauer C., and Giessen H. Light harvesting enhancement in solar cells with quasicrystalline plasmonic structures. Opt. Express. 2013;21:A363.

[44] Munday J. N., and Atwater H. A. Large integrated absorption enhancement in plasmonic solar cells by combining metallic gratings and antireflection coatings. Nano Lett. 2011;11:2195.

[45] Zhang Y., Chen X., Ouyang Z., Lu H., Jia B., Shi Z., et al. Improved multicrystalline Si solar cells by light trapping from Al nanoparticle enhanced antireflection coating. Opt. Express. 2013;3:489.

[46] Juan F., Ramos C. C., Connolly J. P., David C., Abajo F. J., Hurtado J., et al. Effect of Ag nanoparticles integrated within antireflection coatings for solar cells. J. Renew. Sustain. Energy. 2013;5:033116.

[47] Ferry V. E., Sweatlock L. A., Pacifici D., Atwater H. A. Plasmonic nanostructure design for efficient light coupling into solar cells. Nano Lett. 2008;8:4391.

[48] Paetzold U. W., Moulin E., Michaelis D., Bottler W., Hagemann V., Meier M., et al. Plasmonic reflection grating back contacts for microcrystalline silicon solar cells. Appl. Phys. Lett. 2011;99:181105.

[49] Yang M., Li J., Lin F., Zhu X. Absorption enhancements in plasmonic solar cells coated with metallic nanoparticles. Plasmonics. 2013;8:877–83.

[50] Mizuno H., Sai H., Matsubara K., Takato H., Kondo M. Transfer-printed silver nanodisks for plasmonic light trapping in hydrogenated microcrystalline silicon solar cells. Appl. Phys. Express. 2014;7:112302.

[51] Li X., Choy W., Huo L., Xie F., Sha W., Ding B., et al. Dual plasmonic nanostructures for high performance inverted organic solar cells. Adv. Mater. 2012;24:3046–52.

[52] Wen L., Sun F., Chen Q. Cascading metallic gratings for broadband absorption enhancement in ultrathin plasmonic solar cells. Appl. Phys. Lett. 2014;104:151106.

[53] Zhang X., Huang Q., Hu J., Knize R., Lu Y. Hybrid tandem solar cell enhanced by a metallic hole-array as the intermediate electrode. Opt. Express. 2014;22:A1400.

[54] Liu L., Huo Y., Zhao K., Zhao T., Li Y. Broadband absorption enhancement in plasmonic thin-film solar cells with grating surface. Superlattices Microstruct. 2015;86:300–05.

[55] Yue L., Yan B., Attridge M., Wang Z. Light absorption in perovskite solar cell: fundamentals and plasmonic enhancement of infrared band absorption. Solar Energy. 2016;124:143–52.

[56] Mopurisetty S., Bajaj M., Ganguly S. Beyond optical enhancement due to embedded metal nanoparticles in thin-film solar cells. Appl. Phys. Express. 2016;9:032301.

[57] Park J., Park N., Varlamov S. Optimum surface condition for plasmonic Ag nanoparticles in polycrystalline silicon thin film solar cells. Appl. Phys. Lett. 2014;104:033903.

[58] Yang Y., Pillai S., Mehrvarz H., Kampwerth H., Baillie A., Green M. Enhanced light trapping for high efficiency crystalline solar cells by the application of rear surface plasmons. Sol. Energ. Mater. Sol. Cells. 2012;101:217.

[59] Santbergen R., Tan H., Zeman M., Smets A. Enhancing the driving field for plasmonic nanoparticles in thin-film solar cells. Opt. Express. 2014;22:A1023.

[60] Zhang Y., Jia B., Ouyang Z., Gu M. Influence of rear located silver nanoparticle induced light losses on the light trapping of silicon wafer-based solar cells. J. Appl. Phys. 2014;116:124303.

[61] Qu D., Liu F., Huang Y., Xie W., Xu Q. Mechanism of optical absorption enhancement in thin film organic solar cells with plasmonic metal nanoparticles. Opt. Express. 2011;19:24795.

[62] Winans J., Hungerford C., Shome K., Rothberg L., Fauchet P. Plasmonic effects in ultrathin amorphous silicon solar cells: performance improvements with Ag nanoparticles on the front, the back, and both. Opt. Express. 2015;23:A92.

[63] Beck F., Mollapati S., Polman A., Catchpole K. Asymmetry in photocurrent enhancement by plasmonic nanoparticle arrays located on the front or on the rear of solar cells. Appl. Phys. Lett. 2010;96:033113.

[64] Beck F., Verhagen E., Mokkapati S., Polman A., Catchpole K. Resonant SPP modes supported by discrete metal nanoparticles on high-index substrates. Opt. Express. 2011;19:A147.

[65] Abass A., Le K., Alu A., Burgelman M., Maes B. Dual-interface gratings for broadband absorption enhancement in thin-film solar cells. Phys. Rev. B. 2012;85:115449.

[66] Chen Y., Han W., Yang F. Enhanced optical absorption in nanohole-textured silicon thin-film solar cells with rear-located metal particles. Opt. Lett. 2013;38:3973.

[67] Zhang Y., Jia B., Gu M. Biomimetic and plasmonic hybrid light trapping for highly efficient ultrathin crystalline silicon solar cells. Opt. Express. 2016;24:A506.

[68] Li C., Xia L., Gao H., Shi R., Sun C., Shi H., et al. Broadband absorption enhancement in a-Si:H thin-film solar cells sandwiched by pyramidal nanostructured arrays. Opt. Express. 2012;20:A589.

[69] Chriki R., Yanai A., Shappir J., Levy U. Enhanced efficiency of thin film solar cells using a shifted dual grating plasmonic structure. Opt. Express. 2013;21:A382.

[70] Shi W., Fan R., Zhang K., Xu D., Xiong X., Peng R., et al. Broadband light trapping and absorption of thin-film silicon sandwiched by trapezoidal surface and silver grating. J. Appl. Phys. 2015;117:065104.

[71] Shi Y., Wang X., Liu W., Yang T., Ma J., Yang F. Extraordinary optical absorption based on diffraction grating and rear-located bilayer silver nanoparticles. Appl. Phys. Express. 2014;7:062301.

[72] Heidarzadeh H., Rostami A., Dolatyari M., Rostami G. Plasmon-enhanced performance of an ultrathinsilicon solar cell using metal-semiconductor core-shell hemispherical nanoparticles and metallic back grating. Appl. Opt. 2016;55:1779.

[73] Cao L., Fan P., Vasudev A., White J., Yu Z., Cai W., et al. Semiconductor nanowire optical antenna solar absorbers. Nano Lett. 2010;10:439.

[74] Mallick S., Agrawal M., Peumans P. Optimal light trapping in ultra-thin photonic crystal crystalline silicon solar cells. Opt. Express. 2010;18:5691.

[75] Wang W., Wu S., Knize R., Reinhardt K., Lu Y., Chen S. Enhanced photon absorption and carrier generation in nanowire solar cells. Opt. Express. 2012;20:3734.

[76] Zhou K., Guo Z., Li X., Jung J., Jee S, Park K., et al. The tradeoff between plasmonic enhancement and optical loss in silicon nanowire solar cells integrated in a metal back reflector. Opt. Express. 2012;20:A777.

[77] Ren R., Guo Y., Zhu R. Design of a plasmonic back reflector for silicon nanowire decorated solar cells. Opt. Lett. 2012;37:4245.

[78] Zhang X., Yu Y., Xi J., Liu T., Sun X. The plasmonic enhancement in silicon nanocone hole solar cells with back located metal particles. J. Opt. 2015;17:015901.

Chapter 8

Interface Engineering and Electrode Engineering for Organic Solar Cells

Dazheng Chen and Chunfu Zhang

Additional information is available at the end of the chapter

http://dx.doi.org/10.5772/65312

Abstract

Interface engineering and electrode engineering play important roles in the performance improvement for organic solar cells (OSCs). We here would investigate the effect of various cathode modifying layers and ITO-free electrodes on the device performance. First, for inverted organic solar cells (IOSCs) with a poly (3-hexylthiophene-2,5-diyl): [6,6]-phenyl C_{61} butyric acid methyl ester blend, an aqueous solution method using low temperatures is adopted to deposit a ZnO interlayer in IOSCs. When the ZnO annealing temperature is above 80°C, the corresponding IOSCs show senior PCEs over 3.5%. Meanwhile the flexible devices based on poly(ethylene terephthalate) substrate display a PCE of 3.26% and good flexibility. Second, the performance of IOSCs based on AZO cathode and Ca modifier are studied. The resulted IOSCs with an ultrathin Ca modifier (~1 nm) could achieve a senior PCE above 3%, and highly efficient electron transport at AZO/Ca/organic interface, which obviously weakens the light soaking issue. Third, by introducing a 2 nm MoO_3 interlayer for Ag anode deposition, the obtained OSCs show an improved PCE of 2.71%, and the flexible device also achieves a comparable PCE of 2.50%. All these investigations may be instructive for further improvement of device performance and the possible commercialization in the future.

Keywords: organic solar cells, interface engineering, electrode engineering, power conversion efficiency, flexibility

1. Introduction

Organic solar cells (OSCs) have attracted much more attention due to their advantages of low cost, light weight, mechanical flexibility, simple process, and steady improved power conversion efficiency (PCE). Over the past 20 years, many researches about new materials, device structures,

and fabrication processes have been reported for OSCs, and their PCE has remarkably increased from 1% to 10% [1–5]. Nowadays, many efforts have been focused on the further improvement of PCE and long-term stability. Besides the utilizing of novel photoactive materials and device structures, the interface engineering and electrode engineering play important roles in the improvement of device performance and the realization of cost-effective mass manufacture in the future.

In general, the properties of electrode/organic interfaces and transparent electrode materials determine the efficiency of light absorption, charge transport, and collection, which is strongly associated with the open-circuit voltage, short-circuit current density, fill factor, and the overall PCE for IOSCs.

In inverted OSCs (IOSCs), by modifying the indium-tin-oxide (ITO) cathode with functional interface layers and by using high work function metals (Ag, Au) insensitive to air, the IOSCs can obtain improved air-stability while maintaining a PCE comparable to that of conventional structure [6]. Over the past decade, many n-type modifying materials (TiO_2, ZnO) and ultrathin metal films (Ca, Al) have been used to modify the polarity of ITO, so that it can be more effective as an electron-collecting electrode [7–9]. Among these materials, ZnO has a suitable work function, high electron mobility, good optical transmittance, and environmentally friendly nature. Further, it can be prepared by various methods [6, 10], such as the radiofrequency sputtering, atomic layer deposition, sol-gel processing, and so on. All these methods are high cost or high temperature (over 200°C) process, which is not compatible with large area deposition and plastic substrates. For IOSCs, the solution method is time-saving, inexpensive, simple, and compatible with printing techniques and flexible substrates, thus the solution method processed at low temperatures is more desirable. Simultaneously, the ultrathin metal modifier processed by the mature thermal evaporation is also a potential interfacial material, which has been successfully used to modify the ITO cathode and in efficient IOSCs [7, 9].

As we know, ITO is the most commonly used electrode in OSCs; however, the limited reserve of toxic indium element in earth and the increasing price of ITO force us to develop alternatives to ITO. So far, the reported replacements of ITO mainly include the metal films (such as Au, Ag, and oxide/metal/oxide), graphene, carbon nanotubes, and aluminum-doped zinc oxide (AZO) electrodes [3, 11–14]. Among them, AZO is able to meet the requirements of electrode, what is more, Al and Zn are relatively rich in earth, nontoxic and the large area AZO film fabrication is relatively easy. Therefore, the commercial AZO may be more suitable to replace ITO electrode in OSCs. Meanwhile, a smooth and continuous metal thin film (e.g., Ag) can be easily deposited by simple thermal evaporation, suitable for application in the mass production. Moreover, due to their intrinsic flexibility and high conductivity [14], metal thin-film electrodes are also suitable for application in roll-to-roll production of flexible OSCs. It is noted that making the Ag as thin as possible while maintaining its good optical and electrical properties is of vital importance to improve the performance of Ag thin-film electrodes.

In this chapter, besides a simple review of interfacial layers and transparent electrodes, we would like to introduce two efficient modifiers of ZnO and ultrathin Ca films, and two potential ITO-free electrodes of AZO and ultrathin Ag film in IOSCs or OSCs based on poly (3-hexylthiophene-2,5-diyl):[6,6]-phenyl C_{61} butyric acid methyl ester (P3HT:PCBM) blend. Here, not

only the optimization of device parameters, low-temperature process, flexible device, and air stability; but also the energy levels alignment, interface charge transport, metal film growth, light-soaking issue [15], and the underlying mechanism would be investigated. First, an aqueous solution method using low temperature is adopted to deposit a ZnO interlayer in IOSCs. The results show that the transition point of ZnO annealing temperature is approximately 80°C. When the temperature is above 80°C, the corresponding IOSCs show senior photovoltaic performance with PCEs over 3.5%, and the flexible devices based on poly(ethylene terephthalate) (PET) substrates also display a PCE of 3.26% as well as a good flexibility. Second, ITO-free IOSCs based on AZO substrates and ultrathin Ca modifier are studied by optimizing the device parameters and discussing the unexpected light-soaking issue in IOSCs. The results show that IOSCs with an ultrathin Ca modifier (~1 nm) could achieve a senior PCE above 3% and the highly efficient electron transport at AZO/Ca/organic interfaces, which obviously weakens the light soaking issue. Third, by introducing a MoO_3 interlayer for Ag film electrode growth, ITO-free OSCs with a MoO_3 (2 nm)/Ag (9 nm) anode show an improved PCE of 2.71%, and the corresponding flexible device also achieves a comparable PCE of 2.50% to that of ITO-based reference OSCs.

2. ITO-based OSCs with low-temperature ZnO interfacial layer

In this section, IOSCs based on commonly used ITO electrodes and low-temperature solution-processed ZnO interfacial layer are mainly investigated.

2.1. Device fabrication

The aqueous precursor solution used for ZnO production is prepared as follows: ZnO powder (99.9%, particle size <5 μm, Sigma-Aldrich) was dissolved in ammonia (25%, Tianjin Chemical Reagent) to form 0.1 M $Zn(NH_3)_4^{2+}$ solution; then, the solution was ultrasonically processed for 5 min and refrigerated for more than 12 h before use. P3HT and PCBM were purchased from Rieke Metals and Nano-C, respectively. The commercial ITO-coated glass substrate (Zhuhai Kaivo) has a sheet resistance below 10 Ω/square. While the ITO-coated PET substrates show a relatively large resistance (60 Ω/square) and a thickness of 0.15 mm. All the materials are directly used in the device fabrication without any further purification.

Figure 1(a) shows the schematic structure of glass/ITO/ZnO/P3HT:PCBM/MoO_3/Ag for fabricated IOSCs, and the device process was as following: ITO-coated substrates (glass or PET) were ultrasonically cleaned with detergent (Decon 90), deionized water, acetone, and ethyl ethanol, and deionized water for 15–20 min, respectively. Then, the ZnO precursor solution was spin-coated on a nitrogen-dried ITO-coated substrates at 3000 rpm for 40 s and then annealed in an oven at 50, 70, 80, 100, 130, and 150°C for 30 min or 1 h. The deposited ZnO interlayer has a thickness approximately 10 nm. Next, the P3HT:PCBM (1:0.8 wt% in 1,2-dichlorobenzene) solution was spin-coated on ZnO at 1000 rpm for 60 s in a nitrogen-filled glove box. After 150°C preannealing in nitrogen for 10 min, the obtained active layer has a

thickness around 100 nm. Finally, the MoO_3 (8 nm)/Ag (100 nm) anode was thermally evaporated through a shadow mask and the resulted devices have an active area of 10 mm^2.

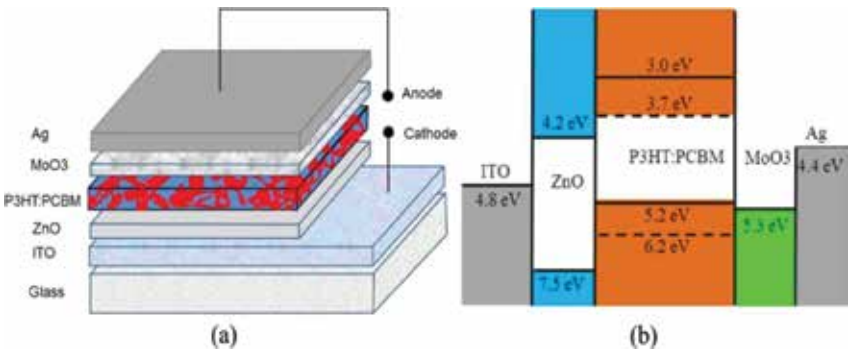

Figure 1. Schematic illustration and ideal energy diagram of materials for the inverted OSCs [6]. Copyright (2015) The Japan Society of Applied Physics.

The current density-voltage (J-V) curves were measured under simulated AM 1.5G solar simulator (Sanei Electric XEC-300M2) using a source-measure unit (Keithley 2400). The illumination intensity is kept at 100 mW/cm^2 using a calibrated Si solar cell. The transmission spectra, film surface morphology, and ZnO film crystal quality were characterized by the ellipsometer (J. A. Woollam WVASE 32), atomic force microscopy (AFM; Agilent 5500), and photoluminescence (PL) spectra (325 nm, He-Cd laser).

2.2. Results and discussion

The fabricated OSCs have a structure shown in **Figure 1**, wherein P3HT:PCBM acts as the photoactive layer, the ZnO film plays the roles of electron transport layer and hole blocking layer. This solution processed ZnO interfacial layer is used to lower ITO work function, modify the ITO polarity, and align the energy levels at ITO/P3HT:PCBM interface. In details, ZnO has the conduction band energy of −4.2 eV and the valence band energy of −7.5 eV, which suggests that electrons from PCBM can be transported into ZnO, while holes from P3HT can be blocked. Meanwhile, the MoO_3 acts as the hole transport layer and electron-blocking layer, and the ITO and Ag play the roles of cathode and anode, respectively.

Figure 2a shows the typical J-V curves under simulated AM 1.5G illumination for IOSCs at different ZnO annealing temperatures. It is well known that the J-V characteristics of solar cells can be described by the single-diode model under illumination, and the relation of J and V is given as follows:

$$J = J_0(\exp(\frac{q(V - R_s J)}{nk_B T}) - 1) + \frac{V - R_s J}{R_{sh}} - J_{ph} \quad (1)$$

where J_0 is the saturation current, q the electron charge, n the ideality factor, k_B the Boltzmann constant, T the temperature, R_s the series resistance, R_{sh} the shunt resistance, and J_{ph} the

http://dx.doi.org/10.5772/65312

photocurrent. Based on Eq. (1) and our previous reported method [16], these photovoltaic parameters extracted from J-V characteristics are shown in **Table 1**. As shown in **Figure 2a**, the experimental data are represented as symbols and the curves calculated from our method are indicated as solid lines. It is clear that the measured data of all devices are well reproduced by the fitting curves.

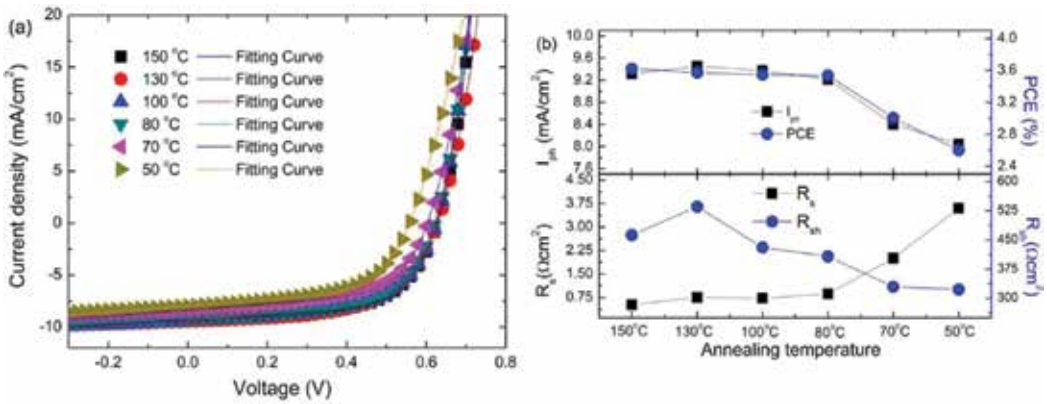

Figure 2. (a) Measured and calculated J-V characteristics of IOSCs with the ZnO interlayer annealed at various temperatures from 50 to 150 °C. (b) Photovoltaic parameters as a function of ZnO annealing temperatures [6]. Copyright (2015) The Japan Society of Applied Physics.

Temperature (°C)	V_{OC} (V)	J_{SC} (mA/cm²)	FF (%)	PCE (%)
150	0.63	−9.30	62.07	3.62
130	0.63	−9.44	60.24	3.57
100	0.62	−9.35	60.66	3.55
80	0.62	−9.19	61.85	3.54
70	0.60	−8.35	59.65	3.00
50	0.56	−7.96	58.57	2.60
Flexible device (80)	0.64	−9.10	56.00	3.26

Table 1. Photovoltaic parameters of inverted OSCs with the ZnO interlayer annealed at different temperatures [6]. Copyright (2015) The Japan Society of Applied Physics.

Figure 2a and **Table 1** show the J-V curves and photovoltaic parameters of IOSCs with ZnO annealed at various temperatures. The device with 150°C annealed ZnO obtains an overall PCE of 3.62% with V_{OC} = 0.63 V, J_{SC} = −9.30 mA/cm², and FF = 62.07%. If the annealing temperature of ZnO decreases from 150 to 80°C, the IOSCs perform well and achieve the almost unchanged PCE of 3.57%, 3.55%, and 3.54 %. However, when the temperature is further decreased (50 or 70°C), the device performance rapidly deteriorates. Although the degradation of the device performance is mainly due to the decrease in photocurrent, it can still be observed

that both V_{OC} and FF also begin to decrease. The effect of the ZnO annealing temperature on the device PCE is also shown in **Figure 2b**. The statistical results in **Figure 3a** show that the temperature approximately 80°C is the transition point, which corresponds to the above discussion. The data are obtained from at least seven devices for each annealing temperature of ZnO interlayer. Meanwhile, the fabricated devices in **Figure 3b** also show good air stability and their PCE could maintain about 90% of the original PCE values after 20 days stored in air.

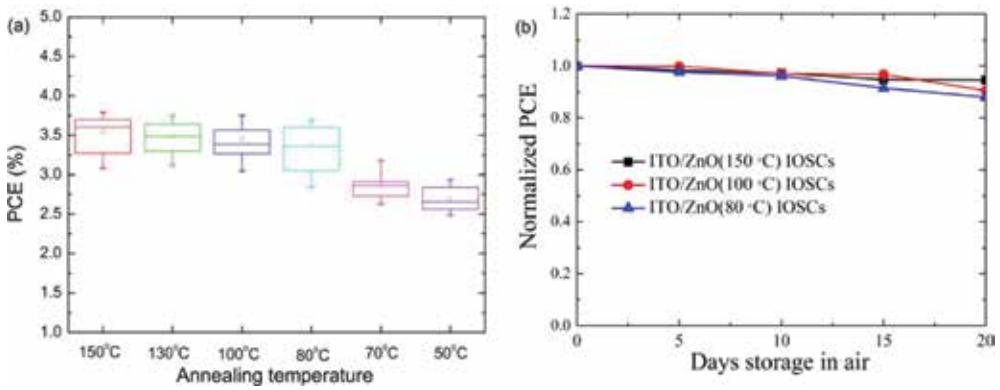

Figure 3. (a) Performance statistical results of the IOSCs with the ZnO interlayer annealed at different temperatures [6]. Copyright (2015) The Japan Society of Applied Physics. (b) PCE degradation of IOSCs in air during 20 days.

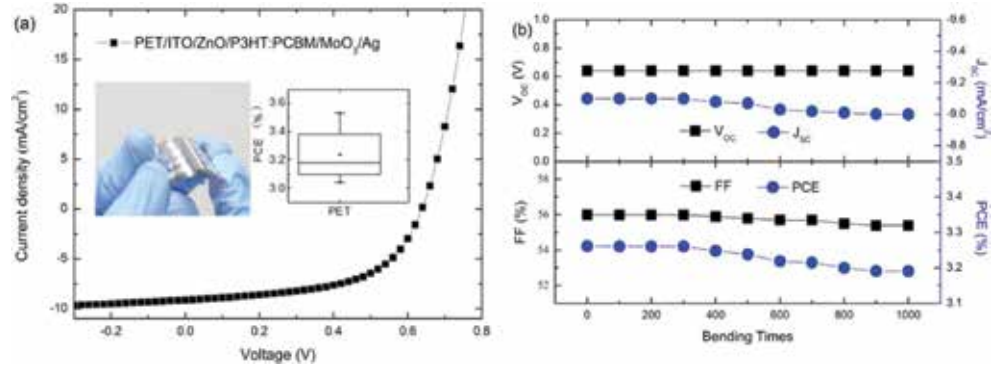

Figure 4. (a) Measured J-V characteristics of and PCE statistical result of flexible IOSCs. (b) Photovoltaic parameters as a function of the number of bending times up to 1000 cycles with a bending radius of about 50 mm [6]. Copyright (2015) The Japan Society of Applied Physics.

Furthermore, IOSCs based on flexible PET substrates were also fabricated with the structure of PET/ITO/ZnO/P3HT:PCBM/MoO_3/Ag. As shown in **Table 1** and **Figure 4a**, the flexible device with ZnO annealed at 80°C shows a PCE of 3.26% with V_{OC} = 0.64 V, J_{SC} = −9.10 mA/cm^2, FF = 56.0%, and the PCE statistical result also shows good device repeatability, which is comparable to that of the reference devices based on glass substrates. Then, the relatively good

http://dx.doi.org/10.5772/65312

ZnO quality achieved at 80°C annealing was again confirmed in the flexible devices. To quantitatively evaluate the device flexibility, a bending test with a number of bending times up to 1000 cycles was carried out. From **Figure 4b**, it could be seen that all the photovoltaic parameters nearly remain unchanged during the first 400 bending cycles, whereas J_{SC} decreases to −9.0 mA/cm^2, FF degrades to 55.4%, and the overall PCE only decreases by 2% from 3.26% to 3.19% after continuous 1000 cycles of bending test. As a result, the device fabricated on flexible PET substrates shows superior flexibility, which proves the potential of low-temperature ZnO deposition method in fabricating flexible IOSCs and other electron devices.

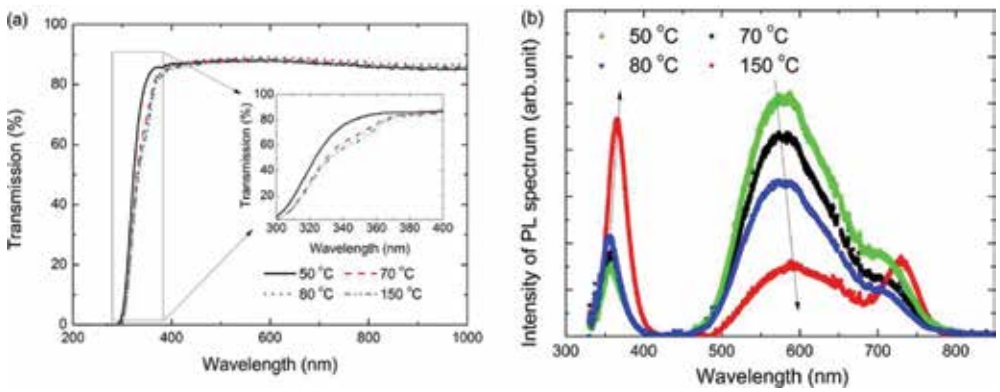

Figure 5. (a) Transmission and (b) PL spectra of ZnO on glass annealed at different temperatures [6]. Copyright (2015) The Japan Society of Applied Physics.

Figure 5a shows the transmission spectra of ZnO/glass samples annealed at 150, 80, 70, and 50°C. All the spectra are very similar and the samples show a transmittance about 88% in the wavelength region from 400 to 1000 nm. And their difference only comes from the shift of transmission edge for ZnO material in the short wavelength region from 300 to 400 nm. It can be seen in the illustration that the transmission edge locates at the lowest wavelength when the ZnO annealing temperature is 50°C and gradually shifts to longer wavelength with the increase in temperatures. Generally, if the material transmittance edge is located at a short wavelength, it has a wide bandgap; otherwise, it has a narrow band gap. A narrow band gap usually means a higher crystalline degree for ZnO [17], so ZnO annealed at higher temperatures has better crystalline quality. From the inset of **Figure 5a**, the relatively smaller shift of the transmission edge for ZnO annealed at 80–150°C means that the ZnO bandgap almost remains unchanged when the annealing temperature is above 80°C, which corresponds to the similar device performance for ZnO annealed at 80–150°C. Meanwhile, from the PL spectra of ZnO in **Figure 5b**, the intrinsic peak in the 350–400 nm range is related to the near-band edge emission of ZnO. With an increase in ZnO annealing temperatures, the intrinsic peak position of ZnO shifts to the longer wavelength and the peak intensity also increases. What is more, the wide peaks in the range from 500 to 800 nm are usually related to the defects in ZnO film, such as interstitial zinc or oxygen atoms, zinc atom vacancy, and oxygen atom or ion vacancy [18]. With an increased temperature, the defect-related peaks are weakened, and thus, the number

of defects is decreased and better ZnO film quality is obtained. Simultaneously, for different ZnO film annealing temperatures of 50, 70, 80, and 150°C, the corresponding root-mean-square surface roughness are 0.673, 0.867, 1.108, and 1.145 nm, respectively. The increased surface roughness corresponds to the more sufficient ZnO crystallization at a high annealing temperature. It is thought that, when the annealing temperature is below 80°C, the ZnO morphology changes markedly, and when the annealing temperature is above 80°C, the ZnO morphology almost remains unchanged. From the morphology results, it is concluded that an annealing temperature of 80°C is sufficient for ZnO crystallization. And the high temperature only slightly improves the film quality, a result agreed to the similar photovoltaic performance of IOSC with ZnO annealed from 80 to 150°C.

According to above discussion, one can draw the conclusion that the 80°C is sufficient for ZnO annealing to obtain a relatively high film quality and act as an interfacial layer, and the resulted devices based glass or PET substrates show the similar photovoltaic performance when the ZnO annealing temperature is higher than 80°C. In short, the senior device performance and good stability show that the aqueous solution method is a more promising low-temperature technique for depositing ZnO in IOSCs and it may be widely applied in flexible and printing devices in the future.

3. ITO-free OSCs based on AZO cathodes and Ca interfacial layer

In this section, ITO-free IOSCs are fabricated on AZO cathodes and ultrathin Ca interfacial layer, the optimization of device performance and light-soaking issue are mainly discussed.

3.1. Device fabrication

The AZO (~980 nm, 2 wt% Al)-coated glass substrates purchased from Zhuhai Kaivo co. were prepared by radiofrequency magnetron sputtering process and they have a sheet resistance of about 7.34 ohm/square and average transmission over 80% in the visible light region. The P3HT:PCBM based bulk heterojunction IOSCs with the AZO transparent cathode was fabricated, and the obtained devices have the structure of Glass/AZO/Ca/P3HT:PCBM/MoO_3/Ag and an active area of 12.5 mm^2. The Ca interfacial modifier with different thicknesses (0, 1, 5, 10 nm) were thermally evaporated on AZO at a base pressure below 5.0×10^{-4} Pa. The detail fabrication process is the same as that in previous section. The J-V characteristics were measured under AM 1.5G solar simulator spectrum before and after 15-min light soaking. The stability of devices was investigated by measuring their J-V characteristics once every 5 days in 1 month.

3.2. Results

From **Figure 6a** and **Table 2**, the AZO only IOSC without an interfacial layer presents a very poor performance and improved V_{OC}, J_{SC}, FF, and PCE after 15 min AM 1.5G continuous illumination (light soaking), shown in **Figures 7a** and **b**. This can be attributed to the energy loss associated with the mismatch of the energy levels between the work function of sputtered AZO (4.5 eV) and the lowest unoccupied molecular orbital (LUMO) level of PCBM (3.7 eV)

http://dx.doi.org/10.5772/65312

(shown in **Figure 8**). During the light soaking, the photogenerated electron-hole pairs in AZO could increase the electron density, fill the trap sites, and thus lower the work function of AZO [15], which improves the electron selectivity from organic layer to AZO cathode and thus induces the improvement of device parameters. However, the performance of AZO only IOSC is still very poor, especially the low V_{OC} of 0.38 V, which indicates that a modifying layer with lower work function must be inserted between AZO and P3HT:PCBM to align their energy levels.

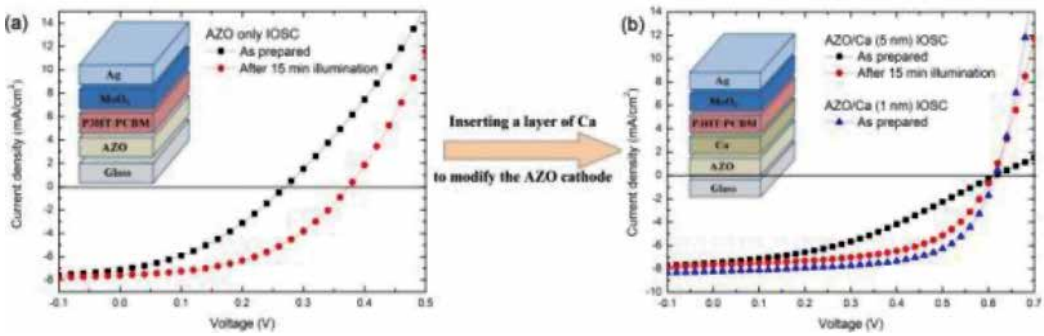

Figure 6. Measured J-V characteristics for as prepared and 15-min illuminated AZO/Ca (0, 1, and 5 nm) IOSCs. Reproduced with permission [20]. Copyright 2014, Elsevier.

Device structures Glass/x/P3HT:PCBM/MoO_3/Ag		V_{OC} (V)	J_{SC} (mA/cm²)	FF (%)	PCE (%)	R_s (Ω cm²)
AZO	As prepared	0.28	−7.11	36	0.72	11.6
	15 min illuminated	0.38	−7.60	46	1.34	4.9
AZO/Ca (5 nm)	As prepared	0.62	−7.49	38	1.74	–
	15 min illuminated	0.60	−7.67	58	2.69	2.3
AZO/Ca (1 nm)		0.62	−8.23	62	3.17	0.7
ITO/Ca (1 nm)		0.64	−7.41	58	2.79	1.5
AZO/Ca (10 nm)		0.62	−7.22	49	2.18	7.1

Table 2. Photovoltaic parameters (PCE, V_{OC}, J_{SC}, and FF) obtained from J-V characteristics of AZO only IOSC, AZO/Ca IOSCs with different Ca thicknesses (1, 5, 10 nm), and the referenced ITO/Ca (1 nm) IOSC. The "–" represents a very large value. For the S-shaped J-V characteristics, the value of R_S is so large that the data are out of the diode model used in the calculation. Reproduced with permission [20]. Copyright 2014, Elsevier.

Then, an electron transport layer of Ca is inserted between AZO and P3HT:PCBM to modify the work function of AZO cathode and the Ca modifier has already been used in ITO based IOSCs [6]. It is clear in **Figure 6** and **Table 2** that, the devices with Ca interfacial layer achieve significant improvement in V_{OC}, J_{SC}, FF, and PCE compared with that of AZO only IOSC. Particularly, an increased V_{OC} (0.60 V) demonstrates that the Ca work function has been pinned to the PCBM Fermi level via the surface states. Consequently, the resulted ohmic contact between Ca and PCBM favors the electron transport and the rectifying contact between Ca and P3HT blocks the hole collection at the AZO cathode. Furthermore, the devices with an ultrathin

Ca (~1 nm) show a superior performance with the highest PCE of 3.17% and lowest R_S of 0.7 Ω cm^2, which is comparable to that of ITO-based device. Thus, the low-cost AZO electrode is one of the promising ITO alternatives.

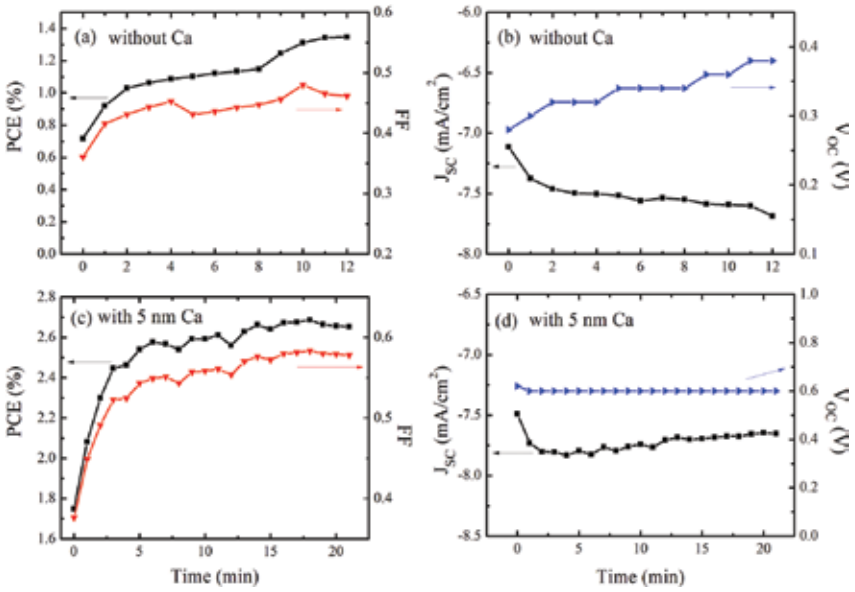

Figure 7. Variations of photovoltaic parameters (PCE, V_{OC}, J_{SC}, and FF) during 15 min light soaking for (a) and (b) the AZO only IOSC, (c) and (d) the AZO/Ca (5 nm) IOSC. Reproduced with permission [20]. Copyright 2014, Elsevier.

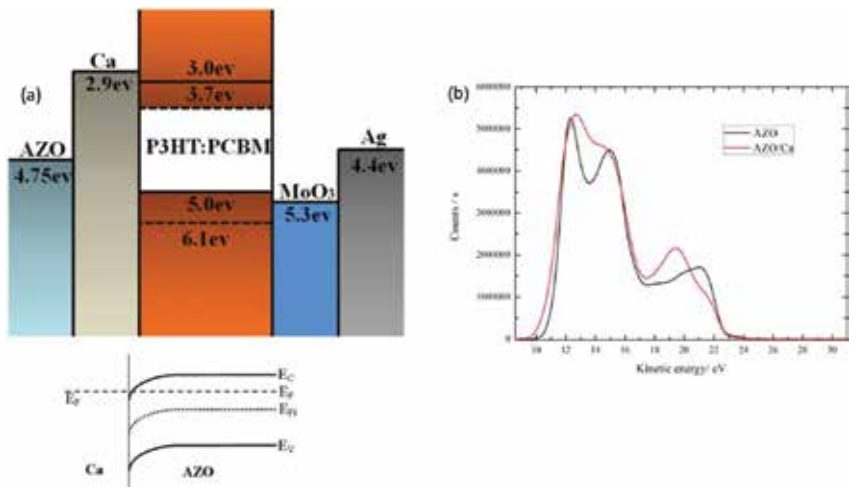

Figure 8. (a) Schematic energy diagram of AZO/Ca IOSCs and ideal band diagram of Ca-AZO contacts according to the ideal metal-n-type semiconductor contact [19]. (b) The AZO work function of 4.5 eV and AZO/Ca work function of 3.8 eV were determined by UPS experiments. Reproduced with permission [20]. Copyright 2014, Elsevier.

http://dx.doi.org/10.5772/65312

One the other hand, for the AZO/Ca (5nm) IOSC, the as prepared device has a low PCE of 1.74% as well as a S-shaped J-V curve, and the PCE increases to 2.69% with the vanish of the S-shaped curve during light soaking, which is observed clearly in **Figures 6b** and **7c**, and **7d**. It is noted that the trend of increasing PCE is nearly identical to that of FF, a slight increase in J_{SC} and nearly unchanged V_{OC} are also observed, which is similar to the reported light-soaking issue [15]. It is obvious in **Table 2** that the R_S of AZO/Ca (5 nm) IOSC shows a remarkable decrease from a very large value to 2.3 Ω cm^2, which is in good agreement with an increase in FF from 38% to 58%. Combining the improved device parameters of AZO only IOSC during light soaking, the strikingly decreased R_S indicates the less energy loss in the charge transport at interfaces and the more efficient charge collection at electrodes. Here, it is thought that the interface electron transport from P3HT:PCBM to AZO is related to the light-soaking issue, which will be discussed in next part. The nearly unchanged V_{OC} demonstrates that an ultrathin Ca layer of 1 nm can also effectively modify the work function of AZO cathode. More remarkably, no light-soaking issue is observed in this device and the detail discussion is shown in next section. Thus, considering the different photovoltaic performances of AZO/Ca (0, 1, 5, and 10 nm) IOSCs, the underlying reasons are deserved to be further investigated.

3.3. Discussion

For a good understanding of different photovoltaic behaviors of AZO-based IOSCs, the following discussions focus on the optical and electrical properties, surface morphology of the AZO/Ca (0, 1, 5, and 10 nm) films. From optical aspect, the transmission spectra of AZO/Ca (x nm) samples in **Figure 9(a)** shows that AZO has a very similar transmission tendency to that of AZO with 1, 5, and 10 nm Ca deposited on it. The lower transmission of AZO/Ca (10 nm) substrate means relatively larger light absorption loss in the active layer, which can be used to explain the relatively poor performance of the AZO/Ca (10 nm) IOSC.

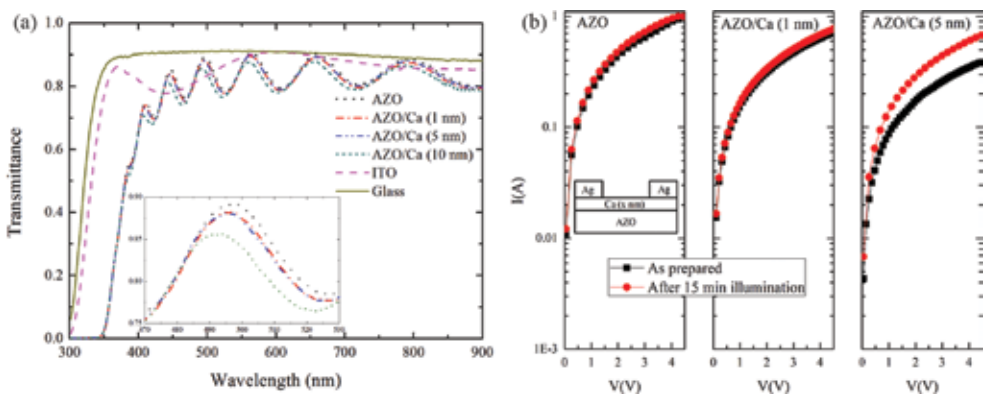

Figure 9. (a) Transmission spectra for the ITO, AZO and AZO/Ca (1, 5, and 10 nm) coated glass substrates. Insert: enlarged pictures for AZO/Ca (0, 1, 5, and 10 nm) substrates in the range from 470 to 530 nm. (b) Photoconductivity measured before and after 15 min AM 1.5 G illumination for the AZO, AZO/Ca (1 nm), and AZO/Ca (5 nm) films on glass substrates. The insert shows the schematic diagram of glass/AZO/Ca (0, 1, and 5 nm)/Ag samples for photoconductivity measurement. Adapted with permission [20]. Copyright 2014, Elsevier.

The coverage of Ca (1, 5, and 10 nm) on AZO films and their surface morphology were characterized by AFM and FE-SEM and no significant differences in morphology could be observed for AZO, AZO/Ca (1 nm), AZO/Ca (5 nm), and AZO/Ca (10 nm) films. This may be related to the very rough surface of AZO films (RMS = 11.59 nm). Fortunately, some useful information may be indirectly acquired from XPS depth profile since the coverage of Ca (1, 5, and 10 nm) on AZO films could be reflected by the different Zn and Ca elements content at the sample surface. The detail XPS analysis and Ca coverage study could be found in our reports [20]. According to the XPS study and the experience Volmer-Weber growth or 3D island growth [21], the AZO film can be completely covered by a Ca layer about 10 nm, while the 1 nm Ca on AZO exists as unclosed islands and the 5 nm Ca could partly cover the AZO surface. From electrical aspect, the measured UPS (He I, 21.2 eV) spectra in **Figure 8** show that the AZO work function (4.5 eV) could be reduced to 3.8 eV by introducing an 5 nm Ca interfacial layer, which is well matched to the LUMO level (3.7 eV) of PCBM. Thus, a Ca modifier can be used to align the energy levels between P3HT:PCBM and AZO cathode.

To further understanding the electron transport in AZO, AZO/Ca (1 nm), and AZO/Ca (5 nm) films, the photoconductivity was investigated as following. It can be observed from **Figure 9b** that the conductivity of AZO and AZO/Ca (1 nm) does not change significantly with the continuous AM 1.5 G illumination; however, the conductivity of AZO/Ca (5 nm) film presents an obvious increase during the 15-min light soaking. From the band diagrams of ideal Ca-AZO contacts shown in **Figure 8**, the different work function between Ca and AZO would cause an electron transport barrier at AZO/Ca interface. For the 5 nm Ca on AZO, the low initial conductivity suggests the large energy loss in the electron transport across AZO/Ca (5 nm) interface, which can be attributed to the electron transport barrier from Ca to AZO as well as the oxidization of Ca layer. During the 15-min light soaking, the photogenerated electron-hole pairs in AZO could increase the electron density, fill the trap sites, and thus lower the work function of AZO, which also lowers the electron transport barrier and improves the electron transport efficiency at AZO/Ca interface, a situation agreed with an increased conductivity of AZO/Ca (5 nm) film and improved J_{SC} in corresponding device. After about 15 min, no further improvement of photovoltaic parameters can be observed and the electron transport reaches a saturated case. For the AZO/Ca (1 nm) sample, its initial conductivity is comparable to the maximum conductivity of AZO/Ca (5 nm) (**Figure 9b**). More importantly, no significant improvement of conductivity is observed upon continuous illumination, which suggests the sufficient charge transport from AZO to Ca. This result is in line with the senior and stable photovoltaic parameters of AZO/Ca (1 nm) IOSC.

According to previous discussion, the high efficient electron transport at AZO/Ca (1 nm)/ organic interface may be related to the Ca coverage on AZO. As we know, the 1 nm Ca only exists as isolated islands on AZO surface, and it is thought that the ultrathin Ca may increase the number of active sites, and these isolated sites with low electric potential provide the fast pathway of electron from P3HT:PCBM to AZO. This process may be understood by introducing the Liebig's law of the minimum [22] that the barrel capacity is limited by the shortest stave. Analogously, the active sites may act as the shortest stave and the electrons play the role of water, and the electron prefers to travel through the low-electric-potential pathway provided

http://dx.doi.org/10.5772/65312

by the island-like ultrathin Ca on AZO film, instead of the direct transport across the larger energy barrier at AZO/organic interface. This discussion agrees with the smaller R_S, larger J_{SC}, FF, and PCE of AZO/Ca (1 nm) IOSCs. In other words, the highly efficient electron transport in AZO/Ca (1 nm) film may be responsible for the removed light-soaking issue of as prepared AZO/Ca (1 nm) IOSC. It also should be noted that the unexpected light soaking issue appears after the un-encapsulated device has been stored in air for several days since the oxidation of Ca, but this does not happen for the device stored in N_2. In short, the observed light-soaking phenomenon is strongly related to the electron transport ability at the AZO/Ca/organic interface and the energy loss caused by the oxidation of Ca, and the more exact mechanism should be further investigated in the future work.

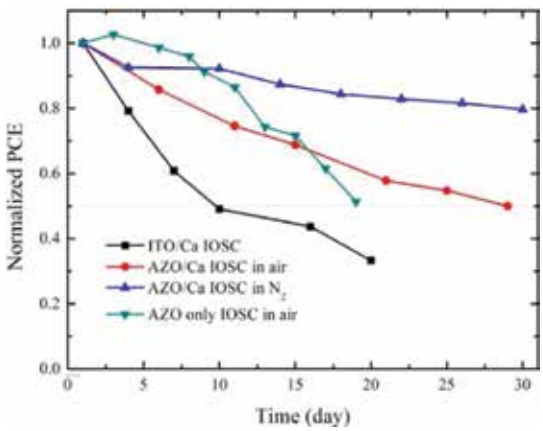

Figure 10. Normalized PCE degradation for AZO/Ca (1 nm) IOSCs and ITO/Ca IOSCs stored in air or N_2. Reproduced with permission [20]. Copyright 2014, Elsevier.

What is more, we investigate the stability of un-encapsulated devices stored in air or N_2 for one month and their normalized PCEs are shown in **Figure 10**. It is very clear that the AZO/Ca (1 nm) IOSC stored in N_2 (measured in air) shows a good stability that its PCE could maintain 80% of the original values after one month. It is noted that the relatively stable V_{OC} demonstrates that the Ca-modified AZO cathode can provide suitable contact for electron collection. Also from **Figure 10**, a degradation of PCE by 50% for the air-stored AZO/Ca (1 nm) IOSC during one month is observed, which can be attributed to the inevitable penetration of oxygen/water from air into the active layer and the oxidization of Ca-modifying layer. Here, the effect of Ca oxidation on the stability could be confirmed from the results of AZO only IOSC. In detail, this device without Ca shows a better stability during the first two weeks in air than that of AZO/Ca (1 nm) IOSC, whereas the mismatch of energy levels at AZO/P3HT:PCBM interface may be responsible for the larger energy loss in charge transport and more un-durable PCE after two weeks. However, the PCE of ITO/Ca (1 nm) IOSC deteriorates by 50% only in 10 days and drops by 80% of the origin values in the next ten days, which further shows the effect of Ca oxidation on the device air-stability. In addition, the increased contact resistance caused by the oxidation and mechanical damages of relatively thin Ag (70 nm) anode

by metal clips during the J-V test may also be a factor of device degradation. As a result, considering the comparable PCEs and better device air-stability, the AZO cathode is a promising alternative of ITO to fabricate the long-lifetime IOSCs.

4. ITO-free OSCs based on Ag thin-film electrodes

In this section, ITO-free OSCs based on (MoO_3/)Ag thin-film electrodes on glass or PET substrates are fabricated, and the best performance of OSCs is obtained by optimizing the thicknesses of Ag film and MoO_3 interlayer. And the underlying mechanism, especially the Ag thin-film growth and film properties are also investigated.

4.1. Device fabrication

The MoO_3/Ag or Ag electrodes were thermally evaporated on glass or PET substrates at a base pressure of 5.0×10^{-4} Pa, with an evaporation rate of 0.02 nm/s for MoO_3 and 0.1 nm/s for Ag, respectively. The thicknesses and evaporation rates of MoO_3, Ag and Al were estimated in situ with a calibrated quartz crystal monitor. Since the 2 nm ultrathin MoO_3 is not smooth and closed, the given thickness had to be a nominal value obtained by the monitor, representing the amount of MoO_3 on the sample. The sheet resistances of these MoO_3/Ag or Ag electrodes were measured by using a four point probe setup system. The transmission spectra were recorded by using a spectrophotometer (Lambda950, PerkinElmer). The fabricated devices has a structure of glass (or PET)/(MoO_3)/Ag/MoO_3/P3HT:PCBM/Al and an active area of 12.5 mm^2. The detail fabrication process is the same as that in previous sections.

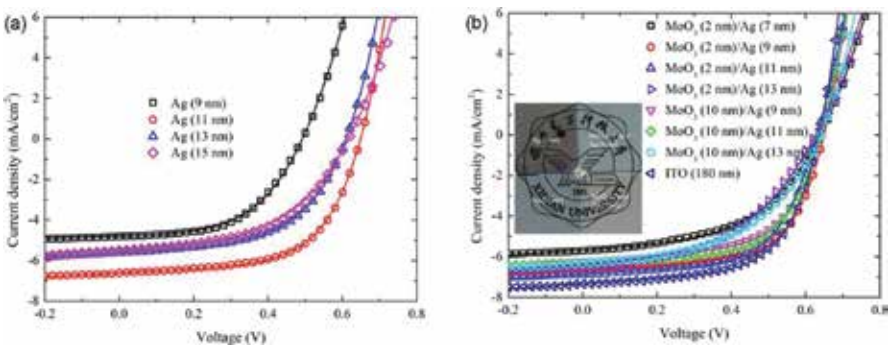

Figure 11. Measured (symbol) and calculated (solid line) J-V characteristics for OSCs fabricated on the (a) Ag or (b) MoO_3/Ag anodes. Inset: A photograph of MoO_3 (2 and 10 nm)/Ag (9 and 11 nm) electrodes. Adapted with permission [11]. Copyright 2014, Elsevier.

4.2. Results and discussion

In details, the OSCs based on Ag thin-film electrode are first fabricated with a structure of glass/Ag/MoO_3/P3HT:PCBM/Al, and then, a MoO_3 interlayer is introduced between glass and

http://dx.doi.org/10.5772/65312

Ag electrode to further improve the device performance. As shown in **Figure 11a** and **Table 3**, the device with 11 nm Ag shows a higher PCE of 2.57% and lower *R*s of 2.0 Ω cm^2. Further, by inserting a MoO_3 interlayer, a senior PCE of 2.71% is obtained by employing a MoO_3 (2 nm)/Ag (9 nm) electrode as well as a relatively low *R*s of 3.0 Ω cm^2, which is comparable to that of reference OSCs based on ITO electrode. Meanwhile, an increase in Ag or MoO_3 layer thickness only degrades the device performance. To understand the underlying mechanism, the optical and electrical properties as well as the surface morphology are studied as follows.

Anodes	J_{sc} (mA/cm^2)	V_{OC} (V)	FF	PCE (%)	*R*s (Ω cm^2)
Ag (9 nm)	4.79	0.49	0.53	1.24	7.5
Ag (11 nm)	6.61	0.65	0.60	2.57	2.0
Ag (13 nm)	5.60	0.61	0.55	1.88	1.9
Ag (15 nm)	5.47	0.62	0.50	1.70	3.6
MoO_3 (2 nm)/Ag (7 nm)	5.67	0.64	0.50	1.82	5.6
MoO_3 (2 nm)/Ag (9 nm)	6.68	0.65	0.63	2.71	3.0
MoO_3 (2 nm)/Ag (11 nm)	6.86	0.63	0.60	2.62	5.8
MoO_3 (2 nm)/Ag (13 nm)	6.41	0.63	0.47	1.90	4.5
MoO_3 (10 nm)/Ag (9 nm)	6.26	0.64	0.59	2.39	3.7
MoO_3 (10 nm)/Ag (11 nm)	6.30	0.64	0.61	2.45	2.8
MoO_3 (10 nm)/Ag (13 nm)	6.26	0.64	0.50	2.02	0.7
ITO (180 nm)	7.33	0.64	0.61	2.85	1.1
PET/MoO_3 (2 nm)/Ag (9 nm)	6.21	0.63	0.64	2.50	–

Table 3. Photovoltaic performance parameters for OSCs fabricated on different anodes/glass substrates. Reproduced with permission [11]. Copyright 2014, Elsevier.

The thermally evaporated Ag film prefers 3D island growth, namely Volmer-Weber growth, which starts from disconnected nuclei [21]. Thus, for the deposition of the first few nanometers of Ag, separate nuclei are formed. According to the SEM images in **Figure 12**, optical transmittance and sheet resistance in **Figure 13**, it can be seen that the percolation threshold thickness of Ag thin film in this study is about 11 nm. At this thickness, the Ag islands are closed and a continuous Ag layer is formed, while the relatively high transmittance and low sheet resistance (6.29 Ω/square) are obtained. This is in good line with the corresponding device performance. By introducing a MoO_3 interlayer, as shown in **Figure 13a**, MoO_3 (2 nm)/Ag (9 nm) anode not only shows similar spectral shape of the transmission curve as Ag (11 nm) electrode but also presents a higher transparency with a maximum of 74% at 361 nm. Particularly, in the visible spectral range, the transparency of the electrode between 56 and 70% is achieved, showing the potential of this electrode. With the introduction of 2 nm thick MoO_3 interlayer between the Ag layer and glass substrate, the sheet resistance of the electrode is decreased to 9.32 Ω/square. The excellent properties of MoO_3 (2 nm)/Ag (9 nm) electrode in

transparency and conductivity lead to the best device performance among all the ITO-free OSCs and verify the fact that the percolation threshold of Ag has been reduced to 9 nm by introducing a 2 nm MoO_3 interlayer. As we know, the thickness of Ag film is strongly related to its transmittance and conductivity, and the percolation threshold thickness determines the smallest thickness for a metal film electrode, which is the most important parameter in the 3D growth of Ag film during the thermal evaporation process. Thus, the decrease in percolation threshold thickness not only could maintain the high conductivity, but also could enhance the optical transmission of Ag film and lower the fabrication cost as well.

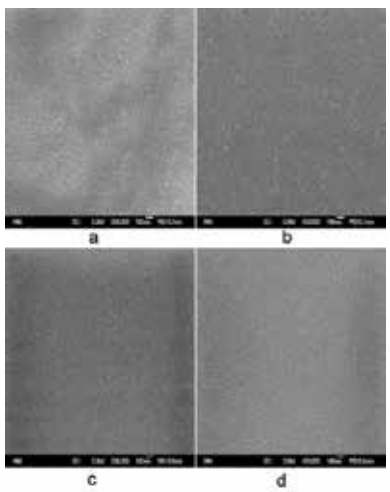

Figure 12. SEM images of (a) Ag (9 nm), (b) Ag (11 nm), (c) MoO_3 (2 nm)/Ag (9 nm) and (d) MoO_3 (10 nm)/Ag (9 nm) electrodes deposited on glass substrates. The white scale bar represents 100 nm. Reproduced with permission [11]. Copyright 2014, Elsevier.

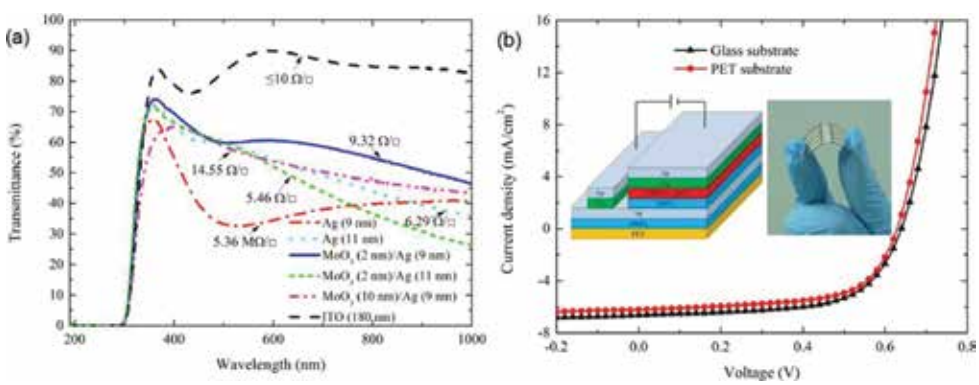

Figure 13. (a) Transmittance spectra with corresponding sheet resistances and (b) J-V characteristics for ITO-free OSCs fabricated on PET or glass substrates. (a) Adapted with permission [11]. Copyright 2014, Elsevier. (b)Reproduced with permission [26]. Copyright 2015, IEEE.

http://dx.doi.org/10.5772/65312

In our opinion, the introduction of the MoO_3 interlayer can effectively improve the wetting of Ag on the substrate and reduce the percolation threshold of Ag. However, the mechanism of the smoothening effect of the MoO_3 layer still remains to be determined. Here, MoO_3 works as a surfactant to modify the surface of Ag film. When the thickness of MoO_3 is 2 nm, the unclosed layer may create preferred nucleation sites on the glass substrate to enhance the lateral growth of Ag film. Similar results are also found in the recent report [23]. However, with an increase in MoO_3 thickness to 10 nm, things become different. Since the surface energy of MoO_3 (γ = 0.06 J m^{-2}) is much less than that of Ag (γ = 1.25 J m^{-2}) [24, 25], the Ag-Ag interactions are stronger than the Ag-substrate interactions, which weakens the surface-modifying effect of the MoO_3 layer. Thus, the effect of a thick MoO_3 interlayer (here 10 nm) on improving the wetting of Ag on the substrate is inferior to that of a thin MoO_3 interlayer (2 nm).

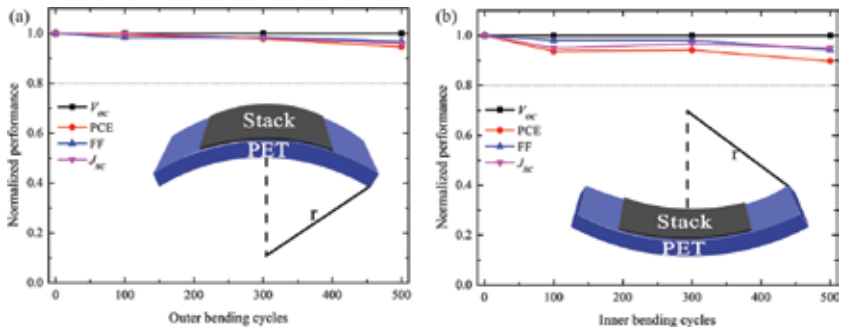

Figure 14. Normalized photovoltaic performance parameters of flexible ITO-free OSCs as a function of the number of (a) outer or (b) inner bending cycles. Adapted with permission [26]. Copyright 2015, IEEE.

Furthermore, flexible devices using our optimized MoO_3 (2 nm)/Ag (9 nm) anode are fabricated on PET substrates with P3HT:PCBM films as the active layer. A PCE of 2.50% is achieved for such flexible ITO-free device (**Table 3**), which is comparable to the PCE (2.71%) of the glass/MoO_3/Ag-based devices and the PCE (2.85%) of glass/ITO-based OSCs. Simultaneously, the corresponding flexible ITO-free OSCs based on MoO_3 (2 nm)/Ag (9 nm) anode show good mechanical flexibility. As shown in **Figure 14**, about 10% degradation in PCE is observed after 500 inner bending cycles with a bending radius of 1.5 cm, whereas a 5% decrease in PCE is observed after 500 outer bending cycles. It shows the huge potential of our flexible electrodes, and it may be instructive for further research on flexible electrodes and roll-to-roll mass production of OSCs.

5. Conclusion

In conclusion, the properties of electrode-organic interfaces and transparent electrode materials have significant impact on the efficiency of light absorption, charge transport and collection, which dominates the overall efficiency of OSCs. Nowadays, the interface engineering and electrode engineering have attracted increased attentions all over the world. In this

chapter, after a simple review of interfacial layers and transparent electrodes reported in OSCs, we have investigated two efficient modifying layers of ZnO and ultrathin Ca films, two potential ITO-free electrodes of AZO and ultrathin Ag film, and their effect on the performance improvement of P3HT:PCBM based OSCs.

By utilizing an aqueous solution method processed ZnO interfacial layer at low temperatures, IOSCs have obtained an obvious improvement of device performance. The results show that the transition point of ZnO annealing temperature is approximately 80°C. When the ZnO annealing temperature is above 80°C, the corresponding IOSCs show senior photovoltaic performances with PCEs higher than 3.5%, and the flexible devices based on PET substrates also display a PCE of 3.26% as well as a good flexibility in bending tests. All devices show good repeatability and air stability. The improved device performance can be attributed to the well-aligned energy levels and improved charge transport between ITO and organic material. Thus, the low-temperature ZnO deposition method based on aqueous solution is a promising technique in fabricating highly efficient IOSCs and flexible devices with long lifetime.

By utilizing an ultrathin Ca modifier and AZO transparent cathodes, ITO-free IOSCs have achieved an obviously improved device performance and weakened light-soaking issue. Although the AZO only IOSC show a very poor performance, IOSCs with a Ca modifier (5 nm or thicker) could obtain the remarkably increased V_{OC} of 0.60 V and PCE of 2.69%, which is attributed to the well-aligned energy levels at AZO/organic interface. When an ultrathin Ca modifier (~1 nm) is introduced, a further improved PCE above 3% is obtained and more importantly, the light soaking issue in the AZO only IOSC and AZO/Ca (5 nm) IOSC has been evidently weakened, which could be explained by the highly efficient electron transport at AZO/Ca/organic interface, while the more exact mechanism should be further investigated in the future work.

By utilizing an ultrathin MoO_3 interlayer for Ag film growth, the MoO_3 (2 nm)/Ag (9 nm) anode not only shows a low sheet resistance of 6.29 Ω/square but also presents a higher transparency with a maximum of 74% at 361 nm, and notably the percolation threshold of Ag film has been decreased from 11 to 9 nm according to the 3D island growth of Ag, confirmed by the SEM, sheet resistance, and transmittance study. The resulted ITO-free OSCs with this MoO_3/Ag anode show an improved PCE 2.71%, and the corresponding flexible device fabricated on PET substrates also achieves a comparable PCE of 2.50% to that of ITO-based OSCs. Thus, the evaporated Ag film electrode with good transmittance and low resistivity is a potential candidate of ITO, and it would find more applications in flexible devices and roll-to-roll production. All investigations in this chapter enrich the understanding of interface and electrode engineering in OSCs, which may be instructive for further research on the improvement of device performance and the possible commercialization in the future.

Acknowledgements

This work is partly financially supported by National Natural Science Foundation of China under Grant 61334002 and 61106063.

Author details

Dazheng Chen* and Chunfu Zhang*

*Address all correspondence to: cfzhang@xidian.edu.cn; dzchen@xidian.edu.cn

State Key Discipline Laboratory of Wide Band Gap Semiconductor Technology, School of Microelectronics, Xidian University, Xi'an, China

References

[1] Yu G, Gao J, Hummelen JC, Wudl F, Heeger AJ. Polymer photovoltaic cells: enhanced efficiencies via a network of internal donor-acceptor heterojunctions. Science. 1995; 270(5243):1789–1791. DOI: 10.1126/science.270.5243.1789

[2] Scharber MC, Sariciftci NS. Efficiency of bulk-heterojunction organic solar cells. Progress in Polymer Science. 2013; 38(12):1929–1940. DOI:10.1016/j.progpolymsci. 2013.05.001

[3] Liu H, Wu Z, Hu J, Song Q, Wu B, Lam Tam H, Yang Q, Hong Choi W, Zhu F. Efficient and ultraviolet durable inverted organic solar cells based on an aluminum-doped zinc oxide transparent cathode. Applied Physics Letters. 2013; 103(4):043309. DOI: http:// dx.doi.org/10.1063/1.4816786

[4] He Z, Xiao B, Liu F, Wu H, Yang Y, Xiao S, Wang C, Russell TP, Cao Y. Single-junction polymer solar cells with high efficiency and photovoltage. Nature Photonics. 2015; 9:174–179. DOI:10.1038/nphoton.2015.6

[5] Chueh CC, Crump M, Jen AKY, Optical enhancement via electrode designs for high-performance polymer solar cells. Advanced Functional Materials. 2016; 26(3):321–340. DOI:10.1002/adfm.201503489

[6] Chen D, Zhang C, Heng T, Wei W, Wang Z, Han G, Feng Q, Hao Y, Zhang J. Efficient inverted polymer solar cells using low-temperature zinc oxide interlayer processed from aqueous solution. Japanese Journal of Applied Physics. 2015; 54(4):042301. DOI: http://dx.doi.org/10.7567/JJAP.54.042301

[7] Shi T, Zhu X, Tu G. Efficient inverted polymer solar cells based on ultrathin aluminum interlayer modified aluminum-doped zinc oxide electrode. Applied Physics Letters. 2014; 104(10):103901. DOI: http://dx.doi.org/10.1063/1.4868101

[8] Lin Z, Jiang C, Zhu CX, Zhang J. Development of inverted organic solar cells with-TiO_2 interface layer by using low-temperature atomic layer deposition. ACS Applied Materials and Interfaces. 2013; 5(3):713–718. DOI: 10.1021/am302252p

[9] Zhao DW, Liu P, Sun XW, Tan ST, Ke L, Kyaw AKK. Indium tin oxide-free and metal-free semitransparent organic solar cells. Applied Physics Letters. 2009; 95(15):153304. DOI: http://dx.doi.org/10.1063/1.3250176

[10] Oh H, Krantz J, Litzov I, Stubhan T, Pinna L, Brabec CJ. Comparison of various sol-gel derived metal oxide layers for inverted organic solar cells. Solar Energy Materials and Solar Cells. 2011; 95(8):2194–2199. DOI:10.1016/j.solmat.2011.03.023

[11] Wang Z, Zhang C, Gao R, Chen D, Tang S, Zhang J, Wang D, Lu X, Hao Y. Improvement of transparent silver thin film anodes for organic solar cells with a decreased percolation threshold of silver. Solar Energy Materials and Solar Cells. 2014; 127:193–200. DOI: 10.1016/j.solmat.2014.04.024

[12] Yambem SD, Haldar A, Liao KS, Dillon EP, Barron AR, Curran SA. Optimization of organic solar cells with thin film Au as anode. Solar Energy Materials and Solar Cells. 2011; 95(8):2424–2430. DOI:10.1016/j.solmat.2011.04.019

[13] Liu ZK, Li J, Yan F. Package-free flexible organic solar cells with graphene top electrodes. Advanced Materials. 2013; 25(31):4296–4301. DOI: 10.1002/adma.201205337

[14] Cao W, Zheng Y, Li Z, Wrzesniewski E, Hammond WT, Xue J. Flexible organic solar cells using an oxide/metal/oxide trilayer as transparent electrode. Organic Electronics. 2012; 13(11):2221–2228. DOI:10.1016/j.orgel.2012.05.047

[15] Trost S, Zilberberg K, Behrendt A, Polywka A, Reckers P, Maibach J, Mayer T, Riedl T. Overcoming the "light-soaking" issue in inverted organic solar cells by the use of Al: ZnO electron extraction layers. Advanced Energy Materials. 2013; 3(11):1437–1444. DOI: 10.1002/aenm.201300402

[16] Zhang C, Zhang J, Hao Y, Lin Z, Zhu C. A simple and efficient solar cell parameter extraction method from a single current-voltage curve. Journal of Applied Physics. 2011; 110(6):064504. DOI: http://dx.doi.org/10.1063/1.3632971

[17] Tan ST, Chen BJ, Sun XW, Fan WJ, Kwok HS, Zhang XH, Chua SJ. Blueshift of optical band gap in ZnO thin films grown by metal-organic chemical-vapor deposition. Journal of Applied Physics. 2005; 98(1):013505. DOI: http://dx.doi.org/10.1063/1.1940137

[18] Wei W, Zhang C, Chen D, Wang Z, Zhu C, Zhang J, Lu X, Hao Y. Efficient "light-soaking"-free inverted organic solar cells with aqueous solution processed low-temperature ZnO electron extraction layers. ACS Applied Materials and Interfaces. 2013; 5(24):13318–13324. DOI: 10.1021/am404291p

[19] Neamen DA. Semiconductor physics and devices: basic principles. 4th ed. Metal-Semiconductor and Semiconductor Heterojunctions. McGraw-Hill. New York. 2011. ISBN-10: 0073529583

[20] Chen D, Zhang C, Wang Z, Zhang J, Tang S, Wei W, Sun L, Hao Y. High efficient ITO free inverted organic solar cells based on ultrathin Ca modified AZO cathode and their

light soaking issue. Organic Electronics. 2014; 15(11):3006–3015. DOI:10.1016/j.orgel.2014.08.042

[21] Sennett R, Scott G. The structure of evaporated metal films and their optical properties. Journal of the Optical Society of America. 1950; 40(4): 203–210. DOI: 10.1364/JOSA.40.000203

[22] Wikipedia. Liebig's law of the minimum [internet]. 2016. Available from< https://en.wikipedia.org/wiki/Liebig%27s_law_of_the_minimum>

[23] Sergeant NP, Hadipour A, Niesen B, Cheyns D, Heremans P, Peumans P, Rand BP. Design of transparent anodes for resonant cavity enhanced light harvesting in organic solar cells. Advanced Materials. 2012; 24(6)728–732. DOI: 10.1002/adma.201104273

[24] Vitos L, Ruban A, Skriver HL, Kollar J. The surface energy of metals. Surface Science. 1998; 411(1–2):186–202. DOI: 10.1016/S0039-6028(98)00363-X

[25] S. Overbury, P. Bertrand, G. Somorjai. Surface composition of binary systems. Prediction of surface phase diagrams of solid solutions. Chemical Review. 1975; 75(5):547–560. DOI: 10.1021/cr60297a001

[26] Wang Z, Zhang C, Chen D, Tang S, Zhang J, Wang Y, Han G., Xu S, Hao Y. Flexible ITO-free organic solar cells based on MoO_3/Ag anodes. IEEE Photonics Journal, 2015; 7(1): 8400109. DOI: 10.1109/JPHOT.2015.2396906

Chapter 9

Copper Indium Gallium Selenide Thin Film Solar Cells

Yang Tang

Additional information is available at the end of the chapter

http://dx.doi.org/10.5772/65291

Abstract

The solar energy as one of the new energy sources and a regenerated energy is abundant and pollution-free. Most photovoltaic devices (solar cells) sold in the market today are based on silicon wafers, the so-called "first generation" technology. The market at present is on the verge of switching to a "second generation" of thin film solar cell technology which offers prospects for a large reduction in material costs by eliminating the costs of the silicon wafers. Cadmium telluride (CdTe), amorphous silicon (a-Si) and copper indium gallium selenide (CIGS) are three thin film technologies which have achieved commercial production. This chapter gives the review of the CIGS solar cells regarding the heterostructures, materials, technology and research advances. It also states the key findings in our research and provides suggestions for future research.

Keywords: Cu(In,Ga)(S,Se)2, solar cell, thin film, photon management, carrier collection, nanostructure

1. Introduction

Nowadays the development of the society and economy raises up the dependence upon the energy sources. However, the energy crisis and the environmental problems induced by using the fossil energy sources have attached much attention. A consensus about developing new energy as well as the reduction of the fossil energy consumption has been reached all over the world. The solar energy as one of the new energy sources and a regenerated energy is abundant and pollution-free. Photovoltaics (PV) is a method of generating electrical power through transforming solar energy into direct current electricity. The transformation is achieved by using semiconductors that exhibit the photovoltaic effect. The photovoltaic effect refers to photons of light exciting electrons into a higher state of energy, allowing them to act as charge carriers for an electric current. Most photovoltaic devices (solar cells) sold in the market today are based on

silicon wafers. There is an argument that the silicon solar cells are the so-called "first generation" technology. The market at present is on the verge of switching to a "second generation" of thin film solar cell technology which offers prospects for a large reduction in material costs by eliminating the costs of the silicon wafers. However, whether the thin film solar cell can be attributed to a "second generation" technology is still a controversial issue. Despite the debate, the silicon photovoltaic industry has reached its industrial maturity. The approach to progress further is to increase the efficiency as well as decrease the cost of the solar cells. The thin film photovoltaic technology is one of the potential alternative approaches.

Classification	Area (cm^2)[a]	Efficiency (%)	References
$Cu(In,Ga)Se_2$ (cell)	0.5 (unknown)	22.3	[2]
$Cu(In,Ga)Se_2$ (module)	808 (da)	17.5	[3]
CdTe (cell)	Unknown	22.1	[4]
CdTe (module)	Unknown	18.6	[5]
a-Si (cell)[b]	1.043 (da)	13.6	[6]
a-Si (module)[c]	14322 (t)	12.3	[7]
Dye sensitized (cell)	1.005 (da)	11.9	[8]
Dye sensitized (minimodule)	26.55 (da)	10.7	[8]
Organic (cell)	0.0429 (ap)	11.5	[9]
Organic (module)	802 (da)	8.7	[10]
Perovskite (cell)	Unknown	22.0	[11]

[a] ap = aperture area; da = designated illumination area (defined in [1]); t = total area.
[b] a-Si/nc-Si/nc-Si triple junction solar cell.
[c] a-Si/nc-Si tandem solar cell.

Table 1. The efficiency table of the thin-film solar cells.

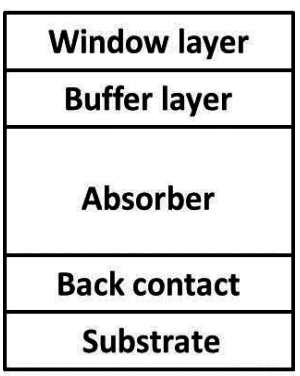

Figure 1. The cell structure of the $Cu(In,Ga)Se_2$ solar cell.

http://dx.doi.org/10.5772/65291

Currently three types of the thin film solar cells have realized industrialization. They are cadmium telluride (CdTe) solar cells, amorphous silicon (a-Si) solar cells and copper indium gallium diselenide (CIGS) solar cells. The other thin film technologies such as perovskite solar cells, dye-sensitized solar cells (DSSCs), organic solar cells and quantum-dot solar cells (QDSCs) remain in the stage of lab research or pilot line. The a-Si solar cells in the PV industry are fading away because of its relative low efficiency and instability. The CdTe and CIGS solar cells show the rapid development trend in recent years. **Table 1** presents the efficiencies of different thin film solar cells. Among them, the CIGS solar cells show the highest efficiency both in cells and modules.

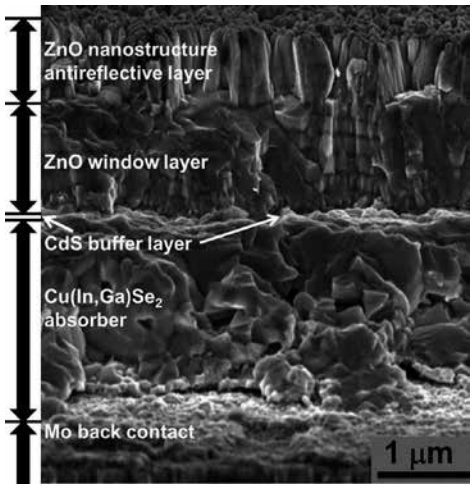

Figure 2. The image of the layers in the CIGS solar cell by scanning electron microscopy.

The structure of the CIGS solar cells is shown in **Figure 1**. The CIGS solar cells consist of a number of films which are deposited onto a rigid or flexible substrate. The first film, typically molybdenum (Mo), serves as a nontransparent back-contact. It is covered by the actual $Cu(In,Ga)Se_2$ film. Most of the light is absorbed by the p-type thin film (absorber) and the photocurrent is generated. The heterojunction is formed by depositing a very thin n-type buffer layer (typically CdS) and an n-type wide gap transparent window layer (usually heavily doped ZnO). **Figure 2** presents the actual image of the layers in the CIGS solar cell, which is measured by a scanning electron microscopy (SEM). From the bottom to the top, they are Mo back contact layer, $Cu(In,Ga)Se_2$ absorber layer, a very thin CdS buffer layer, the ZnO window layer and ZnO nanostructure antireflective coating layer.

2. Fundamental properties of the key materials

The definition of the thin-film given by Chopra et al. [12] provides a good starting point and also yields a criterion to discriminate the term 'thin film' from 'thick film'. According to their

opinion, a thin film is defined as a material that is created ab initio by the random nucleation and growth processes of individually condensing/reacting atomic/ionic/molecular species on a substrate. Thin films may encompass a considerable thickness range, varying from a few nanometers to tens of micrometers and thus are best defined in terms of the production processes rather than by thickness. The layers for constructing the CIGS solar cells are back contact layer, absorber layer, buffer layer and window layer.

2.1. Back contact layer

The back contact layer as the back contact electrode of the solar cell is usually deposited on the substrate such as glass or flexible foils. One of the key requirements for the back contact layer is that the contact between the back contact and the absorber layer should be ohmic contact. The back contact layer should have a good conductivity and can be adhered to substrate firmly in order to make the solar cell stable. Molybdenum (Mo) is used in the majority of the CIGS solar cells. The structural and morphological properties of the Mo thin films will greatly affect the sequent growth of the absorber layer.

2.2. Absorber layer

The absorber layer is deposited on the back contact layer. $CuInSe_2$ (CIS) was the first absorber layer developed in the 1970s. In the next two decades gallium was introduced into the absorber layer, resulting in the deposition of the $Cu(In,Ga)Se_2$ thin films. The invention of the new generation absorber layer boosted the solar cells' efficiency by increasing the absorber's band gap. In addition, the possibility of fabricating graded band gap $Cu(In,Ga)Se_2$ absorber layer further increased the device efficiency. Several other improvements were developed such as the thinner CdS buffer layer (less than 50 nm) and the use of the soda lime glass during this period. These technologies resulted in the progress of the $Cu(In,Ga)Se_2$ absorber layer's performance.

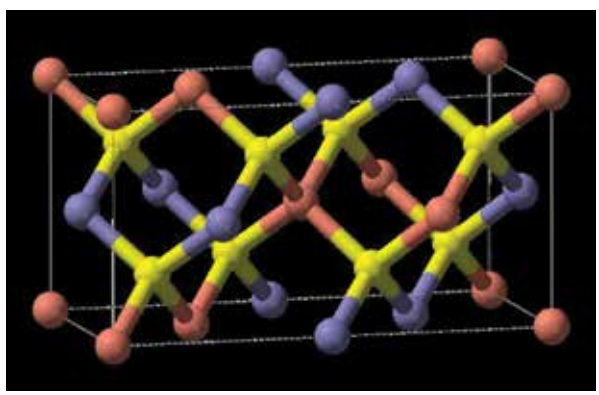

Figure 3. The $Cu(In,Ga)Se_2$ crystal structure. Red = Cu, yellow = Se, blue = In/Ga [13].

The $Cu(In,Ga)Se_2$ material possesses a chalcopyrite crystal structure which is shown in **Figure 3**. Each anion (Se) is coordinated by two cations of each type (Cu, In/Ga). The $Cu(In,Ga)Se_2$ is obtained by partially replacing indium in a CIS structure with Ga. Since the atomic radii of the Ga are smaller than In, the lattice constants will be decreased with increasing Ga content.

The band gap of the $Cu(In,Ga)Se_2$ material depends on the ratio of Cu/(In + Ga). The band gaps of $CuInSe_2$ and $CuGaSe_2$ are 1.02 and 1.67 eV, respectively. The band gap of the $Cu(In,Ga)Se_2$ varies between 1.02 and 1.67 eV by the change in Ga/(In + Ga) ratio.

2.3. Buffer layer

The buffer layer is deposited on the absorber layer. CdS is the most widely used buffer layer in the CIGS solar cells. CdS is an n-type semiconductor with a band gap of ~2.4 eV. The buffer layer improves the CIGS solar cells' performance by forming the optimized band alignment between the absorber layer and the window layer. In addition, the buffer layer possesses more advantages to the CIGS solar cells such as the damage prevention of the absorber layer in the sequent sputtering process, the passivation of the absorber surface, the relief of the lattice misfit and so on. Besides CdS, more new buffer layers are in the development process. For example, the new buffer layers include Zn(S,O), ZnMgO, ZnS and In_2S_3. Since the research on the new buffer layers is a hotspot in the development of the CIGS solar cell in recent years, one can search a lot of published papers regarding the new generation Cd-free buffer layers and some of them showed great progress.

2.4. Window layer

As the window layer, ZnO is deposited on the buffer layer in the CIGS solar cells. ZnO is not really a newly discovered material. Research on ZnO has continued for many decades with interest. In terms of its characterization, reports go back to 1935 or even earlier. For example, lattice parameters of ZnO were investigated for many decades [14–18].

Most of the group II–VI binary compound semiconductors crystallize in either cubic zinc blende or hexagonal wurtzite structure where each anion is surrounded by four cations at the corners of a tetrahedron, and vice versa. **Figure 4** depicts three kinds of crystal structures shared by ZnO which are rocksalt, zinc blende and wurtzite [19]. The zinc-blende ZnO structure can be stabilized only by growth on cubic substrates, and the rocksalt structure may be obtained at relatively high pressures [18].

The wurtzite structure has a hexagonal unit cell with two lattice parameters, a and c, in the ratio of $c/a = \sqrt{8/3} = 1.633$ and belongs to the space group of C_{6v}^4 or P63mc. In a real ZnO crystal, the lattice parameters deviate from the ideal value due to the existence of the Zn interstitials, O vacancies and dislocations in the crystal structure. The properties vary with different material types (bulk material, thin films, powders and nanostructures) and different synthesis processes.

The window layers in the CIGS solar cells usually are consisted of two layers. The first layer deposited on the buffer layer is the intrinsic ZnO thin films. In the following an aluminum-doped ZnO (AZO) layer is deposited on the undoped ZnO layer. The AZO layer processing high conductivity will be used as the front contact for a CIGS module.

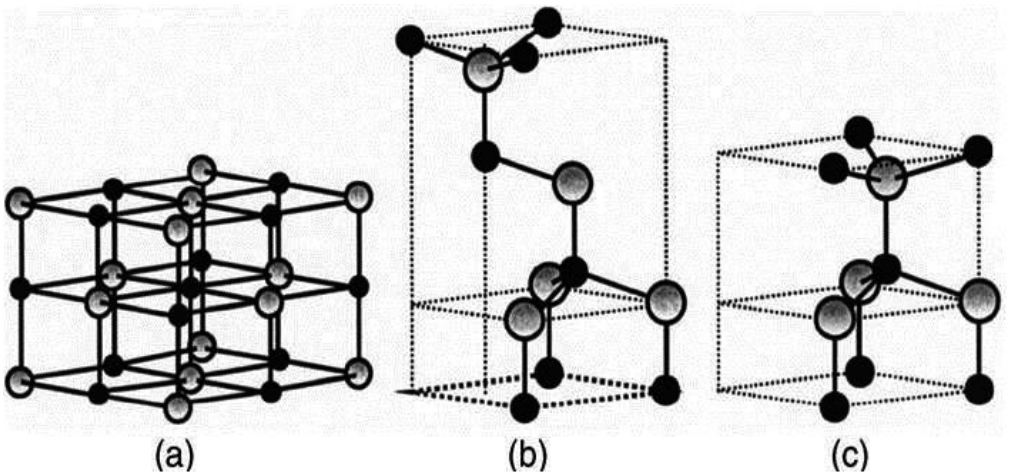

Figure 4. Stick and ball representation of ZnO crystal structures: (a) cubic rocksalt, (b) cubic zinc blende, (c) hexagonal wurtzite. The shaded gray and black spheres denote Zn and O atoms, respectively [19]. Copyright 2005 by AIP Publishing LLC.

3. Technology of the CIGS solar cells

The term "photo-voltaic" has been in use in English since 1849. A photovoltaic cell (also called a solar cell) is an electrical device that converts the energy of light directly into electricity by the photovoltaic effect [20]. The operation of a solar cell requires three basic attributes. At first, the absorption of light generates either electron-hole pairs or excitons. Afterwards, various types of charge carriers are separated. Finally, those carriers are extracted to an external circuit. Conventionally, photovoltaic materials use inorganic semiconductors. Ideally, the absorber material of an efficient solar cell should be a semiconductor with a bandgap of 1–1.5 eV with a high solar optical absorption (10^4 to 10^5 cm^{-1}) in the wavelength region of 350–1000 nm, a high quantum yield for the excited carriers, a long diffusion length and low recombination velocity [21].

The magnetron sputtering is extensively used to deposit the Mo back contact layer and the ZnO window layer. The CdS buffer layer is usually fabricated by a chemical bath deposition method. Several more methods such as atomic layer deposition and spray ion layer gas reaction technique have been adopted to obtain the new buffer layers. Several techniques were developed to fabricate $Cu(In,Ga)Se_2$. Among them the coevaporation method and the two-stage process are two of the most important techniques.

http://dx.doi.org/10.5772/65291

3.1. Coevaporation process

The brief setup of the coevaporation process is shown in **Figure 5**. During the process, Cu, In, Ga and Se sources are heated and evaporated to be grown on a heated substrate. The heating temperature is specific for each source. The temperature for Cu, In and Ga is higher than that for Se. It is very important to control the element flux in the coevaporation process. The in-situ feedback controls based on electron impact emission spectrometry, quadruple mass analysis or atomic absorption spectrometry have been successfully adopted to control the element flux. Although the progress for the coevaporation process is in rapid development, the problems regarding the process control in the absorber deposition remain to be improved.

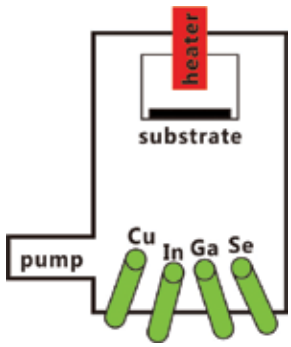

Figure 5. The setup of the coevaporation process.

3.2. Two-stage process

The two-stage process was invented by Boeing company. For the first stage, a stack of precursor layers including the Cu, In and Ga metals is deposited. In the following stage, the deposited precursor alloy layers are transferred to a furnace or a specific reaction setup for selenization. Either H_2Se gas or Se powders are used for selenization process. **Figure 6** shows the brief setup of the selenization furnace.

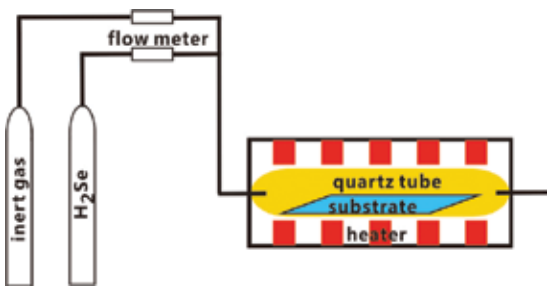

Figure 6. The setup of the selenization furnace.

4. Recent research advances

The approach to progress further is to increase the efficiency as well as decrease the cost of the solar cells. Therefore new concepts and new cell structures should be brought in the development of the film solar cells. One of the plausible solutions is to implant nanostructures in the conventional thin film photovoltaic devices. Zinc oxide (ZnO) nanorod arrays are one of the nanostructures that can be implanted in the solar cells. ZnO nanostructures can be grown on top of the CIGS solar cells' window layers as an antireflective coating layer or implanted into the solar cells. On the one hand, the implanted nanostructures will decrease the reflection and increase the light path due to light coupling effects. On the other hand, the ZnO nanostructures will put the electrode close to the photoinduced carrier generation area with larger carrier collection function. It will assist in boosting the solar cells' efficiency by carrier collection enhancement.

4.1. Photon management

Thin film photovoltaic device technology relies on light management to enhance light absorption in thin absorber layers. One of the plausible solutions is to implant nanostructures in the conventional thin film photovoltaic devices. For example, the zinc oxide (ZnO) nanorod arrays can be implanted in the CIGS solar cells. The use of the ZnO nanorods in the thin film solar cells is an effective way to decrease the reflection. The variation of the geometrical parameters of the ZnO nanorods, such as the diameter, the height and the density can lead to an optimum which results in the maximal absorption in the absorber. An approach of a rigorous three-dimensional (3D) modeling based on the finite element method (FEM) can be used to simulate and optimize the light absorption in the $Cu(In,Ga)Se_2$ absorbers with nanostructures.

Modeling the optical properties of the $Cu(In,Ga)Se_2$ absorbers with nanostructures starts by defining the characteristics of the incident light. In the stationary case, the electric and magnetic field can be expressed as follows.

$$\boldsymbol{E}(x,y,z,t) = \tilde{\boldsymbol{E}}(x,y,z)e^{-i\omega t} \tag{1}$$

$$\boldsymbol{H}(x,y,z,t) = \tilde{\boldsymbol{H}}(x,y,z)e^{-i\omega t} \tag{2}$$

where $\boldsymbol{E}$ is the electric field, $\boldsymbol{H}$ is the magnetic field and ω is the angular frequency related by $\omega = 2\pi f$ to the frequency f of light. The mathematical model of the light propagation is Maxwell's equation:

$$\boldsymbol{E}(x,y,z,t) = \tilde{\boldsymbol{E}}(x,y,z)e^{-i\omega t} \tag{3}$$

http://dx.doi.org/10.5772/65291

$$\nabla \cdot \boldsymbol{H} = 0 \tag{4}$$

$$\nabla \times \boldsymbol{E} = -\frac{\partial \mu \boldsymbol{H}}{\partial t} \tag{5}$$

$$\nabla \times \boldsymbol{H} = \boldsymbol{J} + \frac{\partial \epsilon \boldsymbol{E}}{\partial t} \tag{6}$$

where $\boldsymbol{E}$ is the electric field, $\boldsymbol{H}$ is the magnetic field, ρ is the electric charge density, ε is the permittivity, μ is the magnetic permeability and $\boldsymbol{J}$ is the current density. In the time harmonic case the magnetic field can be determined by the electric field and vice versa. From Maxwell's equations we can find

$$\boldsymbol{H} = -\frac{1}{i\omega \in} \nabla \times \boldsymbol{E} \tag{7}$$

$$\boldsymbol{E} = \frac{1}{i\omega \in} \nabla \times \boldsymbol{H} \tag{8}$$

Thus the electric field in the electromagnetic will be taken into account in the simulation. The electric field distribution of the incident light is described by unpolarized stationary plane waves.

$$\tilde{\boldsymbol{E}} = Ae^{i(\boldsymbol{k}\cdot\boldsymbol{r}+\varphi)} \tag{9}$$

where A is the constant, $\boldsymbol{k}$ is the wave vector, $\boldsymbol{r}$ is the position vector and ϕ is the phase angle. For simplifying the simulation, the wave vector of the incident light is perpendicular to the surface of the Cu(In,Ga)Se_2 absorbers and φ is taken as 0.

The nanorod arrays as a light coupling component can be incorporated into two types of solar cells, i.e., the bifacial solar cells and the superstrate solar cells. As shown in **Figure 7(a)**, both sides of the bifacial solar cells are illuminated and the ZnO nanorods work as a light-coupling component and a nanocontact electrode. The intrinsic ZnO nanorods in the superstrate solar cells play a buffer role. Optionally a buffer layer can be inserted between the ZnO nanorods and the absorber in the superstrate solar cells. Since both the bifacial and superstrate solar cells possess the same components which are glass/transparent conductive oxides/ZnO nanorods/ Cu(In,Ga)Se_2 absorber, the same components are regarded as the simulated structure. As illustrated in **Figure 7(c)**, the simulated structure can be divided into two parts: the glass and the transparent conductive oxides/ZnO nanorods/Cu(In,Ga)Se_2 absorber (TNA) structure.

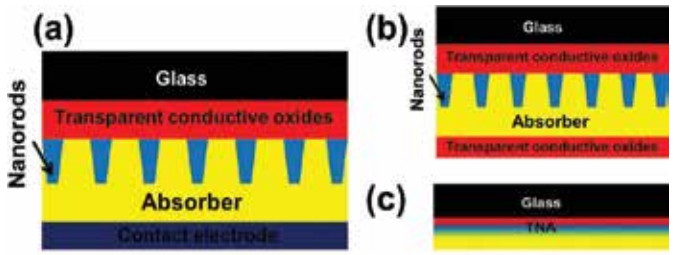

Figure 7. (a) The schematic structure of the bifacial Cu(In,Ga)Se_2 solar cell. (b) The schematic structure of the superstrate Cu(In,Ga)Se_2 solar cell. (c) The schematic drawing of the simulated structure. The TNA is the abbreviation for the transparent conductive oxides/nanorods/absorber.

As shown in **Figure 8**, the total reflection consists of the specular reflectance and the scattered reflectance:

$$R^{Total} = R^S + R^{SC} \tag{10}$$

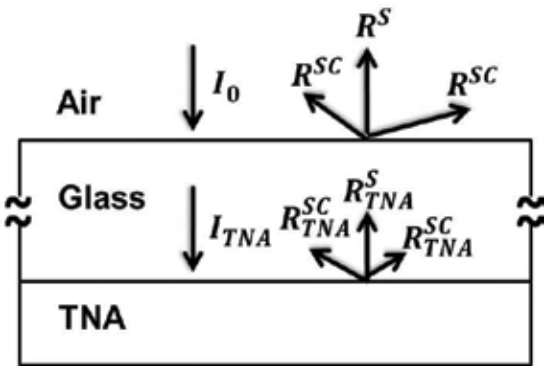

Figure 8. The schematic structure of the simulated structure. The structure is illuminated through the glass side. The figure defines the incident light intensity I_0, the specular intensity I_{TNA} illuminating the glass/TNA interface, the specular reflectance R^s the scattered reflectance , R^{sc} the specular reflectance of the R^s_{TNA} structure and the scattered reflectance of the R^{sc}_{TNA} structure.

where R^S and R^{SC} are the specular reflectance and the scattered reflectance, respectively. The specular reflectance is given as:

$$R^S = R_{glass} + \left(1 - R_{glass}\right)^2 \cdot \tau^2_{glass} \cdot R^S_{TNA} \cdot \sum_{u=0}^{\infty} \left[R_{glass} \cdot \tau^2_{glass} \cdot R^S_{TNA} \right]^u \tag{11}$$

where R_{glass} is the reflectance at the air/glass interface with the incident of light illuminating the interface, τ_{glass} is the absorptance of the thick glass and R^S_{TNA} is the reflectance of the TNA structure illuminated from the glass. The R_{glass} is calculated from the Fresnel's equation:

http://dx.doi.org/10.5772/65291

$$R_{glass} = \left| \frac{\boldsymbol{n}_{glass} - 1}{\boldsymbol{n}_{glass} + 1} \right|^2 \tag{12}$$

$$\boldsymbol{n}_{\boldsymbol{glass}} = n + i \cdot k \tag{13}$$

where $\boldsymbol{n}_{glass}$ is the complex refractive index of the glass, n is the refractive index of the glass and k is extinction coefficient of the glass. The τ_{glass} is calculated as:

$$\tau_{glass} = exp\left(-\alpha_{glass} \cdot d_{glass}\right) \tag{14}$$

$$\alpha_{glass} = \frac{4\pi k}{\lambda 0} \tag{15}$$

where α_{glass} is the optical absorption coefficient of the glass and λ_0 is the vacuum wavelength of light.

The reflection, transmission and absorption in TNA structure can be calculated using the finite element method (FEM) method. The FEM is a numerical technique used in finding solutions of Maxwell equations. The volume of the simulated structure is meshed and electromagnetic field components are computed. Once the simulation of the design (structure, boundary conditions, light sources and frequency range) is set up, FEM process operates through three steps: meshing, solving and postprocessing. In the first step, for a given wavelength, the volume of the designed structure is discretized. During the second step, the resulting system of the equations is solved. In the third step, the reflection, transmission and absorption of the simulated structure is computed. The reflectance R_{TNA} is given by:

$$R_{TNA} = R_{TNA}^{S} + R_{TNA}^{SC} \tag{16}$$

where R_{TNA}^{SC} is the scattered reflectance of the TNA structure. Since tracing the scattered reflected light of the TNA structure in the thick glass and air/glass interface dramatically boosts the computation amount, it is not possible to get the results using FEM. The total reflectance is approximately calculated as:

$$R^{Total} = R_{glass} + R_{TNA} \tag{17}$$

4.2. Nanostructures

An antireflective or antireflection coating (ARC) is a type of optical coating applied to the surface of lenses and other optical devices to reduce reflection. This improves the efficiency of the system since less light is lost. The ARC is generally made of a dielectric layer, e.g., MgF_2, SiN, TiO_2 or ZnS, with a thickness of a quarter-wavelength [22–25]. Another approach of

boosting light coupling is to structure the surface of the solar cells by means of the moth-eye effect. Moths' eyes have an unusual property: their surfaces are covered with a natural nanostructured film which eliminates reflections. The ZnO nanorods have an appropriate refractive index of ~2. Coating an absorber surface leads to continuously varying refractive index profiles in the tapered ZnO nanorods. Consequently they suppress the surface reflection via a subwavelength structure. Therefore the tapered ZnO nanorods are a promising light coupling layer for ARC of solar cells as well as solar thermal selective surfaces.

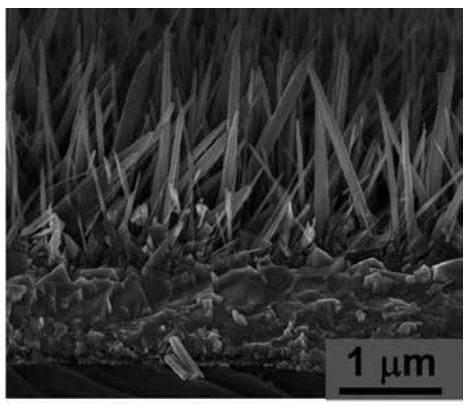

Figure 9. The ZnO nanowire arrays prepared by the hydrothermal method.

Figure 2 has shown the cross section scanning electron microscopy (SEM) images of ZnO nanorods on CIGS. The ZnO nanorod arrays serving as an ARC were electrodeposited on thin film Cu(In,Ga)Se_2 solar cells. According to the research, the weighted reflectance was reduced from 8.6 to 3.5%. Highest increases in both the saturation-current of 5.7% and the solar cells efficiency of 7.2% were achieved [26]. In addition, the ZnO nanorod arrays have been incorporated into a superstrate or a bifacial cell structure of the other thin film photovoltaic devices such as DSSCs [27], QDSCs [28] and organic solar cells [29].

ZnO nanostructures have been prepared by various methods [30–46]. The solution-based fabrication routes including hydrothermal method and electrochemical deposition (ECD) method are the only ways to grow ZnO nanostructures at a low temperature down to the range between 60°C and 90°C [35–46]. Meanwhile the growth can be achieved over large areas up to 10 cm × 10 cm [44–46]. **Figure 9** shows the SEM image of the ZnO nanowire arrays prepared by the hydrothermal method.

The ECD technique consists of an electrochemical cell and accessories for providing a galvanic current which flows through the electrochemical cell. The cell usually contains electrolyte and electrodes. The first of these electrodes has been named the anode. At an anode, electrons go away from the electrolyte to the anode. Hence, an anodic reaction must generate electrons. The second has been named the cathode. The cathode supplies electrons to the positively charged cations which flow to it from the electrolyte. Within the electrolyte, the current flow is always from the anode to the cathode, which means the electron transports from the cathode to the

anode. In the external parts of the closed circuit ("external" relative to the electrolyte), the current flow is from cathode to anode, which equates the electron transport from the anode to the cathode [47].

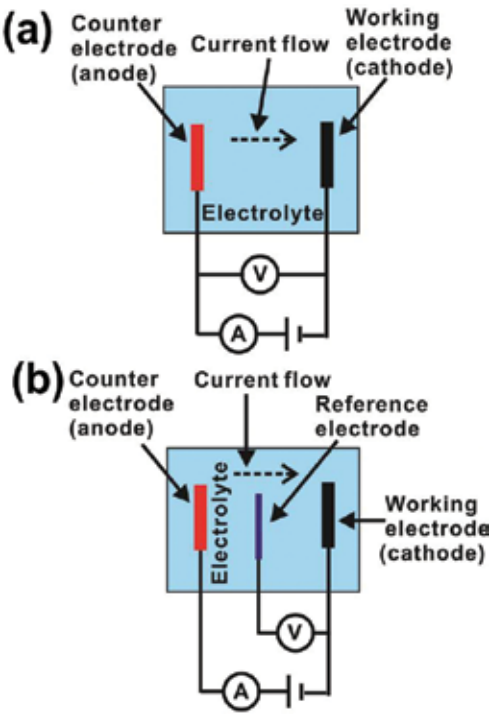

Figure 10. (a) Two-electrode system and (b) three-electrode system.

During the ECD process, the electrodeposited products are deposited on one of the electrodes. The electrode is the working electrode (WE). However, the WE is not enough for the ECD process. At least another electrode is necessary for allowing current to flow. In the simplest case a two-electrode cell is used for ECD (**Figure 10(a)**). The second electrode is used both as the reference electrode (RE) to measure the WE potential and as a counter electrode (CE) to allow current to flow. However, the potential of the second electrode changes accordingly when there is a current flow, which has been termed electrode polarization. In order to measure the accurate WE potential, a three-electrode cell containing a WE, a CE and a RE is more common (**Figure 10(b)**). A current flows between the WE and CE, while the potential of the WE is measured against the RE. No current flows in the circuit of the RE/WE, which therefore is not polarized [48]. The glass substrates coated by FTO and AZO transparent conductive oxides are used as the WE. The electrochemical cell was placed in a thermoregulated bath. The liquid electrolyte contains zinc salts and additives. During the experiments the liquid electrolyte in which there is a magnetic stirring bar is agitated. A schematic illustration of the setup for the ECD process is shown in **Figure 11**. The electrochemical process is controlled and recorded by a potentiostat/galvanostat.

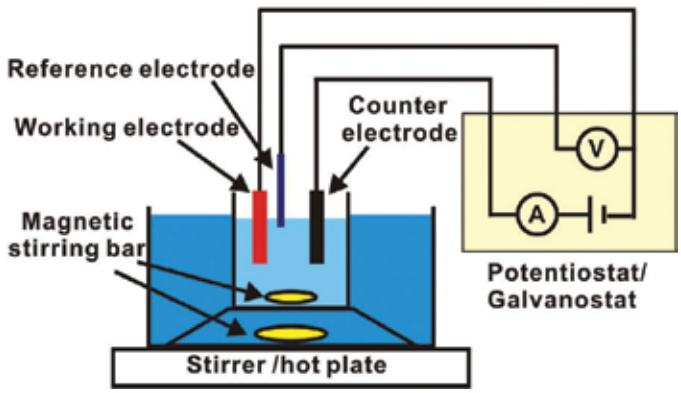

Figure 11. Schematic description of the electrochemical deposition setup.

5. Conclusion

This chapter gives the review of the CIGS solar cells regarding the heterostructures, materials, technology and research advances. The CIGS solar cells consist of a number of films which are deposited onto a rigid or flexible substrate. Mo deposited by magnetron sputtering serves as a nontransparent back-contact. The Mo film is covered by the actual Cu(In,Ga)Se_2 film. The coevaporation method and the two-stage process are two of the most important techniques to fabricate Cu(In,Ga)Se_2. The heterojunction is formed by depositing a very thin n-type buffer layer (typically CdS) and an n-type wide gap transparent window layer (usually heavily doped ZnO). The CdS buffer layer is usually fabricated by a chemical bath deposition method. The magnetron sputtering is extensively used to deposit the ZnO window layer. The chapter also states the key findings in our research and provides suggestions for future research. One of the plausible solutions for boosting solar cells' efficiency is to implant nanostructures such as ZnO nanorod arrays in the conventional thin film photovoltaic devices. ZnO nanostructures can be grown on top of the CIGS solar cells' window layers as an antireflective coating layer or implanted into the solar cells. On one hand, the implanted nanostructures will decrease the reflection and increase the light path due to light coupling effects. On the other hand, the ZnO nanostructures will put the electrode close to the photoinduced carrier generation area with larger carrier collection function. It will assist in boosting the solar cells' efficiency by carrier collection enhancement.

6. Outlook

In the past four decades, the CIGS thin film solar cells have developed steadily. The lab efficiency of the CIGS solar cells has reached to as high as 22.6% [2]. However, the journey to successful large-scale commercialization is going through fire and water. Nowadays the silicon

photovoltaic industry has entered its maturity stage from the industry life cycle point of view. It is ambiguous to estimate that whether the CIGS thin film solar cell is in its introduction stage or in a growth stage. Since very few CIGS companies survive in such an intensively competitive photovoltaic market, it is difficult to conclude that the CIGS is in a growth stage. It is worth noting that new concept solar cells such as the perovskite solar cells are in an astonishing development in recent years, which might make the club of the thin film solar cells more uncertain. The prospect for the CIGS thin film solar cells is facing challenges coming from both the technology and market. For achieving the great expectation of the CIGS photovoltaics, there is still a long way to go.

Acknowledgements

This work was supported by the Beijing Talent Cultivation Support Program for the Top Young Talents in Natural Science (2015000021223ZK38) and the National Natural Science Foundation of China under Grant No. 61404007.

Author details

Yang Tang

Address all correspondence to: tangy118@hotmail.com

National Institute of Clean-And-Low-Carbon Energy, Future Science & Technology City, Beijing, People's Republic of China

References

[1] Green M A, Emery K, Hishikawa Y, Warta W, Dunlop ED. Solar cell efficiency tables (Version 39). Progress in Photovoltaics: Research and Applications, 2011; 20: 12–20. DOI: 10.1002/pip.2163

[2] Press release, ZSW, June 15, 2016.

[3] Sugimoto H. High efficiency and large volume production of CIS-based modules. 40th IEEE photovoltaic Specialists Conference, Denver, June 2014.

[4] Press Release, First solar, February 23, 2016.

[5] Press Release, First solar, July 15, 2015.

[6] Sai H, Matsui T, Koida T, Matsubara K, Kondo M, Sugiyama S, Katayama H, Takeuchi Y, Yoshida I, Triple-junction thin-film silicon solar cell fabrication on periodically

textured substrate with a stabilized efficiency of 13.6%. Applied Physics Letters, 2015; 106: 213902. DOI: 10.1063/1.4921794

[7] Tel solar press release, July 9, 2014.

[8] Komiya R, Fukui A, Murofushi N, Koide N, Yamanaka R, Katayama H, Improvement of the conversion efficiency of a monolithic type dye-sensitized solar cell module, Technical Digest, 21st International Photovoltaic Science and Engineering Conference, Fukuoka, November 2011, 2C-5O-08.

[9] Hu H, Jiang K, Yang G, Li Z, Lin H, Liu Y, Zhao J, Zhang J, Huang F, Qu Q, Ma W, Yan H. Terthiophene-based D-A polymer with an asymmetric arrangement of alkyl chains that enables efficient polymer solar cells. Journal of the American Chemical Society, 2015; 137 (44), 14149–14157. DOI: 10.1021/jacs.5b08556

[10] Hosoya M, Oooka H, Nakao H, Gotanda T, Mori S, Shida N, Hayase R, Nakano Y, Saito M. Organic thin film photovoltaic modules. Proceedings of the 93rd Annual Meeting of the Chemical Society of Japan, 2013; 21–37.

[11] http://www.nrel.gov/ncpv/images/efficiency_chart.jpg

[12] Chopra K L, Paulson P D, Dutta V, Thin-film solar cells: an overview. Progress in Photovoltaics: Research and Applications, 2004; 12: 69–92. DOI: 10.1002/pip.541

[13] https://commons.wikimedia.org/wiki/File:Chalcopyrite-unit-cell-3D-balls.png

[14] Bunn C W. Proceedings of the Physical Society London, 1935; 47: 835.

[15] Heller R B, McGannon J, Weber A H. Precision determination of the lattice constants of zinc oxide. Journal of Applied Physics, 1950; 21: 1283. DOI: 10.1063/1.1699591

[16] Gray T J. Journal of the American Ceramic Society, 1954; 37: 534.

[17] Mohatny G P, Azaroff L V. Electron density distributions in ZnO crystals. The Journal of Chemical Physics, 1961; 35: 1268. DOI: 10.1063/1.1732035

[18] Reeber R R. Journal of Applied Physics, 1970; 41: 506.

[19] Özgür Ü, Alivov Y I, Liu C, Teke A, Reshchikov M A, Dogan S, Avrutin V, Cho S J, Morkoc H. A comprehensive review of ZnO materials and device. Journal of Applied Physics, 2005; 98: 041301. DOI: 10.1063/1.1992666.

[20] http://en.wikipedia.org/wiki/Solar_cell

[21] Poormans J, Arkhipov V. Thin Film Solar Cells Fabrication, Characterization and Applications, John Wiley & Sons Ltd, England, 2006, p. xix.

[22] Richards B S, Comparison of TiO_2 and other dielectric coatings for buried-contact solar cells: a review. Progress in Photovoltaics, 2004; 12: 253. DOI: 10.1002/pip.529

[23] Aberle A G, Overview on SiN surface passivation of crystalline silicon solar cells. Solar Energy Materials and Solar Cells, 2001; 65: 239. DOI: 10.1016/S0927-0248(00)00099-4

[24] Doshi P, Jellison G E, Rohatgi A. Characterization and optimization of absorbing plasma-enhanced chemical vapor deposited antireflection coatings for silicon photovoltaics. Applied Optics, 1997; 36: 7826. DOI: 10.1364/AO.36.007826

[25] Ramanathan K, Contreras M A, Perkins C L, Asher S, Hasoon F S, Keane J, Young D, Romero M, Metzger W, Noufi R, Ward J, Duda A. Progress in Photovoltaics 2003; 11: 225. DOI: 10.1002/pip.494

[26] Ae L, Kieven D, Chen J, Klenk R, Rissom Th, Tang Y, Lux-Steiner M Ch. Progress in Photovoltaics: Research and Applications, 2010; 18: 209-213. DOI: 10.1002/pip.946

[27] Law M, Greene L E, Johnson J C, Saykally R, Yang P. Nanowire dye-sensitized solar cells. Nature Materials, 2005; 4: 455-45. DOI:10.1038/nmat1387

[28] Sun X W, Chen J, Song J L, Zhao D W, Deng W Q, Lei W. Ligand capping effect for dye solar cells with a CdSe quantum dot sensitized ZnO nanorod photoanode. Optics Express, 2010; 18: 1296-1301. DOI: 10.1364/OE.18.001296

[29] Olson D C, Shaheen S E, Collins R T, et al. The effect of atmosphere and ZnO morphology on the performance of hybrid poly(3-hexylthiophene)/ZnO nanofiber photovoltaic devices. Journal of Physical Chemistry C, 2007; 111: 16670-16678. DOI: 10.1021/jp0734225

[30] Kim H W, Kim N H, Shim J H, Cho N H, Lee C. Catalyst-free MOCVD growth of ZnO nanorods and their structural characterization. Journal of Materials Science: Materials in Electronics, 2005; 16: 13.

[31] Park W I, Yi G C, Jang H M. Metal-organic vapor phase epitaxial growth of high-quality ZnO films on Al_2O_3(001). Journal of Materials Research, 2001; 16: 1358. DOI: 10.1557/JMR.2001.0190

[32] Huang M H, Wu Y, Feick H, Tran N, Weber E, Yang P. Catalytic growth of zinc oxide nanowires by vapor transport. Advanced Materials, 2001; 13: 113. DOI: 10.1002/1521-4095(200101)13:2<113::AID-ADMA113>3.0.CO;2-H

[33] Umar A, Kim S H, Suh E-K, Hahn Y B. Nanotechnology, 2006, 17, 4072.

[34] He J H, Wang C W, Liao K F, Chen L J. Advances in Science and Technology, 2006, 51, 38.

[35] Izaki M, Omi T. Transparent zinc oxide films prepared by electrochemical reaction. Applied Physics Letters, 1996; 68: 2439-2440. DOI: 10.1063/1.116160

[36] Izaki M, Omi T, Structural and optical properties of single-crystalline ZnO nanorods grown on silicon by thermal evaporation. Journal of The Electrochemical Society, 1996; 143: L53-55. DOI: 10.1088/0957-4484/17/16/013

[37] Lan C J, Cheng H Y, Chung R J, Li J H, Kao K F, Chin T S, Bi-doped ZnO layer prepared by electrochemical deposition. Journal of The Electrochemical Society, 2007; 154: D117-D12. DOI: 10.1149/1.2422887

[38] Yang J, Qiu Y, Yang S. Studies of electrochemical synthesis of ultrathin ZnO nanorod/nanobelt arrays on Zn substrates in alkaline solutions of amine-alcohol mixtures. Crystal Growth & Design, 2007; 7: 2562-2567. DOI: 10.1021/cg070513i

[39] Chen J, Ae L, Aichele Ch, Lux-Steiner M Ch. High internal quantum efficiency ZnO nanorods prepared at low temperature. Applied Physics Letters, 2008, 92, 161906. DOI: 10.1063/1.2910769

[40] Vayssieres L, Keis K, Lindquist S E. Purpose-built anisotropic metal oxide material: 3D highly oriented microrod array of ZnO. The Journal of Physical Chemistry B, 2001; 105: 3350. DOI: 10.1021/jp010026s

[41] Schmidt-Mende L, MacManus-Driscoll J L. ZnO – nanostructures, defects, and devices. Materials Today, 2007; 10: 40. DOI: 10.1016/S1369-7021(07)70078-0

[42] Ashfold M N R, Doherty R P, Ndifor-Angwafor N G, Riley D J, Sun Y. The kinetics of the hydrothermal growth of ZnO nanostructures. Thin Solid Films, 2007; 515: 8679. DOI: 10.1016/j.tsf.2007.03.122

[43] Govender K, Boyle D S, Kenway P B, O'Brien P. Understanding the factors that govern the deposition and morphology of thin films of ZnO from aqueous solution. Journal of Materials Chemistry, 2004; 14: 2575. DOI: 10.1039/B404784B

[44] Greene L E, Law M, Goldberger J. Low-temperature wafer-scale production of ZnO nanowire arrays. Angewandte Chemie International Edition, 2003, 42, 3031-3034. DOI: 10.1002/anie.200351461

[45] Tak Y, Yong K. Controlled growth of well-aligned ZnO nanorod array using a novel solution method. The Journal of Physical Chemistry B, 2005; 109: 19263-19269. DOI: 10.1021/jp0538767

[46] Lin C-C, Chen H-P, Liao H-C, Chen S-Y. Enhanced luminescent and electrical properties of hydrogen-plasma ZnO nanorods grown on wafer-scale flexible substrates. Applied Physics Letters, 2005, 86, 183103. DOI: 10.1063/1.1904715

[47] Bagotsky V S. Fundamentals of Electrochemistry, John Wiley & Sons, Inc., New Jersey, 2006, second edition, p. 10.

[48] Bagotsky V S. Fundamentals of Electrochemistry, John Wiley & Sons, Inc., New Jersey, 2006, second edition, p. 191.

[49] Shiosaki T, Ohnishi S, Hirokawa Y, Kawabata A. Applied Physics Letters, 1978, 33, 406. DOI: 10.1063/1.90393

Section 4

Nano-Structure Solar Cells - Perovskite Solar Cells

Chapter 10

ZnO-Based Electron Transporting Layer for Perovskite Solar Cells

Lung-Chien Chen and Zong-Liang Tseng

Additional information is available at the end of the chapter

http://dx.doi.org/10.5772/65056

Abstract

Recently, organic/inorganic hybrid perovskite materials, $APbX_3$ (A = CH_3NH_3 or $HC(NH_2)_2$; X = I, Br or Cl), have attracted much interest for their promising application in solar cells as the light-absorbing component to their broad spectral absorption, strong light-harvesting and long exciton diffusion length. The perovskite solar cells (PSCs) can reduce the production costs and achieve high power conversion efficiency significantly compared to standard silicon cells and other thin film cells. On the other hand, ZnO based materials have been recently investigated in the PSCs devices as electron injection layers for low-temperature, low-cost and flexible devices. This chapter aims to review PSCs using ZnO materials as electron extraction layers. We will discuss the electron transmission and effect of the electron-transporting layer in PSCs and the preparation method of the ZnO. ZnO is a potential material for many applications due to their high electron mobility, transparent and various nanostructure. The ZnO was introduced into the PSCs structure to improve electron extraction efficiency. This chapter summaries the effect and parameters of PSCs based on the ZnO layer/nanostructure prepared by several methods as electron transport layers.

Keywords: perovskite, solar cell, ZnO, photovoltaic, hybrid

1. Introduction

Lead halide perovskites materials have been well known for many years [1], but the first incorporation into photovoltaic applications was reported by Miyasaka et al. in 2009 [2]. The lead halide perovskites, $CH_3NH_3PbBr_3$, and $CH_3NH_3PbI_3$ were coated on a mesoporous TiO_2 electron-collector as photosensitized dyes and generated 3.8% power conversion efficiency (PCE), which was based on a dye-sensitized solar cell (DSSC) architecture. However, the cells

were only stable for a matter of minutes because of a liquid corrosive electrolyte. In 2009, using the same dye-sensitized concept to improve upon the PCE, achieving 6.5% PCE [3].

In general, the word "perovskite" is used to describe any material with the same structure as inorganic $CaTiO_3$. Organic halide perovskites present a general formula of AMX_3, where A and M are monovalent and bivalent cations, respectively, and X is a monovalent anion that binds to both cations. M is coordinated to six X anions, and A is coordinated to 12 X anions (**Figure 1**). Consequently, they form anionic M-X semiconducting frameworks and charge-compensating cations [1]. In this case of lead halide perovskites, M is Pb atom and X is a halogen atom (Cl, Br, I, or a combination of them). The PbX_6 octahedra consists of a three-dimensional (3D) framework and small-sized organic or inorganic cations, which can fit into the PbX_6 framework, such as $CH_3NH_3^+$, $HC(NH_2)_2^+$, and Cs+.

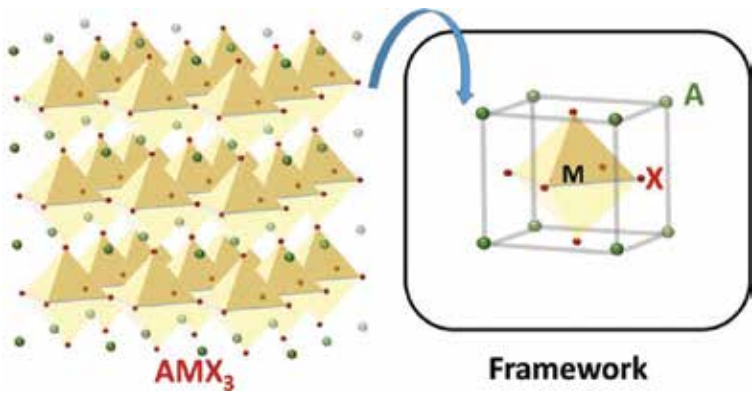

Figure 1. Schematic representation of the 3D inorganic framework of organic halide perovskites.

A breakthrough came in 2012, Michael Grätzel and Park [4] contacted $CH_3NH_3PbI_3$ perovskites with a solid-state electrolyte, spiro-OMeTAD, as a hole-transporting layer (HTL) to improve the device stability. The device structure is shown in **Figure 2**. The all-solid-state mesoscopic solar cells showed the PCE exceeding 9% and began a new perovskite solar cell (PSC) subject in the photovoltaic researches. Subsequently, Lee et al. [5], from the University of Oxford, replaced the mesoporous TiO_2 with an inert Al_2O_3 scaffold, resulting in increased open-circuit voltage and a relative improvement in efficiency of 3–5% more than those with TiO_2 scaffolds, as shown in **Figure 3** [4]. One cell of Al_2O_3-based cells exhibited high efficiency (red solid trace with crosses) and one exhibiting Voc > 1.1 V (red dashed line with crosses); for a perovskite-sensitized TiO_2 solar cell (black trace with circles); and for a planar-junction diode with structure FTO / compact TiO2 / $CH_3NH_3PbI_{3-x}Cl_x$ / spiro-OMeTAD / Ag (purple trace with squares). They showed that the efficiencies of almost 10% were achievable using the 'sensitized' TiO_2 architecture with the solid-state hole transporter, but higher efficiencies, above 10%, were attained by replacing it with an inert scaffold. This showed the PSCs may not require the mesoporous TiO_2 layer in order to transport electrons and the hypothesis that a scaffold is not needed for electron extraction was proved later. A thin-film type PSCs, with no mesoporous scaffold, of >10% efficiency were achieved [6–9].

http://dx.doi.org/10.5772/65056

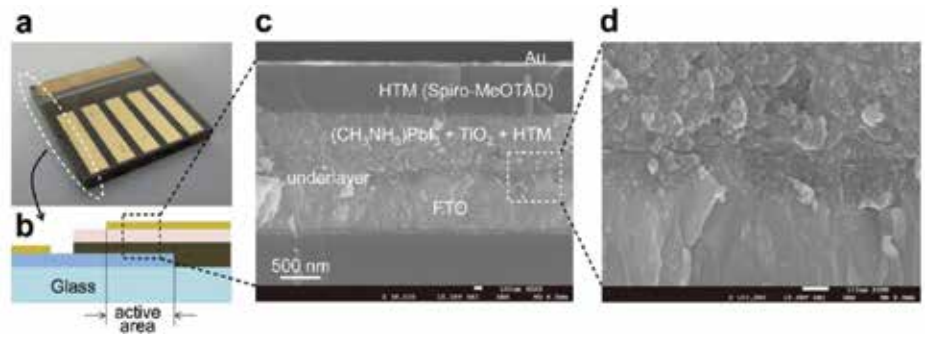

Figure 2. Solid-state device and its cross-sectional mesostructure. (a) Real solid-state device. (b) Cross-sectional structure of the device. (c) Cross-sectional SEM image of the device. (d) Active layer-underlayer-FTO interfacial junction structure.

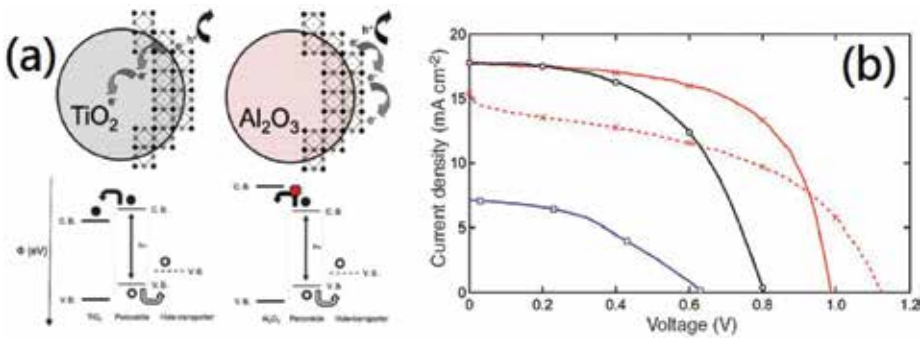

Figure 3. (a) Schematic illustrating the charge transfer and charge transport in a perovskite-sensitized TiO_2 solar cell (left) and a noninjecting Al_2O_3-based solar cell (right). (b) Current density-voltage characteristics under simulated AM1.5 illumination for Al_2O_3-based cells, one cell exhibiting high efficiency (red solid trace with crosses) and one exhibiting VOC > 1.1 V (red dashed line with crosses); for a perovskite-sensitized TiO_2 solar cell (black trace with circles); and for a planar-junction diode with structure FTO/compact TiO_2/$CH_3NH_3PbI_2Cl$/spiro-OMeTAD/Ag (purple trace with squares).

In 2013, both the planar and mesoscopic architectures, **Figure 4**, saw a large amount of developments. Burschka et al. [10] and Bi et al. [11] demonstrated a deposition technique for the mesoscopic-type architecture, exceeding 15% efficiency using a two-step solution processing; Liu et al. [12] showed that it was possible to fabricate planar-type PSCs; using thermal evaporation method at a similar time, over 15% efficiency was achieved. A number of new deposition techniques and even higher efficiencies were reported in 2014 [13, 14]. A reverse-scan efficiency of 19.3% was claimed by Zhou et al. [15] at UCLA using the planar thin-film architecture. In November 2014, a device by researchers from KRICT achieved a record with the certification of a non-stabilized efficiency of 20.1% [15, 16]. In December 2015, a new record efficiency of 21.0% was achieved by EPFL [15]. Subsequently, in March 2016, researchers from KRICT and UNIST created the highest certified record for a single-junction perovskite solar cell with 22.1% [15].

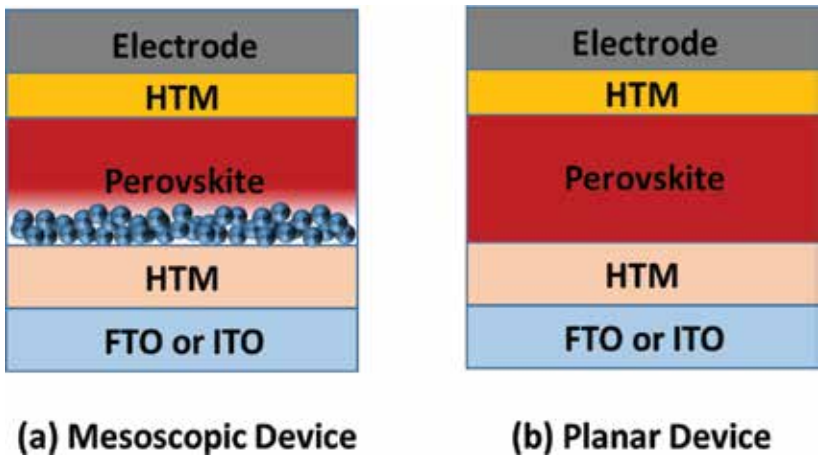

Figure 4. Structure diagram of (a) mesoscopic perovskite solar cell and (b) planar perovskite solar cell.

2. Electron transporting layer in perovskite solar cells

The electron-transporting layer (ETL), one of the most important components in the PSCs for highly efficient performance, plays an essential role in extracting and transporting photogenerated electrons. Simultaneously, it also serves as a hole-blocking layer to suppress carrier recombination. The characteristics of the ETL, especially its carrier mobility, energy band alignment, morphology, trap states, and related interfacial properties are major factors to determine the device behavior and photovoltaic performance of PSCs [17]. A relatively high electron mobility is desirable for ETLs to efficiently transport and collect electrons transport, contributing to the increase of short-circuit current density (Jsc), and fill factor (FF). The better matching energy level between ETLs and the perovskite layer can facilitate electron extraction and transport. Furthermore, the open-circuit voltage (Voc) can be determined by the energy level differences between the Fermi levels (EF) of the ETL and EF of the hole-transporting layer (HTL) [18–20]. Hence, the energy-level engineering is widely used to improve the Voc of a photovoltaic device. Trap states in the ETLs also play important roles in charge transport. Therefore, improving interface contact between ETLs and the perovskite layer is an efficient method to optimize device performance and enhance charge transport. Morphologies of the ETL are also considered to enhance its contact with the perovskite layer for achieving better device behavior.

To date, TiO_2 materials have been used as ETLs in most frequently reported PSCs. The electron injection rates between the perovskite absorber and TiO_2 ETLs are very fast, but the high electron recombination rates are also seen due to the low electron mobility and transporting properties [21]. In addition, a high-temperature process was required for high-quality mesoscopic TiO_2 layer [16, 22]. Hence, these characteristics of TiO_2 materials may act as impediments to improve device performance and their further application for developing low-cost perov-

skite solar cells on various flexible substrates [23, 24]. On the other hand, ZnO is a wide-bandgap semiconductor of the II-VI semiconductor group, which has several favorable properties, including good transparency, high electron mobility, wide bandgap, and strong room-temperature luminescence. Several types of morphologies in ZnO, such as thin film, single-crystal, nanowire, and nanorod has been found and made using the low-temperature solution processes. The native doping of the semiconductor due to oxygen vacancies or zinc interstitials is n-type [25]. Moreover, ZnO is a well-known material that has similar energy level as TiO_2 but has better electron mobility (bulk mobility: 200–300 cm^2/V s [25–27]) than TiO_2, which lets it an ideal candidate for a low-temperature processed electron-selective contact for transparent electrodes, organic solar cell, thin-film transistors, and light-emitting diodes.

3. ZnO film/nanostructure as electron transporting layer

In 2013, ZnO was firstly applied as ETL of PSCs. Kumar et al. [28] reported flexible PSCs employing the ZnO compact layer as a hole-blocking layer and a ZnO nanorods mesoscopic scaffold layer as an electron transporter. The ZnO compact layer was formed by electrodeposition and ZnO nanorods grown by chemical bath deposition, which allow the processing of low-temperature, solution-based ETLs. The planar device, which only uses the ZnO compact layer can also be made, but they presented lower Jsc and FF than nanorod-based devices. Conversion efficiencies of 8.90% were achieved on rigid substrates, while the flexible ones yielded 2.62%. In the same year, Bi et al. [29] used well-aligned ZnO nanorod arrays as ETLs. They consider that the perovskite material has better solar cell stability and is therefore more suited as a sensitizer for ZnO nanorod arrays. Therefore, their results showed the ZnO nanorod-based PSCs had a good long-term stability of PSCs. It was found that the electron transport time and lifetime vary with the ZnO nanorod length, a trend which is similar to that in DSSCs, suggesting a similar charge transfer process in the ZnO nanorod array/$CH_3NH_3PbI_3$ interface as in conventional DSSCs. However, a solar cell efficiency of only 5.0% was achieved under AM 1.5 G illumination due to more recombination losses than TiO_2 devices. The reason indicated that the ZnO nanorod array grown by different processes may affect the PSC performance.

A breakthrough came in the end of 2013, Liu and Kelly [30] reported that a room temperature solution-processed thin compact ZnO ETL was used to fabricate a highly efficient planar perovskite solar cell with a champion efficiency of 15.7%, an average efficiency of 13.7%, and the flexible ones yielded 10.2%, in which ZnO prepared by a co-precipitation method had superior electron mobility, and the ETLs were fabricated without any sintering steps, as shown in **Figure 5**. Besides solution-based co-precipitation ZnO ETLs, a sol-gel solution-processed ZnO ETLs were reported by Kim et al. [31] in 2014. Moreover, a vacuum-processed ZnO ETL has been prepared for high-efficiency PSCs, such as an atom layer deposition (ALD) [32] or sputtering method [33, 34]. Several types of ZnO nanostructures have been studied to replace the mesoporous TiO_2 nanostructures in the conventional PSCs [35–38].

On the other hand, the electrical characteristics of ZnO can be increased by extrinsically doping a small amount of impurities [39, 40], such as Al. The ionic radius of Al^{3+} is 0.54 Å, which is smaller than that of Zn^{2+} (0.74 Å). Therefore, Al^{3+} can replace Zn^{2+} in the lattice point and acts as a donor to increase the conductivity of ZnO [41, 42], and at the same time, it remains the excellent transparence in the visible-light region. This is why a high-quality Al-doped ZnO (AZO) thin film can also be used as a transparent conductive oxide (TCO) electrode, just like other IIIA elements (B, Ga, and In)-doped ZnO [41]. Al-doped ZnO thin film, which was deposited using the electrospraying method, was also used as ETLs in PSCs to suppress charge recombination at the ZnO/perovskite interface, resulting in better efficiency than pure ZnO devices [43]. The charge recombination of the ZnO-based device was also suppressed by appropriate Mg-doping. It mainly attributed to the conduction band offset at the interface between ZnO ETL and perovskite layer [44].

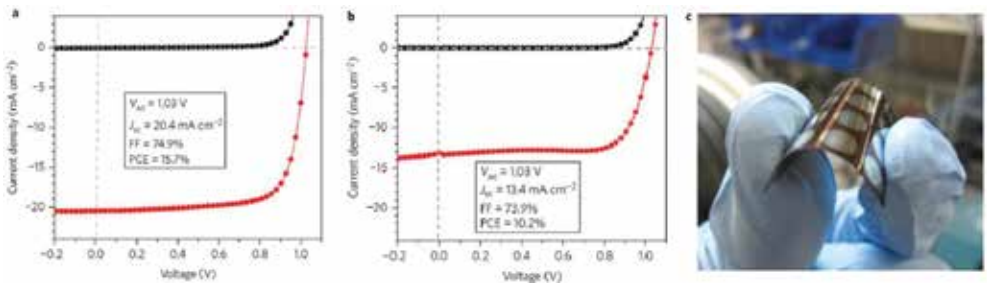

Figure 5. J–V curves of devices on (a) glass and (b) flexible PET substrates in the illumination (red line) and dark (black line) for the highest-performing ITO/ZnO/$CH_3NH_3PbI_3$/spiro-OMeTAD/Ag devices in reference [31]. (c) Photograph of a device prepared on a flexible PET substrate.

The electron extraction by the ETL in perovskite cell strongly depends on the work function (WF) of the ETL. An energy barrier mismatch (a Schottky barrier) between the WF of the ETL and the lowest unoccupied molecular orbital (LUMO) of perovskite absorber could lead to inefficient electron extraction. Therefore, matching the WF of ETL with the absorber could reduce a Schottky barrier or form an Ohmic contact [45, 46] to facilitate the electron injection or collection [47]. Nitrogen-doped ZnO electron materials combined with a dipole layer can increase electron concentration to improve perovskite infiltration and reduce the work function [38]. Above all, doping is an effective way to modify the electrical properties of ZnO.

Self-assembled monolayer (SAM) is well-known that surface treatments can decrease the number of charge carrier traps and tune the surface WF of ETLs. Modification of the interface of solar cells using functional SAMs is an effective method to improve device performance. Modifying the ZnO ETL with 3-aminopropanoic acid monolayer can improve the interfacial energy level alignment due to the formation of permanent dipole moments, which decreased the WF of ZnO from 4.17 to 3.52 eV, and help to obtain highly crystalline perovskite layer with reduced pin-hole and trap-state density [48]. The stoichiometry of ZnO thin film was also affected the photovoltaic device performance. Tseng et al. [33] used sputtered ZnO thin films, which stoichiometry was controlled by adjusting the ratio of working gases (Ar and O_2) during

http://dx.doi.org/10.5772/65056

radio frequency (RF) magnetron-sputtering process, as an ETL in PSCs. As mentioned earlier, the native doping of the ZnO due to oxygen vacancies shows n-type semiconductor. The surface conductivity of ZnO film was affected by the presence of oxygen vacancy of the lattice, which will show even more accentuated variations of the electrical behavior in a thin film. ZnO film with more oxygen vacancies has higher surface conductivity; therefore, device based on ZnO using pure Ar deposition has smaller series resistance. Furthermore, ZnO using pure Ar deposition has lower WF of 4.33 eV than that using Ar/O_2 mixed gas deposition (4.48) but both have a same bandgap. Therefore, ZnO using pure Ar deposition lower conduction band level (down-shift) than that using Ar/O_2 mixed gas deposition to increase the driven force of electron injection (or charge separation) from perovskite (or ZnO/perovskite interface) and lower valance edge can block the hole more efficiently. Both better conductivity and lower conduction band level of ZnO result in high charge extraction efficient; therefore, the corresponding device has high Jsc. (**Figure 6a** and **b**) The hole-blocking ability of ZnO film using pure Ar deposition was also supported by the dark current of the corresponding device illustrated in **Figure 6c**. Cell-based ZnO-Ar electron-transporting layer has smaller dark current indicated that ZnO-Ar has better hole-blocking ability when other components in the cell are supposed to be the same.

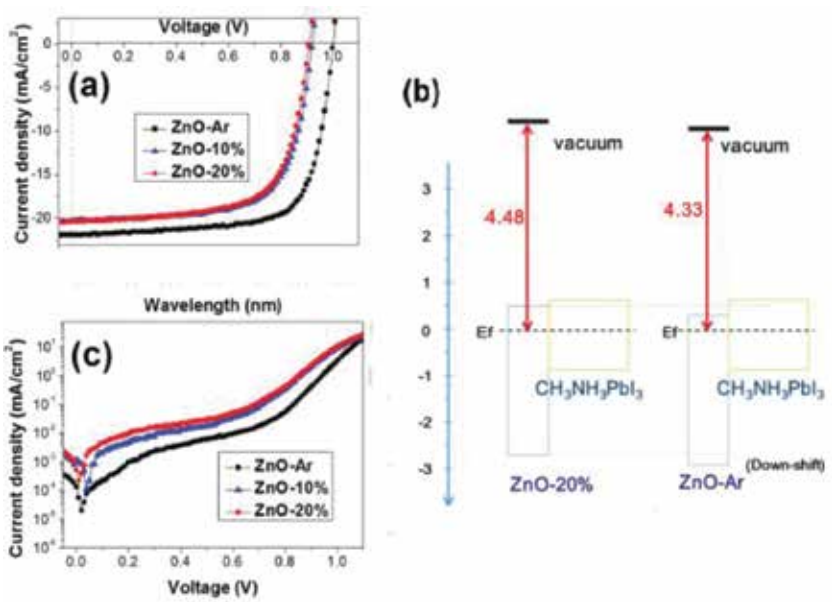

Figure 6. (a) I-V curves, (b) illustration of the frontier orbitals energy levels for ZnO prepared using pure Ar and 20% O_2, and (c) Dark current curves of perovskite solar cell using pure Ar, 10%, and 20% Ar/Ar + O_2 ratio mixed gas as the electron transport layer. The illustration of the frontier orbitals energy levels for ZnO-Ar, ZnO-20%, and perovskite.

Despite the excellent characteristics of ZnO, in 2015, Yang et al. [49] found the thermal instability of PSCs fabricated using ZnO ETLs. They show that the basic nature of the ZnO surface leads to proton-transfer reactions at the $ZnO/CH_3NH_3PbI_3$ interface, which results in

decomposition of the perovskite film PbI_2, as shown in **Figure 7**. The decomposition process is accelerated by the presence of surface hydroxyl groups and/or residual acetate ligands. To reduce the decomposition, Cheng et al. [50] introduced a buffer layer in between the ZnO-NPs and perovskite layers. They found that a commonly used buffer layer with small molecule like [6,6]-phenyl-C_{61}-butyric acid methyl ester (PCBM) can slow down but cannot avoid the decomposition completely. On the other hand, a polymeric buffer layer using poly(ethylenimine) (PEI) can effectively separate the ZnO-NPs and perovskite, which allows larger crystal formation with thermal annealing. Today, thermal instability of PSCs using ZnO ETLs remains the major challenge limiting their further application and device performance.

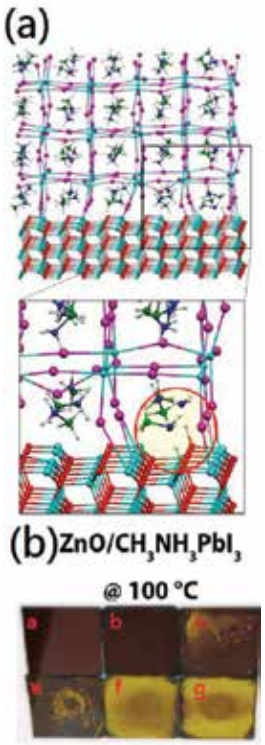

Figure 7. (a) Optimized geometrical structure of the $ZnO/CH_3NH_3PbI_3$ interface. The inset shows a magnified view of the deprotonated methylammonium cations. (b) Photographs of $CH_3NH_3PbI_3$ films deposited on ZnO layers and heated to 100°C with different times (from a to g).

4. Conclusions

In summary, we have given an overview of the efforts focused on the ZnO of ETLs. Their doping effect and interface modification between the ETL and perovskite layer have been developed and applied in PSCs. Because charge extraction, transfer, and recombination mainly occur at

the interfaces of a cell, the interfacial layer between the perovskite layer and the bottom electrode needs to be closely aligned by introducing efficient interfacial materials. For conventional PSCs, a ZnO ETL, good electron-transport ability and a low recombination rate at the interface, works well for high-performance PSC.

Author details

Lung-Chien Chen* and Zong-Liang Tseng

*Address all correspondence to: ocean@ntut.edu.tw

Department of Electro-Optical Engineering, National Taipei University of Technology, Taipei, Taiwan

References

[1] S. Dastidar, Egger, D. A., Tan, L. Z., Cromer, S. B., Dillon, A. D., Liu, S., Kronik, L., Rappe, A. M., Fafarman, A. T. High chloride doping levels stabilize the perovskite phase of cesium lead iodide. Nano Letters. 2016; 16(6), 3563–3570. doi:10.1021/acs.nanolett.6b00635

[2] A. Kojima, Teshima, K., Shirai, Y., Miyasaka, T. Organometal halide perovskites as visible-light sensitizers for photovoltaic cells. Journal of the American Chemical Society. 2009; 131(17), 6050–6051. doi:10.1021/ja809598r

[3] J.-H. Im, Lee, C.-R., Lee, J.-W., Park, S.-W., Park, N.-G. 6.5% efficient perovskite quantum-dot-sensitized solar cell. Nanoscale. 2011; 3(10), 4088–4093. doi:10.1039/C1NR10867K

[4] H.-S. Kim, Lee, C.-R., Im, J.-H., Lee, K.-B., Moehl, T., Marchioro, A., Moon, S.-J., Humphry-Baker, R., Yum, J.-H., Moser, J. E., Grätzel, M., Park, N. G. Lead iodide perovskite sensitized all-solid-state submicron thin film mesoscopic solar cell with efficiency exceeding 9%. Scientific Reports. 2012; 2, doi:10.1038/srep00591

[5] M. M. Lee, Teuscher, J., Miyasaka, T., Murakami, T. N., Snaith, H. J. Efficient hybrid solar cells based on meso-superstructured organometal halide perovskites. Science. 2012; 338(6107), 643–647. doi:10.1126/science.1228604

[6] G. E. Eperon, Burlakov, V. M., Docampo, P., Goriely, A., Snaith, H. J. Morphological control for high performance, solution-processed planar heterojunction perovskite solar cells. Advanced Functional Materials. 2014; 24(1), 151–157. doi:10.1002/adfm.201302090

[7] M. Saliba, Tan, K. W., Sai, H., Moore, D. T., Scott, T., Zhang, W., Estroff, L. A., Wiesner, U., Snaith, H. J. Influence of thermal processing protocol upon the crystallization and

photovoltaic performance of organic–inorganic lead trihalide perovskites. The Journal of Physical Chemistry C. 2014; 118(30), 17171–17177. doi:10.1021/jp500717w

[8] K. W. Tan, Moore, D. T., Saliba, M., Sai, H., Estroff, L. A., Hanrath, T., Snaith, H. J., Wiesner, U. Thermally induced structural evolution and performance of mesoporous block copolymer-directed alumina perovskite solar cells. ACS Nano. 2014; 8 (5), 4730–4739. doi:10.1021/nn500526t

[9] J. M. Ball, Lee, M. M., Hey, A., Snaith, H. J. Low-temperature processed meso-superstructured to thin-film perovskite solar cells. Energy and Environmental Science. 2013; 6(6), 1739–1743. doi:10.1039/C3EE40810H

[10] J. Burschka, Pellet, N., Moon, S.-J., Humphry-Baker, R., Gao, P., Nazeeruddin, M. K., Gratzel, M. Sequential deposition as a route to high-performance perovskite-sensitized solar cells. Nature. 2013; 499(7458), 316–319. doi:10.1038/nature12340

[11] D. Bi, Moon, S.-J., Haggman, L., Boschloo, G., Yang, L., Johansson, E. M. J., Nazeeruddin, M. K., Gratzel, M., Hagfeldt, A. Using a two-step deposition technique to prepare perovskite ($CH_3NH_3PbI_3$) for thin film solar cells based on ZrO_2 and TiO_2 mesostructures. RSC Advances. 2013; 3 (41), 18762–18766. doi:10.1039/C3RA43228A

[12] M. Liu, Johnston, M. B., Snaith, H. J. Efficient planar heterojunction perovskite solar cells by vapour deposition. Nature. 2013; 501(7467), 395–398. doi:10.1038/nature12509

[13] Wikipedia. Perovskite solar cell [Internet]. 2016. Available from: https://en.wikipedia.org/wiki/Perovskite_solar_cell

[14] NREL. Research Cell efficiency records [Internet]. 2016. Available from: http://www.nrel.gov/ncpv/images/efficiency_chart.jpg

[15] H. Zhou, Chen, Q., Li, G., Luo, S., Song, T.-b., Duan, H.-S., Hong, Z., You, J., Liu, Y., Yang, Y. Interface engineering of highly efficient perovskite solar cells. Science. 2014; 345(6196), 542–546. doi:10.1126/science.1254050

[16] W. S. Yang, Noh, J. H., Jeon, N. J., Kim, Y. C., Ryu, S., Seo, J., Seok, S. I. High-performance photovoltaic perovskite layers fabricated through intramolecular exchange. Science. 2015; 348(6240), 1234–1237. doi:10.1126/science.aaa9272

[17] G. Yang, Tao, H., Qin, P., Ke, W., Fang, G. Recent progress in electron transport layers for efficient perovskite solar cells. Journal of Materials Chemistry A. 2016; 4(11), 3970–3990. doi:10.1039/C5TA09011C

[18] S. Ryu, Noh, J. H., Jeon, N. J., Kim, Y. C., Yang, W. S., Seo, J., Seok, S. I. Voltage output of efficient perovskite solar cells with high open-circuit voltage and fill factor. Energy and Environmental Science. 2014; 7(8), 2614–2618. doi:10.1039/C4EE00762J

[19] A. R. b. M. Yusoff, Nazeeruddin, M. K. Organohalide lead perovskites for photovoltaic applications. The Journal of Physical Chemistry Letters. 2016; 7(5), 851–866. doi:10.1021/acs.jpclett.5b02893

[20] Y.-F. Chiang, Jeng, J.-Y., Lee, M.-H., Peng, S.-R., Chen, P., Guo, T.-F., Wen, T.-C., Hsu, Y.-J., Hsu, C.-M. High voltage and efficient bilayer heterojunction solar cells based on an organic-inorganic hybrid perovskite absorber with a low-cost flexible substrate. Physical Chemistry Chemical Physics. 2014; 16(13), 6033–6040. doi:10.1039/C4CP00298A

[21] S. Gubbala, Chakrapani, V., Kumar, V., Sunkara, M. K. Band-edge engineered hybrid structures for dye-sensitized solar cells based on SnO_2 nanowires. Advanced Functional Materials. 2008; 18(16), 2411–2418. doi:10.1002/adfm.200800099

[22] N. J. Jeon, Noh, J. H., Yang, W. S., Kim, Y. C., Ryu, S., Seo, J., Seok, S. I. Compositional engineering of perovskite materials for high-performance solar cells. Nature. 2015; 517(7535), 476–480. doi:10.1038/nature14133

[23] Z. M. Beiley, McGehee, M. D. Modeling low cost hybrid tandem photovoltaics with the potential for efficiencies exceeding 20%. Energy and Environmental Science. 2012; 5(11), 9173–9179. doi:10.1039/C2EE23073A

[24] C. Roldan-Carmona, Malinkiewicz, O., Soriano, A., Minguez Espallargas, G., Garcia, A., Reinecke, P., Kroyer, T., Dar, M. I., Nazeeruddin, M. K., Bolink, H. J. Flexible high efficiency perovskite solar cells. Energy and Environmental Science. 2014; 7(3), 994–997. doi:10.1039/C3EE43619E

[25] Ü. Özgür, Alivov, Y. I., Liu, C., Teke, A., Reshchikov, M. A., Doğan, S., Avrutin, V., Cho, S.-J., Morkoç, H. A comprehensive review of ZnO materials and devices. Journal of Applied Physics. 2005; 98(4), 041301. doi:10.1063/1.1992666

[26] H. Tang, Prasad, K., Sanjinès, R., Schmid, P. E., Lévy, F. Electrical and optical properties of TiO_2 anatase thin films. Journal of Applied Physics. 1994; 75(4), 2042–2047. doi:10.1063/1.356306

[27] H. S. Bae, Yoon, M. H., Kim, J. H., Im, S. Photodetecting properties of ZnO-based thin-film transistors. Applied Physics Letters. 2003; 83(25), 5313–5315. doi:10.1063/1.1633676

[28] M. H. Kumar, Yantara, N., Dharani, S., Graetzel, M., Mhaisalkar, S., Boix, P. P., Mathews, N. Flexible, low-temperature, solution processed ZnO-based perovskite solid state solar cells. Chemical Communications. 2013; 49(94), 11089–11091. doi:10.1039/C3CC46534A

[29] D. Bi, Boschloo, G., Schwarzmuller, S., Yang, L., Johansson, E. M. J., Hagfeldt, A. Efficient and stable $CH_3NH_3PbI_3$-sensitized ZnO nanorod array solid-state solar cells. Nanoscale. 2013; 5(23), 11686–11691. doi:10.1039/C3NR01542D

[30] D. Liu, Kelly, T. L. Perovskite solar cells with a planar heterojunction structure prepared using room-temperature solution processing techniques. Nature Photonics. 2014; 8(2), 133–138. doi:10.1038/nphoton.2013.342

[31] J. Kim, Kim, G., Kim, T. K., Kwon, S., Back, H., Lee, J., Lee, S. H., Kang, H., Lee, K. Efficient planar-heterojunction perovskite solar cells achieved via interfacial modifica-

tion of a sol-gel ZnO electron collection layer. Journal of Materials Chemistry A. 2014; 2(41), 17291–17296. doi:10.1039/C4TA03954H

[32] X. Dong, Hu, H., Lin, B., Ding, J., Yuan, N. The effect of ALD-ZnO layers on the formation of $CH_3NH_3PbI_3$ with different perovskite precursors and sintering temperatures. Chemical Communications. 2014; 50(92), 14405–14408. doi:10.1039/C4CC04685D

[33] Z.-L. Tseng, Chiang, C.-H., Wu, C.-G. Surface engineering of ZnO thin film for high efficiency planar perovskite solar cells. Scientific Reports. 2015; 5, doi:13211.10.1038/srep13211

[34] L. Liang, Huang, Z., Cai, L., Chen, W., Wang, B., Chen, K., Bai, H., Tian, Q., Fan, B. Magnetron sputtered zinc oxide nanorods as thickness-insensitive cathode interlayer for perovskite planar-heterojunction solar cells. ACS Applied Materials and Interfaces. 2014; 6(23), 20585–20589. doi:10.1021/am506672j

[35] J. Zhang, Barboux, P., Pauporté, T. Electrochemical design of nanostructured ZnO charge carrier layers for efficient solid-state perovskite-sensitized solar cells. Advanced Energy Materials. 2014; 4(18), doi:10.1002/aenm.201400932

[36] D.-Y. Son, Im, J.-H., Kim, H.-S., Park, N.-G. 11% efficient perovskite solar cell based on ZnO nanorods: an effective charge collection system. The Journal of Physical Chemistry C. 2014; 118(30), 16567–16573. doi:10.1021/jp412407j

[37] A. K. Chandiran, Abdi-Jalebi, M., Yella, A., Dar, M. I., Yi, C., Shivashankar, S. A., Nazeeruddin, M. K., Grätzel, M. Quantum-confined ZnO nanoshell photoanodes for mesoscopic solar cells. Nano Letters. 2014; 14(3), 1190–1195. doi:10.1021/nl4039955

[38] K. Mahmood, Swain, B. S., Amassian, A. 16.1% efficient hysteresis-free mesostructured perovskite solar cells based on synergistically improved ZnO nanorod arrays. Advanced Energy Materials. 2015; 5(17), doi:10.1002/aenm.201500568

[39] E. Klaus. Magnetron sputtering of transparent conductive zinc oxide: relation between the sputtering parameters and the electronic properties. Journal of Physics D: Applied Physics. 2000; 33(4), R17–R32. doi:http://iopscience.iop.org/0022-3727/33/4/201

[40] Liu, Y., Li, Y..Zeng, H. ZnO-Based Transparent Conductive Thin Films: Doping, Performance, and Processing. Journal of Nanomaterials. 2013; 2013, 196521. DOI: http://dx.doi.org/10.1155/2013/196521.

[41] Sans, J. A., Sánchez-Royo, J. F., Segura, A., Tobias, G..Canadell, E. Chemical effects on the optical band-gap of heavily doped ZnO:MIII (M = Al, Ga, In): An investigation by means of photoelectron spectroscopy, optical measurements under pressure, and band structure calculations. Physical Review B. 2009; 79 (19), 195105. DOI: http://dx.doi.org/10.1103/PhysRevB.79.195105

[42] J. L. Zhao, Sun, X. W., Ryu, H., Moon, Y. B. Thermally stable transparent conducting and highly infrared reflective Ga-doped ZnO thin films by metal organic chemical

vapor deposition. Optical Materials. 2011; 33(6), 768–772. doi:10.1016/j.optmat.2010.12.008

[43] K. Mahmood, Swain, B. S., Jung, H. S. Controlling the surface nanostructure of ZnO and Al-doped ZnO thin films using electrostatic spraying for their application in 12% efficient perovskite solar cells. Nanoscale. 2014; 6(15), 9127–9138. doi:10.1039/C4NR02065K

[44] J. Dong, Shi, J., Li, D., Luo, Y., Meng, Q. Controlling the conduction band offset for highly efficient ZnO nanorods based perovskite solar cell. Applied Physics Letters. 2015; 107(7), 073507. doi:10.1063/1.4929435

[45] H. Kang, Hong, S., Lee, J., Lee, K. Electrostatically self-assembled nonconjugated polyelectrolytes as an ideal interfacial layer for inverted polymer solar cells. Advanced Materials. 2012; 24(22), 3005–3009. doi:10.1002/adma.201200594

[46] J. C. Yu, Kim, D. B., Baek, G., Lee, B. R., Jung, E. D., Lee, S., Chu, J. H., Lee, D.-K., Choi, K. J., Cho, S., Song, M. H. High-performance planar perovskite optoelectronic devices: a morphological and interfacial control by polar solvent treatment. Advanced Materials. 2015; 27(23), 3492–3500. doi:10.1002/adma.201500465

[47] Y. Zhou, Fuentes-Hernandez, C., Shim, J., Meyer, J., Giordano, A. J., Li, H., Winget, P., Papadopoulos, T., Cheun, H., Kim, J., Fenoll, M., Dindar, A., Haske, W., Najafabadi, E., Khan, T. M., Sojoudi, H., Barlow, S., Graham, S., Brédas, J.-L., Marder, S. R., Kahn, A., Kippelen, B. A universal method to produce low–work function electrodes for organic electronics. Science. 2012; 336(6079), 327–332. doi:10.1126/science.1218829

[48] L. Zuo, Gu, Z., Ye, T., Fu, W., Wu, G., Li, H., Chen, H. Enhanced photovoltaic performance of $CH_3NH_3PbI_3$ perovskite solar cells through interfacial engineering using self-assembling monolayer. Journal of the American Chemical Society. 2015; 137(7), 2674–2679. doi:10.1021/ja512518r

[49] J. Yang, Siempelkamp, B. D., Mosconi, E., De Angelis, F., Kelly, T. L. Origin of the thermal instability in $CH_3NH_3PbI_3$ thin films deposited on ZnO. Chemistry of Materials. 2015; 27(12), 4229–4236. doi:10.1021/acs.chemmater.5b01598

[50] Y. Cheng, Yang, Q.-D., Xiao, J., Xue, Q., Li, H.-W., Guan, Z., Yip, H.-L., Tsang, S.-W. Decomposition of organometal halide perovskite films on zinc oxide nanoparticles. ACS Applied Materials and Interfaces. 2015; 7(36), 19986–19993. doi:10.1021/acsami.5b04695

Chapter 11

Fabrication and Characterization of Element-Doped Perovskite Solar Cells

Takeo Oku, Masahito Zushi, Kohei Suzuki,
Yuya Ohishi, Taisuke Matsumoto and Atsushi Suzuki

Additional information is available at the end of the chapter

http://dx.doi.org/10.5772/65768

Abstract

Perovskite solar cells were fabricated and characterized. X-ray diffraction analysis and transmission electron microscopy were used for investigation of the devices. The structure analysis by them showed structural transformation of the crystal structure of the perovskite, which indicated that a cubic-tetragonal crystal system depended on the annealing condition. The photovoltaic properties of the cells also depended on the structures. Metal doping and halogen doping to the perovskite and TiO_2 were also investigated. The results showed an increase in the efficiencies of the devices, due to the structural change of the perovskite compound layers.

Keywords: perovskite, solar cell, doping, structure, $CH_3NH_3PbI_3$, Sb, Cl, TiO_2, Nb, Ge, Cs

1. Introduction

Various organic-inorganic hybrid solar cells with perovskite-type pigments have been broadly studied recently [1–4]. Organic solar cells with a $CH_3NH_3PbI_3$ compound that has a perovskite structure have high conversion efficiencies [5–7]. Since achieving a photoconversion efficiency of 15% [8], higher efficiencies have been reported for various device structures and processes [9–11], and the photoconversion efficiency increased up to ca. 20% [12–18]. The solar cell properties depend on the crystal structures of the perovskite phase, electron transport layers, hole transport layers (HTLs), nanoporous layers, and fabrication process. Especially, the energy band gaps and carrier transport of the perovskite compounds are dependent on the crystal structures [19], and further analyses of the structures and properties are imperative.

In this article, fabrication and characterization of perovskite-type solar cells are reviewed and summarized. Various perovskite compounds, such as $CH_3NH_3PbI_3$, $[HC(NH_2)_2]PbI_3$, and $CsSnI_3$, are expected for solar cell materials. Since these perovskite-type materials often have nanostructures in the solar cell devices, information on the crystal structures, fabrication, and characterization would be useful for fabrication of the perovskite-type crystals. Transmission electron microscopy, electron diffraction, and high-resolution electron microscopy are powerful tools for structure analysis of solar cells [20] and perovskite-type structures in atomic scale [21–23].

The crystals of $CH_3NH_3PbX_3$ (X = Cl, Br, or I) have perovskite structures and provide structural transitions upon heating [24–26]. The crystal structures of cubic, tetragonal, and orthorhombic $CH_3NH_3PbI_3$ are shown in **Figure 1(a)–(c)**, respectively. Space group is *Pm*-3*m*, and the lattice constant a = 6.391 Å at 330 K for cubic $CH_3NH_3PbI_3$ [27]. Hydrogen positions in the orthorhombic $CH_3NH_3PbI_3$ were also determined at 4 K by neutron diffraction [28], as shown in **Figure 1(d)**. Although the crystals of perovskite $CH_3NH_3PbX_3$ provide a cubic system as the high-temperature phase, the $CH_3NH_3^+$ ions are polar and have a symmetry of C_{3v}. This results in formation of cubic phase with disordering [27]. Besides the $CH_3NH_3^+$ions, disordering of the halogen ions is also observed in the cubic perovskite phase, as indicated in **Figure 1(a)**. Site occupancies of I were 1/4, and those of C and N were 1/12, respectively. The CH_3NH_3 ion occupies 12 equivalent orientations of the C_2 axis, and hydrogen atoms have two kinds of configurations on the C_2 axis. Therefore, the total degree of freedom is 24 [26].

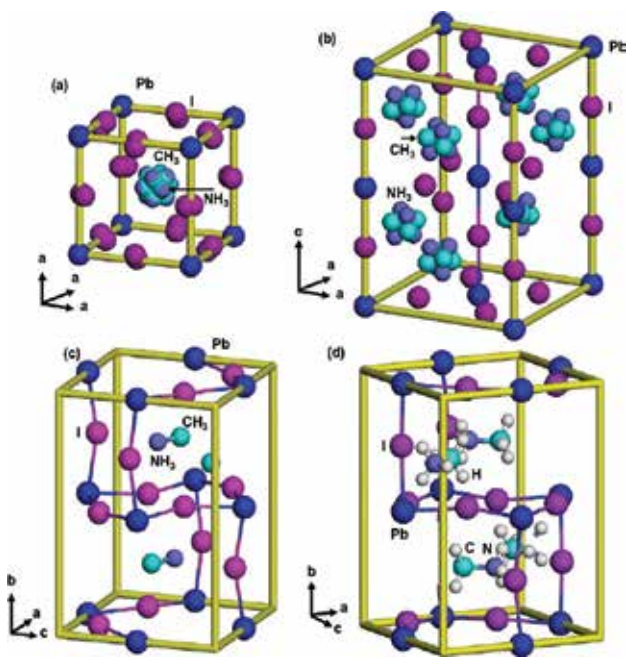

Figure 1. Structure models of $CH_3NH_3PbI_3$ with (a) cubic, (b) tetragonal and (c) orthorhombic structures, and (d) orthorhombic $CH_3NH_3PbI_3$ with hydrogen positions.

http://dx.doi.org/10.5772/65768

In addition to the $CH_3NH_3PbI_3$ ($MAPbI_3$), $[HC(NH_2)_2]PbI_3$ (formamidinium lead iodide, $FAPbI_3$) provided high conversion efficiencies [17, 18]. Structure parameters, including hydrogen positions, were also determined at 298 K by neutron diffraction [29], and the structure model with the lattice constant a = 6.3620 Å is shown in **Figure 2(a)**.

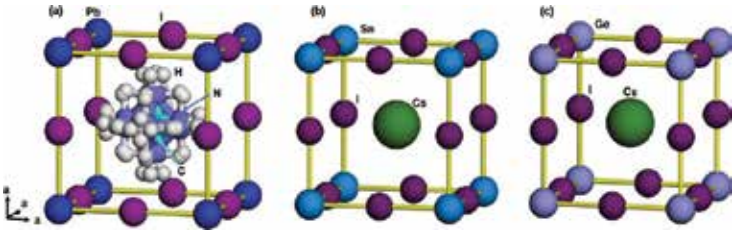

Figure 2. Structure models of (a) $[HC(NH_2)_2]PbI_3$, (b) $CsSnI_3$, and (c) $CsGeI_3$ with cubic structures.

CH_3NH_3 ions can be substituted by other elements such as Cs. The structure models of $CsSnI_3$ and $CsGeI_3$ for high-temperature phase are shown in **Figure 2(b)** and **(c)**, respectively [30–32]. Space group is *Pm*-3*m* (Z = 1), and a = 6.219 Å at 446 K for $CsSnI_3$, a = 6.05 Å at 573 K for $CsGeI_3$, respectively. Solar cells with F-doped $CsSnI_{2.95}F_{0.05}$ provided a photoconversion efficiency of 8.5% [6].

2. Basic device structures

A typical fabrication process of the $TiO_2/CH_3NH_3PbI_3$ photovoltaic devices is described here [8, 33, 34]. Fluorine-doped tin oxide (FTO) substrates were washed in an ultrasonic cleaner using methanol and acetone, and then dried in N_2 gas. Precursor solution of 0.30 M TiO_x was prepared from titanium diisopropoxide bis(acetyl acetonate) with 1-butanol, and the TiO_x precursor solution was spin-coated on the FTO substrate at 3000 rpm and annealed at 125°C for 5 min. This process was carried out two times, and the FTO substrate was annealed at 500°C for 30 min to form the compact TiO_2 layer as an electron transport layer. After that, TiO_2 paste was coated on the substrate by a spin-coating method at 5000 rpm to form a mesoporous structure. For the mesoporous TiO_2 layer, TiO_2 paste was arranged with TiO_2 powder with poly(ethylene glycol) in ultrapure water. The solution was stirred with triton X-100 and acetylacetone for 30 min. The prepared cells were heated at 120°C, and annealed at 500°C for 30 min in air. Designed for the preparation of pigment with a perovskite structure, a solution of CH_3NH_3I and PbI_2 with a mole ratio of 1:1 in γ-butyrolactone was mixed at 60°C. The mixture solution of CH_3NH_3I and PbI_2 was then poured into the TiO_2 mesopores by spin-coating, and annealed at 100°C. After that, the hole transport layer (HTL) was prepared by the spin coating. For preparation of the HTL, a solution of spiro-OMeTAD in chlorobenzene was mixed with a solution of lithium bis(trifluoromethylsulfonyl) imide (Li-TFSI) in acetonitrile for 12 h. The former solution with 4-tert-butylpyridine was mixed with the Li-TFSI solution at 70°C. Finally, gold (Au) metal contacts were evaporated as top electrodes of the cell. Layered structures of

the present photovoltaic cells were represented as FTO/TiO_2/$CH_3NH_3PbI_3$/Spiro-OMeTAD/Au, as shown in **Figure 3**.

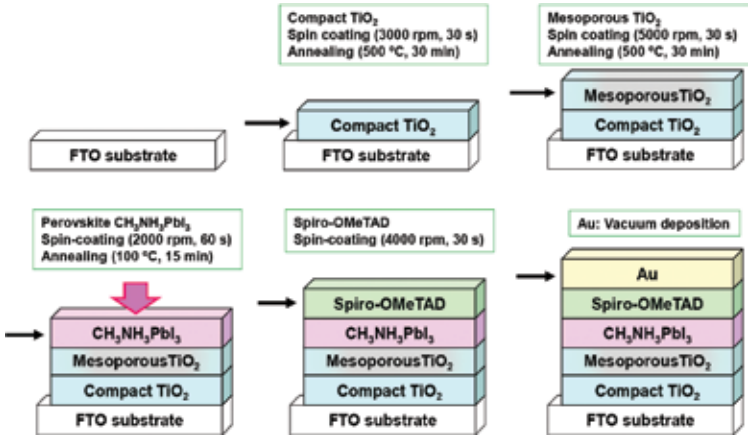

Figure 3. Schematic illustration for the fabrication of $CH_3NH_3PbI_3$ photovoltaic cells.

The typical *J–V* characteristics of the TiO_2/$CH_3NH_3PbI_3$/spiro-OMeTAD photovoltaic cells under illumination are shown in **Figure 4(a)**, which indicates an annealing effect of the $CH_3NH_3PbI_3$ layer. The as-deposited $CH_3NH_3PbI_3$ cell provided a conversion efficiency of 2.83%. The $CH_3NH_3PbI_3$ cell annealed at 100°C for 15 min provided better photovoltaic properties compared with the as-deposited one, as shown in **Figure 4(a)**. The highest efficiency was obtained for the annealed $CH_3NH_3PbI_3$ cell, which provided a power conversion efficiency of 5.16%, a fill factor of 0.486, a short-circuit current density of 12.9 mA cm^{-2}, and an open-

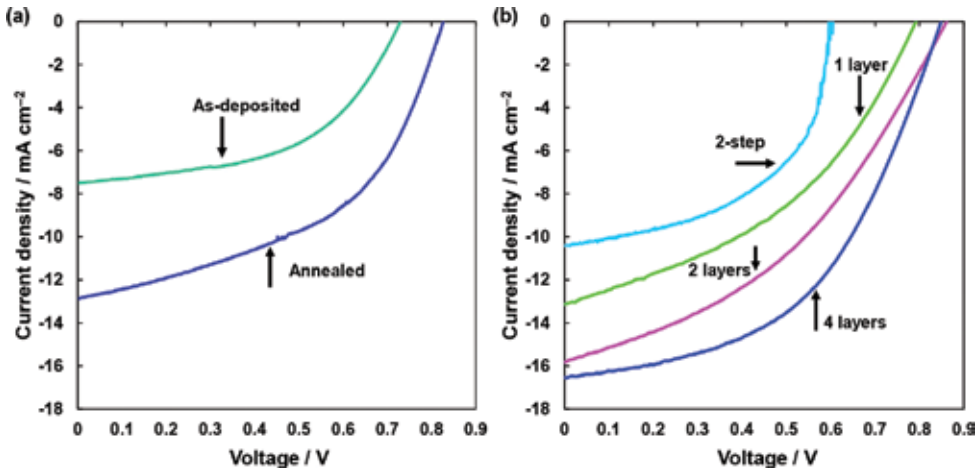

Figure 4. *J–V* characteristics of TiO_2/$CH_3NH_3PbI_3$ photovoltaic cells. (a) As-deposited and annealed samples. (b) $CH_3NH_3PbI_3$ layers prepared by multiple spin-coating.

http://dx.doi.org/10.5772/65768

circuit voltage of 0.827 V [35]. **Figure 4(b)** shows results of multiple spin-coating of $CH_3NH_3PbI_3$, which will be described later.

XRD patterns of $CH_3NH_3PbI_3$ thin films on the glass substrate are shown in **Figure 5(a)**. The diffraction reflections could be indexed with tetragonal and cubic structures for as-deposited and annealed films, respectively. Though the as-deposited film showed a single phase of the perovskite structure, broader diffraction reflections owing to a PbI_2 phase appeared after annealing, as shown in **Figure 5(a)**. **Figure 5(b)** and **(c)** is enlarged XRD patterns at 2θ of ~14° and ~28°, respectively. Split diffraction reflections of 002–110 and 004–220 for the as-deposited sample changed into diffraction reflections of 100 and 200 after annealing, which indicate the

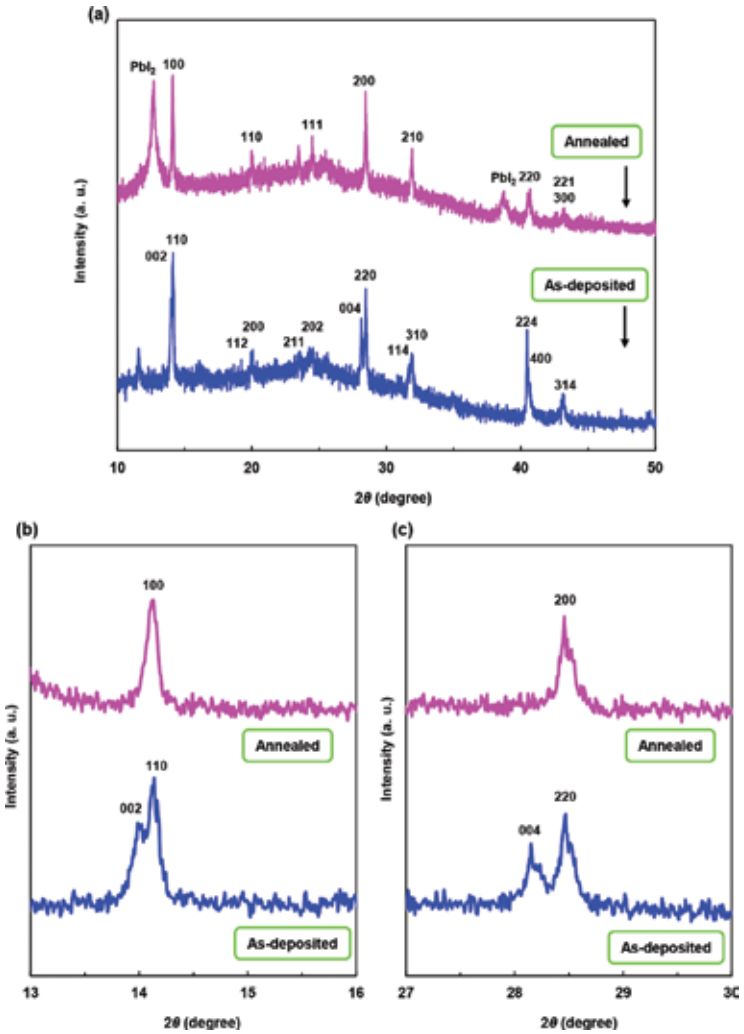

Figure 5. (a) XRD patterns of $CH_3NH_3PbI_3$ thin films before and after annealing. Enlarged XRD patterns at 2θ of (b) ~14° and (c) ~28°.

structural transformation from the tetragonal to cubic system. The $CH_3NH_3PbI_3$ crystals have perovskite structures and provide structural transitions from a tetragonal to a cubic system upon heating at ~330 K, as shown in the structure models of **Figure 1(a)** and **(b)**. For the high-temperature phase, unit cell volume of the cubic system is 261 Å^3, which is bigger compared with that of the tetragonal system (246 Å^3), as shown in **Table 1** [35]. This might be because of both thermal expansion of the unit cell and atomic disordering of iodine in the cubic structure. As the temperature decreases, the tetragonal structure is transformed to the orthorhombic structure because of ordering of CH_3NH_3 ions in the unit cell [37].

Samples	Crystal system	Lattice constants (Å)	V (Å^3)	Z	V/Z (Å^3)
As-deposited	Tetragonal	a = 8.8620 c = 12.6453	993.10	4	248.27
Annealed	Cubic	a = 6.2724	246.78	1	246.78
Ref. [36] (220 K)	Tetragonal	a = 8.800 c = 12.685	982.33	4	245.6
Ref. [27] (330 K)	Cubic	a = 6.391	261.0	1	261.0

V: unit cell volume; Z: number of chemical units in the unit cell.

Table 1. Measured and reported structural parameters of $CH_3NH_3PbI_3$.

The XRD results in **Figure 5** indicated phase transformation of the $CH_3NH_3PbI_3$ perovskite structure from the tetragonal to the cubic system by partial separation of PbI_2 from the $CH_3NH_3PbI_3$ phase at elevated temperatures, which would be related to the decrease of the unit cell volume of the perovskite structure from 248.3 to 246.8 Å^3, as shown in **Table 1**. Besides the iodine atoms, Pb atoms may be deficient, and the occupancy of the Pb sites might be smaller than 1. It should be noted that the structural transition of the $CH_3NH_3PbI_3$ from the tetragonal to cubic system here would be attributed to the formation of PbI_2 by decomposition of the $CH_3NH_3PbI_3$ phase, which is different from the ordinary tetragonal-cubic transition at 330 K [24, 25].

Figure 6(a) and **(b)** is the TEM image and the electron diffraction pattern of TiO_2/$CH_3NH_3PbI_3$, respectively [35]. The TEM image shows TiO_2 nanoparticles with sizes of ~50 nm, and the polycrystalline $CH_3NH_3PbI_3$ phase shows dark contrast, which is due to Pb having the largest atomic number in the present materials.

The electron diffraction pattern of **Figure 6(b)** shows the Debye-Scherrer rings from the nanocrystalline TiO_2 particles, which can be indexed with the 101, 004, and 200 reflections of anatase-type TiO_2. Thickness of the mesoporous TiO_2 layer was found to be ~300 nm from atomic force microscopy measurements. Along with the Debye–Scherrer rings of TiO_2, diffraction reflections agreeing with the $CH_3NH_3PbI_3$ structure [6] were observed and indexed, as shown in **Figure 6(b)**. Other diffraction spots, except for the Debye-Scherrer rings of TiO_2, are also from the $CH_3NH_3PbI_3$ nanoparticles. A structure model and its calculated electron diffraction pattern of a cubic $CH_3NH_3PbI_3$ phase projected along the [210] direction are shown

http://dx.doi.org/10.5772/65768

in **Figure 6(c)** and **(d)**, respectively. The calculated electron diffraction pattern agrees well with the observed pattern of **Figure 6(b)**.

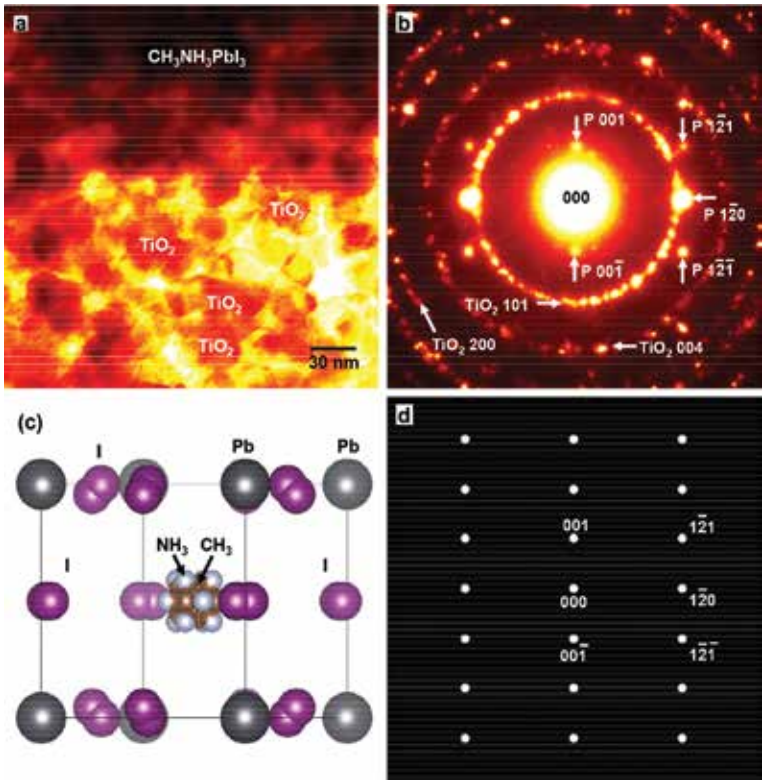

Figure 6. (a) TEM image and (b) electron diffraction pattern of $TiO_2/CH_3NH_3PbI_3$. "P" indicates $CH_3NH_3PbI_3$ perovskite phase. (c) Structure model and (d) its calculated electron diffraction pattern of cubic $CH_3NH_3PbI_3$ projected along the [210] direction.

Figure 7(a) is a high-resolution TEM image of the $CH_3NH_3PbI_3$ taken along the a-axis [33]. The images of thinner parts of the crystals indicate the direct projection of the crystal structure [21, 22]. The darkness and the size of the dark spots corresponding to Pb positions could be directly identified, and atomic positions of iodine (I) in the crystal indicate weak contrast, as compared with the projected atomic structure model of $CH_3NH_3PbI_3$ along the [100] direction in **Figure 7(b)**. NH_3 and CH_3 molecules cannot be represented as dark spots in the image, which is due to the smaller atomic number of N and C. **Figure 7(c)** is a high-resolution image of the surface of a TiO_2 nanoparticle, which indicates {101} lattice fringes.

The *J–V* characteristics of the $TiO_2/CH_3NH_3PbI_3$/spiro-OMeTAD photovoltaic cells prepared by multiple spin-coating of $CH_3NH_3PbI_3$ are shown in **Figure 4(b)**. **Figure 4(b)** indicates the effect of spin-coating times of $CH_3NH_3PbI_3$ on the photovoltaic properties. The highest efficiency of 6.96% was achieved for the cell coated for four times, which provided a J_{SC} of 16.5 mA cm^{-2}, a V_{OC} of 0.848 V, and *FF* of 0.496. More spin-coating reduced the efficiencies of the

cells. Although 2-step deposition [8] (spin-coating PbI_2 and dipping in the CH_3NH_3I solution) was also performed in air, the efficiency was lower compared with that by multiple spin-coating, as observed in **Figure 4(b)**. It is believed that the $CH_3NH_3PbI_3$ phase was embedded inside pores of the mesoporous TiO_2 layer during one- or two-time spin-coating. After the inside pores of the mesoporous TiO_2 were completely filled with the perovskite compound, only the perovskite layer might be formed on the mesoporous TiO_2 layer by four-time spin-coating, which would result in the highest efficiency.

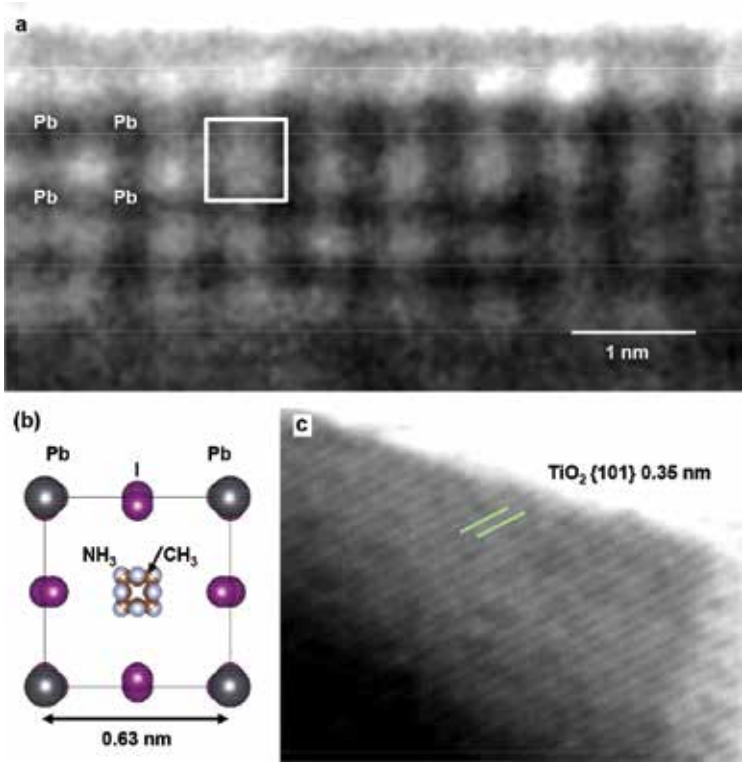

Figure 7. (a) High-resolution TEM image and (b) structure model of $CH_3NH_3PbI_3$. (c) Lattice image of TiO_2.

The IPCE spectrum of the photovoltaic cell with the $TiO_2/CH_3NH_3PbI_3$/spiro-OMeTAD structure exhibits photoconversion efficiencies between 300 and 800 nm, which nearly agrees with the measured energy gaps of 1.51 eV [37] for the $CH_3NH_3PbI_3$ compound. This indicates that excitons might be effectively generated in the perovskite compound layers upon light illumination.

An energy level diagram of $TiO_2/CH_3NH_3PbI_3$ photovoltaic cells is summarized as shown in **Figure 8(a)**. The electronic charge generation is caused by light irradiation from the FTO substrate side. The TiO_2 layer receives the electrons from the $CH_3NH_3PbI_3$ crystal, and the electrons are carried to the FTO. On the other hand, the holes are carried to the Au electrode through the HTL of spiro-OMeTAD. For these processes, the devices were produced in air,

which would induce the reduction of device stability. Perovskite compounds with higher crystal quality would be produced in future works.

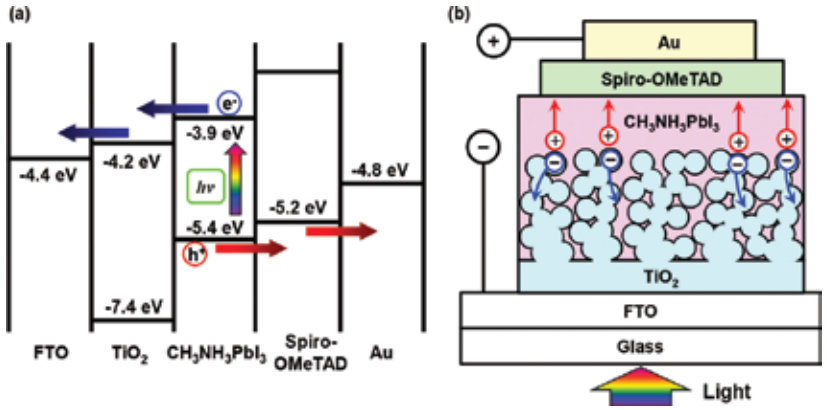

Figure 8. (a) IPCE spectrum and (b) energy level diagram of $TiO_2/CH_3NH_3PbI_3$ cell. (c) Model of interfacial structure.

From the TEM results, size distributions of TiO_2 nanoparticles were observed, indicating a microcrystalline structure, as shown in **Figure 6(b)**, and there seems to be no special crystallographic relation at the interface. The interface between the TiO_2 and $CH_3NH_3PbI_3$ phases would not be perfectly connected over the large area. The cell prepared by four-time spin-coating provided the highest efficiency, which would have an interfacial microstructure as shown in **Figure 8(b)**. The layer thickness of the $CH_3NH_3PbI_3$ phase was too thick for the cells prepared by 10-time spin-coating, which resulted in an increase in the inner electronic resistance and decrease in the efficiency.

As a summary, the structure analysis of $TiO_2/CH_3NH_3PbI_3$ indicated phase transformation of the perovskite structure from the tetragonal to the cubic system by partial separation of PbI_2 from the $CH_3NH_3PbI_3$ compound upon annealing, which was presumed by decrease of the unit cell volume of the perovskite structure and resulted in the enhancement of photovoltaic properties of the devices. Effects of the multiple spin-coating were also investigated, which improved the efficiency when the four-time spin-coating was carried out. The improvement of the devices might attribute to the complete coverage and optimal thickness of the perovskite layer on the porous TiO_2. Additionally, the lattice constants and crystallite sizes of the $CH_3NH_3PbI_3$ increased and decreased, respectively, which indicates the microstructural difference of the perovskite phase between the inside of and above the porous TiO_2.

3. Enlargement of cell

Enlargement of the cell area is especially mandatory to enable the use of perovskite devices such as actual commercial solar cell panels [38]. The photovoltaic properties of perovskite-type solar cells with a substrate size of 70 mm × 70 mm were investigated [39].

The photovoltaic devices consisted of a $CH_3NH_3PbI_3$ compound layer, TiO_2 electron transport layers, and spiro-OMeTAD hole-transport layer, prepared by a simple spin-coating technique. The effect of the distance from the center of the cell on conversion efficiency was investigated based on light-induced *J–V* curves and IPCE measurements. A photograph of a perovskite solar cell measuring 70 mm × 70 mm and a schematic illustration of the arrangement of Au electrodes on the substrate are shown in **Figure 9(a)** and **(b)**, respectively.

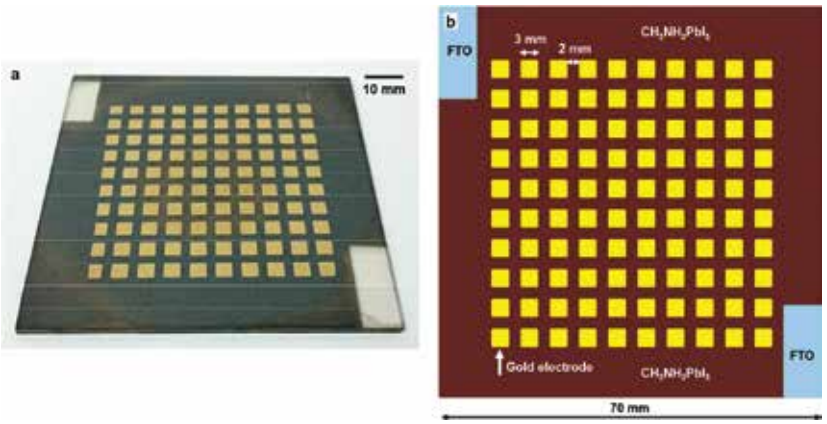

Figure 9. (a) Photograph of perovskite solar cell measuring 70 mm × 70 mm. (b) Schematic illustration of arrangement of Au electrodes on the substrate.

The measured short-circuit current density, open-circuit voltage, fill factor, and photoconversion efficiency of the present $TiO_2/CH_3NH_3PbI_3$ cell as a function of the distance from the center of the cell are shown in **Figure 10(a–d)**, respectively. The highest efficiency was obtained for the electrode at 12.7 mm from the cell center, which provided a photoconversion efficiency of 3.15%, a V_{OC} of 0.653 V, a J_{SC} of 13.0 mA cm^{-2}, and a *FF* of 0.371. Due to the long diffusion length of exciton [40], the J_{SC} values were nearly constant at ~12 mA cm^{-2} for all electrodes on the solar cell, as observed in **Figure 10(a)**. Although the *FF* value slightly decreased as the distance (*d*) from the center of the cell increased, the deviation was small, as observed in **Figure 9(c)**. On the other hand, the value of V_{OC} depended fairly on the *d* values, as observed in **Figure 10(b)**, which led to decreased efficiency, as shown in **Figure 10(d)**. The dependency of V_{OC} values on the *d* values might be related to the thickness of $CH_3NH_3PbI_3$ layer prepared on the large substrate by the spin-coating method. The low V_{OC} and *FF* values would be related to the coverage ratio of $CH_3NH_3PbI_3$ at the $TiO_2/CH_3NH_3PbI_3$ interface, and further multiple spin-coating of $CH_3NH_3PbI_3$ layers on the TiO_2 mesoporous layer would improve the coverage of $CH_3NH_3PbI_3$ on the TiO_2 mesoporous layer, which would induce the increase in the conversion efficiency of the solar cells.

IPCE spectra of electrodes at 4.2, 12.7, and 22.8 mm from the cell center are shown in **Figure 10(e)**. All spectra show similar changes on the wavelength, which agrees with the J_{SC} results shown in **Figure 9(a)**. The perovskite $CH_3NH_3PbI_3$ structure showed photoconversion within the whole measurement range of 300–800 nm, which nearly agrees with the

http://dx.doi.org/10.5772/65768

reported energy gaps for the $CH_3NH_3PbI_3$ phase. Control of the energy levels of the conduction band and valence band is important for carrier transport in the cell. The conversion efficiencies obtained for the present cells are lower than the previously reported values. It might be difficult to control the uniformity of the layer thickness and interfacial structure using the spin-coating. In the present work, the samples were prepared in air, which might result in a decrease in the efficiency of the present cells, and perovskite crystals with higher quality and a uniform surface should be prepared in future works.

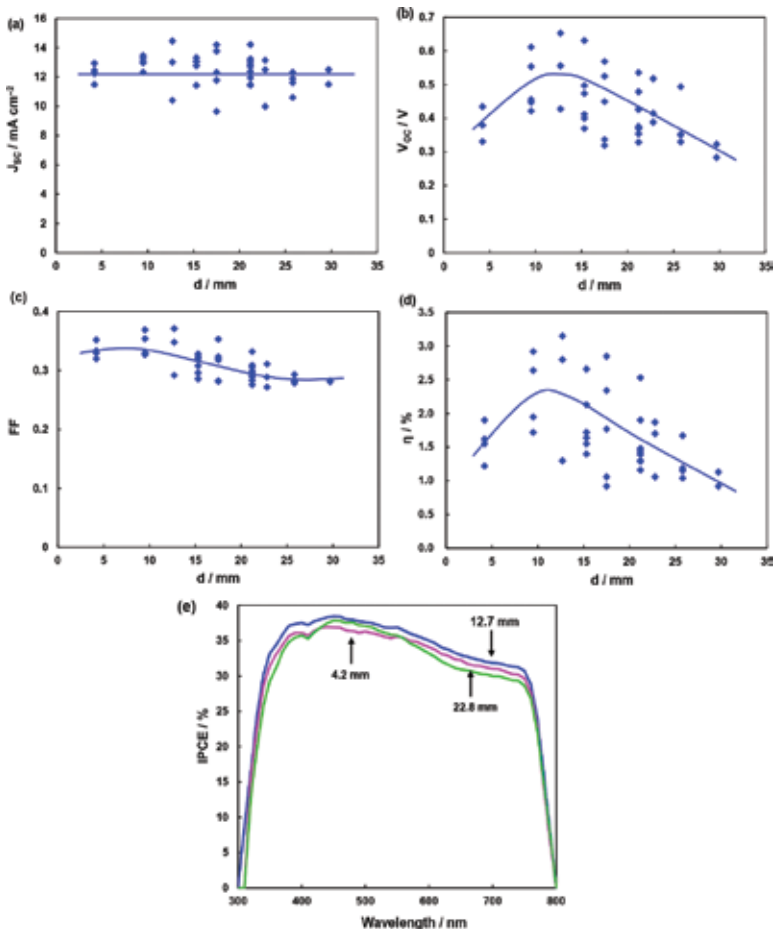

Figure 10. Measured (a) short-circuit current density; (b) open-circuit voltage; (c) fill factor and (d) conversion efficiency of $TiO_2/CH_3NH_3PbI_3$ cell as a function of the distance from the center of the cell. (e) IPCE spectra of the same cell.

As a summary, perovskite solar cell devices with a substrate size of 70 mm were produced by a spin-coating method using a mixture solution. The photovoltaic properties of the solar cells and the size effect of the substrate were investigated by *J–V* and IPCE measurements, and the dependency of their conversion efficiency on the distance from the center of the cell was

investigated. Nearly constant values of short-circuit current density were obtained over a large area, due to the long exciton diffusion length of the $CH_3NH_3PbI_3$ compound. The open-circuit voltage fairly depended on the distance from the center of the cell, which led to a change in conversion efficiency. Optimizing the layer thickness and structure would be important for improving the performance of the devices.

4. Electron transport layers

The electron-transport layers (ETLs) such as TiO_2 are also important for the $CH_3NH_3PbI_3$-based photovoltaic devices. Here, niobium (V) ethoxide was chosen as an additional chemical for TiO_2 [41]. When niobium (Nb) atoms with five valence electrons are introduced at Ti sites with four valence electrons, extra electrons are introduced in the 3d band and could work as a donor. Since the energy level of impurity in the TiO_2 band gap is shallow, transparency could be conserved after the Nb doping [42–46]. Additionally, the radius of Nb ion is close to that of the Ti ion, which leads to a solid solution of titanium and niobium in the anatase-type TiO_2 crystal. The TiO_2 crystal added with Nb is denoted as $Ti(Nb)O_2$ here.

The XRD patterns and crystal structure of TiO_2 and $Ti(Nb)O_2$ thin films on the FTO substrate are shown in **Figure 11(a)** and **(b)**, respectively. Diffraction peaks of TiO_2 101 are observed, and the intensity increased upon Nb-doping. The XRD data indicate that the d-spacing of $Ti(Nb)O_2$ (1.802 Å) is almost the same as that of TiO_2 (1.807 Å). The crystallite size seems to increase a little upon Nb addition (28 nm) to TiO_2 (24 nm).

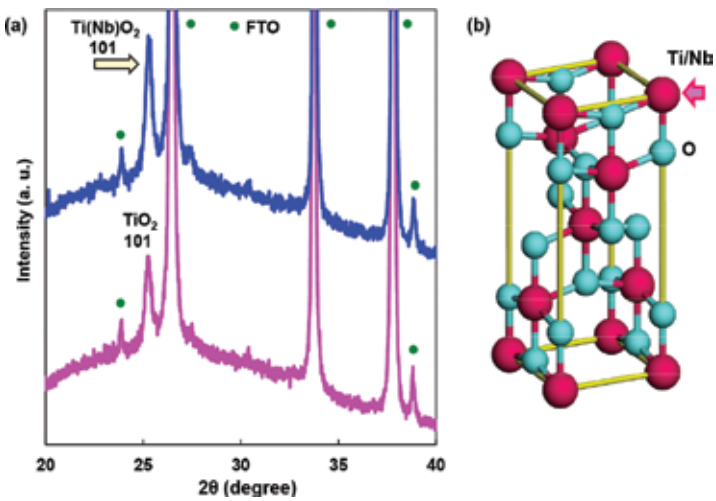

Figure 11. (a) XRD patterns of TiO_2 and $Ti(Nb)O_2$ thin films on FTO. (b) Crystal structure of TiO_2.

A scanning electron microscopy (SEM) image of the $Ti(Nb)O_2$ thin film is shown in **Figure 12(a)**, and the image indicates several particles with sizes of ca. 1 μm on the

http://dx.doi.org/10.5772/65768

smooth surface. Elemental mapping images of Ti and Nb using SEM with energy-dispersive X-ray spectroscopy (EDX) are shown in **Figure 12(b)** and **(c)**, respectively, which indicate that Ti and Nb elements are homogeneously distributed in the films. The elemental ratio of Ti:Nb was estimated to be ~1.00:0.10 from SEM-EDX analysis. The dispersed particles observed in **Figure 12(a)** were found to be Nb-rich phase, as observed in **Figure 12(c)**, which resulted in an Nb-rich (ca. 9 atomic %) composition compared with the preparation composition (ca. 5 atomic %). From XRD analysis, no diffraction peak corresponding to Nb and Nb_2O_5 was observed.

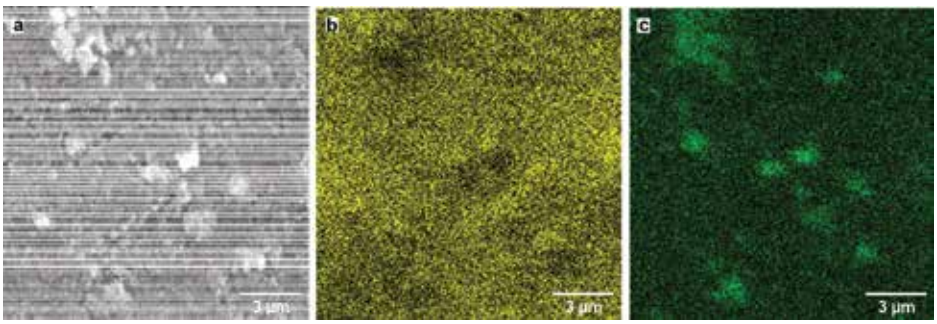

Figure 12. (a) SEM image of Ti(Nb)O_2 thin film. Elemental mapping of (b) Ti (Lα) and (c) Nb (Lα).

The sheet resistances of TiO_2 and Ti(Nb)O_2 thin films were measured to be 1.7×10^6 and 4.2×10^4 Ω/sq, respectively. The sheet resistance significantly decreased upon Nb addition. The *J–V* characteristics of Ti(Nb)O_2/$CH_3NH_3PbI_3$/spiro-OMeTAD photovoltaic cells under illumination are shown in **Figure 13(a)**. The detailed parameters of the best device are listed in **Table 2**. The Ti(Nb)O_2/$CH_3NH_3PbI_3$ photovoltaic cell provided an η of 6.63%, a *FF* of 0.416, a J_{SC} of 20.8 mA cm^{-2}, and a V_{OC} of 0.768 V. The J_{SC} value was especially improved upon Nb

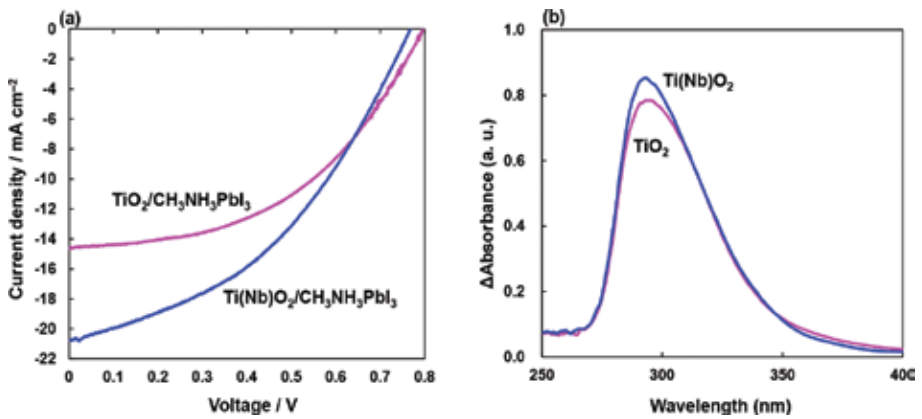

Figure 13. (a) *J–V* characteristics of Ti(Nb)O_2/$CH_3NH_3PbI_3$ photovoltaic cells. (b) Differential absorption spectra of TiO_2 and Ti(Nb)O thin films.

addition, which resulted in increased conversion efficiency. The averaged efficiency (η_{ave}) of three electrodes on the cells is 6.46%, as listed in **Table 2**.

ETL	J_{SC} (mA cm^{-2})	V_{OC} (V)	*FF*	η (%)	η_{ave} (%)
TiO_2	14.6	0.796	0.478	5.56	5.03
$Ti(Nb)O_2$	20.8	0.768	0.416	6.63	6.46

Table 2. Measured parameters of $Ti(Nb)O_2/CH_3NH_3PbI_3$ cells.

Figure 13(b) shows differential absorption spectra of FTO/TiO_2 and FTO/$Ti(Nb)O_2$ after subtracting the spectrum of the FTO substrate. These absorption spectra appear to be closely equal. Based on the band structure of indirect transition [60], energy gaps for TiO_2 and $Ti(Nb)O_2$ were estimated to be 3.54 and 3.52 eV from **Figure 13(b)**, respectively, which indicate that the energy gaps are almost the same for TiO_2 and $Ti(Nb)O_2$.

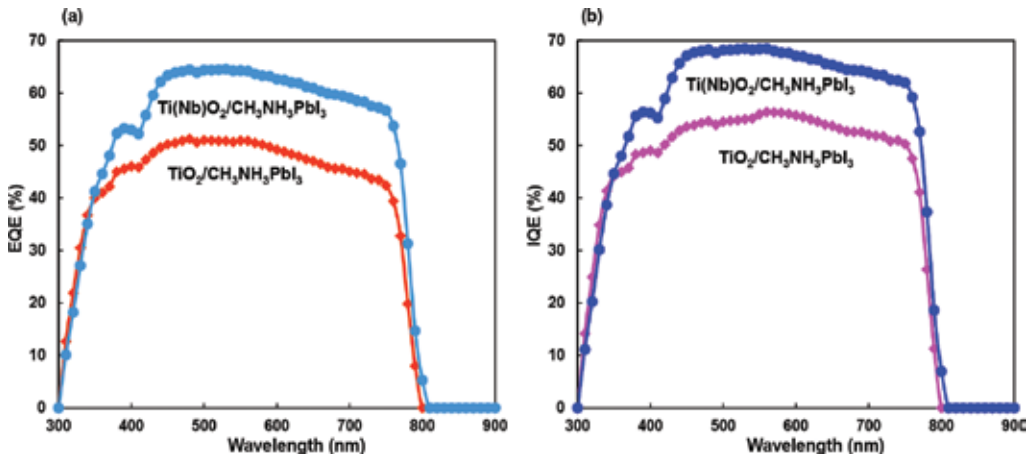

Figure 14. (a) EQE and (b) IQE spectra of $Ti(Nb)O_2/CH_3NH_3PbI_3$ cells.

The IPCE of the cells was also investigated, and the external quantum efficiency (EQE) and internal quantum efficiency (IQE) were measured by a spectral response system. The EQE spectra of the photovoltaic cells with the $Ti(Nb)O_2/CH_3NH_3PbI_3$/spiro-OMeTAD structure are shown in **Figure 14(a)**. The perovskite $CH_3NH_3PbI_3$ phase shows photoconversion efficiencies between 300 and 800 nm. By Nb addition into the TiO_2 layer, the perovskite $CH_3NH_3PbI_3$ structure shows high EQE values of ca. 60% at 500–600 nm and ca. 5% at 800 nm, and the EQE was 0% for ordinary TiO_2 at 800 nm. The IQE spectra of $Ti(Nb)O_2/CH_3NH_3PbI_3$/spiro-OMeTAD cells were computed from the reflectance and EQE, as shown

in **Figure 14(b)**. The IQE of both cells increased in the range of 500–800 nm, which implies that suppression of reflection of light in the range of 500–800 nm could increase the photoconversion efficiencies of the cells. High IQE values of ~70% are seen in the range of 500–600 nm by the Nb addition in the TiO_2 layer.

Two mechanisms could be considered for the decrease in the sheet resistances of TiO_2 by the Nb addition. The first mechanism is niobium doping at the titanium sites in the TiO_2 crystal. Owing to the XRD and differential absorption results of **Figures 11(a)** and **13(b)**, the TiO_2 phase still preserved the crystal structure, energy gap, and transparency of anatase TiO_2. In addition, a small amount of Nb atoms are widely distributed in the TiO_2 phase, as observed by SEM-EDX of **Figure 10(c)** and **(d)**, which could imply a solid solution of titanium and niobium in the TiO_2 structure. The extra electron of Nb might be introduced into the 3d band of Ti and behaves as a donor [60]. The second conceivable mechanism is enhancement of carrier transport by formation of niobium-based particles in the TiO_2 layer, as observed in SEM-EDX images. Nanoparticles in electron-transport and hole-transport layers could facilitate the carrier transport [47, 48], and the present niobium-based particles might contribute to the carrier transport. Both mechanisms could provide an increase in carrier concentration and transport, and an improvement of conversion efficiency through the increase in J_{SC}.

As a summary, $Ti(Nb)O_2/CH_3NH_3PbI_3$-based photovoltaic devices were fabricated by a spin-coating method using a mixture solution of niobium(V) ethoxide, and the effects of Nb addition into the TiO_2 layer were investigated. By adding a simple solution of niobium(V) ethoxide to the TiO_2 precursor solutions, the sheet resistance of the $Ti(Nb)O_2$ thin film decreased, and the J_{SC} value increased, which resulted in the increase in conversion efficiency.

5. Halogen doping to $CH_3NH_3PbI_3$

Effects of Cl-doping $CH_3NH_3PbI_3$ using a mixture solution of perovskite compounds on the microstructures and photovoltaic properties have been investigated [49]. The *J–V* characteristics of the $TiO_2/CH_3NH_3PbI_{3-x}Cl_x$/spiro-OMeTAD photovoltaic cells under illumination are shown in **Figure 15(a)**, which indicate an effect of Cl-doping to the $CH_3NH_3PbI_3$ layer. Measured photovoltaic parameters of $TiO_2/CH_3NH_3PbI_{3-x}Cl_x$ cells are summarized in **Table 3**. The $CH_3NH_3PbI_3$ cell provided a power conversion efficiency of 6.16%, and the averaged efficiency of four electrodes on the cells is 5.53%, as listed in **Table 3**. The highest efficiency was obtained for the $CH_3NH_3PbI_{2.88}Cl_{0.12}$ cell, which provided an η of 8.16%, a *FF* of 0.504, J_{SC} of 18.6 mA cm^{-2}, and a V_{OC} of 0.869 V. As a Cl composition increased, the J_{SC} and V_{OC} decreased, as shown in **Figure 15(b)** and **Table 3**. Energy gaps (E_g) of $CH_3NH_3PbI_3$, $CH_3NH_3PbI_{2.88}Cl_{0.12}$, and $CH_3NH_3PbI_{1.8}Cl_{1.2}$ were estimated to be 1.578, 1.590, and 1.593, respectively, from the optical absorption, which indicated the energy gap of $CH_3NH_3PbI_3$ increased by the Cl-doping.

Preparation composition	J_{SC} (mA cm^{-2})	V_{OC} (V)	*FF*	η (%)	η_{ave} (%)
$CH_3NH_3PbI_3$	17.5	0.844	0.416	6.16	5.53
$CH_3NH_3PbI_{2.94}Cl_{0.06}$	17.7	0.871	0.487	7.53	6.02
$CH_3NH_3PbI_{2.92}Cl_{0.08}$	18.1	0.825	0.478	7.14	6.52
$CH_3NH_3PbI_{2.88}Cl_{0.12}$	18.6	0.869	0.504	8.16	7.77
$CH_3NH_3PbI_{2.77}Cl_{0.23}$	13.9	0.865	0.440	5.29	4.97
$CH_3NH_3PbI_{2.65}Cl_{0.35}$	11.7	0.709	0.347	2.87	2.51
$CH_3NH_3PbI_{1.80}Cl_{1.20}$	14.8	0.598	0.436	3.87	2.00

Table 3. Measured photovoltaic parameters of $TiO_2/CH_3NH_3PbI_{3-x}Cl_x$ cells.

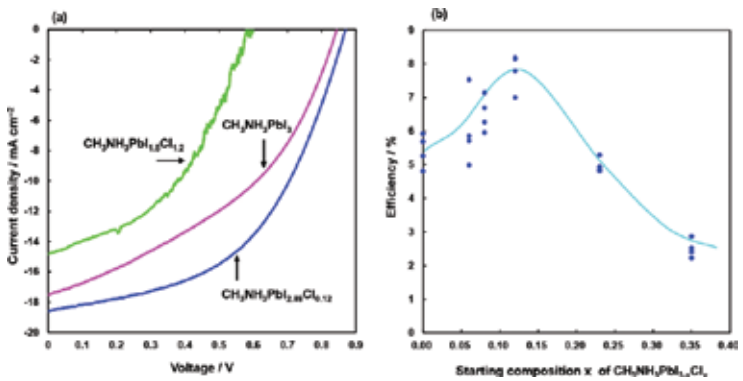

Figure 15. (a) *J–V* characteristic of $TiO_2/CH_3NH_3PbI_{3-x}Cl_x$ photovoltaic cells. (b) Conversion efficiencies of the cells as a function of Cl concentration.

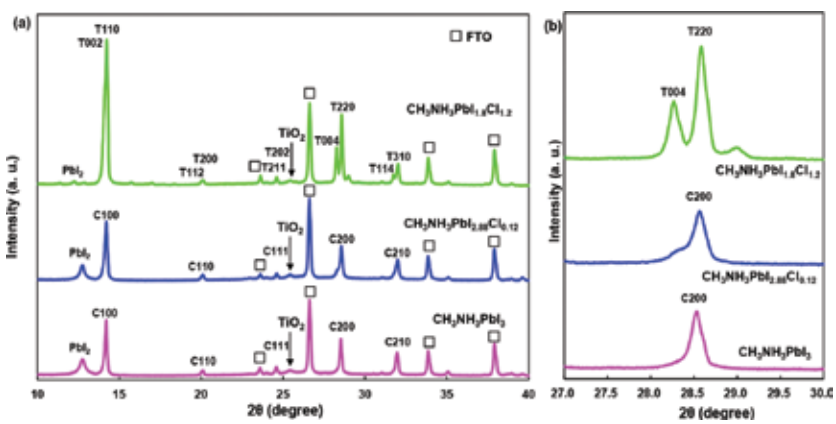

Figure 16. (a) XRD patterns of $CH_3NH_3PbI_{3-x}Cl_x$ thin films. (b) Enlarged XRD patterns at 2θ of ~28.5°.

Preparation composition	Crystal system	Lattice constant (Å)	V (Å^3)	Z	V/Z (Å^3)
$CH_3NH_3PbI_3$	Cubic	a = 6.2524	244.42	1	244.42
$CH_3NH_3PbI_{2.88}Cl_{0.12}$	Pseudocubic	a = 6.2446	243.51	1	243.51
$CH_3NH_3PbI_{1.80}Cl_{1.20}$	Tetragonal	a = 8.8255 c = 12.6180	982.81	4	245.70

V: unit cell volume; Z: number of chemical units in the unit cell.

Table 4. Measured and reported structural parameters of $CH_3NH_3PbI_{3-x}Cl_x$.

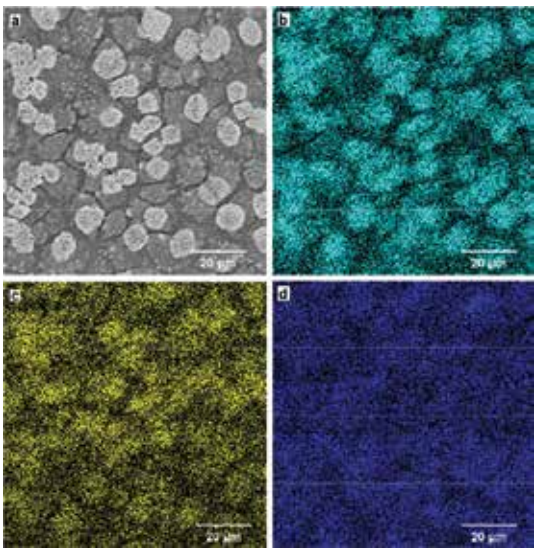

Figure 17. (a) SEM image of $TiO_2/CH_3NH_3PbI_{2.88}Cl_{0.12}$. Elemental mapping images of (b) Pb Mα line, (c) I Lα line, and (d) Cl Kα line.

XRD patterns of $CH_3NH_3PbI_{3-x}Cl_x$ thin films on the FTO/TiO_2 are shown in **Figure 16(a)**. The temperature for XRD measurements was ~292 K. The diffraction peaks can be indexed by cubic and tetragonal crystal systems for $CH_3NH_3PbI_3$ and $CH_3NH_3PbI_{1.8}Cl_{1.2}$ films, respectively. Although the deposited films are a single perovskite phase, broader diffraction peaks due to PbI_2 compound appeared in the $CH_3NH_3PbI_3$ film, as shown in **Figure 16(a)**. **Figure 16(b)** shows enlarged XRD patterns at 2θ of ~28.5°. A diffraction peak of 200 for the $CH_3NH_3PbI_3$ split into diffraction peaks of 004/220 for the $CH_3NH_3PbI_{1.8}Cl_{1.2}$ by the heavy Cl-doping, which indicates the structural transformation from the cubic to tetragonal crystal systems [19]. The heavy Cl-doping suppressed the formation of PbI_2, and no $PbCl_2$ was detected for the $CH_3NH_3PbI_{1.8}Cl_{1.2}$. For the $CH_3NH_3PbI_{2.88}Cl_{0.12}$, a small shoulder is observed just left of the 200 reflection as shown in **Figure 16(b)**, which would be due to the pseudocubic structure between the cubic and tetragonal phases. The measured structural parameters of the $CH_3NH_3PbI_{3-x}Cl_x$ are summarized in **Table 4**.

Figure 17(a) is a SEM image of $TiO_2/CH_3NH_3PbI_{2.88}Cl_{0.12}$, and the image shows particles with sizes of ca. 10 μm. Mapping images of Pb, I, and Cl elements by SEM equipped with EDX are shown in **Figure 17(b–d)**, respectively. These mapping images of elements indicate that the dispersed particles observed in **Figure 17(a)** correspond to the perovskite $CH_3NH_3PbI_{3-x}Cl_x$ phase. The composition ratio of Pb:I:Cl was 1.00:2.70:0.11, which was calculated from their EDX spectra using each element's line after background correction by normalizing the spectrum peaks on the atomic concentration of Pb element. The present result indicates that iodine atoms would be deficient comparing with the starting composition of $CH_3NH_3PbI_{2.88}Cl_{0.12}$, and the deficient I might increase the hole concentration. The $CH_3NH_3PbI_3$ crystals have perovskite structures, and provide structural transitions from tetragonal to cubic system upon heating at ~330 K [27–29].

The XRD results in **Figure 16** indicated phase transformation of the $CH_3NH_3PbI_3$ perovskite structure from tetragonal to cubic system by partial separation of PbI_2 from $CH_3NH_3PbI_3$ phase through the annealing [35], which is related to decrease in the unit cell volume of the cubic $CH_3NH_3PbI_3$ phase from the normal 261 $Å^3$ to the present 244 $Å^3$, as shown in **Table 4**. From the SEM-EDX results, the site occupancies of I atom might be smaller than 1, which would also decrease the cell volume. The conversion efficiencies were reported to be increased by the tetragonal to cubic transformation [35].

The X-ray diffraction pattern indicates division of diffraction peaks from C200 to T004/T220 by means of heavy Cl-doping. This designates reduction of the symmetry of the crystal structures from the cubic to tetragonal system, which resulted in decrease of the photoconversion efficiencies. Once a small amount of Cl was added in the $CH_3NH_3PbI_3$ phase, the cubic structure was still preserved as the pseudocubic phase. The doped Cl atoms would lengthen diffusion length of excitons [7, 40], which would result in the increase of the efficiencies.

EQE spectra of the photovoltaic cell with the $TiO_2/CH_3NH_3PbI_3$-xClx/spiro-OMeTAD structure are shown in **Figure 18(a)**. The perovskite $CH_3NH_3PbI_3$ phase shows photoconversion efficiencies between 300 and 800 nm. In the present work, the energy gap of the $CH_3NH_3PbI_3$ phase increased from 1.578 to 1.590 eV by Cl-doping, which could contribute to the increase in open-circuit voltage. IQE spectra of $TiO_2/CH_3NH_3PbI_3$ and $TiO_2/CH_3NH_3PbI_{2.92}Cl_{0.08}$ were computed from EQE spectra and reflectance, as shown in **Figure 18(b)**. The IQE of both cells increased in the wavelength range of 500–800 nm, and this indicates that improvement of the optical absorption in that range might improve the photoconversion efficiencies of $TiO_2/CH_3NH_3PbI_{3-x}Cl_x$/spiro-OMeTAD cells.

In summary, $TiO_2/CH_3NH_3PbI_{3-x}Cl_x$-based photovoltaic devices were fabricated by a spin-coating method using a mixture solution, and effects of $PbCl_2$ addition to the perovskite $CH_3NH_3PbI_3$ precursor solutions on the photovoltaic properties were investigated. The microstructure analysis showed phase transformation of the perovskite structure from cubic to tetragonal system by heavy Cl-doping to the $CH_3NH_3PbI_3$ phase. A small amount of Cl-doping ($CH_3NH_3PbI_{2.9}Cl_{0.1}$) at iodine sites increased the efficiencies up to ~8%, and it might be owing to conservation of the cubic perovskite structure and to extension of diffusion length of excitons and energy gap. Both the EQE and IQE increased in the range of 300–800 nm by means of a small amount of Cl-doping, and the IQE data designate that the inhibition of the optical

reflection in the wavelength range of 500–800 nm might improve the photoconversion efficiencies further.

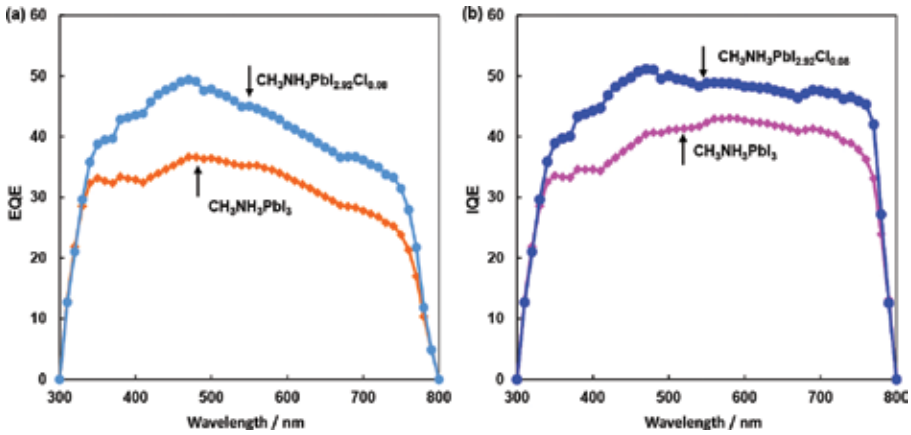

Figure 18. (a) EQE and (b) IQE spectra of $CH_3NH_3PbI_3$ and $CH_3NH_3PbI_{2.92}Cl_{0.08}$ cells.

6. Metal doping to $CH_3NH_3PbI_3$

The properties of solar cells are dependent on the atomic compositions and the crystal structures of perovskite $CH_3NH_3PbI_3$ compounds. Metal atom and halogen doping such as tin (Sn) and chlorine (Cl)/bromine (Br) at the Pb and I sites, respectively, in the $CH_3NH_3PbI_3$ structure have been investigated [12–14, 50–52]. Particularly, researches of the metal element doping at Pb sites are fascinating in the view of Pb-free devices and influence on the photovoltaic properties.

The objective here is to investigate photovoltaic properties and microstructures of photovoltaic devices with perovskite-type $CH_3NH_3Pb_{1-x}Sb_xI_3$ compounds, prepared by a spin-coating technique in ordinary air. Antimony (Sb) is an element in the group 15 and might work as electronic carriers at the Pb sites in the group 14. Effects of SbI_3 addition to a $CH_3NH_3PbI_3$ mixed solution on the microstructures and photovoltaic properties were investigated [53, 54].

The *J*–*V* characteristics of the $TiO_2/CH_3NH_3Pb_{1-x}Sb_xI_3$/spiro-OMeTAD photovoltaic cells under illumination are shown in **Figure 19(a)**, which indicate an effect of Sb addition to $CH_3NH_3PbI_3$. The measured photovoltaic parameters of $TiO_2/CH_3NH_3Pb_{1-x}Sb_xI_3$ cells are summarized in **Table 5**.

The $CH_3NH_3PbI_3$ cell provided a power conversion efficiency of 6.56%, and the averaged efficiency of four electrodes on the cells is 6.37%, as listed in **Table 5**. The highest efficiency was obtained for the $CH_3NH_3Pb_{0.97}Sb_{0.03}I_3$ cell, which provided an η of 9.07%, a *FF* of 0.560, a J_{SC} of 19.2 mA cm^{-2}, and a V_{OC} of 0.843V. As the *x* value (preparation composition of Sb)

increased, the efficiencies decreased, as shown in **Figure 19(b)** and **Table 5**. An η of 9.7% was also reported by addition of SbI_3 and NH_4Cl to the $CH_3NH_3PbI_3$ [54].

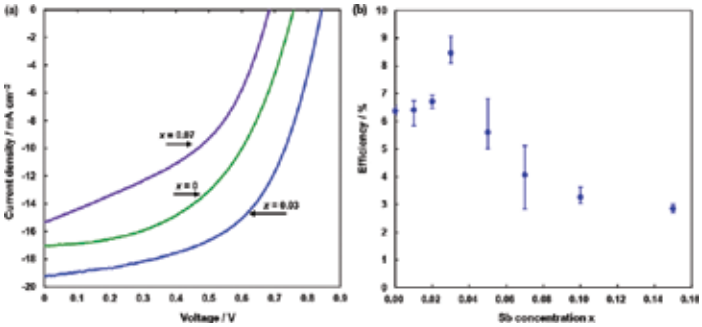

Figure 19. (a) *J–V* characteristics of $TiO_2/CH_3NH_3Pb_{1-x}Sb_xI_3$ photovoltaic cells. (b) Conversion efficiencies of $CH_3NH_3Pb_{1-x}Sb_xI_3$ as a function of Sb concentration.

Sb (*x*)	J_{SC} (mA cm^{-2})	V_{OC} (V)	*FF*	η (%)	η_{ave} (%)
0.00	17.0	0.758	0.509	6.56	6.37
0.01	16.0	0.789	0.534	6.74	6.41
0.02	16.9	0.792	0.518	6.94	6.72
0.03	19.2	0.843	0.560	9.07	8.47
0.05	15.7	0.755	0.575	6.82	5.61
0.07	14.7	0.692	0.502	5.11	4.07
0.10	12.1	0.630	0.476	3.63	3.27
0.15	13.1	0.570	0.402	3.00	2.85

Preparation compositions of Sb are indicated by *x*.

Table 5. Measured photovoltaic parameters of $TiO_2/CH_3NH_3Pb_{1-x}Sb_xI_3$ cells.

IPCE spectra of the $CH_3NH_3PbI_3$ and $CH_3NH_3Pb_{0.97}Sb_{0.03}I_3$ cells are shown in **Figure 20**. The perovskite $CH_3NH_3Pb_{1-x}Sb_xI_3$ shows photoconversion efficiencies between 300 and 800 nm. The IPCE was improved in the range of 350–770 nm by adding a small amount of Sb.

XRD patterns of $CH_3NH_3Pb_{1-x}Sb_xI_3$ cells on the FTO/TiO_2 are shown in **Figure 21(a)**. The diffraction peaks can be indexed by a cubic crystal system (Pm3m) for the $CH_3NH_3Pb_{1-x}Sb_xI_3$ thin films. Although the deposited films are a single perovskite structure, broader diffraction peaks due to the PbI_2 compound appeared in the $CH_3NH_3PbI_3$ film, as shown in **Figure 21(a)**. The Sb addition suppressed the formation of PbI_2, and most of PbI_2 was not detected for the $CH_3NH_3Pb_{1-x}Sb_xI_3$ cells with $x > 0.03$. **Figure 21(b)** shows measured lattice constants a of $CH_3NH_3Pb_{1-x}Sb_xI_3$ as a function of Sb concentration. A small

http://dx.doi.org/10.5772/65768

increase in lattice constants *a* is observed for x = 0.03 and 0.05, and further addition of Sb decreases the lattice constants, which seems to be a significant difference from the error bar. The XRD result of $CH_3NH_3PbI_3$ in **Figure 21(a)** showed the existence of PbI_2 after annealing at 100°C for 15 min. This would indicate partial separation of PbI_2 from $CH_3NH_3PbI_3$ after annealing, which also might correspond to the smaller lattice constant *a* (6.266 Å) of the cubic perovskite structure, compared with that (6.391 Å) of $CH_3NH_3PbI_3$ single crystal reported in Ref. [27].

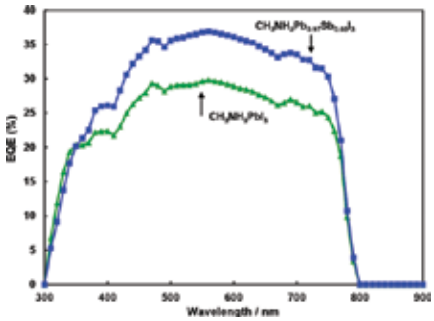

Figure 20. IPCE spectra of $CH_3NH_3PbI_3$ and $CH_3NH_3Pb_{0.97}Sb_{0.03}I_3$ cells.

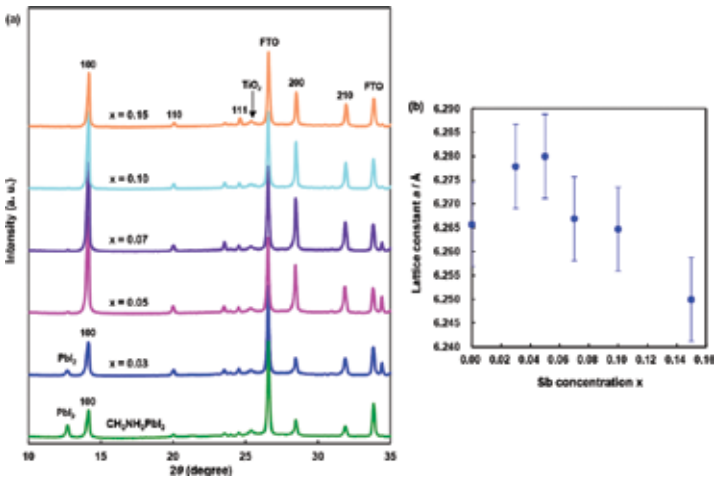

Figure 21. (a) XRD patterns of $CH_3NH_3Pb_{1-x}Sb_xI_3$ solar cells. (b) Lattice constants *a* of $CH_3NH_3Pb_{1-x}Sb_xI_3$ as a function of Sb concentration.

Increase in the photoconversion efficiencies could be explained by two mechanisms. The first mechanism is Sb doping effect at the Pb atom sites. The ionic valence of Sb is three, and it is higher compared with that of Pb^{2+}. Then, the excess charge of Sb^{3+} might work as carriers in the $CH_3NH_3Pb_{1-x}Sb_xI_3$ crystal, and the J_{SC} values were improved. The second mechanism is described as follows: I^- ions might be attracted at the I sites by Sb^{3+} with more ionic valence

compared with that of Pb^{2+}, which resulted in the suppression of PbI_2 elimination from $CH_3NH_3PbI_3$ and in the increase of lattice constants *a* of $CH_3NH_3PbI_3$. The suppression of PbI_2 would improve the interfacial structure of $TiO_2/CH_3NH_3PbI_3$, which might result in improvement of $V_{OC.}$ The lattice constants are expected to be decreased by an increase in the amount of Sb with an ionic size smaller than Pb. Other elemental dopings such as Ge, Tl, and In at the Pb sites were also reported [55, 56].

In summary, $TiO_2/CH_3NH_3Pb_{1-x}Sb_xI_3$-based photovoltaic devices were fabricated, and the effects of SbI_3 addition to the perovskite $CH_3NH_3PbI_3$ precursor solutions on the photovoltaic properties were investigated. The microstructures of the devices indicated that the lattice constant of $CH_3NH_3Pb_{1-x}Sb_xI_3$ increased a little, and that the formation of PbI_2 was inhibited by the addition of a small amount of Sb, which led to the improvement of the conversion efficiencies to ~9%. The IPCE also increased in the range of 350–770 nm by the addition of Sb.

7. Conclusion

Various $TiO_2/CH_3NH_3PbI_3$-based photovoltaic devices were fabricated and characterized. Especially, effects of metal doping and halogen doping to the perovskite and TiO_2 were investigated. Microstructure analysis indicated the changes of the perovskite structure, which resulted in the improvement of photovoltaic properties of the devices. Various elemental dopings to the perovskite structure could be studied further both by experiments and theoretical calculations as follows: Cs, Rb, and K doping to the CH_3NH_3 positions for stability of the structure; Ge, Sn, and Sb doping to the Pb positions for improvement of the semiconducting properties; Cl, Br, and F doping to the I positions for enhancement of carrier mobility.

Acknowledgements

The authors like to acknowledge T. Iwata, Y. Imanishi, M. Kanayama, T. Kida, H. Okada, and T. Akiyama for experimental help and support on the perovskite solar cells. This work was partly supported by Satellite Cluster Program of the Japan Science and Technology Agency and a Grant-in-Aid for Scientific Research (C) 25420760.

Author details

Takeo Oku*, Masahito Zushi, Kohei Suzuki, Yuya Ohishi, Taisuke Matsumoto and Atsushi Suzuki

*Address all correspondence to: oku@mat.usp.ac.jp

Department of Materials Science, The University of Shiga Prefecture, Hikone, Shiga, Japan

References

[1] Kojima A, Teshima K, Shirai Y, Miyasaka T (2009). Organometal halide perovskites as visible-light sensitizers for photovoltaic cells. Journal of the American Chemical Society, 131, 6050–6051.

[2] Im J-H, Lee C-R, Lee J-W, Park S-W, Park N-G (2011). 6.5% efficient perovskite quantum-dot-sensitized solar cell. Nanoscale, 3, 4088–4093.

[3] Kim HS, Lee CR, Im JH, Lee KB, Moehl T, Marchioro A, Moon SJ, Yum JH, Humphry-Baker R, Moser JE, et al (2012). Lead iodide perovskite sensitized all-solid-state submicron thin film mesoscopic solar cell with efficiency exceeding 9%. Scientific Reports, 2, 591–1–591–7.

[4] Grinberg I, West DV, Torres M, Gou G, Stein DM, Wu L, Chen G, Gallo EM, Akbashev A, Davies PK, et al. Perovskite oxides for visible-light-absorbing ferroelectric and photovoltaic materials. Nature, 2013, 503, 509–512.

[5] Lee MM, Teuscher J, Miyasaka T, Murakami TN, Snaith HJ (2012). Efficient hybrid solar cells based on meso-superstructured organometal halide perovskites. Science, 338, 643–647.

[6] Chung I, Lee B, He JQ, Chang RPH, Kanatzidis MG (2012). All-solid-state dye-sensitized solar cells with high efficiency. Nature, 485, 486–489.

[7] Stranks SD, Eperon GE, Grancini G, Menelaou C, Alcocer MJP, Leijtens T, Herz LM, Petrozza A, Snaith HJ (2013). Electron-hole diffusion lengths exceeding 1 micrometer in an organometal trihalide perovskite absorber. Science, 342, 341–344.

[8] Burschka J, Pellet N, Moon S-J, Humphry-Baker R, Gao P, Nazeeruddin MK, Grätzel M (2013). Sequential deposition as a route to high-performance perovskite-sensitized solar cells. Nature, 499, 316–320.

[9] Liu M, Johnston MB, Snaith HJ. Efficient planar heterojunction perovskite solar cells by vapour deposition (2013). Nature, 501, 395–398.

[10] Liu D, Kelly TL (2014). Perovskite solar cells with a planar heterojunction structure prepared using room-temperature solution processing techniques. Nature Photonics, 8, 133–138.

[11] Wang JT-W, Ball JM, Barea EM, Abate A, Alexander-Webber JA, Huang J, Saliba M, Mora-Sero I, Bisquert J, Snaith HJ, Nicholas RJ (2014). Low-temperature processed electron collection layers of graphene/TiO_2 nanocomposites in thin film perovskite solar cells. Nano Letters, 14, 724–730.

[12] Zhou H, Chen Q, Li G, Luo S, Song T-B, Duan H-S, Hong Z, You J, Liu Y, Yang Y (2014). Interface engineering of highly efficient perovskite solar cells. Science, 345, 542–546.

[13] Jeon NJ, Noh JH, Yang WS, Kim YC, Ryu S, Seo J, Seok SI (2015). Compositional engineering of perovskite materials for high-performance solar cells. Nature, 517, 476–480.

[14] Nie W, Tsai H, Asadpour R, Blancon JC, Neukirch AJ, Gupta G, Crochet JJ, Chhowalla M, Tretiak S, Alam MA, Wang HL, Mohite AD (2015). High-efficiency solution-processed perovskite solar cells with millimeter-scale grains. Science, 347, 522–525.

[15] Yang WS, Noh JH, Jeon NJ, Kim YC, Ryu S, Seo J, Seok SI (2015). High-performance photovoltaic perovskite layers fabricated through intramolecular exchange. Science, 348, 1234–1237.

[16] Saliba M, Orlandi S, Matsui T, Aghazada S, Cavazzini M, Correa-Baena JP, Gao P, Scopelliti R, Mosconi E, Dahmen KH, De Angelis F, Abate A, Hagfeldt A, Pozzi G, Graetzel M, Nazeeruddin MK (2016). A molecularly engineered hole-transporting material for efficient perovskite solar cells. Nature Energy, 1, 15017-1–15017-7.

[17] Bi D, Tress W, Dar MI, Gao P, Luo J, Renevier C, Schenk K, Abate A, Giordano F, Baena JPC, Decoppet JD, Zakeeruddin SM, Nazeeruddin MK, Grätzel M, Hagfeldt A. (2016). Efficient luminescent solar cells based on tailored mixed-cation perovskites. Science Advances, 2, e1501170-1–e1501170-7.

[18] Saliba M, Matsui T, Seo JY, Domanski K, Correa-Baena JP, Nazeeruddin MK, Zakeeruddin SM, Tress W, Abate A, Hagfeldtd A, Grätzel M (2016). Cesium-containing triple cation perovskite solar cells: improved stability, reproducibility and high efficiency. Energy Environmental Science, 9, 1989–1997.

[19] Oku T. Crystal structures of $CH_3NH_3PbI_3$ and related perovskite compounds used for solar cells, in Solar Cells – New Approaches and Reviews, Editor, Kosyachenko LA. Rijeka, Croatia (2015). InTech 77–102.

[20] Oku T, Takeda A, Nagata A, Kidowaki H, Kumada K, Fujimoto K, Suzuki A, Akiyama T, Yamasaki Y, Ōsawa E (2013). Microstructures and photovoltaic properties of C_{60} based solar cells with copper oxides, $CuInS_2$, phthalocyanines, porphyrin, PVK, nanodiamond, germanium and exciton diffusion blocking layers. Materials Technology, 28, 21–39.

[21] Oku T (2012). Direct structure analysis of advanced nanomaterials by high-resolution electron microscopy. Nanotechnology Reviews, 1, 389–425.

[22] Oku T (2014). High-resolution electron microscopy and electron diffraction of perovskite-type superconducting copper oxides. Nanotechnology Reviews, 3, 413–444.

[23] Oku T (2014). Structure analysis of advanced nanomaterials: nanoworld by high-resolution electron microscopy. Walter De Gruyter Inc. Berlin, Germany.

[24] Weber D (1978). $CH_3NH_3PbX_3$, a Pb(II)-system with cubic perovskite structure, Zeitschrift für Naturforschung B, 33, 1443–1445.

[25] Poglitsch A, Weber D (1987). Dynamic disorder in methylammonium trihalogenoplumbates (II) observed by millimeter-wave spectroscopy. The Journal of Chemical Physics, 87, 6373–6378.

[26] Onoda-Yamamuro N, Matsuo T, Suga H (1990). Calorimetric and IR spectroscopic studies of phase transitions in methylammonium trihalogenoplumbates (II). Journal of Physics and Chemistry of Solids, 51, 1383–1395.

[27] Mashiyama H, Kurihara Y, Azetsu T (1998). Disordered cubic perovskite structure of $CH_3NH_3PbX_3$ (X=Cl, Br, I). Journal of the Korean Physical Society, 32, S156–S158.

[28] Chen T, Benjamin JF, Ipek B, Tyagi M, Copley JRD, Brown CM, Choi JJ, Lee SH (2015). Rotational dynamics of organic cations in the $CH_3NH_3PbI_3$ perovskite. Physical Chemistry Chemical Physics, 17, 31278–31286.

[29] Weller MT, Weber OJ, Frost JM, Walsh A (2015). Cubic perovskite structure of black formamidinium lead iodide, α-$[HC(NH_2)_2]PbI_3$, at 298 K. Journal of Physical Chemistry Letters, 6, 3209–3212.

[30] Yamada K, Funabiki S, Horimoto H, Matsui T, Okuda T, Ichiba S (1991). Structural phase transitions of the polymorphs of $CsSnI_3$ by means of Rietveld analysis of the X-ray diffraction. Chemistry Letters, 20, 801–804.

[31] Chung I, Song JH, Im J, Androulakis J, Malliakas CD, Li H, Freeman AJ, Kenney JT, Kanatzidis MG (2012). $CsSnI_3$: semiconductor or metal? High electrical conductivity and strong near-infrared photoluminescence from a single material. High hole mobility and phase-transitions. Journal of the American Chemical Society, 134, 8579–8587.

[32] Thiele G, Rotter HW, Schmidt KD (1987). Crystal structures and phase transformations of cesium trihalogenogermanates $CsGeX_3$ (X = Cl, Br, I). Zeitschrift für Anorganische und Allgemeine Chemie, 545, 148–156.

[33] Zushi M, Suzuki A, Akiyama T, Oku T (2014). Fabrication and characterization of $TiO_2/CH_3NH_3PbI_3$-based photovoltaic devices. Chemistry Letters, 43, 916–918.

[34] Oku T, Kakuta N, Kobayashi K, Suzuki A, Kikuchi K (2011). Fabrication and characterization of TiO_2-based dye-sensitized solar cells. Progress in Natural Science: Materials International, 21, 122–126.

[35] Oku T, Zushi M, Imanishi Y, Suzuki A, Suzuki K (2014). Microstructures and photovoltaic properties of perovskite-type $CH_3NH_3PbI_3$ compounds. Applied Physics Express, 7, 121601–1–121601–4.

[36] Kawamura Y, Mashiyama H, Hasebe K (2002). Structural study on cubic–tetragonal transition of $CH_3NH_3PbI_3$. Journal of the Physical Society of Japan, 71, 1694–1697.

[37] Baikie T, Fang Y, Kadro JM, Schreyer M, Wei F, Mhaisalkar SG, Grätzel M, Whitec TJ (2013). Synthesis and crystal chemistry of the hybrid perovskite $(CH_3NH_3)PbI_3$ for solid-state sensitised solar cell applications. Journal of Materials Chemistry A, 1, 5628–5641.

[38] Li X, Bi D, Yi C, Décoppet JD, Luo J, Zakeeruddin SM, Hagfeldt A, Grätzel M (2016). A vacuum flash–assisted solution process for high-efficiency large-area perovskite solar cells. Science, 353, 58–62.

[39] Oku T, Matsumoto T, Suzuki A, Suzuki K (2015). Fabrication and characterization of a perovskite-type solar cell with a substrate size of 70 mm. Coatings, 5, 646–655.

[40] Dong Q, Fang Y, Shao Y, Mulligan P, Qiu J, Cao L, Huang J (2015). Electron-hole diffusion lengths > 175 μm in solution-grown $CH_3NH_3PbI_3$ single crystals. Science, 347, 967–970.

[41] Oku T, Iwata T, Suzuki A (2015). Effects of niobium addition into TiO_2 layers on $CH_3NH_3PbI_3$-based photovoltaic devices. Chemistry Letters, 44, 1033–1035.

[42] Miyagi T, Kamei M, Sakaguchi I, Mitsuhashi T, Yamazaki A (2004). Photocatalytic property and deep levels of Nb-doped anatase TiO_2 film grown by metalorganic chemical vapor deposition. Japanese Journal of Applied Physics, 43, 775–776.

[43] Emeline AV, Furubayashi Y, Zhang X, Jin M, Murakami T, Fujishima A (2005). Photoelectrochemical behavior of Nb-doped TiO_2 electrodes. The Journal of Physical Chemistry B, 109, 24441–24444.

[44] Hirano M, Matsushima K (2006). Photoactive and adsorptive niobium-doped anatase (TiO_2) nanoparticles: influence of hydrothermal conditions on their morphology, structure, and properties. Journal of the American Ceramic Society, 89, 110–117.

[45] Zhang SX, Kundaliya DC, Yu W, Dhar S, Young SY, Salamanca-Riba LG, Ogale SB, Vispute RD, Venkatesan T (2007). Niobium doped TiO_2: intrinsic transparent metallic anatase versus highly resistive rutile phase. Journal of Applied Physics, 102, 013701.

[46] Maghanga CM, Jensen J, Niklasson GA, Granqvist CG, Mwamburi M (2010). Transparent and conducting TiO_2:Nb films made by sputter deposition: application to spectrally selective solar reflectors. Solar Energy Materials and Solar Cells, 94, 75–79.

[47] Tian Y, Tatsuma T (2005). Mechanisms and applications of plasmon-induced charge separation at TiO_2 films loaded with gold nanoparticles. Journal of the American Chemical Society, 127, 7632–7637.

[48] Matsumoto T, Oku T, Akiyama T (2013). Incorporation effect of silver nanoparticles on inverted type bulk-heterojunction organic solar cells. Japanese Journal of Applied Physics, 52, 04CR13–1–04CR13–5.

[49] Oku T, Suzuki K, Suzuki A (2016). Effects of chlorine addition to perovskite-type $CH_3NH_3PbI_3$ photovoltaic devices. Journal of the Ceramic Society of Japan, 124, 234–238.

[50] Shi D, Adinolfi V, Comin R, Yuan M, Alarousu E, Buin A, Chen Y, Hoogland S, Rothenberger A, Katsiev K, Losovyj Y, Zhang X, Dowben PA, Mohammed OF, Sargent

EH, Bakr OM (2015). Low trap-state density and long carrier diffusion in organolead trihalide perovskite single crystals. Science, 347, 519–522.

[51] Hao F, Stoumpos CC, Cao DH, Chang RPH, Kanatzidis MG (2014). Lead-free solid-state organic-inorganic halide perovskite solar cells. Nature Photonics, 8, 489–494.

[52] Hao F, Stoumpos CC, Guo P, Zhou N, Marks TJ, Chang RPH, Kanatzidis MG (2015). Solvent-mediated crystallization of $CH_3NH_3SnI_3$ films for heterojunction depleted perovskite solar cells. Journal of the American Chemical Society, 137, 11445–11452.

[53] Oku T, Ohishi Y, Suzuki A (2016). Effects of antimony addition to perovskite-type $CH_3NH_3PbI_3$ photovoltaic devices. Chemistry Letters, 45, 134–136.

[54] Oku T, Ohishi Y, Suzuki A, Miyazawa Y (2016). Effects of Cl addition to Sb-doped perovskite-type $CH_3NH_3PbI_3$ photovoltaic devices. Metals, 6, 147–1–147–13.

[55] Krishnamoorthy T, Ding H, Yan C, Leong WL, Baikie T, Zhang Z, Sherburne M, Li S, Asta M, Mathews N, Mhaisalkarac SG (2015). Lead-free germanium iodide perovskite materials for photovoltaic applications. Journal of Materials Chemistry A, 3, 23829–23832.

[56] Ohishi Y, Oku T, Suzuki A (2016). Fabrication and characterization of perovskite-based $CH_3NH_3Pb_{1-x}Ge_xI_3$, $CH_3NH_3Pb_{1-x}Tl_xI_3$ and $CH_3NH_3Pb_{1-x}In_xI_3$ photovoltaic devices. AIP Conference Proceedings, 1709, 020020-1–020020-8.

Chapter 12

Perovskite as Light Harvester: Prospects, Efficiency, Pitfalls and Roadmap

Ruby Srivastava

Additional information is available at the end of the chapter

http://dx.doi.org/10.5772/65052

Abstract

In the recent years, perovskite materials have attracted great attention due to their excellent light-harvesting properties. The organic materials of these hybrid inorganic organic light harvesters are used as sensitizers and the inorganic materials have been used as light absorbers. The exceptional properties of these materials such as long diffusion length, high carrier mobility, affordable device fabrication, and adjustable adsorption range have created a new era in optoelectronic technologies. The perovskites have become promising materials due of their versatility in device architecture, flexibility in material growth, and ability to achieve the high efficiency through various processing techniques. The superior performance of silicon-based tandems by achieving efficiency more than 40% has encouraged researchers to further expand the investigations to higher levels. The quest to transit the research curiosity to the market photovoltaic technology has given a new dimension to the remarkable ascension of perovskite solar cells. This chapter introduces the experimental and theoretical aspects, the electrical and optical properties, pitfalls, and a roadmap for the future prospects of perovskite materials.

Keywords: perovskite, power conversion efficiency, energy conversion and storage, toxicity, hysteresis

1. Introduction

The fast-paced industrial development and population growth has increased the consumption of global energy to such an extent that it has become the ultimate necessity to use the renewable energy resources for long-term sustainable development. Now it has become a challenge for both scientists and technologists to generate the cost-effective and environmentally friendly renewable energy resources [1, 2].

Although solar cells based on the photovoltaic effect have attracted great attention due to the advantage of decentralization and sustainability, yet they suffer low cost effectiveness. Another emerging class of thin-film energy devices based on amorphous silicon also tried to capture the market, making headway by processing of costs per unit area [3–5]. The manufacturing of inorganic thin-films solar cells needs high-temperature and high vacuum-based techniques [6]. In addition, these techniques are limited and due to the inclusion of toxic elements, they are limited to large-scale production and wide applications [7].

In 1991, a new breakthrough emerged in the form of dye-sensitized solar cells (DSSCs) that have attracted considerable attention due to their potential application in low-cost solar energy conversion [8–16]. A high efficiency exceeding 12% was obtained by using 10 μm mesoporous TiO_2 film sensitized with a cobalt redox electrolyte and an organic dye [17]. Furthermore, solid-state DSSCs were also investigated where the liquid electrolyte was replaced by a solid hole-transporting material (HTM) [e.g., poly(3-hexylth-iophene)(P3HT),2,2′,7,7′-tetrakis-(N,N-di-p-methoxyphenyl-amine)-9,9′spirobifluorene (spiro-MeOTAD)], polyaniline, and polypyrrole [8] to increase the open circuit voltage and stability of solar cells [18–22]. However, these ss-DSSCs also suffer from faster electron recombination dynamics between electrons (TiO_2) and holes (hole transporter), which results in the low efficiency of ss-DSSCs [23]. So attempts were made to design various types of cells to increase the efficiency of solar cells [24].

This efficiency criterion was increased by the introduction of the perovskite sensitizer ABX_3 (A = CH_3NH_3, B = Pb, Sn, and X = Cl, Br, I), introduced by Prof. Grätzel and team, which has opened a new era in the field of DSSCs due to the excellent light-harvesting capabilities [24–37]. These materials are composed of earth abundant materials, inexpensive, processable at low temperatures (printing techniques), generate charges freely (after absorption) in bulk materials, which qualify them as low energy-loss charge generators and collectors [38–40]. Methylammonium lead trihalide ($CH_3NH_3PbX_3$, where X is a halogen ion such as I^-, Br^-, and Cl^-) have an optical bandgap between 2.3 and 1.6 eV depending on halide content, while formamidinum lead trihalide ($H_2NCHNH_2PbX_3$) also have a bandgap between 2.2 and 1.5 eV. The minimum bandgap is closer to optimum for a single-junction cell than methylammonium lead trihalide, which enhance to higher efficiencies [41]. The power conversion efficiency (PCE) of perovskite cells was improved from 7.2 to 15.9%, which is associated with the comparable optical absorption length and charge-carrier diffusion lengths, making this device the most outperforming relative to the other third-generation thin-film solar cell technologies. Although two different configurations using $CH_3NH_3PbI_3$ perovskite in a classical solid-state DSSC and in a thin-film planar configuration with $CH_3NH_3PbI_{3-x}Cl_x$, having efficiency exceeding 16%, have been reported [26, 42], provided few issues related to the stability and hysteresis are to be solved effectively [43].

Here, it is necessary to mention that the lack of hysteresis that was an obstacle for stable operation in perovskite was observed recently using thin films of organometallic perovskites with millimeter-scale crystalline grains with efficiencies approximately equal to 18% [44].

The three recent reports have given high hopes in the field of solar cells as EPFL scientists have developed a new hole-transporting material FDT that can reduce the cost and achieve

the power conversion efficiency of 20.2% [45]. Another study by Hong Kong University claims that they have achieved the highest efficiency of 25.5% by perovskite-silicon tandem solar cells [46]. In the meantime, it has been claimed that the efficiency of more than 30% can be achieved by tandem solar cells based on silicon and perovskites [47].

2. Structure of perovskite materials

The basic structure of perovskite consists of a 3D network corner-sharing BX_6 octahedra, where A (e.g., A = Cs, CH_3NH_3, NH_2CHNH_2) cations are located in the larger 12-fold coordinated holes between the octahedra [44]. It is composed of a metal cation (M = Sn, Pb, Ge, Cu) and its ligantanions (X = O^{2-}, Cl^-, Br^-, I^-, or S^{2-}). In the case of inorganic perovskite compounds, the structures can be distorted as a result of the cation displacements, which give rise to some useful properties of ferroelectricity and antiferroelectricity due to the stereochemically active pairs of A cations [48]. The simple cubic structure of $CH_3NH_3PbI_3$ is given in **Figure 1**.

These inorganic-organic hybrid compounds have the advantages of inorganic components that include structural order and thermal stability with interesting characteristics of organic materials such as low cost, mechanical flexibility, and functional versatility [49–53]. Numerous compounds have been reported by the covalent bonding between the inorganic and organic bonds [54]. Although the degree of interactions in organic-inorganic systems with the van der Waals interacting system is relatively small, the reason for the small van der Waals interaction is the choice of organic cations, which is limited as the restricted dimension of the cuboctahedral hole formed by the 12 nearest-neighbor X atoms. The synthesis of compounds CH_3NH_3 MX_3 with M = Sn, Pb and X= Cl, Br, and I has been successfully carried out by some groups [55–57]. These organic cations show orientational disorder at high temperature, while at lower temperature the cubic phase results in a structural phase transition as the tolerance factor is smaller than unity. Upon cooling, the structure distorts to lower its symmetry as there are many restrictions to the motion of methylammonium cations [57].

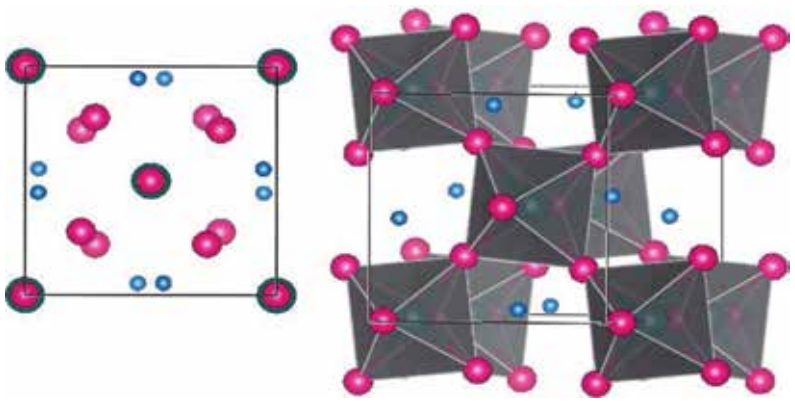

Figure 1. The crystal structure of perovskites, ABX_3, a large cation (A) at center together with metal cation (B) bonded to the surrounded halides (X). Color code: A (CH_3NH_3),blue; B (Pb), green; and X (I), pink.

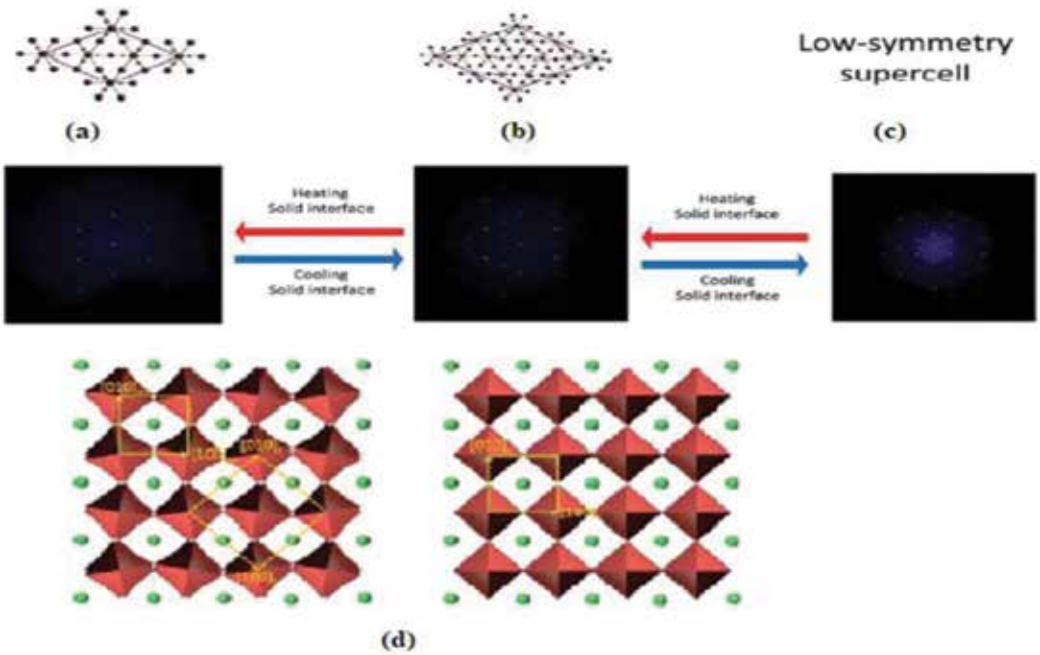

Figure 2. Graphical representation of phase transitions of MA(Pb, Sn)X_3 perovskite materials (a) α-phase, (b) β-phase, (c) γ-phase. Precision images are taken at the [006] view. (d) The structural transformation of Br included in $MAPbI_3$. Adapted with permission from reference [37].

MA, FA, Pb, and Sn perovskite combinations to identify three distinct phase transitions that occur are classified as a high temperature $\boldsymbol{\alpha}$ phase, an intermediate $\boldsymbol{\beta}$ temperature phase, and a low temperature $\boldsymbol{\gamma}$ phase [54]. These different phases are represented in **Figure 2**.

The perovskites were first investigated by Goldschmidt in the 1920s [58] in work related to tolerance factors. The tolerance factor, t, with respect to the ionic radius of the actual ions is given in Eq. (1), where r_A, r_B, and r_C are the ionic radius of the A, B, and C ions, respectively.

$$t = \frac{r_A + r_C}{\sqrt{2}\left(r_B + r_C\right)} \tag{1}$$

The tolerance factor of (0.9–1) is for an ideal cubic structure, for a cubic structure with the tolerance factor (0.7–0.9), the A ion is too small or the B ion is too large. This can be resulted in orthorhombic, rhombohedral, or tetragonal structure. For a large A cation, t becomes larger than one, which results in layered perovskite structures [59, 60]. The compiled results are given in **Table 1** and the different forms of perovskite material $CH_3NH_3PbI_3$ are given in **Figure 3**. The expected structure is also related to Pauling's rules (PRs) [61], given the expected coordination around a two-component radii (cation/anion) system which is summarized in **Table 2**.

The smaller tolerance factor is related to lower symmetry tetragonal or orthorhombic structures, whereas larger t ($t > 1$) could destabilize the three-dimensional (3D) B-X network.

http://dx.doi.org/10.5772/65052

Structure	Tolerance factor	Comment for cation/anion
Tetragonal/rhombohedral/ orthorhombic	0.7–0.9	Cation too large or anion too small
Cubic	0.9–1.0	Ideal perovskite
Layered structures	>1.0	Cation too large

Table 1. Tolerance factors for the perovskite structures

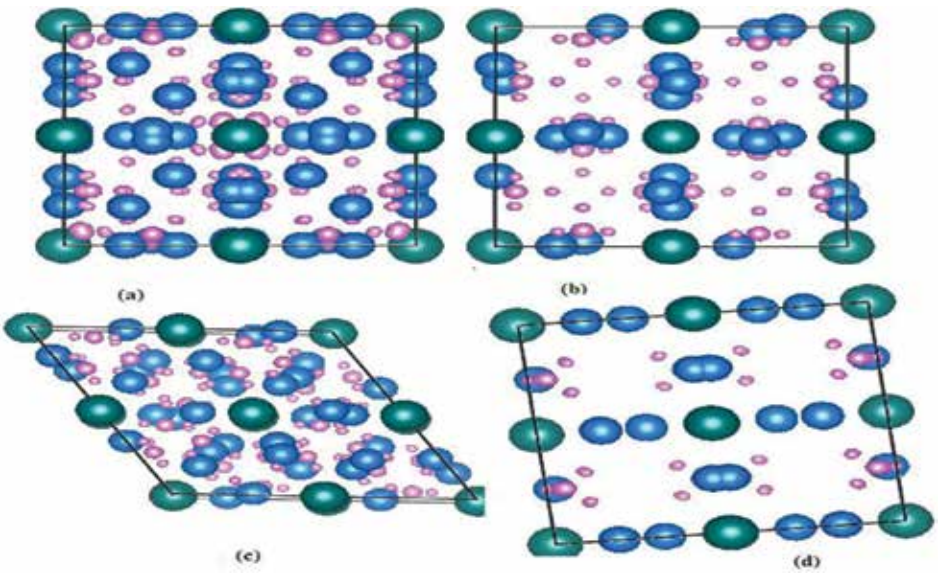

Figure 3. The crystal structure of perovskites ($CH_3NH_3PbI_3$) in different forms: (a) cubic, (b) tetragonal, (c) rhombohedral, and (d) orthorhombic. Color code: CH_3NH_3, pink; Pb, green and I, blue.

Coordination	r_c/r_a	Coordination number
0.15–0.22	Triangular	3
0.22–0.41	Tetrahedral	4
0.41–0.73	Octahedral	6
0.73–1.0	Cubic	8

Table 2. Coordination and ideal $r_c r_a$ (Pauling's rules). r_c and r_a represent the cationic and anionic radii

The other important parameter is an octahedral factor that plays an important role in these materials, and is given by,

$$\mu = R_B / R_A \tag{2}$$

where R_B is the ionic radii of the B cation and R_A is the ionic radii of A anion. If $\mu > 0.442$, the formation of halide perovskite achieves, whereas below this value BX_6 octahedron will

become unstable and a perovskite structure will not form, although these factors provide a guidelines for the formation of halide perovskite, yet they are not sufficient to predict the structural formations within the perovskite family [62].

2.1. Experimental scenario

2.1.1. Origin of perovskite

Although these materials already possessed useful physical properties, organic-like mobility, nonlinear optical properties, enhanced exciton binding energies, electroluminescence, magnetic properties, and conductivity, they have emerged as DSSCs only in 2009 [63–68]. The performance of DSSCs is assessed by three major parameters: short-circuit photocurrent (J_{SC}), open-circuit voltage (V_{OC}), and fill factor (FF), which are further used to calculate the efficiency (PCE). V_{OC} is proportional to the HOMO-LUMO energy gap and J_{SC} reflects the mobility, efficient light-harvesting, and carrier generation. These values of different device structures are presented in **Table 3**.

The first perovskite-sensitized TiO_2 solar cell gave the efficiency of 3.8 and 3.1%, respectively [13]. Later on the titania's surface and $CH_3NH_3PbI_3$-based iodide liquid electrolyte solar cell have increased the efficiency to 6.5% [25]. In 2012, the liquid electrolyte was replaced with a solid electrolyte and a PCE of 9.7% was achieved [69]. A sequential deposition method for the formation of the perovskite pigment within the porous metal oxide film was developed with a PCE of 15% in 2013 (short-circuit current density J_{SC} = 21.5 mA/cm^2, open-circuit voltage V_{OC} = 1.02 V, and fill factor FF = 0.71) [27]. An efficiency of 20% at low temperature was achieved in a processed solar cell, through the end of 2013 [70, 71]. Further, it is reported that the achieved efficiency has above 30% in 2016.

2.1.2. Photoanodes

Mesoporous metal oxide films act as a working electrode for perovskite cells. The charge extraction rates are relatively faster for the perovskite solar cells than the conventional DSSCs [39]. Again the mesoporous TiO_2 was replaced by Al_2O_3 with similar mesomorphology and it was seen that the PCE unexpectedly reached to 10.9% giving hopes for the future increase in efficiency. Furthermore, the DSSC efficiency has improved to 15.9% [27], yet there is the difficulty in pore filling because of the labyrinthine maze structure [72], which was alternatively substituted by a vertically aligned nanowire (NW) and nanotube (NT) structure. These nanotubes and nanowires can be used in pore filling due to their open porous structures. Moreover, they are reported to be better in electron transportation and recombination behavior and hole conductors presenting faster recombination than nanoparticulate films in liquid-based DSSCs [73–75].

As the absorption properties of perovskite are excellent, a possible decrease in the total surface area of the NWs/NTs compared to the nanoparticles does not stimulate the significant reduction of photocurrent. Later it was concluded that perovskite semiconductors in their simple architecture can exhibit sufficiently good ambipolar charge transport and the principal roles of photovoltaic operation, including charge generation, light absorption, and transport

Perovskite	Photo anode	HTM	J_{SC} (mA/cm)	V_{OC} (v)	FF	PCE (%)	References
$CH_3NH_3PbI_3$	mp (TiO_2)	Spiro	17.6	0.88	0.62	9.7	[69]
$CH_3NH_3PbI_3$	TiO_2 NS	Spiro	16.1	0.63	0.57	5.5	[30]
$CH_3NH_3PbI_3$	mp (TiO_2)	Spiro	18.8	0.71	0.66	8	[70]
$CH_3NH_3PbI_3$	mp (TiO_2)	Spiro	18.3	0.87	0.66	10.4	[71]
$CH_3NH_3PbI_2Cl$	mp (Al_2O_3)	Spiro	17.8	0.98	0.63	10.9	[26]
$CH_3NH_3PbI_3$	TiO_2-NWAs	Spiro	10.67	0.74	0.54	4.29	[72]
$CH_3NH_3PbI_2Br$	TiO_2-NWAs	Spiro	10.12	0.82	0.59	4.87	[72]
$CH_3NH_3PbI_3$	mp (TiO_2)	Spiro	20.0	0.99	0.73	15.0	[73]
$CH_3NH_3PbI_3$	Rutile (TiO_2)	Spiro	15.6	0.95	0.63	9.4	[74]
$CH_3NH_3PbI_3$	mp-ZrO_2	Spiro	17.3	1.07	0.59	10.8	[75]
$CH_3NH_3PbI_3$	(TiO_2)crystal	Spiro	12.86	0.79	0.70	7.29	[76]
$CH_3NH_3PbI_3$	mp (Al_2O_3)	Spiro	18.0	1.02	0.67	12.3	[37]
$CH_3NH_3PbI_3$	$CH_3NH_3PbI_3$	Spiro	21.5	1.07	0.67	15.4	[77]
$CH_3NH_3PbI_3$	mp (TiO_2)	P3HT	12.6	0.73	0.73	6.7	[42]
$CH_3NH_3PbI_3$	mp (TiO_2)	PCPDTBT	10.3	0.77	0.67	5.3	[42]
$CH_3NH_3PbI_3$	mp (TiO_2)	PCPDTBT	10.5	0.92	0.43	4.2	[42]
$CH_3NH_3PbI_3$	mp (TiO_2)	PTAA	16.4	0.90	0.61	9.0	[42]
$CH_3NH_3PbI_3$	mp (TiO_2)	PTAA	19.3	0.91	0.70	12.3	[32]
$CH_3NH_3Pb(I_{1-x}Br_x)_3$	Mesoscopic and planar structures	Poly(triarylamine)	19.64	1.11	74.2	16.2	[79]
$CH_3NH_3PbI_3$	Mesoscopic TiO_2	Spiro	1.02	21.2	77.6	16.7	[80]
$FAPbI_3$	Mesoscopic TiO_2	Spiro	1.03	20.97	74	16	[78]
$CH_3NH_3PbI_{3-x}Cl_x$	Planar heterojunction	Spiro	1.13	22.75	75.01	19.3	[81]
$CH_3NH_3PbI_3$		FDT	1.148	22.7	0.76	20.2	[55]

Abbreviations: mp, mesoporous; spiro, spiro OMeTAD.

Table 3. comprehensive summary of the performance of perovskite solar cells, including the perovskite materials, photoanodes, hole-transport materials (HTMs), J_{SC} (mA/cm), V_{OC} (v), FF and PCE (%)

of both electrons and holes. Now the challenge is to determine whether mesostructure is essential or the thin-film p-i-n can lead to a better performance [76].

2.1.3. Perovskite thin films

While using the methylammonium lead halide ($CH_3NH_3PbX_3$, X-halogen) and its mixed-halide crystals, corresponding to the 3D perovskite structures as light harvesters in solar cells,

it is observed that substituting the I with Cl/Br ions, bandgap tuning of $MAPbX_3$ is achieved, which occurred due to the strong dependence of electronic energies on the effective exciton mass [76]. The entire visible region was controlled by tuning the bandgap. Apart from that, the addition of Cl/Br into an iodide-based structure shows a drastic improvement in the charge transport, relative stability, and separation kinetics within the perovskite layer [77]. It was also observed that the bandgap is reduced (1.48–2.23 eV), leading to high short-circuit currents of >23 mA/cm^2 and a PCE of up to 14.2%, when the cation size of perovskite materials is increased [42].

There are a few solution-based techniques that has been used for the fabrication of thin films, where a mixture of two precursors is used to form final absorber, but due to the lack of suitable solvents and high-reaction rate of the perovskite component, the process results in thin film with pinhole formation and incomplete surface coverage, which deteriorates the film quality and thus effect the device performance.

The two-step deposition technique that was used previously to prepare the films of organic-inorganic systems has incompatible solubility characteristics where the organic component is difficult to evaporate. Devices based on the planar $CH_3NH_3PbI_3$ thin film via the modified two-step deposition technique have also achieved the efficiency of 12.1% [78].

Another technique that was developed was dual-source vapor-deposited organometallic trihalide perovskite solar cells based on a p-i-n thin-film architecture with high efficiency. However, the deposition with the vacuum evaporation method will make it cost effective [26].

2.1.4. Hole-transporting materials (HTMs)

The conductivity of perovskite is high, which requires a thick layer of HTM to avoid pinholes. Spiro-OMeTAD, due to being less conductive, offers high resistance because of thick capping layers. A wide variety of polymer hole conductors are also used, which is shown in **Figure 4**. Protic ionic liquids (PILs) are used as effective p dopants in hybrid solar cells [78] based on triarylamine hole-transporting materials. Further, the efficiency is improved by replacing the lithium salts, p-dopants for spiro-OMeTAD with PILs [79]. While using other HTMs as P3HT and DEH HTM, the efficiency of spiro-OMeTAD is much slower than P3HT and DEH HTM, respectively. However, a recent synthesis based on the pyrene-based derivative Py-C also exhibited an overall PCE of 12.7% [76]. As the hole conductors, spiro-OMeTAD and P3HT are costly, so an inexpensive, stable, solution-processable inorganic CuI as the hole conductor has been demonstrated [80]. A solution-processed p-type direct bandgap semiconductor $CsSnI_3$ with a perovskite structure can also be used for hole conduction replacing a liquid electrolyte [34]. Overall we can say that perovskite materials play both the role of light harvesters and hole conductors. Recently, a hole-conductor-free mesoscopic $CH_3NH_3PbI_3$ perovskite/TiO_2 heterojunction solar cell has reported with a PCE of 5.5% [30], yet the photovoltaic performance was inferior to that of HTM. The tuning of bandgap of perovskite materials plays an important role in photophysical properties. The energy bandgaps of different hybrid materials and the hole-transporting materials are given in **Figures 5** and **6**.

http://dx.doi.org/10.5772/65052

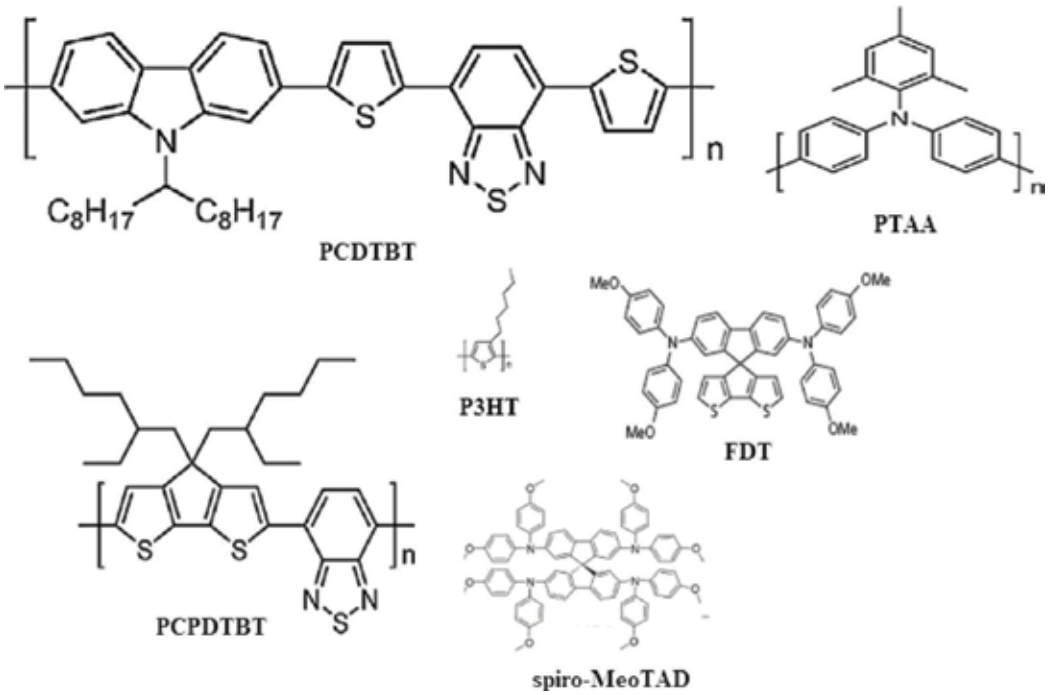

Figure 4. Structural representation of hole-transporting materials (HTMs).

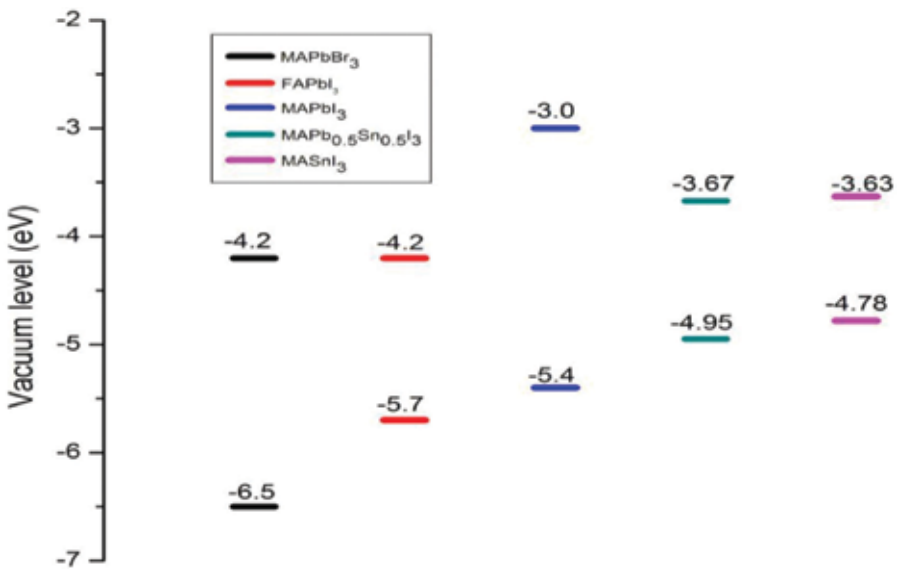

Figure 5. Energy bandgap diagram of hybrid perovskite materials.

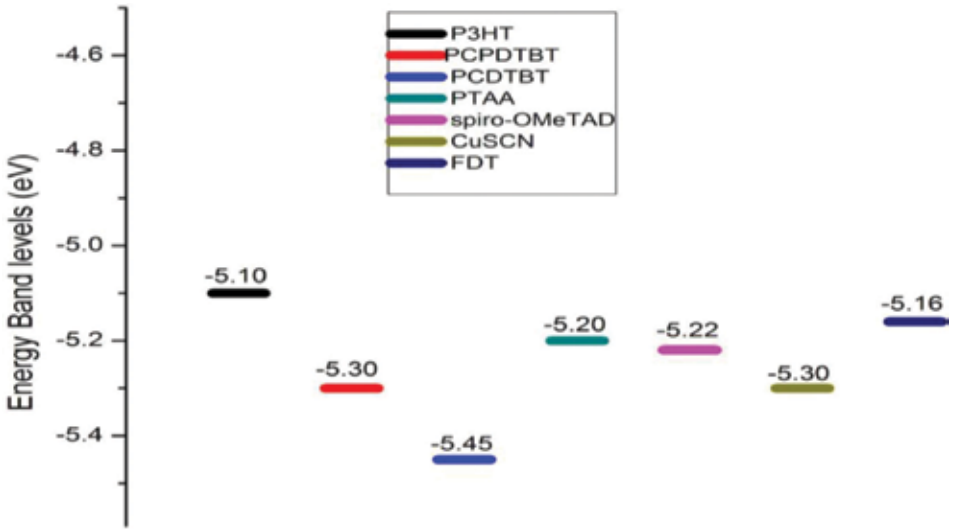

Figure 6. Energy level diagram of hole transporting materials (HTMs).

2.1.5. Measurement of charge-carrier mobility, lifetime and diffusion lengths

Regarding the exciton or the electron and hole diffusion length, it was observed that 100-nm long range diffusion length was obtained in solution-processed $CH_3NH_3PbI_3$ by applying femtosecond transient optical spectroscopy to bilayers that interface this perovskite with either selective-electron or selective-hole extraction materials [38]. The higher efficiency of these materials is only due to the comparable optical absorption length and charge-carrier diffusion lengths. Photoluminescence quenching measurements were performed to extract the electron-hole diffusion lengths in triiodide ($CH_3NH_3PbI_3$) and mixed-halide ($CH_3NH_3PbI_{3-x}Cl_x$) perovskite thin films [39]. In mixed-halide perovskite cells, the larger diffusion length is due to the much longer recombination time, requires both low recombination rates and high charge-carrier mobility; however, the mechanism causing the extended diffusion length is still unclear. Few other things that remain unclear is the relative fraction of free and bound charge pairs at room temperature, the nature of the excited state, and the role of the two species [81, 82].

2.2. Theoretical scenario

There are reports that prove that Density functional theory (DFT) calculations have already carried out before the first perovskite solar cell was reported experimentally [4, 13]. Various theoretical methods were adopted using exchange-correlation functionals such as Local density approximation (LDA) [83], Generalized gradient approximation (GGA) [51], hybrid functional methods (HSE), quasiparticle GW methods, spin-orbit-coupling (SOC), and van der Waals interactions. LDA underestimates and GGA overestimates the lattice parameters.

It is observed that when dispersion interactions are included, the calculated results match well with the experimental results. It is found that adding dispersion corrections increases the binding and corrects the GGA errors.

However, the defects does not affect much as they do not create a detrimental deep level within the bandgap [84, 85] that could be carrier traps and recombination centers for electron-hole in solar cells. Ringwood [86] has included that the contribution of charges depends on the differences in electronegativity. Since lead is considered as a provider of the charge and size, it holds the perovskite crystals all together.

2.2.1. Ambipolar activities

The ambipolar activities of these materials can be defined by taking effective mass into consideration which is defined by formula:

$$m^* = \hbar^2 \left[\frac{\delta^2 \varepsilon(k)}{\delta^2 \varepsilon(k)} \right]^{-1} \tag{3}$$

where $\varepsilon(k)$ is the energy dispersion relation functions, described by the band structures. If the band is more dispersive (flat), near the band edges, the effective mass is lighter (heavier). In perovskite materials, the lone-pair Pb s electrons play a vital role. The electronic structure of $CH_3NH_3PbI_3$ is inverted. The conduction band matrix is derived from Pb p orbitals, and the valence band matrix is a mixture of Pb s and I p (s-p semiconductor) orbitals. A cation Pb p orbital has a much higher energy level than anion p orbitals, although the CBM is derived from Pb p orbitals, Therefore, the lower conduction band of $CH_3NH_3PbI_3$ is more dispersive than the upper valence band, similarly the upper valence band of $CH_3NH_3PbI_3$ is dispersive due to the strong s-p coupling around the Valence band maximum (VBM). Due to the balance between the hole effective mass and the electron effective mass, $CH_3NH_3PbI_3$ leads to higher ambipolar activities. It might be possible that many-body effect plays a role for small carrier effective mass, as the effective mass calculated by the GW + SOC method [87] is even lower. The effective hole and electron masses are given in **Table 4**.

Materials	m_e^*/m_0	m_h^*/m_0	**Bandgap (eV)**
Silicon	0.26	0.29	1.11
GaAs	0.07	0.34	1.43
$CsSnI_3$	0.19	0.09 (0.15)	1.14
$CsSnI_3$ (SOC)	0.16	0.07	
$CH_3NH_3PbI_3$	0.35 (0.32)	0.31 (0.36)	1.5–2.0
$CH_3NH_3PbI_3$ (SOC)	0.18 (0.23)	0.21 (0.29)	

Table 4. Calculated effective masses (electron and holes) and bandgap (eV) for different materials. Experimental values are in parenthesis

2.2.2. Optical absorption spectra

The optical absorption spectra of perovskite materials are determined by the energy bandgaps and partial density of states (pdos). The pdos graph for different materials is depicted in **Figure 7**. The energy bandgap measures the probability of each photoelectric transition and the density of states measures the total number of possible photoelectric transitions. Thus, we can easily conclude that the optical absorption coefficient of a material is closely related to its electronic structure. However, the effect of optical absorption spectra is not considered in the Shockley-Queisser limit [42]. The theoretical maximum efficiency depends on the thickness of the absorber layer. Recently, a method has been developed by Yu et al. [88], in which they calculated the maximum efficiency based on the absorber thickness by taking absorption coefficient and absorber layer thickness both into consideration. So theoretical calculations were carried out on this basis and it was found that halide perovskites ($CH_3NH_3PbI_3$ and $CsPbI_3$) exhibit much higher conversion efficiencies for any given thickness. These materials are also capable of achieving high efficiencies with very thin absorber layers. On the basis of experimental calculations, it is proved that $CH_3NH_3PbI_3$ perovskite has the capability of achieving a high fill factor. Improved interfaces and contact layers also improve the performance of a solar cell, while Pb chalcogenides exhibit abnormal bandgap changes with lattice constant and strain [89].

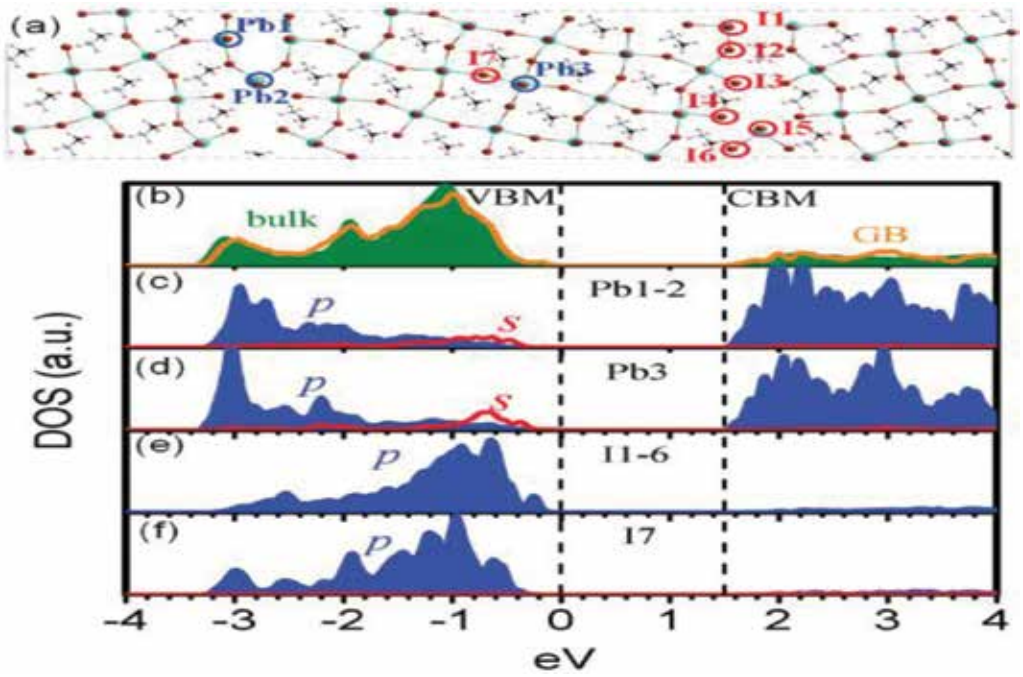

Figure 7. (a) The periodic structural model of Σ5 (310) GB for $CH_3NH_3PbI_3$. (b) Comparison of DOS of bulk $CH_3NH_3PbI_3$calculated from unit cell. (c–f) pdos of selected atoms highlighted in the above structure. Adapted with permission from reference [137].

http://dx.doi.org/10.5772/65052

2.2.3. Ferroelectricity

One more theoretical aspect is the dipole moment of the noncentrosymmetric organic cation in perovskite materials. It was shown from electric dipole calculations of the organic cation that hybrid perovskites exhibit spontaneous electric polarization, which might be due to the two reasons: the alignment of the dipole moments of organic cations and the intrinsic lattice distortion breaking the crystal centrosymmetry. On the basis of this concept, it was proposed in the studies that the presence of ferroelectric domains will result in internal junctions might support electron-hole separation and transportation. However, the calculated value of $CH_3NH_3PbI_3$ bulk polarization is 38 mC/cm^2, which is comparable to the value of ferroelectric oxide perovskites such as $KNbO_3$ (30 mC/cm^2) [90]. Frost and coworkers [91] suggested that it may be possible that the boundaries of ferroelectric domains may form "ferroelectric highways" that facilitate the transportation of electrons and holes. Furthermore, it was proposed that the favorable highways are energetically chosen in such a way that the holes and electrons avoid any collision with the opposite charges. It is directly seen in the recent experiment by direct observation of ferroelectric domains in the β phase of $CH_3NH_3PbI_3$. Another important factor is that V_{OC} can be larger than the bandgap, and charge separation and carrier lifetime can be enhanced due to the internal electric field [92].

2.2.4. Interface and surface

The surface and interface between the absorber, carrier transport layers, and electrode contact layers are also important for efficient carrier transportation. However, the two-step method, vacuum deposition and vapor-assisted solution processing methods [85], have improved the quality much better by the one-step method. The vacuum deposition method is used in small molecule-based devices, which makes the use of insoluble materials more stable than their soluble analogues. There are at least three aspects worth consideration.

2.2.4.1. Band alignment

The bandgaps and band alignments of perovskites can also be tuned by the chemical management of compositional elements, including organic cations [93, 94], Pb [95–97], and halogen elements [98, 99]. This is another way to optimize band alignment at interfaces.

2.2.4.2. Interface structure and passivation

The unusual hysteresis of the *I–V* curve of perovskite solar cells, which would reduce the working cell efficiency, was suspected to be related to the interface properties [99, 100].

2.2.4.3. Surface

Abate et al. [79] reported the existence of trap states at the perovskite surface, which generated charge accumulation and consequent recombination losses in working solar cells. They identified under coordinated iodine ions as responsible and used supramolecular halogen bond complexation for passivation.

2.2.5. Point defects

The p- or n-type absorbers were made from materials with intrinsic defects, or using intentional doping intrinsic defects that create deep energy levels in the absorber usually act as Shockley-Read-Hall nonradiative recombination centers and carrier traps, reducing the carrier lifetime and thus V_{oc}. A good solar cell absorber must exhibit proper doping and defect properties. There are many types of defects as a donor and acceptor which lies in the semiconductors. The formation energy of a defect depends on the chemical potential and environmental factors such as precursors, partial pressure, and temperature. So we can conclude that these experimental conditions play a vital role to determine the formation energies of all the possible defects and further impact the polar conductivity in these materials. Defect formation energies determine the polar conductivity of a semiconductor, whereas defect transition levels determine the electrical effect of any particular defect [101].

Besides point defects, Kim et al. [102] used DFT-GGA to calculate the DOS and partial charge densities of two types of neutral defects in β phase $CH_3NH_3PbI_3$: (a) Schottky defects (equal numbers of positive and negative vacancies) and (b) Frenkel defects (equal numbers of vacancies and interstitials of the same ion). The tunable polar conductivity and shallow defect properties may help to explain why high-performance perovskite solar cells, with extremely long carrier lifetimes [40, 103] can be produced by a diverse range of growth approaches and a wide variety of solar cell architectures. These point defects would suggest new methods for perovskite solar cell architecture. It was observed that deep point defect levels could exist through large atomic relaxations, which is attributed to the strong covalency of the system [104].

2.2.6. Structural disorder

In a recent investigation, Choi et al. [105] found that most of $CH_3NH_3PbI_3$ (70%) is highly disordered with a local perovskite structure extending over a range of only 1.4 nm, which is about 2 lattice constants of the α phase [106].

The mesoporous scaffold confined need the perovskite within the pores and reshaped the structures of perovskites. On the other hand, the low-temperature growth process inevitably leads to polycrystalline perovskites with grain boundaries (GBs). Experimentally, it is very difficult to investigate the structural and electronic properties directly, as it requires a high resolution transmission spectroscopy (HRTEM). So, we have to rely on the theoretical calculations that can give direct insights into the electrical properties of structural disorders and topological defects in hybrid perovskites. Recent combined theoretical and experimental studies [106] have demonstrated that Cl segregated into the GB part of polycrystalline CdTe solar cells effectively taming the detrimental effects at GBs.

Due to the structural complicity of $CH_3NH_3PbI_3$, the GB structures were constructed based on $CsPbI_3$. It was observed that the DOS of the supercells with GBs are very similar to those of single-crystal phases. None of these GBs introduce defect states within the bandgap region. The GW band structure diagram is given in **Figure 8**.

http://dx.doi.org/10.5772/65052

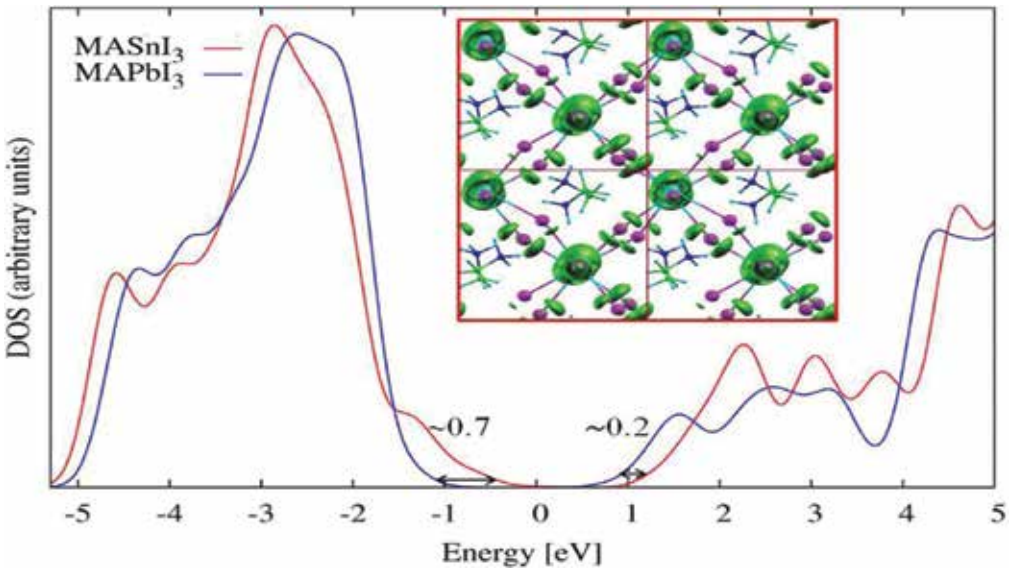

Figure 8. DOS graph of $MASnI_3$ and $MAPbI_3$materials. Adapted with permission from reference [116].

3. Properties

3.1. Electrical properties

Hybrid perovskites exhibit unprecedented carrier transport properties that enable their stellar performance in photovoltaics. So more attention is needed to develop understanding the material properties and ways to improve these properties in all key directions for research. The electrical properties of perovskite materials are seen in the ambipolar carrier transport behavior and long carrier lifetime. These electrical properties are further investigated on the basis of corresponding device structure.

3.1.1. Intrinsic electrical properties

The electrical characteristics of the materials are determined by the carrier type, concentration, and mobility, which is dependent on the method of preparation. It is necessary to use smooth and uniform films to perform measurements. The carrier type is determined by Hall measurements of the conductivity's response to an applied magnetic field, thin-film transistor's response to a gating electric field, and thermoelectric measurements of the Seebeck coefficient. For example, $CH_3NH_3PbI_3$ indicated n-type conductivity, a carrier concentration of ~109 cm^{-3}, and an electron mobility of 66 $cm^2/V/s$ [24]. Carrier concentration can also be adjusted by tuning the stoichiometry of the precursors during solution-phase synthesis and even switch the carrier type to the p-type when excess CH_3NH_3I is used in two-step synthesis.

The electron concentration was measured to be ~1017–1018 cm^{-3}, and it was proposed that the iodide vacancies are responsible for the n-type conductivity [107]. The electron mobility for n-type films deposited from stoichiometric precursors was determined to be 3.9 $cm^2/V/s$ from the Hall measurements, although $CH_3NH_3SnI_3$ prepared by a solid-state reaction in a vacuum-sealed tube showed an electron mobility of 2320 $cm^2/V/s$ [24], while solution processed material measured mobility of 200 $cm^2/V/s$. It was observed that the electron mobility of polycrystalline $CH_3NH_3PbI_3$ films is larger than the thin-film mobility of polymers [107, 108] and colloidal quantum dots (10^{-3}–1 $cm^2/V/s$) [109] comparable to CdTe (10 $cm^2/V/s$) [110] CIGS, Cu_2ZnSnS_4 (CZTS) (10–10^2 $cm^2/V/s$) [111, 112], and polycrystalline Si (40 $cm^2/V/s$) [101]. Film morphology plays an important role as the dark and light conductivities of $CH3NH_3PbI_{3-x}Cl_x$ deposited on a planar scaffold on mesostructured aluminum oxide are quite different [113]. To further increase the photovoltaic performance and radiative lifetime, solvent annealing has been applied to increase the grain size of the films to ~1 μm [114].

3.1.2. Extrinsic electrical properties:

The techniques used to measure the electrical parameters are given in subsections.

3.1.2.1. Impedance spectroscopy (IS) [115, 116]

This technique is used to identify the frequency dependence of capacitance, to measure charge diffusion lengths and lifetimes and to investigate carrier trapping and recombination. The carrier diffusion length was derived and has been estimated to be about ~1 μm for $CH_3NH_3PbI_{3-x}Cl_x$ [83].

3.1.2.2. Electron beam-induced current (EBIC) [117]

Another method to obtain the electrical parameters is EBIC from which the calculated carrier diffusion length for$CH_3NH_3PbI_{3-x}Cl_x$ is 1.5–1.9 μm [40]. The carrier diffusion length is comparable or longer than that of other polycrystalline semiconductors with direct bandgaps used in solar cells [76, 77, 118–120]

3.2. Optical properties

It is very important to understand the optical response of the materials, as optical properties are the most important feature of perovskite materials and they provide insights into the electronic and chemical structures. The ability to tune the optoelectronic properties with ease presents a major attraction among researchers. Few important parameters that are used to define these properties are discussed herein:

3.2.1. Optical constants

A lot of research has been conducted on tuning the bandgap of perovskite, but a more detail understanding of these materials awaits further research. The major problem that occurs in perovskite materials is the difficulty of producing continuous films of sufficient smoothness [121] to avoid measurement artifacts from spectroscopic measurements of transmittance,

reflectance, and ellipsometry. The absorption coefficients determined from the absorption of $CH_3NH_3PbI_3$ films on quartz [122] and glass [123] yield values of ~104 cm^{-1} near the band edge without providing any corrections for the surface's inhomogeneity, so for accurate measurements is important to calculate the absorption coefficients based on the optical constants of $CH_3NH_3PbI_3$ [124]. It is observed that the absorption spectrum for $CH_3NH_3PbI_3$ differs, when deposited within a mesoscopic template and planar substrates, which might be due to the changes in the crystallite morphology that affects the optical transitions [125, 126].

3.2.2. Excitons

Exitons play an important role in perovskites. The studies indicate, however, that there is not significant population of excitons in photovoltaics made from $CH_3NH_3PbI_3$, whose exciton-binding energy has been reported between 20 and 50 meV, comparable to the thermal energy at room temperature [127, 128]. These values have been obtained by fitting temperature-dependent absorption spectra using the measured [88] reduced mass of the exciton. Excitonic radius from the binding energy and an appropriate dielectric constant study is still a subject of debate [129]. The excitonic transition significantly enhances the absorption of hybrid perovskites near the band edge [130, 131].

3.2.3. Photoluminescence

The photoluminescence (PL) efficiency depends on the pump fluence. The trapping of photogenerated charges competes effectively with direct radiative recombination of electrons while holes reduce luminescence at low excitation energies. The PL efficiency of$CH_3NH_3PbI_3$is ~17–30%. The PL efficiency falls at higher pumping and high charge carrier densities. The PL lifetime measurements reported shorter lifetime (between 3 and 18 ns) at low pump fluencies [127, 132–134]. These longer lifetimes have been found in a semiconductor in doped and undoped GaAs films. This might be due to the photon recycling and the PL lifetime dependency on surface recombination than radiative recombination. So we can conclude that photon cycling plays a major role in their excited state dynamics, when nonradiative decay pathways are suppressed. The absorption spectra and photoluminescence for perovskite materials are shown in **Figure 9**.

3.2.4. Vibrational spectroscopy

IR spectroscopy also plays an important role in determining the chemical composition. If we look into the chemical structure of $CH_3NH_3PbI_3$, $CH_3NH_3PbBr_3$, and $CH_3NH_3PbCl_3$, the first one is tetragonal, while the other two are cubic. Raman-active modes are precluded in the symmetry of the lattice for cubic structures [135], though a weak broadband at 66 cm^{-1} is observed in $CH_3NH_3PbCl_3$. For $CH_3NH_3PbI_3$, the resonant Raman spectrum (DFT calculations) has been observed with nodes below 100 cm^{-1} (approximately) related to the inorganic octahedron. The higher energy modes indicate the disorder of $CH_3NH_3^+$ cations. A lot of work in this field is still required to investigate how the modes shift occurs with the structural changes. Raman nodes can provide better tool in understanding the in homogeneity of perovskite films with submicron spatial resolution.

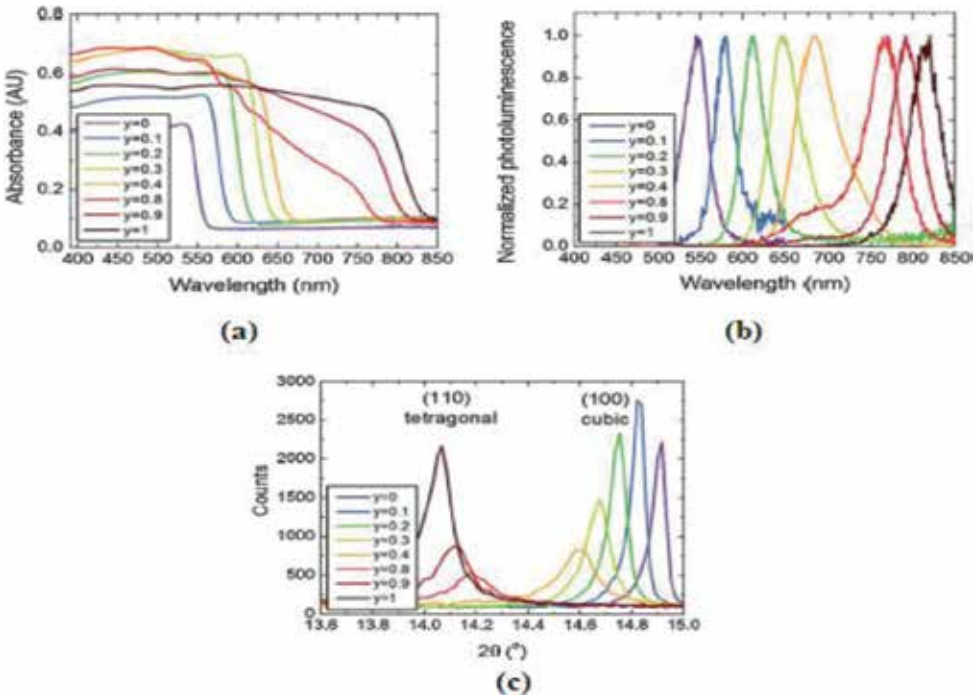

Figure 9. (a) Absorption spectra, (b) photoluminescence spectra of $FAPbI_xBr_{3-x}$ (varying I:Br ratio), (c) XRD spectra of the phase transition Br-rich cubic phase to the I-rich tetragonal phase. Adapted with permission from reference [37].

4. Pitfalls

4.1. Hysteresis

Perovskite solar cells exhibit an anomalous hysteresis in the current-voltage and resistivity-temperature dependence curves [136]. Though it was predicted that the hysteresis on resistivity verses temperature curves is associated with the structural phase transition while the reason for current-voltage curves are still unknown. In an extensive [E-CE6] studies carried out by Prof. Erik Christian Garnett et al. [136], several explanations have been proposed as ion migration, filling of interface, or surface trap states, accumulation of charges at grain boundaries and ferroelectricity, yet no convinced conclusion has been drawn. In structural perception, the cubic phases of the chloride and bromide perovskites do not allow a polar ferroelectric distortion. Various hypotheses have been suggested and it was further predicted that hysteresis should depend on the magnitude of the dipole moment of the organic cationic species and the connecting halide cage. Though the origin of this phenomenon is not yet understood properly, a number of possible causes have been proposed in which the noted causes are ferroelectricity or the presence of mobile ionic species [136]. The illustration for the hysteresis in the electrical transport in hybrid perovskites is given in **Figure 10**.

Here, it is necessary to mention that reporting results from single *J–V* sweeps, even in the absence of hysteresis, or choosing scan rates to report the highest efficiencies, will lead to

http://dx.doi.org/10.5772/65052

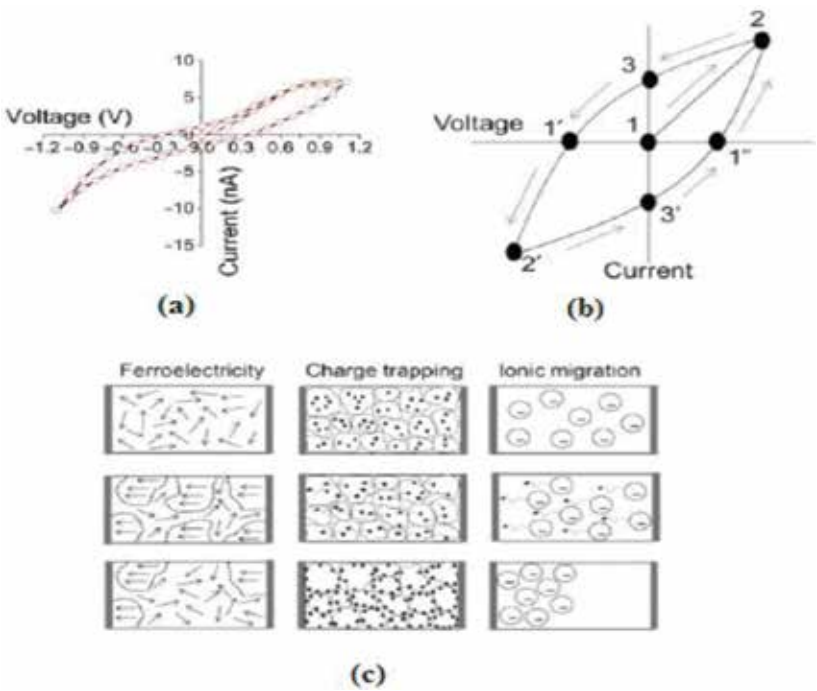

Figure 10. Hysteresis representation in hybrid perovskites. (a) *I-V* graph of $CH_3NH_3PbI_3$ (single crystal) at room temperature, (b) schematic *I-V* curve, (c) proposed phenomena for its origin. Adapted with permission from reference [104].

misleading results. As it might be possible that the certified efficiencies for perovskite solar cells are deemed "not stabilized" though they were measured with negligible hysteresis.

4.2. Thermal and operational stability

There are so many reports that claim that perovskite solar cells have been shown to be stable for many hundreds of hours without any encapsulation. However, the solar cells were stored in the dark and only measured occasionally. So we can conclude that the sealing from environmental ageing is necessary because of operation at elevated temperature and humidity. Stability has become a bigger problem for tin (II) perovskites due to the decrease in stability of the oxidation state of tin (II) compare to lead (II).

4.3. Toxicity

Due to the toxic nature of lead, concerns have been raised on the possible environment and legalization problems from perovskite solar cells based on water soluble lead compounds. So efforts have been made to replace lead with other metal ions without degrading the photophysical properties with quantum mechanical calculations. As lead halogen perovskites are water soluble, the most pessimistic view is the consequences of damaged solar cells and panels with potential exposure to water followed by dissolution and distribution of lead ions into buildings, soil, air, and water.

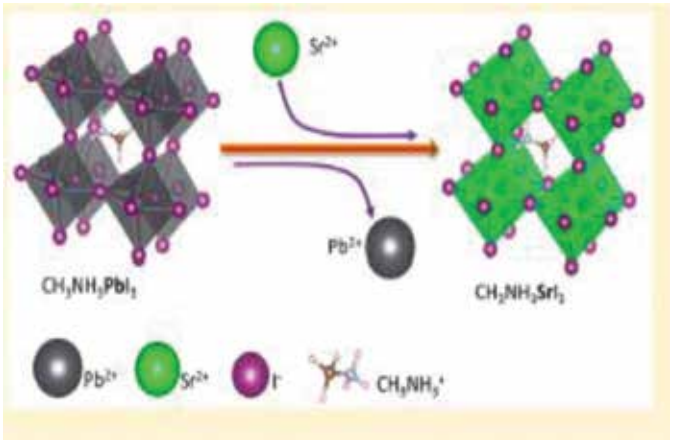

Figure 11. Pictorial representation of replacement of lead by strontium in perovskite solar cells [138].

Lead is known to damage the nervous system and cause brain disorders. In this direction, a theoretical study carried out by De Angelis and group [137] has replaced Pb by Sn (**Figure 11**) with effective development of the GW method with spin-orbit coupling to accurately model the properties of $CH_3NH_3SnI_3$ and then compared it to the $CH_3NH_3PbI_3$. They predicted that $MASnI_3$ is a better electron transporter than $MAPbI_3$ by the SR-DFT method. Another study carried out by Jesper Jacobsson and group [138] has provided deep physical insights into the photophysical nature of a metal-halogen perovskite by removing lead with strontium, which is relatively nontoxic and inexpensive. CCSD calculations and DFT study were performed on the two basic structures of $CH_3NH_3SrI_3$ and $CH_3NH_3PbI_3$ to extract and compare the electronic structures and the optical properties. This is based on the fact that the ionic radii of Sr^{2+} and Pb^{2+} are almost identical, so the exchange could be made as it will not affect the crystal structure. $CH_3NH_3SrI_3$ gives a bandgap of 1.6 eV, which is fairly close to the experimental value reported to be around 1.55 eV [5, 42]. The second effect that was caused by shifting Sr for Pb is that the shape of the pdos graphs for both the halogen and the organic ion is shifted and slightly distorted. The lower electronegativity of Sr compared to Pb shifts the electronic cloud closer to the iodine atoms in the lattice, which perturb the local dipole moment as well as the bonding angles between the iodine octahedra and consequently their columbic interaction with the methylammonium dipoles. The charge distribution is similar to the two structures, with higher charge density around lead compared to strontium due to the higher atomic number of lead.

5. Roadmap

The Perovskite solar cell (PSC) field has now become an emerging field and reports on further improvement in performance are expected in the near future, achieving PCE of more than 30% efficiency has now become a realistic goal. Furthermore, PSC can be used as top cells in two-level tandem configurations using crystalline silicon or copper indium gallium

http://dx.doi.org/10.5772/65052

selenide-based photovoltaic devices as bottom cells. It is expected that by using silicon-based tandems, PCEs of 28–30% can be achieved. Yet there are issues related to the stability and toxicity, hysteresis in perovskite solar cells, which has to be solved. Experimental and theoretical investigations have demonstrated that that halide perovskites exhibit a series of superior electronic and optical properties for solar cell applications, such as proper band-gap and band alignment, high optical absorption, bipolar carrier conductivity, tunable doping ability, and benign defect properties. A lot of studies are required to optimize the material properties and to find new perovskite candidates for high-efficiency, stable solar cells. Band structure engineering of $CH_3NH_3PbI_3$ needs to be extensively investigated by replacing organic cations, Pb or I, with other choices. Furthermore, the mechanisms of performance degradations have to be resolved in a more prominent manner. Water-corroded perovskites as rapid degradation occur in moist environments. So the reaction mechanism between H_2O and the perovskite surface could be carefully studied, leading to the development of new methods for stabilizing perovskites. Although some groups have fabricated the long-term stable perovskites in the laboratory through chemical composition engineering [32, 88], the fundamental reason for alloy stabilization of the structures requires more study. However, it is predicted that the study should converge to the p-i-n planar heterojunction perovskite solar cell to understand the device structure and properties from single crystal.

6. Conclusions

The intense appeal of hybrid organic-inorganic perovskite materials such as solar cells is exceptionally promising. Their enhance optoelectronic properties, deposition techniques, and device structure have led to the higher power conversion efficiencies. Due to the high absorption coefficients and panchromatic absorptions of perovskite, they have become ideal materials for thin film solar cells. However, some complexities as the poor stability in humid air and the toxicity of lead used are a matter of concern. In some perovskite materials, the hysteresis is also pronounced due to the strong dependence of photocurrent to the voltage scan conditions. Still the exceptional performance of hybrid perovskite materials has created revolution in the field of renewable energy with cheap solar cells. Highly efficient solar cells with record performance are still an important milestone to be achieved. The highly innovative and new elegant designs, deep insights into the photophysics and mechanisms of cell operation should now be the main focus of future research.

Finally, we can conclude that the recent advances with perovskite materials will motivate the researchers to expand their horizons to other inorganic or organic pigments, for which the power of mesoscopic solar-cell architectures will emerge to offers more promising opportunities.

The author acknowledges the financial assistance by the DST WOS-A (CS-1005/2014). The author is also thankful to her mentors Dr. G. Narahari Sastry, Head, Center for Molecular Modeling and Dr. K. Bhanuprakash, Chief Scientist, I& PC division, CSIR-Indian Institute of Chemical Technology for the useful discussions and suggestions.

Author details

Ruby Srivastava

CSIR-Indian Institute of Chemical Technology

Hyderabad, Telangana State, India

References

[1] Darling B, You FQ, Veselka T, Velosa A. Assumptions and the levelized cost of energy for photovoltaics. Energy and Environmental Science. 2011;4:3133–3139. DOI: 10.1039/c0ee00698j.

[2] Yue DJ, Khatav P, You FQ, Darling SB. Deciphering the uncertainties in life cycle energy and environmental analysis of organic photovoltaics. Energy and Environmental Science. 2012;5:9163–9172. DOI: 10.1016/j.solmat.2011.08.025.

[3] Ginley D, Green MA, Collins R. Solar energy conversion toward 1 terawatt. MRS Bulletin. 2008;33:355–364. DOI: 10.1557/mrs2008.

[4] Chen X, Jia BH, Zhang YN, Gu M. Exceeding the limit of plasmonic light trapping in textured screen-printed solar cells using Al nanoparticles and wrinkle-like graphene sheets. Light: Science and Applications. 2013;2:e92. DOI: 10.1364/OME.3.000489.

[5] Hibberd CJ, Chassaing E, Liu W, Mitzi DB, Lincot D. Non-vacuum methods for formation of Cu(In,Ga)(Se,S)$_2$ thin film photovoltaic absorbers. Progress in Photovoltaics Research and Applications. 2010;18:434–452. DOI: 10.1002/pip.914.

[6] Samuel SD, Snaith HJ. Metal-halide perovskites for photovoltaic and light-emitting devices. Nature Nanotechnology. 2015;10,391–402. DOI: 10.1039/C4MH00238E.

[7] Robert WM, Guillaume Z, Ian F. Inorganic photovoltaic cells. Materials Today. 2007;10(11):20–27. DOI: 10.1007/BF03353779.

[8] Hagfeldt A, Boschloo G, Sun LC, Kloo L, Pettersson H. Dye-sensitized solar cells. Chemical Review. 2010;110:6595–6663. DOI: 10.1021/cr900356p.

[9] Cong JY, Yang XC, Kloo L, Sun LC. Iodine/iodide-free redox shuttles for liquid electrolyte-based dye-sensitized solar cells. Energy and Environmental Science. 2012;5:9180–9194. DOI: 10.1039/C2EE22095D.

[10] Tetreault N, Grätzel M, Novel nanostructures for next generation dye-sensitized solar cells. Energy and Environmental Science. 2012;5:8506–8516. DOI: 10.1039/C2EE03242B.

[11] Boschloo G, Hagfeldt A. Characteristics of the iodide/triiodideredox mediator in dye-sensitized solar cells. Accounts of Chemical Research. 2009;42:1819–1826. DOI: 10.1021/ar900138m.

[12] Yum JH, Baranoff E, Kessler F, Moehl T, Ahmad S. A cobalt complex redox shuttle for dye-sensitized solar cells with high open-circuit potentials. Nature Communication. 2012;3:631–635. DOI: 10.1038/ncomms1655.

[13] Kojima A, Teshima K, Shirai Y, Miyasaka T. Organometal halide perovskites as visible-light sensitizers for photovoltaic cells. Journal of American Chemical Society. 2009;131:6050–6051. DOI: 10.1021/ja809598r.

[14] Feldt SM, Gibson EA, Gabrielsson E, Sun LC, Boschloo G. Design of organic dyes and cobalt polypyridineredox mediators for high-efficiency dye-sensitized solar cells. Journal of American Chemical Society. 2010;132:16714–16724. DOI: 10.1021/ja1088869.

[15] Xu CK, Wu JM, Desai UV, Gao D. Multilayer assembly of nanowire arrays for dye-sensitized solar cells. Journal of American Chemical Society. 2011;133:8122–8125. DOI: 10.1021/ja202135n.

[16] Law M, Greene LE, Johnson JC, Saykally R, Yang P. Nanowire dye-sensitized solar cells. Nature Materials. 2005;4:455–459. DOI: 10.1038/nmat1387.

[17] Yella A, Lee HW, Tsao HN, Yi CY, Chandiran AK. Porphyrin-sensitized solar cells with cobalt (II/III)-based redox electrolyte exceed 12 percent efficiency. Science. 2011;334:629–634. DOI: 10.1126/science.1209688.

[18] Bach U, Lupo D, Comte P, Moser JE, Weissortel F. Solid-state dye-sensitized mesoporous TiO_2 solar cells with high photon-to-electron conversion efficiencies. Nature. 1998;395:583–585. DOI: 10.1038/26936.

[19] Yang L, Cappel UB, Unger EL, Karlsson M, Karlsson KM. Comparing spiro-OMeTAD and P3HT hole conductors in efficient solid state dye-sensitized solar cells. Physical Chemistry Chemical Physics. 2012;14:779–789. DOI: 10.1039/C1CP22315A.

[20] Zhang W, Zhu R, Li F, Wang Q, Liu B. High-performance solid-state organic dye sensitized solar cells with P3HT as hole transporter. Journal of Physical Chemistry C. 2011;115:7038–7043. DOI: 10.1021/jp064256o.

[21] Tan SX, Zhai J, Wan MX, Meng QB, Li YL. Influence of small molecules in conducting polyaniline on the photovoltaic properties of solid-state dye-sensitized solar cells. Journal of Physical Chemistry B. 2004;108:18693–18697. DOI: 10.1021/jp036786f.

[22] Murakoshi K, Kogure R, Wada Y, Yanagida S. Fabrication of solid-state dye-sensitized TiO_2 solar cells combined with polypyrrole. Solar Energy Materials and Solar Cells. 1998;55:113–125. DOI: 10.3390/ijms11031103.

[23] Krüger J, Plass R, Cevey L, Piccirelli M, Grätzel M. High efficiency solid-state photovoltaic device due to inhibition of interface charge recombination. Applied Physics Letters. 2001;79:2085–2087. DOI: 10.1063/1.1406148.

[24] Bagher AM, Abadi Vahid MM, Mohsen M. Types of solar cells and application. American Journal of Optics and Photonics. 2015;3(5):94–113. DOI: 10.11648/j.ajop.20150305.

[25] Yin WJ, Shi T, Yan Y. Unique properties of halide perovskites as possible origins of the superior solar cell performance. Advance Materials. 2014;26:4653–4658. DOI:10.1002/adma.201306281.

[26] Liu M, Johnston MB, Snaith HJ. Efficient planar heterojunction perovskite solar cells by vapour deposition. Nature. 2013;501:395–398. DOI: 10.1038/nature12509.

[27] Wojciechowski K, Saliba M, Leijtens T, Abate A, Snaith HJ. Sub-150°C processed meso-superstructured perovskite solar cells with enhanced efficiency. Energy and Environmental Science. 2014;7:1142–1147. DOI: 10.1039/C3EE43707H.

[28] Im JH, Lee CR, Lee JW, Park SW, Park NG. 6.5% efficient perovskite quantum-dot-sensitized solar cell. Nanoscale. 2011;3:4088–4093. DOI: 10.1039/c1nr10867k.

[29] Lee MM, Teuscher J, Miyasaka T, Murakami TN, Snaith HJ. Efficient hybrid solar cells based on meso-superstructured organometal halide perovskites. Science. 2012;338:643–647. DOI: 10.1126/science.1228604.

[30] Etgar L, Gao P, Xue ZS, Peng Q, Chandiran AK. Mesoscopic $CH_3NH_3PbI_3/TiO_2$ heterojunction solar cells. Journal of American Chemical society. 2012;134:17396–17399. DOI: 10.1021/ja307789s.

[31] Shin SS, Kim JS, Suk JH, Lee KD, Kim DW. Im-proved quantum efficiency of highly efficient perovskite $BaSnO_3$-based dye-sensitized solar cells. ACS Nano. 2013;7:1027–1035. DOI: 10.1039/c0ee00678e.

[32] Noh JH, Im SM, Heo JH, Mandal TN, Seok SI. Chemical management for colorful, efficient, and stable inorganic–organic hybrid nanostructured solar cells. Nano Letters. 2013;13:1764–1769. DOI: 10.1021/nl400349b.

[33] Bi DQ, Yang L, Boschloo G, Hagfeldt A, Johansson EMJ. Effect of different hole transport materials on re-combination in $CH_3NH_3PbI_3$ perovskite-sensitized mesoscopic solar cells. The Journal of Physical Chemistry Letters. 2013;4:1532–1536. DOI: 10.1021/jz400638x.

[34] Chung I, Lee BH, He JQ, Chang RPH, Kanatzidis MG. All-solid-state dye-sensitized solar cells with high efficiency. Nature. 2012;485:486–489. DOI:10.1038/nature11067.

[35] Kim HS, Lee JW, Yantara N, Boix PP, Kulkarni SA. High efficiency solid-state sensitized solar cell-based on submicrometer rutile TiO_2 nanorod and $CH_3NH_3PbI_3$ perovskite sensitizer. Nano Letters. 2013;13:2412–2417.DOI: 10.1021/nl400286w.

[36] Singh SP, Nagarjuna P. Organometal halide perovskites as useful materials in sensitized solar cells: Dalton Transactions. 2014;43:5247–5251. DOI: 10.1039/c3dt53503g.

[37] Song TB, Chen Q, Zhou H, Jiang CY, Wang HH, Yang Y, Liu YS, You J, Yang Y. Perovskite solar cells: film formation and properties. Journal of Material Chemistry A. 2015;3:9032–9050. DOI: 10.1039/c4ta05246c.

[38] Xing GH, Mathews N, Sun SY, Lim SS, Lam YM. Long-range balanced electron- and hole-transport lengths in organic-inorganic $CH_3NH_3PbI_3$. Science. 2013;342:344–347. DOI: 10.1126/science.1243167.

[39] Stranks SD, Eperon GE, Grancini G, Menelaou C, Alcocer MJP. Electron-hole diffusion lengths exceeding 1micrometer in an organometal trihalide perovskite absorber. Science. 2013;342:341–344. DOI: 10.1126/science.1243982.

[40] Wehrenfennig C, Eperon GE, Johnston MB, Snaith HJ, Herz LM. High charge carrier mobilities and lifetimes in organolead trihalide perovskites. Advance Materials. 2014;26:1584–1589. DOI: 10.1021/acs.accounts.5b00411.

[41] Eperon GE, Stranks SD, Menelaou C, Johnston, Michael MB, Herz, LM, SnaithHJ. Formamidinium lead trihalide: a broadly tunable perovskite for efficient planar heterojunction solar cells. Energy and Environmental Science. 2014;7(3):982. DOI:10.1039/C3EE43822H.

[42] Burschka J, et al. Sequential deposition as a route to high-performance perovskite-sensitized solar cells. Nature. 2013;499:316–319. DOI: 10.1038/nature12340.

[43] Service RF. Turning up the light. Science. 2013;342:794–797. DOI: 10.1126/science.342.6160.794.

[44] Nie W, et al. High-efficiency solution-processed perovskite solar cells with millimeter-scale grains. Science. 2015;347:522–525. DOI: 10.1126/science.aaa0472.

[45] Saliba M, Orlandi S, Matsui T, Aghazada S, Cavazzini M, Correa-Baena JP, Gao P, Scopelliti R, Mosconi E, Dahmen KH, Angelis FD, Abate A, Hagfeldt A, Pozzi G, Grätzel M, Nazeeruddin MK. A molecularly engineered hole-transporting material for efficient perovskite solar cells**.** Nature Energy. 2016;1:15017. DOI: 10.1038/NENERGY.2015.17.

[46] The Hong Kong Polytechnic University. Perovskite-silicon tandem solar cells with the world's highest power conversion efficiency. ScienceDaily. ScienceDaily, 12 April 2016. www.sciencedaily.com/releases/2016/04/160412104814.htm.

[47] McMeekin DP, Sadoughi G, Rehman W, Eperon GE, Saliba M, Horantner MT, Haghighirad A, Sakai N, Korte L, Rech B, Johnston MB, Herz LM, Snaith HJ. A mixed-cation lead mixed-halide perovskite absorber for tandem solar cells. Science. 2016;351(6269):151–155. DOI: 10.1126/science.aad5845.

[48] Bi D, Moon SJ, Haggman L, Boschloo G, Yang L, Johansson EMJ, Nazeeruddin MK, Grätzel M, Hagfeldt A. Using a two-step deposition technique to prepare perovskite (CH3NH3PbI3) for thin film solar cells based on ZrO_2 and TiO_2 mesostructures. RSC Advances. 2013;3:18762–18766. DOI: 10.1039/C3RA43228A.

[49] Borriello I, Cantele G, Ninno D. Ab initio investigation of hybrid organic-inorganic perovskites based on tin halides. Physical Review B. 2008;77:235214–235227. DOI: 10.1103/PhysRevB.77.235214.

[50] Shirane G, Danner H, Pepinshi R. Neutron diffraction study of orthorhombic $BaTiO_3$. Physical Review. 1957;105:856–860. DOI: http://dx.doi.org/10.1103/PhysRev.

[51] Ray SS, Okamoto M. Polymer/layered silicate nanocomposites: a review from preparation to processing. Progress in Polymer Science. 2003;28:1539–1641. DOI:progpolymsci.2003.08.002.

[52] Ray SS, Bousmina M. Biodegradable polymers and their layered silicate nanocomposites: in greening the 21st century materials world. Progress in Materials Science. 2005;50:962–1079. DOI: 10.1016/j.pmatsci.2005.05.002.

[53] Mitzi DB. Synthesis and crystal structure of the alkylbismuth diiodides: a family of extended one-dimensional organometallic compounds. Inorganic Chemistry. 1996;35:7614–7619. DOI: 10.1021/ic961083g.

[54] Stoumpos CC, Malliakas CD, Kanatzidis MG. Semiconducting tin and lead iodide perovskites with organic cations: phase transitions, high mobilities, and near-infrared photoluminescent properties. Inorganic Chemistry. 2013;52:9019–9038. DOI: 10.1021/ic961083g.

[55] Shum K, Chen Z, Qureshi J, Yu CL, Wang JJ. Synthesis and characterization of $CsSnI_3$ thin films. Applied Physics Letters. 2010;96:221903–221906. DOI: 10.1063/1.3442511.

[56] Yamada K, Kuranaga Y, Ueda K, Goto S, Okuda T. Phase transition and electric conductivity of $ASnCl_3$ (A = Cs and CH_3NH_3). Bulletin of the Chemical Society of Japan. 1998;71:127–134. DOI: 10.1021/acs.accounts.5b00229.

[57] Xu Q, Educhi T, Nakayama H, Nakamura N, Kishita M. Molecular motions and phase transitions in solid $CH_3NH_3PbX_3$ (X = Cl, Br, I) as studied by NMR and NQR. Zeitschrift Naturforschung. 1991;46:240–246. DOI: 10.1016/0360-3016(94)90398.

[58] Goldschmidt VM. The laws of crystal chemistry. Naturwissenschaften. 1926;14:477–485. DOI: 10.1007/BF01507527.

[59] Calabrese J, Jones NL, Harlow RL, Herron N, Thorn DL, Wang Y. Preparation and characterization of layered lead halide compounds. Journal of American Chemical Society. 1991;113:2328–2330. DOI: 10.1021/ja00006a076.

[60] Mitzi DB, Wang S, Field CA, Chess CA, Guloy AM. Conducting layered organic-inorganic halides containing (1 1 0)-oriented perovskite sheets. Science. 1995;267:1473–1476. DOI: 10.1126/science.aac7660.

[61] Pauling L. The Nature of the Chemical Bond, 3rd ed. Cornell University Press: New York, 1960. DOI: 10.1021/ja01360a004.

[62] Quarti C, Mosconi E, De Angelis F. Interplay of orientational order and electronic structure in methylammonium lead iodide: implications for solar cell operation. Chemistry of Materials. 2014;26:6557–6569. DOI: 10.1021/cm5032046.

[63] Mitzi DB. Thin-film deposition of organic–inorganic hybrid materials. Chemistry of Materials. 2001;13:3283–3298. DOI: 10.1021/cm0101677.

[64] Valiente R, Rodriguez F. Electron-phonon coupling in charge-transfer and crystal-field states of Jahn–Teller CuCl64-systems. Physical Review B. 1999;60:9423–9429. DOI: 10.1103/PhysRevB.60.6584.

[65] Kagan CR, Mitzi DB, Dimitrakopoulos CD. Organic inorganic hybrid materials as semiconducting channels in thin film field-effect transistors. Science. 1999;286:945–947. DOI: 10.1126/science.286.5441.945.

[66] Zhou P, Drumheller JE, Patyal B, Willet RD. Magnetic properties and critical behavior of quasi-two-dimensional systems $[C_6H_5(CH_2)_nNH_3]_2CuBr_4$ with $n = 1$, 2, and 3. Physical Review B. 1992;45:12365–12376. DOI: 10.1103/PhysRevB.45.5744.

[67] Era M, Morimoto S, Tsutsui T, Saito S. Organic-inorganic heterostructure electroluminescent device using a layered perovskite semiconductor $(C_6H_5C_2H_4NH_3)_2PbI_4$. Applied Physics Letters. 1994;65:676–678. DOI: 10.1063/1.112265.

[68] Hong X, Ishihara T, Nurmikko AV. Dielectric confinement effect on excitons in PbI_4-based layered semiconductors. Physical Review B. 1992;45:6961–6964. DOI: 10.1063/1.4936776.

[69] Kim HS, Lee CR, Im JH, Lee KB, Moehl T. Lead iodide perovskite sensitized all-solid-state submicron thin film mesoscopic solar cell with efficiency exceeding 9%. Scientific Reports. 2012;2:591–597. DOI: 10.1038/srep00591.

[70] Noh JH, Jeon NJ, Choi YC, Nazeeruddin MK, Grätzel M, Seok S, Nanostructured TiO_2/$CH_3NH_3PbI_3$ heterojunction solar cells employing spiro-OMeTAD/Co-complex as hole-transporting material. Journal of Material Chemistry A. 2013;1:11842–11847. DOI: 10.1039/C3TA12681A.

[71] Laban WA, Etgar L. Depleted hole conductor-free lead halide iodide heterojunction solar cells. Energy and Environmental Science. 2013;6:3249–3253.DOI: 10.1039/C3EE42282H.

[72] Snaith HJ, Humphry-Baker R, Chen P, Cesar I, Zakeeruddin SM. Charge collection and pore filling in solid-state dye-sensitized solar cells. Nanotechnology. 2008;19:424003–424015. DOI: 10.1088/0957-4484/19/42/424003.

[73] Zhu K, Neale NR, Miedaner A, Frank AK. Enhanced charge-collection efficiencies and light scattering in dyesensitized solar cells using oriented TiO_2 nanotubes arrays. Nano Letters. 2007;7:69–74. DOI: 10.1021/nl062000o.

[74] Spies JA, Schafer R, Wager JF, Hersh P, PlattHAS, Keszler DA, Schneider G, Kykyneshi R, Tate J, Liu X, Compaan AJ, Shafarman WN. Pin double-heterojunction thin-film solar cell p-layer assessment. Solar Energy Materials and Solar Cells. 2009;93:1296–1308. DOI: 10.1016/J.SOLMAT.2009.01.024.

[75] Crossland JW, Noel N, Sivaram V, Leijtens T, Alexander-Webber JA, Snaith HJ. Mesoporous TiO_2 single crystals delivering enhanced mobility and optoelectronic device performance. Nature. 2013;495:215–220. DOI: 10.1038/nature11691.

[76] Tanaka K, Takahashi T, Ban T, Kondo T, Uchida K. Extremely large binding energy of biexcitons in an organic–inorganic quantum-well material $(C_4H_9NH_3)_2PbBr_4$. Solid State Communications. 2003;127:619–623. DOI: 10.1016/S0038-1098(03)00566-0.

[77] Silvia C, Edoardo M, Paolo F, Andrea L, Francesco G. $MAPbI_{3-x}Cl_x$ mixed halide perovskite for hybrid solar cells: the role of chloride as dopant on the transport and structural properties. Chemistry of Materials. 2013;25:4613–4618. DOI: 10.1016/S0038-1098(03)00566-0.

[78] Chen Q, Zhou HP, Hong ZR, Luo S, Duan HS. Planar heterojunction perovskite solar cells via vapor-assisted solution process. Journal of American Chemical Society. 2014;136:622–625. DOI: 10.1021/ja411509g.

[79] Abate A, Hollman DJ, Teuscher J, Pathak S, Avolio R. Protic ionic liquids as p-dopant for organic hole transporting materials and their application in high efficiency hybrid solar cells. Journal of American Chemical Society. 2013;135:13538–13548. DOI: 10.1021/ja406230f.

[80] Joong Jeon N, Lee J, Noh JH, Nazeeruddin MK, Grätzel M. Efficient inorganic–organic hybrid perovskite solar cells based on pyrenearylamine derivatives as hole-transporting materials. Journal of American Chemical Society. 2013;135:19087–19090. DOI: 10.1021/ja410659k.

[81] Langevin P. Recombination in low mobility semiconductors: Langevin theory. 1903; 28:433–530. DOI: 10.1038/srep08525.

[82] Christians JA, Fung RCM, Kamat PV. An inorganic hole conductor for organo-lead halide perovskite solar cells. Improved hole conductivity with copper iodide. Journal of American Chemical Society. 2014;136:758–764. DOI: 10.1021/ja411014k.

[83] Chang YH, Park CH, Matsuishi K. First-principles study of the structural and the electronic properties of the lead-halide-based inorganic-organic perovskites $(CH_3NH_3)PbX_3$ and $CsPbX_3$ (X = Cl, Br, I). Journal of Korean Physical Society. 2004;44:889–893. DOI: 10.1117/12.2054188.

[84] Yin WJ, Shi T, Yan Y. Unusual defect physics in $CH_3NH_3PbI_3$ perovskite solar cell absorber. Applied Physics Letters. 2014;104:063903–063907. DOI: 10.1063/1.4864778.

[85] Miller J. A battery material charges via an unexpected mechanism. Physics Today. 2014;67:13–15. DOI: 10.1063/PT.3.2368.

[86] Ringwood AE. The principles governing trace element distribution during magmatic crystallization 0.1. The Influence of Electronegativity. Geochimica et Cosmochimica Acta. 1955;7:189–202. DOI: 10.1016/0016-7037(56)90016-3.

[87] Wei SH, Zunger A. Electronic and structural anomalies in lead chalcogenides. Physical Review B. 1997;55:13605–13610. DOI: 10.1103/PhysRevB.55.13605.

[88] Yu LP, Kokenyesi RS, Keszler DA, Zunger A. Inverse design of high absorption thin film photovoltaic materials. Advanced Energy Materials. 2013;3:43–48. DOI:10.1002/aenm.201200538.

[89] Shockley W, Queisser HJ. Detailed balance limit of efficiency of pin junction solar cells. Journal of Applied Physics. 1961;32:510–519. DOI: 10.1063/1.1736034.

[90] Grinberg I, West DV, Torres M, Gou GY, Stein DM, Wu LY, Chen GN, Gallo EM, Akbashev AR, Davies PK, Spanier JE, Rappe AM. Perovskite oxides for visible-light-absorbing ferroelectric and photovoltaic materials. Nature. 2013;503:509–512. DOI: 10.1038/nature12622.

[91] Jarvist KTB, Frost M, Brivio F, Hendon CH, Van Schilfgaarde M, Walsh A. Atomistic origins of high-performance in hybrid halide perovskite solar cells. Nano Letters. 2014;14:2584–2590. DOI: 10.1021/nl500390f.

[92] Abrusci A, Stranks SD, Docampo P, Yip HL, Jen AKY. High performance perovskite-polymer hybrid solar cells via electronic coupling with fullerene monolayers. Nano Letters. 2013;13:3124–3128. DOI: 10.1021/nl401044q.

[93] Shi JJ, Dong J, Lv ST, Xu YZ, Zhu LF, Xiao JY, Xu X, Wu HJ, Li DM, Luo YH, Meng QB. Hole-conductor-free perovskite organic lead iodide heterojunction thin-film solar cells: high efficiency and junction property. Applied Physics Letters. 2014;104:063901–063904. DOI: 10.1039/c4cc04908j.

[94] Pellet N, Gao P, Gregori G, Yang TY, Nazeeruddin MK, Maier J, Grätzel M, Mixed-organic-cation perovskite photovoltaics for enhanced solar-light harvesting. Angewandte Chemie International Edition. 2014;53:3151–3157. DOI: 10.1002/anie.201309361.

[95] Ogomi Y, Morita A, Tsukamoto S, Saitho T, Fujikawa N, Shen Q, Toyoda T, Yoshino K, Pandey SS, Ma TL, Hayase S. $CH_3NH_3Sn_xPb_{(1-x)}I_3$ perovskite solar cells covering up to 1060 nm. Journal of Physical Chemistry Letters. 2014;5:1004–1011. DOI: 10.1021/jz5002117.

[96] Hao F, Stoumpos CC, Chang RPH, Kanatzidis MG. Anomalous band gap behavior in mixed Sn and Pb perovskites enables broadening of absorption spectrum in solar cells. Journal of American Chemical Society. 2014;136:8094–8099. DOI: 10.1021/ja5033259.

[97] Colella S, Mosconi E, Fedeli P, Listorti A, Gazza F, Orlandi TF, Besagni T, Rizzo A, Calestani G, Gigli G, De Angelis F, Mosca R. Band alignment of the hybrid halide perovskites $CH_3NH_3PbCl_3$, $CH_3NH_3PbBr_3$, $CH_3NH_3PbI_3$. Chemistry of Materials. 2013;25:4613–4618. DOI: 10.1021/cm402919x.

[98] Kulkarni SA, Baikie T, Boix PP, Yantara N, Mathews N, Mhaisalkar S. Band-gap tuning of lead halide perovskites using a sequential deposition process. Journal of Material Chemistry A. 2014:2:9221–9225. DOI: 10.1039/C4TA00435C.

[99] Sanchez RS, Gonzalez-Pedro V, Lee JW, Park NG, Kang YS, Mora-Sero I, Bisquert J. Slow dynamic processes in lead halide perovskite solar cells. characteristic times and hysteresis. Journal of Physical Chemistry Letters. 2014;5:2357–2363. DOI: 10.1021/jz5011187.

[100] Snaith HJ, Abate A, Ball JM, Eperon GE, Leijtens T, Noel NK, Stranks SD, Wang JTW. Anomalous hysteresis in perovskite solar cells. Journal of Physical Chemistry Letters. 2014;5:1511–1515. DOI: 10.1021/jz500113x.

[101] Calistru DM, Mihut L, Lefrant S, Baltog I. Identification of the symmetry of phonon modes in $CsPbCl_3$ in phase IV by Raman and resonance-Raman scattering. Journal of Applied Physics. 1997;82:5391–5395. DOI: 10.1063/1.366307.

[102] Kim J, Lee SH, Lee JH, Hong KH. The role of intrinsic defects in methylammonium lead iodide perovskite. Journal of Physical Chemistry Letters. 2014;5:1312–1317. DOI: 10.1039/c4cp04479g.

[103] Agiorgousis ML, Sun YY, ZengH, Zhang S. Electron-hole diffusion lengths exceeding 1 micrometer in an organometal trihalide perovskite absorber. Journal of American Chemical Society. 2014;136:14570–14575. DOI: 10.1021/ja5079305.

[104] Brittman S, Adhyaksa GWP, Garnett EC. The expanding world of hybrid perovskites: materials properties and emerging applications. MRS Communications. 2015;5:7–26. DOI: 10.1557/mrc.2015.6.

[105] Choi JJ, Yang XH, Norman ZM, Billinge SJL, Owen JS. structure of methylammonium lead iodide within mesoporous titanium dioxide: active material in high-performance perovskite solar cells. Nano Letters. 2013;14:127–133.DOI: 10.1021/nl403514x.

[106] Chen Q, Marco ND, Yang YM, Song TB, Chen CC, Zhao HX, Hong Z, Zhou H, Yang Y. Under the spotlight: the organic—inorganic hybrid halide perovskite for optoelectronic applications. Nano Today. 2015;10:355–396. DOI:10.1016/j.nantod.2015.04.009.

[107] Wang Q, Shao Y, Xie H, Lyu L, Liu X, Gao Y, Huang J, Qualifying composition dependent p and n self-doping in CH3NH3PbI3. Applied Physics Letters. 2014;105:163508–163513. DOI: 10.1063/1.4899051.

[108] Venkateshvaran D, et al. Approaching disorder-free transport in high-mobility conjugated polymers. Nature. 2014;515:384–388. DOI: 10.1038/nature13854.

[109] You J, Dou L, Hong Z, Li G, Yang Y. Recent trends in polymer tandem solar cells research. Progress in Polymer Science. 2013;38:1909–1928. DOI:10.1002/advs.201600032.

[110] Long Q, Dinca SA, Schiff EA, Yu M, Theil J. Electron and hole drift mobility measurements on thin film CdTe solar cells. Applied Physics Letters. 2014;105:042106–042111. DOI: 10.1063/1.4891846.

[111] Shin B, Gunawan O, Zhu Y, Bojarczuk NA, Chey SJ, Guha S. Thin film solar cell with 8.4% power conversion efficiency using an earth-abundant Cu_2ZnSnS_4 absorber. Progress in Photovoltaics: Research and Applications. 2013;21:72–76. DOI: 10.1002/pip.1174.

[112] Brown G, Faifer V, Pudov A, Anikeev S, Bykov E, Contreras M, Wu J. Determination of the minority carrier diffusion length in compositionally graded $Cu(In,Ga)Se_2$ solar cells using electron beam induced current. Applied Physics Letters. 2010;96:022104–022107. DOI: 10.1063/1.3291046.

[113] Leijtens T, Stranks SD, Eperon GE, Lindblad R, Johansson EMJ, Ball JM, Lee MM, Snaith HJ, McPherson IJ. Electronic properties of meso-superstructured and planar organometal

halide perovskite films: charge trapping, photodoping, and carrier mobility. ACS Nano. 2014;8:7147–7155. DOI: 10.1021/nn502115k.

[114] Xiao Z, Dong Q, Bi C, Shao Y, Yuan Y, Huang J. Solvent annealing of perovskite-induced crystal growth for photovoltaic-device efficiency enhancement. Advance Materials. 2014;26:6503–6509. DOI: 10.1002/adma.201401685.

[115] Dualeh A, Moehl T, Tétreault N, Teuscher J, Gao P, Nazeeruddin MK, Grätzel M. Impedance spectroscopic analysis of lead iodide perovskite-sensitized solid-state solar cells. ACS Nano. 2014;8:362–373. DOI: 10.1021/nn404323g.

[116] Gonzalez-Pedro V, Juarez-Perez EJ, Arsyad WS, Barea EM, Fabregat-santiago F, Mora-Sero I, Bisquert J. General working principles of $CH_3NH_3PbX_3$ perovskite solar cells. Nano Letters. 2014;14:888–893. DOI: 10.1021/nl404252e.

[117] Edri E, Kirmayer S, Mukhopadhyay S, Gartsman K, Hodes G, Cahen D. Elucidating the charge carrier separation and working mechanism of $CH_3NH_3PbI_{(3-x)}Cl_{(x)}$ perovskite solar cells. Nature Communications. 2014;5:3461–3471. DOI: 10.1038/ncomms4461.

[118] Tarricone L, Romeo N, Sberveglier G, Mora S. Electron and hole diffusion length investigation in CdTe thin films by SPV method. Solar Energy Materials and Solar Cells. 1982;7:343–347. DOI:10.1166/jnn.2014.8029.

[119] Mikhnenko OV, Azimi H, Scharber M, Morana M, Blom PWM, Loi MA. Exciton diffusion length in narrow bandgap polymers. Energy and Environmental Science. 2012;5:6960–6965.DOI: 10.1039/C2EE03466B.

[120] Koleilat GL, Levina L, Shukla H, Myrskog SH, Hinds S, Pattantyus-abraham AG, Sargent EH. Efficient, stable infrared photovoltaics based on solution-cast colloidal quantum dots. ACS Nano. 2008;2:833–840. DOI: 10.1021/nn800093v.

[121] Sum TC, Mathews N. Advancements in perovskite solar cells: photophysics behind the photovoltaics. Energy and Environmental Science. 2014;7:2518–2534. DOI: 10.1039/C4EE00673A.

[122] Xing G, Mathews N, Lim SS, Yantara N, Liu X, Sabba D, Grätzel M, Mhaisalkar S, Sum TC. Low-temperature solution-processed wavelength-tunable perovskites for lasing. Nature Materials. 2014;13;476–480. DOI: 10.1038/nmat3911.

[123] Sutherland BR, et al. Perovskite thin films via atomic layer deposition. Advance Materials. 2014;27:53–58. DOI: 10.1002/adma.201404059.

[124] Stuckelberger M, Niesen B, Filipic M, Moon S, Yum J, Topic M, Ballif C. Complex refractive index spectra of $CH_3NH_3PbI_3$ perovskite thin films determined by spectroscopic ellipsometry and spectrophotometry. Journal of Physical Chemistry Letters. 2015;6:66–71. DOI: 10.1021/jz502471h.

[125] Grancini G, et al. The impact of the crystallization processes on the structural and optical properties of hybrid perovskite films for photovoltaics. Journal of Physical Chemistry Letters. 2014;5:3836–3842. DOI: 10.1021/jz501877h.

[126] Even J, Pedesseau L, Jancu JM, Katan C. Importance of spin–orbit coupling in hybrid organic/inorganic perovskites for photovoltaic applications. Journal of Physical Chemistry Letters. 2013;4:2999–3005. DOI: 10.1021/jz401532q.

[127] D'Innocenzo V, et al. Excitons versus free charges in organo-lead trihalide perovskites. Nature Communications. 2014;5:3586–3590. DOI: 10.1038/ncomms4586.

[128] Huang L, Lambrecht WRL. Electronic band structure, phonons, and exciton binding energies of halide perovskites $CsSnCl_3$, $CsSnBr_3$ and $CsSnI_3$. Physical Review B. 2013;88:165203. DOI: 10.1103/PhysRevB.88.165105.

[129] Lin Q, Armin A, Nagiri RCR, Burn PL, Meredith P. Electro-optics of perovskite solar cells. Nature Photonics. 2014;9:106–112. DOI: 10.1038/nphoton.2015.

[130] Brivio F, Butler KT, Walsh A, Schilfgaarde MV. Relativistic quasiparticle self-consistent electronic structure of hybrid halide perovskite photovoltaic absorbers. Physical Review B. 2014;89:155204–155210.DOI: 10.1103/PhysRevB.89.155204.

[131] Kim HG, Becker OS, Jang JS, Ji SM, Borse PH, Lee JSA. Generic method of visible light sensitization for perovskite-related layered oxides: substitution effect of lead. Journal of Solid State Chemistry. 2006;179:1214–1218. DOI: 10.1016/j.jssc.2006.01.024.

[132] Docampo P, et al. Solution deposition-conversion for planar heterojunction mixed halide perovskite solar cells. Advance Energy Materials. 2014;4:1400355–1400362. DOI: 10.1002/aenm.201400355.

[133] Noel NK, Abate A, Stranks SD, Parrott ES, Burlakov VM, Goriely A, Snaith HJ, Al NET. Enhanced photoluminescence and solar cell performance via Lewis base passivation of organic-inorganic lead halide perovskites. ACS Nano. 2014;8:9815–9821. DOI: 10.1021/nn5036476.

[134] Wehrenfennig C, Liu M, Snaith HJ, Johnston MB, Herz LM. Homogeneous emission line broadening in the organo lead halide perovskite $CH_3NH_3PbI_3$. Journal of Physical Chemistry Letters. 2014;5:1300–1306. DOI: 10.1021/jz500434p.

[135] Maalej A, Abid Y, Kallel A, Daoud A, Lautié A, Romain F. Phase transitions and crystal dynamics in the cubic perovskite $CH_3NH_3PbCl_3$. Solid State Communications. 1997;103:279–284. DOI: 10.1039/c4ee01358a.

[136] Brittman S, Pratama Adhyaksa GW, and Garnett EC, The expanding world of hybrid perovskites: materials properties and emerging applications. MRS Communications. 2015; 5: 7-26.DOI: http://dx.doi.org/10.1557/mrc.2015.6.

[137] Umari P, Mosconi E, De Angelis F. Relativistic GW calculations on $CH_3NH_3PbI_3$ and $CH_3NH_3SnI_3$ perovskites for solar cell applications. Scientific Reports. 2014;4:4467–4470.DOI: 10.1038/srep04467.

[138] Jesper Jacobsson T, Pazoki M, Hagfeldt A, Edvinsson T. Goldschmidt's rules and strontium replacement in lead halogen perovskite solar cells: theory and preliminary experiments on $CH_3NH_3SrI_3$. Journal of Physical Chemistry C. 2015;119:25673–25683. DOI: 10.1021/acs.jpcc.5b06436.

Chapter 13

Recent Progresses in Perovskite Solar Cells

Serafettin Demic, Ahmet Nuri Ozcivan,
Mustafa Can, Cebrail Ozbek and Merve Karakaya

Additional information is available at the end of the chapter

http://dx.doi.org/10.5772/65019

Abstract

Perovskite solar cell (PSC) can be regarded as a continuation of dye sensitized solar cell (DSSC) in terms of the sensitization phenomena that occurred in the functioning molecules. In 2012, a breakthrough propose has been made for the sensitization of PSCs, in which a solid-state structure is offered as an equivalent sensitizer used in DSSC. The power conversion efficiency (PCE) of those solid-state cells reached about twofold of its initial value during the past several years. Immediately after, the researchers followed this propose worldwide. They have introduced an improved efficiency of as much as 20%, which was originally started from its initial value of 4%, just in 4 years. Thus, the new concept, solid perovskite molecules, has eliminated the need for the liquid electrolyte in DSSC while still carrying the advantages of organic solar cells (OSCs). Therefore, the distinctive material of PSC—the organometallic halide molecules (also known as OMH or organic-inorganic trihalides)—inclined an unexpected reputation for solar cell (SC) researches. Hence, it seems that we will witness a new age for solar conversion devices depending on the recent hopeful progresses on PSCs. The high rate of photovoltaic (PV) conversion capacity in PSC is generally expressed by the basic properties possessed by the organic-inorganic perovskite crystal, such as better optical properties and well diffused charges along huge distances during the charge transport. In addition, a low temperature processing is applicable during its production. Moreover, the perovskite layer provides a tunable band gap. Therefore, depending on better developments on designed molecules, PSC may gain extreme performances compared to the other competitors, such as OSC or DSSC devices. This chapter starts with a general discussion on the need for an affordable clean energy conversion device that is urgent for the future of humanity, due to publicly well-known global warming issue. In Section 2, basic properties of PSC are mentioned together with their structure and working principles. Section 3 continues with an overview on organometallic perovskite molecules after a brief introductory history is presented. The absorption and band gap properties are also discussed. Since most perovskite materials need a hole transporting material (HTMs) within the PSC, the kinds of HTMs that are designed for PSCs are described in Section 3. The rendering of long-term stabilization has special importance

for PSCs since the instability issue remained idle in spite of those recent increased efficiency values attained by various research groups. Therefore, the stability issues are discussed in a separate part in Section 4. We finally close the chapter discussing the challenges and opportunities relying on the chapter content. We note that the recent investigations on PSCs have special importance for its large-scale realization in order to make them ready for the photovoltaic industry of the future. Hence, there are various announced meetings focusing on its mass production due to the unexpected sharp rise of the perovskite efficiency in the last 6 years. Hence, all the new cutting-edge scientific findings are also dealt with commercialization issues now, in order to attain the desired low cost fabrication, including the yield of high purity and the formation of smooth films during the continual manufacture of perovskite layers.

Keywords: perovskite solar cells, hole transport materials, spiro-OMeTAD

1. Introduction: the need for new and affordable power converters

The novelties in solar cell (SC) technology may be attracting the widest human attention in the world due to its significance on its effectiveness on electricity production from free and abundant sunlight [1–3]. Namely, petroleum is the main source of energy in the world by a percentage of 40, where most of the petroleum is produced just by a few oil exporting countries. The other countries are the consumers. They exist with increasing petroleum dependency, which means that the most of the countries rely on exporters. Unfortunately, the petroleum consumption accelerates quickly because of energy needs due to expanding industrial zones. It is expected to grow further unless an affordable novel clean energy technology becomes available.

To make a continuous delivery of the energy by means of an environmentally friendly manner, it is mandatory for governments to make immediate precautions against fuel consumption, particularly by strictly improving their alternative energy themes. Among a variety of energy sources, electricity is known as "clean energy". The best quality of electricity is its ease of transformation in other energy forms; thereby, it is crucial for the human society. Accordingly, half of the energy consumption is made by electricity using machinery, for that, conversion of energy into electric energy from other resources is related to fuel saving. This property directed countries to invest on renewable energy transformers (e.g., Germany has already announced that much of the country's consumption is fulfilled through renewables). Hence, many researchers from various institutions worldwide developed new types of alternative energy conversion devices in order to condense their capability more and more. Among them, SCs are the most promising devices since sun energy is accepted to be almost infinite for human needs.

Many new types of SCs in photovoltaic (PV) panels are used in new existing investments for meeting the residential and commercial energy needs. Maximizing efficiency is a must to satisfy those huge consumption needs. Hence, a majority of the investments obliged to use silicon-based PV panels, which have high conversion rates. Whereas for their production

processes, we need to use huge amount of water and energy and to release lots of pollutants to the environment as well. At this point, organic solar cell (OSC) technology attracts attention especially for the utilization of environmentally friendly production procedures. By means of this favorable property, in the last two decades, many new usages of organic materials in electric energy producing devices are proposed and applied. These novel devices are basically expected to satisfy low cost criteria and high efficiency; thereby, recent SC researches are especially shaped around these related topics.

Among SCs, many efficient types of organic materials and devices are present today. For example, commercial dye sensitized solar cells (DSSCs) are in the marketplace for a decade. However, this type of SCs is weak for its possible leaking in electrolyte liquid and imperfect encapsulation. The consistent and cutting-edge studies on this challenge give the fruit of a DSSC like but a novel SC: named, Perovskite Solar Cell (PSC). Relatedly, this chapter mainly deals with the main issues of PSC, i.e., its ideal phenomena, device structure, materials, and manufacturing challenges [4–17].

2. Operating principle and structural layout of PSC

As for the operating principle of PSCs, the present information obtained on "how they operate" is rather insufficient for now. Moreover, the whole working principle is not even well explained [18, 19]. There have already been many different approaches to point out a well-defined PSC operation mechanism. Nevertheless, the proficient working of methylammonium lead iodide (corresponding chemical formula is $CH_3NH_3PbI_3$ and the methylammonium inside the formulas are also introduced as MA or $CH_3NH_3^+$ in the related literature)-based PSC has not yet been completely understood. Accordingly, this confusion raises the necessity for deriving novel clues on (1) light absorption, (2) charge separation, (3) charge transport, and (4) charge collection. This is because these are general SC parameters that are used to express the principal working process during conversion of sunlight into electricity.

Selection of light harvesters is the first step for the determination of the physical layout of a SC. Hence, investigation of perovskite's optoelectronic properties has priority during the design process. This is needed in order to theoretically construct the fundamental energy conversion process, and therefore, to decide the respective SC layout [1]. In this term, we know that organometallic perovskite —like $CH_3NH_3PbI_3$— may exhibit both electron and hole transport features, together. Hence, PSCs can be decided to be layered either using well-known *p-n* junction layout or *p-i-n* junction layout. The decision between the two layouts is made as follows: If the light harvester, perovskite, is an intrinsic semiconductor, a *p-i-n* junction is needed. Whereas a *p-n* junction is required if the light harvester, i.e. perovskite, has an *n*-type or *p*-type property. This is because both types are able to carry electrons or holes to the light harvester [1].

PSCs are fabricated depending on two typical structures of perovskites. These structures are called mesoporous and planar structures. These structures are unique to the perovskite crystal. **Figure 1** illustrates the consequent scheme for the device layout for both mesoporous- and

planar-type PSC. The former contains a mesoporous-type metal oxide layer (i.e., TiO_2 or Al_2O_3) coated with perovskite sensitizer. On the other hand, the latter includes a perovskite film sandwiched between electron and hole transporting layers. Here, in case of perovskite dots are stick to the surface of TiO_2 layer, charge is separated through electron injection. Namely, the charge certainly follows away from perovskite to the metal oxide (also known as transparent conductive oxide layer, TCO), such as TiO_2 [20]. Up to here, the operation principle is considered to be analogous to DSSCs. The remaining operation mechanism, however, is different from DSSCs for both mesoporous- and planar-type PSCs due to the charge accumulation and charge transport characteristics that occur in the PSCs [18, 19, 21]. Comparing these two architectures, it is evident that the charge transport rate is virtually the same for both of them, while mesoporous-type cell performs higher recombination rates [22]. The planar-type PSCs are found applicable to flexible solar cells since the typical high temperature rates are not mandatory in order to fabricate them.

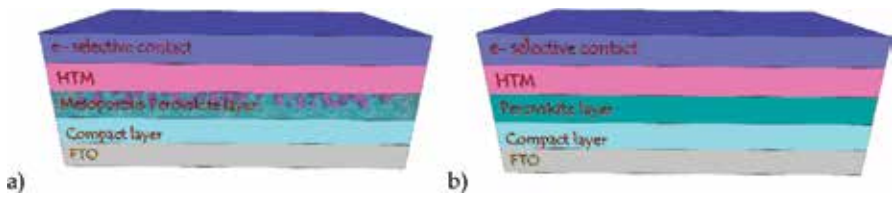

Figure 1. (a) The model structure of mesoporous halide PSC and (b) the model structure of planar hetero-junction structured halide PSC.

Besides these two structures, hole conductor-free (HTM-free) PSCs have also been investigated by many scientists. The first report on HTM-free $CH_3NH_3PbI_3/TiO_2$ hetero-junction SC was released by Etgar et al. [23]. In this study, the mesoporous TiO_2 was coated with a thick perovskite layer having large crystal functioning as both light harvester and hole transport material, simultaneously. In order to obtain highly efficient PSCs and to avoid building shunt pathways, a thick perovskite film having a smooth surface is required. The width of the depletion layer at the $CH_3NH_3PbI_3/TiO_2$ junction plays an important role on the performance of the HTM-free PSC. For instance, it is possible to enlarge the width by increasing the depleted part of TiO_2 according to this study. Such arrangement has given an increased power conversion efficiency (PCE) of almost 11% [24]. Another HTM-free PSC is the one that has tripled layers that is implemented by Han et al. The respective multilayer arrangement consists of simple layout from mesoporous $TiO_2/ZrO_2/C$ layers [25]. Here, the ZrO_2 film is especially used as blocking layer so that the photo-generated electrons could not flow back to the contact. Accordingly, electron hole recombination process occurring inside the device is delayed. With the help of such HTM-free PSC, researchers have already achieved a PCE of around 13% [25].

The charge transfer processes and the latest progresses in PSC are summarized in **Figure 2** and **Table 1** [26]. The explained photonic interaction matches well for a mesoporous-type PSC. Here, the energy level of the perovskite is designed in order to function in the following junction architecture: $TiO_2/CH_3NH_3PbI_3$/spiro-OMeTAD. The charge transfer process for analogous mesoporous architecture requires the steps specified in **Table 1** [26–28]. Here, the

http://dx.doi.org/10.5772/65019

general PCE of mesoporous-type PSC is controlled through the processes given in the table. Where the rate of charge generation as well as charge transport occurred from (1) to (3) should be much faster than the rate of undesired recombination occurred from (4) to (8) given in **Figure 2**. In this way, a high power conversion efficiency can be obtained.

Step no	Event	Occurrence
1	Photoexcitation of the Perovskite	$Perovskite+hv \rightarrow (e^-\ldots h^+)_{Perovskite}$
2	Electron injection	$(e^-\ldots h^+)_{Perovskite} \rightarrow e^-_{cb(TiO2)} + h^+_{(Perovskite)}, h^+_{(Perovskite)} \rightarrow h^+_{(HTM)}$ $h^+_{(Perovskite)}$
3	Hole injection	$(e^-\ldots h^+)_{Perovskite} \rightarrow h^+_{(HTM)} + e^-_{Perovskite}, e^-_{(Perovskite)} \rightarrow e^-_{cb\ (TiO2)}$
4	Photoluminescence	$(e^-\ldots h^+)_{Perovskite} \rightarrow hv$
5	Nonradiative recombination	$(e^-\ldots h^+)_{Perovskite} \rightarrow \nabla$
6	Back electron transfer at TiO_2/Perovskite interface	$e^-_{cb\ (TiO2)} + h^+_{(Perovskite)} \rightarrow \nabla$
7	Back charge transfer at Perovskite/HTM interface	$h^+_{(HTM)+}\ e^-_{(Perovskite)} \rightarrow \nabla$
8	Charge recombination at TiO_2/HTM interface	$e^-_{cb\ (TiO2)} + h^+_{(HTM)} \rightarrow \nabla$

Table 1. The required charge transfer process for analogous mesoporous architecture [26–28].

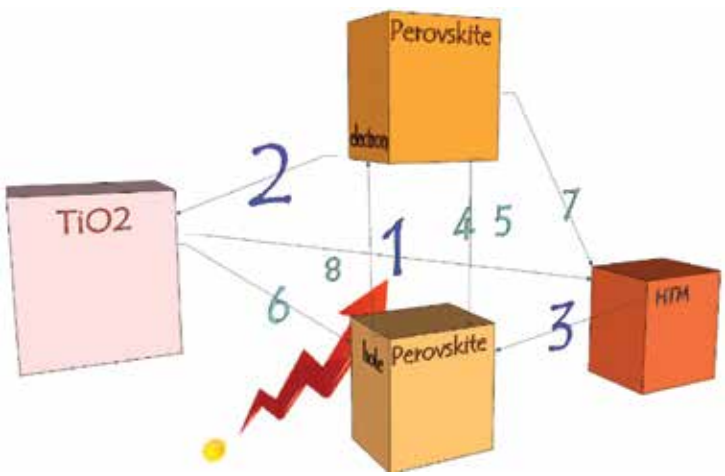

Figure 2. Electron and hole transport process for mesoporous PSC.

It is known that for a single-junction SC the ideal band gap should start from 1.1 and extend to 1.4 eV [27]. One of the most important characteristics related to perovskite material processes is that it is possible to vary this band gap by altering its composition. Fortunately, in PSC, the band gap may be arranged by changing from 1.2 and extend to 2.3 eV. This band gap control can be made by substituting halide composition of $CH_3NH_3Pb(I_{1-x}Br_x)_3$ as

described by Noh et al. [23]. Another way to alter the respective band gap is to increase the cation size, nevertheless it may also result in a decrease in the band gap, unfortunately [28].

The solid-state HTM was first implemented to DSSCs to substitute the undesired liquid electrolyte since it causes fast degradation of the cell if it is used with perovskite crystals. This advancement in structural layout has showed an increase in the open circuit voltage (V_{oc}) of the cell due to the high redox potential of the liquid. Within those cells, HTM layer gradually becomes a solid-state layer instead of a liquid one. Accordingly, the stability of PSC improves. Since after the development of solid-state DSSCs, the most common HTM utilized in PSCs is spiro-OMeTAD (*2,2′,7,7′*-tetrakis (*N,N*-di-*p*-methoxyphenylamine)-*9,9′*-spirobifluorene). This is a kind of small molecule which has improved the PCE of PSC up to 19% [29]. It was shown that an HTM with high conductivity decreases the series resistance and gives rise to improvement in the fill factor (FF) of the device [30]. For example, Seok et al. improved the V_{oc} and FF, just by substituting spiro-OMeTAD with polytriarylamine-type HTM [31]. The FF in turn can also be increased through improving the film quality by achieving enlarged grains and reduced grain boundaries [32].

In addition to replacing organic HTMs with other organic HTMs for the purpose of increasing PCE of the PSCs, there are also some other studies on substitution of organic HTMs with inorganics in order to increase the stability of the PSCs. It is well known that perovskite used as light harvester are rather susceptible to moisture and air resulting in degradation of the cell because of perovskite's low energy of formation [14]. One of the most important reasons why HTM usage is necessary is to protect the photoactive perovskite layer from moisture and air exposure to achieve highly stable PSCs. It is also known that metal oxides have much higher mobility as well as good stability than the generally used organic HTMs mentioned above [33, 34]. In an attempt to increase the stability, therefore, You et al. replaced organic HTM with inorganic charge transport layers [14]. In this study, *p*-type (nickel oxide, NiO_x) and *n*-type (zinc oxide, ZnO) metal oxides were used as electron and hole transport layers, respectively. The device architecture was composed of glass/indium tin oxide/NiO_x/ $CH_3NH_3PbI_3$/ZnO/Al, where NiO_x was used to provide a perovskite layer with better crystallinity and ZnO acted as a coverage layer for perovskite layer, thus preventing degradation. According to the results of this study, the metal oxide-based PSCs demonstrated PCE of around 16% and higher stability compared to those fabricated with other common organic HTMs.

3. PSC materials

3.1. Perovskite as a solar device material: structure

Perovskite is a crystal with a special structure constituting ABX_3 formulation. It contains three same kind cationic ions and two different anionic ions. Here, A, B, and X represent large-dimension earth metal cation, rather smaller-dimension metal cation compared to A, and, either oxygen or halogen, respectively. The perovskite structure is symmetric. Within this structure, A is always larger than X (see **Figure 3**). Here, A-cations hold the octahedral corner coordinates while B-cations hold the octahedral holes; in 3-D structure. Within the composi-

tion, X can be substituted with numerous elements of O, Cl, Br, I, and S. The placements of atoms in 3-D structure are mainly regarded to be related with chemical charge neutralization process that is required for stability [8]. The crucial thing for the perovskite minerals is that, although the fundamental structure appears simple, they perform quite different characteristics under special circumstances, i.e., against structural distortion.

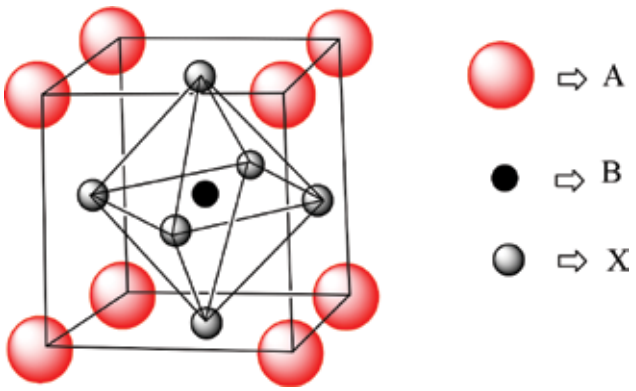

Figure 3. Crystal structure belonging to perovskite structure.

Gustav Rose, a German mineralogist, first recognized perovskite. Nevertheless, its entitlement is given after another mineralogist, Lew Perovskii, from Russia [35–37]. Perovskite is therefore originally a name for the mineral calcium TiO_2 ($CaTiO_3$) discovered by Perovskii, where it is basically used to refer a crystal structure that is the same as $CaTiO_3$. Starting from its discovery, perovskite structure has widely been used in diverse fields of research, such as superconductors, ferroelectricity, thermoelectric, dielectric, magnetoresistive, piezoelectric, conducting, electrooptic, semiconducting, [5, 8, 9, 38–47], etc. The wide range of their application carried out in scientific research is mostly due to their tunable behaviors within the crystal structure observed since its discovery [4]. In particular, researchers have focused on organometallic perovskites which must include anionic halogens (I, Cl, F, and Br) and cationic metals of carbon family like Ge, Pb, and Sn. The attention on them is basically due to their unique structure and their promising response to photovoltaic applications [5–7].

The well-known perovskites are crystals of $MgSiO_3$, $SrFeO_3$, $SrZrO_3$, $BaTiO_3$, $LiNbO_3$, and $KMgO_3$. They originally give clear diffraction peaks at 110, 112, 220, 310, 224, and 314. In spite of its applicability to the mentioned diverse areas, the attention on the original molecules remained rather idle. Mostly, its actual fame has begun with the discovery of organometallic halide perovskite (OMH perovskite) related to the studies made for searching the interactions between the organic-inorganic materials. Namely, a research result claimed that a perovskite material shifts from the semiconducting state to the conduction region along with increased dimensionality [8, 9, 38]. In the mentioned and other related researches, A is exchanged by a cationic organic molecule, B is exchanged by an inorganic transition metal, and X is exchanged by an anionic halide. Hence, the new structure becomes inherently referred to as "OMH perovskite". Among many transition metal alternatives, Sn^{+2} and Pb^{+2} metals substituted for X

are the ones which have collected the scientific interest on the following formulas: "$CH_3NH_3SnI_3$"and "$CH_3NH_3PbI_3$." This attention increases day by day since the respective new molecules inherently carry significant optoelectrical properties and they are able to be processed in rather low temperatures compared to other OMH molecules with rather different formulas [47–49]. Even more, Pb^{+2} and Sn^{+2} cations are nonreactive, stand stable at room temperature, and their supply channels are wide due to being abundant, which makes them easily accessible cheap materials [50].

As for PV applications, Miyasaka et al. are the first group who used perovskite in SC panel production in 2009 [10]. They fabricated a SC with a liquid phase electrolyte based on mesoporous TiO_2 sensitized with $CH_3NH_3X_3$. Here, *X* is able to be substituted by I, Cl, or Br, depending on the application purpose. Similar to this first study on PSCs, the most prevalent organic compound used to fabricate PSCs are (1) $CH_3NH_3^+$ (methyl ammonium), (2) $CH_3CH_2NH_3^+$, (ethyl ammonium), and, (3) $NH_2CH{=}NH_2^+$ (form amidinium) [20, 51, 52]. Though, among all, the most common perovskite material implemented to the recent SC applications perhaps have been methylammonium lead iodide ($CH_3NH_3PbI_3$) with other lead halide structures ($CH_3NH_3PbI_{3-x}Br_x$ or $CH_3NH_3PbI_{3-x}Cl_x$) [37, 53].

3.2. Perovskite's absorption properties

It is beneficial to remind the absorbance of DSSC device here. Namely, the previous form of PSC, DSSCs, contains an *n*-type TiO_2 that has mesoporous structure. The dyes are stick to TiO_2 where the light is absorbed by dye molecules impregnated in a redox electrolyte sea, meantime. Here, the electrolyte regenerates the stable dye again and again by supplying electrons after having each excitation followed by charge transfer. The TiO_2 plays the role of helping the enlargement of the electrode surface as much as possible on behalf of the electrode's job. In this term, the soaring of incident photons become eased. In practice, an approximate 10 μm film thickness of TiO_2 is generally enough in DSSC to make a complete absorption of the visible light [9, 54, 55].

On the other hand, such broad thickness is not appropriate for the solid-state SCs. Because there are various factors that restrict the increase in film thickness. Due to these restrictions, the thickness is limited below 2 μm [9, 30]. In order to relieve these limiting effects, different active semiconducting layers are jointly coated with different thin film types in many research groups. Another approach to resolve this issue is the use of nano-sized quantum dots (QDs). These additional cares are taken in order to increase the sensitivity against the photons. As a result, the absorption band becomes carried to around near-infrared region (NIR) in several researches [30, 56–60].

Under the light of these facts expressed about improved absorption, more sensitization of DSSCs to the incident light worked in 2006 where $CH_3NH_3PbI_3$ and $CH_3NH_3BrI_3$ were used in the redox couple [9, 61, 62]. In some studies, on the other hand, they are applied as solid-state hole conductors. Nevertheless, those applications could only give efficiency as low as 0.2%. Whereas when they were applied to liquid-based DSSCs, it has reached as high as 10 times of this value escalating to around 2%. Therefore, the solid-state applications remained rather idle.

The first fascinating application on the absorbing sensitizer of perovskites is the one that is made with redox couple. Namely, one of the studies reached to around 3.5% efficiency level [9, 20]. Fortunately, improving the surface morphology and perovskite's processing carried the attained efficiency as high as 6.5% in the preceding years [9, 20, 63]. As may be easily guessed, the main obstacle to make a reasonable device was dissolution of the perovskite material inside the liquid electrolyte. Hence, its stability in the electrolyte sea has always remained questionable, since it is distorted after a while and eventually it is dissolved [9, 20, 63]. The removal of this problem needed realization of two ideas: (1) blocking the dissolution in any way, or (2) using them in a HTM that is insoluble in the liquid environment. The latter alternative idea has been applied to devices fabricated in 2006 [9, 64, 65]. Namely, researchers benefited from the insolubility of metilamonium trihalogenplumbate in nonpolar organic solvents. Hence, perovskites became used as sensitizer on TiO_2 as a target. These studies made up a ground for applying this idea to many different materials. Especially, different groups of spiro-OMeTAD have been tested as HTM [9, 11]. The results were surprising, because the use of perovskite molecules reached a respectable efficiency value of around 10% [9, 10, 66]. This result also emphasized the importance of usability of HTMs within the PSC. These records had been a jumping-of-point in terms of their use as alternative to classical dyes since the acquired advantages made PSC more visible among others [9, 67]. This advantage is particularly due to the fact that perovskite (1) makes a stronger absorption in a very wide range of visible colors and (2) realizes this strong absorption in rather small thicknesses compared to the liquid-type DSSCs, namely, a thickness of around 500 nm layer. This property emerged a reform in DSSCs, namely, the replacement of redox liquid with solid-state HTM materials found attractive for solid-state type SCs since the thickness issue become relieved for them. The gain of such property practically meant that the problem of limited thickness of 2 μm for solid-state type SCs has been overcome by use of perovskite. Till those dates, the perovskite material including solid-state type SCs have gained an advantage over other types of solid-state SCs in the scientific community.

Typically, the absorption properties of the PSC are related to the ABX_3-type crystal structure of the perovskite that is coated on the TiO_2 surface as a thin film. Technically, $CH_3NH_3PbI_3$ structure gives 1.5×10^{-4} cm^{-1} of absorption at 450 nm wavelength, whereas it only satisfies 0.3×10^{-4} cm^{-1} of absorption at 750 nm wavelength. Relatedly, the soared light is diffused to a depth starting from 0.7 to 2.2 μm. This typical property of $CH_3NH_3PbI_3$ specifically shows that the perovskite material in the form of a thin film is well enough to absorb the big part of the solar spectrum just being around 2 μm of thickness. This derived fact shows that the $CH_3NH_3PbI_3$ has enough capability in order to be easily used as a solid-state sensitizer material in SCs.

In order to identify the lack of interpretations about the photocarrier dynamics in lead iodide perovskites, the transient absorption should be characterized. These photophysical relations are observed where a quantitative work is presented in a recent paper [68]. Also, photon recycling has been investigated in the papers [69] where the energy transport is found out not to be restricted by diffusion of charge transport. It is figured out that this may occur at distant

intervals by means of several events including absorption, diffusion, and emission together. By means of all, high V_{oc} values are attained [69].

3.3. Optical band gap

Among different atoms, Pb and Sn included in perovskite materials are fair due to that they yield higher efficiency levels due to their tunable band gap values and improved absorption. The main contribution to the tunable band gap comes from the orbitals of additive metals and halides [70–73]. Hence, the metals which will make the electronic contribution should be carefully selected from among numerous metals. Yet, the band gap harmony and proper valence arrangement requires watching the outermost orbital of the metal and one can see that there are highly less metals constituting mentioned configuration. With that, there is no specific procedure or sharp method to eliminate this hardness. Hence, these theoretical issues should be carried along with the observations and some experimental works.

The intrinsic properties of OMH led them to be used in many diverse engineering applications till now, including thin film diode-based devices, such as SCs, transistors, and light-emitting diodes (LEDs). Moreover, it has also been reported that the band gap of OMH perovskite is decreased when the structure is shifted from 2-D to 3-D [9]. The less spaced band gap intervals are especially found applicative for constructing SC devices. Hence, the developed 3-D structure of $CH_3NH_3PbX_3$ is initially tested as an inorganic semiconducting sensitizer in 2009 in DSSCs. Nevertheless, the researchers got unsatisfactory amounts of PCE from the test results compared to those most efficient DSSCs performed till that time (~3.5% versus ~11%) [74]. With that, the testing groups reached a PCE efficiency of 6.5% [10, 11] later on.

The interest on the perovskite material remained poor until a research is exhibited in 2012. The corresponding research results reported 500 hours of stable lifetime of a perovskite thin film coated on TiO_2. The distinguishing specialty of this kind perovskite was its 10 times enlarged absorbing coefficient compared to that of the widely known ruthenium-based sensitizers. The new molecule has been recognized as a breakthrough discovery. In addition to all, the band gap intervals could be reduced more along with the processing of perovskite materials. And more, they can even be processed more to make them gain highly absorbing structure. Together with these improving arrangements, the optical adsorption can become tunable and recombination properties can also become enhanced [50, 75]. Consequently, as a cation for B, Pb is exclusively preferred for SC applications for the assumed reasons when they are put into perovskite molecule. Neatly, Pb including PSC are found to be theoretically ideal. They practically constitute small spaced band gap intervals as well [8–11].

Through the characterization work, the satisfaction of band gap values can be attained through ultraviolet photoelectron spectroscopy and UV-Vis spectral measurements for any kind of material. Namely, the research [8] made for $CH_3NH_3PbI_3$ has revealed that the minimum and maximum valance values are between –5.5 and –3.95 eV interval, giving out approximately 1.5 eV of band gap for this structure [8, 20]. Through looking at the given typical valence-band and conduction-band values, we infer that perovskite material satisfies enough hole and electron separation. The separation gives a band gap value of 1.5 eV that reveals us enough absorption is made using an onset wavelength of 830 nm.

Shortly, the fundamental request for a SC is its strong and wide absorption range. In these terms, OMH perovskite is suitable for its tunable crystal sizes. Namely, with that condition, the band gap value of the absorber material may be arranged by differently utilized cations and anions [23, 28, 76, 77] within the crystal arrangement, as well. As an example, PbI_yBrI_{3-y} crystal structure can be modified to derive different absorption levels through varying the "*y*" value here. Derivation of varied absorption levels is generally referred as "tuning band gap." This is essential for perovskite's future, because the development of various types of advanced molecules is allowed by means of such procedure that makes perovskite attain a tunable band gap [23, 78, 79]. Here, the usability of this strategy is shown for $CH_3NH_3PbBr_{3-x}Cl_x$ SCs, where V_{oc} of 1.5 V is derived. This shows the availability of this idea as a method. One more parameter for getting high power values is reaching high photocurrent values. Namely, this can be made through an engineering on *n*-type and *p*-type materials in order to match wider band gap perovskites. Also, the widened band gap of perovskite may require synthesizing new hole transport materials since valence band is shifted [78–81]. Therefore, engineering for deriving appropriate hole transporters is especially important for PSCs, too.

4. Hole transport materials

The HTMs for PSCs are similar to that of solid-state DSSCs, in view of the general structure. The main distinction between them is that the HTM layers do not fill the pores of TiO_2, and it is because they are currently coated by the perovskite material in a PSC. Fortunately, during the practical selection of the materials, this property eases the determination of HTM molecules for PSC devices for us. This is because it becomes more possible to choose them from a large range of materials—compared to the selections that are made for solid-state DSSCs. Once decided to be used for PSC, the produced HTM layer from chosen molecules should meet the similar requirements as requested for solid-state DSSCs, as follows:

1. The molecules should maintain better hole mobility.
2. They should be good soluble in terms of better film formation.
3. In order to supply a good hole transfer they should carry appropriate HOMO energy level with that of OMH perovskites.
4. They have to be produced by eased synthesis procedure and be low cost molecules.

Among them, spiro-OMeTAD has been the most used HTM as small-molecules in PSCs till now. Because it has already been tested and evaluated as a HTM layer in solid-state DSSCs and OLED devices [67, 74, 82, 83]. Therefore, its interlayer functioning is well known by researchers. Namely, use of hybrid lead halide with spiro-OMeTAD-based HTM has given an efficiency of around 15% PCE [82, 84]. On the other hand, the biggest obstacle yielding spiro-OMeTAD in wide range of applications is its high cost that still remains high due to its difficult synthesis process. This obstacle has been a hindrance for further improvements of PSCs in terms of maintaining high efficiency and low cost production together [74]. At this point, new HTMs that are alternative to spiro-OMeTAD have been an issue for improving cost-effective

designs in recent years. These new molecule designs are generally separated to organic and inorganic HTMs as for PSC applications. Organic molecules can either be polymers or other small molecules. Different types of HTM structures that are already used are given in **Figure 4** with their corresponding HOMO values within the cell.

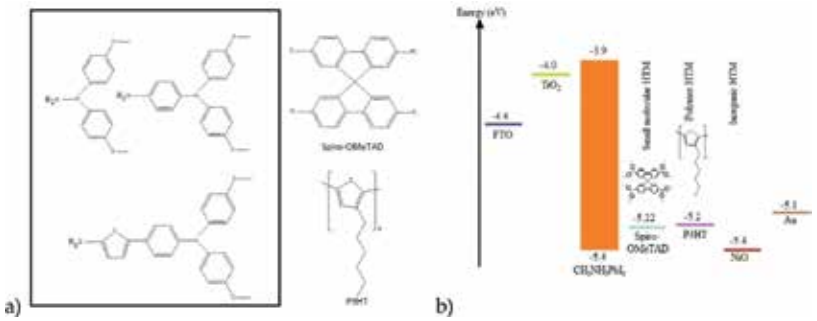

Figure 4. (a) Recently used HTM materials used for PSCs and (b) their corresponding HOMO values.

Spiro-OMeTAD and other small molecule type HTMs have more availability compared to the organic and inorganic HTMs [74] due to its ease of design where the triarylamine is an essential part of the molecule. Here, nitrogen is used as a doping site and can be stabilized through aromatic rings. The nonplanar triarylamine leads to have longer distances between molecules and thus reduces the hole mobility, here. Nevertheless, this makes the molecules more applicable as HTMs for SCs fortunately. Due to the advantages among different molecules, spiro-OMeTAD has been a standard HTM for researchers, where the new small molecules are comparable to that of the standard HTM for this reason. During the application of new types of spiro-OMeTAD and other small molecules some key issues for increasing the efficiency levels are (1) thickness optimization and (2) inclusion of additives, such as making composites [74]. There are also some works done for searching the device's physics on the interface between HTM layer and perovskite layer, as well.

4.1. Early device materials as hole transporters

A HTM layer is needed for sensitizing the TiO_2 layer to satisfy the working of PSCs. The working principle of HTM-based PSC originally depends on DSSCs developed in 1991 by O'Regan and Gratzel based on a liquid electrolyte layer. These cells are photoelectro-chemical cells with a wide surface area of TiO_2 film layer that is sensitized by molecular dyes [54]. The same principle is valid for solid-state sensitized SCs and PSCs, as well. In Gratzel's works, a final efficiency of 12% has been reached. Nevertheless, a leakage is always possible within the corresponding device structure. Shortly, the liquid may leak from the bordered edges. Therefore, the same structure for that of DSSC has been protected in solid-state SCs in principle, on the other side, the electrolyte is altered by a solid hole conductor material instead.

Figure 5 represents the general structure of such solid-state SC and its electron transfer properties. Here, the layered device structure benefits from the TiO_2 layer for blocking the

direct touch of TiO_2 layer to HTM. The working principle of the solid-state SC is the same as that of DSSC, where the only distinction stems from the difference in electron transmission processes occurred inside the liquid electrolyte and solid HTM. Namely, the electron is hopped through the solid HTM instead of reducing in the liquid electrolyte.

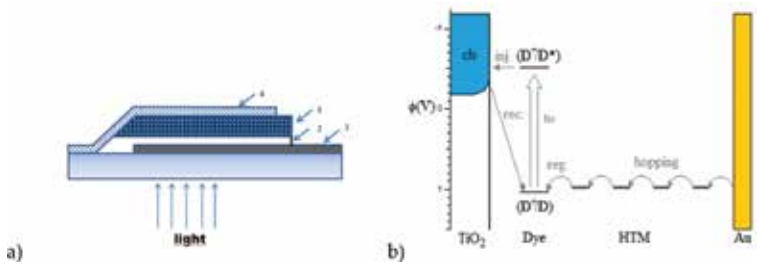

Figure 5. (a) General structure of solid-state solar cells and (b) working principle.

In order to satisfy the HTM's working within the other film layers, the corresponding layer should fill the pores of the mesoporous TiO_2 film layer. With that a heterojunction is produced. For filling process, a molecular HTM structure may be determined. This molecule may be selected from various types of structures, such as small molecule HTM (mostly spiro-OMeTAD is used), and an inorganic or organic HTM. During the layer design, the hole diffusion length and conductivity of HTM is selected at the meantime, because these are parameters directly affecting the layer thickness of the mesoporous TiO_2. Namely, the TiO_2 film layer thickness is inversely proportional to the absorption coefficient. In other words, the less TiO_2 layer thickness, the more the absorption coefficient value. Here, unfortunately, the mesoporous film thickness can only be stretched up to 2 μm, i.e., when spiro-OMeTAD is used [85]. Hence, a breakthrough development in a solid-state DSSC is not expected with typical molecular dyes that constitute $\sim 10^3\ cm^{-1}$ of absorption coefficient. Neatly, in order to wholly collect the incident light arrays using those dyes, a TiO_2 layer with a thickness of 10 μm is needed.

The main problem in the early HTMs leads researchers to think that they may achieve a high efficiency solid-state sensitizer for SCs by means of a stronger light absorbing material. This becomes realized by means of the perovskites' property that has superiority against traditional dyes in terms of absorption. Namely, it has a stronger adsorption over a broad range and therefore full coverage absorption becomes realized within a very low thickness of 500 nm. This property of Perovskite becomes a real advantage for solid-state SCs. Because the previous obstacle for them were that a mesoporous TiO_2 film thickness restricted at around 2 μm length is needed in order to generate photocurrent with the given light absorption [30].

4.2. New small molecules as hole conductors: spiro-OMeTAD

The perovskite basically yield high series and shunt resistances which results in lower FF for SC devices. This is mainly because of the perovskite layer with higher conductivity in contact with the thicker layer of HTM that has lower conductivity. Hence, reduced thickness and better conducting HTM layer is a must to develop more efficient PSC devices [50].

Recently, some efforts on spiro-OMeTAD molecules used as HTM are under attention of researchers in view of their increased hole conductivities [86, 87]. For example, lithium bistrifluoromethanesulfonimide (Li-TFSI) has been found out to increase the hole conductivity when doped to spiro-OMeTAD, within some researches [87]. Using various techniques, spiro-OMeTAD has widely been used for enhancements in conductivity through increasing the hole mobility and charge density in HTM layers [88, 89].

Within the cell, the holes are injected from the perovskite into the spiro-OMeTAD and electrons are passed from perovskite to the mesoporous TiO_2 layer. Here, therefore, the TiO_2 is an active counterpart of the photovoltaic conversion event which makes it a main element of the PSC. Lately, it was fortunately shown that TiO_2 scaffold has leaded a PCE of up to almost 10% [20, 74]. In some studies, spiro-OMeTAD has also been used while coupled with other scaffolds (i.e., Al_2O_3). Where it is mixed with perovskites and good PCE has been attained in [30, 74]. These are famed as meso-super-structured SCs where the $CH_3NH_3PbX_3$ is served as an electron transport material (ETM) in addition to its basic sensitizer duty. Besides with all that, the metal oxide only acts as an insulator with a wide band gap and therefore do not take part in charge transport. Hence, the metal oxide becomes an inactive scaffold here. For that, these are referred as passive scaffolds in the PSC literature. It is good to say that a more uniform perovskite layer formation is applicable with a wide thickness in both of the scaffolds which improves the light absorption of PSCs, thus lead an increase in efficiency [74].

Besides all, new kinds of small molecules as for HTM are continuously introduced to the literature. For example, a Trux-OMeTAD small molecule is reported where an excellent hole mobility is achieved [90]. Here, the constructed PSC has given efficiency as close as to 19%.

4.3. Inorganic and polymer HTM

Inorganic HTMs: The inorganic HTMs are rather low cost materials; on the other hand, they have progressed less in recent years due to the poor existence of such materials. The most known inorganic HTMs are listed as CuI, CuSCN, and NiO with respective PCEs of around 6, 12, and 11%. These inorganic HTMs are evaluated in mesoporous-type PSCs. The main advantage is their stability yielding property in ambient conditions compared to the organic HTMs. On the other hand, they yield a low-quality performance compared to the organic HTMs which makes them disadvantageous against others, as well.

Polymer HTMs: Compared to the inorganic counterparts, organic-based HTMs have tunable oxidization potentials and surface morphology. In addition, high V_{oc} values can be attained together with advanced HOMO levels [78, 91–93]. Basically, polymer HTMs have some drawbacks related to filling the pores which was tested in solid-state DSSCs before. Some kinds of polymer HTMs are known to be PTAA, P3HT, and PANI. It has been shown that they have generally good hole mobility and satisfies a better film formation. Among them, PTAA and P3HT have yielded an efficiency level of around 12 and 6%, respectively [31]. The efficiency of PTAA has later been reported to reach more than 16% using a mixed structure with perovskite material [31, 94, 95]. There has been a study where P3HT is used together with carbon nanotube and formed a novel composite [96] in which the conductivity of the new structure is increased

more. Besides PTAA and P3HT, PANI is also known to satisfy a long-term stable device, which is tested through characterizations.

5. Film formation and stability

The optical and electrical properties of perovskite films show varieties depending on the film formation conditions, such as atmospheric conditions and materials' ratios, which affect the device performance significantly. Up to the present time, several film techniques for fabrications of perovskite have been reported. Generally, these are grouped as (1) solution process and (2) vapor deposition process. The solution processes can be carried out either as a (a) one-step coating technique, or (b) sequential two-step coating technique. The vapor deposition processes are considered through two types of production as well, using (a) the dual-source evaporation process and (b) vapor-assisted solution process (see **Figure 6**).

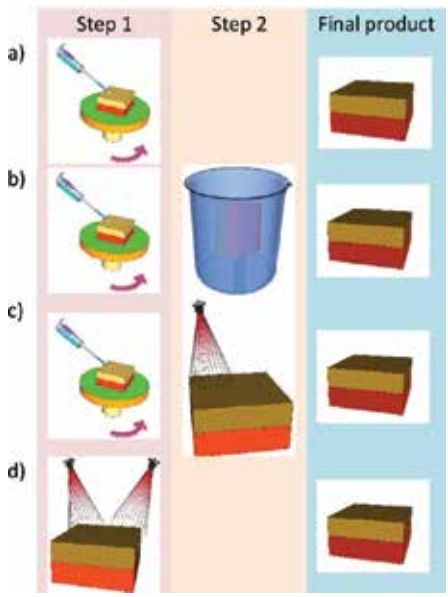

Figure 6. Fabrication of perovskite cells through (a) one-step solution-based, (b) two-steps solution-based, (c) two-step solution and deposition-based, and (d) one-step deposition-based processes.

5.1. Solution processed methods

Two solution process methods have been developed in order to create perovskite film onto substrates: (1) one-step coating and (2) sequential (two-step) coating methods.The first deposition method is the most widespread film coating method for PSCs because of its ease of processing and low production cost. In general, the precursor solution contains the mixture of CH_3NH_3X (or other OMH perovskites) and PbX_2 (where X: I, Br, Cl) at 1:1 or 3:1 molar ratios.

This mixture is dissolved in a polar aprotic solvent, such as *N*,*N*-dimethylformamide (DMF), γ-butyrolactone (GBL), or dimethyl sulfoxide (DMSO). Nevertheless, it is still a challenging issue to form a homogeneous pinhole-free perovskite film using the one-step deposition process. Therefore, the device efficiency is significantly reduced by a poorly coated perovskite layer which causes decreased light absorption and also poor shunting path for charge recombination process [6, 97].

The second deposition method is another kind of solution-based coating process for PSCs. This is first introduced by Mitzi et al. [98], and first used by Burschka et al. [82] for PSC fabrication. In this method, PbX_2 is coated on TiO_2 layer under optimal conditions that is adjusted through spin-coating speed and solution concentration. The optimal coating conditions should yield full penetration of this material into the mesoporous layer. Subsequently, the perovskite layer is obtained either by dipping the substrate into a solution of CH_3NH_3X/isopropanol [82] or by spin-coating of CH_3NH_3X molecules on to the substrate [99]. Here, the perovskite films coated by using the two-step process have a cuboid-like crystal structure, while the one-step method provides a shapeless morphology. Among them the process can be much better controlled to form perovskite morphology by using the two-step method. Namely, better PbX_2 confinement into the nanoporous network of TiO_2 is obtained using this method. Moreover, the two-step sequential coating process provides more uniform and dense perovskite films compared to the single-step coating process. Hence, high efficiency perovskite devices can be fabricated using this process. In addition to all, the two-step process is both well controlled and provides a reproducible treatment.

In the two-step coating process, the perovskite grain size can be controlled by changing molar concentration of the CH_3NH_3X solution. Nevertheless, there are some drawbacks of this coating method related to the trade-off between surface smoothness and perovskite grain size. The perovskite films which have larger grain size also have poor surface morphology which may negatively affect the device efficiency.

The incomplete perovskite conversion is another challenging issue within the two-step coating process. This problem can be overwhelmed using some developed device engineering techniques expressed in the study performed by Song et al. [100]. Recently, the PCE of a perovskite SC has reached 20% through the second-coating method [101].

5.2. Vapor deposition methods

One of the vapor deposition methods consists of a dual-source evaporation process. The vapor deposition method through using dual evaporation sources of $PbCl_2$ and $CH_3NH_3PbI_3$ was first used by Snaith et al. These were realized for $CH_3NH_3PbI_{3-x}Cl_x$-based planar SCs. The manufactured PSCs attained an efficiency level of 15% [84]. In this process, the dual sources contain $PbCl_2$ and $CH_3NH_3PbI_3$. Here the two sources are simultaneously heated to about 120 and 325°C, respectively. Thereafter, the evaporated materials are codeposited onto the TiO_2/FTO substrate in a high vacuum chamber. The pinhole-free and extremely uniform perovskite films can be produced by using this method. However, since it is crucial to use high vacuum for this method, thermal evaporation method is limited because of high cost, low

thermal stability of sources, and unsuitability to mass production. Hence, only a few research groups have published high efficiency PSCs using this method [102, 103].

The other vapor deposition method is called vapor-assisted solution process. The vapor-assisted solution process is almost same as the two-step solution process except an additional modification. In this method, the first step of the two-step solution process is applied initially. Then, CH_3NH_3X is coated onto substrate by vapor deposition. This method provides better grain size and surface morphology control through gas-solid crystallization. In contrast, liquid-solid interactions, which occur in the two-step coating process, may result in delamination of the film. On the other hand, this deposition method allows uniform surface, large grains, and full conversion to the perovskite structure. Nevertheless, this method is restricted by its long processing time passed during the manufacture. For example, the gas-solid reaction takes tens of hours for the full conversion. With all that, the PSCs produced using this method could only attain device efficiencies of up to 12% [104, 105].

5.3. The impact of film composition

The surface morphology of the perovskite film has an important effect on the device performance. As mentioned above, high coverage and uniform crystallinity is required for high power efficiencies. One of the most important effects that influence the surface morphology is the composition of the perovskite films.

In order to increase PSC efficiency, mixed-halide perovskite films have been studied by modifying their film compositions [30]. For instance, a perovskite layer of $(NH_2CH = NH_2PbI_3)_{1-x}$, $(CH_3NH_3PbBr_3)_x$ was used in a SC device. Here, in order to examine the influence of the perovskite materials' composition on the device performance, the proportion of $MAPbBr_3$ in the $FAPbI_3$ was altered. When the composition value is kept at $x = 0.15$, an extremely smooth morphology with EQE > 80% is attained without any noticeable pinholes [106]. Another perovskite film material $MAPbI_{3-x}Cl_x$ was also studied to examine the effect of the chlorine composition on morphology and device performance. It is reported that chlorine allows lower temperature thermal annealing, therefore, it results in reduced pinholes and voids [107, 108].

5.4. The stability of perovskite solar cells

The stability of PSCs is the most critical issue to obtain high performance devices. The stability issues can be related to both perovskite material and SC devices. In order to resolve the related problems and to develop effective strategies, physicochemical processes occurred during the perovskite degradation should be understood. We note that the comparison of stability testing results taken from different studies generally become a challenging issue due to different experimental conditions, such as light intensities, humidity level, temperature, and atmospheric conditions [17].

Air stability: The two molecules in the air, H_2O and O_2, negatively affect the stability of PSCs. Perovskite film color can change from brown to yellow. In order to obtain air stable perovskite

devices, the degradation process should be clearly understood where there are few reports about the effects of O_2 on perovskite films. According to the study about the degradation mechanism of the perovskite under water [109], it is shown that the hydrolysis reaction of $CH_3NH_3PbI_3$ arises under humid condition.

Photo-stability: The mesoporous TiO_2 layer in the device is preferred in order to easily transport photo-generated electrons. On the other hand, TiO_2 is inherently sensitive to ultraviolet light, which may cause degradation in PSCs. The instability of encapsulated and nonencapsulated perovskite devices was investigated through considering the device efficiency by Snaith et al. [110], and it is showed that the degradation of the first-type device occurs faster than that of the second type. Nevertheless, the first device has given a more stable condition in the lack of UV light. In order to overcome this photo-instability due to the TiO_2 layer, the respective authors suggest some methods such as pacifying the trap states, replacing the TiO_2 layer with other materials, and avoiding UV light from the TiO_2 layer. For example, stability at over 1000 hours at 40°C is accomplished when mesoporous Al_2O_3 is used instead of TiO_2 layer in the PSC device. Nonetheless, the PCE was decreased to around by half of its first value after the first 200 hours. A continuing reduction is also observed in both V_{oc} and FF values.

Thermal stability: Thermal stability is an issue regarding both perovskite material and in HTM layer. The intrinsic thermal instability of a perovskite material was reported in the literature [111], and it is showed that even though the film was maintained in an inert condition, the degradation of perovskite is seen at 85°C. It means that the SCs may not be used properly in cases where the SC temperature exceeds this temperature level.

6. Summary

Perovskite has been the most initiative and promising material in terms of energy harvesting among organic, inorganic, and organic-inorganic SCs [8]. In case the difficulties, which are mainly about stability, are overcome, the humanity would face to a new and affordable solar energy harvester for future use. Therefore, the novelties in PSC technology attract a large amount of attention in our recent world due to its significance on its effectiveness on electricity production from free and abundant sunlight.

The main prospects for the future cover the strategies in terms of reducing the band gap, enhancing the light absorption capacity, and improving the conversion efficiency. In addition, exposing the charge transport properties and improving interfacial engineering methods in device fabrication are important. Especially, the chemistry work on chemical composition has great value. Hence, the lion's share for future work should be explaining the photo-physical mechanism of solid-state SCs with respect to different chemicals.

Unfortunately, the present information obtained on "how PSCs operate?" is rather insufficient at least for now. Because the complete working principle is not well explained [18, 19]. Therefore, deriving novel clues on (1) light absorption, (2) charge separation, (3) charge transport, and (4) charge collection are needed during research since these four key issues are general SC parameters to identify the principal working of solar conversion process.

The PSC is mostly accompanied with a HTM layer. In view of the available HTMs, the inorganic ones are rather less progressed reaching an applied efficiency of 11%. On the other hand, these applications are promising in view of their improved stability against ambient conditions. With respect to these, polymeric HTMs offer tunable oxidization potential and better surface morphology. In addition, the researchers also attained advanced HOMO levels [78, 91–93]. The efficiency of polymer HTMs-based SCs is reported to reach more than 16% [31, 94, 95]. The third kind of HTMs is small molecules. Among these, spiro-OMeTAD has been the most used HTM in PSCs till now since it has already been evaluated in solid-state DSSCs and OLED devices [67, 83, 112] (that is, spiro-OMeTAD has already been a standard HTM for researchers). The use of hybrid lead halide with spiro-OMeTAD-based HTM is reported to give an efficiency of around 15% PCE [82, 84]; however, the cost of spiro-OMeTAD remains high due to its difficult synthesis process. Therefore, novel small molecules should be designed and synthesized in order to develop cost-effective PSC devices.

We note that PSCs evolved rapidly and the semiconducting phenomena occurred within the cell remained shaded until now. Hence, the semiconducting behavior is continuously investigated benefitting from the current-voltage characteristics of SCs in some research groups [113]. Deriving an increased efficiency level in PSCs is also related to the way how deposition is carried out. The perfection within the selected coating method is also important [114, 115]. Besides all discussion presented here, we note that the use of completely wet processing method during the production of SCs is especially important for an easy fabrication. Therefore, studies made on "all-solution production process" are highly valuable since vacuum production is expensive and highly energy dependent [116].

Author details

Serafettin Demic[1*], Ahmet Nuri Ozcivan[2], Mustafa Can[3], Cebrail Ozbek[1,2] and Merve Karakaya[4]

*Address all correspondence to: serafettin.demic@gmail.com

1 Department of Materials Science and Engineering, Izmir Katip Celebi University, Izmir, Turkey

2 Department of Electrical and Electronics Engineering, Izmir Katip Celebi University, Izmir, Turkey

3 Department of Engineering Sciences, Izmir Katip Celebi University, Izmir, Turkey

4 Depertment of Materials Science and Engineering, Izmir Institute of Technology, Izmir, Turkey

References

[1] Jung H S, Park N G. Perovskite solar cells: from materials to devices. Small 2015;11:10–25.

[2] 姚鑫, 丁艳丽, 张晓丹, 赵颖. 钙钛矿太阳电池综述. 物理学报 2015;64:38805–038805.

[3] Zhou Y, Zhu K. Perovskite solar cells shine in the "Valley of the Sun". ACS Energy Letters 2016;1:64–67.

[4] Lotsch B V. New light on an old story: perovskites go solar. Angewandte Chemie International Edition 2014;53:635–637.

[5] Loi M A, Hummelen J C. Hybrid solar cells: perovskites under the sun. Nature Materials 2013;12:1087–1089.

[6] Sum T C, Mathews N. Advancements in perovskite solar cells: photophysics behind the photovoltaics. Energy & Environmental Science 2014;7:2518–2534.

[7] Xu Z, Mitzi D B. [CH3 (CH2) 11NH3] SnI3: a hybrid semiconductor with MoO3-type Tin (II) iodide layers. Inorganic Chemistry 2003;42:6589–6591.

[8] Park N-G. Perovskite solar cells: an emerging photovoltaic technology. Materials Today 2015;18:65–72.

[9] Ahmed M I, Habib A, Javaid S S. Perovskite solar cells: potentials, challenges, and opportunities. International Journal of Photoenergy 2015;2015:1.

[10] Kojima A, Teshima K, Shirai Y, Miyasaka T. Organometal halide perovskites as visible-light sensitizers for photovoltaic cells. Journal of the American Chemical Society 2009;131:6050–6051.

[11] Im J-H, Lee C-R, Lee J-W, Park S-W, Park N-G. 6.5% efficient perovskite quantum-dot-sensitized solar cell. Nanoscale 2011;3:4088–4093.

[12] Babayigit A, Ethirajan A, Muller M, Conings B. Toxicity of organometal halide perovskite solar cells. Nature Materials 2016;15:247–251.

[13] Sun Y-Y, Shi J, Lian J, Gao W, Agiorgousis M L, Zhang P, et al. Discovering lead-free perovskite solar materials with a split-anion approach. Nanoscale 2016.

[14] You J, Meng L, Song T-B, Guo T-F, Yang Y M, Chang W-H, et al. Improved air stability of perovskite solar cells via solution-processed metal oxide transport layers. Nature Nanotechnology 2016;11:75–81.

[15] Jiang Z, Chen X, Lin X, Jia X, Wang J, Pan L, et al. Amazing stable open-circuit voltage in perovskite solar cells using AgAl alloy electrode. Solar Energy Materials and Solar Cells 2016;146:35–43.

[16] Back H, Kim G, Kim J, Kong J, Kim T K, Kang H, et al. Achieving long-term stable perovskite solar cells via ion neutralization. Energy & Environmental Science 2016;9:1258–1263.

[17] Shahbazi M, Wang H. Progress in research on the stability of organometal perovskite solar cells. Solar Energy 2016;123:74–87.

[18] Stranks S D, Eperon G E, Grancini G, Menelaou C, Alcocer M J, Leijtens T, et al. Electron-hole diffusion lengths exceeding 1 micrometer in an organometal trihalide perovskite absorber. Science 2013;342:341–344.

[19] Xing G, Mathews N, Sun S, Lim S S, Lam Y M, Grätzel M, et al. Long-range balanced electron-and hole-transport lengths in organic-inorganic $CH_3NH_3PbI_3$. Science 2013;342:344–347.

[20] Kim H-S, Lee C-R, Im J-H, Lee K-B, Moehl T, Marchioro A, et al. Lead iodide perovskite sensitized all-solid-state submicron thin film mesoscopic solar cell with efficiency exceeding 9%. Scientific Reports 2012;2.

[21] Kim H-S, Mora-Sero I, Gonzalez-Pedro V, Fabregat-Santiago F, Juarez-Perez E J, Park N-G, et al. Mechanism of carrier accumulation in perovskite thin-absorber solar cells. Nature Communications 2013;4.

[22] Gonzalez-Pedro V, Juarez-Perez E J, Arsyad W-S, Barea E M, Fabregat-Santiago F, Mora-Sero I, et al. General working principles of CH3NH3PbX3 perovskite solar cells. Nano Letters 2014;14:888–893.

[23] Noh J H, Im S H, Heo J H, Mandal T N, Seok S I. Chemical management for colorful, efficient, and stable inorganic–organic hybrid nanostructured solar cells. Nano Letters 2013;13:1764–1769.

[24] Koh T M, Fu K, Fang Y, Chen S, Sum T, Mathews N, et al. Formamidinium-containing metal-halide: an alternative material for near-IR absorption perovskite solar cells. The Journal of Physical Chemistry C 2013;118:16458–16462.

[25] Mei A, Li X, Liu L, Ku Z, Liu T, Rong Y, et al. A hole-conductor–free, fully printable mesoscopic perovskite solar cell with high stability. Science 2014;345:295–698.

[26] Marchioro A, Teuscher J, Friedrich D, Kunst M, Van De Krol R, Moehl T, et al. Unravelling the mechanism of photoinduced charge transfer processes in lead iodide perovskite solar cells. Nature Photonics 2014;8:250–255.

[27] Meillaud F, Shah A, Droz C, Vallat-Sauvain E, Miazza C. Efficiency limits for single-junction and tandem solar cells. Solar Energy Materials and Solar Cells 2006;90:2952–2959.

[28] Eperon G E, Stranks S D, Menelaou C, Johnston M B, Herz L M, Snaith H J. Formamidinium lead trihalide: a broadly tunable perovskite for efficient planar heterojunction solar cells. Energy & Environmental Science 2014;7:982–988.

[29] Zhou H, Chen Q, Li G, Luo S, Song T-B, Duan H-S, et al. Interface engineering of highly efficient perovskite solar cells. Science 2014;345:542–546.

[30] Lee M M, Teuscher J, Miyasaka T, Murakami T N, Snaith H J. Efficient hybrid solar cells based on meso-superstructured organometal halide perovskites. Science 2012;338:643–647.

[31] Heo J H, Im S H, Noh J H, Mandal T N, Lim C-S, Chang J A, et al. Efficient inorganic-organic hybrid heterojunction solar cells containing perovskite compound and polymeric hole conductors. Nature Photonics 2013;7:486–491.

[32] Chiang C-H, Wu C-G. Bulk heterojunction perovskite–PCBM solar cells with high fill factor. Nature Photonics 2016.

[33] Hau S K, Yip H-L, Baek N S, Zou J, O'Malley K, Jen A K-Y. Air-stable inverted flexible polymer solar cells using zinc oxide nanoparticles as an electron selective layer. Applied Physics Letters 2008;92:253301.

[34] Qian L, Zheng Y, Xue J, Holloway P H. Stable and efficient quantum-dot light-emitting diodes based on solution-processed multilayer structures. Nature Photonics 2011;5:543–548.

[35] Marchioro A. Interfacial Charge Transfer Dynamics in Solid-State Hybrid Organic-Inorganic Solar Cells: École Polytechnique Fédérale De Lausanne; 2014.

[36] Jäntti P P. Solar Cells with Methylammonium Lead Halide Perovskites; 2015.

[37] Emami S, Andrade L, Mendes A. Recent progress in long-term stability of perovskite solar cells. U Porto Journal of Engineering 2015;1:52–62.

[38] Mitzi D B. Synthesis, structure, and properties of organic-inorganic perovskites and related materials. Progress in Inorganic Chemistry 1999;48:1–121. DOI: 10.1002/9780470166499.ch1

[39] Kim H-S, Im S H, Park N-G. Organolead halide perovskite: new horizons in solar cell research. The Journal of Physical Chemistry C 2014;118:5615–5625.

[40] Bokov A, Ye Z-G. Recent progress in relaxor ferroelectrics with perovskite structure. Frontiers of Ferroelectricity 2006:31–52.

[41] Frost J M, Butler K T, Brivio F, Hendon C H, Van Schilfgaarde M, Walsh A. Atomistic origins of high-performance in hybrid halide perovskite solar cells. Nano Letters 2014;14:2584–2590.

[42] Juarez-Perez E J, Sanchez R S, Badia L, Garcia-Belmonte G, Kang Y S, Mora-Sero I, et al. Photoinduced giant dielectric constant in lead halide perovskite solar cells. The Journal of Physical Chemistry Letters 2014;5:2390–2394.

[43] Batra A K, Bhattacharjee S, Chilvery A K, Aggarwal M D, Edwards M E, Bhalla A. Simulation of energy harvesting from roads via pyroelectricity. Journal of Photonics for Energy 2011;1:014001–014012.

[44] Takahashi Y, Obara R, Lin Z-Z, Takahashi Y, Naito T, Inabe T, et al. Charge-transport in tin-iodide perovskite CH 3 NH 3 SnI 3: origin of high conductivity. Dalton Transactions 2011;40:5563–5568.

[45] Bhalla A, Guo R, Roy R. The perovskite structure—a review of its role in ceramic science and technology. Material Research Innovations 2000;4:3–26.

[46] Stoumpos C C, Malliakas C D, Kanatzidis M G. Semiconducting tin lead iodide perovskites with organic cations: phase transitions, high mobilities, and near-infrared photoluminescent properties. Inorganic Chemistry 2013;52:9019–9038.

[47] Mitzi D B, Feild C, Harrison W, Guloy A. Conducting Tin Halides with a Layered Organic-Based Perovskite Structure; 1994.

[48] Gao P, Grätzel M, Nazeeruddin M K. Organohalide lead perovskites for photovoltaic applications. Energy & Environmental Science 2014;7:2448–2463.

[49] Koutselas I, Ducasse L, Papavassiliou G C. Electronic properties of three-and low-dimensional semiconducting materials with Pb halide and Sn halide units. Journal of Physics: Condensed Matter 1996;8:1217.

[50] Chilvery A K, Batra A K, Yang B, Xiao K, Guggilla P, Aggarwal M D, et al. Perovskites: transforming photovoltaics, a mini-review. Journal of Photonics for Energy 2015;5:057402.

[51] Hao F, Stoumpos C C, Cao D H, Chang R P, Kanatzidis M G. Lead-free solid-state organic-inorganic halide perovskite solar cells. Nature Photonics 2014;8:489–494.

[52] Im J-H, Chung J, Kim S-J, Park N-G. Synthesis, structure, and photovoltaic property of a nanocrystalline 2H perovskite-type novel sensitizer (CH3CH2NH3) PbI3. Nanoscale Research Letters 2012;7:1–7.

[53] Ball J M, Lee M M, Hey A, Snaith H J. Low-temperature processed meso-superstructured to thin-film perovskite solar cells. Energy & Environmental Science 2013;6:1739–1743.

[54] O'regan B, Grfitzeli M. A low-cost, high-efficiency solar cell based on dye-sensitized. Nature 1991;353:737–740.

[55] Umari P, Mosconi E, De Angelis F. Relativistic GW calculations on $CH_3NH_3PbI_3$ and CH3NH3SnI3 perovskites for solar cell applications. Scientific Reports 2014;4.

[56] Snaith H J, Schmidt-Mende L. Advances in liquid-electrolyte and solid-state dye-sensitized solar cells. Advanced Materials 2007;19:3187–3200.

[57] Snaith H J, Stavrinadis A, Docampo P, Watt A A. Lead-sulphide quantum-dot sensitization of tin oxide based hybrid solar cells. Solar Energy 2011;85:1283–1290.

[58] Lee H, Leventis H C, Moon S J, Chen P, Ito S, Haque S A, et al. PbS and CdS quantum dot-sensitized solid-state solar cells: "old concepts, new results". Advanced Functional Materials 2009;19:2735–2742.

[59] Kamat P V. Quantum dot solar cells. Semiconductor nanocrystals as light harvesters. The Journal of Physical Chemistry C 2008;112:18737–18753.

[60] Itzhaik Y, Niitsoo O, Page M, Hodes G. Sb2S3-sensitized nanoporous TiO_2 solar cells. The Journal of Physical Chemistry C 2009;113:4254–4256.

[61] Kojima A, Teshima K, Miyasaka T, Shirai Y, editors. Novel photoelectrochemical cell with mesoscopic electrodes sensitized by lead-halide compounds (2). Meeting Abstracts. The Electrochemical Society; 2006.

[62] Kamat P V. Quantum dot solar cells. The next big thing in photovoltaics. The Journal of Physical Chemistry Letters 2013;4:908–918.

[63] Kojima A, Teshima K, Shirai Y, Miyasaka T, editors. Novel photoelectrochemical cell with mesoscopic electrodes sensitized by lead-halide compounds (11). Meeting Abstracts. The Electrochemical Society; 2008.

[64] Laban W A, Etgar L. Depleted hole conductor-free lead halide iodide heterojunction solar cells. Energy & Environmental Science 2013;6:3249–3253.

[65] Green M A. Silicon solar cells: evolution, high-efficiency design and efficiency enhancements. Semiconductor Science and Technology 1993;8:1.

[66] Hardin B E, Snaith H J, McGehee M D. The renaissance of dye-sensitized solar cells. Nature Photonics 2012;6:162–169.

[67] Bach U, Lupo D, Comte P, Moser J, Weissörtel F, Salbeck J, et al. Solid-state dye-sensitized mesoporous TiO_2 solar cells with high photon-to-electron conversion efficiencies. Nature 1998;395:583–585.

[68] Yang Y, Ostrowski D P, France R M, Zhu K, van de Lagemaat J, Luther J M, et al. Observation of a hot-phonon bottleneck in lead-iodide perovskites. Nature Photonics 2016;10:53–59.

[69] Pazos-Outón L M, Szumilo M, Lamboll R, Richter J M, Crespo-Quesada M, Abdi-Jalebi M, et al. Photon recycling in lead iodide perovskite solar cells. Science 2016;351:1430–1433.

[70] Stranks S D, Snaith H J. Metal-halide perovskites for photovoltaic and light-emitting devices. Nature Nanotechnology 2015;10:391–402.

[71] Filip M R, Eperon G E, Snaith H J, Giustino F. Steric engineering of metal-halide perovskites with tunable optical band gaps. Nature Communications 2014;5.

[72] Castelli I E, García-Lastra J M, Thygesen K S, Jacobsen K W. Bandgap calculations and trends of organometal halide perovskites. APL Materials 2014;2:081514.

[73] Even J, Pedesseau L, Katan C. Analysis of multivalley and multibandgap absorption and enhancement of free carriers related to exciton screening in hybrid perovskites. The Journal of Physical Chemistry C 2014;118:11566–11572.

[74] Salim T, Sun S, Abe Y, Krishna A, Grimsdale A C, Lam Y M. Perovskite-based solar cells: impact of morphology and device architecture on device performance. Journal of Materials Chemistry A 2015;3:8943–8969.

[75] Knutson J L, Martin J D, Mitzi D B. Tuning the band gap in hybrid tin iodide perovskite semiconductors using structural templating. Inorganic Chemistry 2005;44:4699–4705.

[76] Pang S, Hu H, Zhang J, Lv S, Yu Y, Wei F, et al. NH2CH=NH2PbI3: an alternative organolead iodide perovskite sensitizer for mesoscopic solar cells. Chemistry of Materials 2014;26:1485–1491.

[77] Mitzi D B, Chondroudis K, Kagan C R. Organic-inorganic electronics. IBM Journal of Research and Development 2001;45:29–45.

[78] Edri E, Kirmayer S, Kulbak M, Hodes G, Cahen D. Chloride inclusion and hole transport material doping to improve methyl ammonium lead bromide perovskite-based high open-circuit voltage solar cells. The Journal of Physical Chemistry Letters 2014;5:429–433.

[79] Hoke E T, Slotcavage D J, Dohner E R, Bowring A R, Karunadasa H I, McGehee M D. Reversible photo-induced trap formation in mixed-halide hybrid perovskites for photovoltaics. Chemical Science 2015;6:613–617.

[80] Heo J H, Song D H, Im S H. Planar CH3NH3PbBr3 hybrid solar cells with 10.4% power conversion efficiency, fabricated by controlled crystallization in the spin-coating process. Advanced Materials 2014;26:8179–8183.

[81] Schulz P, Edri E, Kirmayer S, Hodes G, Cahen D, Kahn A. Interface energetics in organo-metal halide perovskite-based photovoltaic cells. Energy & Environmental Science 2014;7:1377–1381.

[82] Burschka J, Pellet N, Moon S-J, Humphry-Baker R, Gao P, Nazeeruddin M K, et al. Sequential deposition as a route to high-performance perovskite-sensitized solar cells. Nature 2013;499:316–319.

[83] Shirota Y, Kageyama H. Charge carrier transporting molecular materials and their applications in devices. Chemical Reviews 2007;107:953–1010.

[84] Liu M, Johnston M B, Snaith H J. Efficient planar heterojunction perovskite solar cells by vapour deposition. Nature 2013;501:395–398.

[85] Kim H-S, Lee C-R, Jang I-H, Kang W-K, Park N-G. Effect of overlayer thickness of hole transport material on photovoltaic performance in solid-sate dye-sensitized solar cell. Bulletin Korean Chemical Society 2012;33:671.

[86] Bi D, Moon S-J, Häggman L, Boschloo G, Yang L, Johansson E M, et al. Using a two-step deposition technique to prepare perovskite (CH 3 NH 3 PbI 3) for thin film solar cells based on ZrO_2 and TiO_2 mesostructures. RSC Advances 2013;3:18762–18766.

[87] Snaith H J, Grätzel M. Enhanced charge mobility in a molecular hole transporter via addition of redox inactive ionic dopant: implication to dye-sensitized solar cells. Applied Physics Letters 2006;89:2114.

[88] Schölin R, Karlsson M H, Eriksson S K, Siegbahn H, Johansson E M, Rensmo H. Energy level shifts in spiro-OMeTAD molecular thin films when adding Li-TFSI. The Journal of Physical Chemistry C 2012;116:26300–26305.

[89] Liu F, Zhu J, Wei J, Li Y, Lv M, Yang S, et al. Numerical simulation: toward the design of high-efficiency planar perovskite solar cells. Applied Physics Letters 2014;104:253508.

[90] Huang C, Fu W, Li C-Z, Zhang Z, Qiu W, Shi M, et al. Dopant-free hole-transporting material with a C 3 h symmetrical truxene core for highly efficient perovskite solar cells. Journal of the American Chemical Society 2016;138:2528–2531.

[91] Cai B, Xing Y, Yang Z, Zhang W-H, Qiu J. High performance hybrid solar cells sensitized by organolead halide perovskites. Energy & Environmental Science 2013;6:1480–1485.

[92] Ryu S, Noh J H, Jeon N J, Kim Y C, Yang W S, Seo J, et al. Voltage output of efficient perovskite solar cells with high open-circuit voltage and fill factor. Energy & Environmental Science 2014;7:2614–2618.

[93] Kwon Y S, Lim J, Yun H-J, Kim Y-H, Park T. A diketopyrrolopyrrole-containing hole transporting conjugated polymer for use in efficient stable organic–inorganic hybrid solar cells based on a perovskite. Energy & Environmental Science 2014;7:1454–1460.

[94] Green M A, Emery K, Hishikawa Y, Warta W, Dunlop E D. Solar cell efficiency tables (Version 45). Progress in Photovoltaics: Research and Applications 2015;23:1–9.

[95] Jeon N J, Noh J H, Kim Y C, Yang W S, Ryu S, Seok S I. Solvent engineering for high-performance inorganic–organic hybrid perovskite solar cells. Nature Materials 2014;13:897–903.

[96] Chen H, Pan X, Liu W, Cai M, Kou D, Huo Z, et al. Efficient panchromatic inorganic–organic heterojunction solar cells with consecutive charge transport tunnels in hole transport material. Chemical Communications 2013;49:7277–7279.

[97] Jeng J Y, Chen K C, Chiang T Y, Lin P Y, Tsai T D, Chang Y C, et al. Nickel oxide electrode interlayer in $CH_3NH_3PbI_3$ perovskite/PCBM planar-heterojunction hybrid solar cells. Advanced Materials 2014;26:4107–4113.

[98] Liang K, Mitzi D B, Prikas M T. Synthesis and characterization of organic-inorganic perovskite thin films prepared using a versatile two-step dipping technique. Chemistry of Materials 1998;10:403–411.

[99] Im J-H, Jang I-H, Pellet N, Grätzel M, Park N-G. Growth of $CH_3NH_3PbI_3$ cuboids with controlled size for high-efficiency perovskite solar cells. Nature Nanotechnology 2014;9:927–932.

[100] Song Z, Watthage S C, Phillips A B, Heben M J. Pathways toward high-performance perovskite solar cells: review of recent advances in organo-metal halide perovskites for photovoltaic applications. Journal of Photonics for Energy 2016;6:022001.

[101] Yang W S, Noh J H, Jeon N J, Kim Y C, Ryu S, Seo J, et al. High-performance photovoltaic perovskite layers fabricated through intramolecular exchange. Science 2015;348:1234–1237.

[102] Chen C W, Kang H W, Hsiao S Y, Yang P F, Chiang K M, Lin H W. Efficient and uniform planar-type perovskite solar cells by simple sequential vacuum deposition. Advanced Materials 2014;26:6647–6652.

[103] Lin Q, Armin A, Nagiri R C R, Burn P L, Meredith P. Electro-optics of perovskite solar cells. Nature Photonics 2015;9:106–112.

[104] Hao F, Stoumpos C C, Liu Z, Chang R P, Kanatzidis M G. Controllable perovskite crystallization at a gas–solid interface for hole conductor-free solar cells with steady power conversion efficiency over 10%. Journal of the American Chemical Society 2014;136:16411–16419.

[105] Chen Q, Zhou H, Hong Z, Luo S, Duan H-S, Wang H-H, et al. Planar heterojunction perovskite solar cells via vapor-assisted solution process. Journal of the American Chemical Society 2013;136:622–625.

[106] Jeon N J, Noh J H, Yang W S, Kim Y C, Ryu S, Seo J, et al. Compositional engineering of perovskite materials for high-performance solar cells. Nature 2015;517:476–480.

[107] Yantara N, Yanan F, Shi C, Dewi H A, Boix P P, Mhaisalkar S G, et al. Unravelling the effects of Cl addition in single step $CH_3NH_3PbI_3$ perovskite solar cells. Chemistry of Materials 2015;27:2309–2314.

[108] Zhang W, Saliba M, Moore D T, Pathak S K, Hörantner M T, Stergiopoulos T, et al. Ultrasmooth organic–inorganic perovskite thin-film formation and crystallization for efficient planar heterojunction solar cells. Nature Communications 2015;6.

[109] Dualeh A, Tétreault N, Moehl T, Gao P, Nazeeruddin M K, Grätzel M. Effect of annealing temperature on film morphology of organic–inorganic hybrid pervoskite solid-state solar cells. Advanced Functional Materials 2014;24:3250–3258.

[110] Leijtens T, Eperon G E, Pathak S, Abate A, Lee M M, Snaith H J. Overcoming ultraviolet light instability of sensitized TiO_2 with meso-superstructured organometal tri-halide perovskite solar cells. Nature Communications 2013;4.

[111] Conings B, Drijkoningen J, Gauquelin N, Babayigit A, D'Haen J, D'Olieslaeger L, et al. Intrinsic thermal instability of methylammonium lead trihalide perovskite. Advanced Energy Materials 2015;5.

[112] Burschka J, Dualeh A, Kessler F, Baranoff E, Cevey-Ha N-L, Yi C, et al. Tris (2-(1 H-pyrazol-1-yl) pyridine) cobalt (III) as p-type dopant for organic semiconductors and its application in highly efficient solid-state dye-sensitized solar cells. Journal of the American Chemical Society 2011;133:18042–18045.

[113] Meloni S, Moehl T, Tress W, Franckevičius M, Saliba M, Lee Y H, et al. Ionic polarization-induced current-voltage hysteresis in CH3NH3PbX3 perovskite solar cells. Nature Communications 2016;7.

[114] Back H, Kim J, Kim G, Kim T K, Kang H, Kong J, et al. Interfacial modification of hole transport layers for efficient large-area perovskite solar cells achieved via blade-coating. Solar Energy Materials and Solar Cells 2016;144:309–315.

[115] Li H, Li S, Wang Y, Sarvari H, Zhang P, Wang M, et al. A modified sequential deposition method for fabrication of perovskite solar cells. Solar Energy 2016;126:243–251.

[116] Yang K, Li F, Zhang J, Veeramalai C P, Guo T. All-solution processed semi-transparent perovskite solar cells with silver nanowires electrode. Nanotechnology 2016;27:095202.

Edited by Narottam Das

Nanostructured solar cells are very important in renewable energy sector as well as in environmental aspects, because it is environment friendly. The nano-grating structures (such as triangular or conical shaped) have a gradual change in refractive index which acts as a multilayer antireflective coating that is leading to reduced light reflection losses over broadband ranges of wavelength and angle of incidence. There are different types of losses in solar cells that always reduce the conversion efficiency, but the light reflection loss is the most important factor that decreases the conversion efficiency of solar cells significantly. The antireflective coating is an optical coating which is applied to the surface of lenses or any optical devices to reduce the light reflection losses. This coating assists for the light trapping capturing capacity or improves the efficiency of optical devices, such as lenses or solar cells. Hence, the multilayer antireflective coatings can reduce the light reflection losses and increases the conversion efficiency of nanostructured solar cells.

ISBN 978-953-51-4110-5

Photo by Rost-9D / iStock

IntechOpen